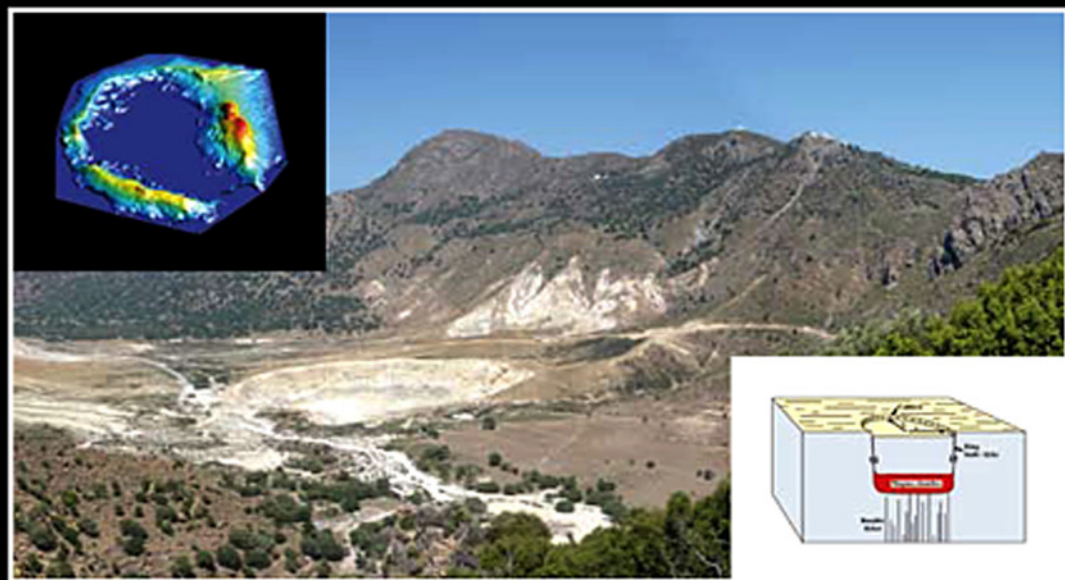# CALDERA VOLCANISM

## ANALYSIS, MODELLING AND RESPONSE

EDITED BY

JOACHIM GOTTSMANN AND JOAN MARTÍ

# DEVELOPMENTS IN VOLCANOLOGY

# CALDERA VOLCANISM: ANALYSIS, MODELLING AND RESPONSE

# DEVELOPMENTS IN VOLCANOLOGY

# CALDERA VOLCANISM: ANALYSIS, MODELLING AND RESPONSE

*Editors*

JOACHIM GOTTSMANN
*Department of Earth Sciences,*
*University of Bristol,*
*Bristol, United Kingdom*

JOAN MARTÍ
*Institute of Earth Sciences,*
*CSIC, Lluis Sole Sabaris s/n,*
*Barcelona, Spain*

Notice
No responsibility is assumed by the publisher for any injury and/or damage to persons
or property as a matter of products liability, negligence or otherwise, or from any use
or operation of any methods, products, instructions or ideas contained in the material
herein. Because of rapid advances in the medical sciences, in particular, independent
verification of diagnoses and drug dosages should be made

For information on all Elsevier publications
visit our website at books.elsevier.com

Working together to grow
libraries in developing countries

www.elsevier.com | www.bookaid.org | www.sabre.org

ELSEVIER    BOOK AID International    Sabre Foundation

# Contents

## 8. Magma-Chamber Geometry, Fluid Transport, Local Stresses and Rock Behaviour During Collapse Caldera Formation   313

Agust Gudmundsson

## 9. Facilitating Dike Intrusions into Ring Faults   351

Thomas R. Walter

## 10. A New Uplift Episode at Campi Flegrei Caldera (Southern Italy): Implications for Unrest Interpretation and Eruption Hazard Evaluation   375

Claudia Troise, Giuseppe De Natale, Folco Pingue,
Umberto Tammaro, Prospero De Martino, Francesco Obrizzo and
Enzo Boschi

This page intentionally left blank

# Contributors

**Valerio Acocella**
Dip. Scienze Geologiche Roma Tre, Roma, Italy

**Gerardo J. Aguirre-Díaz**
Centro de Geociencias, Universidad Nacional Autónoma de México, Campus Juriquilla, Querétaro, Qro., 76230, Mexico

**Maurizio Battaglia**
Department of Earth Sciences, University of Rome I "La Sapienza", P.le A. Moro 5, 00185 Rome, Italy

**Enzo Boschi**
Istituto Nazionale di Geofisica e Vulcanologia-Osservatorio Vesuviano, Via Diocleziano 328, 80124 Naples, Italy

**Roberto Carniel**
Dipartimento di Georisorse e Territorio, Università di Udine, Via Cotonificio 114, 33100 Udine, Italy

**R.A.F. Cas**
School of Geosciences, Monash University, Victoria, 3800, Australia; Department of Earth and Ocean Sciences, University of Waikato, Private Bag 3105, Hamilton, 3216, New Zealand

**P.L. Corcoran**
Department of Earth Sciences, University of Western Ontario, London, Ontario, Canada N6A 5B7

**Fidel Costa**
CSIC, Institut de Ciències de la Terra 'Jaume Almera', Lluís Solé i Sabarís s/n, 08028 Barcelona, Spain

**R. Daigneault**
Sciences de la terre, Université du Québec à Chicoutimi, Canada G7 H 2B1

**Pierfrancesco Dellino**
Dipartimento Geomineralogico, Università di Bari, via Orabona 4, 70125 Bari, Italy

**Prospero De Martino**
Istituto Nazionale di Geofisica e Vulcanologia-Osservatorio Vesuviano, Via Diocleziano 328, 80124 Naples, Italy

**Giuseppe De Natale**
Istituto Nazionale di Geofisica e Vulcanologia-Osservatorio Vesuviano, Via Diocleziano 328, 80124 Naples, Italy

**A. Folch**

Osservatorio Vesuviano (OV-INGV), Napoli, Italy

**Alicia García**

Departamento de Volcanología. Museo Nacional de Ciencias Naturales, CSIC, Madrid, Spain

**A. Geyer**

Laboratory for the Simulation of Geological Processes (SIMGEO), Department of Geophysics and Geohazards, Institute of Earth Sciences 'Jaume Almera', CSIC, Barcelona, Spain

**Joachim Gottsmann**

Department of Earth Sciences, University of Bristol, Wills Memorial Building, Queens Road, Bristol BS8 1RJ, UK

**Agust Gudmundsson**

Department of Structural Geology and Geodynamics, GZG, University of Göttingen, Germany; Department of Earth Sciences, Royal Holloway, University of London, Queens Building, Egham, Surrey, TW20 0EX, UK

**Isaac Gutiérrez-Palomares**

Centro de Geociencias, Universidad Nacional Autónoma de México, Campus Juriquilla, Querétaro, Qro., 76230, Mexico

**Olivier Jaquet**

In2Earth Modelling Ltd., Switzerland

**Guillermo Labarthe-Hernández**

Instituto de Geología, Universidad Autónoma de San Luis Potosí, S.L.P., México

**B. Lafrance**

Cogitore, 1300 Saguenay, Suite 200 Rouyn–Noranda, Québec, Canada J9X 7C3

**P.B. Larson**

School of Earth and Environmental Sciences, Washington State University, Pullman, Washington, 99164, U.S.A.

**J. Martí**

Institute of Earth Sciences 'Jaume Almera', CSIC, c/Lluis Sole Sabaris s/n, 08028 Barcelona, Spain

**W.U. Mueller**

Sciences de la terre, Université du Québec à Chicoutimi, Canada G7 H 2B1

**H.J. Nichols**

School of Earth and Environmental Sciences, Washington State University, Pullman, Washington, 99164, U.S.A.

**Jorge Nieto-Obregón**

Centro de Geociencias, Universidad Nacional Autónoma de México, Campus Juriquilla, Querétaro, Qro., 76230, Mexico

**Francesco Obrizzo**

Istituto Nazionale di Geofisica e Vulcanologia-Osservatorio Vesuviano, Via Diocleziano 328, 80124 Naples, Italy

**Ramon Ortiz**

Departamento de Volcanología. Museo Nacional de Ciencias Naturales, CSIC, Madrid, Spain

**Folco Pingue**

Istituto Nazionale di Geofisica e Vulcanologia-Osservatorio Vesuviano, Via Diocleziano 328, 80124 Naples, Italy

**A. Pittari**

School of Geosciences, Monash University, Victoria, 3800, Australia; Department of Earth and Ocean Sciences, University of Waikato, Private Bag 3105, Hamilton, 3216, New Zealand

**J.B. Stix**

Department of Earth & Planetary Sciences, McGill University, Canada

**Roberto Sulpizio**

Dipartimento Geomineralogico, Università di Bari, via Orabona 4, 70125 Bari, Italy

**Umberto Tammaro**

Istituto Nazionale di Geofisica e Vulcanologia-Osservatorio Vesuviano, Via Diocleziano 328, 80124 Naples, Italy

**Marta Tárraga**

Departamento de Volcanología. Museo Nacional de Ciencias Naturales, CSIC, Madrid, Spain

**Micol Todesco**

Istituto Nazionale di Geofisica e Vulcanologia, Sezione di Bologna, via Donato Creti, 12, 40128 Bologna, Italy

**Margarito Tristán-González**

Instituto de Geología, Universidad Autónoma de San Luis Potosí, S.L.P., México

**Claudia Troise**

Istituto Nazionale di Geofisica e Vulcanologia-Osservatorio Vesuviano, Via Diocleziano 328, 80124 Naples, Italy

**Thomas R. Walter**

GFZ Potsdam, Telegrafenberg, 14473 Potsdam, Germany

**J.D.L. White**

Geology Department, University of Otago, Dunedin, New Zealand

**J.A. Wolff**

School of Earth and Environmental Sciences, Washington State University, Pullman, Washington, 99164, U.S.A.

This page intentionally left blank

# Preface

Caldera–forming eruptions are among the most awe-inspiring and powerful displays of nature's force, yet at the same time they constitute a major natural hazard. An eruption on this scale can wreak large-scale havoc, claim significant losses in lives and assets and can significantly impact regional and global climate and living conditions. Calderas are undoubtedly enigmatic displays of Earth's evolution and often display the most scenic landscapes on this planet, attracting millions of visitors each year. Despite their potential ferocious nature, calderas play a crucial role in modern society's life. Calderas host essential economic deposits and supply power for many via the exploitation of geothermal reservoirs and thus receive considerable scientific, economic and industrial attention. Yet, they also pose a serious threat to our livelihood in case of their reactivation as they can significantly impact our environment both locally and globally (Lipman, 1997, 2000). Volcanic hazards associated with collapse calderas differ markedly in space and time from hazards associated with solitary volcanoes. Probably one of the most remarkable hazards related to caldera-forming eruptions are the effects on global climate and thus on global socioeconomics. Historical caldera–formations such as at Tambora in 1815, at Krakatau in 1883 and at Pinatubo in 1991, although several orders of magnitude smaller than the largest prehistoric eruptions, appear to have had a significant impact on our climate, including visible atmospheric effects such as bizarrely coloured skies, halos around the sun and the moon, vibrant sunsets and sunrises and anomalously cold weather conditions leading to crop failure and famine.

Since volcanoes and their eruptions are merely the surface manifestation of large-scale magmatic processes operating in the Earth's interior, calderas also provide key insights into the generation and evolution of large-volume silicic magma bodies (Self et al., 1984, 1986; Lipman, 1984, 2000). Volcanic processes are the culmination of a complex interaction of geological processes occurring at global, regional and local scales and the study of volcanoes (including collapse calderas) provides us with relevant information on lithospheric dynamics.

The relationship between caldera formation and pyroclastic activity became evident after the historical eruption of Krakatau in 1883 (Verbeek, 1886). Verbeek noted that the volume of the deposits was much less than that of the missing structure. Consequently, he rejected the idea that the mountain had been blasted away and concluded that most of the mass had foundered into the space evacuated by a rapid discharge of huge volumes of magma. Earlier, Fouqué (1879) inferred from similar reasoning, that the bay enclosed by the islands of Thera and Therasia in Santorini had resulted from a collapse associated with a strong pyroclastic eruption. Fouqué concluded that whatever the mechanism, it was the collapse of the roof that had triggered the explosive eruptions. The main explosive discharge was the

consequence, not the cause of the collapse. At Kilauea Volcano in Hawaii, the concept of caldera formation by post-eruptive collapse was also recognised by Dutton (1884).

At the beginning of the 20th century, some examples of eroded calderas (cauldrons) were first interpreted as subsided blocks associated with igneous activity, e.g. Glen Coe in Scotland (Clough et al., 1909) and the eroded calderas in the Tertiary San Juan volcanic field, Colorado (Burbank, 1933). Subsequent investigations recognised a collapse origin for Crater Lake, Oregon (Diller and Patton, 1902), and identified the Toba caldera in Indonesia and the post-collapse resurgent uplift of its floor (Van Bemmelen, 1929). A few years later, large Pleistocene calderas associated with voluminous explosive volcanism were recognised in southwestern Japan (Matumoto, 1943).

In 1941, Williams presented an insightful analysis of calderas and their origin. He assumed the reverse relation as suggested by Fouqué (1879), that most large calderas form by collapse after the eruption of magma during pyroclastic volcanism. In the 60s and 70s, several studies (Smith, 1960, 1979; Smith and Bailey, 1968) provided a conceptual framework for stratigraphic studies of ash flow sheets, a model of collapse resurgence within ash flow calderas and a petrologic framework for ash flow magmatism. Also important were the studies of pyroclastic deposits (e.g. Sparks and Walker, 1977; Walker, 1980; Wilson and Walker, 1982) that showed the way for correlating the physical properties of pyroclastic deposits with their emplacement mechanism.

The tremendous progress made since the 1960s in the related fields of pyroclastic flow analysis, caldera geology and caldera dynamics are difficult to summarise. However, after these pioneering works, collapse calderas have been the subject of studies of diverse disciplines. In fact, during the last decades, analogue modelling has become a useful tool in the study of caldera–collapse processes. The first experiments were performed by Ramberg (1967, 1981), who carried out centrifuge experiments using putty (the magma chamber analogue) under a roof of clay (the host rock analogue). These experiments and posterior works (e.g. Komuro et al., 1984; Komuro, 1987; Martí et al., 1994; Roche et al., 2000; Roche and Druitt, 2001) focused on understanding caldera-collapse mechanisms and resulting caldera structures. The use of analogue models for caldera studies is currently increasing, and new questions such as the influence of regional tectonics and the effect of pre-existing topography (volcanic edifice) on the formation of collapse calderas are arising (Acocella et al., 2002, 2004).

Simultaneously, theoretical models based on the application of thermodynamics and solid and fluid mechanics have progressively become an indispensable tool for the investigation of caldera-forming processes. These theoretical studies are oriented towards different aspects of the collapse caldera formation, mainly the behaviour of magma (Druitt and Sparks, 1984; Bower and Woods, 1997; Martí et al., 2000; Roche and Druitt, 2001) or the behaviour of host rocks (Komuro et al., 1984; Gudmundsson et al., 1997; Gudmundsson, 1998; Folch and Martí, 2004).The geophysical disciplines have also significantly contributed to our understanding of calderas in recent years: first, by providing unprecedented insights into their subsurface structure using in particular seismic signals to construct

subsurface images (Aprea et al., 2002; Nishimura et al., 1997), and second, by recording time series to capture the dynamic behaviour of calderas (Tikku et al., 2006; Gottsmann et al., 2007). Ground deformation monitoring has evolved into a standard technique by either land-based or air–borne instrumentation. Combined with gravimetry (to detect mass changes at depth), geodetic investigations are regarded important tools for the quantification of precursor signals during unrest (Rymer and Williams-Jones, 2000).

However, some important aspects of the dynamics and the structure of collapse calderas still remain poorly understood. A collapse caldera is defined as the volcanic depression that results from the disruption of the geometry of the magma chamber roof due to down faulting during the course of an eruption (Williams, 1941; Smith and Bailey, 1968; Williams and McBirney, 1979; Smith, 1979; Lipman, 1997, 2000). This definition embraces a diversity of structures, processes and deposits, but we are still far from having a complete understanding of the causes that drive a shallow magmatic system to caldera formation. A number of problems are still unresolved:

- Do the different caldera morphologies observable in the field really represent different genetic processes related to the shallow magmatic system or are they merely a product of variations in the collapse mechanism due to differences in the mechanical behaviour of host rocks and tectonic structures?
- How much does a geophysical image of the internal structure of a restless caldera correspond to the original subsurface architecture prior to the caldera-forming event?
- Is caldera unrest controlled by the deep caldera structure or by shallow structures, or a combination of both?
- Is a present shallow magmatic system beneath an active caldera an analogue to the magmatic system during the caldera-forming events, or are both systems completely unrelated?

These are just a few of the crucial, yet unresolved problems pertaining to collapse calderas and to which we do not yet have satisfying answers.

One of the most important future tasks for volcanologists is to identify precursors to potentially devastating caldera-forming eruptions. Any cluster of active volcanoes should be evaluated as a possible site of a growing upper crustal magma chamber that could lead to a future caldera formation (Lipman, 2000). However, herein lies the crux in determining whether caldera-collapse is an inevitable result of an ensuing eruption; caldera-formations are rare events in human timescales and thus our current knowledge of precursory signals is very limited if not absent. Not enough data or information exist to clearly define precursory events as indicators for impending major eruptions and critical parameters indicating whether a caldera–collapse will or will not occur during a major eruption are still mostly unknown. The same applies to the question of characteristic time intervals between the occurrence of anomalous (precursory) signals and an eruption. From the experience of several important periods of caldera unrest over the past decades (e.g., Yellowstone, Long Valley, Campi Flegrei) it is safe to state that most periods of unrest do not terminate with a volcanic eruption,

let alone with a caldera-forming event. The general idea that all unrest is triggered by the arrival of new magma at shallow depth is also eroded by the fact that few historic unrest periods culminated in eruptions and by the increasing evidence for a significant role of shallow hydrothermal fluid migration during unrest (Bonafede and Mazzanti, 1998; Battaglia et al., 2006; Gottsmann et al., 2007).

With the aim to sample state-of-the-art of caldera studies and to contribute to the understanding of collapse calderas and their processes, we organised an international workshop entitled Caldera Volcanism: Analysis, Modelling and Response, in Tenerife, Canary Islands, in October 2005. More than 40 dedicated scientists, covering a wide range of disciplines (structural geology, melt physics, geophysical monitoring, stratigraphy, numerical modelling and gas monitoring, to list just a few), attended the workshop and presented the most recent results from their studies. One of the most interesting results emerging from the passionate and down-to-the-nitty-gritty scientific discussions during that workshop was the general acknowledgment of the desperate need for a joint multi-disciplinary cross-boundary collaboration to tackle the many outstanding and unresolved issues on the formation and the behaviour of collapse calderas. We need to put together geologists, physicists, modellers, geophysicists, geochemists, mathematicians and others in order to fully comprehend caldera dynamics, their potential effects on our environment in general, their associated hazards and their economic benefits in order to give informed advise to decision makers for risk mitigation.

The idea of locking up a bunch of scientist in a remote mountain resort for one week with not much more to do except talk science (and astonishingly devour the hotel's bar of any liquid carbonhydrates) proved the right concept. Several major questions were raised during the workshop, testing to the bone our current knowledge on collapse calderas. Some of these questions were:

- How do collapse calderas form? What are the conditions to create fractures and slip along them to initiate caldera-collapse and when are these conditions fulfilled? How do these conditions relate to explosive volcanism?
- Does extensional tectonism drive caldera volcanism or vice versa?
- Most products of large caldera-forming eruptions show evidence for pre-eruptive reheating. Is this a pre-requisite to produce large volume eruptions and large calderas?
- What is the time-scale of caldera processes? How long does it take for magma to reach conditions ripe enough to generate a caldera-forming eruption?
- Do magma chamber walls behave elastically, viscoelastically or rigidly during caldera-collapse?
- Do calderas form by underpressure following a certain level of magma chamber withdrawal during a previous eruptive episode or by magma chamber loading due to deep doming (underplating), or both?
- How to generate underpressure in a magma chamber?
- How can we interpret unrest signals in active caldera systems? What is the origin of seismic tremor?
- Which criteria could be used to differentiate between pit craters and collapse calderas?

- Which are the mechanisms of fracture propagation during ring fault formation?
- Are caldera-forming faults outward or inward dipping ring faults?

This volume aims at providing some answers to these puzzling questions by exploring the current understanding of these complex geological processes in the form of 14 contributions to this volume. The book includes some of the contributions presented at the workshop but it is also seeded with invited papers to cover the broad spectra of studies dedicated to caldera volcanism. Although we aimed at integrating quite diverse disciplines, it is clear that we cannot provide an exhaustive treatment of all flavours of caldera studies. There are of course additional and equally important disciplines of caldera research, which are not covered by this volume and there is still a significant amount of work to be done. We intended this volume to be another step forward in attempting to capture the full dynamics of volcanic calderas.

The volume starts with a treatment of geological and geochemical investigations at collapse calderas. Costa reviews the approaches to and existing data on magma residence times and rates of igneous activity related to major calderas. The paper also explores how this time information contributes to establishing the rates of magmatic differentiation, mass and thermal budgets of caldera-forming reservoirs. Residence times are highly variable for different systems and range from a few thousand years to several hundred thousand years.

Sulpizio and Dellino describe the analysis of pyroclastic products of caldera volcanism. They illustrate how the geological record can be read in order to deduce the eruption mechanism and the physical processes that influence the mobility, sedimentology and depositional mechanisms of pyroclastic density currents (PDCs) generated during both caldera formation as well as post-caldera volcanism. In this context, a particular emphasis is given to the influence of various types of morphological settings and obstacles on the deposition and the mobility of PDCs.

Pittari et al. reconstruct pre- and syn-caldera-collapse processes associated with the 186 ka caldera-forming event on Tenerife via detailed geological and geochemical analyses of ignimbrite deposits. They show that significant lateral variations in the proportions of lithic clast types, within depositional units, are consistent with an eruption involving multiple vents around a caldera that underwent piecemeal collapse. Based on evidence from vertical variations in lithic clast proportions between depositional units, the authors infer an increasing depth of conduit wall rock fragmentation during the eruption.

Aguirre-Diaz et al. report on the large ignimbrite province of the Sierra Madre Occidental in Mexico, presenting a particular type of caldera formation associated with the generation of tectonic grabens during vertical collapse and the formation of thick ignimbrite deposits. After the main collapses and ignimbrite emplacements during a flare-up period between 38 and 23 Ma, faulting and subsidence continued for several millions of years displacing the intra-graben-caldera products downward into the tectonic depression, but preserving the chaotic arrangement of the collapsed blocks. In many cases, the graben-caldera vents are related to gold and silver hydrothermal mineralisation and thus the findings constitute an important

contribution to the understanding of the relationship among ignimbrites, graben–caldera vents and post-caldera fills for economic prospecting.

Turning to Archean times and highlighting the economic importance of geological caldera investigations, Mueller et al. report on subaqueous calderas in Canada, which are primary sites for volcanogenic massive sulfide (VMS) deposits. Based on detailed volcanic facies mapping, they distinguish caldera subsettings in the ancient deposits of the Hunter Mine and Normetal calderas, two little-known effusive-dominated edifices and the explosive-dominated Sturgeon Lake caldera. The authors propose a new hydrothermal alteration model that helps in explaining the formation of chert–Fe-carbonate assemblages in Archean sequences and in pinpointing highly favourable sites for VMS exploration.

With a review on collapse caldera modelling, Martí et al. summarise recent development in investigating caldera formation via analogue and numerical modelling and cross-correlate key findings with results from geophysical imaging of the sub-surface architecture at calderas. They conclude that the combination of field studies with experimental, theoretical and geophysical modelling enables identifying and quantifying the main controlling factors for the formation of collapse calderas. These include magma chamber size and shape, magma chamber depth, host rock rheology, previous history of deformation, topography, regional tectonics, temperature field around the magma chamber and magma composition and rheology.

Acocella explores the structural development of calderas as investigated by analogue experiments. He finds that despite differences in the instrumental setup and imposed boundary conditions, a complete collapse can be summarised through four main stages, proportional to the amount of subsidence and progressively characterised by a downsag, reverse ring fault, peripheral downsag and peripheral normal ring fault. This proposed evolutionary scheme incorporates not only the geometric features of calderas, but more importantly, also their genetic features.

Focussing on rock mechanical conditions, Gudmundsson discusses the initiation of ring faults to trigger caldera-collapse as opposed to mere dyke emplacement. He finds that underpressure and excess pressure in a shallow, crustal chamber normally results in dyke injection rather than caldera formation. Dyke injection is also favourable over ring-fault initiation for doming or tension above a spherical magma chamber. Numerical results indicate that the local stresses in composite volcanoes most likely to initiate caldera faults are associated with sill-like chambers subject to tension, doming or both.

Via a systematic set of numerical models, Walter summarises a variety of types, mechanisms and patterns of caldera ring-dykes that can be observed in nature. The findings suggest that caldera deformation may be affected by pre-existing and reactivated tectonic faults and ring fractures, and that sites of ring-dyke intrusions are controlled by various tectonic and magmatic loading processes. The models suggest that ring-dykes commonly form incompletely, i.e. only part of a ring can be intruded, as a result of a non-uniform stress field around the ring-fault.

The following three papers focus on the analysis and interpretation of geophysical time series collected during unrest periods at caldera volcanoes

to infer causative sources. Troise et al. report on a new uplift episode at the Campi Flegrei caldera after a prolonged period of overall ground subsidence. They show that this new episode, which appears slower but longer than previous small uplifts, sheds light both on the origin of small and large unrests, and on the conditions to evolve towards large unrests. Evaluating an almost 25-year-long record of geodetic observations, the authors propose that the maximum horizontal to vertical displacement ratio can be a powerful indicator of source changes, and can give important information for volcanic eruption forecast.

Todesco focuses on the role that hydrothermal systems may play in caldera unrest. It is stressed that magma emplacement at depth as well as shallow circulating hydrothermal fluids can generate geophysical signals measured at the ground surface. Effective hazard evaluation requires a proper understanding of unrest phenomena and correct interpretation of their causes. The author shows that simultaneous modelling of different independent parameters is a powerful tool for understanding caldera unrest. Her results highlight the importance of comprehensive conceptual models that incorporate all the available geochemical and geophysical information, and the need for high-quality, multi-parameter monitoring and modelling of volcanic activity.

Echoing the need for cross-boundary multi-parameter investigations during unrest episodes, Gottsmann and Battaglia present a review of recent advances of gravimetric and ground deformation studies. They show that with deformation data alone one cannot discriminate between magma and aqueous fluid intrusions, but in combination with gravimetric data, the density of the intrusive fluids can be assessed which helps in better constraining the nature of the causative source. Through a series of case studies they highlight limitations of current standard procedures, discuss different data inversion techniques and problems caused by data aliasing and by the use of oversimplified models for the interpretation of geophysical signals.

The final two papers explore the use of statistics for forecasting volcanic phenomena. Tarraga et al. assess the failure forecast method (FFM) and its applicability to the analysis of reawakening volcanoes and caldera unrest. Using an automated FFM procedure, the authors present results from data collected during the recent episode of unrest at the Las Cañadas caldera in Tenerife (Spain). The authors note the importance of the long-term use of the FFM at a quiet or dormant volcano as an essential prerequisite to define the baseline or normal behaviour of the FFM, thus effectively reducing the number of potential false alarms during reactivation.

Finally, Carniel et al. examine the memory or persistence of a given time series collected at a volcano. They note that a time series that does not keep some memory of its past cannot provide information about the future of an evolving volcanic process, i.e. it cannot help to forecast an eruption. The authors report on stochastic models developed for hazard estimation in the short-term by inspecting time series sampled at Stromboli and Soufrière Hills volcanoes and in the long-term using space–time data from the Osteifel and Tohoku volcanic regions. For the case of the Las Cañadas caldera they show how the stochastic approach can provide evidence for unrest.

In closing, we express our gratitude to a number of people who helped in making this volume:

Tirza van Daalen and Pauline Riebeek at Elsevier for accepting our proposal, walking us through the publication process and their impeccable support throughout the realisation of this project;
Janine Kavanagh (Bristol) for her editorial help and correction of English spelling and grammar in many manuscripts;
the staff of the Parador de Las Cañadas for their impeccable support in helping organising the 2005 Calderas Workshop in Tenerife;
all authors for contributing to this volume;
the numerous referees who provided constructive criticism for the submitted manuscripts
and our families for their love and support.

We believe the creation of this volume was well-worth the effort and we hope it stimulates further fruitful discussion and fosters additional lateral thinking. We would of course be pleased to witness an update of this community effort in a few years' time.
Joachim Gottsmann
Joan Martí
Bristol, United Kingdom and Barcelona, Spain
January 2008

## REFERENCES

Acocella, V., Funiciello, R., Marotta, E., Orsi, G., de Vita, S., 2004. The role of extensional structures on experimental calderas and resurgence. J. Volcanol. Geotherm. Res., 129(1–3), 199–217.

Acocella, V., Korme, T., Salvini, F., Funiciello, R., 2002. Elliptic calderas in the Ethiopian rift: control of pre-existing structures. J. Volcanol. Geotherm. Res., 119, 189–203.

Aprea, C., Hildebrand, S., Fehler, M., Steck, L., Baldridge, W., Roberts, P., Thurber, C., Lutter, W., 2002. Three-dimensional Kirchhoff migration: imaging of the Jemez volcanic field using teleseismic data. J. Geophys. Res., 107(B10), doi: 10.1029/2000JB000097.

Battaglia, M., Troise, C., Obrizzo, F., Pingue, F., De Natale, G., 2006. Evidence for fluid migration as the source of deformation at Campi Flegrei caldera (Italy). Geophys. Res. Lett., 33(L01307), doi: 10.1029/2005GL024904.

Bonafede, M., Mazzanti, M., 1998. Modelling gravity variations consistent with ground deformation in the Campi Flegrei caldera (Italy). J. Volcanol. Geotherm. Res., 81(1–2), 137–157.

Bower, S.M., Woods, A.W., 1997. Control of magma volatile content and chamber depth on the mass erupted during explosive volcanic eruptions. J. Geophys. Res., 102, 10273–10290.

Burbank, W.S., 1933. Vein system of the Arrastre Basin and regional structure in the Silverton and Telluride quadrangles, Colorado. Colorado Sci. Soc. Proc., 13, 135–214.

Clough, B.J., Maufe, H.B., Bailey, E.B., 1909. The cauldron-subsidence of Glen Coe, and the associated igneous phenomena. Quart. J. Geol. Soc. Lond., 65, 611–678.

Diller, J.S., Patton, H.B., 1902. Geology and petrology of Crater Lake National Park. US Geological Survey Professional Paper, 3: 167 pp.

Druitt, T.H., Sparks, R.S.J., 1984. On the formation of calderas during ignimbrite eruptions. Nature, 310, 679–681.

Dutton, C.E., 1884. Hawaiian volcanoes. In: Fourth Annual Report, US Geological Survey, Washington D.C., pp. 75–219.

Folch, A., Martí, J., 2004. Geometrical and mechanical constraints on the formation of ring-fault calderas. Earth Planet. Sci. Lett., 221(1–4), 215–225.

Fouqué, F., 1879. Santorin et ses eruptions. Masson, Paris, 39, 440 pp.

Gottsmann, J., Carniel, R., Coppo, N., Woller, L., Hautmann, S., Rymer, H., 2007. Oscillations in hydrothermal systems as a source of periodic unrest at caldera volcanoes: multiparameter insights from Nisyros, Greece. Geophys. Res. Lett., 34(L07307), doi: 10.1029/2007GL029594.

Gudmundsson, A., 1998. Formation and development of normal-fault calderas and the initiation of large explosive eruptions. Bull. Volcanol., 60, 160–171.

Gudmundsson, A., Martí, J., Turón, E., 1997. Stress fields generating ring faults in volcanoes. Geophys. Res. Lett., 24, 1559–1562.

Komuro, H., 1987. Experiments on cauldron formation: a polygonal cauldron and ring fractures. J. Volcanol. Geotherm. Res., 31, 139–149.

Komuro, H., Fujita, Y., Kodama, K., 1984. Numerical and experimental models on the formation mechanism of collapse basins during the Green Tuff orogenesis of Japan. Bull. Volcanol., 47, 649–666.

Lipman, P.W., 1984. The roots of ash flow calderas in western North America: windows into the tops of granitic batholiths. J. Geophys. Res., 89(B10), 8801–8841.

Lipman, P.W., 1997. Subsidence of ash-flow calderas: relation to caldera size and magma-chamber geometry. Bull. Volcanol., 53(3), 198–218.

Lipman, P., 2000. Caldreas. In: Sigurdsson, H., Houghton, B.F., McNutt, S.R., Rymer, H., Stix, J. (Eds), Encyclopedia of Volcanoes. Academic Press, San Diego, pp. 643–662.

Martí, J., Ablay, G.J., Redshaw, L.T., Sparks, R.S.J., 1994. Experimental studies of collapse calderas. J. Geol. Soc. Lond., 151, 919–929.

Martí, J., Folch, A., Macedonio, G., Neri, A., 2000. Pressure evolution during caldera forming eruptions. Earth Planet. Sci. Lett., 175, 275–287.

Matumoto, T., 1943. The four gigantic caldera volcanoes of Kyushu. Jpn. J. Geol. Geogr., 19, 57.

Nishimura, T., Fehler, M., Baldridge, W.S., Roberts, P., Steck, L., 1997. Heterogeneous structure around the Jemez volcanic field, New Mexico, USA, as inferred from the envelope inversion of active-experiment seismic data. Geophys. J. Int., 131(3), 667–681.

Ramberg, H., 1967. Gravity, Deformation and the Earth's Crust: As Studied by Centrifuged Models. Academic Press, London, 214 pp.

Ramberg, H., 1981, Gravity, Deformation and the Earth's Crust in Theory, Experiments and Geologic Application, 2nd edn. Academic Press, London, 452 pp.

Roche, O., Druitt, T.H., Merle, O., 2000. Experimental study of caldera formation. J. Geophys. Res., 105(B1), 395–416.

Roche, O., Druitt, T.H., 2001. Onset of caldera collapse during ignimbrite eruptions. Earth Planet. Sci. Lett., 191(3–4), 191–202.

Rymer, H., Williams-Jones, G., 2000. Volcanic eruption prediction: magma chamber physics from gravity and deformation measurements. Geophys. Res. Lett., 27(16), 2389–2392.

Self, S., Goff, F., Gardner, J.N., Wright, J.V., Kitte, W.M., 1986. Explosive rhyolitic volcanism in the Jemez Mountains: vent locations, caldera development and relation to regional structures. J. Geophys. Res., 91, 1779–1798.

Self, S., Rampino, M.R., Newton, M.S., Wolf, J.A., 1984. Volcanological study of the great Tambora eruption of 1815. Geology, 12, 659–663.

Smith, R.L., 1960. Ash flows. Geol. Soc. Am. Bull., 71, 795–842.

Smith, R.L., 1979. Ash flow magmatism. Special Papers Geological Society of America, 180: 5–27.

Smith, R.L., Bailey, R.A., 1968. Resurgent cauldrons. Geological Society of America Memories, 116, 613–622.

Sparks, R.S.J., Walker, G.P.L., 1977. The significance of vitric-enriched air-fall ashes associated with crystal-enriched ignimbrites. J. Volcanol. Geotherm. Res., 2, 329–341.

Tikku, A.A., McAdoo, D.C., Schenewerk, M.S., Willoughby, E.C., 2006. Temporal fluctuations of microseismic noise in Yellowstone's Upper Geyser Basin from a continuous gravity observation. Geophys. Res. Lett., 33(L11306), doi: 10.1029/2006GL026113.

Van Bemmelen, R.W., 1929. Het Caldera Probleem. De Mijningenieur, 4, 101–102.

Verbeek, R.D.M., 1886. Krakatau. Imprimerie l'Etat, Batavia, Indonesia, 495 pp.

Walker, G.L.P., 1980. The Taupo pumice: product of the most powerful Known (ultraplanian) eruption? J. Volcanol. Geotherm. Res., 8, 69–94.

Williams, H., 1941. Calderas and their origin. Bull. Dep. Geol. Sci., 25(6), 239–346.

Williams, H., McBirney, A.R., 1979. Volcanology. Freeman, Cooper and Co., San Francisco, 397 pp.

Wilson, C.J.L., Walker, G.P.L., 1982. Ignimbrites depositional facies: the anatomy of a pyroclastic flow. J. Geophys. Res., 139, 581–592.

CHAPTER 1

# Residence Times of Silicic Magmas Associated with Calderas

Fidel Costa*

## Contents

*Corresponding author. Tel.: ++34-93-4095410; Fax: ++34-93-4110012
*E-mail address:* fcosta@ija.csic.es

CSIC, Institut de Ciències de la Terra 'Jaume Almera', Lluís Solé i Sabarís s/n, 08028 Barcelona, Spain.

## Abstract

This paper reviews the times that silicic magmas related to major caldera systems spend in the crust prior to eruption. The significance of the time information is evaluated and combined with magma volumes and temperatures to quantify the mass and thermal fluxes associated to calderas. The data discussed includes the largest explosive eruptions on Earth: Taupo Volcanic Zone (New Zealand), the Youngest Toba Tuff (Indonesia), Yellowstone system (USA), Long Valley (USA), Carter Lake (USA), Valles-Toledo complex (USA), La Garita caldera (USA), La Pacana (Chile) and Kos (Greece). Magma residence times are calculated from the difference between the eruption age and the age obtained by radioactive clocks and minerals that are a closed system at high magmatic temperatures (e.g., U–Pb system in zircon).

Large ranges of residence times between different systems are found. The shortest residences (4–19 ky) are those of some magmas from the Taupo Volcanic Zone (Oruanui and Rotoiti) and Yellowstone (Dry Creek and Lava Creek). There is not a good correlation between magma volume and residence time, although most eruptions $<10\,\mathrm{km}^3$ have residence times $<100$ ky, and those $>100\,\mathrm{km}^3$ have longer residences, some up to 300–500 ky (Fish Canyon, La Pacana). The residence times of some small ($<10\,\mathrm{km}^3$) pre- and post-caldera magmas indicate that they were extracted from the same reservoir as the caldera-forming magma (e.g., Long Valley, Taupo). However, the time information from most small-volume magmas seems to reflect the recycling of crystals from previous cycles of caldera-forming magmas (Yellowstone), from plutonic rocks of the same caldera cycle with or without erupted equivalents on the surface (Crater Lake, Taupo, Long Valley), or from a partially solidified magma reservoir (Taupo). These interpretations are in agreement with cooling rates and solidification times obtained from simple thermal models of magma reservoirs.

Magma production rates were calculated from the ratio of erupted volume and residence time, and they vary between $<0.001\,\mathrm{km}^3\,\mathrm{y}^{-1}$ for small deposits ($<10\,\mathrm{km}^3$) and ca. $0.1\,\mathrm{km}^3\,\mathrm{y}^{-1}$ for the Oruanui eruption ($530\,\mathrm{km}^3$). Estimates for most eruptions $>500\,\mathrm{km}^3$ are within $2\pm2\times10^{-2}\,\mathrm{km}^3\,\mathrm{y}^{-1}$. These high magma production rates are probably transient and comparable to global eruptive fluxes of basalts (e.g., Hawaii). Magma cooling rates for deposits $>100\,\mathrm{km}^3$ were calculated from the difference between the liquidus and pre-eruptive temperatures over their residence times, and they vary between $2\times10^{-4}$ and $3\times10^{-3}\,\mathrm{K}\,\mathrm{y}^{-1}$. Integration of the calculated residence times and magma fluxes with a simple rheological model of the crust is not possible and should be a main topic of research if we are to understand the mechanisms and rates which permit large amounts of silicic magma to be stored below calderas.

## 1. INTRODUCTION

Caldera-forming eruptions produce the most voluminous (up to $5{,}000\,\mathrm{km}^3$) explosive eruptions on Earth, and their activity appears to provide clues for understanding climatic and evolutionary biological changes (e.g., Lipman, 2000a; Francis and Oppenheimer, 2003). Collapse calderas are among the most investigated geological objects also because of their association with economic deposits and geothermal energy. The distinctive feature of caldera–related silica–rich

volcanism is the topographical depressions left after the eruption. These are thought to be the result of either tremendous explosions that blew apart a pre-existing volcanic cone or due to subsidence of the roof of the reservoir after or during magma evacuation. High-level magma emplacement (typically $<10\,km$ depth) seems to be required for caldera formation, but when combined with the apparent large size of some reservoirs, questions arise as to the thermal and mechanical states of the crust and the magma, the rates and mechanisms of vapour- and silica-rich magma differentiation, and the timescales of transport and storage of huge quantities of eruptible silicic magma (e.g., Smith, 1979; Hildreth, 1981; Shaw 1985; Jellinek and DePaolo, 2003). These issues were addressed by Shaw (1985) who noted that "the interaction of magma generation rates, stress domains and injection rates leads to a spectrum of residence times which effectively determine the types of intrusive and volcanic suites seen at high crustal levels and at the surface." Almost 25 years later, progress in analytical techniques have enabled the quantification of the time over which crystals and magma are stored before a caldera-forming eruption. This allows analysing the relations between the volumes, compositions, temperatures and depths of magma reservoirs below calderas from a new perspective. The purpose of this manuscript is to describe the approaches used to obtain the time scales of magmatic processes, to compile the data on residence times of major caldera-related complexes, and to use this information for deriving modes and rates of silica-rich magma production and storage in the Earth's crust.

## 1.1. What is the residence time of a magma?

It can be defined as the time elapsed since the magma was formed and its eruption. Uncertainties arise with the meaning of 'when' a magma is formed because what is finally erupted is a mixture of phases that might have very different origins in time and space (e.g., Bacon and Lowenstern, 2005). The most widespread use of residence time involves pinpointing when a given mineral started to crystallise, presumably during storage in a magma reservoir. This is different from the definition used in oceanic geochemistry or in highly active volcanic systems where it refers to the (mean) time that a given element or isotope spends in a reservoir before being removed (e.g., Holland, 1978; Albarède, 1993). In practice, one can calculate the residence time as the difference between the eruption age as obtained by K–Ar (or $^{40}Ar/^{39}Ar$), (U, Th)/He and $^{14}C$ methods (for prehistorical eruptions) and the age provided by other radioactive clocks, such as Rb–Sr, and U–Th–Pb. From this definition it is apparent that the residence time does not need to be a single value, and might depend on the phases and radioactive isotopes that are used. Multiple values of residence times may arise from different crystallisation ages of different minerals, but also from the fact that the very definition of an age requires knowledge of when the radioactive system became closed. This condition depends on several factors but strongly on the diffusion rate of the daughter isotope, and has been quantified with the use of a closure temperature (Dodson, 1973). This explains the *a priori* paradoxical situation that, for example, a sanidine might have two different ages and both could be correct: dated by the K–Ar system the mineral gives the eruption age but using Rb–Sr clock it may give a much older

crystallisation age, simply because the K–Ar system becomes closed at much lower temperatures (e.g., on quenching of the magma upon eruption). Most of the age data used in this manuscript were obtained using zircon and the U–Th–Pb decay system and thus reflect the time since the beginning of zircon crystallisation and final eruption. It is worth mentioning that there might be a systematic bias between the radioactive clocks of the K–Ar and that of U–Pb systems, the latter giving slightly older ages (<1%; e.g., Renne et al., 1998; Min et al., 2000; Renne, 2000; Villeneuve et al., 2000; Schmitz and Bowring, 2001; Schoene et al., 2006). Since the issue is not resolved at the time of writing it has not been considered for calculating residence times. Recent reviews of the methods and time scales of magmatic processes can be found in Condomines et al. (2003), Reid (2003), Turner et al. (2003), Hawkesworth et al. (2004) and Peate and Hawkesworth (2005).

## 1.2. Magma production and cooling rates

Aside from compiling residence times and rates of processes, two other parameters were calculated. One is a 'magma production rate,' which is the ratio of the erupted volume over the residence time (e.g., Christensen and DePaolo, 1993; Davies et al., 1994). It is not *sensu stricto* a magma production rate because it only accounts for the erupted magma. It should be called 'erupted magma production rate' but this would be very cumbersome. These rates are different from the 'average magma eruption rate' (or output rate) calculated using the total erupted volume and time span of magmatic activity at a given volcanic system (Crisp, 1984; White et al., 2006). They are also different from the rates obtained from the erupted volume divided by the time interval between two subsequent eruptions (Bacon, 1982). A magma cooling rate has also been calculated for eruptions $>100\,km^3$. This is the difference between the magma temperature at pre-eruptive conditions and its liquidus calculated by MELTS (Ghiorso and Sack, 1995), over the residence time. The significance of such cooling rates is debatable: it could be a maximum if the magma delivered to the reservoir was crystal-rich, or a minimum if the magma was reheated prior to eruption. The magma cooling rates reported here should be considered as first-order estimates and are applicable only to the erupted magma rather than to the entire magmatic system at depth (which likely has many cooling rates).

## 1.3. Choice of caldera systems and organisation of the manuscript

The systems described are those that have produced large silicic eruptions for which residence time data exists (Figure 1): Taupo Volcanic Zone (New Zealand), Toba caldera (Indonesia), Yellowstone (USA), Long Valley (USA), Valles–Toledo complex (USA), and La Garita (USA). The time information from Crater Lake (USA), Kos Tuff (Greece) and La Pacana (Chile) are also briefly discussed. A summary of residence times and rates of processes for major eruptions are shown in Tables 1 and 2. The rest of this manuscript is organised in four more sections: Section 2 discusses the methods used to obtain time information. Section 3 contains the time information and other basic geological features of each caldera system. Section 4 is a general discussion of what the residence times mean in the context of
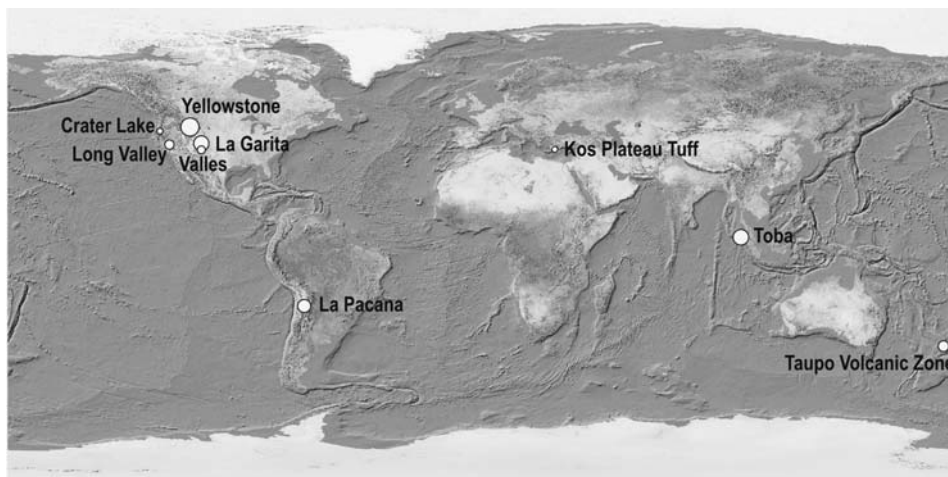
**Figure 1**    Location of the caldera systems discussed in the manuscript. The sizes of the circles are roughly proportional to the difference in caldera diameters.

some simple thermal and mechanical calculations of magma reservoirs. Section 5 summarizes the main findings of the manuscript.

## 2. Methods for Obtaining Time Constraints of Magmatic Processes

### 2.1. Radioactive isotopes

The age determination is based on radioactive decay laws which state that the rate of spontaneous decay of an unstable radioactive parent is proportional to the number of parent atoms. One can obtain an age if: (1) the initial number of daughter atoms since the system's closure is known, and (2) the system that is dated (e.g., mineral, phases or rock associations) has remained closed to additions or losses of parent and daughter atoms (e.g., Faure and Mensing, 2004). In analogy to the chemical diffusion approach described below, the first requirement is related to the initial conditions of the system, and the second to the boundary conditions and because of its importance it is discussed below in some detail.

The advent of in-situ analytical techniques enabled multiple isotope determinations for age purposes in a single crystal using secondary ion mass spectrometry (SIMS), although thermal ionisation mass spectrometry (TIMS) on bulk materials (single crystal or not) are more commonly used. A good example of the power of SIMS is the possibility to obtain isochrons from multiple in situ analyses of single zircon crystals (Lowenstern et al., 2000). Details about the dating methods and radioactive systems used to obtain time scales of magmatic process can be found in McDougall and Harrison (1999), Condomines et al. (2003), Turner et al. (2003) and Dickin (2005).

**Table 1**　Summary of characteristics, residence times and magmatic rates of major caldera-forming silicic eruptions for the systems discussed in the manuscript organised by geochronological order.

| | Member or unit | Vol[a] (km$^3$) | Eruption age[b] | Magma residence time[c] | Magma production rate (km$^3$ y$^{-1}$)[d] | Magma cooling rate (Ky$^{-1}$)[e] |
|---|---|---|---|---|---|---|
| Crater Lake | Wineglass Tuff and Mazama ash | 50 | 7.0 ka | n.d. | n.d. | n.d. |
| Taupo Volcanic Zone | Oruanui | 530 | 26.5 ka | 4 to 70 ky | $7.5 \times 10^{-3}$–$1.3 \times 10^{-1}$ | $(0.1$–$2) \times 10^{-2}$ |
| | Rotoiti | ca 100 | 62 ka | 9–50 ky | $(0.2$–$1) \times 10^{-2}$ | n.d. |
| | Whakamaru | 300–1000 | 320–340 ka | Up to 250 ky | $(1$–$4) \times 10^{-3}$ | $5 \times 10^{-4}$ |
| | Ongatiti | 300–1000 | 1.21 Ma | Up to 240 ky | $(1$–$4) \times 10^{-3}$ | n.d. |
| Toba | Youngest Toba | 2800 | 75 ka | Up to 160 ky | $1.8 \times 10^{-2}$ | $(0.8$–$1) \times 10^{-3}$ |
| Kos | Kos Plateau Tuff | 60 | 161 ka | 180 ky | $3.3 \times 10^{-4}$ | n.d. |
| Yellowstone | Lava Creek | 1000 | 600 ka | 19–57 ky | $(2$–$5) \times 10^{-2}$ | $(0.2$–$2) \times 10^{-3}$ |
| | Mesa Falls | 280 | 1.3 Ma | 160–170 ky | $1.7 \times 10^{-3}$ | $(0.6$–$2.3) \times 10^{-4}$ |
| | Huckleberry | 2500 | 2.0 Ma | 77–234 ky | $(1$–$3) \times 10^{-2}$ | $(0.4$–$4.5) \times 10^{-4}$ |
| Long Valley | Bishop | 600 | 760 ka | 50–390 ky | $(0.2$–$1) \times 10^{-2}$ | $(0.2$–$1) \times 10^{-3}$ |
| Valles Toledo | Upper Bandelier | 250 | 1.2 Ma | n.d. | n.d. | n.d. |
| | Lower Bandelier | 400 | 1.6 Ma | n.d. | n.d. | n.d. |
| La Pacana | Atana and Toconao | 2700 | ca.4 Ma | 500–750 ky | ca $4 \times 10^{-3}$ | n.d. |
| La Garita | Fish Canyon | 5000 | 28 Ma | 80–360 ky (perhaps 900 ky) | $(0.5$–$6) \times 10^{-2}$ | $(0.3$–$3) \times 10^{-3}$ |

*Note:* [a]Vol = Volumes in dense rock equivalent. [b]This is the age obtained by $^{40}$Ar/$^{39}$Ar, or K–Ar or $^{14}$C methods. [c]Calculated from the time difference between the eruption age and the age of the deposit obtained by other radioactive clocks with higher closure temperatures (e.g., Rb–Sr, U–Th–Pb). [d]Ratio of erupted volume and residence time. [e]Calculated using the difference between the pre-eruptive and the liquidus temperature (determined by MELTS, Ghiorso and Sack, 1995) over the residence time. Data sources can be found in Tables 3–8 and in the text. n.d.=not determined.

**Table 2** Summary of time scales and process rates derived from studies of caldera-related silicic magmas described in this manuscript.

| Magmatic process | Time scale (prior to eruption) | Rate | Method | Magmatic system |
|---|---|---|---|---|
| Crystal fractionation | ca 100 ky | | Sr and Ba diffusion in sanidine | Long Valley |
| and magma differentiation | ca 160 ky | Fractionation (% per ky)= 0.1–0.4 | U–Th series disequilibria and other trace elements data on allanite | Toba |
| Large scale remobilization of magma reservoir | 100–200 ky | Heating (degrees y$^{-1}$)= $3 \times 10^{-4}$ | Thermal modeling | La Garita |
| Last magma replenishment | 0.1–10 ky | | Sr diffusion in sanidine, O isotopes and Ti zoning in quartz | Long Valley, Valles–Toledo |
| Melting of intracaldera rocks | 0.5–5 ky | Heating (degrees y$^{-1}$)= $(3–30) \times 10^{-2}$ | O diffusion in quartz and zircon | Yellowstone |
| Assimilation of wall-rocks | 1–200 y | | O diffusion in quartz and sanidine | Valles–Toledo |
| Partial assimilation of xenocrysts | 2–25 y | | Ar diffusion in feldspars, Sr in biotite | Long Valley, Yellowstone, Valles–Toledo, Toba |

*Note:* Data sources can be found in the Tables 3–8 and in the text for each individual system.

## 2.1.1. Comments on closed system and boundaries: closure temperature

The degree to which the system has been open to exchange with the environment via diffusion has been quantified using the notion of closure temperature. Dodson (1973) provided a formulation of the closure temperature that is commonly used:

$$\frac{E}{RT_c} = \ln\left(-\frac{AD_o RT_c^2}{Esa^2}\right) \qquad (1)$$

where $T_c$ is the closure temperature; $E$ the activation energy for diffusion of the daughter isotope; $R$ the gas constant; $D_o$ the pre-exponential factor of the diffusion coefficient (e.g., $D = D_o \exp[-E/RT]$) of the daughter isotope; $A$ a geometric factor; $s$ the cooling rate; and $a$ the diffusing distance. The following simplifications are built into this equation: (1) a single cooling rate, (2) it is applicable only to the mean concentration, and thus $T_c$ is a mean closure temperature, (3) it considers a finite crystal with an infinitely sized reservoir of infinitely fast diffusion and (4) the composition at the centre of the crystal has been removed by diffusion from that at

the onset of cooling. Later, Dodson (1986) introduced the closure profile which allows for different zones of a crystal to 'close' at different temperatures (e.g., centres at higher temperature than rims). Ganguly and Tirone (1999, 2001) presented new formulations in which the closure profiles and temperatures can be calculated for minerals with an arbitrary extent of diffusion. This effectively eliminates condition (4) (above) and thus should be of wide applicability to igneous systems. Using the Dodson (1973, 1986) equations when condition (4) does not apply leads to higher closure temperatures than the correct values (see Ganguly and Tirone, 1999, 2001).

   A set of calculations of the mean closure temperature show that the K–Ar method has the lowest values, followed by Rb–Sr and U- and Th–Pb system (Figure 2). Accordingly, the K–Ar system is the most reliable to obtain eruption ages, whereas Rb–Sr ages may or may not be good records of existing residence time. The U- and Th–Pb based age determinations in zircons should be able to
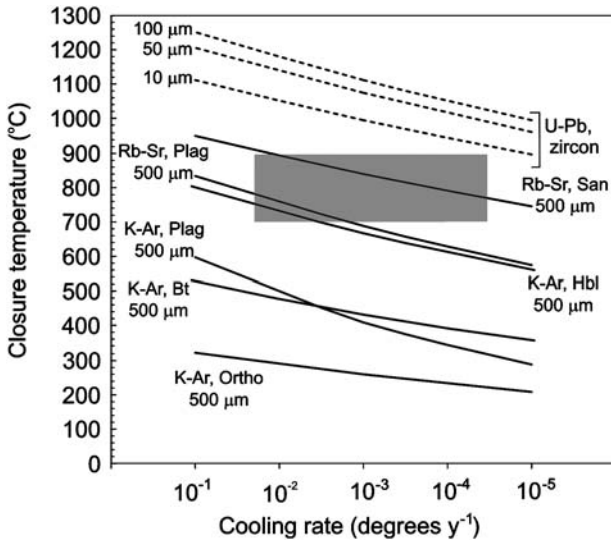


**Figure 2**  Calculated mean closure temperatures (Dodson, 1973) for several radioactive systems, minerals and cooling rates. The calculations are for a sphere of 500 μm radius, except for zircon where radius varies between 10 and 100 μm. Mineral abbreviations: Plag, plagioclase, San, sanidine, Ortho, orthoclase, Bt, biotite, Hbl, hornblende. Sources for the diffusion coefficients are: Ar in Ortho from Foland (1994), Ar in Plag from Kelley et al. (2002), Ar in Bt from Grove and Harrison (1996), Ar in Hbl from Harrison (1981), Sr in San from Cherniak (1996), Sr in Plag (27 mol % of anorthite) from Giletti and Casserly (1994), Pb in zircon from Cherniak and Watson (2001). The area below each line defines the conditions where the system can be considered 'closed'. The grey area encompasses the ranges of temperature and cooling rates of caldera-forming magmas described in the manuscript (see text). The closure temperatures are for values of: $M[M = (D_{T_o} \times R \times T_c^2)/(E \times s \times a^2)$; $D_{T_o} = D$ at peak temperature] larger than 1, and thus the Dodson (1973) formulation applies (see Ganguly and Tirone, 1999, 2001). The exception is Pb in zircon which are an overestimate because the $M$ values are much smaller than 1. This was not corrected because the low calculated $M$ values (Log $[M^{0.5}]$ between $-2$ and $-4$) are not found in Ganguly and Tirone (1999, 2001).

record any prolonged magmatic history. From this perspective, subtracting the ages obtained from U- and Th–Pb methods form those of K–Ar or $^{40}$Ar/$^{39}$Ar should be a reliable proxy for magma residence time. One can also start with Fick's second law of diffusion and include an additional term for the production of the daughter isotope:

$$\frac{\partial C_{DA}}{\partial t} = D(t)_{DA} \frac{\partial^2 C_{DA}}{\partial x^2} + \lambda N_o \exp(-\lambda t) \tag{2}$$

where $C_{DA}$ is the concentration of the daughter, $N_o$ the number of parent atoms present initially, $D(t)_{DA}$ the diffusion coefficient which depends on time through the thermal history, $D(t)=D_o \exp[-E/RT(t)]$, but not on composition or position, and $x$ is distance (in one dimension). Solving this equation with finite difference numerical techniques can also address the closure temperature and enables the implementation of almost any initial and boundary condition and cooling history. The attainable information using the closure temperature concept has not been much exploited for magmatic processes but has a long history in metamorphic rocks (e.g., Ganguly, 2002) and in low-temperature chronology (e.g., thermo-chronology; Reiners and Ehlers, 2005). Recent detailed geochronological results of the Fish Canyon system (Bachmann et al., 2007b) show that $^{40}$Ar/$^{39}$Ar total fusion ages of sanidine are slightly younger than those of the other minerals (plagioclase, hornblende and biotite) which could be explained by the effects the closure temperatures discussed here.

## 2.2. Chemical diffusion, relaxation of mineral zoning

The discussion above has already introduced the notion of using diffusion modelling to retrieve time scales of magmatic processes. The technique exploits the presence of gradients of concentration (or chemical potential) which dissipate or tend to equilibrium at a rate that has been experimentally calibrated (e.g., diffusion coefficient). The idea is that the zoning in minerals records the conditions and composition from the environment in which they reside. Depending on the rate of chemical diffusion of the elements in the crystal and surrounding matrix, different elements will reequilibrate to different extents. Because diffusion is exponentially dependent on temperature, and diffusion rates of typical elements in most geological materials are quite slow at room temperature, the mineral compositions that we measure reflect conditions of much higher temperatures; i.e., closure temperature above. To solve Fick's second law (e.g., Equation (2) without the production term on the RHS) we need initial and boundary conditions. It is crucial to have criteria to establish these as close as possible to the natural system we are studying. In this sense, the uncertainties in initial and boundary conditions are similar to those discussed above for the radioactive isotopes techniques.

### 2.2.1. Initial and boundary conditions
The initial conditions are the concentration distribution within the crystal prior to the main episode of diffusion. They vary depending on the problem at hand.

One possibility is to use the zoning patterns of slowly diffusing elements to constraint those that move faster and which we are interested in modelling (e.g., Costa et al., 2003). A similar approach was taken by Morgan and Blake (2006) to model Ba and Sr zoning in sanidine of the Bishop Tuff. Other studies suggest that an initial homogeneous concentration is a good assumption (e.g., Costa and Chakraborty, 2004; Costa and Dungan, 2005) and was used by Bindeman and Valley (2001) to model oxygen isotope zoning in zircon of Yellowstone magmas.

The boundary conditions refer to whether the crystal exchanges matter with its surrounding matrix (open to flux) or not (isolating boundary). The boundary conditions also include whether the concentration at the boundary remains constant or not. In many situations related to magmatic processes a boundary open to flux to an infinite reservoir is applicable. A constant composition at the boundary is the simplest case but for example, Christensen and DePaolo (1993) presented a model of Sr with changing boundary conditions due to in situ $^{87}$Rb decay in the case of the Bishop Tuff. The equilibration of glass inclusions by volume diffusion can also be used to obtain time scales but we need to take into account other boundary conditions, such as the solubility of the element in the host (e.g., Qin et al., 1992).

## 2.3. Other methods of obtaining time scales of magmas related to calderas

Thermal or crystallisation models, where viscosities and densities of liquids play a prominent role can also be used to obtain time information (e.g, Wolff et al., 1990; Bachmann and Bergantz, 2003; Michaut and Jaupart, 2006). For a first approximation to the cooling times of magma reservoirs the following solution of the heat diffusion equation can be used (Carslaw and Jaeger, 1986):

$$\frac{T - T_1}{T_o - T_1} = \frac{1}{2} \left\{ \mathrm{erf} \frac{RR + a}{2(\kappa t)^{0.5}} - \mathrm{erf} \frac{RR - a}{2(\kappa t)^{0.5}} - \frac{2(\kappa t)^{0.5}}{r \pi^{0.5}} \right.$$
$$\left. \times \left( \exp \frac{-(RR - a)^2}{4 \kappa t} - \exp \frac{-(RR + a)^2}{4 \kappa t} \right) \right\} \qquad (3)$$

which is for the case of a half sphere of at an initial temperature $T_o$, and where $\kappa$ is thermal diffusivity; $T_1$ the initial temperature of the host rock; $r$ distance measured from the centre of the intrusion and $RR$ the radius of the intrusion. This equation is used in Section 4 to compare magma solidification with crystal residence times.

Crystal size distribution (CSD; Marsh, 1988) studies can also provide time information. However, one should keep in mind that the times are directly dependent on an arbitrarily chosen growth rate, which can be a variable (e.g., Cashman, 1991; Lasaga, 1998). The common syn-eruptive fragmentation of crystals during explosive eruptions can also make the results difficult to interpret (e.g., Bindeman, 2005). First-order inferences about magma residence times are the periodicity or time gaps between two successive eruptions from the same system (Smith, 1979; Bacon, 1982).

> ## 3. Residence Times of Magmas Associated with Selected Calderas

The caldera complexes (Figure 1) are described from the youngest to the oldest. Each section contains a brief introduction to the main geological and petrological features of the system and is followed by the residence times and process rates. The data sources are cited in the text and/or shown in Tables 3–8 and Figures 3–8.

## 3.1. Taupo volcanic zone

The Taupo volcanic zone (New Zealand) is 300 km long and up to 60 km wide and lies above a subduction zone. At least 34 caldera-forming events have produced a complex of overlapping volcanic centres over 1.6 My, with a total estimated volume of 15,000–20,000 km$^3$ (Figure 3). Houghton et al. (1995) presented the following eruptive history: (1) Period I from 1.68 to 1.53 Ma is the earliest ignimbrite volcanism. Three units erupted from the Mangakino volcanic centre and a fourth from an eastern source. (2) Period II (1.21–0.89 Ma) during which two of the largest ignimbrites were erupted (e.g., Ongatiti). The main active centres were Mangakino and Kapenga. (3) Period III (0.34 Ma –present) includes the voluminous ignimbrites (300–1,000 km$^3$) of the Whakamaru group at ca. 330 ka, and the Oruanui eruption at 26.5 ka (Figure 3). Pre-eruptive temperatures for dacitic to rhyolitic compositions vary between 940 and 730°C, whereas their liquidus obtained with the whole-rock compositions are about 1–60°C higher (Smith et al., 2005).
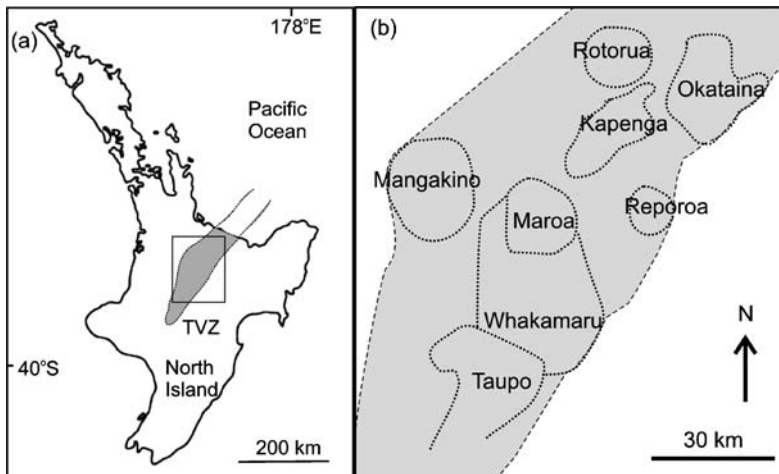


**Figure 3**   Location of Taupo Volcanic Zone (a), and of the main calderas (b), Maps modified after Houghton et al. (1995).

### 3.1.1. Eruptive products between 1.2 Ma and 300 ka

Brown and Smith (2004) reported zircon ages from the Ongatiti ignimbrite ($300–1,000\,km^3$; erupted at 1.21 Ma) ranging from 1.44 Ma to that of eruption, with a peak at 1.31 Ma. Although no systematic age differences between crystal cores and rims were found, the largest difference between eruption and the zircon ages is about 240 ky, and this is the maximum residence time (Table 3 and Figure 4). There are no rocks erupted at ca 1.40 Ma (Houghton et al., 1995) which means that if the old ages are partly inherited zircons, their sources cannot be identified on the surface. In a similar study, Brown and Fletcher (1999) reported the ages of zircons from the Whakamaru group ignimbrites ($300–1,000\,km^3$, erupted at ca. 340 ka). In this case the age of the crystal rims overlapped with that of eruption, but cores extended up to 608 ka, indicating residence times of up to 250 ky. These old ages cannot be correlated with any other erupted rock in the Taupo volcanic zone. The spectacular zoning in age from core to rim in these zircons is probably the best evidence for long magma residence times (see Figure 3 of Brown and Fletcher, 1999). However, there is also the possibility that some of the old ages are inherited from previous (but unerupted) magmas (Brown and Fletcher, 1999). A cooling rate of $5 \times 10^{-4}\,K\,y^{-1}$ has been calculated for the Type A low-silica Whakamaru ignimbrites from the temperature difference at the average pre-eruptive conditions ($790°C$, water content of ca 3 wt%, pressure of 150 MPa; Brown et al., 1998) and the liquidus at the same conditions ($915°C$, as calculated by MELTS; Ghiorso and Sack, 1995) over the residence time.

### 3.1.2. Eruptive products between 300 and 45 ka

Charlier et al. (2003) investigated the Rotoiti and Earthquake Flat events (ca. 100 and $10\,km^3$, respectively, both erupted at ca. 62 ka) using a combination of SIMS analyses of zircon and separated phases analysed by TIMS. They determined model ages (isochrons obtained with only two points) using U-Th series disequilibria. The results are complex, and the SIMS and TIMS ages on the same material do not always overlap. Comparison of eruption ages of Rotoiti with the TIMS zircon data gives 9 ky of residence time. The SIMS analyses show more spread in ages from about 50 to >350 ka. This may indicate that zircon crystallised up to eruption. Crystals older than 100 ky might be an inherited fraction rather than part of a continuous growth of a single magma body, and Charlier et al. (2003) concluded that the Rotoiti magma accumulated and crystallised zircon for a period of ca. 50 ky. The data from the Earthquake Flat eruption show residence times of about 100 ky and could mean that the magma was a largely crystalline pluton which was partly remobilised shortly prior to eruption (Charlier et al., 2003).

### 3.1.3. Eruptive products <45 ka

The ages of zircons from deposits erupted from the Taupo volcanic centre between 45 and 3.5 ka (including the Oruanui eruption) were investigated by Charlier et al. (2005). They found no significant age variation between crystal centres and rims.

**Table 3** Units, volumes, age data, residence times and process rates of the caldera-related silicic rocks of the Taupo volcanic zone.

| Taupo volcanic zone | Vol (km$^3$) | $^{40}$Ar/$^{39}$Ar, K–Ar or $^{14}$C age[a] (eruption) | Zircon U–Th disequilibrium model age (SIMS) | Zircon U–Th disequilibrium model age (TIMS) | U–Th disequilibrium bulk-rock, minerals or glass age | Zircon U–Pb age (SIMS) | Oldest ages | Magma residence time[b] | Magma production rate km$^3$ y$^{-1}$ (vol/residence time) |
|---|---|---|---|---|---|---|---|---|---|
| *Taupo volcano and caldera* | | | | | | | | | |
| Unit Y | 13.4 [W93] | 1.8 ka [F&L90] | | | 12.6 (+20.2/−16.7) ka [C00] | | | Unknown | |
| Unit S | 5.1 [W93] | 3.6 ka [W93] | | 29.7±1.1 ka [C05] | | | | Up to 26 ka | 2 × 10$^{-4}$ |
| Unit G | <0.21 [W93] | 6.7 ka [W93] | 9–>350 ka, peaks at 18, 43 and 109 ka [C05] | 40.7±0.7 ka–113.2±2.9 ka [C05] | | 92–527 Ma [C05] | | Up to 105 ky (w/oldest peak), up to 12 ky (w/youngest peak) | 2 × 10$^{-5}$–2 × 10$^{-6}$ |
| Unit E | 1.4 [W93] | 10.0 ka [W93] | | 18.9±0.6 ka–23.6±0.5 ka [C05] | | | | Up to 13 ky (w/oldest peak), up to 9 ky (w/youngest peak) | 2 × 10$^{-4}$–10$^{-4}$ |
| Unit D/Acacia Bay dome | 0.06 [W93] | 11.4 ka [W93] | | 25.4±0.6 ka and 27.9±1.1 ka [C05] | | | | Up to 15±1 ky | 4 × 10$^{-6}$ |
| Unit B | 0.42 [W93] | 11.8 ka [W93] | ca. 12–100 ka, peaks at 23 and 34 ka [C05] | 16.0±0.9–23.8±0.6 ka [C05] | | | | Up to 22 ky (w/oldest peak), up to 4 ky (w/youngest peak) | 10$^{-4}$–2 × 10$^{-5}$ |
| Unit Omega | 0.03 [W93] | 20 ka (bracket only) [N03] 18.8 ka [W93] | ca. 30–>350 ka [C05] | | | 244 ka–524 Ma [C05] | | No clear peak | |
| Oruanui eruption | 530 [W01] | 26.5 ka [W88 & W01] | <26.5–200 ka, peaks at 32–39 ka and 94–96 ka [C05] | 32.0±0.5–36.9±1.0 ka [C05] | 33 (+18/−16) ka [C05] | | | Up to 70 ky (w/oldest peak), up to 4 ky (w/youngest peak), min. *ca.* 2.5 ky [C05], max. *ca.* 40 ky [C05], | 1.3 × 10$^{-1}$–7.5 × 10$^{-3}$ |

**Table 3** (*Continued*)

| Taupo volcanic zone | Vol (km³) | ⁴⁰Ar/³⁹Ar, K–Ar or ¹⁴Cᵃ age (eruption) | Zircon U–Th disequilibrium model age (SIMS) | Zircon U–Th disequilibrium model age (TIMS) | U–Th disequilibrium bulk-rock, minerals or glass age | Zircon U–Pb age (SIMS) | Oldest ages | Magma residence timeᵇ | Magma production rate km³ y⁻¹ (vol/residence time) |
|---|---|---|---|---|---|---|---|---|---|
| Poihipi/ Rubbish Tip Dome | 0.5 [F&L90] | 27.3 ka [N03] | 40–52 ka [C05] | <27–*ca.* 90 ka peak at 54 ka [C05] | | | | Up to 27 ky (w/oldest peak), up to 13 ky (w/youngest peak) | $2 \times 10^{-5}$–$4 \times 10^{-5}$ |
| Okaia | 3 [F&L90] | 29 ka [N03] | 47–69 ka [C05] | <27–*ca.* 180 ka peaks at 27 and 95 ka [C05] | | | | Up to 65 ky (w/oldest peak), up to 18 ky (w/youngest peak) | $2 \times 10^{-4}$–$5 \times 10^{-5}$ |
| Tihoi | 3 [F&L90] | *ca.* 45 ka [CJNW] | 63–76 ka [C05] | 45–*ca.* 200 ka, peaks at 61 and 104 ka [C05] | | | | Up to 50 ky (w/oldest peak), up to 18 ky (w/youngest peak) | $2 \times 10^{-4}$–$6 \times 10^{-5}$ |
| *Another caldera?* | | | | | | | | | |
| Earthquake flat | 10 [C03] | inferred *ca.* 62 ka [C03] | 70 (+34/−26) ka–>350 ka [C03] | | 173±5 ka [C03] | | | *ca.* 100 ky | $10^{-4}$ |
| *Okataina volcano and caldera* | | | | | | | | | |
| Kapenga volcano | | | | | | | | | |
| Rotoiti xenoliths | | | 60–90 ka [C03] | | 57±8 ka [C03] | | | | |
| Rotoiti | 100 [C03], 120.5 [F&L90] | 62±2 ka [C03] | 50±24 ka to >350 ka, peaks at 70 to 90 ka, mean=83±14 ka [C03] | | 69±3–76±6 ka, mean=71±2 ka [C03] | | | Bulk mean=9±2 ky, zircon ca. 50 ky [C03] | $1 \times 10^{-2}$–$2 \times 10^{-3}$ |
| *Whakamaru caldera* | | | | | | | | | |
| Whakamaru group ignimbrites | 300–1000 [H95] | 320–340 ka [H95] | | | | 346±21 ka (rims)–608±20 ka (cores) [B&F99] | | Up to 250 ky [B&F99] | $10^{-3}$–$4 \times 10^{-3}$ |
| *Mangakino caldera* | | | | | | | | | |
| Ongatiti | 300–1000 [H95] | 1.21±0.04 Ma [H95] | | | | 1.18–1.44 Ma, peak 1.31±0.03 Ma [B&S04] | 119–340 Ma [B&S04] | Up to 240 ky | $10^{-3}$–$4 \times 10^{-3}$ |

*Note:* If both ⁴⁰Ar/³⁹Ar and K–Ar ages are available only the former are given. ¹⁴Cᵃ age determinations are calendar calibrated; Vol = Volumes in dense rock equivalent. ᵇthis is taken as the difference between the eruption ages and those of other radioactive clocks (e.g., U–Th–Pb). w/=with. Data sources: [B&F99], Brown and Fletcher (1999); [B&S04], Brown and Smith (2004); [CJNW], unpublished data of C.J.N. Wilson (cited in Charlier et al., 2005); [C00], Charlier (2000); [C03], Charlier et al. (2003); [C05], Charlier et al. (2005); [F&L90], Froggatt and Lowe (1990); [H95], Houghton et al. (1995); [N03], Newnham et al. (2003); [W88], Wilson et al. (1988); [W93], Wilson (1993); [W01], Wilson (2001).
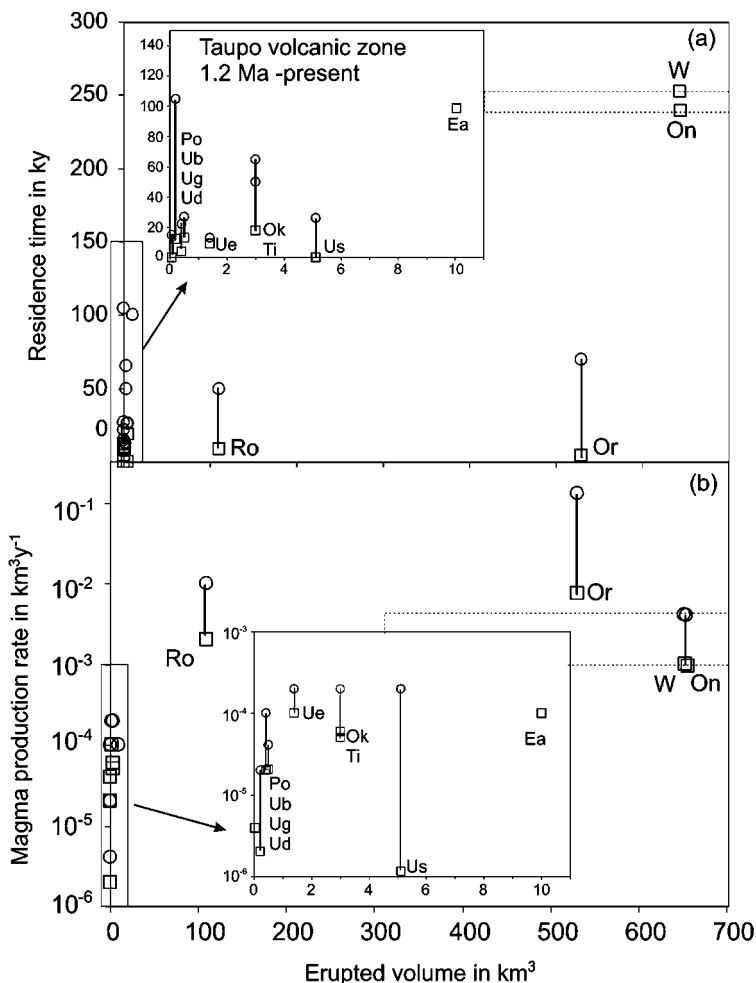
**Figure 4** Taupo Volcanic Zone. (a) Erupted volume versus residence time. Dots are maxima and squares the minima values (or single estimates), and lines are shown connecting the two. The dashed lines show the uncertainties on the estimated volumes for the large Whakamaru and Ongatiti ignimbrites. Inset is a magnification of the zone shown in the box. Abbreviations for the units: On, Ongatiti, W, Whakamaru, Ro, Rotoiti, Ea, Earth quake flat, Ti, Tihoi, Ok, Okaia, Po, Poihipi, Or, Oruanui, Ub, Unit B, Ud, Unit D, Ue, Unit E, Ug, Unit G, Us, Unit S. (b) Erupted volume versus magma production rate ( = erupted volume/residence time). Large eruptions tend to have higher magma production rates. This could be explained by recycling of old zircons in smaller eruptions, a real difference in magma fluxes, or by the pre-caldera deposits being issued from same reservoir as the caldera collapse magma (see discussion Section 4). Data sources are in Table 3.

In detail, the age data are rather convoluted, with typically multiple age peaks within a single deposit, the peaks defined by SIMS results are not always as those defined by TIMS. The youngest ages of many deposits overlap with eruption (e.g., the Oruanui eruption), although the youngest crystals can be also ca. 15 ky

older (e.g., Taupo units D and E). If we neglect crystals older than 0.5 My, most zircons have maximum model ages of up to 200 ka. Moreover, when all the data are taken together, there are two peaks, at about 35 and 100 ka. These peaks do not correspond to any eruption and thus if some of the old zircons are inherited from previous magmas these were never erupted. The exceptions are the 100 ka ages found in the deposits of three consecutive eruptions of Tihoi, Okaia, and Oruanui. This might reflect that they share a similar (common?) reservoir or petrogenetic history (see Section 4).

   The residence times were calculated using the oldest and the youngest zircon peak ages determined by Charlier et al. (2005) either by SIMS or TIMS data, and they vary between 13 and 100 ky (Table 3). The residence of the Oruanui magma can be up to ~70 ky, but can also be as short as 4–26 ky if the youngest peak ages as used (Figure 4). Charlier et al. (2005) argue that the zircon model ages at ca. 100 ka are from inherited crystals from previous but young intrusive episodes, and they propose residence times that are somewhat intermediate between the two extremes noted above. Moreover, they suggest that bimodal (or multi-modal) zircon model age spectra indicate remobilization of zircons from a crystal mush, rather than a long-lived magma body. Perhaps the complexities of the data partly reflect the current limitations in spatial resolution and precision of the analytical techniques. For example, the detailed in situ zircon age data for the Whakamaru group ignimbrites (Brown and Fletcher, 1999; their Figure 3) shows crystals with ages that progressively decrease from core to rim (e.g., with no jumps). If this is the case, one would expect no modality in the age distribution, and the origin of the bimodality found by Charlier et al. (2005) in the Whakamaru data is unclear (their Figure 22a).

   The cooling rate of the Oruanui magma obtained from the difference between the pre-eruptive temperature of $760^{\circ}$C (water content of 4.5 wt% and pressure of 150 MPa; Wilson et al., 2006) and the liquidus ($830^{\circ}$C, as calculated by MELTS; Ghiorso and Sack, 1995) over the range of residence times varies between $2 \times 10^{-2}$ and $10^{-3}$ K y$^{-1}$. This is almost two orders of magnitude higher than for the Whakamaru ignimbrites discussed above (Table 1). The calculated magma production rates (Figure 4) range from $< 10^{-5}$ for small eruptions up to 0.1 km$^3$ y$^{-1}$ for the Oruani, the highest found in all caldera related magmas (e.g., Table 1).

## 3.2. Toba Caldera complex

The Toba Caldera complex is located in Sumatra, Indonesia, in a subduction-zone setting. During the past 1.2 Ma, at least 3,400 km$^3$ of magma have been erupted in four ash-flow units, three from the Toba caldera (Chesner and Rose, 1991; Chesner, et al., 1991; Chesner, 1998). The tuffs are compositionally zoned from minor andesite to predominant rhyolite with relatively high crystal content (12–40 wt%; Chesner, 1998). Toba is the largest resurgent quaternary caldera on Earth, measuring 100 km by 30 km, and was the source of the voluminous (2,800 km$^3$) Youngest Toba Tuff at 73 ka (Table 4). Chesner (1998) reports pre-eruptive conditions of 701–780$^{\circ}$C, 300 MPa, and magmatic water content of

**Table 4** Units, volumes, age data, residence times and process rates of the Toba silicic caldera complex.

| Toba caldera complex | Vol (km³) | $^{40}$Ar/$^{39}$Ar, K–Ar, F–T[a] or Oxis[b] age (eruption) | Allanite U-Th disequilibrium age (SIMS) | Oldest ages | Magma residence time[c] | Time from diffusion modeling | Magma production rate km³ y$^{-1}$ (vol/residence time) |
|---|---|---|---|---|---|---|---|
| Youngest Toba Tuff [R&C87] | 2800 [R&C87] | 73±4 ka (San [C91]) 68±7[a] ka (ash, [C91]) 74±3 ka (San [N78]) 75±12 ka (Bt [N78]) 75[b] ka [N78] 75±7 ka (San [G02]) 78±6 ka (Bt [G02]) | 66±7 ka (rims)–236±16 ka (cores) [V&R04] | 1.5 Ma (Hbl [G02]) ca. 450 ka (Plag [G02]) | Up to ca. 160 ky [V&R04] | <25 y [G02] | $1.8 \times 10^{-2}$ |

*Note:* If both $^{40}$Ar/$^{39}$Ar and K–Ar ages are available only the former are given. [a]F–T, Fission track date; [b]Oxis, astronomically tuned oxygen isotope stratigraphy, Vol, Volumes in dense rock equivalent. [c]this is taken as the difference between the eruption ages and those of other radioactive clocks (e.g., U–Th–Pb). calc., calculation, Plag, plagioclase, Hbl, hornblende, San, sanidine, Bt, biotite. Data sources: [C91], Chesner et al. (1991); [C&R91], Chesner and Rose (1991); [G02], Gardner et al. (2002); [N78], Ninkovich et al. (1978); [R&C87], Rose and Chesner (1987); [V&R04], Vázquez and Reid (2004).

5–6 wt%. The liquidus calculated with MELTS (Ghiorso and Sack, 1995) vary between 840 and 970°C.

### 3.2.1. Unfolding the building stages of large silicic magma bodies

The Youngest Toba Tuff was investigated for its residence time using U-series disequilibria measured in allanite by SIMS (Vazquez and Reid, 2004). The crystals are zoned in age and composition, from cores with ages at 100–236 ka and rims with eruption ages. This gives magma residence times of up to 160 ky (Figure 1 of Vazquez and Reid, 2004). Combining the allanite's age and compositional zoning Vazquez and Reid (2004) calculated magma fractionation rates of 0.1–0.4% per ky. Moreover, they proposed a magmatic history consisting of a quiescent early period followed by multiple episodes of mixing of melts differentiated to different degrees. The development of the chemical zoning of the deposits seems to have occurred close to eruption. Calculated cooling rates are $0.8–1.1 \times 10^{-3}\,\mathrm{K\,y}^{-1}$, and magma production rates are ca. $0.02\,\mathrm{km^3\,y}^{-1}$ (Table 1).

The eruption age of the Youngest Toba Tuff has been determined by $^{40}\mathrm{Ar}/^{39}\mathrm{Ar}$ and K–Ar using sanidine and biotite with consistent results between laboratories (Table 4). However, the $^{40}\mathrm{Ar}/^{39}\mathrm{Ar}$ data of Gardner et al. (2002) on hornblende and plagioclase indicates ages of up to 1.5 Ma. This result, together with experimental work, was interpreted evidence for the hornblende and part of the plagioclase being xenocrystic. Gardner et al. (2002) calculated that about 25 years is the maximum time that plagioclase crystals of 1.5 Ma would be able to retain any old age, and thus this is the maximum time since xenocrysts incorporation and eruption. An alternative interpretation for the age data is that sanidine and biotite were as old and from the same source as the hornblende and plagioclase xenocrysts (perhaps of an earlier intrusion?) but their ages were completely reset to that of eruption because of their lower closure temperatures (Figure 2).

## 3.3. Yellowstone calderas

The Yellowstone volcanic field encompasses part of the USA states of Wyoming, Idaho and Montana and its caldera-related activity about 2 My ago. Volcanism could be related to a hotspot but not necessarily a plume (e.g., Christiansen et al., 2002). The geologic history defines three caldera cycles, each culminating with the eruption of a voluminous rhyolitic ash–flow (e.g., Christiansen, 2001). The three major caldera-forming eruptions (Table 5; Figure 5) have been dated at 2.0 Ma (Huckleberry Tuff; $2,500\,\mathrm{km^3}$), 1.3 Ma (Mesa Falls Tuff; Henrys Fork Caldera; $280\,\mathrm{km^3}$) and 0.6 Ma (Lava Creek Tuff; Yellowstone caldera; $1,000\,\mathrm{km^3}$). Yellowstone caldera-related magmas are stored at shallow levels, have low water contents, and pre-eruptive temperatures between 810 and 940°C (Hildreth, 1981; Hildreth et al., 1984; Bindeman and Valley, 2001). These are only 10–35°C lower than the liquidus of the bulk-rocks calculated using MELTS (Ghiorso and Sack, 1995; Bindeman and Valley, 2001).

**Table 5**  Units, volumes, age data, residence times and process rates of the Yellowstone caldera system.

| Yellowstone system | Vol (km³) | ⁴⁰Ar/³⁹Ar or K–Ar age (eruption) | Zircon U–Pb or U–Th disequilibrium age (SIMS) | Oldest ages | Magma residence time[a] | Time from diffusion modeling | Magma production rate $km^3\,y^{-1}$ |
|---|---|---|---|---|---|---|---|
| Pitchstone Plateau | <50 [C01e] | 70±2 ka [O92] | 101(+11/−10) ka [V&R02] | Up to 350 ka [V&R02] | 30±11 ky | | $<1.6 \times 10^{-3}$ |
| Solfatara Plateau | <50 [C01e] | 110±3 ka [O92] | 167 (+12/−11) ka [V&R02] | Up to 300 ka [V&R02] | 57±12 ky | | $<8.7 \times 10^{-4}$ |
| West Yellowstone | <50 [C01e] | 120±3 ka [O92] | 163 (+20/−17) ka [V&R02] | Up to 199 ka [V&R02] | 40±18 ky | | $<1.2 \times 10^{-3}$ |
| Dry Creek | <50 [C01e] | 160±2 ka [O92] | 167(+26/−21) ka [V&R02] | Up to 280 ka [V&R02] | 7–20 ky | | $<2.5 \times 10^{-3}$ |
| Tuff of Sulphur Creek | <50 [C01e] | 0.479±0.010 Ma [G96] | | Up to 370 Ma [G96] | | <2 y [G96]* | |
| Canyon Flow | <50 [C01e] | 0.484±0.041 Ma [G96] | 0.53–0.63 Ma [B01] | 92–97 Ma [B01] | 46–146 ky | 0.5–5 ky [B&V01] | $<3.3 \times 10^{-4}$ |
| Dunraven Road Flow | <50 [C01e] | 0.486±0.041 Ma [G96] | 0.54–2.15 Ma [B01] | 3.52±0.2 Ma [B01] | 54 ky–1.6 My | 0.5–5 ky [B&V01] | $<9.2 \times 10^{-4}$ |
| Middle Biscuit Basin Flow | <50 [C01e] | 0.516±0.06 Ma [G96] | 0.516–2.03 Ma [B01] | | 60 ky–1.5 My | 0.5–5 ky [B&V01] | $<8.3 \times 10^{-4}$ |
| South Biscuit Basin Flow | <50 [C01e] | n.d. (between 0.6 and 0.5 Ma) | | | | 0.5–5 ky [B&V01] | |
| Lava Creek Tuff | 1000 [C01] | 0.640±0.002 Ma [L02] 0.602±0.004 Ma [G98] | 0.659±0.044 Ma [B01] | Up to 1 Ma [G98] | 19–57 ky | | $1.7–5.2 \times 10^{-2}$ |
| Mesa Falls Tuff | 280 [C01] | 1.304±0.011 Ma [L02] 1.293±0.012 Ma [G98] | 1.463±0.046 Ma [B01] | Up to 1.7 Ma [G98] | 160–170 ky | | $1.6–1.8 \times 10^{-3}$ |
| Blue Creek Flow | | 1.75, 1.78 Ma [O92] | 1.87–2.2 Ma [B01] | 64±1 Ma [B01] | 120–450 ky | 10 ky [B&V01] | |
| Huckleberry Tuff | 2500 [C01] | 2.057±0.002 Ma [L02] 2.003±0.014 Ma [G98] | 2.134±0.234 Ma [B01] | | 77–234 ky | | $1.0–3.2 \times 10^{-2}$ |

*Notes*: If both ⁴⁰Ar/³⁹Ar and K–Ar ages are available only the former are given. Vol, Volumes in dense rock equivalent. * These data refer to one multiple geographically related units. calc., calculation, Plag, plagioclase, Zrc, zircon, Qtz, quartz. Data sources: [B01], Bindeman et al. (2001), [B&V01], Bindeman and Valley (2001), [C01], Christiansen (2001), [G96], Gansecki et al. (1996), [G98], Gansecki et al. (1998), [L02], Lamphere et al. (2002), [O92], Obradovich (1992), [V&R02], Vazquez and Reid (2002). [C01e], the volumes are rough estimates from the publication of Christiansen (2001). ᵃThis is taken as the difference between the eruption ages and those of other radioactive clocks (e.g., U–Th–Pb).
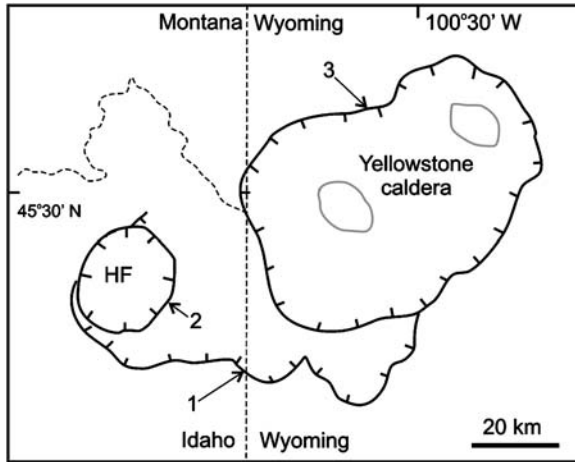
**Figure 5** Location of the Yellowstone magmatic system with the tectonic features related to the three caldera collapse cycles (I, II, III; hachure towards collapse) and their respective tuffs. I is related to Huckleberry, II to Mesa Falls, and III to Lava Creek. Also shown are the two resurgent domes of Yellowstone caldera in gray. HF, Henry's Fork caldera. Figure modified after Christiansen (2001).

### 3.3.1. Residence times of the caldera-forming Huckleberry, Mesa Falls and Lava Creek magmas

The residence times of the main tuffs (Figure 6 and Table 5) were obtained from the eruption dates and the zircon ages reported by Bindeman et al. (2001). The ages of these two events overlap for the Huckleberry Tuff, although the error of the U–Pb zircon age still allows 77–234 ky of residence time. The data on the Mesa Falls magma gives a residence time of ca. 165 ky, and ca. 60 ky for the Lava Creek magma. The calculated cooling rates are $0.4 \times 10^{-4}$–$2 \times 10^{-3} \, K \, y^{-1}$, and magma production rates vary between 0.002 and $0.01 \, km^3 \, y^{-1}$ (Table 5 and Figure 3).

### 3.3.2. Residence times of the post-caldera magmas (mainly <0.6 Ma)

The relatively close agreement between the U–Pb and $^{40}Ar/^{39}Ar$ ages for the three major tuffs contrasts with the variety and spread of ages for the presumably small ($< 50 \, km^3$ ?) post-caldera magmas (Figure 6). For example, three units erupted between 0.51 and 0.48 Ma contain zircons with ages ranging from those of eruption but can be as old as the Huckleberry Tuff (Bindeman et al., 2001). This gives residence times that are incredibly long (450 ky–1.6 My). The simplest explanation is that some of the zircons in these post-caldera units are recycled from the major tuffs. This is in accord with the $\delta^{18}O$ disequilibrium between minerals and glass of the post-caldera units found by Bindeman and Valley (2001). They proposed that the change towards low $\delta^{18}O$ values after caldera collapse was due to complete melting of hydrothermally altered rocks that were part of the down-dropped block. Bindeman and Valley (2001) used a diffusion model to obtain 500–5,000 years for
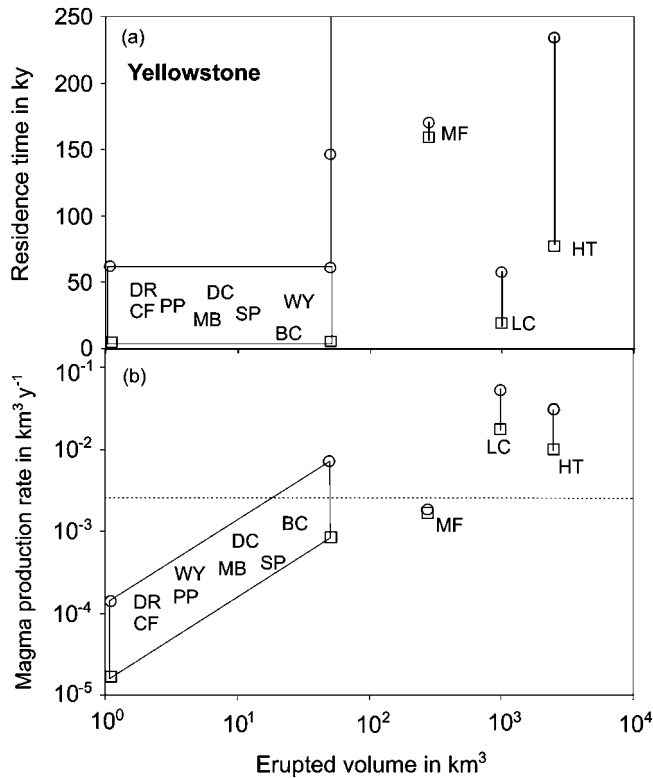
**Figure 6**  Yellowstone system. Erupted volume vs. (a) residence times and (b) magma production rates. Circles are maxima and squares the minima values (or single estimates), and lines are shown connecting the two. The data of the maximum estimates (>0.4 My) for Blue Creek (BC), Middle Biscuit (MB) and Dunraven Road (DR) are not shown. The deposits from two eruptions at ca. 115 ka (Solfatara Plateau, SF, and West Yellowstone, WY) show inherited zircon crystals from the previous one at 160 ky (Dry Creek, DC; Vazquez and Reid, 2002). Abbreviations for the units are: MF, Mesa Falls Tuff, LC, Lava Creek Tuff, CF, Canyon flow, PP, Pichstone Plateau. The volumes of the small eruptions are estimated from the publication of Christiansen (2001) to be <50 km$^3$ and are only very rough values and thus they are shown as a box. There does not seem to be a correlation between volume and residence times, although larger eruptions seem to have higher magma production rates. Data sources are in Table 5.

the time since total melting and eruption of the post-caldera lavas, and requires heating rates of $3 \times 10^{-1}$–$3 \times 10^{-2}$ K y$^{-1}$. These melting times are about an order of magnitude shorter than the lowest estimate of the residence times (ca. 50 ky).

The residence times of much younger post-caldera deposits (the so-called Central Plateau Member, 70–160 ka) were investigated by Vazquez and Reid (2002). They found that none of the zircons were related to any of the three major collapse caldera tuffs. The eruption age of the oldest investigated flows overlap with the zircon $^{238}$U–$^{230}$Th disequilibrium ages, although the precision of the data still allow residence times of several ky (Table 5, Figure 6). For flows erupted down to 110 ka they found zircon model ages (isochrons obtained with two points) at ca. 167 ka implying residence times of ca. 50 ka and probably crystal recycling from

previously erupted post-caldera magmas. In contrast, the youngest flow erupted at 70 ka contains zircons with model ages at 101 ka and indicates a new zircon crystallisation episode. Combining this age information with the changes of Sr and Nd isotopes or element ratios indicative of magma evolution, Vazquez and Reid (2002) proposed that the magmatic system of the Central Plateau member might have been differentiating for $>100$ ky.

Finally, the $^{40}Ar/^{39}Ar$ data reported by Gansecki et al. (1996, 1998) shows the presence of sanidine and plagioclase xenocrysts (up to 370 My old). Diffusion calculations indicate maximum times for immersion in magma of a couple of years or less. Such short times were interpreted as xenocrysts entrapment during fracturing and conduit propagation (Gansecki et al., 1996).

## 3.4. Long Valley system

The Long Valley volcanic field is located in east-central California, within and east of the Sierra Nevada. It is part of an active regional transtensional zone at the Sierra Nevada-Basin and Range transition (e.g., Bailey et al., 1976; Bailey, 2004; Hildreth, 2004). Hildreth (2004) distinguished six successive foci of silicic volcanism driven by basaltic intrusion of the deep crust, the location of which has moved repeatedly. The simplified chronology of events involves (1) a pre-caldera dacite field (2.5–3.5 Ma) and the Glass mountain rhyolites ($\sim$100 km$^3$; 0.79–2.2 Ma), (2) caldera collapse and eruption of the Bishop Tuff (600 km$^3$; 0.76 Ma) and (3) a long history of post-caldera volcanism, starting with the Early Rhyolite (ca. 100 km$^3$, 650–760 ka), and followed by series of small volume Moat Rhyolites (101–527 ka). In younger times, there are two distinct focus of activity at the Mono Craters chain and Inyo domes (Holocene to ca. 50 ka), and Mono Lakes (0.25–14 ka) (Figure 7). The volume of deposits $<650$ ka is ca. 7–8 km$^3$ (Hildreth, 2004). The reader is referred to Reid (2003) for a summary of residence time data in Long Valley and also to Simon and Reid (2005) for the most recent data and interpretation.

### 3.4.1. Pre-caldera magmas: petrological attributes and time scale information
Glass Mountain includes $>60$ phenocryst poor ($<5$ wt%) high-silica rhyolite flows. They comprise an old sequence (2.2–1.3 Ma) of variable compositions and erupted from discrete magma bodies, and a young sequence (1.2–0.79 Ma) which is compositionally similar to the most evolved units of the Bishop Tuff and thus probably issued from the same reservoir (Metz and Mahood, 1985, 1991; Hildreth, 2004). Pre-eruptive conditions for these magmas are ca. 700–770°C, ca. 200 MPa, and water contents of 2.5–6 wt% (Metz and Mahood, 1991).

*3.4.1.1. Residence times of the pre-caldera magmas.*   Current interest in the application of geochemical methods to determine the residence times of silicic magmas probably started with the study of pre-caldera lavas of Glass Mountain and the publication of Halliday et al. (1989). They obtained Rb–Sr isochrons of ages from ca. 1 to 2 Ma. These overlapped with eruption ages of the oldest lavas available at that time (K–Ar; Metz and Mahood, 1985) but also implied residence times of ca.
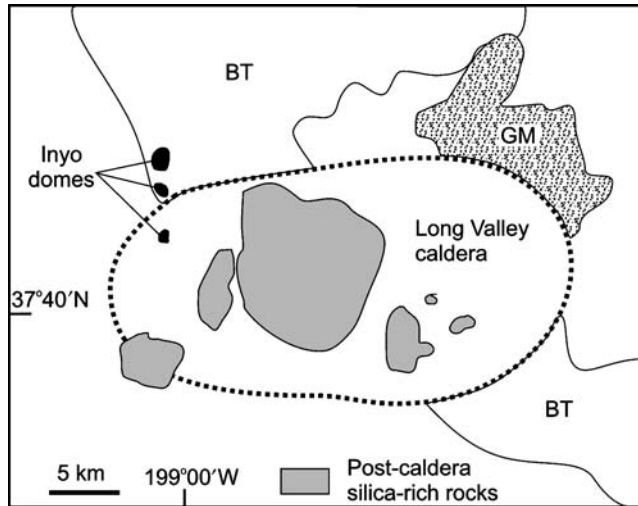
**Figure 7**    Very simplified map showing Long Valley caldera (topographic margin) and the main units discussed in the text. BT, Bishop Tuff, GM, Glass Mountain (pre-caldera). Figure based on Bailey (1989) and on a simplified map published on the USGS web page.

0.3 My for the younger lavas, and up to 0.7 My for the old lavas. Halliday et al. (1989) proposed that high Rb/Sr values and low Sr concentrations of the lavas were due to extreme crystal fractionation and the isochrons were dating such a process. The geochemical similarity of the younger Glass Mountain lavas and the Bishop Tuff led them to suggest that the chamber containing the magma later to erupt as the Bishop Tuff was already formed, including the chemical zoning, by about 1.1 Ma. This implied the existence of relatively small volumes of mostly liquid magma at shallow depths for long periods of time. Sparks et al. (1990) raised questions on the Halliday et al. (1989) interpretation mainly related to the feasibility of keeping such volumes of magma in a mostly liquid state without freezing in the upper crust. Their alternative interpretation was that the silicic magmas were the result of remelting of a granite source region (presumably in deep portions of the crust) where they develop the 'old isochrons' but the residence times in the shallow crust could be short. In a new model by Mahood (1990) the volumes of erupted rhyolites were small compared to the size of the entire reservoir, minimising the thermal problems of keeping small and mainly liquid magma batches for a long time in the shallow crust. Moreover, Mahood (1990) argued that parts of the reservoir can be 'frozen' as crystallised rind or immobile mush, and a portion can be 'defrosted' for eruption at a later date by input of new magma without causing the magma to be shifted off the isochron. Thus, the long residence times could be explained if the erupted magmas were solidified in the upper crust for some time and later remelted close to eruption.

Davies et al. (1994) and Davies and Halliday (1998) reported more precise $^{40}$Ar/$^{39}$Ar and Rb–Sr and Sm–Nd isotope data, and the residence times for the Glass Mountain magmas were reduced to about half that originally proposed, with a maximum time of ca. 350 ky (Table 6). Moreover, Davies et al. (1994) and

**Table 6** Units, volumes, age data, residence times and process rates of the Long Valley system.

| Long Valley Caldera | Vol (km³) | ⁴⁰Ar/³⁹Ar, K–Ar or ¹⁴C age (eruption) | Zircon U–Th disequilibrium model age (SIMS) | U–Th disequilibrium isochron age | Zircon U–Pb age (SIMS and TIMS) |
|---|---|---|---|---|---|
| *Postcaldera* | | | | | |
| Inyo dome (South dead man) | 0.13 [M85] | ca. 0.6 ka [M85]* | 30–278 ka [R97], 208±18 ka [R97] | | |
| Mammoth knolls domes | <1 [H04] | 110±22 ka–97±12 ka [M86], 110±3 ka [H02] | | 139.1±5.3 ka– 143.8±0.9 ka [H02] | |
| Deer Mountain dome | <1 [H04] | 115±3 ka [M86], 101±8 ka [H02] | 120–375 ka [R97], 224±16 ka [R97] | 179.8±2.0 ka– 257.7±3.3 ka 235.6±1.2 ka [H02] | |
| West Moat Coulee (or Low Silica flow) | 4 [H04] | 151 and 147±4 ka [H02] | | 152.6±2.0 ka– 202.6±0.9 ka 175.6±12.9 ka [H02] | |
| *Caldera* | | | | | |
| Bishop Tuff (BT) | >600 [H79] | 762±12 ka [I&O94], 759±3 ka [P92], 760±1 ka [vdB&S95] | | | 811±7 ka (early BT [S&R05]), 823±11 ka (early BT [R&C00]), 841±8 ka (late BT [S&R05]) |
| *Precaldera* | | | | | |
| Glass mountain (GM) center Young Units | 100±20 [H04] | 2.1-0.79 Ma [M&M85] | | | |
| GM-Dome YA | <3 [M&M91e] | 790±20 ka [M&M85] | | | 981±18 ka [S&R05] |
| GM-Dome YG | <3 [M&M91e] | 900±30 ka [M&M85] | | | 933±17 ka [S&R05] |
| *Old units* | | | | | |
| GM-Dome OD | <2 [M&M91e] | 1.35±0.10 Ma [M&M85], 1.686±0.011 Ma [D94] | | | 1.853±0.013 Ma (interiors [S&R05]), 1.706±0.035 Ma (surfaces [S&R05]) |
| GM-Dome OL | <1 [M&M91e] | 1.6±0.1 Ma [M&M85], 1.867±0.005 Ma [D94] | | | |
| GM-Dome OC | <1 [M&M91e] | 1.92±0.05 Ma [M&M85], 1.999±0.012 Ma [D94] | | | |

*Notes:* If both ⁴⁰Ar/³⁹Ar and K-Ar ages are available only the former are given. Vol, Volumes in dense rock equivalent. [a]This is taken as the difference between the eruption ages and those of other radioactive clocks (e.g., Rb–Sr, U–Th–Pb). [b]These data refer not only to one dome but use multiple geographically related units. calc., calculation, San, sanidine, Bt, biotite, Qtz, quartz. Data sources: [A00], Anderson et al. (2000); [B&W02], Bindeman and Valley (2002); [C&D93], Christensen and DePaolo (1993); [C&H96], Christensen and Halliday (1996); [D94], Davies et al. (1994); [D&H98], Davies and Halliday (1998); [H79], Hildreth (1979); [H89], Halliday et al. (1989); [H04], Hildreth (2004); [H&D92], Hervig and Dunbar (1992), [H&D97], Heumann and Davies (1997); [H02], Heumann et al. (2002); [I&O94], Izett and Obradovich (1994); [M&M85], Metz and Mahood (1985); [M&M91e], Metz and Mahood (1991), the [e] means that no estimate was found in the literature, and the volumes were calculated from Figure 1of Metz and Mahood (1991) using a thickness of 0.5 km. [M85], Miller (1985); [M86], Mankinen et al. (1986); [M&B06], Morgan and Blake (2006); [P92], Pringle et al. (1992); [R97], Reid et al. (1997). Data of [R97] are including all zircons. [R&C00], Reid and Coath (2000); [S&R05], Simon and Reid (2005). Data of [S&R05] are mean values. [vdB&S95], Van den Bogaard and Schirnick (1995); [W01], Winick et al. (2001), [W07], Wark et al. (2007).

| Rb–Sr isochron age | Oldest ages | Magma residence time[a] | Time from diffusion modeling | Magma production rate km³ y⁻¹ (vol/ residence time) |
|---|---|---|---|---|
| | | 30–200 ky [R97] | | $<1 \times 10^{-6}$ |
| 277 ± 124 ka [H&D97][b] 257 ± 39 ka [H02][b] | | 167 ky [H&D97] 33–150 ky [H02] | | $<1 \times 10^{-5}$ |
| 277 ± 124 ka [H&D97][b], 188 ± 41 ka–277 ± 124 ka 257 ± 39 ka [H02][b] | | 177 ky [H&D97], ca. 88–125 ky [R97], up to 160 ky [H02] | | $<1 \times 10^{-5}$ |
| | | Up to 50 ky [H02] | | $8 \times 10^{-5}$ |
| 1.4–2.5 Ma (Early BT, [C&H96]), ca. 1.0 Ma (Late and intermediate BT [C&H96]), 0.77–1.15 Ma (feldspars, [D&H98]) | 2.3 ± 0.3 Ma [vdB&S95], ca. 210 Ma [R&C00], 3.7 ± 1.00 Ma [W01] | ca. 1.1 My [vdB&S95], ca. 300 ky [C&H96], ca. 390 ky [D&H98], ca. 100 ky [R&C00], 50–80 ky [S&R05] | $<10$ ky [H&D92], 100 ky– 1 My [A00], $<10$ ky [B&W02], 114 ky [M&B06] $<100$ y [W07] | $1.4 \times 10^{-3}$ [C&D93], 0.4–0.75 × 10⁻² [D&H98], $2 \times 10^{-3}$– $1 \times 10^{-2}$ [S&R05] |
| | | | | $0.75 \times 10^{-3}$ [D94 and D&H98] |
| 1.14 ± 0.08 Ma [H89][b], 1.15 ± 0.01 Ma [D&H98][b], 0.77–1.08 Ma (feldspars, [D&H98]) | | 0.35 My [H89], 0.36 My [D&H98], 190 ky [S&R05] | | $<1 \times 10^{-5}$ |
| 1.09 ± 0.03 Ma [D&H98][b], 0.84–1.01 Ma (feldspars, [D&H98]) | 1.4-2.1 Ma [S&R05] | $<17$ ky [S&R05], up to 0.3 My [D&H98] | | $<2 \times 10^{-4}$ |
| 2.09 ± 0.06 Ma [H89][b], 2.047 ± 0.013 Ma [D94][b] | | 0.7 My [H89], 0.36 My [D94], up to 170 ky [S&R05] | | $<1 \times 10^{-5}$ |
| 1.90 ± 0.02 Ma [H89][b] 1.894 ± 0.013 Ma [D94][b] | | 0.5 My [H89], 180 ky [D94] | | $<5 \times 10^{-6}$ |
| 2.09 ± 0.06 Ma [H89][b], 2.047 ± 0.013 Ma [D94][b] | | $<170$ ky [H89], $<50$ ky [D94], | | $<2 \times 10^{-5}$ |

Davies and Halliday (1998) found differences in crystallisation times between and within minerals of $<10\,ky$ (within error of most individual glass–mineral isochrons). Differences of $20$–$70\,ky$ (up to ca. $300\,ky$) between feldspar centres and rims were also found. They calculated crystal growth rates between $7 \times 10^{-13}$ and $9 \times 10^{-14}\,cm\,s^{-1}$.

More recent data of Simon and Reid (2005) show that ages of zircons rims overlap with eruption, but centres are up to $150\,ky$ older. The oldest zircon ages are significantly younger than those previously obtained by whole-rock–glass–minerals Rb–Sr isochrons (Figure 8), and thus reduce the residence times of the Glass Mountain magmas to a maximum of $190\,ky$ (Table 6 and Figure 8). The difference between the Rb–Sr and U–Pb ages could reflect that the minerals defining the Rb–Sr isochrons crystallised earlier than the zircons. However, recent interpretations (e.g., Simon and Reid, 2005) propose that the Rb–Sr model isochrons are not dating the crystal fractionation. They probably are the result of a complex history involving open system, including in situ $^{87}Rb$ decay in the reservoir and the presence xenocrysts.

### 3.4.2. Caldera magma: Bishop Tuff petrological attributes and time scale information

The Bishop magma was thermally (ca. $720$–$790°C$) and compositionally zoned in major and trace elements and also in $^{87}Sr/^{86}Sr$ values (Hildreth, 1979; Christensen and DePaolo, 1993; Hildreth and Wilson, 2007) prior to eruption. The first erupted units are crystal poor, colder and more evolved than the later ones (Hildreth, 1979). Water contents vary from ca. 6 to 4 wt% (Anderson et al., 1989), and a pressure of ca. $200\,MPa$ was determined for the roof of the reservoir (Wallace et al., 1999). The liquidus temperatures of the early and late magmas calculated with MELTS (Ghiorso and Sack, 1995) are ca. 795 and $855°C$, respectively. The origin of the zoning of the Bishop magma has been highly debated and investigated. Hildreth (1979) proposed that it resulted from convective circulation driven by thermogravitational diffusion, complexation and wall-rock exchange. Other interpretations include crystal liquid fractionation (Michael, 1983), side-wall crystallization (Wolff et al., 1990; Bindeman and Valley, 2002), wall-rock assimilation (Duffield et al., 1995) or mafic intrusion at the base of the reservoir (Hervig and Dunbar, 1992). Hildreth and Wilson (2007) have recently proposed that the zoning was created by numerous batches of crystal-poor melt released from a mush zone at the floor of the accumulating rhyolitic magma body. Crystal-melt fractionation was the dominant zoning process. A major role for a magma intrusion at the base of the reservoir for triggering the eruption of the Bishop Tuff has been recently proposed by Wark et al. (2007).

### 3.4.2.1. Residence times of the Bishop magma.

The study of residence times in the Bishop magma also started with a long estimate from Christensen and DePaolo (1993) who proposed a model of the Bishop magma being mainly liquid for long periods of time (e.g., $0.5\,My$) based on Rb–Sr isotope systematics. A later $^{40}Ar/^{39}Ar$ study by Van den Bogaard and Schirnick (1995) reported ages of glass inclusions in quartz at $1.9$–$2.3\,Ma$, and thus residence times $>1\,My$. A later
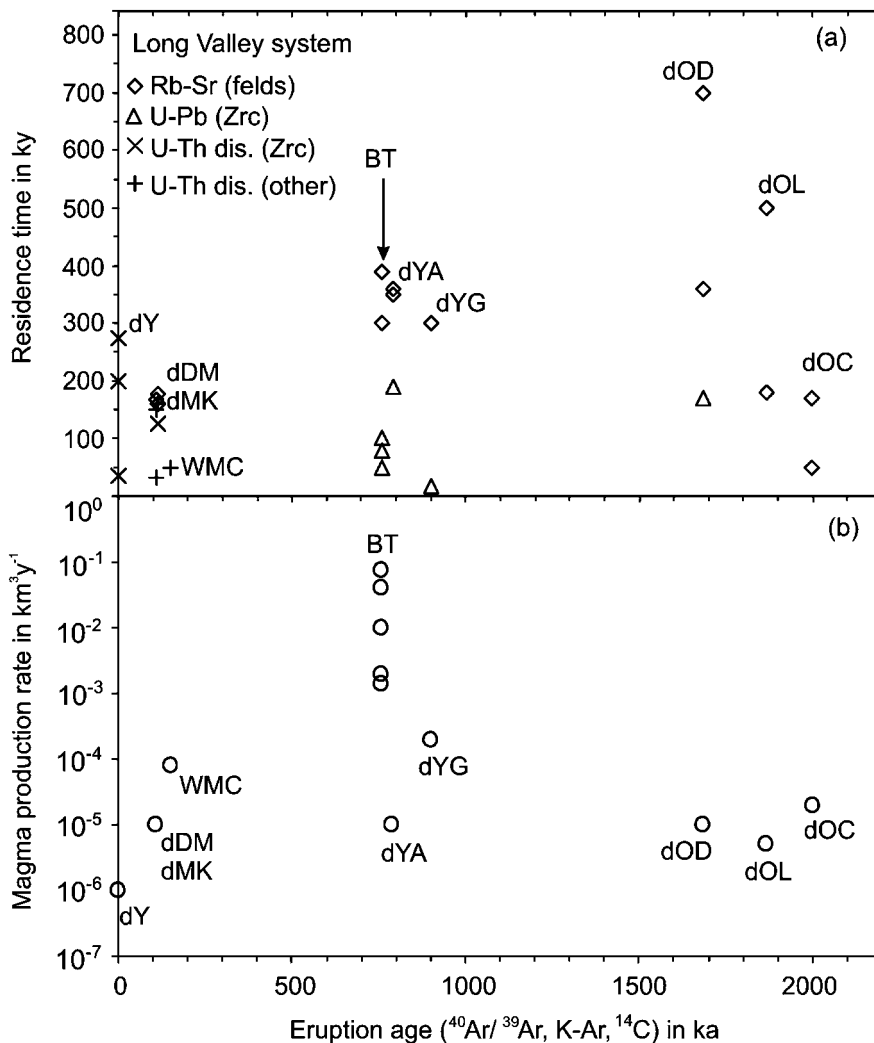
**Figure 8** Long Valley system. (a) Eruption ages obtained by K—Ar, $^{40}Ar/^{39}Ar$ and $^{14}C$ vs. calculated residence times for all ages obtained by other radioactive clocks (if K—Ar and $^{40}Ar/^{39}Ar$ ages were both available only the most recently published $^{40}Ar/^{39}Ar$ data have been used; see Table 6 for all data). The very long (ca. 1 Ma) residence times of Van den Bogaard and Schirnick (1995) are not shown. The residence times defined by the Rb—Sr feldspar ages are typically longer than U—Th—Pb system, although for some post-caldera units they overlap. Abbreviations used: felds, feldspar, Zrc, zircon, U—Th dis, U—Th series disequilibria, other, multi-minerals (including zircon or not) and glass isochrons. Units: dOC, Glass Mountain old dome C, dOL, Glass Mountain old dome L, dOD, Glass Mountain old dome, dYG, Glass Mountain young dome G, dYA, Glass Mountain young dome A, BT, Bishop Tuff, WMC, West Moat Coulee, dDM, Deer Mountain dome, dMK, Mammoth Knolls domes, dY, Inyo dome. (b) Eruption ages vs. calculated magma production rates which imply higher influx of magma for the Bishop Tuff compared to smaller pre- and post-caldera eruptions (see discussion Section 4). Data sources are given in Table 6.

$^{40}$Ar/$^{39}$Ar study on the same material (Winick et al., 2001) found even older ages at 4 Ma, but since the data were obtained using laser step heating, they were interpreted as the result of excess $^{40}$Ar presumably derived from degassing of old rocks. Why the Ar isotope compositions of the glass inclusion did not homogenize during residence times of several hundreds of ky is discussed in the next section.

Christensen and Halliday (1996) and Davies and Halliday (1998) measured the Nd and Sr isotopes of glass inclusions in quartz and assuming an initial $^{87}$Sr/$^{86}$Sr they obtained ages of 1.4–2.5 Ma for the early and ca. 1 Ma for the intermediate and late erupted units. This gave residence times of 250–450 ky (Table 6, Figure 8). They were also able to determine age differences between feldspar cores and rims of up to 250 ky.

Reid and Coath (2000) found a collective mean age (including rims and centre of crystals from different units) for zircon at ca. 820 ka, which gives a residence time of ca. 40 ky. This is about 10 times shorter than the time obtained from feldspars and the Rb–Sr system (Figure 8). Later, Simon and Reid (2005) reported mean ages for zircons that are 50–90 ky older than the eruption age, implying also residence times for the Bishop magma of < 100 ky. Simon and Reid (2005) cast doubts on the validity of the Rb–Sr isochrons and propose that the Sr isotope characteristics of the Bishop Tuff which were used to support inheritance from the Glass Mountain can be explained by radiogenic in growth and crystal growth from isotopically heterogeneous domains.

### 3.4.2.2. Diffusion studies applied to the time scales of processes of the Bishop magma.
Hervig and Dunbar (1992) calculated the time for complete homogenisation of Sr zoning in sanidine (e.g., using the relation: $x^2 = D \times t$) to be between 2 and 13 ky. Although it is a maximum time, it is about a factor of four smaller than the shortest residence time obtained from zircon U–Pb data (40–50 ky; Reid and Coath, 2000; Simon and Reid, 2005). Bindeman and Valley (2002) calculated that between 0.1 and 10 ky occurred since the last replenishment plus a fractionation event using CSD's of quartz and zircons and the presence of $\delta^{18}$O zoning in quartz. Anderson et al. (2000) used the trace element zoning patterns in sanidine to calculate complete equilibration times of 140 ky–2.8 My, whereas Morgan and Blake (2006) used the same crystals to obtain times of ca. 100 ky from a more detailed diffusion model. This last estimate agrees with the longer residence times obtained from zircon. The new diffusion model of Wark et al. (2007) based on Ti in quartz indicates that less than 100 years occurred since the last magma replenishment and eruption.

A remaining issue related to Bishop magma is why the $^{40}$Ar/$^{39}$Ar data on glass inclusion in quartz by Van den Bogaard and Schirnick (1995) and Winick et al. (2001) did not homogenise within the residence times on the order of 100 ky's (this should be the case if a simple $x^2 = D \times t$ relation is used for the calculations). This can be evaluated using the Ar solubility (crystal/melt) and volume diffusion data in quartz (Watson and Cherniak, 2003) and an analytical solution of diffusion of glass inclusions in a spherical crystal (Qin et al., 1992). Using a temperature of 750$^{\circ}$C and a ratio of 0.1–0.05 for the inclusion to the crystal radius,

with the inclusion located in the centre of a 500 μm (radius) sized crystal, it would take >0.5 My to homogenize 50% of the Ar isotopes. Thus, the presence of excess $^{40}Ar$ in some of the glass inclusion in quartz is consistent with residence times ca. of 100 ky for the Bishop magma and the example highlights the need of considering all parameters to retrieve time information from diffusion models.

### 3.4.3. Post-Caldera magmas: petrological attributes and time scale information

There is a long history of post-caldera silicic volcanism at Long Valley proper (e.g., Bailey et al., 1976; Bailey, 2004; Heumann, 1999; Hildreth, 2004; Mankinen et al., 1986; Ring, 2000). It started with the ca. $100 \, km^3$ of the Early Rhyolite (652–751 ka), and was followed by the Moat Rhyolite with ages of 481–527 ka, the Southeastern rhyolite cluster (329–362 ka), and the west Moat rhyolites (97–162 ka). Western post-caldera volcanism includes Mammoth Mountain (57–111 ka), mafic scoria cones and lavas (65–160 ka), a series of dacites (27–40 ka) and finally the Mono-Inyo chain (Holocene–20 ka, Wood, 1983; Miller, 1985). There is a time gap between ca. 160 and 320 ka without volcanic activity.

Reid et al. (1997) reported zircon model ages (two-point isochrons) for Deer Mountain ranging from eruption to 110 ky older (mean at 224 ka). For the South Dead Man dome (erupted at 0.6 ka) ages range from 30 to 278 ka, implying long residence times for such a small volume ($0.13 \, km^3$, Miller 1985). The similar ages found in the oldest parts of the zircons of both units could mean that the South Dead Man dome zircons are recycled from Deer Mountain. Notwithstanding, no deposits have been dated in that range and thus zircon ages between 200 and 300 ka are probably from crystals recycled from 'plutonic' magmas.

Heumann and Davies (1997) and Heumann et al. (2002) reported $^{40}Ar/^{39}Ar$, Rb–Sr and U-series disequilibria systematics for several post-caldera lavas. The West Moat Coulee (referred to by Heumann et al., 2002 as the Low Silica Flow) was the largest (ca. $4 \, km^3$) and oldest one (ca. 150 ka), and yields $^{238}U–^{230}Th$ isochrons that range from eruption age to ca. 200 ka, giving residence times of up to 50 ky (Table 6 and Figure 8). The data for the younger Deer Mountain and Mammoth Knolls (both at ca. 105 ka) define Rb–Sr isochrons at ca. 260 ka. This was interpreted as a feldspar fractionation and magma differentiation event where melts accumulated at the top of the reservoir where they remained for 150 ky prior to eruption. In contrast, the $^{238}U–^{230}Th$ isochrons from the two domes are different. Deer Mountain defines ages at ca. 235 ka which overlap with the Rb–Sr ages (when errors are taken into account) and also agrees with the zircon U–Th series disequilibria data of Reid et al. (1997). The Mammoth Knolls $^{238}U–^{230}Th$ isochron ages are at ca. 140 ka which is ca. 50 ky younger that the Rb–Sr ages. Heumann et al. (2002) explained age differences between radiogenic clocks and phases by considering a cooling history where feldspars and some zircon crystallised earlier (at a higher temperature) than the allanite which gives younger ages, and inferred maximum cooling rates between $7 \times 10^{-4}$ and $10^{-3} \, K \, y^{-1}$.

### 3.4.4. Summary of residence times for the Long Valley system

The chronology of the studies of residence times for the Long Valley system described above indicates that the residence times have been somehow getting shorter with publication year. The initially long estimates of half a million years or more for the pre-caldera and Bishop magmas obtained with the Rb–Sr system seem now to be probably not correct. They probably reflect the effects of in situ isotopic in growth of $^{87}$Sr and also the presence of xenocrysts and/or assimilation (e.g., Simon and Reid, 2005). Likewise, the long times of millions of years suggested by some $^{40}$Ar/$^{39}$Ar data appear to be the result of excess $^{40}$Ar (e.g., Winick et al., 2001) probably due to contamination from old rocks. The zircon age data indicates residence times for some pre-caldera and Bishop magmas of $< 100$ ky (e.g, Simon and Reid, 2005), and the longer estimates that have also been found in some zircons are probably reflecting recycling of crystals from previous intrusive episodes (see discussion Section 4).

## 3.5. Valles-Toledo complex

This system is located in the Jemez Mountains (New Mexico) on the margin of the Rio Grande rift. Here we are concerned only with the two major eruptions (Table 7; Smith and Bailey, 1966; Self et al., 1986, 1996; Spell et al., 1990, 1996). The lower Bandelier Tuff or Otowi Member (1.61 Ma, 400 km$^3$) is related to the Toledo caldera, and the upper Bandelier Tuff or the Tshigere Member (1.21 Ma, 250 km$^3$) erupted from the present-day Valles caldera that coincides with the older Toledo. Both tuffs are high-silica rhyolites rather homogenous in major elements but chemically zoned in trace elements, with incompatible elements always being more abundant in the early erupted rocks (e.g., Smith, 1979). Between the two caldera collapses, a series of rhyolitic lava flows, domes and pyroclastic units were erupted (Cerro Toledo Rhyolite; e.g., Stix et al., 1988; Table 7).

### 3.5.1. Time scale information: disruption of silicic carapace and mixing

The available Rb–Sr data for this system do not permit residence times to be calculated with confidence (Table 7). Wolff and Ramos (2003) note that the Sr isotope data are consistent with $^{87}$Sr in growth over 270 ky prior to eruption of the Otowi magma. This approximately coincides with the time lag since the previous ignimbrite eruption from the system (at 1.85 Ma). However, the clear evidence of open system magmatic processes means that no confidence can be attached to this residence time, and parallels the problems discussed for the Long Valley estimates (J. Wolff, personnel communication). A maximum residence time of 380 ky for the Tshigere magma can be obtained if we assume that the two members were erupted from a common reservoir. Other time information has been obtained using the elemental and isotopic disequilibrium found between different phases of the Bandelier rocks and diffusion models. Wolff et al. (2002) found oxygen isotope disequilibrium between feldspars and quartz of the Tshigere Member which could have only survived for 1–200 years prior to eruption (Tables 2 and 7). This is the time since disruption of a silicic carapace, assimilation and eruption. Such time

**Table 7** Units, volumes, age data, times and process rates of the Valles-Toledo system.

| Valles/Toledo system | Vol (km³) | $^{40}$Ar/$^{39}$Ar or K–Ar age (eruption) | Oldest ages | Time from diffusion modeling | Mineral and elements used for diffusion calc. |
|---|---|---|---|---|---|
| Upper Bandelier Tuff or Tshirege member | 250 [Se96] | 1.212 Ma ± 0.006 Ma [S96] 1.256 ± 0.009 Ma [P03] | 14.60 ± 1.50 Ma [W01] | 1–200 y [W02] | [W02] O isotopes in Qtz and San (at 700°C) |
| Cerro Toledo Rhyolites | | From 1.550 ± 0.008 Ma to 1.212 ± 0.007 Ma [S96] | | 1–200 y [W02] | [W02] O isotopes in Qtz and San (at 700°C) |
| Lower Bandelier Tuff or Otowi member | 400 [Se96] | 1.611 ± 0.008 Ma [S96] | 11.54 ± 0.87 Ma [W01] | 1–200 y [W02] <10 ky [H&D92] | [W02] O isotopes in Qtz and San (at 700°C) [H&D92] Sr in San (at 800°C) |

*Note:* If both $^{40}$Ar/$^{39}$Ar and K–Ar ages are available only the former are given. Vol, Volumes in dense rock equivalent. calc., =calculation, San, sanidine, Qtz, quartz. [H&D92], Hervig and Dunbar (1992), [P03], Phillips et al. (2003), [S96], Spell et al. (1996), [Se96], Self et al. (1996), [W01], Winick et al. (2001), [W02], Wolff et al. (2002).

scales are presumably in accord with the $^{87}Sr/^{86}Sr$ and $^{206}Pb/^{204}Pb$ disequilibria reported by Wolff et al. (1999) and Wolff and Ramos (2003) between quartz–bearing glass inclusions, sanidines and the rest of the phases of the Otowi member. Hervig and Dunbar (1992) also calculated the time for complete homogenisation of Sr zoning in sanidine to be between 2 and 13 ky. Finally, the results of $^{40}Ar/^{39}Ar$ experiments on glass inclusion bearing quartz from the Bandelier Tuffs of Winick et al. (2001) seem to confirm the interpretation of Wolff and co-workers. Winick et al. (2001) found unrealistically old ages between 11 and 14 Ma (Table 7) which were interpreted as the result of excess $^{40}Ar$, similar to the Bishop Tuff case.

## 3.6. La Garita caldera

La Garita is part of a caldera cluster located in the San Juan volcanic field of southern Colorado. The Fish Canyon Tuff (5,000 km$^3$) was erupted from La Garita and is the largest known pyroclastic eruption on Earth (Lipman, 2000b). The tuff was preceded by the pre-caldera Pagosa Peak dacite, a large (200 km$^3$) and poorly fragmented pyroclastic deposit (Bachmann et al., 2000). A time gap of a few months occurred between the two eruptions (Bachmann et al., 2007b). The intracaldera tuff is overlain by the Nutras Creek dacite lava (<1 km$^3$; Table 8). All the deposits have almost identical geochemistry and very similar mineralogy and textures suggesting they were erupted from the same reservoir. The Fish Canyon Tuff is proposed to be the result of rejuvenation of a near solidus upper–crustal intrusive body of batholithic dimensions (Bachmann and Dungan, 2002; Bachmann et al., 2002). The pre-eruptive conditions of the Fish Canyon magma were experimentally determined by Johnson and Rutherford (1989) to be 760°C, 240 MPa and 3–3.5 wt% $H_2O$, and the liquidus obtained from MELTS (Ghiorso and Sack, 1995) is ca. 1,015°C. The Fish Canyon Tuff has been used as a test to establish age concordance between K–Ar and U–Pb isotopic systems, and its sanidine and biotite are commonly used standards (Table 8).

### 3.6.1. Time scale information: rejuvenation and remobilization of crystal-rich mushes

The age the Fish Canyon Tuff has been intensively investigated (e.g., Lanphere and Baadsgaard, 2001; Schmitz and Bowring, 2001; Dazé et al., 2003; Bachmann et al., 2007b), and is a matter of debate (e.g., Schmitz et al., 2003; Lanphere, 2004). Almost all minerals have been dated (plagioclase, sanidine, biotite, hornblende, zircon, titanite) and using different methods (Table 8). In general, the ages obtained by $^{40}Ar/^{39}Ar$ on, for example, sanidine, are younger than zircons or titanites dated by U–Pb system by several hundreds of thousands of years. The detailed geochronological study of Bachmann et al. (2007b) showed that total fusion $^{40}Ar/^{39}Ar$ ages of all phases almost overlap, with the youngest being those of sanidine at 28.04 Ma, and those of biotite, plagioclase or hornblende being <250 ky older. The sanidine total fusion $^{40}Ar/^{39}Ar$ ages of the pre- and post-caldera deposits are slightly younger (<100 ky) and older (30 ky), respectively,

**Table 8** Volume, age data, residence times and process rates for the Fish Canyon Tuff.

| La Garita system | Vol (km$^3$) | $^{40}$Ar/$^{39}$Ar age (eruption) | Rb–Sr isochron age | U–Pb age | Magma residence time[a] | Thermal modelling | Magma production rate km$^3$ y$^{-1}$ (vol/residence time) |
|---|---|---|---|---|---|---|---|
| Pagosa Peak Dacite | 200 [B07b] | San=27.93±0.09 Ma [B07b] Bt=28.25±0.10 Ma [B07b] | | Zrc=28.33±0.15 Ma [B07b] | Up to 400 ky | | |
| Fish Canyon Tuff | 5000 [L00b] | Bt=28.13±0.24 Ma [D03] San=28.04±0.09 Ma [B07b] Plag=28.31±0.11 Ma [B07b] Hbl=28.23±0.12 Ma [B07b] Bt=28.25±0.09 Ma [B07b] San and Bt=27.57±0.18 Ma [LB01] | Felds and Bt=27.44± 0.16 Ma [LB01] | Zrc=28.41±0.10 Ma [B07b] Zrc=27.52±0.09 Ma [LB01] Zrc=28.476±0.029 Ma [SB01] Tit=28.395±0.049 Ma [SB01] | Min.80 ky, max.900 ky 360 ky [B07b] | 100–200 ky [B&B03] | 1.3–6 × 10$^{-2}$ |
| Nutras Creek Dacite Flow | <1 [B07b] | San=28.07±0.09 Ma [B07b] | | Zrc=28.31±0.30 Ma [B07b] | Up to 250 ky | | |

*Note*: Vol, Volume in dense rock equivalent. [a]this is taken as the difference between the eruption ages and those of other radioactive clocks (e.g., U–Th–Pb, Rb–Sr). San, sanidine, Bt, biotite, Zrc, zircon, Tit, titanite, Felds, feldspars. Data sources: [B&B03], Bachmann and Bergantz (2003), [B07b], Bachmann et al. (2007b); [D03], Dazé et al. (2003); [L00b], Lipman (2000b); [LB01], Lamphere and Baadsgaard (2001), [SB01], Schmitz and Bowring (2001). The $^{40}$Ar/$^{39}$Ar data shown for Bachmann et al. (2007b) are total fusion results only, whereas those of zircon of the Fish Canyon Tuff are for the Fun Valley location.

although when errors of about 100 ky are considered, the ages of the three deposits overlap. Geochronological data on zircon (mainly single crystal) were also obtained by Bachmann et al. (2007b) and found a spread in ages from about 28.03 to 28.67 Ma. The mean age of the zircons from the main tuff was determined to be 28.41 Ma (using $^{206}Pb/^{238}U$) and overlaps with the zircon of the pre- and post-caldera deposits when errors are considered (Table 8).

It is apparent from the foregoing discussion that there is an age difference between the $^{40}Ar/^{39}Ar$ results on several minerals and those of the U/Pb system on zircon of about 300–400 ky. There are two main interpretations for this discrepancy: (1) it represents the residence time of the Fish Canyon magma (e.g., Bachmann et al., 2007b) or (2) it is due to a systematic bias of the $^{40}Ar/^{39}Ar$ and U–Pb methods (e.g., Schmitz and Bowring, 2001). Bachmann et al. (2007b) noted that even if one allows for the 1% of bias between the two radioactive systems, a residence time of about 300 ky still remains, and thus it seems that the prolonged residence time of the Fish Canyon magma is a robust conclusion (see Bachmann et al., 2007b for detailed discussion). The uncertainties of the most precise dates are in the order of 100 ky, and this remains a minimum estimate for the residence time.

Insights into the time scales of the Fish Canyon magma were also given by Bachmann and Bergantz (2003, 2006) who tested the hypothesis of remobilisation of a crystal–rich magma with a thermal model where heat was transported by a $H_2O$–$CO_2$ fluid phase. Their calculations show that to raise the temperature of the Fish Canyon by about 40°C it requires 100–200 ky if the amount of mafic magma or intrusion time remained within reasonable limits. This implies heating rates on the order of $3 \times 10^{-4} K y^{-1}$. Such time scales agree with age data that indicates residence times on the order of a few 100 ky, and can be taken as the time since remobilisation and eruption.

## 3.7. Other calderas

Other caldera-related magmas that have been investigated for their residence times include those of Crater Lake (Oregon), the Kos Plateau Tuff (Greece), and La Pacana (Chile). Other data on time scales of small and non-silicic caldera-related magmas can be found in Reid (2003) and Condomines et al. (2003).

### 3.7.1. Crater Lake caldera

It was formed during the eruption of ca. 50 km$^3$ of rhyodacite magma from Mount Mazama about 7,700 years ago (Bacon, 1983). Together with the main tuff there are many xenoliths, including blocks of granodiorite that are thought to be the wall-rock of the magma reservoir of the climatic eruption. Bacon et al. (2000) found zircon ages of ca. 100 ka for the granodiorite and indicates the presence of a sizeable pluton beneath Mount Mazama at the depth of the caldera-forming magma. These ages coincide with those of some silicic flows preserved on the north caldera wall (between 130 and 100 ka, Bacon and Lanphere, 2006). More recent determinations from the granodiorite blocks vary from 20 ka to >300 ka, with peaks at ca 60, 100 and 200 ka (Bacon and Lowenstern, 2005). Similar ages were found in pre-caldera

rhyodacite lavas of Steel Bay (2–3 km$^3$; erupted at 27 ka), and thus the residence times for these pre-caldera lavas vary between 20 and >100 ky. Bacon and Lowenstern (2005) used zircon dissolution rates to obtain a time of several decades between zircon entrapment and eruption, and the absence of zircons in the climatic eruption magma is probably the result of complete zircon dissolution in these hotter caldera-forming magmas.

### 3.7.2. Kos plateau tuff

The caldera associated with this rhyolitic tuff (60 km$^3$) is probably between the Greek islands of Kos and Nisyros, and has an inferred diameter of ca. 20 km (Keller 1969; Allen, 2001). The deposits contain numerous granitoid xenoliths (some with textures indicative of partial melting) of almost the same mineralogy as the tuff (Keller 1969; Bachmann et al., 2007a). Single crystal sanidine $^{40}$Ar/$^{39}$Ar analysis gave eruption ages at $161.3 \pm 1.1$ ka (Smith et al., 1996), although the $^{40}$Ar/$^{39}$Ar ages of plagioclase and quartz are up to $925 \pm 22$ ka, and are thought to be xenocrysts from earlier events (Smith et al., 2000). In situ dating of zircons from the tuff and the granitoid xenoliths (Bachmann et al., 2007a) shows that all crystals have similar age distributions, from that of eruption to ca. 160 ka–340 ka (except for one point at 500 ka). This gives residence times and zircon crystallization period of about 180 ky. Since the ages of the tuff and the xenoliths are the same, the latter are probably pieces of nearly completely crystallised rind of the magma reservoir which was disrupted during eruption (Bachmann et al., 2007a).

### 3.7.3. La Pacana caldera

It is located in the Chilean Andes and is the largest described in South America. It was the source of two voluminous crystal–rich ignimbrites, the Atana (2,500 km$^3$) and Toconao (180 km$^3$). They erupted (based on K–Ar data) in a small but not well resolved time interval, with ages at $3.77 \pm 0.09$–$4.23 \pm 0.12$ Ma, and $4.0 \pm 0.9$–$5.27 \pm 0.12$ Ma, respectively (Lindsay et al., 2001). Schmitt et al. (2002) determined zircon ages from Toconao a pumice of $4.65 \pm 0.13$ Ma, whereas those from a bulk ignimbrite sample are much older, at ca. 13 and 470 Ma. The ages for the Atana zircons are $4.11 \pm 0.2$ Ma, considerably younger than the pumice zircon ages of the Toconao. Schmitt et al. (2002) calculated average residence times for the two units of the order of 0.5–0.75 My, the longest residence times calculated so far from ages obtained by U–Pb on zircon.

## 4. INTERPRETATION OF RESIDENCE TIMES AND INTEGRATION WITH THERMAL AND MECHANICAL CONSTRAINS

### 4.1. What do the residence times indicate?

Large ranges of residence times are found within single deposits, between deposits of single systems, and between systems (Figure 9). The shortest times are those of
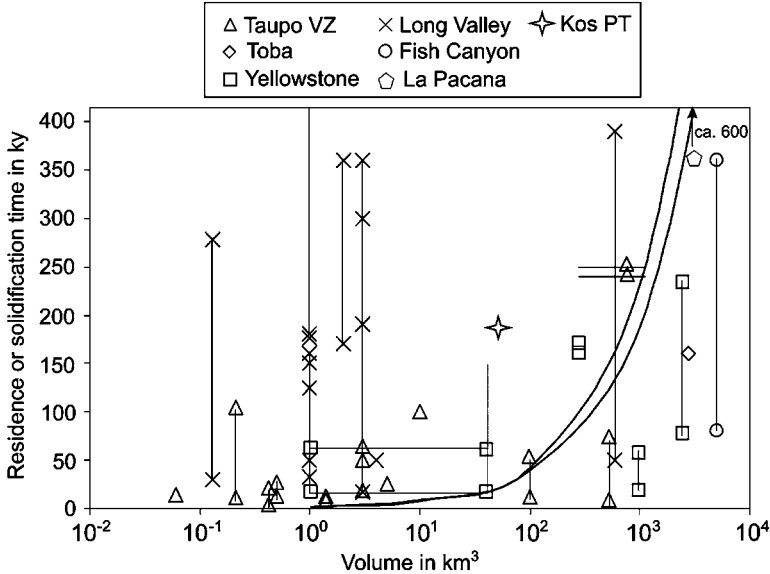
**Figure 9**   Calculated residence times vs. volume for all deposits. The two curves are solidification models calculated using Equation (3) and the following parameters: (1) an initial temperature of 900°C for the magma. This is $\pm 25$ degrees of the liquidi of most magmas treated in this manuscript, (2) a thermal diffusivity of $10^{-6}\, m^2\, s^{-1}$ (e.g., Guéguen and Palciauskas, 1994), (3) a solidus of 650°C, which is representative for silicic and water bearing systems (e.g., Johannes and Holtz, 1996), and (4) two different conditions for the initial temperature of the host rock. In one case a temperature of 200°C was used as representative of a depth of 6 km (curve that reaches solidification faster). In the other, the temperature of the host rock increased with increasing size of the reservoir at typical geothermal gradient of 30 K km$^{-1}$, starting from 200°C at 6 km for a 1 km$^3$ body. As can be seen from the figure the effect of incorporating a geothermal gradient does not significantly change the results. Most magmas < ca. 100 km$^3$ lie to the left of the solidification curves suggesting their residence times reflect probably crystal recycling from previous igneous activity (although see Section 4.1.1) rather than the time they spend above the solidus.

Oruanui and Rotoiti magmas at 4 and 9 ky, respectively (both from Taupo volcanic zone), followed by the Dry Creek and Lava Creek Yellowstone magmas at 7 and 19 ky, respectively. There is not a good correlation between the volume and residence time, but most eruptions < 10 km$^3$ have residence times < 100 ky, and those > 100 km$^3$ have longer residence times, up to ca. 400 ky for the Fish Canyon and > 500 ky for La Pacana. A positive correlation between the volume of the deposit and the residence time can be expected if magma fluxes of small and large systems are the same (see magma production rate section below). The question is what these magma residence times indicate. If we first exclude the possibilities of (1) the effect of different closure temperatures consequent upon the use of different phases and radioactive systems, (2) the obvious xenocrysts which are several My older than the host and (3) the possible effects of sample bias due to the analytical method used (in situ vs. bulk mineral separates), at least two additional end–member possibilities remain. The residence times could constrain the duration that the

magma was above the solidus, or they reflect the recycling of crystals from previous intrusive episodes of the same magmatic system, and thus provide artificially long residence times for the studied magma. Evidence for both cases is discussed below.

### 4.1.1. Residence times as a record of the duration that magmas spend above their solidus

The most robust data for this case are the zircon age distributions from the large volume (300–1,000 km$^3$) Whakamaru ignimbrites (Brown and Fletcher, 1999) and from allanite of the Youngest Toba Tuff (2,800 km$^3$; Vazquez and Reid, 2004). In both systems the ages decrease progressively (i.e., without a major gap) from the centre to the rim of crystals. This is crucial because it could mean that the crystals were able to grow from a melt without interruption and for these two systems it amounts to about 200 ky.

A simple test of this possibility is to consider the thermal evolution of a magma reservoir based on a conduction model of an instantaneous heat source (e.g., Equation (3); see Figures 9 and 10 and their captions for more details on the parameters used). Considering the latent heat of crystallisation and multiple
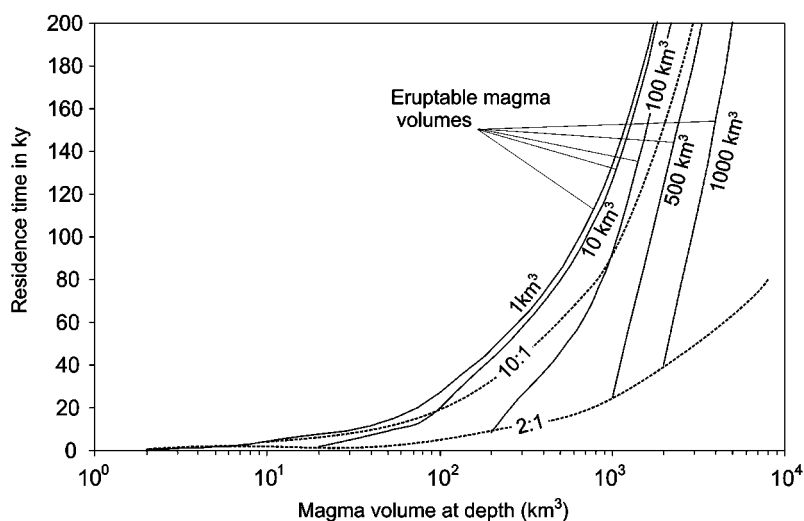


**Figure 10** Residence time vs. calculated magma volume at depth for different volumes of erupted magma. The curves were calculated using the thermal model parameters from previous figure but using 750°C as the lowest temperature that a magma would be able to erupt. This is a simplification and the effect of viscosity and crystallinity should also be considered. However, since the lowest pre-eruptive temperatures of most magmas discussed in the text are at 750 ± 25°C it appears a valid simplification to use only temperature as a eruptability criterion. The figure highlights that small volumes of magma (e.g., 1 km$^3$) with long residence times (e.g., 100 ky) imply very large amounts of unerupted magma at depth (e.g., ca. 800 km$^3$). Such a ratio of 800:1 of intrusive over extrusive volumes is much larger than the maximum value of 10 determined by other authors (e.g., White et al., 2006). Dashed lines indicate intrusive to extrusive ratios of 10:1 and 2:1. Most residence times of large eruptions fall within these values of intrusive to intrusive volumes.

intrusions in the model would produce longer equilibration times, but the endothermic reactions associated with the wall–rock and magma or hydrothermal convection might partly balance this effect (e.g., Norton and Knight, 1977; Bowers et al., 1990). For example, detailed studies of contact areoles around exposed plutons do not deviate significantly from the results of the simple approach used here (e.g., Bowers et al., 1990; Furlong et al., 1991). The results of the modelling can be seen first in Figure 9. The region above or to the left of the two curves are those where magmas would have reached the solidus. The majority of eruptions $<10 \, km^3$ lie in this field, whereas most eruptions $>100 \, km^3$ lie below or to the right of the solidification curves. Thus, the long residence times calculated for small magmas could be unrealistic because they would have long solidified before eruption. Note that the difference is large, with a factor of ten or more of difference between the magma solidification and residence times. However, it has been pointed out (Mahood, 1990) that small eruptions might be only the 'mobile' parts of a larger magmatic system that would take longer to solidify. In other words, the intrusive to extrusive ratios are also an important factor. This has been tested by calculating the time that a system reaches a given volume of still eruptible magma (Figure 10). For erupted volumes between 1 and $10 \, km^3$, residence times $>$ ca. 100 ky imply that the magma at depth is $10^2$–$10^3$ times larger, which is much higher than the highest reported values of 10 for intrusion to extrusion ratios (e.g., Wadge, 1982; Crisp, 1984; Pritchard and Simons, 2004; White et al., 2006). Thus, it seems very unlikely that the residences $>10^4$ y of small eruptions ($<10 \, km^3$) reflect times the magmas stayed above their solidus. Nonetheless, it will be shown in the next section that it is useful to consider the data in context of the caldera cycle (pre- and post-collapse activity) of individual systems before reaching conclusions.

In contrast, almost all residence times for deposits $>100 \, km^3$ fall to the right or below the solidification curve (Figure 9). This indicates that their residence times are not in contradiction with the time-temperature path of such a cooling model. Moreover, the data for these large eruptions have intrusive to extrusive ratios from 1:1 to 10:1 in accord with other estimates listed above (Figure 10). These thermal arguments together with the in situ age variation in single crystals in the Whakamaru ignimbrites and the Toba Tuff indicate that the residence times of ca. 100 ky or more for magmas $>100 \, km^3$ are probably a good indication of the amount of time that they stayed above the solidus.

#### 4.1.1.1. The caldera cycle, the time evolution of a single reservoir and crystal ageing.    The discussion above considers a scenario where the erupted magmas are extracted from individual and isolated magma reservoirs. However, caldera collapse is commonly pre- and post-dated by volcanic activity (e.g., Lipman, 2000a) and there is the possibility that the long residence times of some small magmas reflect that they were extracted from the same reservoir as the large caldera collapse magma. This can be tested with a diagram where the residence times are plotted against the eruption ages recalculated to a 'caldera-collapse reference time frame'. The eruption age of the pre- and post-caldera deposits are calculated with respect to a 'zero time' of caldera collapse (Figure 11). If the pre- or post-caldera volcanics were extracted from the same reservoir as the caldera-forming magma, their
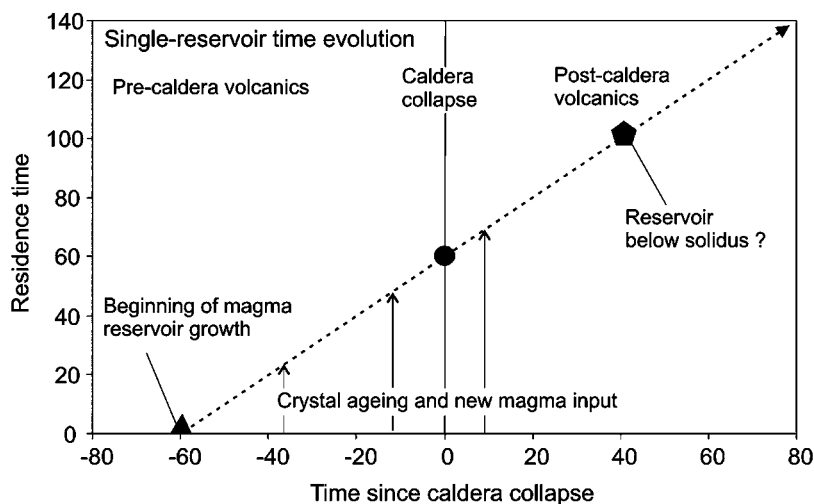
**Figure 11**    Single-reservoir evolution diagram where the absolute time is recalculated to the caldera collapse episode and plotted vs. magma residence time. If the residence time of the caldera collapse magma is known, it is possible to calculate when the reservoir started to exist (e.g., the minerals used to obtain the residence time begin to crystallise). This line has a slope of one and any pre- or post-caldera magma erupted from the same reservoir as the caldera forming magma should plot on this line. If the magma reservoir is growing, shorter residence times could also be expected from newly crystallised melt after of each magma increment. After caldera collapse the main reservoir will cool down and crystallise if there is also a decrease in magma input. No time units are shown on the axes. As long as the units are equal on either axis, any temporal unit is possible.

residence times should increase with eruption (or absolute) time. The maximum residence time of any batch erupted from a common reservoir should fall on a line with a slope of 1; the minimum times of the different deposits do not need to be related since they might reflect progressive magma additions to the reservoir. After caldera collapse the remaining magma might eventually solidify. Even if post-caldera lavas are not erupted from the same caldera left-over magma (e.g., erupted after the solidification limit), if their residence times fall in the time evolution of the main reservoir the sources of their crystals are partly recycled from caldera-related material (Figure 11).

This diagram has been constructed for the Long Valley, Taupo and Yellowstone caldera systems (Figure 12). The long residence times of some small pre-caldera volcanics in Long Valley and Taupo systems (Oruanui Tuff) seem to be consistent with them being from the same magma reservoir as the caldera collapse magma. Such a relation was also proposed by the geochemical similarity between the pre- and caldera-related rocks (e.g., Long Valley and Taupo sections). Other pre-caldera magmas clearly deviate from the single reservoir evolution (e.g., old domes in Long Valley). The majority of the post-caldera deposits have residence times that despite being long for their volumes, are short compared to the time evolution lines of the single reservoir. Note that in Taupo (Figure 12b), the very long residence times of
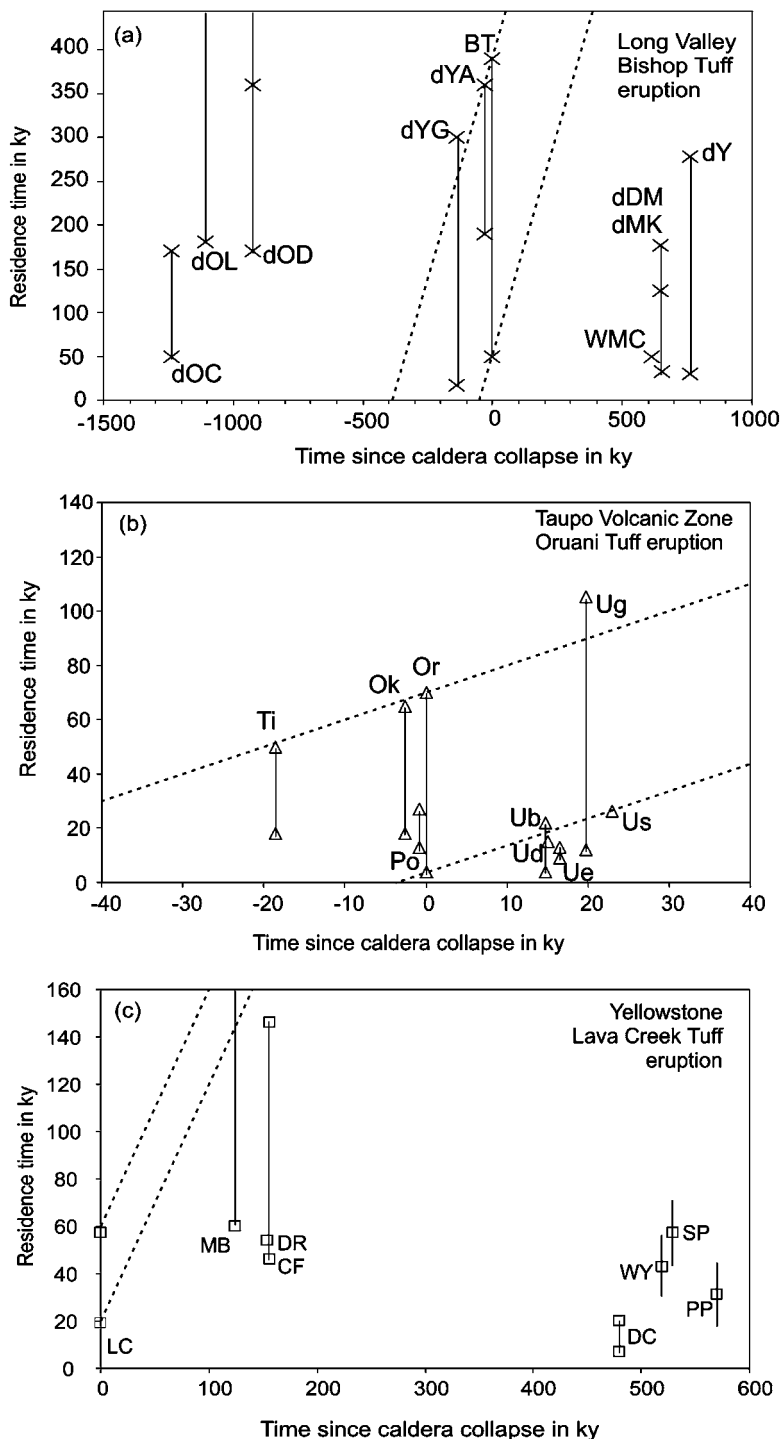
**Figure 12** Single-reservoir evolution diagram for (a) Long Valley, (b) Taupo (caldera collapse related to Oruanui eruption) and (c) Yellowstone (caldera collapse related to Lava Creek Tuff). Abbreviations and data sources as in Figures 4, 6, and 8. The dashed lines are the single reservoir time evolution (maxima and minima) as described in previous Figure 10. Note that the long residence times of some small pre-caldera volcanics from Long Valley and Taupo can be the result of sampling the much larger magma reservoir of the caldera forming eruption (see text for discussion).

one unit fall in the time evolution of the main reservoir suggesting that either it was derived from the still remaining melt or that the crystals are recycled from an already crystallised part of the same reservoir.

### 4.1.2. Residence times recording previous magmatic episodes (erupted or not)

The long residence compared to the solidification times of some small eruptions, as well as their positions with respect to the caldera cycle above, open the question about the sources of these crystals. At least two possibilities have been proposed: they are recycled from previous magmatic episodes that have been erupted; or where the crystals' ages have no correspondence with the erupted record, they are derived from plutonic magmas or rocks.

Recycling of crystals from well identified magmatic activity has been documented in Yellowstone, where the ages of the crystals in some young and small post-caldera lavas (<0.6 Ma) are the same as those of the Huckleberry Tuff (Bindeman et al., 2001) or the same as other post-caldera products (Vazquez and Reid, 2002). Recycling of crystals from non-erupted magmas has been invoked in many other systems. For example, zircons in deposits <45 ka of Taupo volcanic zone display two main peaks at ca. 30 and 100 ka but such ages have no correspondence with the erupted record (Charlier et al., 2005). This is also found in post-caldera lavas of the Long Valley system, where several units contain zircons with ages between 200 and 300 ka, which corresponds to a gap in the post-caldera volcanism at Long Valley (e.g., Hildreth, 2004). Once crystal inheritance has been recognised, the plutons could be from the same magmatic system (or even reservoir) as the magmas that carried the crystals to the surface or not. Evidence for the former is found in the Taupo system (see above) and another is from Crater Lake. Bacon et al. (2000) and Bacon and Lowenstern (2005) showed that the zircon ages from granodiorite xenoliths from the caldera forming deposits are the same as those of pre-caldera rhyodacite lavas.

### 4.2. Time scales of magmatic processes

Other time information obtained from caldera-related magmas is the duration and rates of magmatic processes (Table 2). Residence times establish a crystallisation episode or history of the phases used to derive the age. Geochronological studies that use Rb–Sr isotope systematics of main phenocrysts could quantify differentiation rates of silicic magmas. Unfortunately, the systems that have been studied in detail show that the role of open system process is so important that the time information is difficult to be interpreted (e.g, Long Valley, Valles-Toledo). The most reliable results appear to be those obtained from accessory minerals. Although, it is not clear how these may relate to a significant event of magma differentiation their time information seems more robust. For example, the study of Vazquez and Reid (2004) of allanites from the Toba Tuff quantified fractionation rates of silicic magmas to be 1–4% every 10 ky.

Time information on magmatic processes and rates is also derived from relaxation of chemical zoning in minerals by diffusion or from thermal models
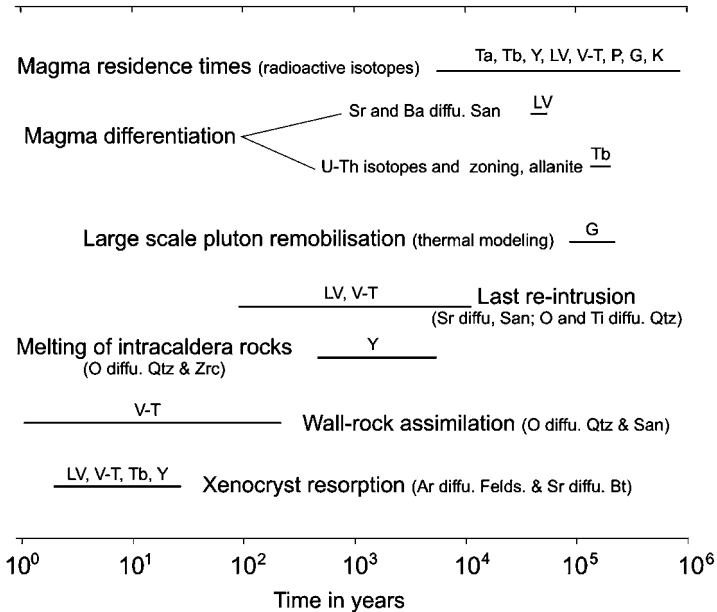
**Figure 13** Summary of time scales of magmatic processes obtained from caldera related silicic magmas. Abbreviations used: Ta, Taupo volcanic zone, Tb, Toba, Y, Yellowstone, LV, Long Valley, V-T, Valles–Toledo, P, La Pacana, G, La Garita, K, Kos Plateau Tuff, San, sanidine, Qtz, quartz, Zrc, zircon, Felds., feldspars, Bt, biotite, Diffu., diffusion. Data sources for this figure can be found in Tables 3—8 and in Section 3.7.

(Table 2 and Figure 13). In many cases the time scales of individual magmatic processes are shorter than the residence time. This probably reflects that during magmatic evolution different short-lived processes occur repeatedly. The duration of the process that we may determine is probably only the last one before eruption. This can be exemplified with the data from the Bishop Tuff. Magma residence times based on zircon ages are 50–90 ky (Simon and Reid, 2005) but recent estimates from Ti diffusion within quartz are much shorter, in the range of 100 years (Wark et al., 2007). The short times obtained from diffusion only reflect last arrival of magma to the reservoir prior eruption and not the entire growth of the Bishop magma.

## 4.3. Magma production and cooling rates related to calderas

Magma production rates have been calculated from the ratio of erupted volume and residence time. They are shown in Table 1 for large eruptions and in Figure 14 for all eruptions. Magma production rates appear to decrease with decreasing volume of the deposits. They vary from ca. $0.1 \, \text{km}^3 \, \text{y}^{-1}$ of the Oruanui eruption to $10^{-6} \, \text{km}^3 \, \text{y}^{-1}$ of some small post-caldera deposits of Taupo and Long Valley. With a couple of exceptions, deposits larger than $500 \, \text{km}^3$ have similar and high magma production rates bracketed at ca. $2 \pm 1 \times 10^{-2} \, \text{km}^3 \, \text{y}^{-1}$ (collective volume
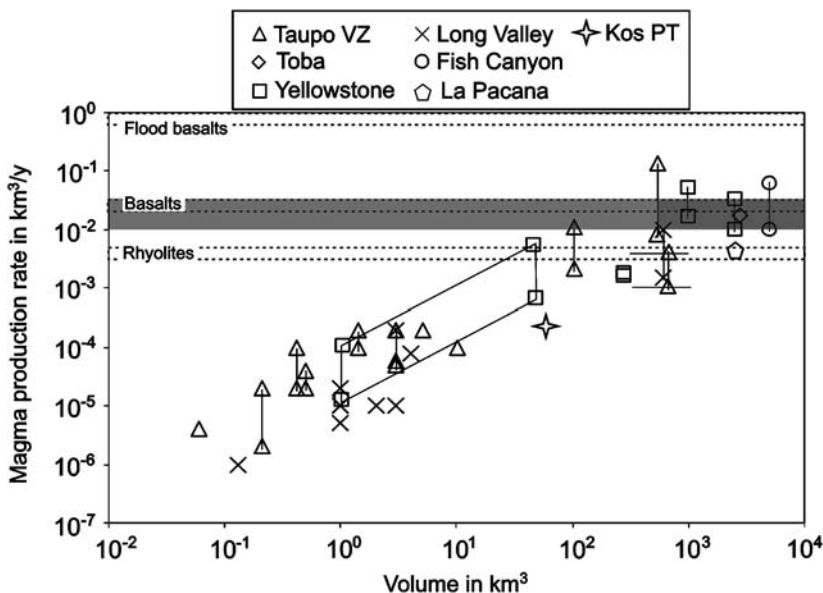
**Figure 14** Calculated magma production rates vs. erupted volume for all available data. Dashed lines are the global estimates of eruption rates for different rock types from White et al. (2006) and grey band is the estimate of this publication ($2 \pm 2 \times 10^{-2} \, \mathrm{km^3 \, y^{-1}}$) for most eruptions $> 500 \, \mathrm{km^3}$. Note that the magma production rates of large eruptions overlap with magma eruption rates of basaltic compositions excluding flood basalts. Data sources for this figure are numerous and cited in Tables 3—8 and in Section 3.7.

of ca. $15 \times 10^3 \, \mathrm{km^3}$). This is five times higher than the global eruption rate estimates of ca. $4 \pm 1 \times 10^{-3} \, \mathrm{km^3 \, y^{-1}}$ for rhyolitic compositions (White et al., 2006), but overlaps with the estimates of ca. $3 \pm 1 \times 10^{-2} \, \mathrm{km^3 \, y^{-1}}$ for basaltic eruptions. The higher rates obtained in this manuscript show that residence times are shorter than repose time between successive eruptions, and thus are better estimates of magma production rates. However, they are still low values because not all intruded magma is erupted. Using a nominally high value of intrusion to extrusion rates of 10 (e.g., Wadge, 1982; Crisp, 1984; Pritchard and Simons, 2004; White et al., 2006), more realistic magma production rates for rhyolitic magmas are close to $0.1 \, \mathrm{km^3 \, y^{-1}}$. This is about an order of magnitude lower than the highest eruption rate estimates of flood basalts (ca. $1 \, \mathrm{km^3 \, y^{-1}}$; White et al., 2006), but overlaps with some of them (e.g., Grande Ronde basalts of Columbia River), and also with active oceanic hotspots like Hawaii in the last 100 ky ($0.15 \, \mathrm{km^3 \, y^{-1}}$; Lipman, 1995). Note that for this comparison to be appropriate (i.e., mafic to silicic magma production rates), intrusive to extrusive ratios of mafic magmas are assumed much lower and closer to 1 (e.g., Wadge, 1982). The lifetimes of caldera-related magmatic cycles span a few million years or less (except perhaps for the caldera complexes of the San Juan Mountains; Lipman, 2000b) which suggest that the high magma production rates related to calderas are transient phenomena. How such high and transient magma production rates can be achieved

should be tested by transport and thermal models for silicic magma generation (e.g., Petford et al., 2000; Annen and Sparks, 2002; Dufek and Bergantz, 2005; Michaut and Jaupart, 2006).

The interpretation of the low magma production rates for small eruptions involves other factors related to the significance of the residence times. The evidence for crystal recycling discussed above for some post-caldera deposits can explain their artificially low magma production rates. However, if the low magma production rates estimated for other small pre- and post-caldera magmas are correct, they could be interpreted as 'the rise and the fall' of a large caldera-related magmatic episode where magma input rates change with time.

## 4.3.1. Magma cooling rates

The calculated cooling rates for some large magmas vary between $4 \times 10^{-5}$ and $2 \times 10^{-2}\,K\,y^{-1}$, although most data fall between $5 \times 10^{-4}$ and $3 \times 10^{-3}\,K\,y^{-1}$ (Table 1 and Figure 15). These cooling rates are in general agreement with those obtained from the numerical simulations described above (Figure 15). This shows that there is a degree of internal consistency between the residence times and cooling rates for large magmas. Cooling rates are a main parameter controlling crystal growth, and thus these estimates should help to better constrain the crystal
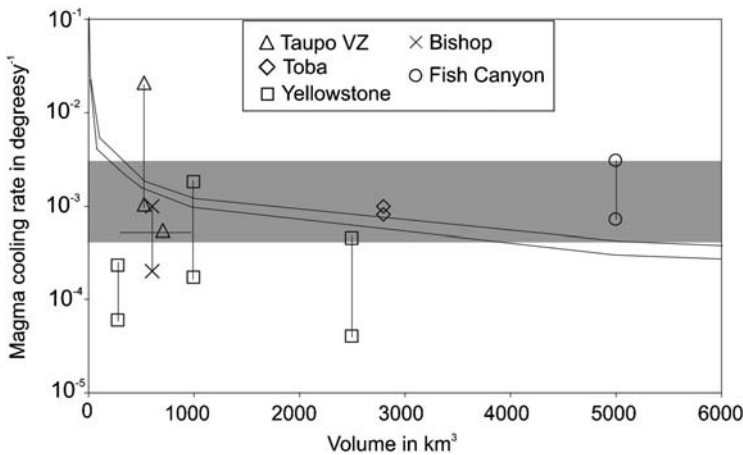


**Figure 15**   Calculated magma cooling rates vs. erupted volume for large ($>100\,km^3$) caldera forming deposits. The cooling rates were obtained from the difference between the pre-eruptive and the liquidus temperatures (calculated with MELTS, Ghiorso and Sack, 1995) over the residence time. Note that there is no correlation between the size of the eruption and the cooling rates, with most of cooling rates (grey area) are between $5 \times 10^{-4}$ and $3 \times 10^{-3}\,K\,y^{-1}$. The two curves are the cooling rates at the centre of the sphere of the given volume for $750^{\circ}C$ and $650^{\circ}C$. The cooling rates were extracted from the numerical simulations and thermal model described in the text and Figures 5 and 6 and are meant to be only guidelines for comparison to the cooling rates extracted from the rocks.

growth rates in silicic magmas. They also allow calculating the closure temperatures of multiple phases and radioactive systems (Figure 2).

## 4.4. Magma residence times, caldera collapse and the rheology of the crust

The knowledge of residence times can also contribute to understand the relation between magma fluxes and rheological behaviour of the crust and thus caldera-related volcanism. This topic was addressed by Jellinek and DePaolo (2003) using a visco-elastic model for the crust. Their equations 11 and 12 allow calculating the time needed to reach a critical overpressure in the elastic and viscous regimes and also the maximum chamber overpressure. The results from the calculations show that the high magma fluxes of ca. $0.01\,km^3\,y^{-1}$ inferred for most large caldera collapse eruptions ($>500\,km^3$) require pressurisation times up to the critical overpressure of decades to hundreds of years (e.g., Figure 4 of Jellinek and DePaolo, 2003). This is several orders of magnitude shorter than most residence times. Moreover, these high magma fluxes do not allow for the construction of a large magma volume because the critical overpressure is reached before any significant amount of magma can be accumulated. The apparent contradiction between the residence times and the rheological model can be due to several reasons. The model of Jellinek and DePaolo (2003) contains elastic and viscous behaviour of the crust, but it does not include damage (e.g., Gray and Monaghan, 2004) or how this might change with time. The overpressure could be reached by other factors than the magma influx rate, like the crystallisation and progressive build up of volatiles (Tait et al., 1989). A much larger uncertainty is probably introduced by using the mean magma production rates derived from the residence time and volume as if they would be instantaneous rates. Jellinek and DePaolo (2003) pointed out the difficulty of building large magma reservoirs that erupt with large periodicities (ca. 500 ky), and noted that peak intrusion fluxes higher than the average would be necessary to trigger large caldera-collapse eruptions. Some model calculations using their equation 8 show that aside from an intrusion peak higher than average, the increasing volume of the reservoir with time exacerbates this effect even more. Using linear, exponential or abrupt increases of magma flux rates with time does not lead to eruption in the frame of the residence times. From this discussion it is apparent that more feedback between rheological and residence time models is necessary to understand the processes that lead to eruption of such large volumes of magma. A main contribution to such an understanding may also arise from studies of the growth rates of granitoid plutons and their thermal and mechanical effects in the crust (e.g., Yoshinobu and Girty, 1999; Petford et al., 2000; Gerbi et al., 2004; Glazner et al., 2004; Oberli et al., 2004; Titus et al., 2005; Žák and Paterson, 2005).

## 5. SUMMARY AND CONCLUSIONS

A review of the data produced in the last 30 years from silicic deposits of major caldera systems allows to quantify the rates of magmatic differentiation and the mass

and thermal budgets of this type of igneous activity. The most important findings are:

(1) The residence times of large volume caldera-forming eruptions ($>100\,\mathrm{km}^3$) range from a few ky to up to a few 100 ky, and may be a robust indication for the duration that magma spends above the solidus. This is indicated by in-situ age data of crystals from the Whakamaru and Toba ignimbrites which show progressive age changes from core to rim over a couple of 100 ky. This time frame is consistent with numerical simulations of conductive cooling models of igneous bodies, magma production rates, and intrusive to extrusive ratios. The cooling rates of such large magmas are calculated to be between $5 \times 10^{-4}$ and $3 \times 10^{-3}\,\mathrm{K\,y}^{-1}$ which are also within the results of the thermal models.

(2) Residence times of smaller ($<10\,\mathrm{km}^3$) pre-and post-caldera magmas are comparable or shorter than most caldera-forming magmas. Aside from genuinely reflecting the times that these magmas were in the crust, other interpretations come into play. The long residence times (e.g., 50–300 ky) of some pre-caldera deposits can be explained if they are batches from the same reservoir as the caldera-forming magma (e.g., Long Valley, Taupo). The long residences of other small magmas reflect that the dated crystals are recycled from a caldera-forming deposit of a previous caldera cycle (Yellowstone), from plutonic rocks of the same caldera cycle with or without erupted equivalents on the surface (Crater Lake, Taupo, Long Valley), or perhaps from a not completely solidified caldera-forming magma reservoir (Taupo).

(3) Time scales of specific magmatic processes are in general shorter than overall magma residence times. The geochemical imprint of assimilation and partial melting of wall-rocks (e.g., Valles–Toledo) or of previously erupted intracaldera lavas (e.g., Yellowstone) can occur rather quickly, in less than a thousand years. Even shorter times are obtained for the time since the last magma replenishment and eruption (ca. 100 years for the Bishop Tuff) and for xenocrysts incorporation and eruption ($<$a decade).

(4) The majority of magma production rates from large caldera forming eruptions, including the tuffs of Bishop, Fish Canyon, Toba, Huckleberry, Lava Creek, Oruanui and Rotoiti, (ca. $15 \times 10^3\,\mathrm{km}^3$ in total) fall within the range of $2 \pm 2 \times 10^{-2}\,\mathrm{km}^3\,\mathrm{y}^{-1}$, values that are comparable to global eruptive fluxes of basalts. When combined with the high intrusive to extrusive values expected for silicic magmas of 10:1 they suggest that the mass fluxes related to caldera forming volcanism are of the same order as that of some flood basalts (e.g., Grande Ronde basalts of Columbia River). Such high magma fluxes are transient phenomena and insights should be gained from thermal models of the crust that lead to episodic and silicic magma generation. Magma production rates derived from pre- and post-caldera lavas are much lower and might reflect the initiation or decline of a caldera cycle, although care has to be exercised as other factors might bias the residence time estimates towards higher values (e.g., recycling of old crystals).

(5) These magma production rates and residence times are important parameters for rheological models of the crust and their relation to magmatic inputs and eruption. However, the retrieved times are much longer and the fluxes inappropriate to reach the critical overpressure necessary for eruption of a large reservoir as indicated by a simplified rheological model of the crust. The discrepancy may be partly explained if the magma production rates are mean values of a highly variable magma influx. Further interactions between residence times and rheological models are necessary for the understanding of the mechanisms by which large magma reservoirs are constructed and stored in the shallow crust awaiting to produce a caldera–forming eruption.

## ACKNOWLEDGMENTS

## REFERENCES

Albarède, F., 1993. Residence time analysis of geochemical fluctuations in volcanic series. Geochim. Cosmochim. Acta, 57, 615–621.

Allen, S.R., 2001. Reconstruction of a major caldera-forming eruption from pyroclastic deposit characteristics: Kos Plateau Tuff, eastern Aegean Sea. J. Volcanol. Geotherm. Res., 105, 141–162.

Anderson, A.T., Davis, A.M., Lu, F., 2000. Evolution of Bishop Tuff rhyolitic magma based on melt and magnetite inclusions and zoned phenocrysts. J. Petrol., 41, 449–473.

Anderson, A.T., Newman, S., Williams, S.N., Druitt, T.H., Skirius, C., Stolper, E., 1989. $H_2O$, $CO_2$, Cl and gas in plinian and ash-flow Bishop rhyolite. Geology, 17, 221–225.

Annen, C., Sparks, R.S.J., 2002. Effects of repetitive emplacement of basaltic intrusions on thermal evolution and melt generation in the crust. Earth Planet. Sci. Lett., 203, 937–955.

Bachmann, O., Bergantz, G.W., 2003. Rejuvenation of the Fish Canyon magma body: a window into the evolution of large-volume silicic magma systems. Geology, 31, 789–792.

Bachmann, O., Bergantz, G.W., 2006. Gas percolation in upper-crustal silicic crystal mushes as a mechanism for upward heat advection and rejuvenation of near-solidus magma bodies. J. Volcanol. Geotherm. Res., 149, 85–102.

Bachmann, O., Dungan, M.A., 2002. Temperature-induced Al-zoning in hornblende of the Fish Canyon magma, Colorado. Am. Mineral., 87, 1062–1076.

Bachmann, O., Dungan, M.A., Lipman, P.W., 2000. Voluminous lava-like precursor to a major ash-flow tuff: low-column pyroclastic eruption of the Pagosa Peak Dacite, San Juan Volcanic field, Colorado. J. Volcanol. Geotherm. Res., 98, 153–171.

Bachmann, O., Charlier, B.L.A., Lowenstern, J.B., 2007a. Zircon crystallization and recycling in the magma chamber of the rhyolitic Kos Plateau Tuff (Aegean Arc). Geology, 35, 73–76.

Bachmann, O., Dungan, M.A., Lipman, P.W., 2002. The Fish Canyon magma body, San Juan Volcanic Field, Colorado: rejuvenation and eruption of an upper-crustal batholith. J. Petrol., 43, 1469–1503.

Bachmann, O., Oberli, F., Dungan, M.A., Meier, M., Mundil, R., Fischer, H., 2007b. $^{40}$Ar/$^{39}$Ar and U–Pb dating of the Fish Canyon magmatic system, San Juan Volcanic field, Colorado: evidence for an extended crystallization history. Chem. Geol., 236, 134–166.

Bacon, C.R., 1982. Time-predictable bimodal volcanism in the Coso Range, California. Geology, 10, 65–69.

Bacon, C.R., 1983. Eruptive history of Mount Mazama and Crater Lake caldera, Cascade Range, U.S.A. J. Volcanol. Geotherm. Res., 18, 57–115.

Bacon, C.R., Lanphere, M.A., 2006. Eruptive history and geochronology of Mount Mazama and the Crater Lake region, Oregon. Bull. Geol. Soc. Am., 118, 1331–1359.

Bacon, C.R., Lowenstern, J.B., 2005. Late Pleistocene granodiorite source for recycled zircon and phenocrysts in rhyodacite lava at Crater Lake, Oregon. Earth Planet. Sci. Lett., 233, 277–293.

Bacon, C.R., Persing, H.M., Wooden, J.L., Ireland, T.R., 2000. Late Pleistocene granodiorite beneath Crater Lake caldera, Oregon. Geology, 28, 467–470.

Bailey, R.A., 1989. Geologic map of the Long Valley caldera, Mono-Inyo craters volcanic chain, and vicinity, Eastern California. U.S. Geological Survey Map I–1933, scale 1:62,500.

Bailey, R.A., 2004. Eruptive history and chemical evolution of the precaldera and postcaldera basalt-dacite sequences, Long Valley, California: implications for magma sources, current magmatic unrest, and future volcanism. U.S. Geological Survey, Professional. Paper 1692, 76 pp.

Bailey, R.A., Dalrymple, G.B., Lanphere, M.A., 1976. Volcanism, structure, and geochronology of Long Valley Caldera, Mono County, California. J. Geophys. Res., 81, 104–122.

Bindeman, I.N., 2005. Fragmentation phenomena in populations of magmatic crystals. Am. Mineral., 90, 1801–1815.

Bindeman, I.N., Valley, J.W., 2001. Low $\delta^{18}$O rhyolites from Yellowstone: magmatic evolution based on analyses of zircons and individual phenocrysts. J. Petrol., 42, 1491–1517.

Bindeman, I.N., Valley, J.W., 2002. Oxygen isotope study of the Long Valley magma system, California: isotope thermometry and convection in large silicic magma bodies. Contrib. Mineral. Petrol., 144, 185–205.

Bindeman, I.N., Valley, J.W., Wooden, J.L., Persing, H.M., 2001. Post-caldera volcanism: *in situ* measurement of U–Pb age and oxygen isotope ratio in Pleistocene zircons from Yellowstone caldera. Earth Planet. Sci. Lett., 189, 197–206.

Bowers, J.R., Kerrick, D.M., Furlong, K.P., 1990. Conduction model for the thermal evolution of the Cupsuptic aureole, Maine. Am. J. Sci., 290, 644–665.

Brown, S.J.A., Fletcher, I.R., 1999. SHRIMP U–Pb dating of the preeruption growth history of zircons from the 340 ka Whakamaru ignimbrite, New Zealand: evidence for > 250 k.y. magma residence times. Geology, 27, 1035–1038.

Brown, S.J.A., Smith, R.T., 2004. Crystallization history and crustal inheritance in a large silicic magma system: $^{206}$Pb/$^{238}$U ion probe dating of zircons from the 1.2 Ma Ongatiti ignimbrite, Taupo Volcanic Zone. J. Volcanol. Geotherm. Res., 135, 247–257.

Brown, S.J.A., Wilson, C.J.N., Cole, J.W., Wooden, J., 1998. The Whakamaru group ignimbrites, Taupo Volcanic Zone, New Zealand: evidence for reverse tapping of a zoned silicic magmatic system. Jour. Volcanol. Geotherm. Res., 84, 1–37.

Carslaw, H.S., Jaeger, J.C., 1986. Conduction of Heat in Solids. Oxford University press, Oxford, 510 pp.

Cashman, K.V., 1991. Textural constraints on the kinetics of crystallization of igneous rocks. In: Nicholls, J. and Russell, J.K. (Eds), Modern methods of igneous petrology. Rev. Mineral., Vol. 24, pp. 259–314.

Charlier, B.L.A., 2000. U–Th isotopic constraints on the pre-eruptive dynamics of large-scale silicic volcanism: examples from New Zealand. Ph.D. Thesis, The Open University, Milton Keynes (U.K.).

Charlier, B.L.A., Peate, D.W., Wilson, C.J.N., Lowenstern, J.B., Storey, M., Brown, S.J.A., 2003. Crystallization ages in coeval silicic magma bodies: $^{238}$U–$^{230}$Th disequilibrium evidence from the Rotoitii and Earthquake Flat eruption deposits, Taupo Volcanic Zone, New Zealand. Earth Planet. Sci. Lett., 206, 441–457.

Charlier, B.L.A., Wilson, C.J.N., Lowenstern, J.B., Blake, S., Van Calsteren, P.W., Davidson, J.P., 2005. Magma generation at a large, hyperactive silicic volcano (Taupo, New Zealand) revealed by U–Th and U–Pb systematics in zircon. J. Petrol., 46, 3–32.

Cherniak, D.J., 1996. Strontium diffusion in sanidine and albite, and general comments on strontium diffusion in alkali feldspars. Geochim. Cosmochim. Acta, 60, 5037–5043.

Cherniak, D.J., Watson, E.B., 2001. Pb diffusion in zircon. Chem. Geol., 172, 5–24.

Chesner, C.A., 1998. Petrogenesis of the Toba Tuffs, Sumatra, Indonesia. J. Petrol., 39, 397–438.

Chesner, C.A., Rose, W.I., 1991. Stratigraphy of the Toba Tuffs and evolution of the Toba Caldera Complex, Sumatra, Indonesia. Bull. Volcanol., 53, 343–356.

Chesner, C.A., Rose, W.I., Deino, A., Drake, R., Westgate, J.A., 1991. Eruptive history of Earth's largest Quaternary caldera (Toba, Indonesia) clarified. Geology, 19, 200–203.

Christensen, J.N., DePaolo, D.J., 1993. Timescale of large volume silicic magma systems: Sr isotopic systematics of phenocrysts and glass from the Bishop Tuff, Long Valley. Contrib. Mineral. Petrol., 113, 100–114.

Christensen, J.N., Halliday, A.N., 1996. Rb–Sr ages and Nd isotopic compositions of melt inclusions from the Bishop Tuff and the generation of silicic magma. Earth Planet. Sci. Lett., 144, 547–561.

Christiansen, R.L., 2001. The Quaternary and Pliocene Yellowstone Plateau volcanic field of Wyoming, Idaho, and Montana. U.S. Geological Survey Professional Paper, 729-G.

Christiansen, R.L., Foulger, G.R., Evans, J.R., 2002. Upper-mantle origin of the Yellowstone hotspot. Bull. Geol. Soc. Am., 114, 1245–1256.

Condomines, M., Gauthier, P.-J., Sigmarsson, O., 2003. Timescales of magma chamber processes and dating of young volcanic rocks. In: Bourdon, B., Henderson, G.M., Lundstrom, C.C. and Turner, S.P. (Eds), Uranium series geochemistry, Rev. Mineral. Geochem., Mineralogical Society of America, Washington D.C., Vol. 52, 125–174.

Costa, F., Chakraborty, S., 2004. Decadal time gaps between mafic intrusion and silicic eruption obtained from chemical zoning patterns in olivine. Earth Planet. Sci. Lett., 227, 517–530.

Costa, F., Chakraborty, S., Dohmen, R., 2003. Diffusion coupling between trace and major elements and a model for calculation of magma residence times using plagioclase. Geochim. Cosmochim. Acta, 67, 2189–2200.

Costa, F., Dungan, M., 2005. Short time scales of magmatic assimilation from diffusion modelling of multiple elements in olivine. Geology, 33, 837–840.

Crisp, J.A., 1984. Rates of magma emplacement and volcanic output. J. Volcanol. Geotherm. Res., 20, 177–211.

Davies, G.R., Halliday, A.N., 1998. Development of the Long Valley rhyolite magma system: strontium and neodymium isotope evidence from glasses and individual phenocrysts. Geochim. Cosmoch. Acta, 62, 3561–3574.

Davies, G.R., Halliday, A.N., Mahood, G.A., Hall, C.M., 1994. Isotopic constraints on the production rates, crystallization histories and residence times of pre-caldera silicic magmas, Long Valley, California. Earth Planet. Sci. Lett., 125, 17–37.

Dazé, A., Lee, J.K.W., Villeneuve, M., 2003. An intercalibration study of the Fish Canyon sanidine and biotite $^{40}Ar/^{39}Ar$ standards and some comments on the age of the Fish Canyon Tuff. Chem. Geol., 1999, 111–127.

Dickin, A.P., 2005. Radiogenic isotope geology. Cambridge University Press, Cambridge, 510 pp.

Dodson, M.H., 1973. Closure temperature in cooling geochronological and petrological systems. Contrib. Mineral. Petrol., 40, 259–274.

Dodson, M.H., 1986. Closure profiles in cooling systems. Mater. Sci. Forum, 7, 145–154.

Dufek, J., Bergantz, G.W., 2005. Lower crustal magma genesis and preservation: a stochastic framework for the evaluation of basalt–crust interaction. J. Petrol., 46, 2167–2195.

Duffield, W.A., Ruiz, J., Webster, J.D., 1995. Roof-rock contamination of magma along the top of the reservoir for the Bishop Tuff. J. Volcanol. Geotherm. Res., 69, 187–195.

Faure, G., Mensing, T.M., 2004. Isotopes: Principles and Applications. Wiley, Hoboken, 928 pp.

Foland, K.A., 1994. Argon diffusion in feldspars. In: Parsons, I. (Ed.), Feldspars and Their Reactions. Kluwer, Dordrecht, pp. 415–447.

Francis, P., Oppenheimer, C., 2003. Volcanoes. Oxford University Press, Oxford, 534 pp.

Froggatt, P.C., Lowe, D.J., 1990. A review of late Quaternary silicic and some other tephra formations from New Zealand: their stratigraphy, nomenclature, distribution, volume, and age. N. Z. J. Geol. Geophys., 33, 89–109.

Furlong, K.P., Hanson, R.B., Bowers, J.R., 1991. Modeling thermal regimes. In: Kerrick, D.M. (Ed.), Contact metamorphism, Rev. Mineral. 26, 437–505.

Ganguly, J., 2002. Diffusion kinetics in minerals: principles and applications to tectono-metamorphic processes. EMU Notes Mineral., 4, 271–309.

Ganguly, J., Tirone, M., 1999. Diffusion closure temperature and age of a mineral with arbitrary extent of diffusion: theoretical formulation and applications. Earth Planet. Sci. Lett., 170, 131–140.

Ganguly, J., Tirone, M., 2001. Relationship between cooling rate and cooling age of a mineral: theory and applications to meteorites. Meteoritics Planet. Sci., 36, 167–175.

Gansecki, C.A., Mahood, G.A., McWilliams, M.O., 1996. [40]Ar/[39]Ar geochronology of rhyolites erupted following collapse of the Yellowstone caldera, Yellowstone Plateau volcanic Field: implications for crustal contamination. Earth Planet. Sci. Lett., 142, 91–107.

Gansecki, C.A., Mahood, G.A., McWilliams, M.O., 1998. New ages for the climatic eruption at Yellowstone: single crystal [40]Ar/[39]Ar dating identifies contamination. Geology, 26, 343–346.

Gardner, J.E., Layer, P.W., Rutherford, M.J., 2002. Phenocrysts versus xenocrysts in the youngest Toba Tuff: implications for the petrogenesis of 2800 km[3] of magma. Geology, 30, 347–350.

Gerbi, C., Johnson, S.E., Paterson, S.R., 2004. Implications of rapid, dike-fed pluton growth for host-rock strain rates and emplacement mechanisms. J. Struct. Geol., 26, 583–594.

Ghiorso, M.S., Sack, R.O., 1995. Chemical mass transfer in magmatic processes IV. A revised and internally consistent thermodynamic model for the interpolation and extrapolation of liquid–solid equilibria in magmatic systems at elevated temperatures and pressures. Contrib. Mineral. Petrol., 119, 197–212.

Giletti, B.J., Casserly, J.E.D., 1994. Strontium diffusion kinetics in plagioclase feldspars. Geochim. Cosmoch. Acta, 58, 3785–3797.

Glazner, A.F., Bartley, J.M., Coleman, D.S., Gray, W., Taylor, R.Z., 2004. Are plutons assembled over millions of years by amalgamation from small magma chambers? Geol. Today, 14, 4–11.

Gray, J.P., Monaghan, J.J., 2004. Numerical modeling of stress fields and fracture around magma chambers. J. Volcanol. Geotherm. Res., 135, 259–283.

Grove, M., Harrison, T.M., 1996. [40]Ar* in Fe-rich biotite. Am. Mineral., 81, 940–951.

Guéguen, Y., Palciauskas, V., 1994. Introduction to the Physics of Rocks. Princeton University Press, Princeton, 294 pp.

Halliday, A.N., Mahood, G.A., Holden, P., Metz, J.M., Dempster, T.J., Davidson, J.P., 1989. Evidence for long residence times of rhyolite magma in the Long Valley magma system; the isotopic record in the pre-caldera rhyolite lavas of Glass Mountain. Earth Planet. Sci. Lett., 94, 274–290.

Harrison, T.M., 1981. Diffusion of [40]Ar in hornblende. Contrib. Mineral. Petrol., 78, 324–331.

Hawkesworth, C., George, R., Turner, S., Zellmer, G., 2004. Time scales of magmatic processes. Earth Planet. Sci. Lett., 218, 1–16.

Hervig, R.L., Dunbar, N.W., 1992. Cause of chemical zoning in the Bishop (California) and Bandelier (New Mexico) magma chambers. Earth Planet. Sci. Lett., 111, 97–108.

Heumann, A., 1999. Timescales of processes within silicic magma chambers. Ph.D. Thesis Vrije Univesiteit, Amsterdam, 198 pp.

Heumann, A., Davies, G.R., 1997. Isotopic and chemical evolution of the post-caldera rhyolitic system at Long Valley, California. J. Petrol., 38, 1661–1678.

Heumann, A., Davies, G.R., Elliot, T., 2002. Crystallization history of rhyolites at Long Valley, California, inferred from combined U–series and Rb–Sr isotope systematics. Geochim. Cosmochim. Acta, 66, 1821–1837.

Hildreth, E.W., 1979. The Bishop Tuff: evidence for the origin of the compositional zonation ins silicic magma chambers. Geol. Soc. Am. Special Paper, 180, 43–76.

Hildreth, E.W., 2004. Volcanological perspectives on Long Valley, Mammoth Mountain, and Mono Craters: several contiguous but discrete systems. J. Volcanol. Geotherm. Res., 136, 169–198.

Hildreth, E.W., 1981. Gradients in silicic magma chambers: implications for lithospheric magmatism. J. Geophys. Res., 86, 10153–10192.

Hildreth, E.W., Christiansen, R.L., O'Neil, J.R., 1984. Catastrophic isotopic modification of rhyolitic magma at times of caldera subsidence, Yellowstone Plateau Volcanic field. J. Geophys. Res., 89, 8339–8369.

Hildreth, E.W., Wilson, C.J.N., 2007. Compositional zoning of the Bishop Tuff. J. Petrol., 48, 951–999.

Holland, H.D., 1978. The Chemistry of the Atmosphere and Oceans. Wiley, New York.

Houghton, B.F., Wilson, C.J.N., McWilliams, M.O., Lanphere, M.A., Weaver, S.D., Briggs, R.M., Pringle, M.S., 1995. Chronology and dynamics of a large silicic magmatic system: Central Taupo Volcanic Zone, New Zealand. Geology, 23, 13–16.

Izett, G.A., Obradovich, J.D., 1994. $^{40}$Ar/$^{39}$Ar age constraints for the Jaramillo Normal Subchron and the Matuyama–Brunhes geomagnetic boundary. J. Geophys. Res., 99, 2925–2934.

Jellinek, M., DePaolo, D., 2003. A model for the origin of large silicic magma chambers: precursors of caldera-forming eruptions. Bull. Volcanol., 65, 363–381.

Johannes, W., Holtz, F., 1996. Petrogenesis and experimental petrology of granitic rocks. Springer-Verlag, Berlin, 335 pp.

Johnson, M., Rutherford, M.J., 1989. Experimentally determined conditions in the Fish Canyon Tuff, Colorado, Magma chamber. J. Petrol., 30, 711–737.

Keller, J., 1969. Origin of rhyolites by anatectic melting of granitic crustal rocks; the example of rhyolitic pumice from the island of Kos (Aegean sea). Bull. Volcanol., 33, 942–959.

Kelley, S.P., Wartho, J.-A., Elphick, S.C., 2002. Experimental determinations of Ar diffusion and solubility in plagioclase and leucite. Geochim. Cosmochim. Acta, 66(Suppl. 1), A390.

Lanphere, M.A., 2004. Reply to comment on 'Precise K–Ar, $^{40}$Ar/$^{39}$Ar, Rb–Sr and U/Pb mineral ages from the 27.5 Ma Fish Canyon Tuff reference standard' by M.A. Lanphere and H. Baadsgaard. Chem. Geol., 211, 389–390.

Lanphere, M.A., Baadsgaard, H., 2001. Precise K–Ar, $^{40}$Ar/$^{39}$Ar, Rb–Sr and U/Pb mineral ages from the 27.5 Ma Fish Canyon Tuff reference standard. Chem. Geol., 175, 653–671.

Lanphere, M.A., Champion, D.E., Christiansen, R.L., Izett, G.A., Obradovich, J.D., 2002. Revised ages for tuffs of the Yellowstone Plateau volcanic field: assignment of the Huckleberry Ridge Tuff to a new geomagnetic polarity event. Bull. Geol. Soc. Am., 114, 559–568.

Lasaga, A.C., 1998. Kinetic theory in the Earth Sciences. Princeton University Press, Princeton, 811 pp.

Lindsay, J.M., de Silva, S., Trumbull, R., Emmermann, R., Wemmer, K., 2001. La Pacana caldera, N. Chile: a reevaluation of the stratigraphy and volcanology of one of the world's largest resurgent calderas. J. Volcanol. Geotherm. Res., 106, 145–173.

Lipman, P., 1995. Declining growth of Mauna Loa during the last 100,000 years: rates of lava accumulation vs. gravitational subsidence, in Mauna Loa revealed: structure, composition, history, and hazards. In: Rhodes, J.M. and Lockwood, John P. (Eds), Geophys. Monogr., Vol. 92, pp. 45–80.

Lipman, P.W., 2000a. Calderas. In: Sigurdsson, H. (Ed.), Encyclopedia of Volcanoes, Academic Press, London, pp. 643–662.

Lipman, P.W., 2000b. The central San Juan caldera cluster: regional volcanic framework. In: Bethke, P.M. and Hay, R.L. (Eds), Ancient Lake Creede: its volcano-tectonic setting, history of sedimentation, and relation of mineralization in the Creed mining district. Geological Society of America Special Paper, 346, 9–69.

Lowenstern, J.B., Persing, H.M., Wooden, J.L., Lanphere, M., Donnelly-Nolan, J., Grove, T.L., 2000. U–Th dating of single zircons from young granitoid xenoliths: new tools for understanding volcanic processes. Earth Planet. Sci. Lett., 183, 291–302.

Mahood, G.A., 1990. Evidence for long residence times of rhyolitic magma in the Long Valley magmatic system: the isotopic record in the pre-caldera lavas of glass mountain-reply. Earth Planet. Sci. Lett., 99, 395–399.

Mankinen, E.A., Grommé, C.S., Dalrymple, G.B., Lanphere, M.A., Bailey, R.A., 1986. Paleomagnetism and K–Ar ages of volcanic rocks from Long Valley caldera, California. J. Geophys. Res., 91, 633–652.

Marsh, B.D., 1988. Crystal size distribution (CSD) in rocks and the kinetics and dynamics of crystallization. 1. Theory. Contrib. Mineral. Petrol., 99, 277–291.

McDougall, I., Harrison, T.M., 1999. Geochronology and Thermochronology by the $^{40}Ar/^{39}Ar$ method, Second Edition. Oxford University Press, New York, 269 pp.

Metz, J.M., Mahood, G.A., 1985. Precursors to the Bishop Tuff eruption: Glass Mountain, Long Valley, California. J. Geophys. Res., 90, 11121–11126.

Metz, J.M., Mahood, G.A., 1991. Development of the Long Valley magma chamber recorded in precaldera rhyolite lavas of Glass Mountain, California. Contrib. Mineral. Petrol., 106, 379–397.

Michael, P.J., 1983. Chemical differentiation of the Bishop Tuff and other high-silica magmas through crystallization processes. Geology, 11, 31–34.

Michaut, C., Jaupart, C., 2006. Ultra-rapid formation of large volumes of evolved magma. Earth Planet. Sci. Lett., 250, 38–52.

Miller, C.D., 1985. Holocene eruptions of the Inyo Volcanic Chain, California: implications for possible eruptions in Long Valley caldera. Geology, 13, 14–17.

Min, K., Mundil, R., Renne, P.R., Ludwig, K.R., 2000. A test for systematic errors in 40Ar/39Ar geochronology through comparison with U–Pb analysis of a 1.1 Ga Rhyolite. Geochim. et Cosmochim. Acta, 64, 73–98.

Morgan, D.J., Blake, S., 2006. Magmatic residence times of zoned phenocrysts: introduction and application of the binary element diffusion modelling (BEDM) technique. Contrib. Mineral. Petrol., 151, 58–70.

Newnham, R.M., Eden, D.N., Lowe, D.J., Hendy, C.H., 2003. Rerewhakaaitu Tephra, a land–sea marker for the Last Termination in New Zealand, with implications for global climate change. Quat. Sci. Rev., 22, 289–308.

Ninkovich, D., Shackleton, N.J., Abdel-Monem, A.A., Obradovich, J.D., Izett, G., 1978. K–Ar age of the late Pleistocene eruption of Toba, north Sumatra. Nature, 276, 574–577.

Norton, D., Knight, J., 1977. Transport phenomena in hydrothermal systems: cooling of plutons. Am. J. Sci., 277, 937–981.

Oberli, F., Meier, M., Berger, A., Rosenberg, C.L., Giere, R., 2004. U–Th–Pb and $^{230}Th/^{238}U$ disequilibrium isotope systematics: precise accessory mineral chronology and melt evolution tracing in the Alpine Bergell intrusion. Geochim. Cosmochim. Acta, 68, 2543–2560.

Obradovich, J.D., 1992. Geochronology of the late Cenozoic volcanism of Yellowstone National Park and adjoining areas, Wyoming and Idaho, U.S. Geological Survey Open-File Report, 92–408, 1–45.

Peate, D.W., Hawkesworth, C.J., 2005. U series disequilibria: insights into mantle melting and the timescales of magma differentiation. Rev. Geophys., 43, doi: 10.1029/2004RG000154.

Petford, N., Cruden, A.R., McCaffrey, K.J.W., Vigneresse, J.-L., 2000. Granite magma formation, transport and emplacement in the Earth's crust. Nature, 408, 669–673.

Phillips, E., McIntosh, W., Kyle, P., Goff, F., Gardner, J.N., 2003. Age constraints on the timing and duration of resurgence of the Valles Caldera, New Mexico, Eos Trans. AGU, 84 (46), Fall Meet. Suppl., Abstract V52-04.

Pringle, M., McWilliams, M., Houghton, B.F., Lanphere, M.A., Wilson, C.J.N., 1992. $^{40}Ar/^{39}Ar$ dating of Quaternary feldspar: examples from the Taupo Volcanic Zone, New Zealand. Geology, 20, 531–534.

Pritchard, M.E., Simons, M., 2004. An InSAR-based survey of volcanic deformation in the central Andes. Geochem., Geophys., Geosys., 5, doi: 10.1029/2003GC000610.

Qin, Z., Lu, F., Anderson, A.T., Jr., 1992. Diffusive reequilibration of melt and fluid inclusions. Am. Mineral., 77, 565–576.

Reid, M., 2003. Timescales of magma transfer and storage in the crust. In: Holland, H.D. and Turekian, K.K. (Eds), Treatise on geochemistry: The crust, Elsevier Pergamon, San Diego, Vol. 3, pp. 167–193.

Reid, M.R., Coath, C.D., 2000. In situ U–Pb ages of zircons from the Bishop Tuff: no evidence for long crystal residence times. Geology, 28, 443–446.

Reid, M.R., Coath, C.D., Harrison, T.M., McKeegan, K.D., 1997. Prolonged residence times for the youngest rhyolites associated with Long Valley Caldera: $^{230}Th$ $^{238}U$ ion microprobe dating of young zircons. Earth Planet. Sci. Lett., 150, 27–39.

Reiners, P.W. Ehlers, T.A., 2005. Past, present, and future of thermochronology. In: Reiners, P.W. and Ehlers, T.A (Eds), Rev. Mineral. Geochem., 58, 1–18.

Renne, P.R., 2000. $^{40}$Ar/$^{39}$Ar age of plagioclase from Acapulco meteorite and the problem of systematic errors in cosmochronology. Earth Planet. Sci. Lett., 175, 13–26.

Renne, P.R., Karner, D.B., Ludwig, K.R., 1998. Absolute ages aren't exactly. Science, 282, 1840–1841.

Ring, J.H., 2000. Young volcanism in western Long Valley, California. MS Thesis, Stanford University, 202 pp.

Rose, W.I., Chesner, C.A., 1987. Dispersal of ash in the great Toba eruption, 75 ka. Geology, 15, 913–917.

Schmitt, A.K., Lindsay, J.M., de Silva, S., Trumbull, R.B., 2002. U–Pb zircon chronostratigraphy of early-Pliocene ignimbrites from La Pacana, north Chile: implications for the formation of stratifies magma chambers. J. Volcanol. Geotherm. Res., 120, 43–53.

Schmitz, M.D., Bowring, S.A., 2001. U–Pb zircon and titanite systematics of the Fish Canyon Tuff: an assessment of high precision U–Pb geochronology and its application to young volcanic rocks. Geochim. Cosmochim. Acta, 65, 2571–2587.

Schmitz, M.D., Bowring, S.A., Ludwig, K.R., Renne, P.R., 2003. Comment on "Precise K–Ar, $^{40}$Ar/$^{39}$Ar, Rb–Sr and U/Pb mineral ages from the 27.5 Ma Fish Canyon Tuff reference standard" by M.A. Lanphere and H. Baadsgaard. Chem. Geol., 199, 277–280.

Schoene, B., Crowley, J.L., Condon, D.J., Schmitz, M.D., Bowring, S.A., 2006. Reassessing the uranium decay constants for geochronology using ID–TIMS U–Pb data. Geochim. Cosmochim. Acta, 70, 426–445.

Self, S., Goff, F., Gardner, J.N., Wright, J.V., Kite, W.M., 1986. Explosive rhyolitic volcanism in the Jemez Mountains, vent locations, caldera development, and relation to regional structure. J. Geophys. Res., 91, 1779–1798.

Self, S., Heiken, G., Sykes, M.L., Wohletz, K., Fisher, R.V., Deiter, D.P., 1996. Field excursions to the Jemez mountains, New Mexico. New Mexico Bureau of Mines and Mineral Resources Bulletin, 134, 72 pp.

Shaw, H.R., 1985. Links between magma-tectonic rate balances, plutonism and volcanism. J. Geophys. Res., 90, 11275–11288.

Simon, J.I., Reid, M.R., 2005. The pace of rhyolite differentiation and storage in an 'archetypical' silicic magma system, Long Valley, California. Earth Planet. Sci. Lett., 235, 123–140.

Smith, P.E., Evensen, N.M., York, D., 2000. Under the volcano. A new dimension in Ar–Ar dating of volcanic ash. Geophys. Res. Lett., 27, 585–588.

Smith, P.E., York, D., Evensen, N.M., 1996. Single crystal $^{40}$Ar–$^{39}$Ar dating of a Late Quaternary paroxysm on Kos, Greece: concordance of terrestrial and marine ages. Geophys. Res. Lett., 21, 3047–3050.

Smith, R.L., 1979. Ash-flow magmatism, In: Chapin, C.E. and Elston, W.E. (Eds), Ash-flow Tuffs. Geological Society of America Special Paper 180, 5–27.

Smith, R.L., Bailey, R.A., 1966. The Bandelier Tuff– a study of ash-flow eruption cycles from zoned magma chambers. Bull. Volcanol., 29, 83–104.

Smith, V.C., Shane, P., Nairn, I.A., 2005. Trends in rhyolite geochemistry, mineralogy, and magma storage during the last 50 kyr at Okataina and Taupo volcanic centres, Taupo Volcanic Zone, New Zealand. J. Volcanol. Geotherm. Res., 148, 372–406.

Sparks, R.S.J., Huppert, H.E., Wilson, C.J.N., 1990. Discussion of "Evidence for long residence times of rhyolite magma in the Long Valley magma system; the isotopic record in the pre-caldera rhyolite lavas of Glass Mountain" by A.N Halliday, G. Mahood, P. Holden, J.M. Metz, T.J. Dempster and J.P. Davidson. Earth Planet. Sci. Lett., 99, 387–389.

Spell, T.L., Harrison, T.M., Wolff, J.A., 1990. $^{40}$Ar/$^{39}$Ar dating of the Bandelier Tuff and San Diego Canyon ignimbrites, Jemez Mountains, New Mexico-temporal constraints on magmatic evolution. J. Volcanol. Geotherm. Res., 43, 175–193.

Spell, T.L., McDougall, I., Doulgeris, A.P., 1996. Cerro Toledo Rhyolite, Jemez Volcanic field, New Mexico: $^{40}$Ar/$^{39}$Ar geochronology of eruptions between two caldera-forming events. Bull. Geol. Soc. Am., 108, 1549–1566.

Stix, J., Goff, F., Gorton, M.P., Heiken, G., Garcia, S.R., 1988. Restoration of compositional zonation in the Bandelier silicic magma chamber between two caldera-forming eruptions:

geochemistry and origin of the Cerro Toledo Rhyolite, Jemez Mountains, New Mexico. J. Geophys. Res., 93, 6129–6147.

Tait, S., Jaupart, C., Vergniole, S., 1989. Pressure, gas content and eruption periodicity of a shallow, crystallizing magma chamber. Earth Planet. Sci. Lett., 92, 107–123.

Titus, S.J., Clark, R., Tikoff, B., 2005. Geologic and geophysical investigation of two fine grained granites, Sierra Nevada Batholith, California: evidence for structural controls on emplacement and volcanism. Bull. Geol. Soc. Am., 117, 1256–1271.

Turner, S., Bourdon, B., Gill, J., 2003. Insights into magma genesis at convergent margins from U-series isotopes. In: Bourdon, B., Henderson, G.M., Lundstrom, C.C. and Turner, S.P. (Eds), Uranium series geochemistry, Rev. Mineral. Geochem., Mineralogical Society of America, Washington D.C., Vol. 52. pp. 255–315.

Van den Bogaard, P., Schirnick, C., 1995. $^{40}$Ar/$^{39}$Ar laser probe ages of Bishop Tuff quartz phenocrysts substantiate long-lived silicic chamber at Long Valley, United States. Geology, 23, 759–762.

Vazquez, J., Reid, M.R., 2002. Time scales of magma storage and differentiation of voluminous high-silica rhyolites at Yellowstone caldera, Wyoming. Contrib. Mineral. Petrol., 144, 274–285.

Vazquez, J.A., Reid, M.R., 2004. Probing the accumulation history of voluminous Toba magma. Science, 305, 991–994.

Villeneuve, M., Sandeman, H.A., Davis, W.J., 2000. A method for intercalibration of U–Th–Pb and $^{40}$Ar/$^{39}$Ar ages in the Phanerozoic. Geochim. Cosmochim. Acta, 64, 4017–4030.

Wadge, G., 1982. Steady state volcanism: evidence from eruption histories of polygenetic volcanoes. J. Geophys. Res., 87, 4035–4049.

Wallace, P.J., Anderson, A.T., Jr., Davis, A.M., 1999. Gradients in $H_2O$, $CO_2$, and exsolved gas in a large-volume silicic magma system: interpreting the record preserved in melt inclusions from the Bishop Tuff. J. Geophys. Res., 104, 20097–20122.

Wark, D.A., Hildreth, W., Spear, F.S., Cherniak, D.J., Watson, E.B., 2007. Pre-eruption recharge of the Bishop magma system. Geology, 35, 235–238.

Watson, E.B., Cherniak, D.J., 2003. Lattice diffusion of Ar in quartz, with constraints on Ar solubility and evidence of nanopores. Geochim. Cosmochim. Acta, 67, 2043–2062.

White, S.M., Crisp, J.A., Spera, F.J., 2006. Long-term volumetric eruption rates and magma budgets. Geochem., Geophys., Geosys., 7, doi: 10.1029/2005GC001002.

Wilson, C.J.N., 1993. Stratigraphy, chronology, styles and dynamics of late Quaternary eruptions from Taupo Volcano, New Zealand. Phil. Trans. Royal Soc. Lond. Ser. A, 343, 205–306.

Wilson, C.J.N., 2001. The 26.5 ka Oruanui eruption, New Zealand: an introduction and overview. J. Volcanol. Geotherm. Res., 112, 133–174.

Wilson, C.J.N., Blake, S., Charlier, B.L.A., Sutton, A.N., 2006. The 26.5 ka Oruanui eruption, Taupo Volcano, New Zealand: development, characteristics and evacuation of a large Rhyolitic magma body. J. Petrol., 47, 35–69.

Wilson, C.J.N., Switsur, V.R., Ward, A.P., 1988. A new 14C age for the Oruanui (Wairakei) eruption, New Zealand. Geol. Mag., 125, 297–300.

Winick, J.A., McIntosh, W.C., Dunbar, N.W., 2001. Melt-inclusion-hosted excess $^{40}$Ar in quartz crystals of the Bishop and Bandelier magma systems. Geology, 29, 275–278.

Wolff, J.A., Balsley, S.D., Gregory, R.T., 2002. Oxygen isotope disequilibrium between quartz and sanidine from the Bandelier Tuff, New Mexico, consistent with a short residence time of phenocrysts in rhyolitic magma. J. Volcanol. Geotherm. Res., 116, 119–135.

Wolff, J.A., Ramos, F.C., 2003. Pb isotope variations among Bandelier Tuff feldspar: no evidence for a long-lived silicic magma chamber. Geology, 31, 533–536.

Wolff, J.A., Ramos, F.C., Davidson, J.P., 1999. Sr isotope disequilibrium during differentiation of the Bandelier Tuff: constraints on the crystallization of a large rhyolitic magma chamber. Geology, 27, 495–498.

Wolff, J.A., Wörner, G., Blake, S., 1990. Gradients in physical parameters in zoned felsic magma bodies: implications for evolution and eruptive withdrawal. J. Volcanol. Geotherm. Res., 43, 37–55.

Wood, S.H., 1983. Chronology of late Pleistocene and Holocene volcanics, Long Valley and Mono Basin geothermal areas, eastern California. US Geological Survey Open file report 83–747, 76 pp.

Yoshinobu, A.S., Girty, G.H., 1999. Measuring host rock volume changes during magma emplacement. J. Struct. Geol., 21, 111–116.

Žák, J., Paterson, S., 2005. Characteristics of internal contacts in the Tuolumne Batholith, central Sierra Nevada, California (USA): implications for episodic emplacement and physical processes in a continental arc magma chamber. Bull. Geol. Soc. Am., 117, 1242–1255.

This page intentionally left blank

# Sedimentology, Depositional Mechanisms and Pulsating Behaviour of Pyroclastic Density Currents

Roberto Sulpizio* *and* Pierfrancesco Dellino

## Contents

## Abstract

This work is an exploratory effort to address some key concepts about physical
processes that influence the mobility, sedimentology and depositional mechanisms of

*Corresponding author. Tel.: +39-0805442608; Fax: +39-0805442591
*E-mail address:* r.sulpizio@geomin.uniba.it

Dipartimento Geomineralogico, Università di Bari, via Orabona 4, 70125, Bari, Italy.

pyroclastic density currents. The main mechanisms of particle support are critically reviewed and their influence on depositional mechanisms is discussed. The depositional behaviour of pyroclastic density currents is discussed in the light of new models that consider the different typologies within a continuum spectrum that spans from very dilute (fluid-dominated) to very concentrated (solid-dominated) flows. The combination of progressive aggradation and *en masse* freezing models is proposed on the basis of a model that takes into account the stepwise aggradation of discrete pulses that develop within a single current and that stop *en masse* when resisting bulk forces exceed driving ones. The influence of various types of morphological settings and obstacles on depositional mechanisms and mobility of pyroclastic density currents is examined and discussed in detail. Some examples of stepwise aggradation within pulsating PDCs are discussed using analyses of lithofacies and lithofacies associations of deposits emplaced under different flow-boundary conditions.

# 1. INTRODUCTION: WHAT ARE PYROCLASTIC DENSITY CURRENTS?

Pyroclastic density currents (PDCs) are among the most amazing, complex and dangerous volcanic phenomena. They are moving mixtures of particles and gas that flow across the ground, and originate in different ways and from various sources, during explosive eruptions or gravity-driven collapse of domes. They may be short-lived (highly unsteady) or relatively long-lived (sustained unsteady to quasi-steady) phenomena, driven by both magmatic or phreatomagmatic melt fragmentation (e.g., Cas and Wright, 1987; Carey, 1991; Branney and Kokelaar, 2002; Figure 1).

From a fluid dynamic point of view, PDCs macroscopically behave as dense fluids (the pyroclastic mixture) immersed in a less dense, almost isothropic one (the atmosphere). They mainly move under the effect of gravity (e.g., Burgissier and Bergantz, 2002) and their mobility (distance travelled vs. difference in height from source and deposit) is greatly controlled by mass and height of generation (potential energy) and efficiency of conversion from potential to kinetic energy (i.e. loss of momentum due to frictional processes both within the current and at current edges). Because mass and frictional processes mainly relate to solid particles, the particle concentration in a PDC is crucial in determining the physical parameters of the moving flow (i.e. velocity, density, clast-support mechanism; Sparks, 1976; Middleton and Neal, 1989; Bonnecaze et al., 1993; Hallworth and Huppert, 1998; Branney and Kokelaar, 2002; Cao et al., 2003; Sulpizio et al., 2007). In currents that initiate explosively, the clast concentration of the pyroclastic mixture relates to the eruption style (collapse of a pyroclastic fountain or radial expansion of an over-pressurised jet), the volatile content of the erupting mixture, the mechanical energy released at fragmentation and the abundance of accidental fragments (Sparks et al., 1997a; Dingwell, 1998; Alidibirov and Dingwell, 2000). In currents generated by gravitational failures (e.g., dome collapses), the clast concentration in the mixture relates to the amount of gas released during failure and by block breakage during transport.
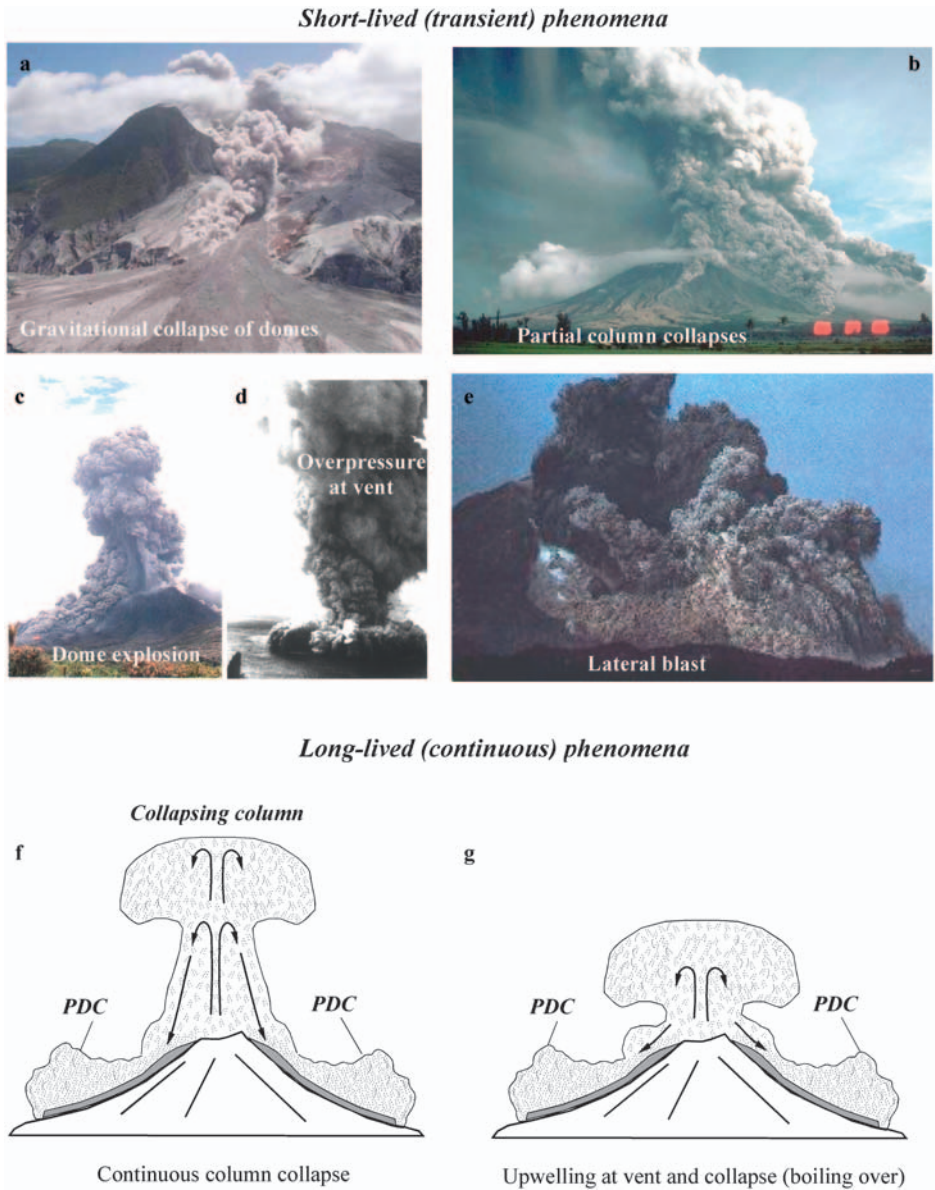
**Figure 1** Examples of generation of PDCs from different eruptive mechanisms. (a) Dome collapse at Soufriere Hills volcano, Montserrat (photo from Montserrat Volcano Observatory website); (b) PDCs generated by partial column collapses during the eruption of September 23, 1984 eruption of Mayon volcano (photo from Newhall, USGS website); (c) PDC generation by dome explosion at Soufriere Hills, Montserrat (photo from Montserrat Volcano Observatory website); (d) radial expanding PDC generated during phreatomagmatic activity at Capelinhos, Azores (photo from San Diego State University website); (e) generation of PDC by a lateral blast at the onset of May 18, 1980 eruption of St Helens volcano (photo from USGS website); (f) sketch of PDC generation by continuous column collapse; (g) sketch of PDC generation by boiling over mechanism.

Regardless of whether they are concentrated or diluted suspensions of gas and particles, PDCs consist of two essential and intergradational counterparts: an underflow and a phoenix plume (e.g., Fisher, 1966; Dade and Huppert, 1996; Baer et al., 1997; Branney and Kokelaar, 2002). The underflow is denser than the atmosphere and flows in direct contact with the ground. It usually comprises a basal part dominated by particle–particle interaction overlaid by a turbulent part dominated by traction processes (also known as ash-cloud surge; e.g. Cas and Wright, 1987). The phoenix (or coignimbrite plume) is less dense than atmosphere and lofts convectively (Dobran et al., 1993; Sparks et al., 1997a). Mass partitioning between the underflow and phoenix changes continuously during motion, particularly when: (1) a slope change induces sedimentation (concave local curvature; Denlinger and Iverson, 2001; Macias et al., 1998; Saucedo et al., 2004); or (2) mixing with air is enhanced (i.e. an accelerating moving mixture, convex local curvature; Branney and Kokelaar, 2002), or (3) where a change in the substrate (e.g. topographic jumps, surface roughness, standing water) affects the current (Fisher, 1990; Carey et al., 1996; Gurioli et al., 2002). The rate and behaviour of mass partitioning between the underflow and the phoenix plume influence the runout distance of a current as well as mass flux (e.g. Bursik and Woods, 1996; Branney and Kokelaar, 2002), density and grain size of pyroclasts (e.g. Taddeucci and Palladino, 2002) and rate of air entrainment (e.g. Huppert et al., 1986; Woods and Bursik, 1994; Nield and Woods, 2003).

The complex interplay between sedimentation and depositional mechanisms, coupled with the difficulty of direct observation of the internal flow organisation, make the study of PDCs a great challenge for volcanologists. The resulting literature is extensive, complex and sometimes contradictory. In this work, we will review and reinterpret some of the most crucial points in the physics of PDCs over topography. We will also illustrate some examples of PDC behaviour inferred from their deposits.

## 2. KEY CONCEPTS

### 2.1. The flow-boundary zone approach

PDC deposits record processes and physical conditions in a generically defined flow-boundary zone that includes the lowermost part of the current, the flow-deposit boundary and the uppermost part of the deposit (Branney and Kokelaar, 2002; Figure 2). From a sedimentological point of view, the flow-boundary zone can be considered that (lower) part of the current where particle–particle interaction dominates the transport mechanisms and promotes deposition.

It is important to note that the concept of flow-boundary zone (Branney and Kokelaar, 2002) neither contains limitations on its thickness nor takes into account the behaviour of the overriding flow. The concept of flow-boundary zone has been used in describing deposition of both fully turbulent and granular flow dominated small-scale PDCs (Sulpizio et al., 2007), with the thickness of the flow-boundary zone ranging between several centimetres and meters. The extreme case of a
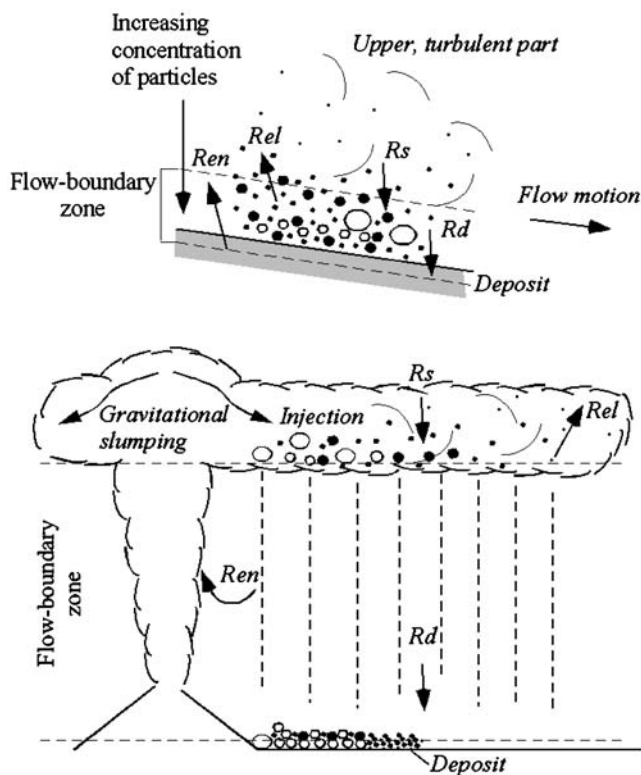
**Figure 2** Examples of flow-boundary zones. $R_{en}$, rate of re-entrainment of particles in the flow; $R_{el}$, rate of elutriation of particles from the flow-boundary zone; $R_s$, rate of supply from the upper part of the flow into the flow-boundary zone; $R_d$, rate of deposition from flow-boundary zone into deposit.

flow-boundary zone is that of fallout of pyroclastics from a convective plume and umbrella, with thickness up to tens of kilometres (Figure 2). The thickness of the flow-boundary zone can fluctuate during PDC motion and critically depends upon the ratio between rate of supply ($R_s$) and rate of deposition ($R_d$) reduced by the rate of elutriation ($R_{el}$). The rate of re-entrainment ($R_{en}$) increases the flow-boundary thickness only if removed particles are too heavy to be elutriated (Figure 2). Deposition from the flow-boundary zone can occur progressively or stepwise (Branney and Kokelaar, 1992).

## 2.2. Pyroclastic flows vs. pyroclastic surges

The deposits of PDCs vary from stratified to massive. The recognition of these two different lithofacies has motivated the development of two end-member models of PDCs (e.g. Cas and Wright, 1987; Walker, 1983). Stratified deposits have been proposed to be the products of dilute suspensions, pyroclastic surges, in which particles are mainly carried in turbulent suspension and in a thin flow-boundary

layer. Massive deposits result from highly concentrated mixtures, pyroclastic flows, in which particle–particle interactions dominate the pyroclast motion.

Recent works (e.g. Burgissier and Bergantz, 2002; Branney and Kokelaar, 2002; Sulpizio et al., 2007) have demonstrated how these two categories are just the end members of a continuous spectrum of PDCs, whose sedimentological character-istics mainly depend on the interplay of particle concentration, shear rate and depositional rate over time and space. Hereafter, we will discard the terms pyroclastic flow and pyroclastic surge as deposit characteristics. We will refer instead to the different typologies of PDCs using the terms diluted or concentrated, with sedimentological information supplied by lithofacies codes and architecture.

## 2.3. Steady vs. unsteady currents

A given PDC can experience variations of physical parameters (velocity, concentration, mass flux, etc.) with time at a fixed location. A current can be defined as steady with respect to a given parameter if that parameter does not vary with time at a fixed location. If the parameter fluctuates with time, the current is unsteady (Kneller and Branney, 1995). This means that we observe the current in an Eulerian reference frame and we can define the current as time variant or time invariant.

There are three main types of unsteadiness: waxing is when a given parameter at a fixed location increases with time, waning is when a given parameter at a fixed location decreases with time, and quasi-steady is when a parameter fluctuates only slightly around some average value (Branney and Kokelaar, 2002).

It is important to note that the concept of steadiness and unsteadiness applies to parameters that characterise the whole current. In comparison to behaviour of particles within the PDC as a whole, particles at the point of observation can exhibit contrasting behaviour. For example, even for waxing and steady currents, a particle can experience a decrease in the considered parameter. If we consider the velocity, a particle can decelerate and settle down the current thickness in waxing, waning and steady flows, depending on the support mechanisms that act within the flow and their spatial distribution. This means that using a Lagrangian reference frame we can describe the variation of parameters for a single particle within the PDC.

## 2.4. Sedimentation vs. deposition

The terms sedimentation and deposition are sometimes confused and improperly used in describing the processes that influence PDC behaviour. Therefore, it is important to clarify their relationships here. The term sedimentation describes all processes that accompany the motion of a particle throughout the current thickness down to the flow-boundary zone. The mass flux of particles that settle across the upper part of the flow-boundary zone define the $R_s$. This implies that only hypotheses on the sedimentation processes can be made based on deposit characteristics. The term deposition describes all processes that affect a particle in the flow-boundary zone until the definitive rest in the deposit. The mass flux of

particles that pass from the flow-boundary zone to the deposit defines the $R_d$. This implies that the deposition processes can be inferred on the basis of deposit characteristics.

## 3. Sedimentology: Main Particle Support and Segregation Mechanisms in PDCs

PDCs are intrinsically heterogeneous media that comprise a fluid and a solid phase. Several factors can influence the heterogeneity of PDCs and the transport of solid particles, including: (i) variability at the source in time and space (e.g. velocity fluctuation, concentration, etc.), due to non-homogeneous injections of pyroclastic material into the atmosphere from the vent; (ii) segregation processes within the current (e.g. due to development of density stratification); (iii) different characteristics of the upper and lower flow-boundary zones, due to processes of elutriation, entrapment and turbulence; (iv) ingestion of air; (v) influence of topography; (vi) sedimentation and/or erosional processes that induce changes in the physical properties of PDCs and substrate in time and space (Branney and Kokelaar, 2002).

The fluid phase supports solid particles through different mechanisms, which are usually: suspension due to fluid turbulence, intermittent saltation, traction (sliding and rolling) and fluid support (fluidisation). Additional mechanisms of particle support are particle–particle collisions and matrix support. The combination of different mechanisms acting on a particle changes in time and space, as it experiences different concentrations and shear intensities during settling. Support mechanisms influence the segregation processes and determine the settling velocity of a particle.

Segregation processes induce density stratification within PDCs and determine their depositional characteristics and subsequently, their lithofacies. Segregation processes can occur within the whole PDC, at the flow boundary and/or within the deposit (e.g. loading processes that induce sinking of large particles and/or elutriation pipes).

## 3.1. Support due to fluid turbulence

Fluid turbulence acts as particle support mechanism through fluid drag and lift forces (Figure 3a). If the concentration of particles in a PDC is lower than a few volume percent, the particle interactions are negligible and turbulence dominates the support mechanisms.

Clasts within a fully turbulent PDC segregate vertically. This implies that clasts with different hydraulic properties occupy three partially overlapping levels within the current, according to their main transport/support mechanism: suspension, intermittent suspension and traction (Middleton and Southard, 1984; Figure 3). Some dimensionless numbers and criterions describe the physical conditions necessary to maintain suspension. In particular, the Rouse number

Suspension population. They gentle settle from the dilute ash cloud that accompanies the main current. During flow motion they belong to and are part of the fluid phase

Saltation, sliding and rolling population. Ash and fine lapilli transported by fluid turbulence through fluid drag (rolling and sliding) and fluid lift (saltation). Gravity-driven motion on lee sides of dunes (sliding and rolling) can cause local reverse grading of beds.

Traction carpet or traction population. Imbrication of large clasts due to the drag force exerted by the overriding current.

**Figure 3**    Different sediment support mechanisms and related deposits in a diluted, fully turbulent PDC. (a) Different mechanisms of fluid support of particles with different shapes (after Branney and Kokelaar, 2003; modified); (b) theoretical mechanism of formation of lithofacies lensL(n,i) at the very base of the current; (c) effect of fluid drag and fluid lift on saltation and rolling mechanisms of particle transport (lithofacies xsA); (d) gentle settling (direct fallout regime) of fine particles from the ash cloud that accompanies the waning phase of the current (lithofacies maccrA); (e) real deposit left by a dilute, fully turbulent PDC of the Pollena eruption (AD 472, Somma-Vesuvius, Italy).

($Pn_i$; Rouse, 1937; Valentine, 1987) defines suspension conditions for particles of a given grain size:

$$Pn_i = \frac{w_i}{ku^*} \tag{1}$$

where $w_i$ is the settling velocity of particles of a given grain size, $k$ the von Karman's coefficient (~0.4) and $u^*$ the shear velocity. Low Rouse numbers ($Pn_i \sim {<} 0.5$) correspond to small or light particles that can be efficiently transported in suspension by fluid turbulence, while Rouse numbers $> 2.5$ characterise coarser or heavier particles transported by mechanisms other than suspension (Valentine, 1987).

Recently, Leeder et al. (2005) proposed a dimensionless criterion, $\Lambda$, needed to maintain suspension for a given load. $\Lambda$ is defined as the ratio of the maximum vertical turbulent stress to the immersed weight of the suspended load above a unit bed area:

$$\Lambda = \frac{\rho(\overline{v'^2})_{max}}{m(\sigma - \rho/\sigma)g} \geq 1 \tag{2}$$

where $v'$ is fluctuating (instantaneous) vertical turbulent velocity, $\sigma$ and $\rho$ are solid and fluid densities, respectively, $m$ the suspended load dry mass and $g$ the acceleration of gravity.

Within the initial grain size population of a PDC, turbulence supports only the particles with low terminal velocity (smaller and/or lighter). This means that, with the exception of very energetic PDCs, the size of particles fully supported by turbulence never exceeds fine ash. These particles constitute the suspension population, and they are transported at any level within a PDC as fluid components (Figure 3d).

Particles with higher terminal velocity (coarser and/or denser) are intermittently supported by fluid turbulence. This is because turbulence produces fluctuations in the near-bed velocity that give rise to fluctuations in the forces on, and resultant motion of, particles in the flow-boundary zone (Schmeeckle and Nelson, 2003). These velocity fluctuations act on particles that spend the majority of their time in the lower part of the current, where they form the intermittent suspension population (Figure 3c). The motion of particles only intermittently supported by turbulence is named saltation, common in unsteady and turbulent PDCs. The term saltation indicates any process of clast bouncing at an interface, with the interface supplying intermittent support.

A typical dimensionless relation characterising the limiting conditions for the entrainment of bed particles into bedload motion can be written as (Raudkivi, 1990):

$$f(Re_p^*, \tau^*) = 0 \qquad (3)$$

where $Re_p^* = u^* d_p / \nu$ denotes a particle Reynolds number, with $u^*$ denoting the flow shear velocity, $d_p$ denoting a representative mean diameter of the entrained particles and $\nu$ denoting the kinematic viscosity of the fluid. The term $\tau^* = u^{*2}/(gRd_p)$ denotes a dimensionless bed shear stress (i.e. Shields' stress), with $g$ denoting gravitational acceleration, $R = (\rho_s - \rho)/\rho$ denoting the submerged specific density and $\rho_s$ and $\rho$ denoting the density of the entrained particle and the density of the fluid, respectively. It can be argued that Equation (3) can also be used to represent a dimensionless relation characterising the limit of entrainment into suspension of particles lying over a granular bed (Niño et al., 2003). In fact, $u^*$ is a measure of the turbulence intensity in the near-bed region, and $\tau^*$ can be interpreted as a measure of the ratio of turbulent lift to gravitational forces acting on the particle.

Particles with the highest terminal velocity are transported at the current-deposit interface by drag forces, and constitute the traction population (Figure 3b). This type of support occurs when the terminal velocity of particles is comparable to the drag force exerted by the fluid, causing the sliding and rolling of particles at the flow boundary (a process also known as traction; Middleton and Southard, 1984). Sliding and rolling processes are very common at the base of fully diluted and turbulent PDCs, but can also occur in more concentrated PDCs, where large blocks can roll at the flow-boundary under the drag force exerted by overriding flowing material. The clasts transported by intermittent or continuous support at an interface (e.g. at the deposit surface) can experience different segregation processes. As an example, clasts that roll under the effect of fluid drag in turbulent PDCs can result in alignments of clasts and/or crudely stratified layers with imbrication of

larger clasts (traction carpet; Sohn, 1997; Dellino et al., 2004; Figure 3b). Elongated clasts usually exhibit a preferential orientation of long axis perpendicular to the flow motion.

The proposed division of three partially overlapping layers is useful for a comprehensive description of main support mechanisms that act within a fully turbulent PDC. However, it is an oversimplification of reality because a particle can experience different support mechanisms during its down-current movement, or the support mechanisms can change according to current unsteadiness. Regardless, the progressive density stratification of turbulent PDCs with time increases the importance of particle-interaction processes, and may limit or suppress the effects of turbulence in the lower part of the current.

## 3.2. Fluid-escape regime and matrix support

Gas fluidisation has long been considered one of the main particle support mechanisms in PDCs. It is frequently invoked to explain both the mobility of concentrated PDCs and some characteristics of their deposits, such as gradation, sorting and the presence of elutriation pipes.

Several fluidisation mechanisms have been hypothesised to act in a moving PDC, and exhaustive reviews of these mechanisms can be easily found in the literature (Sparks, 1976, 1978; Wilson, 1980; Carey, 1991; Branney and Kokelaar, 2002). The escaping fluid supplies the clast support, but only for particles with terminal velocity comparable or lower than the force exerted by upward fluid movement (e.g. Roche et al., 2004). The particles with lower terminal velocity are elutriated, whereas those with higher terminal velocity should sink towards the base (Figure 4). Sinking processes occur only if the density of the particle is greater than the fluid density in which it is immersed. Since PDCs are usually density stratified, the larger clasts can be supported by the lower part of the current (a process also known as matrix support). PDCs can only be partially fluidised due to the wide grain-size spectra present in typical volcanic eruptions.

Fluid-escape processes and matrix support can be important mechanisms in highly concentrated PDCs. In these cases, the sedimentation and deposition of particles induces fluid expulsion from the flow-boundary zone, and the upward motion of escaping fluid delays the settling of particles toward the deposition zone. At the same time, part of the fluid remains entrapped in the flow-boundary zone. The amount of this fluid depends mainly on the porosity of particulate and on rate of new gas released by breakage or degassing of juvenile material (Figure 4). This type of fluidisation is probably the most effective and most common in PDCs that contain a broad range of particles, and does not require the occurrence of complicated external mechanisms that continuously induce fluidisation. The pressure drop with height induced by fluidisation has been demonstrated to be directly proportional to the escaping gas velocity and inversely proportional to the porosity of the particulate through the gas flows (Ergun equation; Roche et al., 2004). This implies that fines-rich grain sizes (low porosity) and/or large amounts of gas content/generation (increasing pore fluid pressure and/or escaping gas velocity) within a PDC are favourable conditions for
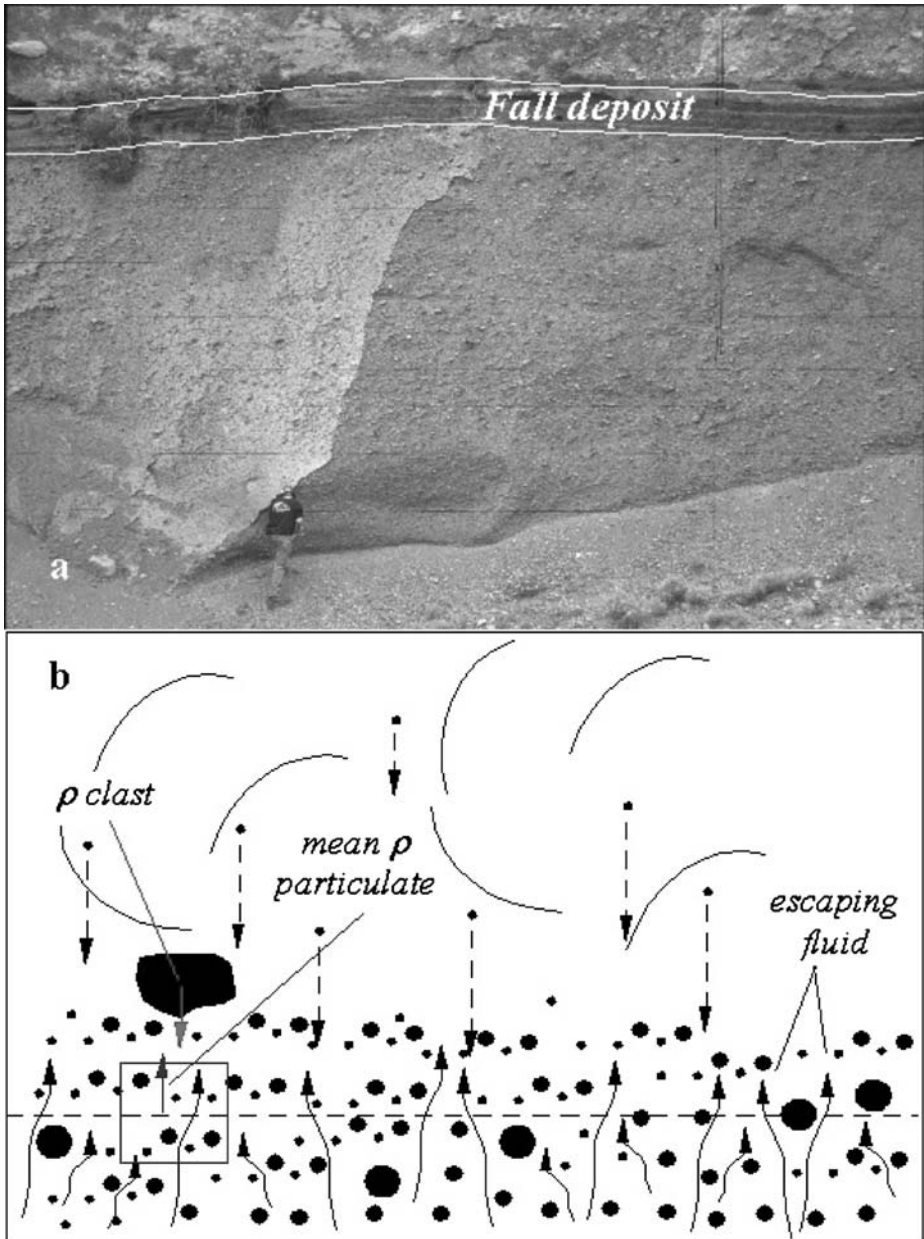
**Figure 4** Example of deposit (a) and mechanisms of particle support and segregation (b) for a flow-boundary zone dominated by fluid escape regime.

development of an effective fluid-escape regime. Deposits of PDCs dominated by fluid-escape regimes are fines-rich and usually show poor or absent grading of large, heavy clasts. Upward increases in concentration of large pumice and/or lighter clasts can occur due to floating processes related to density contrasts

with respect to the matrix (e.g. normal grading of lithic clasts and reverse grading of pumice).

Another mechanism that can support clasts and promote segregation in fines-rich concentrated PDCs is particle cohesion. Cohesion is a force characteristic of moist clay that aggregates and imparts a yield strength (or matrix strength) to the particulate. The amount of clay controls the strength, defined as the ability of a given material to absorb a finite amount of stress without deformation. Cohesion is often a characteristic of volcaniclastic flows, especially of those generated by erosion or failure of weathered, soil-rich and/or hydrothermally altered volcanic terrains. Cohesion effects in PDCs are usually negligible, although some ignimbrite characteristics have been interpreted in terms of current segregation induced by current yield strength (Wright and Walker, 1981; Freundt and Schmincke, 1986; Carey, 1991). However, PDCs are unlikely to contain moist clay aggregates because they are usually hot and do not contain large amounts of very fine particles ($<2\,\mu$m). An exception could be represented by low-temperature, fines-rich phreatomagmatic PDCs, in which the presence of water could induce sticky effects among particles, promoting agglutination and subsequently increasing the yield strength of the particulate.

## 3.3. Support due to particle interactions

The granular flow theory (Campbell, 1990; Iverson and Vallance, 2001) is important in understanding some important sedimentological characteristics of PDCs. In a rapid, gravity-driven, shearing mass of sediment, the repulsion force originated by particle–particle collisions causes their motion in each direction, irrespective of the mean shear flow direction of the whole PDC. Clast vibration can be considered as an analogue for thermal motion of molecules in the kinetic theory of gases, and is known as granular temperature (Savage, 1983, 1984; Iverson, 1997). Similar to the thermodynamic temperature, the granular temperature generates pressure and governs the transfer of mass and momentum. However, the granular temperature cannot auto-sustain because particle collisions are inelastic and mechanical energy dissipates as thermodynamic heat. This implies that the granular temperature is maintained by conversion of kinetic energy to mechanical energy during the motion of the granular mass. The granular temperature varies as function of the square of the shear rate of the granular mass (Campbell and Brennen, 1985) and then is influenced by the slope angle or by the shear stress exerted by the more diluted, upper part of the flow.

The pressure associated with the granular temperature is called dispersive pressure (Bagnold, 1954), and causes inflation of the whole granular mass. At high granular temperatures, the dispersive pressure can maintain a granular mass in a liquefied state, while the inflation of the granular mass promotes segregation processes due to kinetic sieving. Kinetic sieving promotes the migration of small particles toward the base of the current because smaller particles can easily fall in the intergranular voids among larger particles (Figure 5). This induces an apparent migration of the coarser clasts towards the top of the flow-boundary zone, a process also promoted by the kinematic squeezing undergone by larger clasts because of their more frequent collisions when compared to smaller clasts (Savage and Lun, 1988; Sohn and Chough, 1993; Le Roux, 2003; Figure 5).
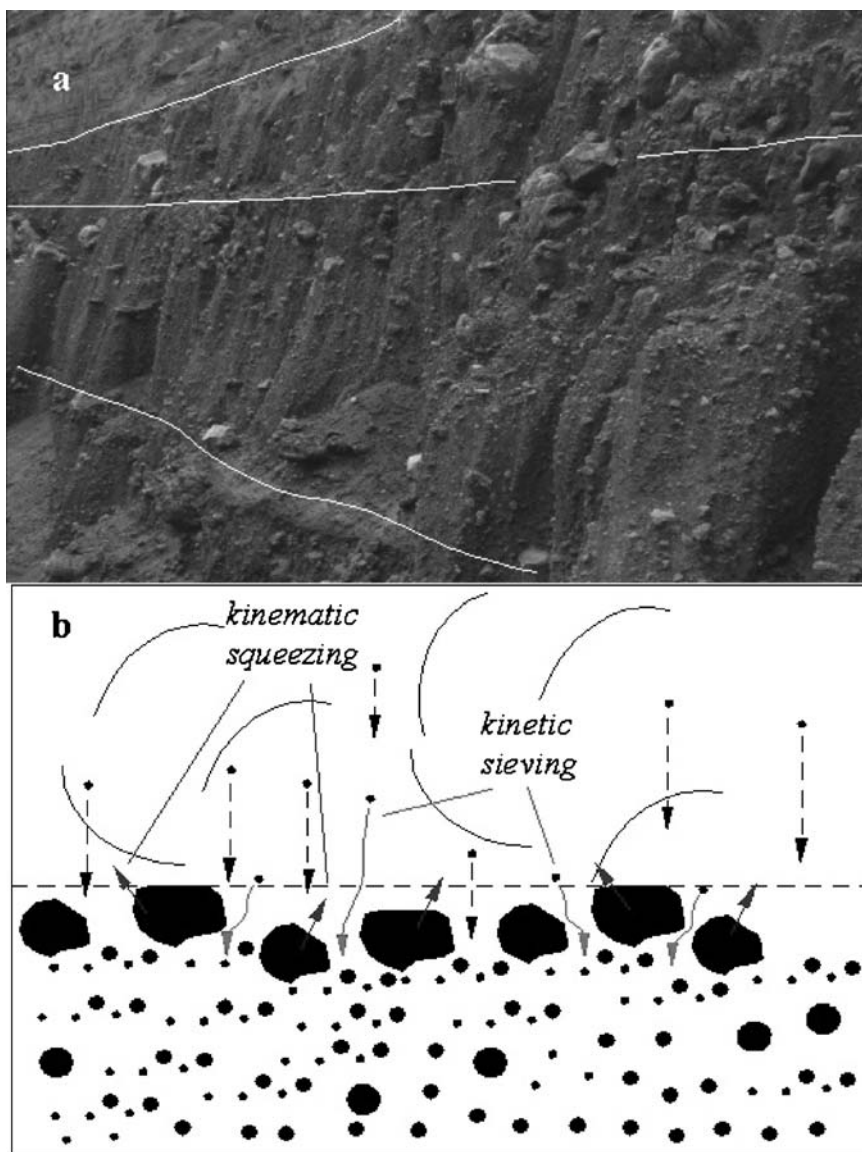
**Figure 5** Example of deposits (a) and mechanisms of particle support and segregation (b) for a flow–boundary zone dominated by granular flow regime.

Currents dominated by granular temperatures are also called non–cohesive debris flows (Postma, 1986). They can be classified as: (i) true grainflows, in which the interstitial fluid has a negligible effect on the physical state of the granular mass; and (ii) modified grainflows (Lowe, 1982), in which the physical characteristics of the moving granular mass are modified by the intergranular fluid (Iverson and Vallance, 2001). The wide spectrum of PDCs contains both end–members,

although modified grainflows are more common due to the abundance of gas in pyroclastic mixtures.

In PDCs, dominated by grain interaction, large clasts can bounce downcurrent, driven by both gravity and their momentum, causing a particular type of clast saltation called debris-fall (Sohn and Chough, 1993). The debris-fall process, also known as overpassing, requires slopes very close to or steeper than the repose angle of falling clasts (Nemec, 1990; Branney and Kokelaar, 2002). The larger clasts can overpass the smaller ones because: (i) the larger clasts migrate toward the top of the flow-boundary zone due to collisional forces (kinematic squeezing), where they experience greater shear intensities; (ii) in debris-fall regimes, the larger clasts have greater momentum; and (iii) the larger clasts that move along an interface are less influenced by surface roughness than smaller clasts. In turn, small clasts can easily be stopped by surface irregularities and/or can fill intergranular voids when they move over coarse-grained deposits (Branney and Kokelaar, 2002). Laboratory experiments have demonstrated that for this type of segregation, clast size is more important than clast density (Drahun and Bridgewater, 1983).

# 4. Depositional Processes in PDCs

Depositional mechanisms affect all particles in the flow-boundary zone until they come to a complete stop to form the deposit. Deposition accompanies transport, and transport may be affected by deposition (Branney and Kokelaar, 2002). Deposition can occur grain by grain or *en masse*, when shear velocity fall below the resistance force in large parts of the flow-boundary zone. Deposition can be a steady, discontinuous or stepwise process. Steady deposition (Branney and Kokelaar, 1992) is a continuous phenomenon in which the thickness of a deposit increases at constant rate with time (Figure 6). Stepwise deposition (Branney and Kokelaar, 1992) defines periods of steady or sharp increase in deposit thickness alternating with periods of non-deposition (Figure 6). Alternating periods of steady or stepwise deposition with erosion of deposits characterises discontinuous deposition, resulting in fluctuation of deposit thickness with time (Figure 6). Here, we review the main "historical models" and discuss some new ideas about depositional mechanisms in PDCs.

## 4.1. *En masse* freezing vs. progressive aggradation

Historically, two main models of deposition have been proposed for PDCs: *en masse* freezing (Sparks, 1976; Wright and Walker, 1981; Carey, 1991) and progressive aggradation (Fisher, 1966; Branney and Kokelaar, 1992). In *en masse* freezing, the flow comes to an abrupt halt over its entire depth, whereas in the progressive aggradation model, the deposit builds progressively due to the continuous supply of material from the current through the flow-boundary layer. The debate about the two models has been vigorous in the past, although it was recognised early that some internal shear occurs even in avalanche-type flows and that progressive
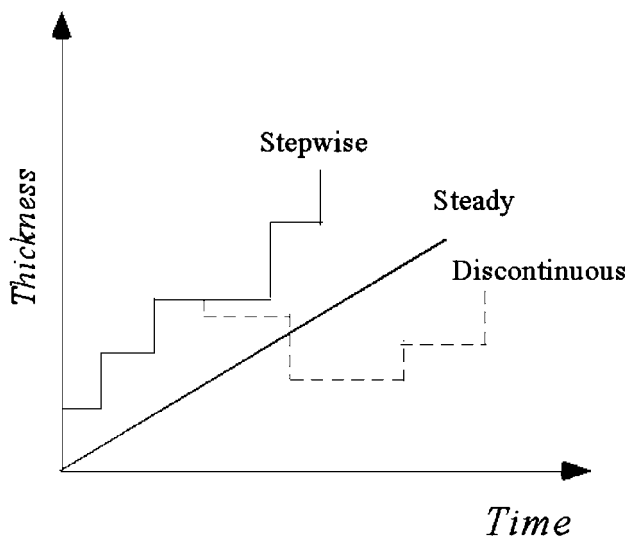
**Figure 6**   Diagram showing the variation in thickness of deposit with time for steady, stepwise and discontinuous deposition.

aggradation model is less consistent with small volume PDCs. Indeed, different geological evidence supports both models. The existence of steep levées and lobate fronts in PDC deposits (e.g. Rowley et al., 1981; Miyabuchi, 1999; Iverson and Vallance, 2001) has been interpreted as indicative of flows with Bingham rheology and internal yield strength (Johnson, 1970; Sparks, 1976). However, the rheological approach to granular mass–flow behaviour has been recently questioned (Iverson and Vallance, 2001; Iverson and Denlinger, 2001; Iverson, 2003), and the characteristics of these deposits have been attributed to the contrasting effects of pore–fluid pressure, mixture agitation (granular temperature) and forces exerted by grain interlocking at flow borders (Druitt, 1998; Iverson and Vallance, 2001; Iverson and Denlinger, 2001).

On the other hand, several lines of evidence support the idea that extensive ignimbrite sheets form by progressive aggradation. Their range as well as their thickness and lateral grain–size variations are successfully predicted by models that assume deposition by progressive aggradation from dilute turbulent suspension (Bursik and Woods, 1996; Dade and Huppert, 1996; Freundt and Bursik, 1998). Some ignimbrites show vertical variations in chemical composition (Branney and Kokelaar, 1992, 1997) or in abundance, type or size of lithic clasts (Bryan et al., 1998), which are thought to reflect temporal changes in the material supplied to the flow–boundary zone of the flow.

Although the progressive aggradation model is satisfactory in describing large ignimbrite sheet deposits, it is more difficult to apply to small–volume PDCs because certain characteristics of their deposits (e.g. alignment of large blocks, concentration of pumice and lithics at the base or at the top of the deposit) require fluctuations in physical characteristics of the current (e.g. competence) that are unlikely to occur at very short time scale.

## 4.2. Development of self-organised pulses in a PDC and stepwise aggradation

Recently, Sulpizio et al. (2007) proposed a model for small-scale PDCs that joins together the *en masse* and aggradation approaches. This model successfully explains characteristics of small-scale PDCs from the subplinian eruption of Pollena from Somma-Vesuvius (Rosi and Santacroce, 1983; Rolandi et al., 2004; Sulpizio et al., 2005), but it can also satisfactorily describe some general characteristics of PDC deposits.

The model assumes that most PDC deposits originate from stratified flows, in which the segregation of particles with higher terminal velocities in the lowermost part of the flow can develop a high-concentration zone (Valentine, 1987; Branney and Kokelaar, 2002; Dellino et al., 2004). This basal portion of the flow can move down-slope as a succession of high-concentration pulses whose thickness varies as a function of turbulence and kinematics of different density waves (Figure 7a, d and f). This allows consideration of a single-pulse as a flow-boundary zone for its entire thickness, in which the interplay among shear-rate, rate of deposition and concentration of particles determines the depositional regime (fallout, fluid-escape, granular flow and traction; Figure 7n). Pulse stoppage occurs *en masse* when resistance forces overpass the driving ones (e.g. when grain interlocking forces overpass gravitational forces). The four types of flow-boundary zones are completely intergradational (Burgissier and Bergantz, 2002; Branney and Kokelaar, 2002) and mixed regimes are common (Sulpizio et al., 2007).

This implies that, due to the masking effect of the phoenix cloud on the underflow, the current appears to move as a steady mass flow, but, in reality, the main body is segmented into different pulses that run very close to each other. The development of multiple pulses within a gravity current have been observed during large flume experiments (Major, 1997; Iverson, 1997), small-scale laboratory experiments (Savage, 1979; Brennen et al., 1983; Huppert et al., 1986) and hypothesised for both volcaniclastic and pyroclastic deposits on the basis of field evidence (Chough and Sohn, 1990; Schwarzkopf et al., 2005; Sulpizio et al., 2006, 2007). The mechanisms responsible for pulsating behaviour in a gravity-driven current are still not completely understood, but can be related to the successive release of material during generation (i.e. during column or dome collapse and failure of soils or slopes; Pierson, 1980; Scott et al., 2001; Cole et al., 2002; Loughlin et al., 2002) and/or to the inhomogeneous mass distribution within the current that induces development of kinetic waves (Lee and Leibig, 1994; Major and Iverson, 1999; Schwarzkopf et al., 2005). Lee and Leibig (1994) numerically demonstrated how a system with an initially random density field evolves to a configuration in which neighbouring regions have a high-density contrast. At the early stage of development, the density contrast between nearby regions increases linearly with time. In a gravitational field, this results in different velocities in adjacent portions of the current:

$$U(1, 2) = \frac{j(\rho_1) - j(\rho_2)}{\rho_1 - \rho_2} \qquad (4)$$
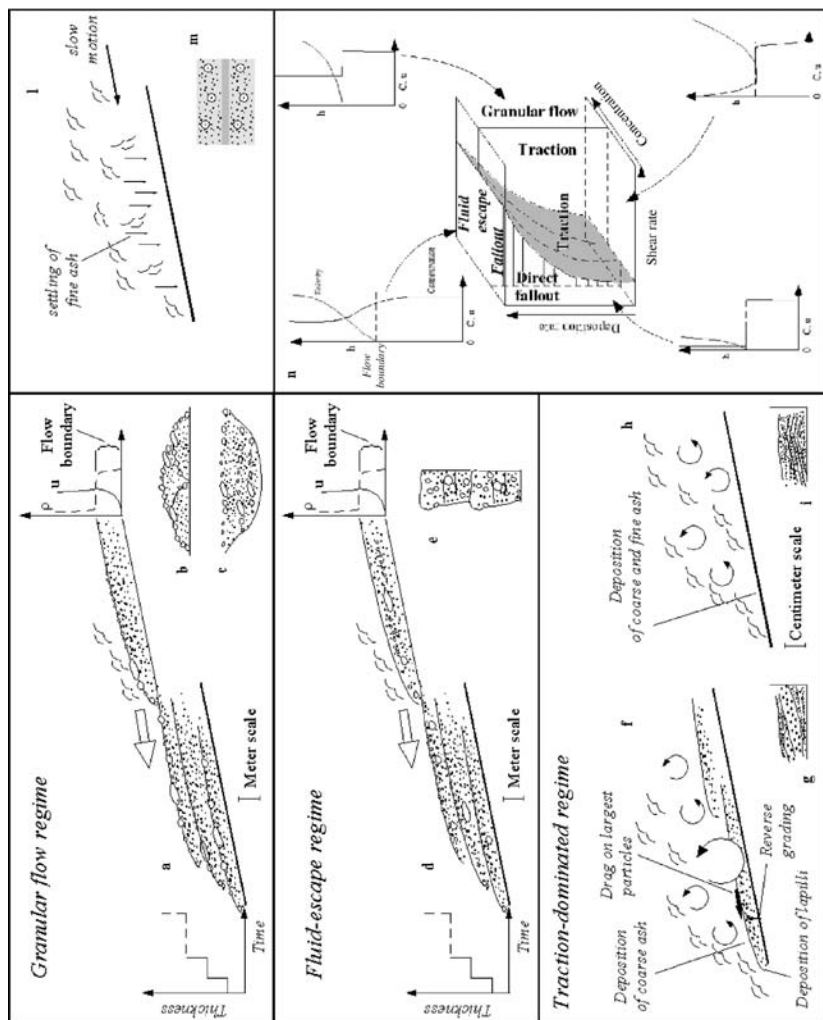
**Figure 7** Sedimentological model for stepwise aggradation of different pulses within the same PDC for four depositional regimes. (a) granular flow regime with aggradation of thick pulses; (b) aggradation of pulses that generate stacked deposits over a flat surface; (c) deposits from aggradation of different pulses in a valley (valley–pond deposits); (d) fluid–escape flow regime with aggradation of thick pulses; (e) sketch of a stratigraphic column from aggradation of different pulses dominated by fluid escape regime; (f) development of thin pulses at the base of fully turbulent PDC; (g) deposits left by aggradation of thin pulses at the base of a traction-dominated current; (h) dilute, fully turbulent flow without development of granular pulses at the very base; (i) cross-stratified deposits left by the current described at point (h); (l) Gentle settling of fine ash from an ash cloud dominated by a direct fallout regime; (m) stacked deposits of massive, accretionary lapilli-bearing fine ash deposited in the direct fallout regime of point l); (n) conceptualisation of the relative fields of the four types of flow-boundary zone (after Branney and Kokelaar, 2002; modified).

where $U(1, 2)$ is the velocity of the interface that separates regions with different densities $\rho_1$ and $\rho_2$, and $j(\rho_1) - j(\rho_2)$ the difference in density flux between the two regions. The evolution of the system is determined by the motion of the interfaces, and the nature of their interactions leads to a final state in which large density contrasts occur (Lee and Leibig, 1994).

The contrasting effects of shear stress and particle concentration control the distribution of turbulence within each pulse and subsequently determine its sedimentological character (Figure 7n). The organisation of the current into trains of pulses occurs in both concentrated and dilute PDCs (Sulpizio et al., 2007). This determines two important consequences: (i) PDCs are intrinsically unsteady phenomena; and (ii) deposition occurs stepwise (Figure 7).

Field evidence that supports a wide spectra of PDC behaviour is illustrated in Section 5.

## 4.3. Influence of topography on deposition

With the exception of completely flat topography, the landscape morphology exerts a major influence on depositional mechanisms of gravity-driven currents (e.g. Fisher, 1990; Woods et al., 1998; Kneller and Buckee, 2000; Branney and Kokelaar, 2002; Pittari et al., 2006). The mechanisms that can influence mobility and deposition in PDCs are basically: (i) changes in turbulence within the current; (ii) changes in particle concentration in the flow-boundary zone; (iii) blocking or stripping of the current. The influence of topography on gravity-driven currents has been demonstrated in many field-based studies (e.g. Cas and Wright, 1987; Saucedo et al., 2004; Branney and Kokelaar, 2002; Sulpizio et al., 2007 among many others), but the effective mechanisms have been investigated primarily through small-scale laboratory experiments (e.g. Edwards et al., 1994; Kneller and McCaffrey, 1999; Woods et al., 1998) and numerical modelling (e.g. Dobran et al., 1994). However, both simple laboratory conditions (use of fluids with different densities, limited grain sizes distributions) and very dilute flows used in numerical simulations (particle sizes between 10 and 100 μm, concentrations below a few volume percent) only partially resemble the complexities of natural cases. This implies that field data, which represent natural cases, have to be accurately collected and interpreted in order to better understand the influence of topography on the physical behaviour of PDCs. Here, some real examples of interactions between PDCs and common landscape morphologies will be illustrated and discussed, although they do not exclusively represent possible natural conditions.

### 4.3.1. Break in slope (concave local curvature)

PDCs may flow along the ground for some distance without significant deposition, due to the prevalence of driving forces over resisting ones. The simplest way to change the partition between the two forces in gravity-driven currents is to reduce the gravitational driving force by reduction in local curvature of the topographic slope (Figure 8a). The response of the moving flow includes two components. One component reflects a simple trade-off between reduced driving stress and increased
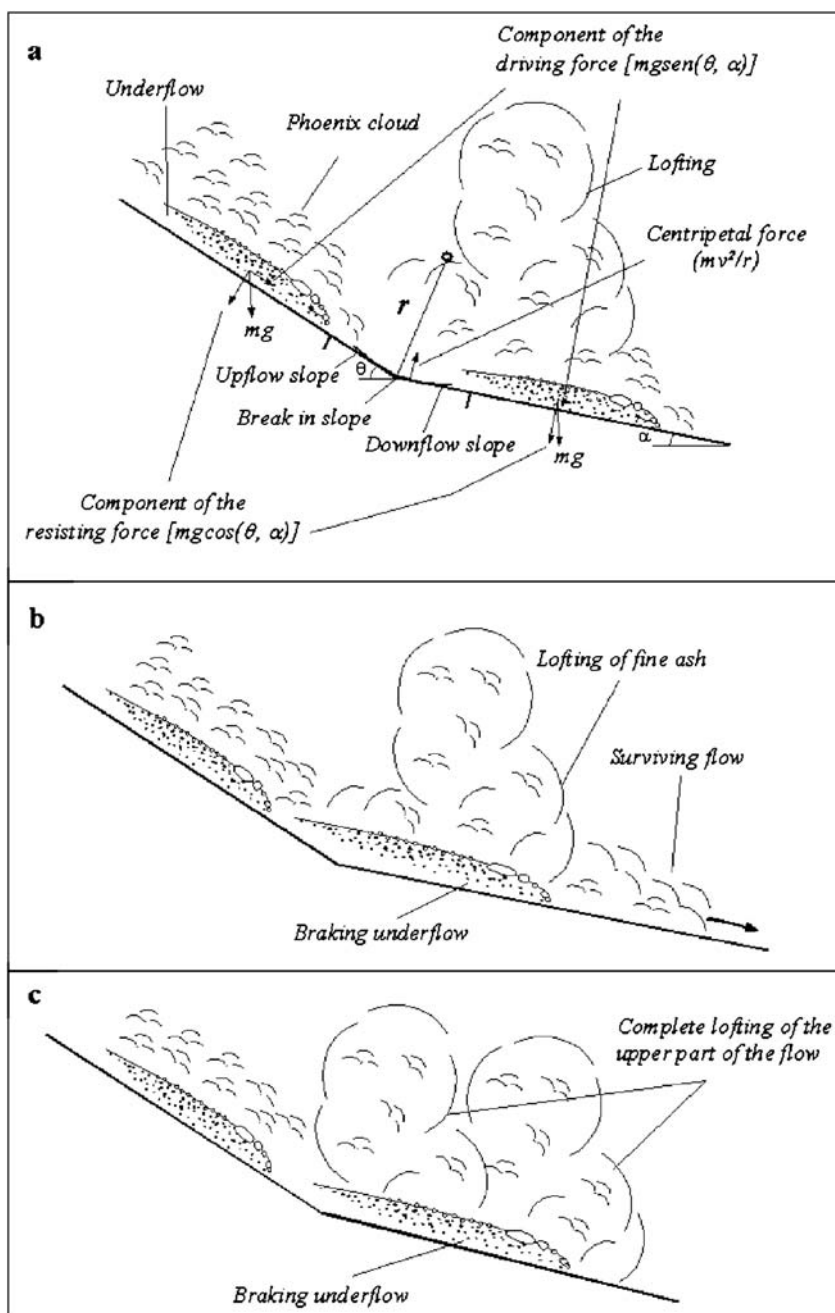
**Figure 8** (a) Sketch of the changes in driving and resisting forces for a PDC that moves over a change in slope (concave upward curvature); (b) conceptual sketch of an underflow that brakes over a change in slope. The elutriated and lofted fine material is sufficient to generate a PDC denser than the atmosphere that propagates further; (c) conceptual sketch of an underflow that brakes over a change in slope. The elutriated and lofted fine material is lighter than the atmosphere and the PDC does not propagate further.

resisting stress that occurs as bed slopes decline (Figure 8a). The other component takes into account that, where the bed slope decreases in the downstream direction, part of the depth-averaged momentum flux per unit area $\rho v^2$ is directed into the bed and resisted by the reaction force provided by the underlying Earth (assumed to be infinitely massive and immobile). This external reaction force redirects the flow's depth-averaged momentum flux to keep it parallel to the bed. However, the action–reaction at the bed also locally increases the normal stress at the bed by an amount $(\rho h v^2)/r$, where $r$ is the radius of local bed curvature, $v^2/r$ the associated centripetal acceleration, $\rho$ the density of the flow and $h$ the flow height (Figure 8a; Iverson and Denlinger, 2001). Hence, a strong change in slope increases the normal stress (small $r$ value) more than a weaker change (high $r$ value), resulting in greater normal bed frictional forces. Similar evaluation of such an influence of break in slope on depositional behaviour of gravity-driven currents was claimed by Zanchetta et al. (2004a) for volcaniclastic flows in the Vesuvian area. They demonstrated how, at equal (or similar) flow characteristics and boundary conditions, the distance travelled was related to the value of the slope ratio (SR), defined as the ratio between the downflow and the upflow slopes (Figure 8a). The deceleration of the current due to an increase in normal bed stress and lowering of the slope enhances the turbulence (Gray et al., 2005), which may increase the elutriation of fines and lofting (Figure 8a).

Deposition induced by change in slope has been documented in many papers for dry granular flows (e.g. Denlinger and Iverson, 2001; Felix and Thomas, 2004) volcaniclastic flows (e.g. Zanchetta et al., 2004a), PDCs (e.g. Macias et al., 1998; Cole et al., 2005; Sulpizio et al., 2007) and turbidites (e.g. Mulder and Alexander, 2001; Gray et al., 2005). However, changes imposed by deposition in proximity of a break in slope may also induce major flow transformations in fluid-bearing currents. Beyond the break in slope, the flow braking induces deposition of material in the flow-boundary zone and partial transfer of momentum to turbulence generation and elutriation of fines (Figure 8a). At this point, the part of the flow above the flow-boundary zone can respond in two ways: (i) its bulk density is still greater than the surrounding ambient fluid and it propagates further as an independent gravity-driven current (Figure 8b); or (ii) its bulk density is less than the surrounding ambient fluid and it lofts convectively and stops (Figure 8c). The fate of a gravity-driven current is then function of its mass and grain-size, the local curvature at the break in slope and efficiency in energy transformation. All these parameters control both the amount of material remaining in the transport system as the flow crosses the break in slope and the subsequent physical characteristics of the surviving gravity-driven current. Natural examples of PDC decoupling in proximity of a break in slope were observed during the 1991 eruption of Colima volcano (Saucedo et al., 2004) and inferred for the Avellino eruption of Somma–Vesuvius (Figure 9; Sulpizio et al., 2008a).

## 4.3.2. Ability to surmount a ridge

When the path of a gravity-driven flow includes a steepening of the slope, the change in local curvature lessens the partition between driving and resisting forces,
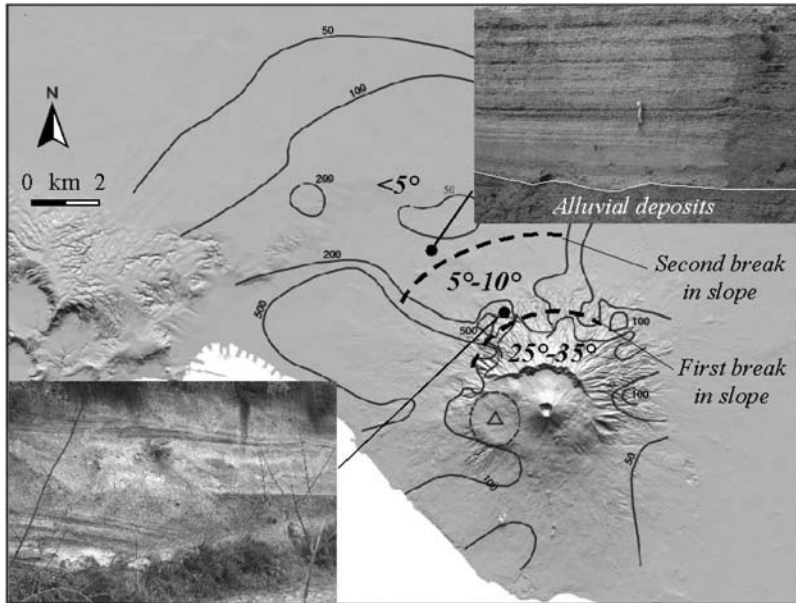
**Figure 9**   Different lithofacies association of PDC deposits of Avellino eruption (3.8 ka BP, Somma-Vesuvius, Italy). The exposures are located beyond the first and the second breaks in slope that connect the steep upper slopes of the volcano to the flat alluvial plain. The numbers indicate the range of slope. The solid black lines are the isopachs of Avellino PDC deposits (thickness in cm).

promoting deposition and flow stoppage (Figure 10a). Assuming a steady, homogeneous flow and neglecting deposition or bulking, we can develop a simple model to assess the travel distance along a slope. For a PDC (or any other gravity-driven current) approaching a break in slope, the momentum flux per unit area is given by:

$$M_f = \rho h v^2 \tag{5}$$

where $v$ is the velocity, $h$ the flow depth and $\rho$ its density. As shown in Section 4.3.1, the local curvature affect the momentum flux because part of it is converted on normal bed stress by an amount of $(\rho h v^2)/r$, where $r$ is the radius of local bed curvature and $v^2/r$ the associated centripetal acceleration. Conservation of mass implies that the loss in momentum flux affects only velocity. Therefore, if we consider changes in velocity just within the vicinity of the break in slope, the approaching velocity ($v_0$, Figure 10b) is separated in two components ($v_t$ and $v_n$, Figure 10b), a consequence of actions related to centripetal acceleration. In particular, the term $v_t$ represents the velocity of the flow at the base of the inclined slope, and can be written as:

$$v_t = v_0 \cos(\theta - \alpha) \tag{6}$$

where $\alpha$ and $\theta$ are the slope angles before and beyond the break in slope (Figure 10). This implies that for $\theta - \alpha = 0°$ (i.e. curvature radius $r \to \infty$) $v_t = v_0$, and for $\theta - \alpha = 90°$
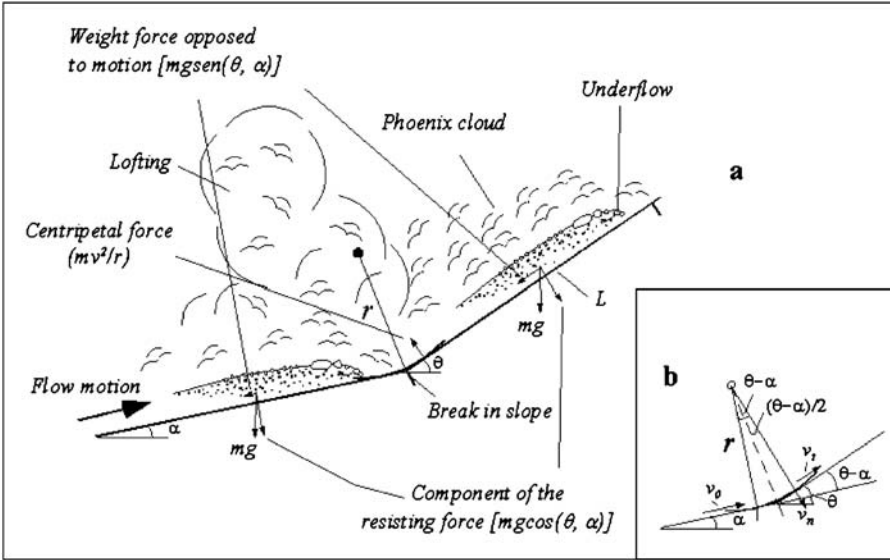
**Figure 10**    (a) Sketch of the changes in driving and resisting forces for a PDC that moves over an inclined obstacle; (b) simple diagram showing the splitting of the initial velocity ($v_0$) into the normal ($v_n$) and the tangential ($v_t$) components due to the steepening of slope.

($r = 0$) $v_t = 0$. Hence, the kinetic energy of the moving flow can be written as:

$$E_c = \frac{1}{2}\rho h v_t^2 \tag{7}$$

To reach a complete stop of the moving current, the work exerted by frictional forces ($W_f$) and transformation in potential energy ($E_p$) must equal the available kinetic energy:

$$E_c + E_p + W_f = 0 \tag{8}$$

under the assumption that frictional forces are dissipated only as work ($W_f$) at the flow base:

$$W_f = \kappa \rho h g L \, \cos\theta \tag{9}$$

where $\kappa$ is the coefficient of dynamic friction, $L$ the travelled length on slope and $\theta$ the slope angle (Figure 10), and:

$$E_p = \rho h g L \, \sin\theta \tag{10}$$

then, we can obtain the length travelled along slope, $L$:

$$L = v_t^2 [2g(\kappa \cos\theta + \sin\theta)]^{-1} \tag{11}$$

Inspection of Equation (11) reveals that it represents a power-law function (i.e. a parabola in $L$ vs. $v$ space) and that $L$ critically depends on slope but increases dramatically for very fast currents.

Because momentum decreases due to deceleration on a slope also reduce turbulence generation, a fully turbulent, homogeneous flow may develop density stratification. Depending on the balance achieved between driving and resisting forces, the fate of the basal, more concentrated part of the flow, may be different than that of its diluted upper part. Increasing concentration of particles at the base of the flow may result in enhanced deposition and loss of mass from the current, with feedback effects on the momentum equation (Legros and Kelfoun, 2000):

$$M_f = \frac{v \, dv}{dx} + v^2 \frac{(dm/m)}{dx} \tag{12}$$

where $m$ is the initial mass. The deposited material may either rest on the slope or start to flow backward, depending whether the Coulomb equilibrium is exceeded or not (neglecting cohesion):

$$mg \, \sin\theta > [(mg \, \cos\theta) - \delta]tg\phi \tag{13}$$

where $\theta$ is the slope angle, $\delta$ the pore fluid pressure and $\phi$ the internal friction angle of the material.

Because the rate of material delivered to the flow-boundary zone depends on the rate of supply ($R_s$), the upper part of the current loses mass at a rate proportional to $dm/dt$. At the same time, the flow decelerates on a slope at a rate proportional to $dv/dt$. Therefore, the upper part of the flow may stop on a slope if $R_s$ drives the bulk density of the flow below that of the surrounding atmosphere in a time less than that necessary for the flow to overcome the length of the slope. If the time is not enough, the upper part of the flow can overcome the slope to form a new flow with different physical characteristics than the previous one, driven by residual kinetic energy and potential energy transformation. An example of this behaviour is represented by PDCs originated during the Upper Pollara eruption (13 ka; Calanchi et al., 1993; De Rosa et al., 2002) at Salina Island (southern Italy; Sulpizio et al., 2008b; Figure 11). The eruption was characterised by several Vulcanian explosions that generated small-volume PDCs, which propagated in the Pollara depression, overcame the rim and finally stopped beyond the break in slope between the outer slopes and the Malfa terrace (Figure 11a). On the inner slopes of the depression, coarse-grained, poorly sorted, massive deposits characterise the entire stratigraphic succession (Figure 11b), indicative of rapid deposition from a flow-boundary zone with a high concentration of material. The inner slopes were not great enough to stop the whole flow, which passed over the depression rim and flowed along the outer slopes of the depression. In these areas, the deposits comprise lapilli and ash, with diffuse stratification, indicative of a flow-boundary zone affected by traction processes (Figure 11c). The deposits are, as a whole, finer grained than those on the inner slopes. The more distal deposits include fine and coarse ash with lenses of lapilli (Figure 11d), indicative of a flow-boundary zone dominated by granular interaction. The deposits thicken close to the break in slope zone and disappear within 1 km beyond this point (Figure 11a).
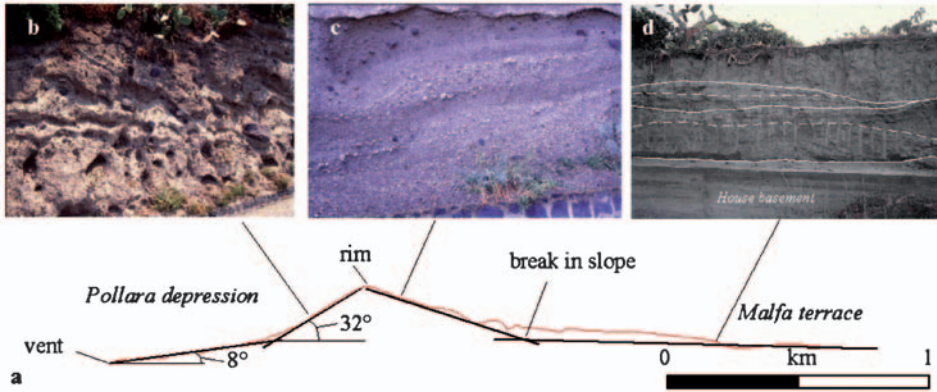
**Figure 11**   Variation of lithofacies of PDC deposits from Upper Pollara eruption (Salina Island, Aeolian Archipelago, Italy) in response to changes in topography. (a) Morphological profile (red line) from the Pollara depression (vent area) to the Malfa terrace. The black lines indicate approximately the topography before the eruption; (b) massive, coarse-grained deposits on the inner slopes of Pollara depression; (c) diffusely stratified deposit on the outer slopes of Pollara depression; (d) massive, fine-grained, lenticular deposits in the Malfa terrace area. The white lines indicate different eruptive units, while the dashed lines indicate different depositional units within a single eruptive unit.

### 4.3.3. Vertical barrier

The occurrence in which a PDC encounters a vertical barrier is the extreme case of a flow encountering an increase in slope. The effects of a vertical topographic barrier can vary in function of: (i) physical properties of the PDC (e.g. density stratification, height); (ii) height of the obstacle; (iii) angle of incidence; and (iv) topography of the surroundings.

Physical properties are important because they define how a current behaves as a fluid or as a granular mass of solid particles. If the current behaves as a fluid (e.g. fully diluted PDCs) we can imagine different mechanisms of interaction with a vertical obstacle, with effects on flow propagation and deposition that depend mainly on height of the flow ($h_f$), height of the obstacle ($h_b$) and Froude number (Rottman et al., 1985; Branney and Kokelaar, 2002; Figure 12a).

In the case of stratified currents, only the part of the flow above a certain critical height, known as the dividing streamline (Sheppard, 1956; Snyder et al., 1985; Valentine, 1987; Figure 12b), is able to overcome the obstacle. In this case, the denser levels of the current are blocked or diverted, depending on the incidence angle with respect to the obstacle. The diverted current can flow along the obstacle and pass through saddles or valleys (Figure 12b).

The higher, less-dense levels of the current are less constrained by topography and can pass over the obstacle. The separation of the basal, concentrated flow and the upper less dense one is known as flow-stripping (Piper and Normark, 1983). The stripped upper part of PDCs caused the most devastation and fatalities in the 1902 eruption of Mt. Pelèe (Fisher and Heiken, 1982), in 1991 at Unzen volcano (Yamamoto et al., 1993) and in 1997 at Montserrat (Loughlin et al., 2002).
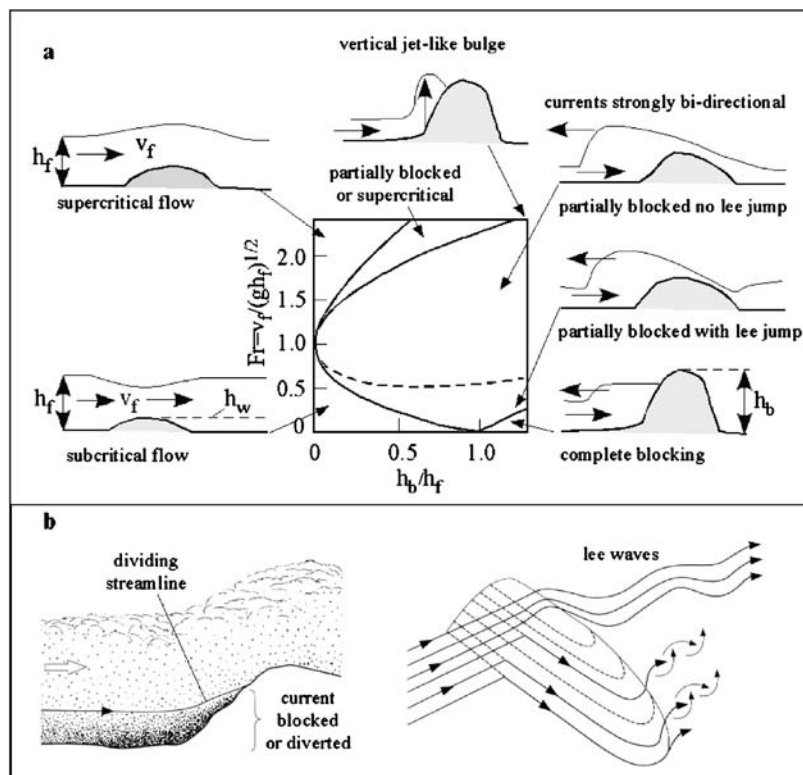
**Figure 12** Scheme of possible interactions among a fluid–like current and obstacles with different heights. (a) Diagram of Froude number vs. ratio between obstacle ($h_b$) and flow heights ($h_f$) (after Branney and Kokelaar, 2002; modified); (b) interaction between a density-stratified flow with ridges. Only the part above the dividing streamline is able to pass over the obstacle. If diverted, the basal part can pass over the obstacle through saddles or at the end of the barrier (after Valentine, 1987; modified).

An example of interaction between a radial, expanding PDC with a vertical barrier has been recently recognised in the Avellino eruption of Somma–Vesuvius (Sulpizio et al., 2008a; Figure 13). This eruption was characterised by extensive generation of PDCs during the final phreatomagmatic phase, whose deposits show large lithofacies variability from proximal to distal sites. In particular, massive, accretionary lapilli–bearing beds crop out on eastern and southern slopes of Somma-Vesuvius volcano (Figure 13), in a stratigraphic position that corresponds to the dune-bedded, thick PDC deposits of the western and north-western sectors. This dramatic change in lithofacies was caused by the presence of the morphologic obstacle of the Mount Somma caldera wall, which blocked the basal, coarse-grained part of the currents and caused the stripping of the upper, finer grained, more diluted flows that gently settled beyond the obstacle.
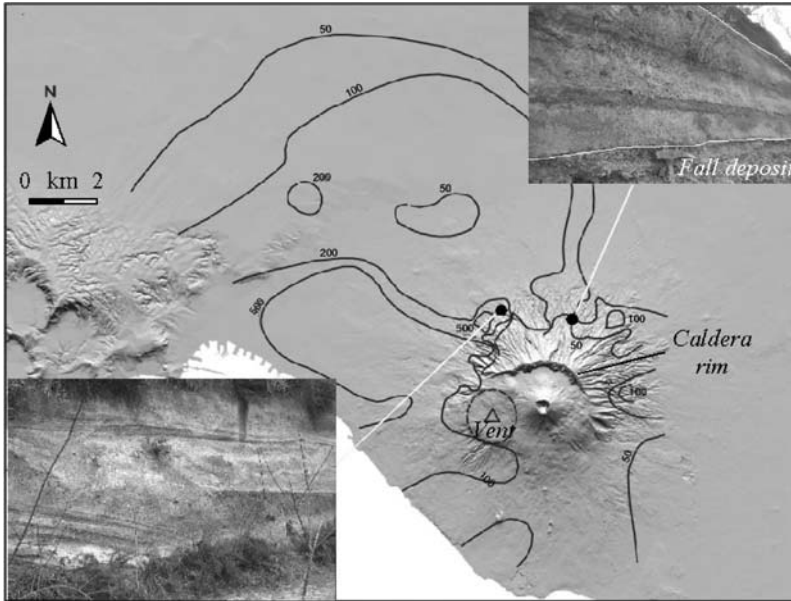
**Figure 13** Different lithofacies association of PDC deposits of Avellino eruption (3.8 ka BP, Somma-Vesuvius, Italy). The exposures are located in areas free of topographic obstacles or sheltered by the vertical barrier of the Mount Somma caldera wall. The solid black lines are the isopachs of Avellino PDC deposits (thickness in cm).

## 4.3.4. Interaction with town buildings

When gravity-driven currents flow across terrains with significant topographic obstacles, they develop flow variations, which affect not only the loci of deposition but also the depositional lithofacies (Kneller and McCaffrey, 1999). The complex urban morphology, characterised by road networks and agglomerates of buildings with different heights and shapes, represents a very rough and complex topography that can greatly affect runout and deposition of gravity-driven currents. Despite several works that have investigated the impact of different types of gravity-driven flows on buildings and infrastructures (Newhall and Punongbayan, 1996; Baxter et al., 1998; Valentine, 1998; Cioni et al., 2000; Gurioli et al., 2002; Druitt and Kokelaar, 2002; Luongo et al., 2003a, b; Nunziante et al., 2003; Petrazzuoli and Zuccaro, 2004; Spence et al., 2004; Zanchetta et al., 2004a; Zuccaro and Ianniello, 2004), little quantitative data are available on the influence of urban environments on transport and deposition behaviours of these flows. The most detailed works about this topic consider the interaction of PDCs from the AD 79 (Pompeii) eruption of Somma–Vesuvius (Sigurdsson et al., 1985) with Roman urban settlements of Herculaneum and Pompeii (Gurioli et al., 2002, 2005). In particular, these works demonstrated how basal parts of PDCs can experience rapid variations in both flow direction and temperature when entering an urban area (Cioni et al., 2004; Gurioli et al., 2005). The effects of this interaction can be modelled

qualitatively in terms of the internal structure of the currents (the vertical gradients of velocity and density) with respect to the scale of the local substrate roughness. The anisotropy of magnetic susceptibility (AMS) shows both how building-induced roughness was able to strongly influence flow directions and that the more concentrated underflows in several streams followed external walls of the city and filled internal roads (Figure 14; Gurioli et al., 2005). The roughness induced by the close assemblage of buildings and roads locally increased turbulence, and the vortex production was particularly enhanced when the space between edifices equalled their heights (Oke, 1987). The development of strong vortices can cause a decrease in temperature of hot PDCs in the order of $150-200\,^{\circ}C$ (Gurioli et al., 2005).

The interaction with urban structures probably limited the runout of PDCs by loss of kinetic energy on impacts against obstacles, deflection, bore formation and increasing turbulence. As an example, a decrease in runout of 15–25% was observed for volcaniclastic flows that interacted with urban settlements in the Sarno area in comparison to others that flowed over undeveloped areas (Zanchetta et al., 2004a).
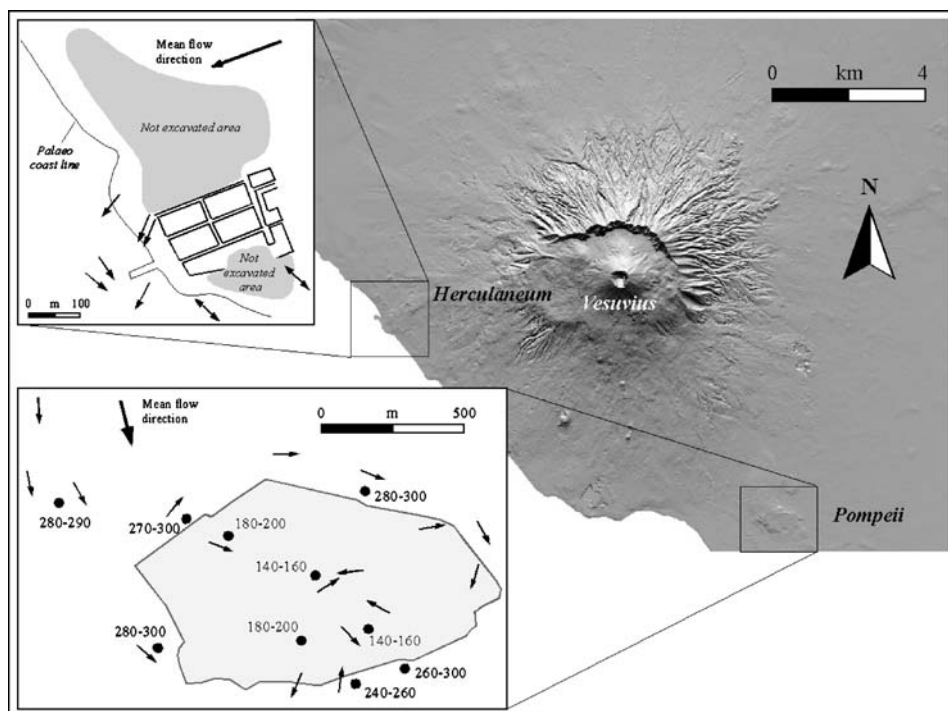


**Figure 14** Influence of city buildings and roads on flow directions of PDCs from the AD 79 eruption of Vesuvius. For the archaeological excavations of Pompeii the assessed equilibrium temperatures are also reported for the town and in its surroundings (after Gurioli et al., 2005; modified).

## 5. FIELD EVIDENCES OF STEPWISE AGGRADATION IN PULSATING PDCs

Following the previous discussion about recent developments in depositional models for PDCs and their interaction with topography, this section will illustrate some examples of real deposits interpreted using the model of stepwise aggradation of discrete pulses. The range of the chosen examples is testament to the applicability of the model to a wide spectrum of PDCs. The examples comprise various typologies of flow-boundary zones developed within each aggrading pulse, varying from traction- to granular flow- or fluid escape-dominated.

Lithofacies analysis and association are the main tools used in reconstructing the architecture of chosen PDC deposits and in supporting their sedimentological interpretation. Lithofacies analysis is commonly used in sedimentological studies of marine (e.g. Lowe, 1982), fluvial (Miall, 1978, 1985; Mathisen and Vondra, 1983; Smith, 1986, 1987) and alluvial fan environments (Waresback and Turbeville, 1990; Zanchetta et al., 2004b), and has also been applied to the study of complex sequences of pyroclastic deposits (e.g. Walker et al., 1980; Walker, 1985; Sohn and Chough, 1989; Chough and Sohn, 1990; Colella and Hiscott, 1997; Gurioli et al., 2002; Sulpizio, 2005; Sulpizio et al., 2007). Lithofacies analysis was also successfully applied in describing the lateral and vertical variations of sedimentary structures in single flow units within widespread ignimbrites (e.g. Freundt and Schmincke, 1986; Druitt, 1992; Cole et al., 1993; Allen and Cas, 1998). Lithofacies analysis allows us to gain insight into some physical conditions that characterise the flow-boundary zone of a PDC at the time of deposition, and provides some constraints on transport mechanisms and interactions between solid and fluid phases.

The time-space association of different lithofacies represents the lithofacies architecture. The different lithofacies record the physical conditions at the flow-boundary at the time of deposition, while changes in lithofacies record the non-uniformity of the current in time and space. Therefore, the study of lithofacies architecture allows for inferences about changes in depositional regime that occurred in time and space for a given PDC or for a set of PDCs.

## 5.1. Case studies

The repetitive occurrence of stacked, massive bodies with lithofacies mLA and mLB, sometimes with reverse grading of lithic blocks (lithofacies $mLA_{(il)}$ and $mLB_{(il)}$; Figure 15) is common in PDC successions. These successions have been interpreted in the past as having been deposited *en masse* from different PDCs when the driving gravitational force fell below the resistance force due to friction between grains and between the flowing mass and the topographic surface (*en masse* freezing; e.g. Sparks, 1976). An alternative model considers these deposits as aggraded from sustained currents that changed their transportability with time (aggrading model; e.g. Branney and Kokelaar, 1992).
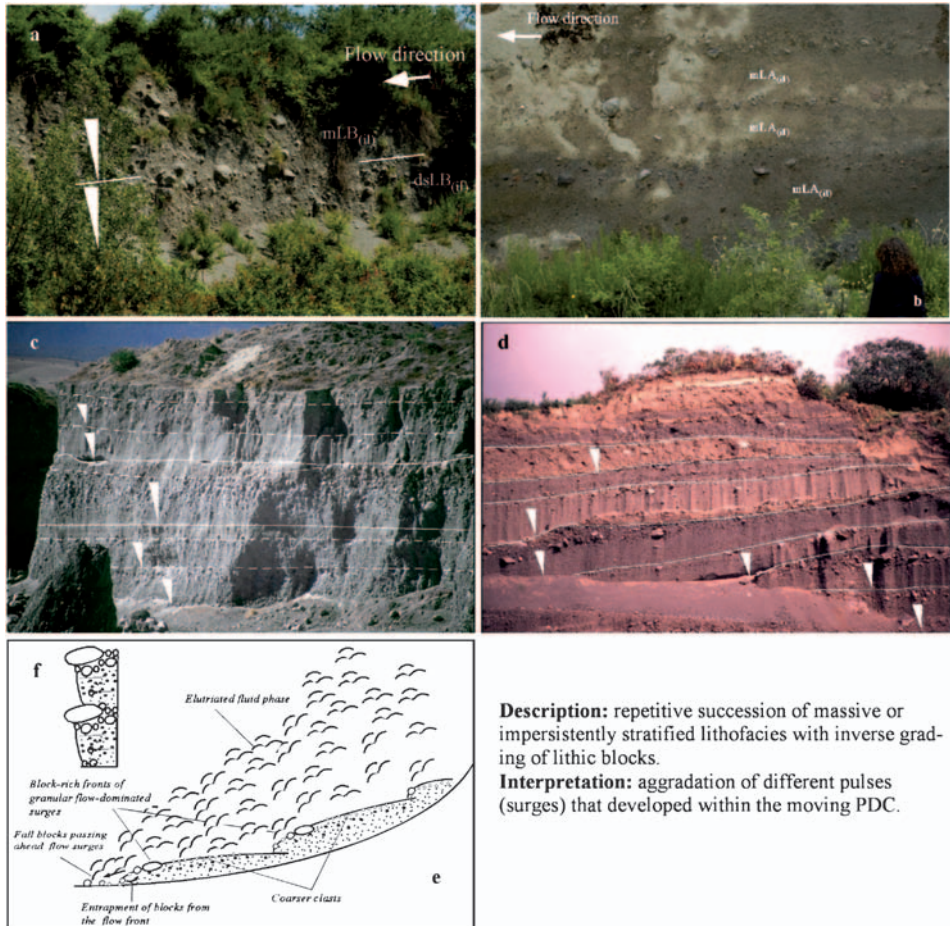
**Figure 15**  Examples of PDC deposits originated by aggradation of different pulses developed within the same current. Inverse grading of lithic blocks indicate a flow-boundary zone dominated by granular flow regime. (a, b) Massive deposits of Pollena eruption (Somma–Vesuvius, Italy). Inverse grading of large lithic blocks indicates the aggradation of three main pulses; (c) block and ash flow deposits at Nevado de Toluca (Mexico). The white solid lines indicate different eruptive units, while dashed lines indicate depositional units within the same current; (d) stacked, massive PDC deposits with inverse grading of large lithic blocks at Tungurahua volcano (Ecuador); (e, f) sedimentological scheme that illustrates the development of different pulses within a current and their stepwise aggradation.

A more convincing interpretation of this lithofacies architecture is offered by stepwise aggradation of different pulses developed within a PDC (see Section 4.2; Sulpizio et al., 2007). This model explains the repetitive occurrence of lithofacies $mLA_{(il)}$ and $mLB_{(il)}$ (Figure 15) as the progressive deposition of different pulses developed within a single PDC (Figure 15e). These pulses are dominated by grain interaction (granular flow regime), with the processes of kinetic sieving and kinematic squeezing causing an increased concentration of larger blocks toward the top of each single pulse. In this model, each pulse stops *en masse* when the driving force falls

**Description:** alternating lithofacies mLA(il) and mA.
**Interpretation:** aggradation of different pulses (surges) and entrapment of fine ash at change in slope.
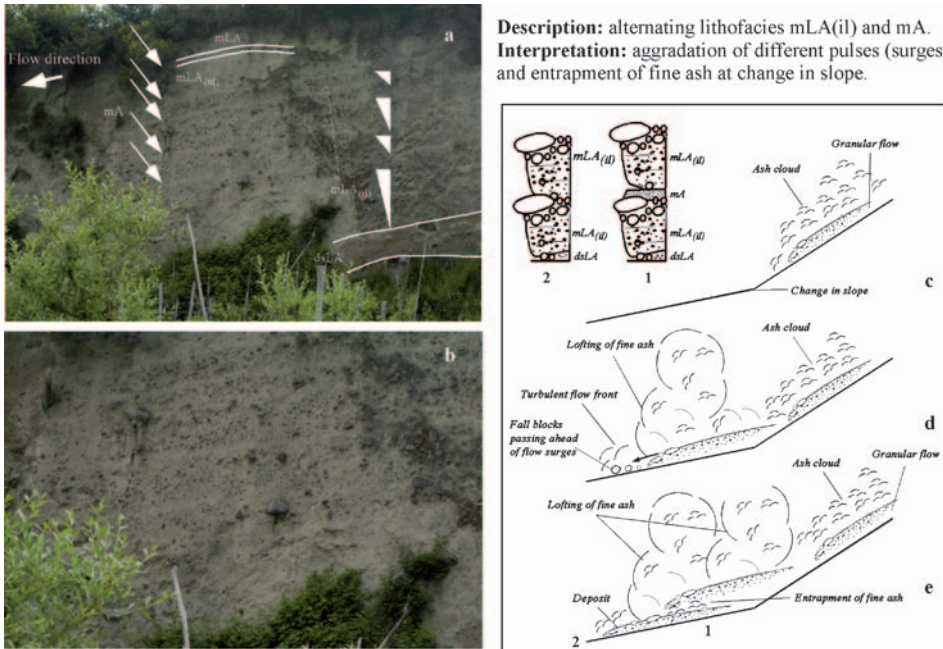
**Figure 16** (a, b) Alternating massive deposits with inverse grading of lithic blocks and fine ash (Pollena eruption, Somma-Vesuvius); (c — e) sedimentological model that illustrates the observed alternation of pictures (a) and (b).

below the resistance force due to friction and grain interlocking. Since different pulses form within the PDC, the deposition occurs stepwise (Figures 6 and 7).

Figure 16 shows another good example of stepwise aggradation of granular pulses. In this case, the lithofacies mLA$_{(il)}$ have interbeds of massive ash (lithofacies mA; Figure 16a and b). When each single pulse approaches the change in slope between the upper and lower slopes of the volcano, the sharp decrease in velocity causes loss of some finer materials due to convective lofting (Figure 16c). The lofting fine material is successively entrapped by the following granular pulse (Figure 16d). This occurrence preserves the succession of lithofacies mLA$_{(il)}$–mA (Figure 16e). Further support for this mechanism is the rapid disappearing of lithofacies mA a few hundred meters down valley, where the succession includes only lithofacies mLA (Figure 15b).

Another common occurrence in PDC deposits is the alternation of massive and stratified lithofacies (Figure 17). This type of lithofacies architecture generally records different events of deposition, with alternation of diluted PDCs, dominated by tractive processes, and concentrated PDCs, dominated by fluid-escape or granular flow regimes. However, this does not necessarily imply different eruptive mechanisms because traction-dominated deposits can be generated at the front of highly concentrated PDCs (e.g. Branney and Kokelaar, 2002), which travel in advance of granular flow- or fluid escape-dominated pulses from the main body and tail of the PDC.

**Description:** Passage from diffusely stratified lithofacies to massive lithofacies in the same eruptive unit.
**Interpretation:** The lithofacies dsLA records a flow-boundary zone influenced by tractive processes at the head of a PDC. The lithofacies mLA records the deposition from the main body of the PDC in which the high concentration of particles suppressed the turbulence.

**Figure 17** Examples of lithofacies associations in PDC deposits of Pollena (left) and Avellino (right) eruptions of Somma-Vesuvius (Italy).

Many deposits from diluted PDCs show a chaotic alternation of coarse-grained lenses (lapilli) and coarse to fine ash (Figure 18). This lithofacies architecture has been interpreted as the result of deposition by two different portions of the various pulses that constitute the entire PDC (Sulpizio et al., 2007). In this model, the coarse-grained lenses represent the basal part of the pulse, dominated by grain interaction. The lenses can exhibit inverse grading and imbrication of larger clasts. The stratified ash represents the tail of the pulse, less concentrated and richer in fine-grained material. In this case, the thickness of each pulse is only a few centimetres, and the turbulence that dominates the upper part of the current can, in some cases, penetrate the deposit and truncate the sedimentary structures (Figure 7f). The extreme case of interaction between deposition processes and turbulence is shown in Figure 7h and i, in which the current is fully turbulent and the low concentration of material does not allow the development of any granular flow–dominated layer. In these cases, deposition occurs grain by grain with development of dune-bedding and internal cross-stratification (lithofacies xsA; Figure 18e). Fluid drag can induce traction on the material previously deposited and cause imbrication of clasts in the upper part of the deposit (lithofacies lensL$_{(i)}$; Figure 18e).

# 6. Conclusive Remarks and Future Perspectives

Research on PDC behaviour is one of the main topics in present day volcanology, and involves disciplines ranging from sedimentology to geophysics to laboratory experiments to numerical simulations. The vast interest is justified by the complex nature of these currents and by their very dangerous nature that threaten millions of people around the world. In recent years, significant goals have been reached in understanding the physics of PDCs. Perhaps the most important
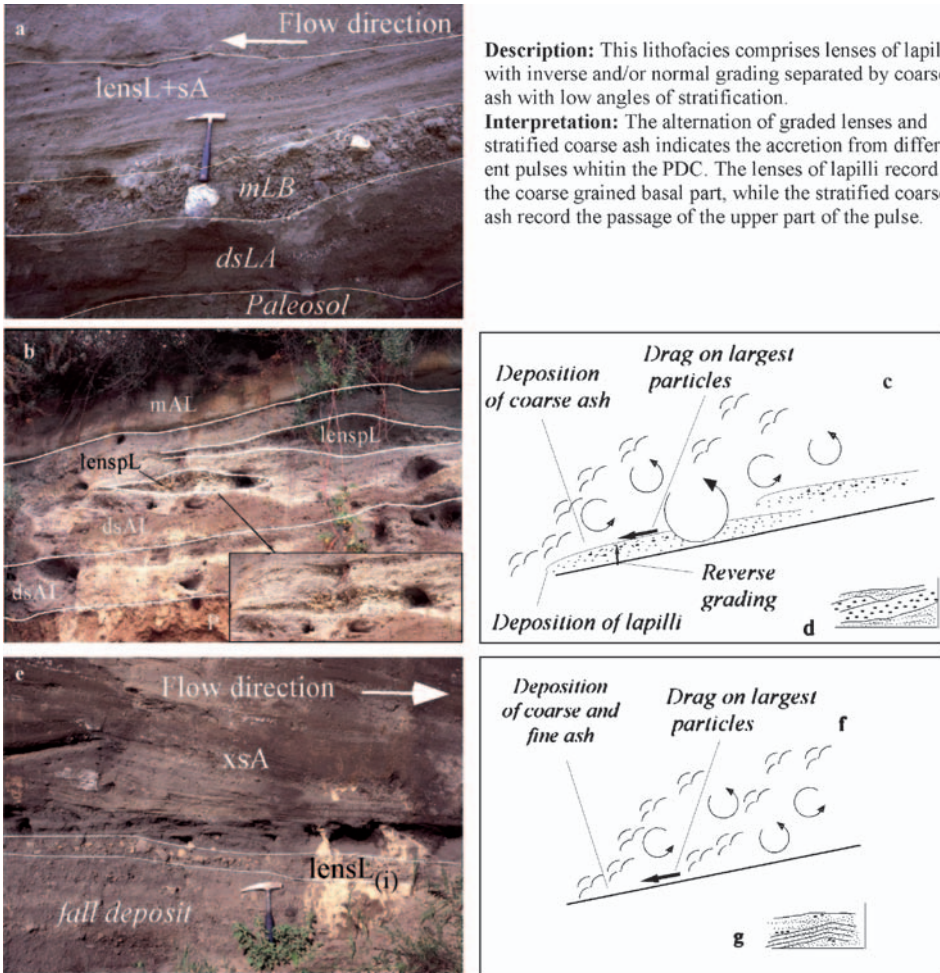
**Figure 18**  Examples of lithofacies associations in PDC deposits of Pollena (a) and (e) and Upper Pollara (b) eruptions; (c, d) sedimentological model that illustrates the observed lithofacies association of picture (a) and (b); (f, g) sedimentological model that illustrates the observed lithofacies association of picture (e).

achievement is the description of different types of PDCs within a continuum of phenomena, in which the dominance of fluid or solid particles on motion determines the wide range of observed deposits. Of primary importance is also the involvement of the granular flow theory in description of the particle–particle dominated (lower) part of PDCs. Since PDCs are density stratified, particle–particle interaction plays a role in all types of PDCs, although with the likely exception of extremely diluted currents. The interpretation of some deposits using granular flow theory has opened some interesting perspectives for future research. The first is

unification of the current two major models for PDC deposition: progressive aggradation and *en masse* freezing. The second is that a PDC does not move as a single body but comprises different pulses that move at different velocities down valley.

Nevertheless, a considerable gap in understanding remains between documented deposit features, such as sorting, texture and sedimentary structures and the conceptual models of PDCs. The new approaches, descriptive schemes and models presented here represent a tentative attempt to illustrate both modern research and to address some key concepts on PDC behaviour. However, high-quality research urges us to enhance our understanding of the physical behaviour of PDCs and other gravity-driven currents. This is needed to ameliorate both our comprehension of the natural phenomenon and our forecasting ability.

Being that PDCs are physical phenomenon, their nature and behaviour can be investigated by future research in three primary ways: observation in nature, reproduction in laboratory and theoretical prediction (numerical modelling). These three ways are not independent, as any progress in one of these has to be validated by the other two. Because PDCs are very hazardous phenomena, real time observations are limited to small or intermediate-scale events, although in the last 25 years, the observation of some PDC-producing eruptions have greatly pushed ahead the research (e.g. St Helens, 1980; Arenal, 1987–2001; Unzen, 1990–1995; Colima, 1991; Pinatubo, 1991; Montserrat, 1995-present day; Lipman and Mullineaux, 1981; Yamamoto et al., 1993; Newhall and Punongbayan, 1996; Ui et al., 1999; Druitt and Kokelaar, 2002; Saucedo et al., 2004; Cole et al., 2005). This implies that only real time observation and measurements of physical parameters of PDCs generated in future explosive eruptions will significantly enhance our knowledge.

To partially get around this lack of information from direct observation, a number of laboratory experiments have been performed, ranging from small laboratory flumes (Gladstone et al., 1998; Choux and Druitt, 2002; Choux et al., 2004; Roche et al., 2004) to open air experiments (Dellino et al., 2007). Despite some problems due to the use of synthetic material, limited mass and scaling processes, laboratory experiments have highlighted important mechanisms in both transport and depositional mechanisms of PDCs, which have been used to interpret natural deposits. Nevertheless, further experimentation is required to learn about the physics of density-stratified currents that have polydispersed clast populations and a gaseous fluid phase (dusty gas). The reproduction of small PDCs in large-scale experiments is the main research direction for future. To date, this approach has allowed the observation of PDC generation and the measurements of some important parameters (work, rate of turbulence, potential to kinetic energy transformation, velocity) over flat topography (Dellino et al., 2007). In the near future, additions of complexities in topography and enhancement of the ability to record different parameters are very promising avenues to shed new light on PDC behaviour.

At the same time, numerical modelling has undergone tumultuous growth during the last 15 years, with complexities that have constantly been added to numerical codes to obtain a better fit with natural phenomena (e.g. Dobran et al.,

1993; Neri et al., 2003). These computations have yielded invaluable constraints to the basic physical processes that characterize motion and deposition of particles within a PDC, but some complexities of natural currents are still difficult to replicate using the available computational capabilities. The addition of new results and constraints from field data and experiments into numerical codes is the main challenge for future research in numerical modelling. Although recent developments in multiphase, Lagrangian codes represent a significant improvement toward description of complex phenomena, the results are still not able to fully describe the variability of natural PDCs.

## ACKNOWLEDGEMENTS

## REFERENCES

Alidibirov, M.A., Dingwell, D.B., 2000. Three fragmentation mechanisms for highly viscous magma under rapid decompression. J. Volcanol. Geotherm. Res., 100, 413–421.

Allen, S.R., Cas, R.A.F., 1998. Rhyolitic fallout and pyroclastic density current deposits from a phreatoplinian eruption in the eastern Aegean Sea, Greece. J. Volcanol. Geotherm. Res., 86, 219–251.

Baer, E.M., Fisher, R.V., Fuller, M., Valentine, G., 1997. Turbulent transport and deposition of the Ito pyroclastic flow: determinations using anisotropy of magnetic susceptibility. J. Geophys. Res., 102(B10), 22565–22586.

Bagnold, R.A., 1954. Experiments on a gravity-free dispersion of large solid spheres in a Newtonian fluid under shear. Proc. Royal Soc., London, A, 225, 49–63.

Baxter, P.T., Neri, A., Todesco, M., 1998. Physical modeling and human survival in pyroclastic flows. Nat. Hazard., 17, 163–176.

Bonnecaze, R.T., Huppert, H.E., Lister, J.R., 1993. Particle driven gravity currents. J. Fluid Mech., 250, 339–369.

Branney, M.J., Kokelaar, P., 1992. A reappraisal of ignimbrite emplacement: progressive aggradation and changes from particulate to non-particulate flow during emplacement of high-grade ignimbrite. Bull. Volcanol., 54, 504–520.

Branney, M.J., Kokelaar, P., 1997. Giant bed from a sustained catastrophic density current flowing over topography: Acatlan ignimbrite, Mexico. Geology, 25, 115–118.

Branney, M.J., Kokelaar, P., 2002. Pyroclastic Density Currents and the Sedimentation of Ignimbrites. Geological Society, London, Memoirs, 27, 143 pp.

Brennen, C.E., Sieck, K., Paslasky, J., 1983. Hydraulic jumps in granular material flow. Powd. Technol., 35, 31–37.

Bryan, S.E., Cas, R.A., Marti, J., 1998. Lithic breccias in intermediate volume phonolitic ignimbrites, Tenerife (Canary Islands). Constraints on pyroclastic flow depositional processes. J. Volcanol. Geotherm. Res., 81, 269–296.

Burgissier, A., Bergantz, G.W., 2002. Reconciling pyroclastic flow and surge: the multiphase physics of pyroclastic density currents. Earth Plan. Sci. Lett., 202, 405–418.

Bursik, M.I., Woods, A.W., 1996. The dynamics and thermodynamic of large ash flows. Bull. Volcanol., 58, 175–193.

Calanchi, N., De Rosa, R., Mazzuoli, R., Rossi, P., Santacroce, R., Ventura, G., 1993. Silicic magma entering a basaltic magma chamber: eruptive dynamics and magma mixing-an example from Salina (Aeolian islands, southern Tyrrhenian sea). Bull. Volcanol., 55, 504–522.

Campbell, C.S., 1990. Rapid granular flows. Ann. Rev. Fluid Mech., 22, 57–92.

Campbell, C.S., Brennen, C.E., 1985. Computer simulation of granular shear flows. J. Fluid Mech., 151, 167–188.

Cao, Z., Egashira, S., Carling, P.A., 2003. Role of suspended-sediment particle size in modifying velocity profiles in open channel flows. Water Resour. Res., 39, 1–15.

Carey, S.N., 1991. Transport and deposition of tephra by pyroclastic flows and surges. In: Fisher, R.V. and Smith, G.A. (Eds), Sedimentation in volcanic settings, SEPM, Special Publications, p. 45.

Carey, S.N., Sigurdsson, H., Mandeville, C., Bronto, S., 1996. Pyroclastic flows and surges over water: an example from the 1883 Krakatau eruption. Bull. Volcanol., 57, 493–511.

Cas, R., Wright, J.W., 1987. Volcanic Successions: Modern and Ancient. Allen and Unwin, London, 528 pp.

Chough, S.K., Sohn, Y.K., 1990. Depositional mechanics and sequences of base surges, Songaksan tuff ring, Cheju Island, Korea. Sedimentology, 37, 1115–1135.

Choux, C., Druitt, T., Thomas, N., 2004. Stratification and particle segregation in flowing polydisperse suspensions, with applications to the transport and sedimentation of pyroclastic density currents. J. Volcanol. Geotherm. Res., 138, 223–241.

Choux, C.M., Druitt, T.H., 2002. Analogue study of particle segregation in pyroclastic density currents, with implications for the emplacement mechanisms of large ignimbrites. Sedimentology, 49, 907–928.

Cioni, R., Gurioli, L., Lanza, R., Zanella, E., 2004. Temperatures of the A.D. 79 pyroclastic density current deposits (Vesuvius, Italy). J. Geophys. Res., 109, 1–18.

Cioni, R., Gurioli, L., Sbrana, A., Vougioukalakis, G., 2000. Precursory phenomena and destructive events related to the Late Bronze Age Minoan (Thera, Greece) and A.D. 79 (Ve-suvius, Italy) Plinian eruptions: Inferences from the stratigraphy in the archaeological areas. In: McGuire, B., et al., (Eds), The archaeology of geological catastrophes: Geological Society (London) Special Publication, Vol. 171, pp. 123–141.

Cole, P.D., Calder, E.S., Sparks, R.S.J., Clarke, A.B., Druitt, T.H., Young, S.R., Herd, R.A., Harford, C.L., Norton, G.E., 2002. Deposits from dome-collapse and fountain-collapse pyroclastic flows at Soufriére Hills volcano, Montserrat. In: Druitt, T.H. and Kokelaar, B.P. (Eds), The eruption of Soufriére Hills Volcano, Montserrat, from 1995 to 1999. Geological Society of London Memoir, London, Vol. 21, pp. 231–262.

Cole, P.D., Fernandez, E., Duarte, E., Duncan, A.M., 2005. Explosive activity and generation mechanisms of pyroclastic flows at Arenal volcano, Costa Rica between 1987 and 2001. Bull. Volcanol., 67, 695–716.

Cole, P.D., Guest, J.E., Duncan, A.M., 1993. The emplacement of intermediate volume ignimbrite: a case study from Roccamonfina volcano, southern Italy. Bull. Volcanol., 55, 467–480.

Colella, A., Hiscott, R.N., 1997. Pyroclastic surges of the Pleistocene Monte Guardia sequence (Lipari island, Italy): depositional processes. Sedimentology, 44, 47–66.

Dade, B.W., Huppert, H.E., 1996. Emplacement of the Taupo Ignimbrite by a dilute turbulent flow. Nature, 381, 509–512.

Dellino, P., Isaia, R., Veneruso, M., 2004. Turbulent boundary layer shear flows as an approximation of base surge at Campi Flegrei (Southern Italy). J. Volcanol. Geotherm. Res., 133, 211–228.

Dellino, P., Zimanowski, B., Buettner, R., La Volpe, L., Mele, D., Sulpizio, R., 2007. Large scale experiments on the mechanics of pyroclastic flows: design, engineering and first results. J. Geophys. Res., 112, B04202.

Denlinger, R.P., Iverson, R.M., 2001. Flow of variably fluidized granular masses across three dimensional terrain, 2. Numerical predictions and experimental texts. J. Geophys. Res., 106, 553–566.

De Rosa, R., Donato, P., Ventura, G., 2002. Fractal analysis of mingled/mixed magmas; an example from the Upper Pollara eruption (Salina Island, southern Tyrrhenian Sea, Italy. Lithos, 65, 299–311.

Dingwell, D.B., 1998. Recent experimental progress in the physical description of silicic magma relevant to explosive volcanism. In: Gilbert, J.S. and Sparks, R.S.J. (Eds), The Physics of Explosive Volcanic Eruptions. Geological Society, London Special Publications, Vol. 145, pp. 9–26.

Dobran, F., Neri, A., Macedonio, G., 1993. Numerical simulations of collapsing volcanic columns. J. Geophys. Res., 98, 4231–4259.

Dobran, F., Neri, A., Todesco, M., 1994. Assessing the pyroclastic flow hazard at Vesuvius. Nature, 367, 551–554.

Drahun, J.A., Bridgewater, J., 1983. The mechanism of free surface segregation. Powd. Technol., 36, 39–53.

Druitt, T.H., 1992. Emplacement of the 18 May 1980 lateral blast deposits east–northeast of Mount St Helens, Washington. Bull. Volcanol., 54, 554–572.

Druitt, T.H., 1998. Pyroclastic density currents. In: Gilbert, J.S. and Sparks, R.S.J. (Eds), The Physics of Explosive Volcanic Eruptions. Geological Society, London, Special Publications, Vol. 145, pp.145–182.

Druitt, T.H., Kokelaar, B.P., 2002. The Eruption of Soufriére Hills Volcano, Montserrat, from 1995 to 1999. Geological Society of London Memoir, 21, 664 pp.

Edwards, D.A., Leeder, M.R., Best, J.L., Pantin, H.M., 1994. On experimental reflected density currents and the interpretation of certain turbidites. Sedimentology, 41, 437–461.

Felix, G., Thomas, N., 2004. Relation between dry granular flow regimes and morphology of deposits; formation of levees in pyroclastic deposits. Earth Plan. Sci. Lett., 221, 197–213.

Fisher, R.V., 1966. Mechanism of deposition from pyroclastic flows. Am. J. Sci., 264, 350–366.

Fisher, R.V., 1990. Transport and deposition of a pyroclastic surge across an area of high relief — the 18 May 1980 eruption of Mount St Helens, Washington. GSA Bull., 102, 1038–1054.

Fisher, R.V., Heiken, G., 1982. Mt. Pelée, Martinique: May 8 and 20, 1902, pyroclastic flows and surges. J. Volcanol. Geotherm. Res., 13, 339–371.

Freundt, A., Bursik, M.I., 1998. Pyroclastic flow transport mechanisms. In: Freundt, A. and Rosi, M. (Eds), From Magma to Tephra, Modelling Physical Processes of Explosive Volcanic Eruptions. Elsevier, Amsterdam, pp. 173–231.

Freundt, A., Schmincke, H.U., 1986. Emplacement of small-volume pyroclastic flows at Lacher See (East Eifel, Germany). Bull. Volcanol., 48, 39–59.

Gladstone, C., Phillips, J.C., Sparks, R.S.J., 1998. Experiments on bidisperse, constant-volume gravity currents: propagation and sediment deposition. Sedimentology, 45, 833–843.

Gray, T.E., Alexander, J., Leeder, M.R., 2005. Quantifying velocity and turbulence structure in depositing sustained turbidity currents across breaks in slope. Sedimentology, 4, 1–22.

Gurioli, L., Cioni, R., Sbrana, A., Zanella, E., 2002. Transport and deposition of pyroclastic density currents over an inhabited area: the deposits of the AD 79 eruption of Vesuvius at Herculaneum, Italy. Sedimentology, 49, 1–26.

Gurioli, L., Pareschi, M.T., Zanella, E., Lanza, R., Deluca, E., Bisson, M., 2005. Interaction of pyroclastic density currents with human settlements: evidence from ancient Pompeii. Geology, 33(6), 441–444.

Hallworth, M.A., Huppert, H., 1998. Abrupt transitions in high-concentration, particles driven gravity currents. Phys. Fluids, 10, 1083–1087.

Huppert, H.E., Turner, J.S., Carey, S.N., Sparks, R.S.J., Hallworth, M.A., 1986. A laboratory simulation of pyroclastic flows down slopes. J. Volcanol. Geotherm. Res., 30, 179–199.

Iverson, R.M., 1997. The physics of debris flows. Rev. Geophys., 35, 254–296.

Iverson, R.M., 2003. The debris flow rheology myth. In: Rickenmann, D. and Chen, C.I. (Eds), Debris flow hazard mitigation: mechanics, prediction, and assessment. Millpress, Rotterdam, Netherlands, pp. 303–314.

Iverson, R.M., Denlinger, R.P., 2001. Flow of variably fluidized granular masses across three dimensional terrain, I. Coulomb mixture theory. J. Geophys. Res., 106, 537–552.

Iverson, R.M., Vallance, J.M., 2001. New views of granular mass flows. Geology, 29, 115–118.

Johnson, A.M., 1970. Physical processes in geology. Freeman, San Francisco, CA.

Kneller, B., Branney, M.J., 1995. Sustained high-density turbidity currents and the deposition of thick massive sands. Sedimentology, 42, 607–616.

Kneller, B., Buckee, C., 2000. The structure and fluid mechanics of turbidity currents: a review of some recent studies and their geological implications. Sedimentology, 47, 62–94.

Kneller, B.C., McCaffrey, W., 1999. Depositional effects of flow nonuniformity and stratification within turbidity currents approaching a bounding slope: deflection, reflection, and facies variation. J. Sediment. Res., 69, 980–991.

Lee, J., Leibig, M., 1994. Density waves in granular flow: a kinetic wave approach. J. Phys. I France, 4, 507–514.

Leeder, M.E., Gray, T.E., Alexander, J., 2005. Sediment suspension dynamics and a new criterion for the maintenance of turbulent suspensions. Sedimentology, 52, 683–691.

Legros, F., Kelfoun, K., 2000. On the ability of pyroclastic flows to scale topographic obstacles. J. Volcanol. Geotherm. Res., 98, 235–241.

Le Roux, J.P., 2003. Can dispersive pressure cause inverse grading in grain flows? — discussion. J. Sediment. Res., 73, 333–334.

Lipman, P.W., Mullineaux, D.R., Eds., 1981. The 1980 eruptions of Mount St. Helens, Washington. USGS Prof. Paper 1250, 844 pp.

Loughlin, S.C., Calder, E.S., Clarke, A., Cole, P.D., Luckett, R., Mangan, M.T., Pyle, D.M., Sparks, R.S.J., Voight, B., Watts, R.B., 2002. Pyroclastic flows and surges generated by the 25 June 1997 dome collapse, Soufrière Hills Volcano, Montserrat. In: Druitt, T.H. and Kokelaar, B.P. (Eds), The Eruption of Soufriére Hills Volcano, Montserrat, from 1995 to 1999. Geological Society, London, Memoirs, Vol. 21, pp. 191–210.

Lowe, D.R., 1982. Sediment gravity flows: II. Depositional models with special references to deposits of high-density turbidity currents. J. Sediment. Petrol., 52, 279–297.

Luongo, G., Perrotta, A., Scarpati, C., 2003a. Impact of the AD 79 eruption on Pompeii, I. Relations amongst the depositional mechanisms of the pyroclast products, the framework of the buildings and the associated destructive events. J. Volcanol. Geotherm. Res., 126, 201–223.

Luongo, G., Perrotta, A., Scarpati, C., De Carolis, E., Patricelli, G., Ciarallo, A., 2003b. Impact of the A.D. 79 eruption on Pompeii, II. Causes of death of the inhabitants inferred by stratigraphic analysis and areal distribution of the human causalities. J. Volcanol. Geotherm. Res., 126, 169–200.

Macias, J.L., Espindola, J.M., Bursik, M., Sheridan, M.F., 1998. Development of lithic-breccias in the 1982 pyroclastic flow deposits of El Chichon volcano, Mexico. J. Volcanol. Geotherm. Res., 83, 173–196.

Major, J.J., 1997. Depositional processes in large-scale debris flow experiments. J. Geol., 105, 345–366.

Major, J.J., Iverson, R.M., 1999. Debris-flow deposition: effects of pore-fluid pressure and friction concentrated at flow margins. Geol. Soc. Am. Bull., 111, 1424–1434.

Mathisen, M.E., Vondra, C.F., 1983. The fluvial and pyroclastic deposits of the Cagayan basin, Northern Luzon, Philippines—an example of non-marine volcaniclastic sedimentation in an interarc basin. Sedimentology, 30, 369–392.

Miall, A.D., 1978. Lithofacies types and vertical profiles models in braided river deposits: a summary. In: Miall, A.D. (Ed.), Fluvial Sedimentology. Canadian Society of Petroleoum Geologists Memoir, 5, 597–604.

Miall, A.D., 1985. Architectural-element analyses: a new method of facies analyses applied to fluvial deposits. Earth Sci. Rev., 22, 261–308.

Middleton, G.V., Neal, W.J., 1989. Experiments on the thickness of beds deposited by turbidity currents. J. Sediment. Petrol., 59, 297–307.

Middleton, G.V., Southard, J.B., 1984. Mechanics of sediment movements. SEPM, Tulsa, OK, 401 pp.

Miyabuchi, Y., 1999. Deposits associated with the 1990–1995 eruption of Unzen volcano, Japan. J. Volcanol. Geotherm. Res., 89, 139–158.

Mulder, T., Alexander, J., 2001. The physical character of subaqueous sedimentary density flows and their deposits. Sedimentology, 48, 269–299.

Nemec, W., 1990. Aspects of sediment movement on steep delta slopes. In: Colella, A. and Prior, D.B., (Eds.), Coarse grained deltas. International Association of Sedimentology, special publication, Vol. 10, 29–73.

Neri, A., Ongaro, T.E., Macedonio, G., Gidaspow, D., 2003. Multiparticle simulation of collapsing volcanic columns and pyroclastic flow. J. Geophys. Res., 108(B4), 2202.

Newhall, C.G. and Punongbayan, R.S. (Eds), 1996. Fire and mud: eruptions and lahars of Mount Pinatubo, Philippines, Philippine Institute of Volcanology and Seismology & University of Washington Press, Quezon City & Seattle, 1126 pp.

Nield, S.E., Woods, A.W., 2003. Effects of flow density on the dynamics of dilute pyroclastic density currents. J. Volcanol. Geotherm. Res., 132, 269–281.

Niño, Y., Lopez, F., Garcia, M., 2003. Threshold for particle entrainment into suspension. Sedimentology, 50, 247–263.

Nunziante, L., Fraldi, M., Lirer, L., Petrosino, P., Scotellaro, S., Cicirelli, C., 2003. Risk assessment of the impact of pyroclastic currents eruption. Nature, 345, 519–521.

Oke, T., 1987. Boundary layer climates. Routledge, London, 464 pp.

Petrazzuoli, S.M., Zuccaro, G., 2004. Structural resistance of reinforced concrete buildings under pyroclastic flows: a study of the Vesuvian area. J. Volcanol. Geotherm. Res., 133, 1–15.

Pierson, T.C., 1980. Erosion and deposition by debris flows at Mt. Thomas, North Canterbury, New Zealand. Earth Surf. Process., 5, 227–247.

Piper, D.J.W., Normark, W.R., 1983. Turbidite depositional patterns and flow characteristics, Navy submarine fan, California borderland. Sedimentology, 30, 681–694.

Pittari, A., Cas, R.A.F., Edgar, C.J., Nichols, H.J., Wolf, J.A., Martì, J., 2006. The influence of palaeotopography on facies architecture and pyroclastic flow processes of a lithic-rich ignimbrite in a high gradient setting: the Abrigo Ignimbrite, Tenerife, Canary Islands. J. Volcanol. Geotherm. Res., 152, 273–315.

Postma, G., 1986. Classification for sediment gravity flow deposits based on flow conditions during sedimentation. Geology, 14, 291–294.

Raudkivi, A.J., 1990. Loose Boundary Hydraulics, 3rd edn. Pergamon Press, New York.

Roche, O., Gilbertson, M.A., Phillips, J.C., Sparks, R.S.J., 2004. Experimental study of gas–fluidized granular flows with implications for pyroclastic flow emplacement. J. Geophys. Res., 109, B10201.

Rolandi, G., Munno, R., Postiglione, I., 2004. The A.D. 472 eruption of the Somma volcano. J. Volcanol. Geotherm. Res., 129, 291–319.

Rosi, M., Santacroce, R., 1983. The A.D. 472 "Pollena" eruption: volcanological and petrological data for this poorly-known, Plinian-type event at Vesuvius. J. Volcanol. Geotherm. Res., 17, 249–271.

Rottman, J.W., Simpson, J.E., Hunt, J.C.R., 1985. Unsteady gravity current flows over obstacles: some observations and analyses related to Phase II trials. J. Hazard. Mater., 11, 325–340.

Rouse, H., 1937. Modern conceptions of the mechanics of fluid turbulence. Trans. Am. Soc. Civ. Eng., 102, 436–505.

Rowley, P.D., Kuntz, M.A., Macleod, N.S., 1981. Pyroclastic flow deposits. In: Lipmann, P.W. and Mullineaux, D.R. (Eds). The 1980 eruption of Mount St Helens, Whashinghton. USGS Professional Paper, Vol. 1250, pp. 489–512.

Saucedo, R., Macias, J.L., Bursik, M., 2004. Pyroclastic flow deposits of the 1991 eruption of Volcan de Colima, Mexico. Bull. Volcanol., 66, 291–306.

Savage, S.B., 1979. Gravity flow of cohesionless granular materials in chutes and channels. J. Fluid Mech., 92, 53–96.

Savage, S.B., 1983. Granular flows down rough inclines — review and extension. In: Jenkins, J.T. and Satake, M. (Eds), Mechanics of granular materials: new models and constitutive relations. Elsevier, Amsterdam, pp. 261–281.

Savage, S.B., 1984. The mechanics of rapid granular flows. Adv. Appl. Mech., 24, 289–366.

Savage, S.B., Lun, C.K.K., 1988. Particle size segregation in inclined chute flow of dry cohesionless granular solids. J. Fluid Mech., 189, 311–335.

Schmeeckle, M.W., Nelson, J.M., 2003. Direct numerical simulation of bedload transport using a local, dynamic boundary condition. Sedimentology, 50, 279–301.

Schwarzkopf, L.M., Schmincke, H.U., Cronin, S.J., 2005. A conceptual model for block-and-ash flow basal avalanche transport and deposition, based on deposit architecture of 1998 and 1994 Merapi flows. J. Volcanol. Geotherm. Res., 139, 117–134.

Scott, K.M., Macìas, J.L., Naranjo, J.A., Rodriguez, S., McGeehin, J.P., 2001. Catastrophic debris flows transformed from landslide in volcanic terrains: mobility, hazard assessment and mitigation strategies. U.S. Geol. Surv. Prof. Pap., 1630, 1–59.

Sheppard, P.A., 1956. Airflow over mountains. Q.J.R. Meteorol. Soc., 82, 528–529.

Sigurdsson, H., Carey, S., Cornell, W., Pescatore, T., 1985. The eruption of Vesuvius in A.D. 79. Nat. Geog. Res., 1, 332–387.

Smith, G.A., 1986. Coarse-grained nonmarine volcaniclastic sediment: terminology and depositional process. GSA Bull., 97, 1–10.

Smith, G.A., 1987. The influence of explosive volcanism on fluvial sedimentation: the Deschutes formation (Neogene) in central Oregon. J. Sediment. Petrol., 57, 613–629.

Snyder, W.H., Thompson, R.S., Eskridge, R.E., Lawson, R.E., Castro, I.P., Lee, J.T., Hunt, J.C.R., Ogawa, Y., 1985. The structure of strongly stratified flow over hills: dividing-streamline concept. J. Fluid Mech., 152, 249–288.

Sohn, Y.K., 1997. On traction-carpet sedimentation. J. Sediment. Res., 67, 502–509.

Sohn, Y.K., Chough, S.K., 1989. Depositional processes of the Suwolbong Tuff Ring, Cheju Island (Korea). Sedimentology, 36, 837–855.

Sohn, Y.K., Chough, S.K., 1993. The Udo tuff cone, Cheju Island, south Korea — transformation of pyroclastic fall into debris fall and grain flow on a steep volcanic cone slope. Sedimentology, 40, 769–786.

Sparks, R.S.J., 1976. Grain size variations in ignimbrites and implications for the transport of pyroclastic flows. Sedimentology, 23, 147–188.

Sparks, R.S.J., 1978. Gas release rates from pyroclastic flows: an assessments of the role of fluidization in their emplacement. Bull. Volcanol., 41, 1–9.

Sparks, R.S.J., Gardeweg, M.C., Calder, E.S., Matthews, S.J., 1997. Erosion by pyroclastic flows on Lascar volcano. Chile. Bull. Volcanol., 58, 557–565.

Spence, R.J.S., Baxter, P.J., Zuccaro, G., 2004. Building vulnerability and human casualty estimation for a pyroclastic flow: A model and its application to Vesuvius. J. Volcanol. Geotherm. Res., 133, 1–23.

Sulpizio, R., 2005. Lithofacies and lithofacies architecture analyses in the study of pyroclastic density current deposits. Acta Vulcanologica, 17, 101–116.

Sulpizio, R., Bonasia, R., Dellino, P., Di Vito, M.A., La Volpe, L., Mele, D., 2008a. The Avellino eruption of Somma-Vesuvius (3.8 ka BP) part II: Sedimentology and physical volcanology of pyroclastic density current deposits. Bull. Volcanol., Submitted for publication.

Sulpizio, R., De Rosa, R., Donato, P., 2008b. The influence of variable substrate morphology on sedimentology of pyroclastic density currents: the example of Upper Pollara eruption (Salina Island, southern Italy). J. Volcanol. Geotherm Res., Submitted for publication.

Sulpizio, R., Mele, D., Dellino, P., La Volpe, L., 2005. A complex, Subplinian-type eruption from low-viscosity, phonolitic to tephri-phonolitic magma: the AD 472 (Pollena) eruption of Somma-Vesuvius (Italy). Bull. Volcanol., 67, 743–767. doi 10-1007/s00445-005-0414-x.

Sulpizio, R., Mele, D., Dellino, P., La Volpe, L., 2007. High variability of sedimentology and physical properties of pyroclastic density currents during complex Subplinian eruptions: the example of the AD 472 (Pollena) eruption of Somma-Vesuvius, Italy. Sedimentology, 54, 607–635.

Sulpizio, R., Zanchetta, G., Demi, F., Di Vito, M.A., Pareschi, M.T., Santacroce, R., 2006. The Holocene syneruptive volcaniclastic debris-flows in the Vesuvian area: geological data as a guide for hazard assessment. In: Siebe, C., Macias, J.L. and Aguirre-Diaz, G.J. (Eds), Neogene—Quaternary continental margin volcanism: a perspective from Mexico. GSA Special Paper. 402, pp. 203–221.

Taddeucci, J., Palladino, D.M., 2002. Particle size-density relationships in pyroclastic deposits: inferences for emplacement processes. Bull. Volcanol., 64, 273–284.

Ui, T., Matsuwo, N., Sumita, M., Fujinawa, A., 1999. Generation of block and ash flows during the 1990–1995 eruption of Unzen volcano, Japan. J. Volcanol. Geotherm. Res., 89, 123–137.

Valentine, G., 1987. Stratified flow in pyroclastic surges. Bull. Volcanol., 49, 616–630.

Valentine, G.A., 1998. Damage to structures by pyroclastic flows and surges, inferred from nuclear weapons effects. J. Volcanol. Geotherm. Res., 87, 117–140.

Walker, G.P.L., 1983. Ignimbrite types and ignimbrite problems. J. Volcanol. Geotherm. Res., 17, 65–88.

Walker, G.P.L., 1985. Origin of coarse lithic breccias near ignimbrite source vents. J. Volcanol. Geotherm. Res., 25, 157–171.

Walker, G.P.L., Wilson, C.J.N., Froggat, P.C., 1980. Fines depleted ignimbrite in New Zealand — the product of a turbulent pyroclastic flow. Geology, 8, 245–249.

Waresback, D.B., Turbeville, B.N., 1990. Evolution of a Plio–Pleistocene volcanogenic alluvial fan: the Puye formation, Jemez Mountains, New Mexico. GSA Bull., 102, 298–314.

Wilson, C.J.N., 1980. The role of fluidization in the emplacement of pyroclastic flows: an experimental approach. J. Volcanol. Geotherm. Res., 8, 231–249.

Woods, A.W., Bursik, M.I., 1994. A laboratory study of ash flows. J. Geophys. Res., 99(B3), 4375–4394.

Woods, A.W., Bursik, M.I., Kurbatov, A.V., 1998. The interaction of ash flows with ridges. Bull. Volcanol., 60, 38–51.

Wright, J.V., Walker, G.P.L., 1981. Eruption, transport and deposition of ignimbrite — a case study from Mexico. J. Volcanol. Geotherm. Res., 9, 111–131.

Yamamoto, T., Takarada, S., Suto, S., 1993. Pyroclastic flows from the 1991 eruption of Unzen volcano, Japan. Bull. Volcanol., 55, 166–175.

Zanchetta, G., Sulpizio, R., Pareschi, M.T., Leoni, F.M., Santacroce, R., 2004a. Characteristics of May 5–6 1998 volcaniclastic debris flows in the Sarno area (Campania, Southern Italy): relationships to structural damage and hazard zonation. J. Volcanol. Geotherm. Res., 133, 377–393.

Zanchetta, G., Sulpizio, R., Di Vito, M.A., 2004b. The role of volcanic activity and climate in alluvial fan growth at volcanic areas: an example from southern Campania (Italy). Sediment. Geol., 168, 249–280.

Zuccaro, G., Ianniello, D., 2004. Interaction of pyroclastic flows with building structures in an urban settlement: a fluid-dynamic simulation impact model. J. Volcanol. Geotherm. Res., 133, 1–8.

# The Use of Lithic Clast Distributions in Pyroclastic Deposits to Understand Pre- and Syn-Caldera Collapse Processes: A Case Study of the Abrigo Ignimbrite, Tenerife, Canary Islands

A. Pittari[1],[*], R.A.F. Cas[1], J.A. Wolff[2], H.J. Nichols[2], P.B. Larson[2] *and* J. Martí[3]

## Contents

[*]Corresponding author. Tel.: +61-39905-4885, +64-7-838 4466, Ext.: 8582; Fax: +61-39905-4903; +64-7-856 0115
*E-mail address:* apittari@waikato.ac.nz

[1] School of Geosciences, Monash University, Victoria, 3800, Australia; Department of Earth and Ocean Sciences, University of Waikato, Private Bag 3105, Hamilton, 3216, New Zealand
[2] School of Earth and Environmental Sciences, Washington State University, Pullman, Washington, 99164, U.S.A.
[3] Institute of Earth Sciences ' Jaume Almera', CSIC, c/Lluis Sole Sabaris s/n, 08028 Barcelona, Spain

## Abstract

Lithic-rich pyroclastic units and facies are often associated with caldera-forming eruptions. Petrographic and quantitative studies on the variety of lithic types, and the spatial and vertical variations in their proportions, provide a powerful tool for understanding (a) the subsurface and pre-caldera geology, and (b) conduit-vent processes during caldera eruptions. In particular, lithic assemblages may include unique samples of deep plutonic-basement features, hydrothermal systems and ancient volcanic landforms destroyed by caldera fragmentation. When interpreting caldera eruptions, studies of lithic clasts can constrain vent configurations, and the depth and style of conduit wall rock fragmentation.

The 186 ka Abrigo ignimbrite, representing the last major caldera-forming eruption of the Las Cañadas volcanic edifice, Tenerife, contains a diverse lithic population including (a) syenite, and rare syenogabbroid and gabbroid fragments from a deep plutonic-contact metamorphic core, (b) abundant altered fragments, representing a relatively deep extensive zone of hydrothermal alteration, and (c) shallow- and surface-derived mafic to felsic, crystalline and glassy volcanic clasts, and welded to non-welded pyroclastic and epiclastic breccia clasts, all of which are consistent with being derived from a pre-Abrigo constructive phase of the Las Cañadas edifice. Significant lateral variations in the proportions of lithic clast types, within depositional units, is consistent with an eruption involving multiple vents around a caldera that underwent piecemeal collapse, and this is further supported by lateral geochemical variations in juvenile clast populations. Vertical variations in lithic clast proportions between depositional units suggest an increasing depth of conduit wall rock fragmentation during the eruption. This study highlights vertical caldera collapse as a major process in the evolution of the Las Cañadas caldera complex.

## 1. INTRODUCTION

Pyroclastic ejecta from explosive volcanic eruptions are key tracers for subsurface volcanic processes. In particular, lithic clasts, or lapilli and block–sized dense rock fragments, are often unique samples of the interior geology of volcanic edifices (e.g. Eichelberger and Koch, 1979; Suzuki–Kamata et al., 1993; Cole et al., 1998; Krippner et al., 1998). Whilst juvenile volcanic components (pumice, crystals, vitric ash) are useful in understanding plutonic, conduit flow and magma fragmentation processes, lithic clasts provide insight into destructive/erosional conduit–vent dynamics (e.g. Heiken and McCoy, 1984; Hildreth and Mahood, 1986; Suzuki–Kamata et al., 1993; Rosi et al., 1996), which may be complex during caldera–forming eruptions. Hence, lithic–rich pyroclastic deposits provide sound geological evidence for the conditions leading to and dynamic processes occurring during caldera–collapse events.

Debate over the dynamic processes related to the formation of the Las Cañadas caldera, Tenerife, has centred on arguments in favour of a vertical collapse origin

(e.g. Hausen, 1956; Araña, 1971; Martí et al., 1994; Martí and Gudmundsson, 2000) versus a landslide origin (e.g. Bravo, 1962; Anchochea et al., 1990, 1999; Cantagrel et al., 1999; Huertas et al., 2002). The Abrigo eruption, representing the last major explosive eruption on Tenerife, produced a moderate volume ignimbrite, which is consistent with a caldera–forming eruption. Studies of lithic clasts from the Abrigo ignimbrite, described here, confirm that caldera-collapse processes occurred during this eruption.

This chapter firsts reviews the use of lithic clast compositional variations in pyroclastic deposits to understand volcanic edifices and calderas, then provides a case study of the Abrigo ignimbrite to further constrain the subsurface geology and dynamic caldera processes of the Las Cañadas edifice. Although this chapter is mainly concerned with lithic clast variations, reference is made to geochemical variations among juvenile pumice clasts, which complement the results of lithic clast analyses.

## 2. Review of Lithic Component Studies and Inferred Caldera Processes

### 2.1. Lithic-rich pyroclastic deposits

Plinian fall deposits and ignimbrites, which are the deposits of gas-supported, high particle concentration pumice and ash granular density currents or pyroclastic flows (e.g. Iverson, 1997; Iverson and Vallance, 2001; Sulpizio et al., 2007), constitute the main products of explosive caldera-forming eruptions, and are the focus of this review. Pyroclastic deposits from eruptions of minor intensity (e.g. subplinian, vulcanian) also occur at calderas and may contain lithic populations that are useful for understanding eruption dynamics, although they are generally not associated with caldera-collapse events. Lithic clast component studies rely on a sound pre-existing knowledge of the distribution, stratigraphy and facies architecture of lithic-rich pyroclastic deposit packages. The following is a summary of the different types of lithic-rich deposits associated with plinian fall deposits and ignimbrites.

#### 2.1.1. Fall deposits

Most plinian fallout deposits consist predominantly of juvenile pumice lapilli or ash. Lithic clasts, at any one location, are usually a minor component and finer-grained than juvenile clasts as a result of hydraulic sorting (Cas and Wright, 1987), although they are well-documented in many fall deposits (e.g. Aramaki, 1984; Heiken and McCoy, 1984; Fierstein and Hildreth, 1992; Suzuki-Kamata et al., 1993; Allen et al., 1999; Rosi et al., 1999; Thouret et al., 1999, 2002; Allen, 2001; Adams et al., 2001). Some fall deposits contain graded or discrete lithic-enriched horizons, which could reflect intermittent episodes of vent wall rock instability, collapse and erosion or phreatomagmatic pulses (e.g. van den Bogaard and Schmincke, 1984; Criswell, 1987; Macedonio et al., 1994; Perrotta et al., 1996; Bryan et al., 2000; Jurado-Chichay and Walker, 2001; Schumacher et al., 2001).

## 2.1.2. Ignimbrites

Along with vesiculated juvenile clasts, free crystals and glass shards, lithic fragments (fine lithic and vitric ash may be indistinguishable) are an important component of ignimbrites, although they may vary from trace to greater than 50 vol.% in abundance and occur in a diversity of associated facies types. Relatively high lithic clast abundances may be widespread throughout massive to stratified ignimbrite body facies (e.g. Calvache and Williams, 1992; Bryan et al., 1998b; Calder et al., 2000; Pittari and Cas, 2004; Pittari et al., 2006; Edgar et al., 2007). Relatively larger isolated "outsized" lithic clasts may be dispersed throughout massive ignimbrite facies (e.g. Bryan et al., 1998a; Pittari et al., 2006). Lithic-rich breccias may occur as stratigraphically confined or spatially localised facies or concentrations within broader ignimbrite deposits. The different types are discussed below.

*Ground breccias* or "ground layers" (Walker et al., 1981; Druitt and Sparks, 1982; Suzuki-Kamata, 1988), which are a type of Layer 1 deposit of Sparks et al. (1973), or layer 1(H) of Wilson and Walker (1982), are sharply bounded layers enriched in dense clasts and commonly depleted in fine ash relative to overlying pumiceous ignimbrite facies. Ground breccias may frequently occur well away from proximal areas and are interpreted to have formed at the head of a pyroclastic flow (Walker et al., 1981).

*Co-ignimbrite lag breccias* (Wright and Walker, 1977; Wright, 1981; Druitt and Sparks, 1982; Druitt, 1985; Bacon, 1983; Walker, 1985; Druitt and Bacon, 1986; Suzuki-Kamata et al., 1993; Freundt and Schmincke, 1985; Self et al., 1986; Fierstein and Hildreth, 1992; Cole et al., 1993; Rosi et al., 1996; Nairn et al., 2004; Sottili et al., 2004; Pittari et al., 2006) are coarse (largest lithic clasts >2 m diameter), thick (20–30 m), often fines-depleted, clast-supported and stratified lithic breccias which occur in vent-proximal locations. They are often deposited at the peak of an eruption, particularly at the onset of caldera collapse, from expanded pyroclastic flows near their point of initiation at the base of a collapsing eruption column.

*Outer slope fines-depleted lithic breccias* (e.g. Roobol et al., 1987; Pittari et al., 2006) are generally finer-grained than co-ignimbrite lag breccias, and were deposited from pyroclastic flows that experienced enhanced flow-turbulence-induced fines elutriation as a response to steep and/or highly vegetated slopes.

*Widespread intra-ignimbrite matrix-supported lithic breccias* or *lithic concentration zones* can occur near the base (2bL of Sparks, 1976; see also Sparks et al., 1973; Yokoyama, 1974; Freundt and Schmincke, 1985; Suzuki-Kamata and Kamata, 1990; Palladino and Valentine, 1995; Allen and Cas, 1998; Pittari et al., 2006), or at higher stratigraphic levels (e.g. Bryan et al., 1998a; Pittari et al., 2006) within the main body deposit of single ignimbrite depositional units. These types of breccias may be locally discontinuous, but their occurrence at specific stratigraphic levels is widespread. They can be single or multiple clast-thick horizons typically less than 1 m thick. Controls on their occurrence are generally related to variations in supply from the vent and/or in response to specific topographic situations and local substrate flow entrainment processes (Druitt and Sparks, 1982; Freundt and Schmincke, 1985; Buesch, 1992; Allen and Cas, 1998; Bryan et al., 1998a; Pittari et al., 2006).

A variety of *localised lithic bedforms*, such as lithic trails, low- and high–profile bedforms, discontinuous lenses and stratification, are commonly documented within ignimbrite depositional units (e.g. Freundt and Schmincke, 1985; Bryan et al., 1998a; Allen and Cas, 1998; Pittari et al., 2006). These are generally the result of localised flow processes controlled by topographic features and/or changing flow regimes. Lithic clasts may also be concentrated into vertical *gas escape pipes* (Wilson, 1980, 1984) immediately after emplacement (Druitt, 1995; Roche et al., 2002).

## 2.2. Quantifying spatial variations in lithic assemblages

Grainsize analysis techniques (e.g. sieve analysis, point counting) may be applied to pyroclastic deposits to estimate average grainsize, degree of sorting and the spatial variations in the grainsize and relative proportions of the major pyroclastic components (pumice, lithic clasts, free crystals, ash). The maximum lithic clast size (ML) of a particular pyroclastic unit, taken as the average of the length of the long axis of 3–7 largest lithic clasts within a sample area, is a useful quantity which can be related to the eruption intensity. Isopleth maps, which are contoured representations of the spatial variation of ML, have been constructed for ignimbrite deposits to constrain vent locations (e.g. Aramaki, 1984; Smith and Houghton, 1995; Allen, 2001) and to assess the effect of palaeotopography on lithic distributions in pyroclastic flows (e.g. Giordano, 1998). Similarly, isopleth maps of both maximum pumice and lithic clast sizes can be constructed for pyroclastic fall deposits to estimate mass eruption rates and eruption column heights (Carey and Sparks, 1986; Wilson and Walker, 1987; Fierstein and Hildreth, 1992; Bryan et al., 2000).

Hand specimen identification, further constrained by detailed microscopic petrographic study, forms the basis for classifying the major lithic compositional types within pyroclastic units. Major- and trace-element geochemistry may further refine the classification criteria (e.g. Cole et al., 1998). To assess the relative proportions of the different lithic types, a variety of sampling methods have been used, including (a) field or laboratory grid and line point counting, or counting of only in situ or extracted lithic clasts within a specified sampling area (Heiken and McCoy, 1984; Druitt, 1985; Potter and Oberthal, 1987; Buesch, 1992; Suzuki-Kamata et al., 1993; Rosi et al., 1996), or (b) weighing clast populations from grainsize fractions (Hildreth and Mahood, 1986; Suzuki-Kamata, 1988; Druitt, 1992; Calder et al., 2000). Individual samples generally contain 50 to over 300 lithic clasts, although desirable sampling statistics are only approached with the latter number (Suzuki-Kamata et al., 1993). Depending on the classification criteria, lithic analyses, especially in the field, are generally restricted to lapilli and block grainsize fractions, which could involve textures or fabrics visible to the naked eye. In some cases, only a specific grainsize fraction(s) is analysed.

A popular way to visually represent spatial lithic component variations is to construct a series of pie charts assorted around a locality map, showing the relative proportion of lithic clast types at each sample site (Figure 1a; Heiken and McCoy, 1984; Potter and Oberthal, 1987; Suzuki-Kamata, 1988; Suzuki-Kamata et al., 1993). Bar charts and histograms (Suzuki-Kamata et al., 1993; Calder et al., 2000) or ternary diagrams (Druitt, 1992) can be used to the same effect (Figure 1b).

Alternatively, the distribution of each lithic type can be shown on separate maps (Figure 1c; Druitt, 1985). The vertical variation in lithic component abundances, or just in their occurrence, can be plotted against stratigraphic logs (Figure 1d; Druitt, 1985; Suzuki-Kamata et al., 1993; Bryan et al., 2000; Allen, 2001) and combined with spatial variation maps to show three-dimensional variations (Rosi et al., 1996).

## 2.3. Lithic clast provenance

Lithic clasts are either: (a) *juvenile (cognate)* dense fragments of the erupting magma chamber, (b) *accessory* country rock fragments eroded from the walls of the magma chamber, conduit and vent, and (c) *accidental* fragments of the exposed surface eroded and entrained into pyroclastic flows (Cas and Wright, 1987). To ascertain the provenance of specific lithic types, it is necessary to understand the regional geology of the volcanic terrain, which can often be complex. Conversely, where lithic types are not represented by any known surface exposure, the nature of the subsurface geology can be inferred.

Accessory and accidental lithic clasts in volcanic regions are often texturally and compositionally similar, and difficult to distinguish. Plinian fall deposits contain solely vent-derived lithologies and can help to establish vent-derived lithic clasts in ignimbrites from the same eruption (e.g. Potter and Oberthal, 1987; Bryan et al., 2000; Calder et al., 2000), although later ignimbrites may contain additional accessory lithologies if the vent location changes. Lithic fragments embedded in juvenile pumice clasts must also be vent-derived (e.g. Bryan et al., 2000). Both accidental and accessory lithic clasts are present in variable proportions within ignimbrite deposits. Vent-derived lithologies generally decrease in size and proportion away from the vent, whereas local substrate-derived lithologies increase, especially on the lee side of topographic highs (Suzuki-Kamata, 1988; Buesch, 1992; Calder et al., 2000).

Accessory lithic clasts represent samples of a thick subsurface rock succession (4–7 km in the case of the Las Cañadas edifice, Tenerife; Bryan et al., 2000). Cole et al. (1998) presented a detailed petrological and geochemical provenance study of ignimbrite lithic clasts from the Taupo volcanic centre, New Zealand, attempting to correlate these to local outcrop exposures and inferring a complex subsurface geology and constraining caldera locations. Fresh volcanic lithic clasts, with no equivalent outcrop exposure, have been interpreted to represent pre-caldera

**Figure 1** Examples of representations of quantitative spatial lithic assemblage variations. (a) Pie diagrams showing relative lithic proportions within a continuous lithic-rich layer in the Wineglass Welded Tuff, W, and underlying lithic-rich layers, W′, around the rim of Crater Lake caldera (modified from Suzuki-Kamata et al., 1993). (b) Bars showing relative lithic assemblage variations of the Soncor ignimbrite, Lascar volcano, Chile, across three down flow transects within quebradas (valleys) (modified from Calder et al., 2000). (c) Qualitative lithic distribution maps for each lithic type identified in lag breccias from the Cape Riva eruption, Santorini (modified from Druitt, 1985). (d) Qualitative vertical variations in lithic clast assemblage through the Granadilla pumice fallout deposit, Tenerife (modified and simplified from Bryan et al., 2000). Abbreviations: cog. cl., cognate clast; phen., phenocryst; phon., phonolite; weld., welded.

edifice features (e.g. stratovolcanoes or dome complexes), which were destroyed by the subsequent caldera-forming eruption (Suzuki-Kamata et al., 1993; Cole et al., 1998; Allen, 2001; Jurado-Chichay and Walker, 2001); or buried beneath later caldera in-fill deposits (e.g. Krippner et al., 1998; Bryan et al., 2000). Altered volcanic, plutonic and metasedimentary lithic clasts are often derived from deeper source rocks (e.g. Eichelberger and Koch, 1979; Suzuki-Kamata et al., 1993; Bryan et al., 2000) representing the pre-volcanic basement, earlier volcanic edifice products, and the intruded plutonic–hypabyssal complex and surrounding metamorphic aureole associated with ongoing magmatism. At some volcanoes, hydrothermal alteration may be extensive at the surface (e.g. Yellowstone and Valles calderas) and, in these cases, not all altered lithic clasts were necessarily derived from deep source rocks.

## 2.4. Hydrothermally altered lithic clasts

Hydrothermally altered lithic clasts often comprise a significant fraction of the lithic population in explosive pyroclastic deposits and have been used to infer the presence of ancient hydrothermal systems in the subsurface (Heiken and McCoy, 1984; Rocher and Westercamp, 1989; Suzuki-Kamata et al., 1993; Rosi et al., 1996; Cole et al., 1998; Bryan et al., 2000; Thouret et al., 1999, 2002; Adams et al., 2001). In many volcanic systems, they are the only samples of hydrothermally altered rocks that are otherwise not exposed at the surface, yet they are rarely used to understand hydrothermal systems. Common alteration processes affecting volcanic edifices and surrounding basement rock include: hydrothermal bleaching; glass devitrification; rock dissolution, fracturing and brecciation; and replacement or cementation by secondary minerals (e.g. Rocher and Westercamp, 1989; López and Williams, 1993; Suzuki-Kamata et al., 1993). Secondary alteration minerals (e.g. clay minerals, quartz, carbonates, sulphides, oxides, zeolites, serpentine, epidote, albite, chlorite and micas) are dependent on the chemistry of the original rock, and the composition and temperature of the hydrothermal fluids.

Hydrothermal alteration zones are likely to be discontinuous, concentrated around volcano–tectonic structures (Rocher and Westercamp, 1989) and interacting with contact metamorphic aureoles (Eichelberger and Koch, 1979). Increasing alteration of the rock pile above magma chambers, especially along pre-existing structures, destabilises volcanic edifices and increases the potential for caldera collapse (Calvache and Williams, 1992; Calvache et al., 1997; López and Williams, 1993). Furthermore, interactions between magma chambers and large volumes of hydrothermal fluids may contribute to the explosivity of volcanic eruptions (Criswell, 1987; Scandone, 1990; Mellors and Sparks, 1991; Calvache and Williams, 1992; Rosi et al., 1996), increasing country rock fragmentation and the capability to expel lithic debris. However, although the abundance of altered lithic clasts in a pyroclastic deposit implies the existence of active hydrothermal systems before an explosive eruption, their presence alone cannot ascertain the role of hydrothermal systems in initiating or fuelling the eruption itself.

## 2.5. Vent configurations

Lithic clast studies have assisted in constraining vent locations of caldera eruptions through the use of isopleth maps in conjunction with deposit thickness isopach maps (Aramaki, 1984; Bryan et al., 2000; Allen, 2001), the occurrence of near-to-vent lithic lag breccias (e.g. Lindsay et al., 2001) and correlating lithic clast types to near-to-vent outcrop exposures (e.g. Self et al., 1986; Hildreth and Mahood, 1986; Potter and Oberthal, 1987; Cole et al., 1998).

Many caldera-forming eruptions have been interpreted to evolve from a single vent plinian phase to multiple vents along a ring fissure accompanying caldera collapse (Druitt and Sparks, 1984; Lipman, 1984; Legros et al., 2000) marked by an increase in the proportion and diversity of lithic clasts (Heiken and McCoy, 1984; Druitt, 1985; Druitt and Bacon, 1986; Hildreth and Mahood, 1986; Cole and Scarpati, 1993; Rosi et al., 1996; Perrotta et al., 1996; Burgisser, 2005). Circumcaldera lithic component variations within caldera-related ignimbrite deposits indicate that pyroclastic flows were sourced from multiple vents during caldera collapse, erupting simultaneously and/or propagating along the ring fracture (Bacon, 1983, 1985; Hildreth and Mahood, 1986; Potter and Oberthal, 1987; Suzuki-Kamata et al., 1993; Cole et al., 1998).

Variations in the chemical composition of juvenile clast (pumice) types (e.g. Wolff, 1985) may also support changes in the configuration of conduits and position of magma withdrawal (e.g. Druitt, 1985; Druitt and Bacon, 1986), complementing evidence gleaned from lithic analysis. For example, although the initial plinian fall deposit of the Cape Riva eruption (Santorini) shows a normal vertical gradation to less-evolved compositions, reflecting tapping of deeper magma chamber levels (Spera, 1984; Blake and Ivey, 1986), the overlying pyroclastic flow deposit is reversely zoned (Druitt, 1985), interpreted to be the result of a change in conduit position above the magma chamber.

## 2.6. Conduit-vent dynamics

Conduit wall rock erosion and vent-widening processes result from gas-magma shear stress on conduit walls and significant differences in gas-magma and lithostatic pressures (Dobran, 1992; Papale and Dobran, 1993, 1994; Macedonio et al., 1994). Shear stresses exerted by the rising coherent magma or the fragmented eruption mixture, during high magma discharge events result in pneumatic fracturing and entrainment of conduit wall rock. At the fragmentation level, the magma–gas pressure drops rapidly below lithostatic pressure causing significant exfoliation of the wall rock into the conduit. This may also draw in large volumes of groundwater, fuelling phreatomagmatic explosions, further contributing to conduit wall rock fragmentation (Dobran, 1992). Near the conduit exit, where velocity and viscosity gradients of the gas–pyroclast mixture are high, the stripping of the conduit wall by particle impacts becomes a dominant erosive mechanism and may contribute to flaring at the vent (Dobran, 1992; Papale and Dobran, 1994; Macedonio et al., 1994). High proportions of shallow-derived fresh lithic fragments may indicate significant vent flaring (e.g. Eichelberger and Koch, 1979; Suzuki-Kamata et al., 1993).

During waning eruptive phases where the gas–magma pressure decreases, previously fractured rock, which was held in place by high conduit gas pressures during peak magma discharge stages, may collapse gravitationally into the conduit. Periodically, the conduit may become choked by excessive wall collapse or fall back of lithic debris, which may then be ejected during periods of greater eruption intensity (Wilson et al., 1980; Wright, 1981; Aramaki, 1984; Druitt, 1985; Dobran, 1992).

Although multiple levels of a conduit may be sampled simultaneously by an accelerating magma/pyroclast–gas mixture, an overall vertical increase in the proportion of deeper-derived lithic clasts within pyroclastic eruption packages is often attributed to progressive deepening of the magma and conduit wall rock fragmentation levels (Suzuki-Kamata et al., 1993; Rosi et al., 1996, Thouret et al., 1999, 2002; Bryan et al., 2000; Allen, 2001). If the deepest-derived accessory lithic clasts can be correlated to stratigraphic formations of known depth, then the maximum depth of fragmentation can be estimated. Maximum fragmentation depths of 1–2 km have been suggested for Novarupta (Hildreth, 1987), Reunion Island (Rocher and Westercamp, 1989) and Crater Lake (Suzuki-Kamata et al., 1993).

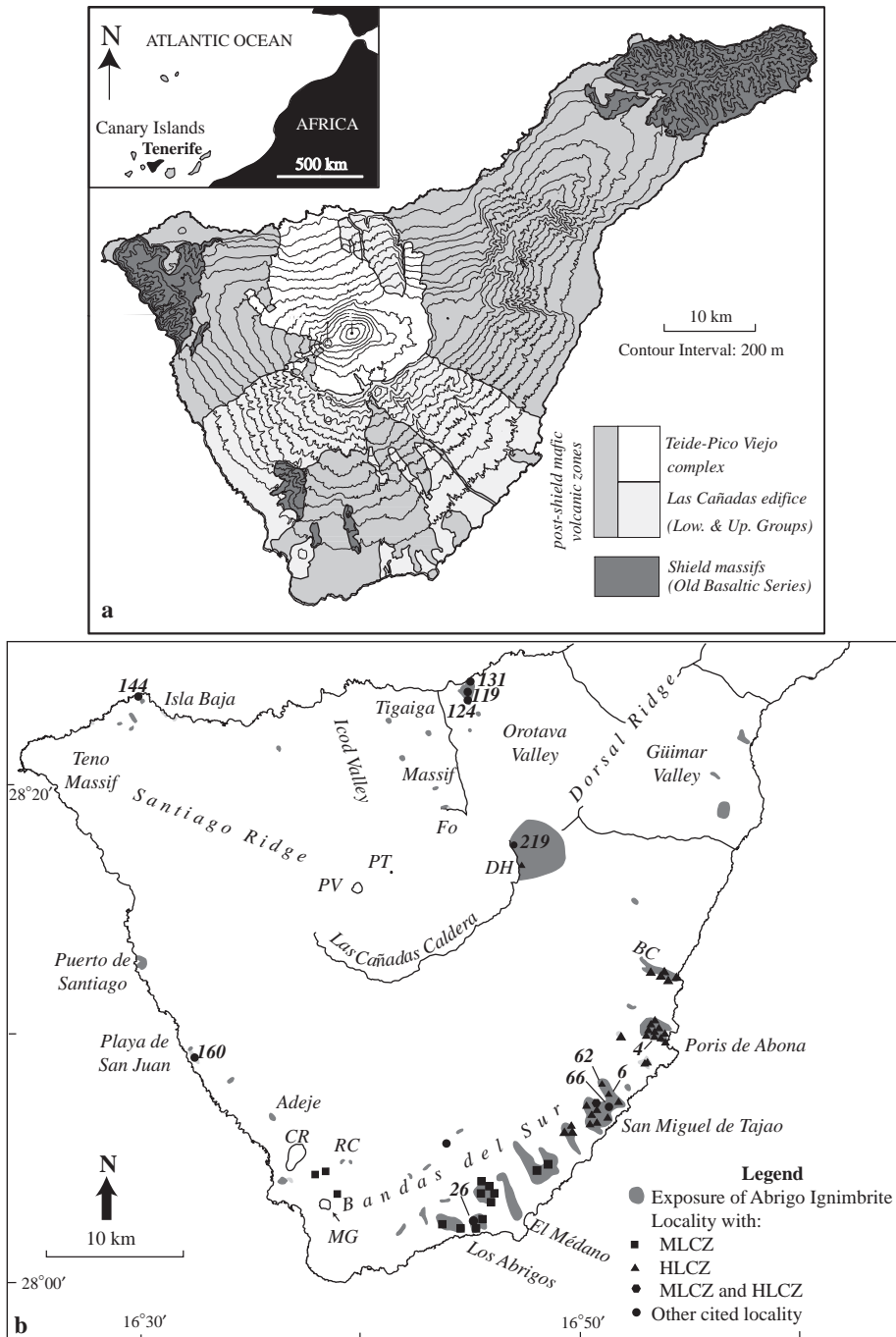## 3. Case Study of the Abrigo Ignimbrite

The Abrigo ignimbrite is a voluminous deposit with a high lithic content and clast diversity, and widespread exposure around the Las Cañadas edifice, Tenerife. A detailed study of the lithic clast population within the deposit provides a useful tool for interpreting key aspects of the pre-Abrigo subsurface geology, evidence for caldera collapse, conduit-vent dynamics and processes of lithic clast dispersal.

### 3.1. Geology of Tenerife

Figure 2a is a highly simplified geological map of Tenerife (Ablay and Martí, 2000). The earliest shield-building stage of subaerial volcanism ("Old Basaltic Series"; >12–3.3 Ma) is preserved as three massifs (Anaga, Teno and Roque del Conde; Figure 2b) consisting of alkali basalt lava flows and tuffs, and minor late-stage intermediate to phonolitic dykes, domes and pyroclastics (Fúster et al., 1968; Anchochea et al., 1990; Thirlwall et al., 2000).

The largely phonolitic central Las Cañadas edifice has been active since 3.8 Ma (Ablay and Kearey, 2000) and underwent an early constructive phase preserved in the caldera wall as basaltic, intermediate and phonolitic lavas and welded and non-welded pyroclastics (Lower Group; Martí et al., 1994). Extracaldera rocks of Lower Group age have also been identified on the southwestern, upper southern and southeastern flanks of the Las Cañadas edifice and on the Tigaiga Massif (Anchochea et al., 1990, 1999; Ibarrola et al., 1993; Fúster et al., 1994; Huertas et al., 1994, 2002).

The Las Cañadas edifice underwent a late explosive phase of volcanism (Upper Group; 1.6–0.2 Ma), characterised by at least three major basaltic to phonolitic

**Figure 2** (a) Simplified topographic and geological map of Tenerife and (inset) the location of the Canary Islands (modified from Ablay and Kearey, 2000). (b) Map of Tenerife showing the distribution of the Abrigo ignimbrite, lithic clast analysis localities, geographical features and towns referred to in the text, and the localities where mono/bilithologic (MLCZ) and heterolithologic (HLCZ) lithic pebble to boulder concentration zones are found. Abbreviations: MG, Montaña de Guaza; RC, Roque del Conde; CR, Caldera del Rey; BC, Barranco de la Cera; DH, Diego Hernández caldera wall; PT, Pico Teide; PV, Pico Viejo; Fo, La Fortaleza.

eruption cycles represented by the Ucanca, Guajara and Diego Hernández formations (Martí et al., 1994). Geophysical, structural, stratigraphical, volcano-logical and geochronological data suggest that major vertical collapse events at the end of each cycle led to the formation of the summit caldera (Araña, 1971; Ortiz et al., 1986; Vieira et al., 1986; Camacho et al., 1991; Martí et al., 1994, 1996, 1997; Bryan et al., 1998b, 2000; Ablay and Kearey, 2000; Araña et al., 2000; Martí and Gudmundsson, 2000; Pous et al., 2002; Edgar et al., 2002, 2007). However, the final shape of the caldera and the northern flanks of Tenerife have been influenced by the interplay between giant lateral flank collapse causing landslides and vertical collapse resulting from magma withdrawal (Martí et al., 1994, 1996, 1997; Anchochea et al., 1999; Cantagrel et al., 1999; Ablay and Hürlimann, 2000; Martí and Gudmundsson, 2000).

Within the caldera wall, the Upper Group consists mainly of basaltic to phonolitic lavas, and welded and non-welded phonolitic pyroclastic deposits (Fúster et al., 1994; Martí et al., 1994). Correlative pyroclastic deposits on the mid to lower slopes are generally non-welded, with one or two exceptions (e.g. Arico Ignimbrite, von Fritsch and Reiss, 1868; Alonso et al., 1988; Bryan et al., 1998b).

Basaltic volcanism has been contemporaneous with the formation of the Las Cañadas edifice leading to the construction of the Dorsal (Féraud et al., 1985; Anchochea et al., 1990) and Santiago ridges and basaltic lavas intercalated with Upper Group pyroclastic deposits on the southern coastal plain (Fúster et al., 1968; Bryan et al., 1998b). In addition, a tephritic to phonolitic flow/dome complex (Montaña de Guaza, Fernández Santín and Nafría López, 1978) and maar (Caldera del Rey, Paradas Herrero and Fernández Santín, 1984), both of Upper Group age are preserved in the southwest corner of Tenerife.

The Abrigo ignimbrite (Pittari et al., 2006; emplaced between 202 and 170 ka, see Brown et al., 2003; Edgar et al., 2007) is the uppermost unit of the Diego Hernández formation and post-dates all of the above stratigraphic units. Volcanism post-dating the Abrigo eruption has resulted in the intracaldera Teide–Pico Viejo stratovolcano and extracaldera basaltic scoria cones and lava fields.

## 3.2. The Abrigo ignimbrite

The non-welded, phonolitic, lithic-rich (up to 50% of the whole rock) Abrigo ignimbrite (Pittari et al., 2006) occurs as scattered outcrop and sheets on the lower slopes and coastal plains around the Las Cañadas edifice (Figure 2b). It correlates with a proximal lithic breccia on the Diego Hernández and La Fortaleza sectors of the caldera wall, based on stratigraphic position, lithic content and geochemistry (Martí et al., 1994). The deposit thickens and thins across palaeotopography, but has a maximum cumulative thickness of 25 m within the Barranco de la Cera (Figure 2b). The minimum inferred tephra volume of the extracaldera Ignimbrite deposit is 1.8 km$^3$, of which 0.74 km$^3$ consists of lithic clasts (Pittari et al., 2006). This does not take into account an expected much greater volume for Abrigo ignimbrite deposits offshore, buried within the caldera, removed by erosion and elutriated from the pyroclastic flow into the ash clouds. The actual

volume could be at least an order of magnitude greater than the calculated $1.8\,km^3$ proposed on land.

Two widespread depositional units of massive lithic-rich ignimbrite (Abrigo Sur-A and C, Pittari et al., 2006) occur across the southern to eastern flanks of the Las Cañadas edifice commonly separated by a discontinuous accretionary lapilli-bearing fine ash layer (Sur-B) (Figure 3). The Sur-A unit commonly contains cobble-sized lithic concentration zones, which are either (a) mono/bilithologic and locally derived, occurring in the lower part of the unit, or (b) heterolithologic and largely vent-derived, near the top of the unit. The Sur-C unit generally has a lower relatively fine-grained, massive to stratified zone and an upper, coarser-grained, massive, lithic-rich zone. Lateral facies variations in both the Sur-A and −C units are strongly controlled by the underlying palaeotopography (e.g. thinner, stratified ignimbrite packages occur on palaeotopographic highs, Pittari et al., 2006). Along the northern and western flanks of the Las Cañadas edifice, the Abrigo ignimbrite consists of multiple depositional units of massive, lithic-rich ignimbrite.
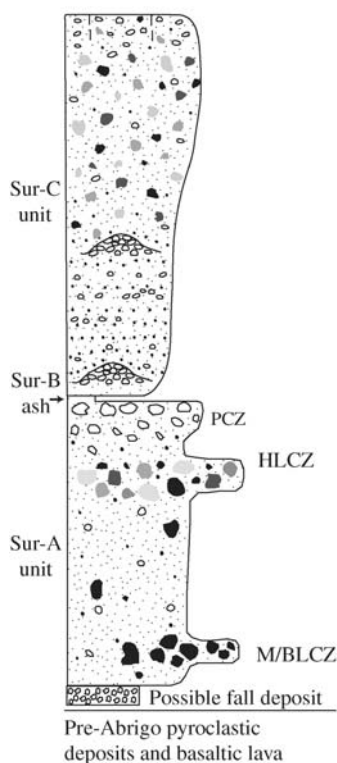


**Figure 3** Composite stratigraphic log of the Abrigo ignimbrite on the SW to NE flanks of the Las Cañadas edifice. Abbreviations: HLCZ and M/BLCZ, heterolithologic and mono-/bilithologic lithic pebble to boulder concentration zones, respectively; PCZ, pumice concentration zone.

## 3.3. Lithic clast types and their provenance

Eight major groups of lithic clasts in the Abrigo ignimbrite have been recognised (Tables 1–4): nepheline syenite (S); syeno-gabbroids and gabbroids (G); mafic and intermediate crystalline volcanics (MV); felsic crystalline volcanics (FV); glassy volcanics (GV); welded or lava-like volcanic breccias (W); pyroclastic and epiclastic breccias (C) and altered clasts (A). The major subgroups (e.g. MV1) were identified in the field, and then described in more detail through petrographic analysis of hand samples and thin sections. Quantitative analysis of the lithic distributions both vertically and laterally in the Abrigo ignimbrite was undertaken using this lithic classification scheme.

Coarse-grained coherent lithologies were defined as having an average grainsize of greater than 3 mm, medium-grained, between 1 and 3 mm, and fine-grained, less than 1 mm. Fine-grained coherent lithologies have been subdivided further according to McArthur et al. (1998): coarsely crystalline (500 µm–1 mm); medium crystalline (250–500 µm); finely crystalline (125–250 µm); very finely crystalline (63–125 µm); microcrystalline (4–63 µm) and cryptocrystalline (<4 µm).

### 3.3.1. Nepheline syenite (S), syeno-gabbroids and gabbroids (G)

Nepheline syenite clasts of the Abrigo ignimbrite have been described by Wolff (1987), Wolff et al. (2000) and Nichols (2001) and consist of a coarse-grained intergranular framework of alkali feldspar ($\sim$60%) and feldspathoids (nepheline and sodalite; 25–30%, Figure 4a, b); lesser interstitial aegirine-augite, arfvedsonite and ilmenite; minor biotite, titanite and magnetite; late-stage stellate aegirine clusters; and exotic accessory minerals. Wolff (1987) and Wolff et al. (2000) identified both fresh syenite (<10% of syenite clasts; S1, Table 1) and accessory hydrothermally altered syenite (>90% of syenite clasts; S4, Table 1). Fresh clasts have strong chemical affinities with Abrigo pumice and, being holocrystalline, form one end of a textural continuum in glass content that includes glass-bearing syenites (>90% crystals), quenched "crystal mush" (50–90% crystals) and porphyritic pumice (<50% crystals); hence, they are considered to be essentially juvenile in origin (Wolff, 1987; Wolff and Toney, 1993; Wolff et al., 2000; Nichols, 2001). The primary crystalline texture within some clasts is partly corroded and replaced by a micro- to medium-crystalline granular mosaic of subhedral to anhedral feldspar (Figure 4c; S3, Table 1). Fresh microsyenite has also been observed (S2, Table 1).

Coarsely crystalline mafic clasts (i.e. gabbro, syeno-gabbroid/gabbroid, pyroxenite, Figure 4d; G1–G6, Table 1) are a rare component of the lithic assemblage and have only been found on the northeastern and southeastern flanks of the Las Cañadas edifice. The mineral assemblages and textures are variable and most have compositions intermediate between syenite and alkali gabbro.

Nepheline syenite, syeno-gabbroid and gabbroid clasts are derived from plutonic and hypabyssal rocks, which are not exposed at the surface on Tenerife. Fresh cognate syenite clasts (S1) are thought to represent crystallised margins of the Abrigo magma chamber (Wolff, 1987; Nichols, 2001), extracted from depths of 4–7 km (Wolff, 1987; Ablay et al., 1995, 1998; Bryan et al., 2000). Fresh microsyenite (S2)

**Table 1** Description and classification of nepheline syenite, syenogabbroid and gabbroid clasts.

| Classification: clast type | Description |
| --- | --- |
| S1: Fresh nepheline syenite | *Coarse-grained, crystalline; Afs+Ne (± Sdl)+Agt+Aeg*+Arf±Bi±Tte[a] |
| S2: Fresh nepheline microsyenite | As for S1, but medium-grained |
| S3: Recrystallised syenite and microsyenite | *White to grey-blue, peppery appearance; micro- to medium-crystalline;* granular mosaic Fsp groundmass; minor glassy domains; minor FeOx and Fe–Mg silicate-rich domains; strongly corroded relict syenitic textures; occasional spherulitic texture |
| S4: Hydrothermally altered nepheline syenite and microsyenite | *As for S1, but cloudy-white altered appearance;* sericite, calcite, cancrinite, FeOx and Fe-rich clay alteration phases |
| G1: Fine-grained subhedral granular gabbro | *Equigranular, fine-grained; Cpx (∼ 45%)+Pl (∼ 40%)+Mag (∼ 10–15%)*±Ap (up to 5%)±glass (2–3%), subhedral crystals |
| G2: Porphyritic syeno-gabbroid | *∼ 50% coarse-grained (up to 4.5 mm) Fsp phenocrysts in a fine-grained Fsp+mafic-rich groundmass;* Fsp (Pl+An) (∼75%)+Am (∼8%)+Cpx (∼4%)+Bi (∼5%)+Foids (∼2%)+FeOx (∼5%)+Ap (∼1%); commonly partially resorbed Fsp; diffuse grain boundaries across groundmass |
| G3: Vitric hornblende melagabbro | *Coarse-grained; brown Am (50%)+Fsp (10%)+Mag (10%);* 15% interstitial yellow-brown glass; 10% pore space and vesicles |
| G4: Porphyritic microgabbro | *Medium to coarse-grained Cpx+Mag phenocrysts in an equigranular fine-grained groundmass;* Cpx > Pl > Mag; partially altered |
| G5: Pyroxenite | *Equigranular, coarse-grained, mostly pyroxene;* TiAug+minor FeOx |
| G6: Coarse-grained gabbroid | Cpx (up to 30 mm) > Pl (+ minor Bi) *(Handsample of C. Edgar)* |

*Note:* Essential visually identifiable field classification criteria are highlighted in italics; additional characteristics observed from thin sections of representative samples are listed in regular font. Mineral abbreviations: Fsp, feldspar; Afs, alkali feldspar; An, anorthoclase; Pl, plagioclase; Ol, olivine; Cpx, clinopyroxene; Aug, augite; TiAug, titanaugite; Aeg, aegirine; Agt, aegirine-augite; Am, amphibole; Arf; arfvedsonite; Krs, kaersutite; Bi, biotite; Foid, feldspathoid; Ne, nepheline; Sdl, sodalite; Hyn, haüyne; Tte, titanite; Ap, apatite; FeOx, iron oxide; Mag, magnetite; Cal, calcite. *Percentages* represent visual estimates of the whole rock or of a mineral group.
[a]Mineralogy from Wolff (1987), Wolff et al. (2000) and Nichols (2001).

was probably derived from the outer extremities of the magma chamber and within the proximal hypabyssal system. Heavily altered syenite clasts (S4), that are chemically distinct from the cognate clasts, have been attributed by Wolff et al. (2000) to one or more solidified pre-Abrigo plutons, constituting a portion of the wall rock around the Abrigo magma chamber/conduit (cf. Bryan et al., 1998b, 2000). It is

**Table 2**   Description and classification of mafic/intermediate and felsic crystalline to glassy volcanic clasts.

| Classification: clast type | Description |
| --- | --- |
| MV1: Aphyric basalt (may include intermediate rocks) | *Aphyric, grey micro-to finely crystalline groundmass; intergranular to trachytic groundmass (Pl+Cpx+FeOx$\pm$rare Ne); rare phenocrysts, Ol+Cpx+FeOx* |
| MV2: Porphyritic basalt and ankaramite | *Porphyritic (mostly Cpx, up to 8 mm and/or Ol, up to 5 mm); grey micro- to medium crystalline groundmass; TiAug>Ol>>FeOx$\pm$rare Pl phenocrysts; intergranular to trachytic groundmass (Pl+Cpx+FeOx)* |
| MV3: Porphyritic dark grey intermediate rock | *Porphyritic (mostly Pl, up to 1 mm and/or Cpx); dark grey, crypto- to medium crystalline groundmass; Pl+Cpx+Mag$\pm$Am$\pm$Ne$\pm$Sdl/Hyn phenocrysts, may also contain An and Tte; Pl may be resorbed or glomerophyric; intergranular to trachytic groundmass (Pl+Cpx/Am+FeOx); Fsp laths commonly curved, branching; some flow banding* |
| MV4: Finely porphyritic pale grey intermediate rock | *Finely porphyritic; light grey, micro- to finely crystalline groundmass; Pl+Krs+Cpx+Mag+Tte$\pm$Bi$\pm$Foids (Sdl/Hyn and/or Ne) phenocrysts; intergranular to trachytic groundmass (Fsp+Am/Cpx+Mag$\pm$Ap); some flow banding* |
| MV5: Vesicular basalt and intermediate rocks | *Mafic to intermediate compositions; vesicularity, 20 to >40% of the whole rock* |
| FV1: Highly Afs-phyric green phonolite | *Porphyritic ($\sim$ 30%, up to 8 mm, randomly oriented Afs laths); green, very finely crystalline groundmass; Afs >> (Agt+Mag+Ne$\pm$Bi$\pm$Sdl/Hyn) phenocrysts; intergranular groundmass with acicular, fibrous and spherulitic textures* |
| FV2: Mottled green phonolite | *Mottled appearance defined by fine-grained, anastomosing white felsic and green mafic domains; minor Afs$\pm$rare Cpx phenocrysts; felsic domains are Afs-rich, and form a trachytic texture which wraps around phenocrysts and less common equigranular mosaic-textured subdomains; mafic domains have abundant sodic Am and minor Aeg/agt intergrown with Afs, dendritic textures* |
| FV3: Foliated green phonolite | *Foliated ("slaty cleavage"); felsic-mafic domains as in FV2, but stronger mineral alignment; very fine to coarsely crystalline groundmass; Afs+Ne+Sdl/Hyn+Mag phenocrysts; trachytic groundmass; curved and branching Fsp microlites and spherulites; equigranular Fsp mosaic domains.* |

**Table 2** (*Continued*)

| Classification: clast type | Description |
|---|---|
| FV4: Massive green phonolite | *Massive, sugary to glassy appearance; green crypto- to medium crystalline groundmass; Minor Afs+Agt+Mag+Sdl/Hyn+Tte phenocrysts; intergranular to weakly trachytic groundmass* (Afs+sodic Cpx$\pm$sodic Am+Mag), which may contain minor curved Fsp microlites or spherulites; or very fine to very coarsely crystalline equigranular Fsp mosaic groundmass with minor Agt, Tte and FeOx |
| FV5: Aphyric to porphyritic spherulitic phonolite | *Light grey-blue and/or white micro- to medium crystalline groundmass; non- to weakly trachytic; spherical, bow-tie and fan spherulites; straight and curved Fsp microlites; minor intersertal glass or cryptocrystalline texture* |
| FV6: Porphyritic brown phonolite | *Porphyritic (mostly Fsp); caramel-brown; very fine to finely crystalline groundmass*; Afs+Pl+Bi+Mag+Tte phenocrysts, Afs>Pl; trachytic groundmass, straight, curved and branching Afs laths and interstitial brown glass |
| GV1: Dense, glassy volcanic clasts | *Aphyric to porphyritic; glassy groundmass*; felsic phenocrysts − Afs+Agt+Bi+Mag+Tte+Sdl/Hyn+Ap; mafic/intermediate phenocrysts − Pl+Afs+Cpx+Krs+Bi+FeOx (Mag)+Tte+Sdl/Hyn+Ap; amorphous to cryptocrystalline groundmass; some crystallites, spherulites; <30% microvesicles |

*Note:* Essential visually identifiable field classification criteria are highlighted in italics (NB: groundmass grainsize was constrained from thin sections of representative samples); additional characteristics observed from representative thin sections are listed in regular font. See Table 1 for definition of mineral abbreviations and percentages.

noted that some mildly altered syenite clasts are chemically similar to the fresh cognate Abrigo syenite suite, and their relationship to either the Abrigo or older plutons has not been established. The finer-grained granular feldspar mosaic groundmass observed in some corroded syenite clasts is likely to be the result of thermal metamorphism of the wall rock (Bryan et al., 2000). Gabbroids and syeno-gabbroids are interpreted to be juvenile and/or accessory mafic cumulates (Neumann et al., 2000; Nichols, 2001).

## 3.3.2. Mafic/intermediate (MV) and felsic (FV) crystalline volcanic clasts

Grey, fine-grained basaltic to intermediate crystalline volcanic clasts are common and range from dense (MV1–4, Table 2) to vesicular (MV5, Table 2), and from

**Table 3** Description and classification of clasts of welded or lava-like breccia, and clastic breccia.

| Classification: clast type | Description |
|---|---|
| W1: Green heterolithologic welded pyroclastic breccia | *Angular fine-grained green and brown clasts in a partially altered flow banded, green cryptocrystalline groundmass*; clasts include (a) altered light green, microcrystalline phonolite, (b) dark green, slightly coarser crystalline phonolite, (c) brown, microcrystalline phonolite, (d) strongly banded glassy to microcrystalline-textured lithology and (e) fiamme, with spherulites |
| W2: Heterolithologic glassy volcanic breccia | *Angular clasts of various altered and fresh feldspathic lithologies in a partially altered glassy to microcrystalline, groundmass*; lithic types include (a) altered lithology; (b) coarsely crystalline phonolite/microsyenite; (c) microcrystalline feldspathic lithology; (d) medium to coarsely crystalline, trachytic, aphyric feldspathic lithology and (e) coarsely crystalline equigranular mosaic groundmass-textured lithology; also contains broken crystals |
| W3: Porphyritic heterolithologic glassy volcanic breccia | Crystals (Pl+minor Afs+Bi+Cpx+FeOx+Sdl/Hyn) *and subordinate angular clasts of (a) altered lithology*, (b) trachytic-textured *felsic fine-grained, coherent lithology* and (c) fiamme; in a *glassy to cryptocrystalline partially altered groundmass* with microlites |
| W4: Irregular laminated volcanic rock with broken crystals | *Broken Afs crystals in a partially altered, irregular laminated crypto- to microcrystalline groundmass* |
| W5: Deformed obsidian–rich pyroclastic breccia | *Poorly sorted; angular clasts of (a) deformed, attenuated obsidian (abundant) wrapped around or squeezed between other fragments, (b) various phonolite types and (c) rare vesicular ultramafic rock; in a green, altered groundmass* |
| C1: Grey, lithic-rich breccia | *Poorly sorted, clast-supported; angular fragments of (a) massive to vesicular basalt and (b) light grey and white altered rock, in a grey mud matrix* |
| C2: Pink ignimbrite | *Subangular basalt to phonolite, and minor red altered lithic clasts ($\sim 20\%$); subrounded altered pumice ($\sim 20\%$); crystals ($\sim 5\%$); in a pink fine ash matrix* |

*Note:* Essential visually identifiable field classification criteria are highlighted in italics (NB: groundmass grainsize was constrained from thin sections of representative samples); additional characteristics observed from representative thin sections are listed in regular font. See Table 1 for definition of mineral abbreviations and percentages.

aphyric (MV1, Table 2) to porphyritic (MV2–4, Table 2). Alkali basalt and basanite (MV1, Table 2, Figure 5a), which cannot be distinguished in the field, have previously been observed on Tenerife (Fúster et al., 1968; Scott, 1969; Araña, 1971; Ridley, 1970; Borley, 1974; Ablay et al., 1998; Wolff et al., 2000; Bryan et al., 2002).

**Table 4** Description and classification of pervasively altered lithic types.

| Classification: clast type | Description |
|---|---|
| A1: Amorphous Fe-rich clay and FeOx altered rock | *Distinctive red, purple, pink and/or orange appearance* due to Fe-rich clay and FeOx, sericitisation of Fsp, cancrinitisation of Foids, and Cal precipitation; alteration textures include reddish blebs, disseminated FeOx, pseudomorphs of phenocrysts, colloform banding, banding defined by variations in the concentration of disseminated Fe-rich clay, irregular hairline vein networks, open and in-filled vughy porosity; relict primary textures variably preserved |
| A2: Carbonatised alteration breccia with relict clasts | *Breccia, often with mosaic or jigsaw fit texture of relict volcanic clasts within a pervasive anastomosing network of microcrystalline Cal*; disseminated FeOx; relict microphenocrysts |
| A3: Non-descript clay and carbonate altered rock | *Pale grey, brown, yellow, yellowish-brown, cream appearance*; massive or with relict phenocrysts; pervasive alteration to phyllosilicates and Cal; minor amorphous Fe-rich clay, disseminated or streaks of FeOx and zeolites; Cal in fractures and vughs and as groundmass clots/blebs; relict primary textures variably preserved |
| A4: Silky altered phonolite | *Massive, greyish-white and greenish-brown, silky lustre*; strong alteration to phyllosilicates and abundant FeOx often replacing phenocrysts; minor colloform banding within cavities; relict large tabular Afs and trachytic textures |

*Note:* Essential visually identifiable field classification criteria are highlighted in italics; additional characteristics observed from thin sections of representative samples are listed in regular font. See Table 1 for definition of mineral abbreviations.

Ankaramite (MV2, Table 2) is a highly porphyritic variety of alkali basalt or basanite (>30% total olivine and pyroxene phenocrysts, Borley, 1974). Grey intermediate volcanics (MV3–5, Table 2, Figure 5b) of the Las Cañadas edifice follow the plagioclase basanite–phonotephrite–tephriphonolite and trachybasalt–trachyandesite trends (Fúster et al., 1968; Scott, 1969; Ridley, 1970; Araña, 1971; Borley, 1974; Ablay et al., 1998; Wolff et al., 2000; Bryan et al., 2002). Porphyritic intermediate clasts (MV3–4, Table 2) in the Abrigo ignimbrite are distinguished from basaltic clasts in the field by their visible phenocryst assemblage and occasional lighter colour. Aphyric intermediate clasts are difficult to distinguish from mafic clasts in the field and are included with MV1.

Felsic volcanic clasts (Figure 5c–h) are generally phonolitic in composition and are commonly identified in the field by their distinct green groundmass (FV1–5, Table 2), although some are also brown (FV6) ones. The groundmass consists
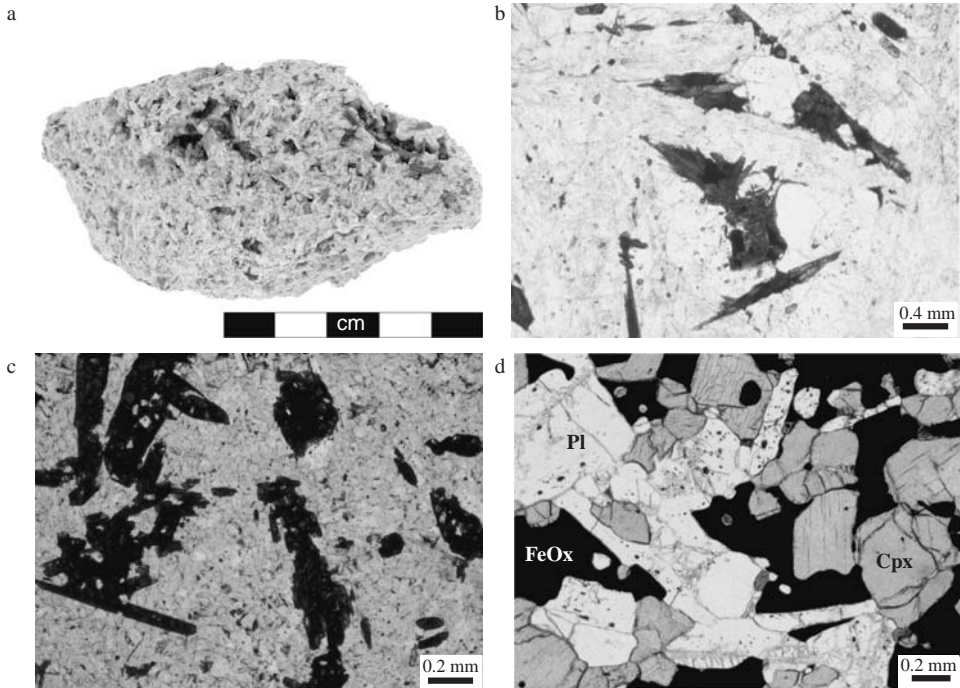
**Figure 4** (a) Photograph of fresh syenite, and photomicrographs of (b) syenitic alkali feldspar framework with interstitial aegirine and aegirine—augite (ppl), (c) corroded syenitic framework minerals in a sub- to anhedral feldspathic mosaic groundmass (ppl) and (d) fine-grained, subhedral granular gabbro (ppl). Mineral abbreviations: Pl, plagioclase; Cpx, clinopyroxene; FeOx, iron oxide.

predominantly of alkali feldspar and subordinate clinopyroxenes, amphiboles and iron oxides. Felsic clasts vary from aphyric to porphyritic (Figure 5c), and occur in a variety of textural types (Table 2). Massive clasts (FV4, Table 2) have groundmass textures varying from intergranular to weakly trachytic with straight, curved or branching feldspar laths, to an equigranular felsic mosaic (Figure 5e). Spherulitic textures may also be present (Figure 5f). Mottled (FV2, Table 2, Figure 5d) or foliated (FV3, Table 2) felsic volcanic clasts commonly contain felsic and dendritic mafic domains (Figure 5g) and a strongly trachytic groundmass of fibrous, curved and branching feldspar microlites (Figure 5h).

Mafic, intermediate and felsic crystalline volcanic rocks appear to be derived mainly from lava flow units, although some could also be derived from shallow dykes and sills. Clasts that are altered, or occur as lithic inclusions in pumice clasts, are likely to be accessory in origin (see Section 2.3) and include some foliated, massive and spherulitic felsic lithologies and minor aphyric and plagioclase-phyric intermediate/mafic volcanic clasts.

Basaltic source rocks are ubiquitous throughout Tenerife, and it is difficult to constrain whether fresh basaltic lithic clasts are accidental or accessory. However, pebble- and cobble-sized basalt lithic concentration zones on the Bandas del Sur, or
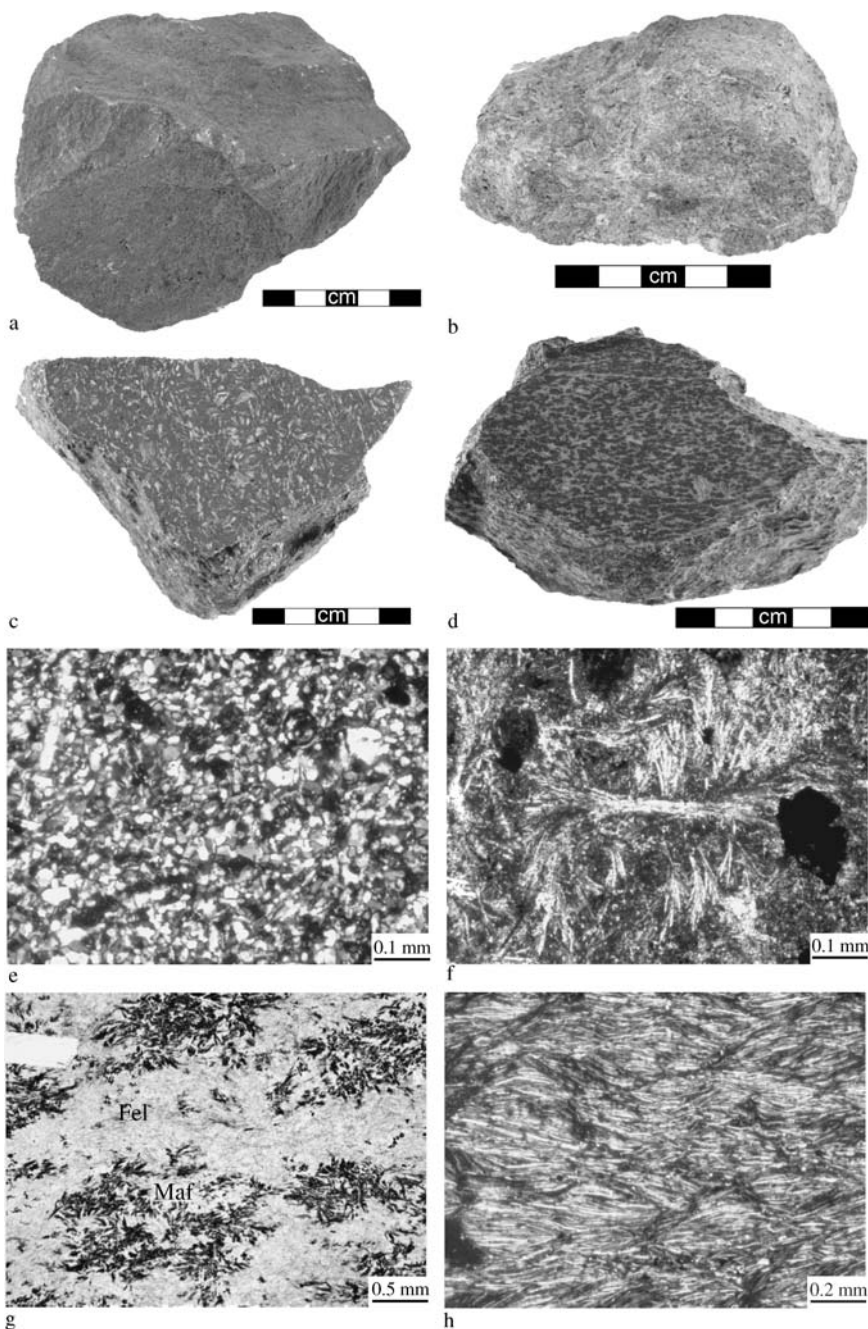
**Figure 5**   Photographs of: (a) aphyric basalt, (b) pale grey intermediate clast, (c) porphyritic phonolite, and (d) mottled phonolite; and photomicrographs of textural variations in felsic volcanic lithic clasts: (e) equigranular mosaic groundmass (crossed polars), (f) bow-tie and fan spherulites (crossed polars), (g) mafic (clinopyroxene/amphibole–rich, Maf) and felsic (clinopyroxene/amphibole–rich-poor, Fel) domains (ppl) and (h) groundmass of curved and branching feldspar microlites (crossed polars).

isolated, anomalously large basalt clasts within massive ignimbrite, are most logically accidental and derived from nearby basalt lavas.

Intermediate and felsic volcanic rocks are largely confined to the central Las Cañadas edifice (Lower Group and Ucanca formation, Upper Group, Martí et al., 1994) and most are exposed within the caldera wall and upper edifice slopes, hence, constraining an accessory or near-to-vent accidental origin for most intermediate-felsic volcanic clasts. Limited outcrop of the Lower Group on the mid-southern flanks and along the north coast, as well as younger small felsic centres (Caldera del Rey and Montaña de Guaza) near the southwest coast (see Fúster et al., 1968), could have contributed a minor fraction of the intermediate-felsic volcanic lithic population locally.

### 3.3.3. Dense, glassy volcanic clasts (GV)

Dense, glassy volcanic clasts (GV1, Table 2) are aphyric to porphyritic, dense and poorly vesicular (<30% microvesicles) and have an amorphous or cryptocrystalline groundmass, sometimes with acicular microlites. Felsic/phonolitic (green) to mafic (black) and banded compositional types occur. Most dense, glassy volcanic clasts are interpreted to be juvenile clasts as they geochemically duplicate Abrigo pumice (Nichols, 2001) are unaltered, and dense glassy bands are often co-mingled within juvenile pumice clasts. However, care must be taken in interpreting all of these lithic clasts as juvenile because older obsidian lavas have also been observed within the caldera wall (e.g. Zafrilla, 2001).

### 3.3.4. Welded or lava-like volcanic breccias (W) and clastic breccias (C)

Clasts of welded or lava-like volcanic breccias (Table 3) consist of angular fragmental components within a groundmass that displays cooling features suggestive of a fluidal or plastic rheology, such as a glassy to devitrified crypto- to microcrystalline texture or flow banding. Some clasts contain fiamme (e.g. W1, W3, Table 3), deformed obsidian fragments (W5, Table 3), broken crystals (W4) and/or a heterolithologic suite of lithic fragments (W1–3, W5, Table 3), all of which indicate a pyroclastic origin.

Non-welded, matrix- or clast-supported lithic-rich clastic breccias, either epiclastic or pyroclastic in origin, also occur. Two distinctive clastic breccia clast types have been identified in the Abrigo ignimbrite (Table 3): grey, lithic-rich breccia (C1) and pink ignimbrite (C2), although this list is probably not exhaustive.

Welded and rheomorphic pyroclastic deposits are common around the caldera wall and on the upper slopes of the Las Cañadas edifice (Martí et al., 1994; Zafrilla, 2001; Soriano et al., 2002, 2006). There is also limited exposure of welded ignimbrites, which are lithologically distinct from proximal welded deposits, on the western and southern coastal plains (i.e. Adeje Ignimbrite, Fúster et al., 1994; Arico Ignimbrite, Alonso et al., 1988), although clasts derived from these deposits have not been identified within the Abrigo ignimbrite. Hence, most welded lithic clasts are either accessory or near vent-derived accidental clasts.

Pyroclastic and/or epiclastic deposits occur intermittently around the Las Cañadas edifice and within the caldera wall, and the provenance of individual lithic clast types is uncertain. The abundance and variety of angular lithic fragments, poor sorting and interclast mud/ash matrix suggests that these clasts were derived from widely exposed ignimbrite deposits on Tenerife.

### 3.3.5. Pervasively altered lithic clasts (A)

The Abrigo ignimbrite is characterised by an abundance of pervasive hydrothermally altered clay-rich, red, orange, yellow, brown, white and/or grey lithic clasts (A1–A4, Table 4; Figure 6a). Relict primary textures of mafic to phonolitic lavas include phenocrysts, the remnant intergranular or trachytic feldspar groundmass texture, and unaltered textural domains or pseudoclasts. Coarse-grained samples are likely to be syenitic. Alteration includes conversion of ferromagnesian minerals to clay and disseminated iron oxides, sericitisation of feldspars, cancrinitisation of feldspathoids, calcite precipitation and zeolitisation. Iron-rich clay minerals and phyllosilicates often occur as amorphous masses, irregular blebs or in-filling cavities. Calcite occurs as clots, irregular anastomosing veins or in-filling fractures. Some cavities show clear fibrous, botryoidal and colloform textures with alternating layers of secondary minerals (Figure 6b).

Exposure of hydrothermally altered volcanic rocks around the Las Cañadas edifice is limited to a few isolated patches associated with fractures within the southern and western parts of the caldera (Araña, 1971). The abundance of altered lithic clasts within the Abrigo ignimbrite cannot be accounted for by the sparse surface exposure of hydrothermally altered rock. It is possible that surface alteration was more extensive prior to the destructive Abrigo eruption; however, there is little evidence for this as much of the older caldera wall lithologies are still quite fresh. Hence, a large fraction of the altered clast population was likely to have been derived from hydrothermally altered rocks occurring at depth.



a                                                                b
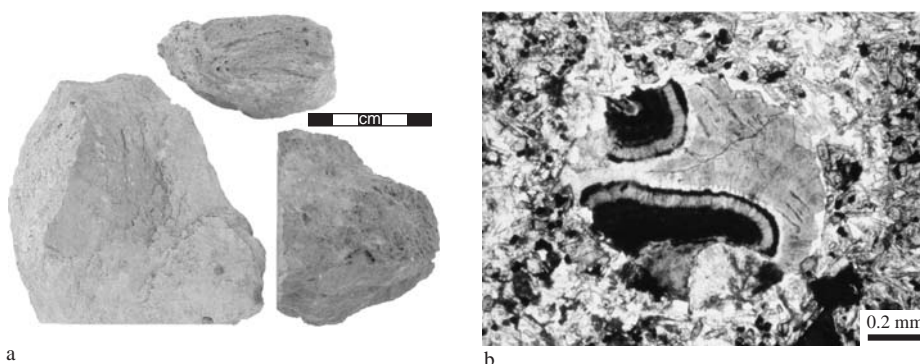
**Figure 6**    (a) Photograph of pervasively altered lithic clasts and (b) photomicrograph of an altered clast showing botryoidal and colloform banded alteration textures (ppl).

## 3.4. Quantitative analysis of lithic clast populations

### 3.4.1. Method

Fifteen field lithic clast analyses within the Abrigo ignimbrite were conducted at 11 locations around Tenerife in order to gain an understanding of the proportions of the different lithic clast types and their spatial variation. Sites of individual analyses were chosen so as to obtain the vertical, down-slope and lateral variations of lithic clast populations within the ignimbrite. For each analysis, the number of each lithic clast type larger than a threshold grainsize (0.5 cm apparent maximum diameter on outcrop surface, for 14 analyses) was counted within a box drawn over the ignimbrite surface. The area of the box varied (0.2–0.36 m$^2$, for 14 analyses) so that a minimum of 400 (up to 700) lithic clasts were counted in each case. In the case of a cobble-sized lithic concentration zone in the upper Sur-A unit (Locality 4), a minimum clast size of 1 cm and a box-size of 1 m$^2$ was used. It was assumed that lithic clasts were thoroughly mixed within the pyroclastic flow prior to deposition so that the square represents the bulk lithic clast distribution of the ignimbrite deposit at the specified locality and stratigraphic level.

Different lithic clast types are sometimes difficult to distinguish from each other in the field, especially for small clast sizes or clasts that are masked by surface weathering. Clast types that are categorised by dispersed phenocryst assemblages may be mistaken for aphyric varieties where the clast size is small if there are no distinguishing groundmass features (e.g. small clasts of MV3 or MV2 may be mistaken for MV1, see Table 2). Gradational boundaries exist between the different compositional types (i.e. mafic, intermediate and felsic class) and between fresh and pervasively altered types, and textural and appearance (e.g. colour) descriptors may overlap. In addition to the large sample sizes and assignment of a minimum threshold grainsize (see above), the error in clast identification was reduced through the use of simple, visually identifiable descriptors to classify clast types, which are highlighted in Tables 1–4. Given these constraints, it is estimated that the error in assigning a clast to one of the eight major groups is insignificant. The error in assigning different subgroups is dependant on how distinct a particular subgroup's distinguishing features are, but, for each subgroup, an estimated 90% or more clasts were identified correctly.

### 3.4.2. Results

Figures 7–12 show bar charts representing the proportions of different lithic clast groups, and the position of each lithic clast analysis within each stratigraphic log. The geographic locations for each analysis are shown in Figure 2. The main results of the quantitative analysis are summarised below, and definitions for abbreviated lithic clast types are shown in Figure 7 and Tables 1–4. Quoted percentages are relative abundances within the total lithic clast population.

The range in relative abundances of each of the major lithic groups is: 26–59% mafic crystalline volcanic clasts (MV1, MV3 and lesser MV4 are most common, MV2 and MV5 are minor, see Table 2); 14–40% altered lithic clasts (A1 and A3 are more abundant than A2, A4 is rare, see Table 4); 3–35% felsic crystalline
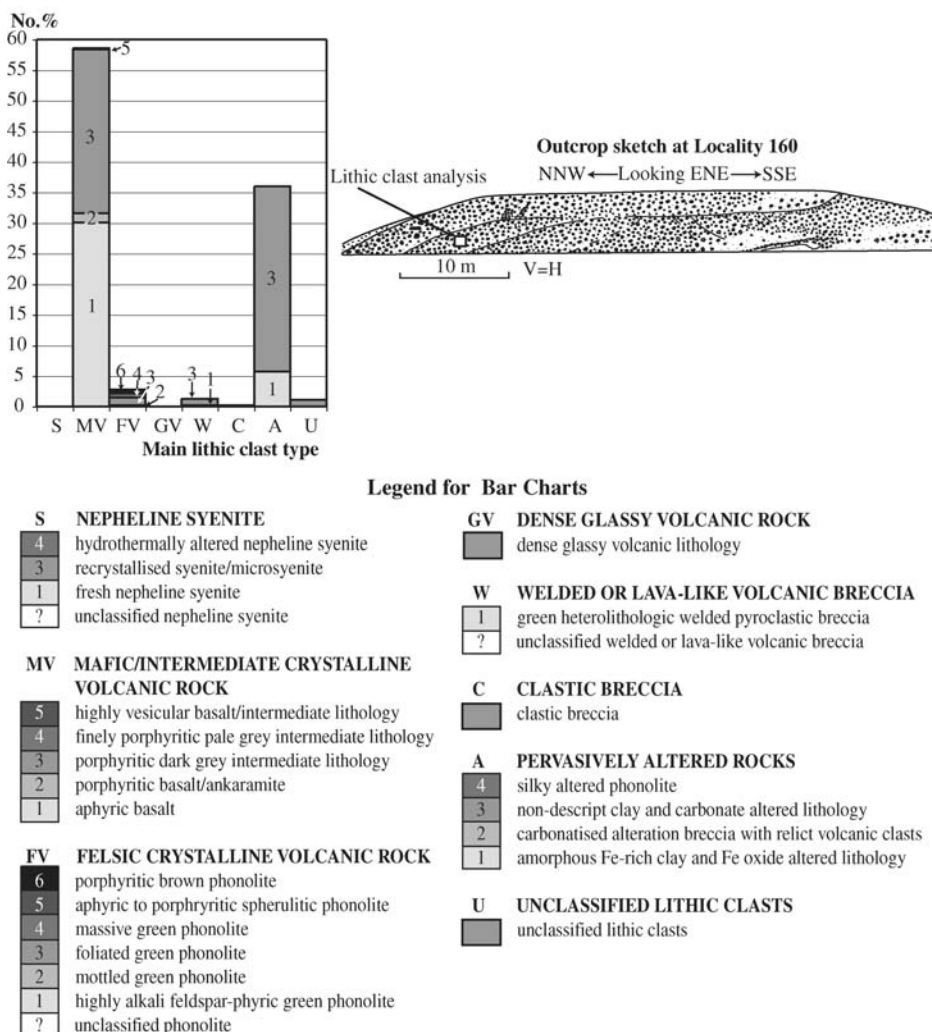
**Figure 7** Field lithic clast analysis and sample location on outcrop at Locality 160, near San Juan (includes legend of lithic clast abbreviations and numbers which is also used for Figures 7–12). Abbreviation: Lit. Cl., Lithic clast.

volcanic clasts (generally FV4 > FV3 ≈ FV6 > FV2 > FV1 with some local exceptions, FV5, where present, is relatively common, see Table 2); < 1–20% syenite (S4 > > S1 > > S3, S2 is rare and not observed in sample counts, see Table 1); and rare, dense, glassy volcanics, welded volcanics and non–welded clastic clasts. Syeno-gabbroids and gabbroid clasts were not observed in the selected sample boxes.

Major vertical lithic component variations were observed at both Poris de Abona (Figure 10) and El Medano (Figure 8) across the Bandas del Sur. In general, there is a greater variety of lithic types and a greater abundance of altered lithic
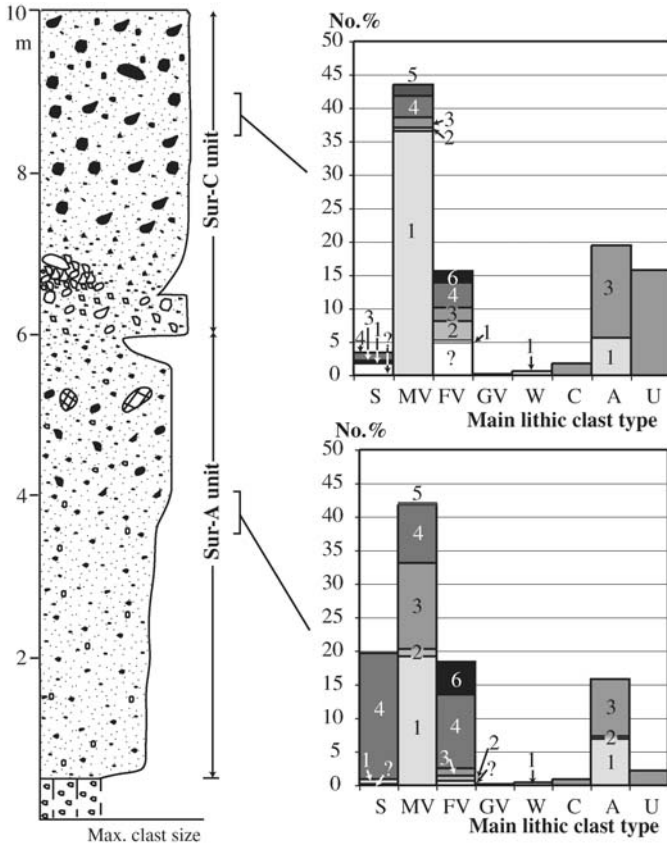
**Figure 8**    Field lithic clast analyses and sample locations on stratigraphic log at Locality 26, La Mareta (see Figure 7 for legend of lithic clast abbreviations and numbers).

clasts in the Sur-C unit compared to the Sur-A unit across the Bandas del Sur. Near Poris de Abona, from the base to the upper lithic concentration zone of the Sur-A unit, there is an increase in mafic crystalline volcanic clasts (34–47%) along with felsic crystalline volcanic, welded volcanic and clastic clasts, and a decrease in syenite (13–7%) and altered lithic clasts (27–17%). Into and toward the top of the Sur-C unit, the proportion of syenite clasts increases slightly and then remain constant, mafic crystalline volcanic clasts first decrease to 26%, then increase upwards to 32%, felsic crystalline volcanic clasts remain constant (28%), and altered lithic clasts first increase to 33% and then decrease to 29%. The vertical trend at El Medano differs from that at Poris de Abona in that syenite decreases and mafic crystalline volcanic clasts become increasingly dominated by type MV1 (see Table 2, Figure 8) from the Sur-A unit to the Sur-C unit.

The most significant variation over distances of 1.5–2 km downslope is an increase in felsic crystalline volcanic clasts (20-35%, San Miguel de Tajao, Figure 9) or mafic crystalline and welded volcanic clasts (Orotava Valley, Figure 11),
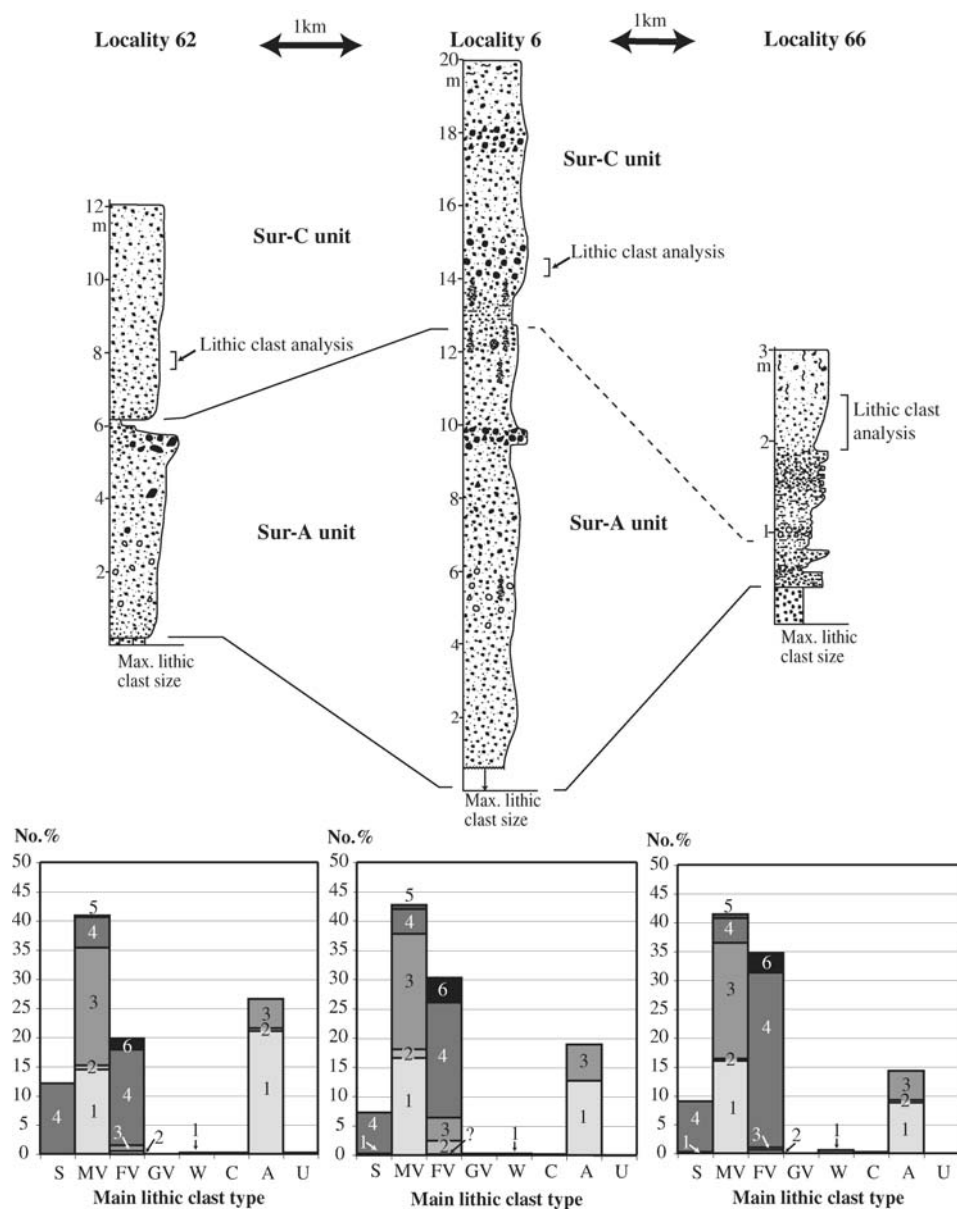
**Figure 9**    Field lithic clast analyses and sample location on stratigraphic logs along a down–slope transect near San Miguel de Tajao, proximal (Locality 62), medial (Locality 6) and distal (Locality 66) from the break in slope (see Figure 7 for legend of lithic clast abbreviations and numbers).

accompanied by a decrease in altered lithic clasts (27–14%, San Miguel de Tajao; 36–24%, Orotava Valley). In addition, the relative proportions of lithic clasts observed in the caldera wall (Figure 12) resemble those in the Orotava Valley (Figure 11) (cf. Bandas del Sur sites).
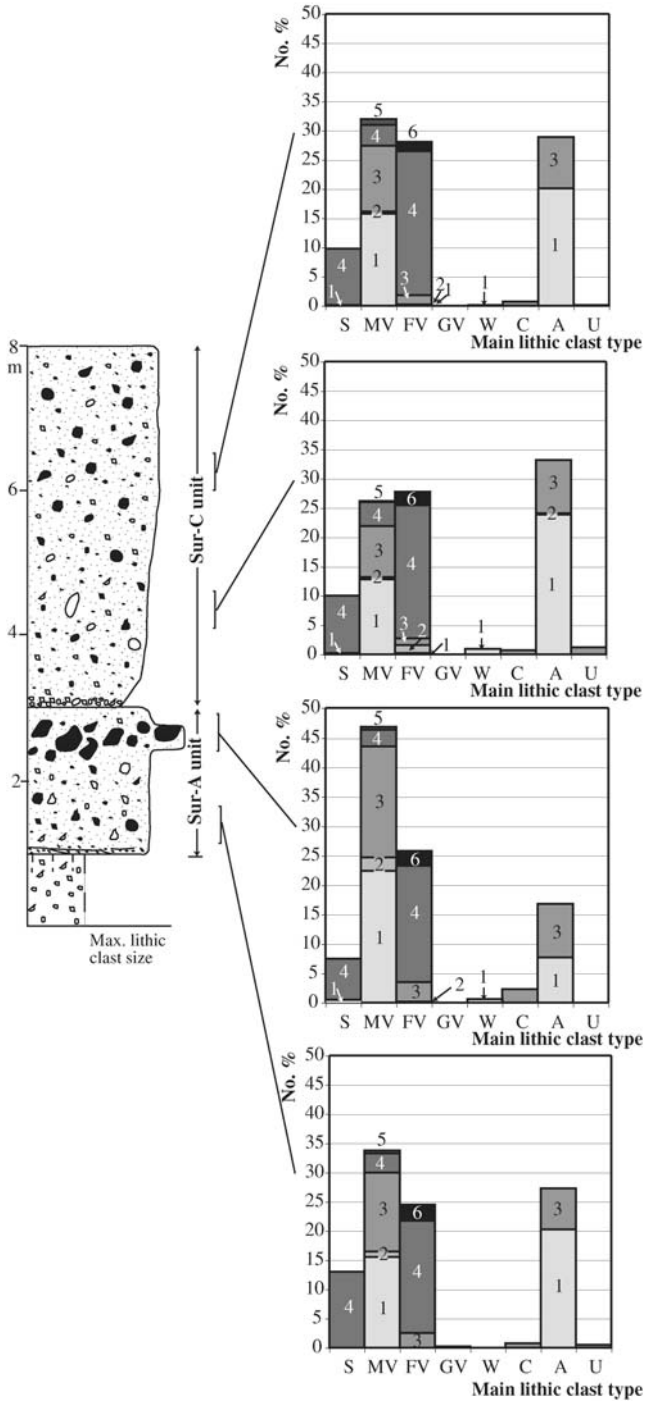
**Figure 10** Field lithic clast analyses and sample locations on stratigraphic log at Locality 4, Poris de Abona (see Figure 7 for legend of lithic clast abbreviations and numbers).
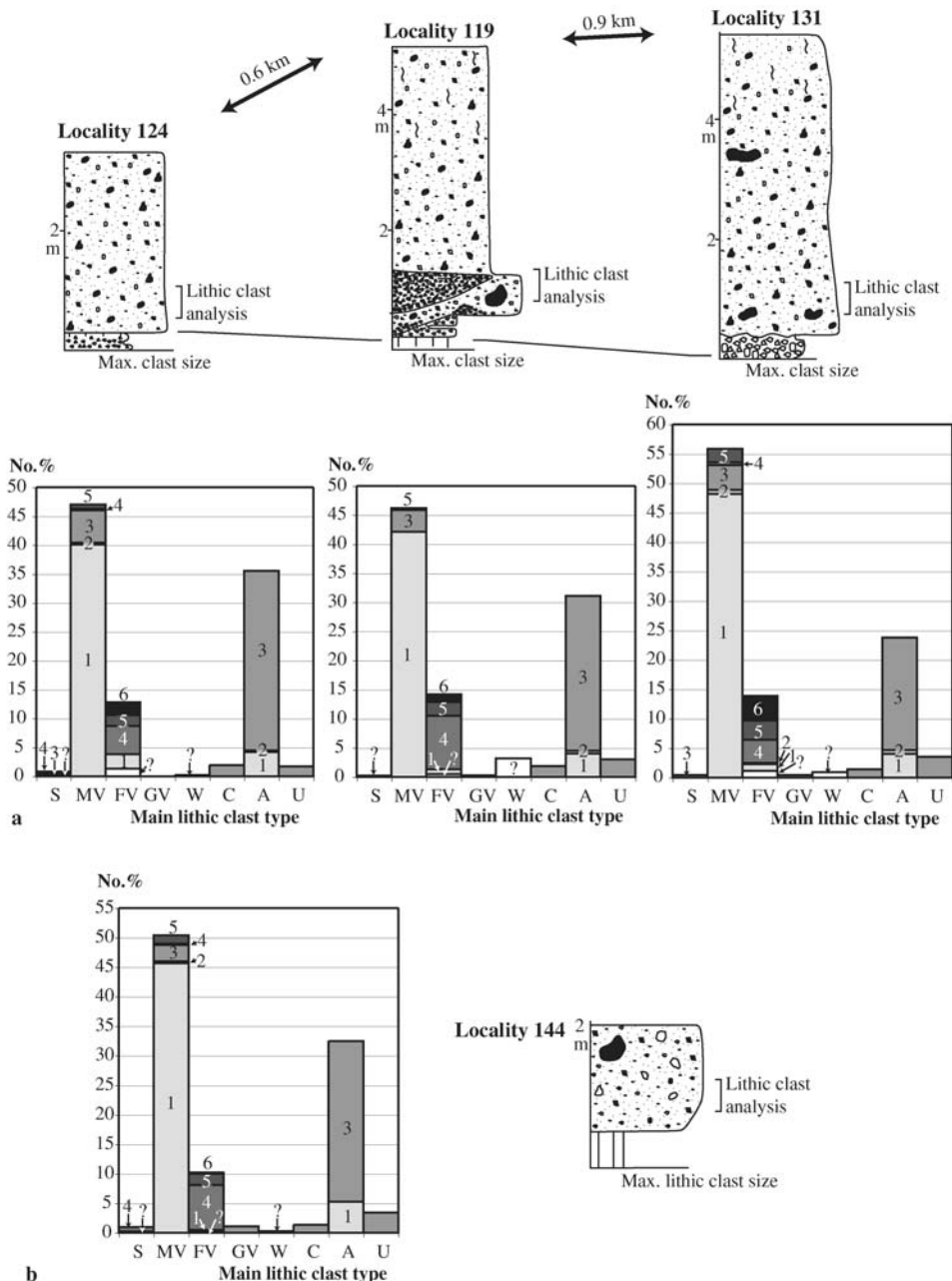
**Figure 11**  Field lithic clast analyses and sample location on stratigraphic logs on the north coast: (a) along a traverse down slope of the Orotava Valley from Locality 124 to Locality 119 to Locality 131; and (b) at Locality 144, Isla Baja (see Figure 7 for legend of lithic clast abbreviations and numbers).
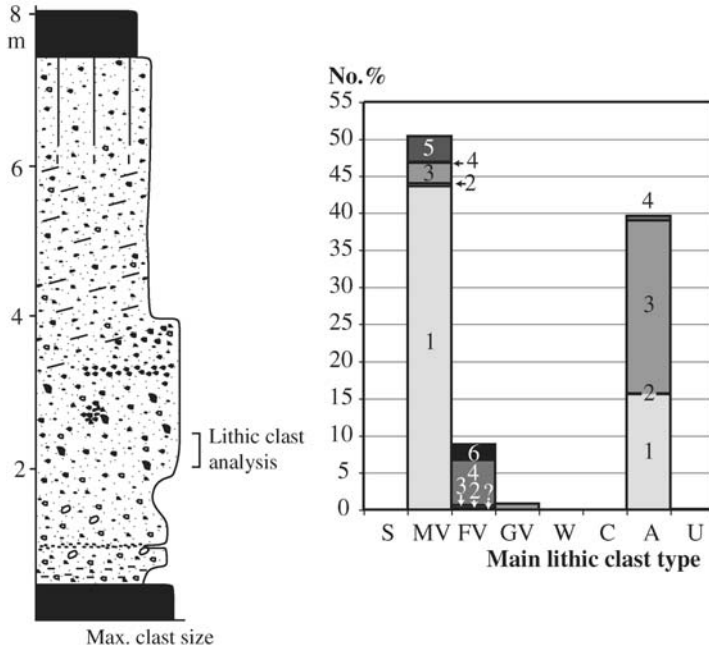
**Figure 12**    Field lithic clast analysis and sample location on stratigraphic log at Locality 219, Diego Hernández caldera wall (see Figure 7 for legend of lithic clast abbreviations and numbers).

Radially around the lower slopes of the Las Cañadas edifice:

(a) there is a greater abundance of syenite on the Bandas del Sur (4–20%) than on the north coast (≤1%) (Figure 12);

(b) mafic crystalline volcanic clasts (i) are more abundant on the north coast (47–56%) than on the Bandas del Sur (26–47%) and are also relatively common at San Juan (59%); (ii) the relative proportions of each subgroup (i.e. MV1 > MV3 > MV4 > MV2+MV5, see Table 2) are consistent across the Bandas del Sur and San Juan with minor deviations; and (iii) a similar consistency occurs across the north coast, but differs from the south in that MV1 and, to a lesser extent, MV5, are relatively more abundant, and MV4 is insignificant;

(c) felsic crystalline volcanic clasts are (i) less abundant on the western Bandas del Sur (16–19%) than on the eastern side (20–35%), whereas the relative abundance is consistent (10–14%) across the north coast; (ii) FV2 and FV3 (see Table 2) are rare on the north coast but relatively common everywhere else; and (iii) FV5 is only common on the north coast; and

(d) A3 is more common than A1 (see Table 4) on the north coast and near San Juan, but typically less than A1 on the Bandas del Sur.

There are several additional field observations of lithic clast distributions, which are not shown in the quantitative analyses. First, the upper Sur-A lithic

concentration zone contains a larger variety of lithic types than shown in the quantitative analysis including GV and FV1. Second, the quantitative analysis at San Juan does not represent the lithic clast population of the entire west coast; in particular, a larger variety of lithologies have been observed around Puerto de Santiago to the north (S4, relatively common; S3, MV1, MV2 MV5, FV3, FV4, FV6, C, A1 and 3 also observed; see Tables 1–4); dense, glassy volcanic clasts around San Juan and Adeje; and welded pyroclastic breccia clasts around Adeje. Third, syenite is common on the Diego Hernàndez and La Fortaleza caldera wall sections (S1, S2, G1 and G2 are common at La Fortaleza). Finally, gabbroid/syeno–gabbroid clasts have only been observed on the eastern side of the Las Cañadas edifice in the Orotava Valley, on the Tigaiga Massif and near San Miguel de Tajao.

## 3.5. Supporting evidence from juvenile clast and syenite geochemical compositions

Spatial variations in juvenile clast geochemistry within temporally equivalent zones across the Abrigo ignimbrite should reflect tapping and eruption of different parts of the magma chamber. Such variations should complement regional variations in lithic clast componentry. Field studies (Pittari, 2004) indicate that the proportion of banded and/or mafic juvenile clasts increases from west to east across the Bandas del Sur, although anomalously high proportions also occur near Puerto de Santiago on the west coast. Fresh gabbro clasts have only been found in the eastern part of the island.

Bulk rock geochemical analyses of major and trace elements within juvenile pumice and dense glassy clasts, further constrain regional compositional variations within the Abrigo deposit around the island. A detailed examination of the geochemical data is beyond the scope of this paper; however, the data can be found in Nichols (2001) and Pittari (2004). Juvenile clasts of the Abrigo ignimbrite follow the basanite/tephrite–phonotephrite–tephriphonolite–phonolite trend, although the majority are phonolitic in composition (Nichols, 2001). Individual localities of the Abrigo deposit are characterised by one of the four geochemically distinct juvenile clast populations identified in this study (South groups A and B, North group, San Juan group, Figure 13a), and further constrained, especially the San Juan group, by differences in the ranges of Mn, Zn and Nb/Zr associated with the phonolitic portion of clasts (Figure 13b).

(a) South group A, which spans the southern coastline from Playas de las Américas to the Güimar Valley, has the broadest range in juvenile clast compositions, and is distinct from the North group, spanning the northern coastline and Puerto de Santiago on the west coast, which has a limited variation (Figure 13a, b).

(b) South group B, which is localised between San Miguel de Tajao and the Barranco de la Cera in Abrigo deposits that are within close proximity to deposits of the more widespread South group A population, is dominated by more evolved compositions (Figure 13a).
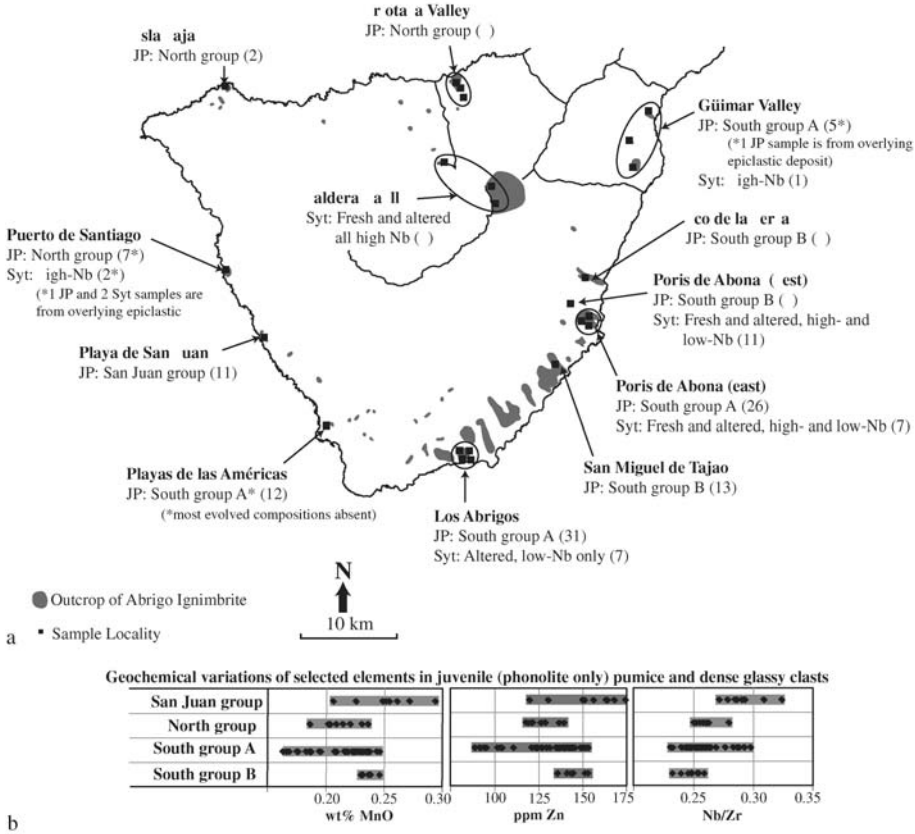
**Figure 13** (a) Major geochemical groups of juvenile pumice and dense glassy clasts ( JP; North group, South groups A and B, San Juan group; see text for definition of groups) and variations in cognate and accessory syenite clasts (Syt) within the Abrigo ignimbrite around the Las Cañadas edifice. Geochemical sample localities or groups of localities (ellipses) are indicated and the number of analysed samples are shown in parentheses. (b) Geochemical variations in Mn, Zn and Nb/Zr within *only* the phonolitic population of juvenile clasts between the San Juan, North, South A and South B geochemical groups as depicted in (a).

(c)  Localised San Juan group, at Playa de San Juan on the west coast, is unique with the phonolitic juvenile clasts having distinctly high Nb/Zr, Zn and Mn (Figure 13b).

Geochemical variations in cognate and accessory syenite lithic clasts also occur within the Abrigo ignimbrite (Figure 13a). Cognate Abrigo syenite is generally fresh and classified as high–Nb/Zr type, although some partly altered varieties could also be cognate. Older accessory syenites are generally altered and may be of low- and high–Nb/Zr type (Wolff et al., 2000). High–Nb/Zr syenites dominate the fresh and altered Abrigo syenite population, with the following exceptions (Figure 13a): (a) both high- and low–Nb/Zr syenites occur locally near Poris de Abona; and (b) only altered low–Nb/Zr syenites have been recognised geochemically around Los Abrigos.

## 3.6. Geological configuration of the Las Cañadas edifice prior to the Abrigo eruption

The large variety of lithic types and the high lithic clast volume indicate that the Abrigo ignimbrite sampled a large number of lithological units both in the subsurface of the Las Cañadas caldera and from the ground surface on the flanks of the edifice. A large fraction of the lithic population within the Abrigo ignimbrite is likely to be accessory, although the exact proportions of accidental to accessory clasts are unknown. Deep-level accessory lithic clasts (i.e. plutonic and most of the hydrothermally altered clasts) constitute approximately 35% of the lithic population. The variety of fresh volcanic accessory lithic clasts embedded in juvenile pumice clasts also suggest that a substantial proportion of the volcanic lithic population was derived from shallow subsurface unaltered zones.

### 3.6.1. Plutonic/metamorphic core and the Abrigo magma chamber

Shallow syenitic plutons were emplaced at depths of 4–7 km below the Las Cañadas summit, multiple times over the depositional history of the Upper Group (1.6 Ma) (Wolff, 1987; Wolff et al., 2000; Ablay et al., 1995, 1998; Bryan et al., 2000) and a solidified plutonic complex is likely to form much of the core of Tenerife. The Diego Hernández formation consists of four distinct chemostratigraphic sequences, characterised by Nb/Zr ratios from phonolitic juvenile clasts, and are named from oldest to youngest: DHFbs (high Nb/Zr), DHF I (low Nb/Zr), DHF II (very low Nb/Zr) and DHF III (high Nb/Zr, also represented by cognate syenites in the Abrigo ignimbrite; Wolff, 1987; Nichols, 2001; Wolff et al., 2000; Edgar et al., 2007). Each sequence represents a unique cycle of volcanic eruptions with a common magma chemistry (e.g. DHF III includes the Abrigo ignimbrite and pre-Abrigo plinian eruptions). At least three earlier geochemically distinct pre-DHF plutons have been identified: (a) one of low Nb/Zr type, represented by accessory syenites found in the Caleta and Fasnia Members (Diego Hernández formation, Edgar et al., 2007; cf. Wolff et al., 2000); (b) another that conforms to a high Nb/Zr trend, represented by syenite clasts in units of the Guajara and Ucanca formations; and (c) an additional augite syenite to alkali gabbro pluton beneath the southern coastal plain.

Most hydrothermally altered syenite clasts from the Abrigo ignimbrite are derived from pre-DHF I plutons. Hence, the Abrigo magma chamber is likely to have formed within or adjacent to significantly older pre-Diego Hernandez formation pluton(s) and erupted fragments of these crystallised plutonic lithologies (Figure 14).

The pre-eruption configuration of the Abrigo magma chamber probably involved: (a) an upward zoned body of less evolved (relatively low Zr content) to more evolved (higher Zr) crystal mush, capped by a crystal-poor supernatant liquid layer; (b) crystallised syenite chamber walls, from which fresh syenite lithic clasts were derived; and (c) a mafic magma body which had intruded from below (Nichols, 2001). Rare microsyenite and recrystallised syenitic lithic clast types were possibly sourced from finer-grained outer parts of the crystallised chamber wall, related sills and dykes and/or an associated metamorphic aureole.
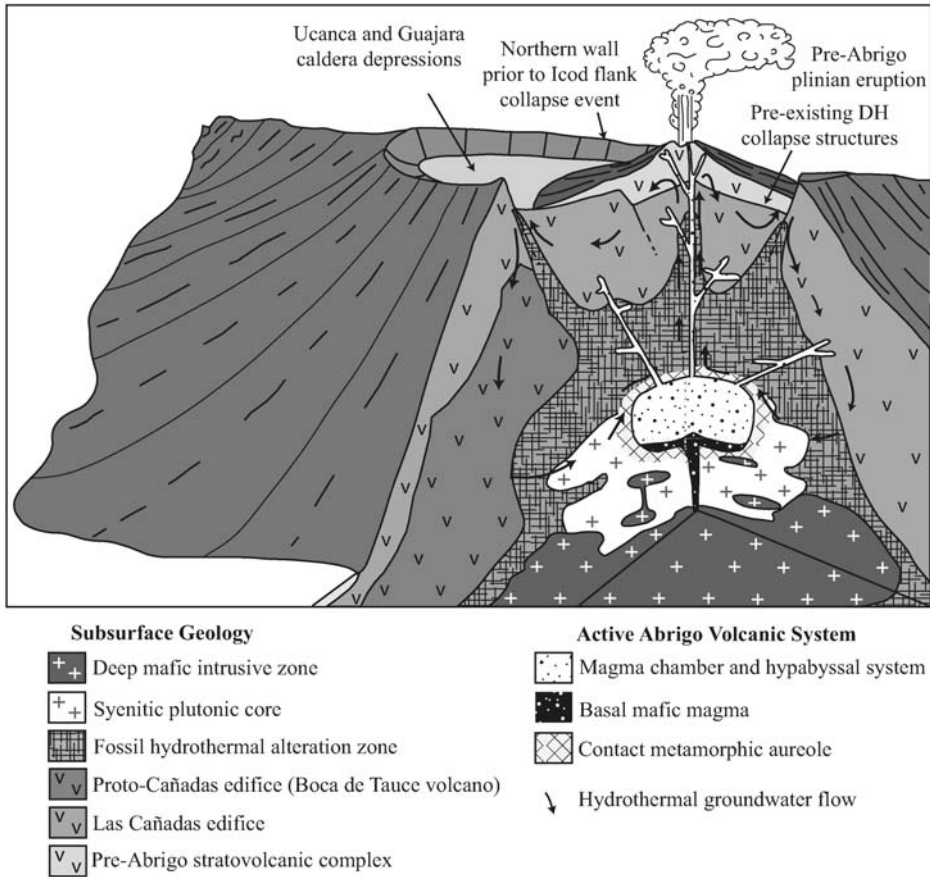
**Figure 14**   Schematic representation of the substrate geology and the superimposed active volcanic system just prior to the climactic destructive Abrigo eruption. Abbreviation: DH, Diego Hernández.

Mafic cumulate body(s) have been identified from geophysical studies at depths of 5–14 km below central Tenerife (Ablay and Kearey, 2000; Araña et al., 2000) and are probably the source of the very rare syeno-gabbroid and gabbroid lithic clasts within the Abrigo ignimbrite. It is likely that syenite was a more dominant wall rock lithology. Mafic plutonic lithic clasts within the Abrigo ignimbrite are more common on the eastern flanks of the edifice and could be evidence for a higher abundance of syeno-gabbro/gabbros at the eastern end of the Abrigo chamber wall.

## 3.6.2. Ancient hydrothermal systems

The abundance of hydrothermally altered lithic clasts within the Abrigo ignimbrite (often up to 40%) indicates that a large subsurface region of hydrothermally altered rock was sampled during the eruption (Figure 14). Hydrothermal altered rocks are locally exposed along the margin of the caldera wall (Araña, 1971) and may be the

cause of a magnetotelluric anomaly up to 1 km below the current caldera floor associated with the structural boundary of the caldera (Pous et al., 2002).

A currently active hot hydrothermal system on Tenerife is evident from fumaroles on top of Teide, thermal groundwater anomalies (Albert-Beltrán et al., 1990; Valentin et al., 1990), and from seismic (Jiménez and García–Fernández, 1996) and magnetotelluric (Ortiz et al., 1986; Pous et al., 2002) data. The aquifer system on Tenerife consists of a series of groundwater bodies/compartments within fractured volcanic rocks and minor pyroclastic and alluvial deposits, which are bound by relatively impermeable barriers (e.g. dykes, baked palaeosoils and geological contacts), and are interconnected by permeable pathways, such as fractures (Ecker, 1976; Pous et al., 2002).

Ancient hydrothermal activity on Tenerife may have varied with magmatic activity during each phonolitic magmatic cycle associated with the Upper Group (< 1.6 Ma, Martí et al., 1994; Wolff et al., 2000), reaching peak activity during the evolution of each phonolitic magma chamber, then reduced to background levels by climactic caldera-forming eruptions, subsequent removal of the plutonic heat source and reconfiguration of the central aquifer system. Hydrothermal activity may also have varied between individual eruptions associated with the same magma chamber. Multiple generations of secondary minerals in altered lithic clasts record variations in temperature and chemistry of the hydrothermal fluids during long-term magmatic cycles and shorter periods of eruption and quiescence.

The pervasiveness of hydrothermal alteration is reflected in the strongly altered lithic clasts. The higher proportion of reddish altered lithic clasts (A1) compared to lighter-coloured altered lithic clasts (A3) within the Abrigo ignimbrite on the south coast and the converse situation on the north coast reflects the asymmetry of the hydrothermally altered wall rocks around the magma chamber/conduit. Hydro-thermally altered basaltic lithologies probably made up over half of the altered wall rock portion of the southern chamber/conduit wall. On the northern, and possibly western, chamber/conduit wall, the hydrothermally altered rocks were predomi-nantly of more felsic lithologies.

The Abrigo magma chamber had been active for some 36,000 years prior to the Abrigo eruption and was the source of as many as 15 preceding plinian eruptions (Nichols, 2001; Edgar et al., 2007). This was sufficient time to develop a mature hydrothermal system. However, the state or intensity of hydrothermal activity at the time of the eruption cannot be inferred from the presence of hydrothermally altered lithic clasts within the Abrigo ignimbrite alone.

### 3.6.3. Evidence for a "Teide–Pico Viejo-like" stratovolcano

A constructive volcanic phase may have occurred in at least the 36,000 years before the Abrigo eruption, represented in part by the preceding 15 or more plinian fall deposits (Nichols, 2001; Edgar et al., 2007). Construction of the present intracaldera Teide-Pico Viejo stratovolcano has been ongoing since the Abrigo eruption (i.e. for a maximum of 202 ka) evolving from early basanitic to predominantly phono-tephritic to phonolitic compositions (Ablay et al., 1998; Ablay and Martí, 2000). A recent subplinian eruption (Moñtana Blanca, ∼ 2 ka,

Ablay et al., 1995) may be a smaller-scale analogy to the pre-Abrigo plinian eruptions (Edgar et al., 2007 also likens the Moñtana Blanca eruption to early explosive activity at the start of the Diego Hernández cycle). Effusive volcanism has continued since the Moñtana Blanca eruption, and it is possible that intracaldera effusive eruptions also occurred between the pre-Abrigo plinian eruptions although there are no interbedded lava flow units within this succession at the caldera wall.

Abundant, fresh, volcanic lithic clasts in the Abrigo ignimbrite, much of which are likely to be shallow conduit-derived accessory or near-to-vent accidental clasts, include basaltic to phonolitic compositions and a large variety of textures. This suggests that the conduit system and near-extra-vent ground surface consisted of a laterally and vertically variable stratigraphic architecture constructed during multiple effusive eruptions. This is consistent with the idea of a possible stratovolcano-building phase preceding the Abrigo eruption (Figure 14), although its size, morphology and position within the caldera is unknown.

## 3.7. Destruction of the pre-Abrigo volcanic system

The Abrigo eruption is considered to be the final caldera-forming eruption of the Diego Hernández cycle (Martí et al., 1994), which probably included earlier incremental collapse events (Edgar et al., 2007). The Icod landslide, which occurred around the same time, removed part of the northern caldera wall although its significance in determining the final shape of the caldera is uncertain (Watts and Masson, 1995, 2001; Ablay and Kearey, 2000; Ablay and Hürlimann, 2000). Evidence for caldera collapse associated with the Abrigo eruption includes (a) the large deposit volume ($>>1.8\,\mathrm{km}^3$) of which about 60% is juvenile material, and which represents the withdrawal of a large volume of magma; (b) the occurrence of a co-ignimbrite lithic lag breccia on the caldera rim (see Section 3.2; Pittari et al., 2006); and (c) clast component variations. The latter provides further insight into caldera-forming processes, which are discussed below.

### 3.7.1. Relationship between caldera dynamics and hydrothermal activity

The abundance of altered lithic clasts within the Abrigo ignimbrite suggests that an extensive hydrothermal alteration zone existed above the Abrigo magma chamber, probably concentrated along pre-existing structures associated with older caldera-collapse events (Martí et al., 1994; Edgar et al., 2007). During the hypothetical pre-Abrigo constructive phase, continued pervasive hydrothermal alteration and an increase in overburden by the addition of pyroclastic material and possible lavas, would have contributed to an increasing instability in the rock pile above the magma chamber (c.f. Calvache and Williams, 1992; López and Williams, 1993; Calvache et al., 1997). A hydrothermal system may have, at least in part, contributed to the explosive activity associated with the caldera-forming eruption (c.f. Criswell, 1987; Scandone, 1990; Mellors and Sparks, 1991; Calvache and Williams, 1992; Rosi et al., 1996), although the configuration of the aquifer system and availability of water to the magma chamber at the time of the eruption is not known.

## 3.7.2. Conduit-vent evolution

Large lithic volumes and lateral lithic clast variations within the Abrigo ignimbrite suggest that multiple vents along a ring fissure existed during the eruption (c.f. Eichelberger and Koch, 1979; Heiken and McCoy, 1984; Hildreth and Mahood, 1986; Suzuki-Kamata et al., 1993; Rosi et al., 1996; Cole et al., 1998; Legros et al., 2000). Deposits on the Bandas del Sur contain more syenite and felsic crystalline volcanic clasts, fewer mafic crystalline volcanic clasts and significant variations in the type of altered clasts compared to those on the north coast, indicating that northward- and southward-directed pyroclastic flows were fed from different vents. This is further supported by variations in juvenile clast geochemical populations on the northern (North group) and southern to eastern coasts (South A group), reflecting different vents tapping geochemically different parts of the magma chamber.

Subtle lateral variations in lithic componentry are also evident within both the Sur-A and -C units across the Bandas del Sur (e.g. increase in felsic crystalline volcanic and gabbroic clasts from west to east) suggesting that each southerly directed pyroclastic flow was fed from multiple, simultaneously active vents sourcing different country rock lithologies (e.g. Druitt, 1985). However, slight lateral lithic clast variations may also be an artefact of point counting sites being at slightly different stratigraphic levels within each unit, which is difficult to constrain in vertically continuous sequences of massive ignimbrite. Thus, the variations could also be explained by changes in wall rock excavation levels within a single vent. Nevertheless, the west to east increase in the proportion of mafic juvenile clasts across Tenerife, within laterally continuous Abrigo depositional units, reflects similar west to east compositional variations within the Abrigo magma chamber system and is consistent with simultaneous tapping of different parts of the magma chamber from multiple vents.

Furthermore, localised concentrations of low-Nb syenite at Los Abrigos and of only evolved juvenile clast compositions at San Miguel de Tajao, Poris de Abona west and Barranco de la Cera (South Group B, Figure 13a) could have been caused by imperfect mixing between the products from different vents. Mixing from different vent-sourced pyroclastic flow pulses could occur either within the caldera depression before spilling out into barrancos through passes in the caldera wall, or by partial overlapping of pyroclastic flow lobes as they travel down the upper slopes. A higher degree of mixing from multiple vents may be represented in the Abrigo deposit at Poris de Abona (east), which has the most diverse suite of juvenile clast and syenite compositions (Figure 13a).

The unique lithic clast population and juvenile clast geochemical group at Playa de San Juan (west coast) is consistent with a separate pyroclastic flow lobe sourced from a geochemically distinct part of the magma chamber and thus a different vent from those that fed other Abrigo pyroclastic flow lobes.

The vent-derived lithic concentration zone in the upper Sur-A unit is restricted to the southeastern flanks of the Las Cañadas edifice. This could be attributed to a significant incremental (piecemeal) collapse event of the southeastern sector of the caldera.

The Sur-C unit contains a higher abundance of deep lithic clasts (plutonic and altered clasts) than the Sur-A unit and suggests that the focus of wall rock

fragmentation progressed to greater depths (c.f. Suzuki-Kamata et al., 1993; Rosi et al., 1996; Thouret et al., 1999, 2002; Bryan et al., 2000; Allen, 2001). The upper Sur-A lithic concentration zone contains a relatively higher proportion of shallow fresh crystalline volcanic and clastic lithic clasts than the underlying and overlying deposit, suggesting shallower fragmentation levels during the southeastern piecemeal collapse event.

### 3.7.4. Implication for caldera evolution

Many caldera-forming eruptions proceed through two stages: an early central vent plinian stage and a later collapse, ring vent stage (e.g. Druitt and Sparks, 1984; Druitt, 1985; Druitt and Bacon, 1986; Hildreth and Mahood, 1986; Suzuki-Kamata et al., 1993; Rosi et al., 1996; Bryan et al., 2000). Remnants of a possible 30 cm thick Abrigo plinian fall deposit occurs beneath the ignimbrite near Poris de Abona; however, its distribution is very localised (Pittari et al., 2006). Thus, an early plinian phase may have been very short-lived due to early collapse of the eruption column.

Multiple vents are suggested by the lateral lithic clast variations within the Sur-A unit, and a similar inference can be made for the Sur-C unit. Timing of onset of caldera collapse is poorly constrained. However, a significant conduit-vent wall fragmentation event, likely to have been triggered by partial subsidence within the southeastern sector of the caldera, is thought to have occurred during the latter stages of the Sur-A phase, as represented by the deposition of the upper Sur-A lithic concentration zone.

After an eruption hiatus, a renewed collapsing eruption column fed a pyroclastic flow during the Sur-C phase. The latter stage of the Sur-C phase was characterised by large-scale conduit erosion as represented by the coarse maximum lithic clast size (typically up to 14 cm), high lithic content ($\sim$40%) and large variety of vent-derived lithic clasts. It represents the final climactic stage of the eruption where large-scale caldera collapse occurred at least along the southern margin of the caldera.

Northward- and westward-directed pyroclastic flows were sourced from vents on the north and possibly the west side of the caldera rim, although their timing with respect to those directed to the south is poorly constrained. Relatively high lithic contents within the north coast deposits and the Sur-C unit reflect high eruption intensities, and both may have been deposited during the final climactic stage of the eruption.

### 3.8. Implications for pyroclastic flow processes

In the downslope transects near both San Miguel de Tajao (Localities 6, 62 and 66; Figures 2b, 9) and the Orotava Valley (Localities 119, 124 and 131; Figures 2b, 11), the proportion of altered lithic clasts, relative to other fresh lithic clast types, decreases with increasing distances from the source caldera. In a granular flow mixture of hard fresh volcanic clasts and relatively softer altered clasts, the latter will tend to be ground to smaller grainsizes more quickly. The distance available for study along both downslope transects is small (1.5–2 kms) relative to the total

distance from the source-vent region to the end of each transect (at least 10–15 kms). If a relatively high rate of communion of altered lithic clasts had been ongoing along the entire distance to the source region, then a significantly higher proportion and size of altered clasts would have been ejected from the vent(s) than is represented in the preserved coastal ignimbrite. A slight increase in the proportion of mafic crystalline volcanic clasts (46–56%, Figure 11) downslope within the Orotava Valley may be due to entrainment of basalt lithic clasts from the ground surface. Additionally or alternatively, this may be an artefact of the pulverisation and decrease in the proportion of vent-derived altered clasts.

Pittari et al. (2006) provide evidence that the massive ignimbrite facies of the Abrigo ignimbrite was deposited by progressive or step-wise aggradation of material from the base of the pyroclastic flow (Fisher, 1966; Branney and Kokelaar, 1992). The vertical variation in the proportion of different lithic types, especially mafic crystalline volcanic and altered clasts (Figure 10), further supports the upward aggradation of the ignimbrite deposit with a changing influx of lithic clast componentry over time.

## 4. Conclusions

The detailed qualitative and quantitative lithic clast study of the Abrigo ignimbrite highlights the diverse applications of lithic clasts in understanding syn- and inter-eruptive processes within caldera systems. The abundance of syenite to gabbroid and altered lithic clasts within the Abrigo ignimbrite show that, prior to the Abrigo eruption, the active magma chamber was, at least partially hosted within a deep mafic to syenitic, intrusive complex surrounded by a widespread zone of hydrothermal alteration (Figure 14). Increasing hydrothermal alteration over time may have destabilised the edifice and contributed to caldera collapse. A diverse variety and abundance of fresh volcanic clasts, along with similarities between the pre-Abrigo plinian eruptions and the recent subplinian eruption of the active Pico Viejo-Teide stratovolcano suggest that a stratovolcanic complex may also have existed prior to the Abrigo eruption (Figure 14). Differences in the proportions of lithic clast types between the northern, western (San Juan) and southern flanks of the Las Cañadas edifice and additional variations across the southern flanks, along with geochemical variations in juvenile clasts, also provide unequivocal evidence for syn-eruptive piecemeal caldera collapse and eruption from multiple vents. Conduit fragmentation progressed to greater depths, along with increased eruption intensity, during the latter stages of the Sur-C phase.

Lithic clasts, along with juvenile components, if studied within the stratigraphic and facies framework of the pyroclastic deposits that host them, offer a unique window into subsurface volcanic and hydrothermal processes. In many cases, especially when structural components of calderas have been eroded or buried, lithic clast analyses may provide the only evidence for caldera collapse events and associated caldera dynamics. Component analyses of pyroclastic deposits provide important data, which would constrain numerical and experimental caldera models.

## *ACKNOWLEDGEMENTS*

## *REFERENCES*

Ablay, G., Hürlimann, M., 2000. Evolution of the north flank of Tenerife by recurrent giant landslides. J. Volcanol. Geotherm. Res., 103, 135–159.

Ablay, G.J., Carroll, M.R., Palmer, M.R., Martí, J., Sparks, R.S.J., 1998. Basanite–phonolite lineages of the Teide–Pico–Viejo volcanic complex, Tenerife, Canary Islands. J. Petrol., 39, 905–936.

Ablay, G.J., Ernst, G.G.J., Martí, J., Sparks, R.S.J., 1995. The ~2 ka subplinian eruption of Montaña Blanca, Tenerife. Bull. Volcanol., 57, 337–355.

Ablay, G.J., Kearey, P., 2000. Gravity constraints on the structure and volcanic evolution of Tenerife, Canary Islands. J. Geophys. Res., 105, 5783–5796.

Ablay, G.J., Martí, J., 2000. Stratigraphy, structure, and volcanic evolution of the Pico Teide–Pico Viejo formation, Tenerife, Canary Islands. J. Volcanol. Geotherm. Res., 103, 175–208.

Adams, N.K., de Silva, S.L., Self, S., Salas, G., Schubring, S., Permenter, J.L., Arbesman, K., 2001. The physical volcanology of the 1600 eruption of Huaynaputina, southern Peru. Bull. Volcanol., 62, 493–518.

Albert–Beltrán, J.F., Araña, V., Diez, J.L., Valentin, A., 1990. Physical–chemical conditions of the Teide volcanic system (Tenerife, Canary Islands). J. Volcanol. Geotherm. Res., 43, 321–332.

Allen, S.R., 2001. Reconstruction of a major caldera-forming eruption from pyroclastic deposit characteristics: Kos Plateau Tuff, eastern Aegean Sea. J. Volcanol. Geotherm. Res., 105, 141–162.

Allen, S.R., Cas, R.A.F., 1998. Lateral variations within coarse co-ignimbrite lithic breccias of the Kos Plateau Tuff, Greece. Bull. Volcanol., 59, 356–377.

Allen, S.R., Stadlbauer, E., Keller, J., 1999. Stratigraphy of the Kos Plateau Tuff: product of a major Quaternary explosive rhyolitic eruption in the eastern Aegean, Greece. Int. J. Earth Sci., 88, 132–156.

Alonso, J.J., Araña, V., Martí, J., 1988. La ignimbrita de Arico (Tenerife): mecanismos de emisión y de emplazamiento. Rev. Soc. Geol. Esp., 1, 15–24.

Anchochea, E., Fúster, J.M., Ibarrola, E., Cendrero, A., Coello, J., Hernan, F., Cantagrel, J.M., Jamond, C., 1990. Volcanic evolution of the island of Tenerife (Canary Islands) in the light of new K–Ar data. J. Volcanol. Geotherm. Res., 44, 231–249.

Anchochea, E., Huertas, M.J., Cantagrel, J.M., Coello, J., Fúster, J.M., Arnaud, N., Ibarrola, E., 1999. Evolution of the Cañadas edifice and its implications for the origin of the Cañadas caldera (Tenerife, Canary Islands). J. Volcanol. Geotherm. Res., 88, 177–199.

Aramaki, S., 1984. Formation of the Aira caldera, Southern Kyushu, ~22,000 years ago. J. Geophys. Res., 89, 8485–8501.

Araña, V., 1971. Litología y estructura del Edificio Cañadas, Tenerife (Islas Canarias). Est. Geol., 27, 95–135.

Araña, V., Camacho, A.G., Garcia, A., Montesinos, F.G., Blanco, I., Vieira, R., Felpeto, A., 2000. Internal structure of Tenerife (Canary Islands) based on gravity, aeromagnetic and volcanological data. J. Volcanol. Geotherm. Res., 103, 43–64.

Bacon, C.R., 1983. Eruptive history of Mount Mazama and Crater Lake caldera, Cascade Range, U.S.A. J. Volcanol. Geotherm. Res., 18, 57–115.

Bacon, C.R., 1985. Implications of silicic vent patterns for the presence of large crustal magma chambers. J. Geophys. Res., 90, 11243–11252.

Blake, S., Ivey, G.N., 1986. Magma-mixing and the dynamics of withdrawal from stratified reservoirs. J. Volcanol. Geotherm. Res., 27, 153–178.

Borley, G.D., 1974. Aspects of the volcanic history and petrology of the island of Tenerife, Canary Islands. Proc. Geol. Assoc., 85, 259–279.

Branney, M.J., Kokelaar, P., 1992. A reappraisal of ignimbrite emplacement: progressive aggradation and changes from particulate to non-particulate flow during emplacement of high-grade ignimbrite. Bull. Volcanol., 54, 504–520.

Bravo, T., 1962. El circo de Las Cañadas y sus dependencias. Bol. R. Soc. Esp. Hist. Nat., 60, 93–108.

Brown, R.J., Barry, T.L., Branney, M.J., Pringle, M.S., Bryan, S.E., 2003. The quaternary pyroclastic succession of southeast Tenerife, Canary Islands: explosive eruptions, related caldera subsidence, and sector collapse. Geol. Mag., 140, 265–288.

Bryan, S.E., Cas, R.A.F., Martí, J., 1998a. Lithic breccias in intermediate volume phonolitic ignimbrites, Tenerife (Canary Islands): constraints on pyroclastic flow depositional processes. J. Volcanol. Geotherm. Res., 81, 269–296.

Bryan, S.E., Cas, R.A.F., Martí, J., 2000. The 0.57 Ma plinian eruption of the Granadilla Member, Tenerife (Canary Islands): an example of complexity in eruption dynamics and evolution. J. Volcanol. Geotherm. Res., 103, 209–238.

Bryan, S.E., Martí, J., Cas, R.A.F., 1998b. Stratigraphy of the Bandas del Sur formation: an extracaldera record of Quaternary phonolitic explosive eruptions from the Las Cañadas edifice, Tenerife (Canary Islands). Geol. Mag., 135, 605–636.

Bryan, S.E., Martí, J., Leosson, M., 2002. Petrology and geochemistry of the Bandas del Sur formation, Las Cañadas edifice, Tenerife (Canary Islands). J. Petrol., 43, 1815–1856.

Buesch, D.C., 1992. Incorporation and redistribution of locally derived lithic fragments within a pyroclastic flow. Geol. Soc. Am. Bull., 104, 1193–1207.

Burgisser, A., 2005. Physical volcanology of the 2,050 bp caldera-forming eruption of Okmok volcano, Alaska. Bull. Volcanol., 67, 497–525.

Calder, E.S., Sparks, R.S.J., Gardeweg, M.C., 2000. Erosion, transport and segregation of pumice and lithic clasts in pyroclastic flows inferred from ignimbrite at Lascar volcano, Chile. J. Volcanol. Geotherm. Res., 104, 201–235.

Calvache, V.M.L., Cortés, J.G.P., Williams, S.N., 1997. Stratigraphy and chronology of the Galeras volcanic complex, Colombia. J. Volcanol. Geotherm. Res., 77, 5–19.

Calvache, V.M.L., Williams, S.N., 1992. Lithic-dominated pyroclastic flows at Galeras volcano, Colombia — an unrecognised volcanic hazard. Geology, 20, 539–542.

Camacho, A.G., Vieira, R., de Toro, C., 1991. Microgravimetric model of the Las Cañadas caldera (Tenerife). J. Volcanol. Geotherm. Res., 47, 75–88.

Cantagrel, J.M., Arnaud, N.O., Anchochea, E., Fúster, J.M., Huertas, M.J., 1999. Repeated debris avalanches on Tenerife and genesis of Las Cañadas caldera wall (Canary Islands). Geology, 27, 739–742.

Carey, S., Sparks, R.S.J., 1986. Quantitative models of the fallout and dispersal of tephra from volcanic eruption columns. Bull. Volcanol., 48, 109–125.

Cas, R.A.F., Wright, J.V., 1987. Volcanic Successions: Modern and Ancient. A Geological Approach to Processes, Products and Successions. Allen and Unwin, London, 518 pp.

Cole, J.W., Brown, S.J.A., Burt, R.M., Beresford, S.W., Wilson, C.J.N., 1998. Lithic types in ignimbrites as a guide to the evolution of a caldera complex, Taupo volcanic centre, New Zealand. J. Volcanol. Geotherm. Res., 80, 217–237.

Cole, P.D., Guest, J.E., Duncan, A.M., 1993. The emplacement of intermediate volume ignimbrites: a case study from Roccamonfina volcano, southern Italy. Bull. Volcanol., 55, 467–480.

Cole, P.D., Scarpati, C., 1993. A facies interpretation of the eruption and emplacement mechanisms of the upper part of the Neapolitan Yellow Tuff, Campi Flegrei, southern Italy. Bull. Volcanol., 55, 311–326.

Criswell, C.W., 1987. Chronology and pyroclastic stratigraphy of the May 18, 1980 eruption of Mount St. Helens, Washington. J. Geophys. Res., 92, 10237–10266.

Dobran, F., 1992. Nonequilibrium flow in volcanic conduits and application to the eruptions of Mt. St. Helens on May 18, 1980, and Vesuvius in AD 79. J. Volcanol. Geotherm. Res., 49, 285–311.

Druitt, T.H., 1985. Vent evolution and lag breccia formation during the Cape Riva eruption of Santorini, Greece. J. Geol., 93, 439–454.

Druitt, T.H., 1992. Emplacement of the 18 May 1980 lateral blast deposit ENE of Mount St. Helens, Washington. Bull. Volcanol., 54, 554–572.

Druitt, T.H., 1995. Settling behaviour of concentrated dispersions and some volcanological applications. J. Volcanol. Geotherm. Res., 65, 27–39.

Druitt, T.H., Bacon, C.R., 1986. Lithic breccia and ignimbrite erupted during the collapse of Crater Lake caldera, Oregon. J. Volcanol. Geotherm. Res., 29, 1–32.

Druitt, T.H., Sparks, R.S.J., 1982. A proximal ignimbrite breccia facies on Santorini, Greece. J. Volcanol. Geotherm. Res., 13, 147–171.

Druitt, T.H., Sparks, R.S.J., 1984. On the formation of calderas during ignimbrite eruptions. Nature, 310, 679–681.

Ecker, A., 1976. Groundwater behaviour in Tenerife, volcanic island (Canary Islands, Spain). J. Hydrol., 28, 73–86.

Edgar, C.J., Wolff, J.A., Nichols, H.J., Cas, R.A.F., Martí, J., 2002. A complex Quaternary ignimbrite-forming phonolitic eruption: the Poris Member of the Diego Hernández formation (Tenerife, Canary Islands). J. Volcanol. Geotherm. Res., 118, 99–130.

Edgar, C.J., Wolff, J.A., Olin, P.H., Nichols, H.J., Pittari, A., Cas, R.A.F., Reiners, P.W., Spell, T.L., Marti, J., 2007. The late Quaternary Diego-Hernandez formation, Tenerife: volcanology of a complex cycle of voluminous explosive phonolitic eruptions. J. Volcanol. Geotherm. Res., 160, 59–85.

Eichelberger, J.C., Koch, F.G., 1979. Lithic fragments in the Bandelier Tuff, Jemez Mountains, New Mexico. J. Volcanol. Geotherm. Res., 5, 115–134.

Féraud, G., Giannérini, G., Campredon, R., Stillman, C.J., 1985. Geochronology of some Canarian dike swarms: contribution to the volcano-tectonic evolution of the archipelago. J. Volcanol. Geotherm. Res., 25, 29–52.

Fernández Santín, S., Nafría López, R., 1978. La extrusión fonolítico-traquítica de Montaña de Guaza, Tenerife (Canarias). Estud. Geol., 34, 375–387.

Fierstein, J., Hildreth, W., 1992. The plinian eruptions of 1912 at Novarupta, Katmai National Park, Alaska. Bull. Volcanol., 54, 646–684.

Fisher, R.V., 1966. Mechanism of deposition from pyroclastic flows. Am. J. Sci., 264, 350–363.

Fúster, J.M., Araña, V., Brandle, J.L., Navarro, M., Alonso, U., Aparicio, A., 1968. Geologia y Volcanologia de las Islas Canarias. Instituto "Lucas Mallada", CSIC, Madrid, 218 pp.

Fúster, J.M., Ibarrola, E., Snelling, N.J., Cantagrel, J.M., Huertas, M.J., Coello, J., Anchochea, E., 1994. Cronología K–Ar de la Formación Cañadas en el sector Suroeste de Tenerife: implicaciones de los episodios piroclásticos en la evolución volcánica. Bol. R. Soc. Esp. Hist. Nat. (Sec. Geol.), 89, 25–41.

Freundt, A., Schmincke, H.-U., 1985. Lithic-enriched segregation bodies in pyroclastic flow deposits of Laacher See volcano (East Eifel, Germany). J. Volcanol. Geotherm. Res., 25, 193–224.

Giordano, G., 1998. The effect of paleotopography on lithic distribution and facies associations of small volume ignimbrites: the WTT Cupa (Roccamonfina volcano, Italy). J. Volcanol. Geotherm. Res., 87, 255–273.

Hausen, H., 1956. Contributions to the geology of Tenerife (Canary Islands). Soc. Sci. Fenn. Comm. Phys.-Math., 18, 247.

Heiken, G., McCoy, F., Jr., 1984. Caldera development during the Minoan eruption, Thira, Cyclades, Greece. J. Geophys. Res., 89, 8441–8462.

Hildreth, W., 1987. New perspectives on the eruption of 1912 in the Valley of Ten Thousand Smokes, Katmai National Park, Alaska. Bull. Volcanol., 49, 680–693.

Hildreth, W., Mahood, G.A., 1986. Ring-fracture eruption of the Bishop Tuff. Geol. Soc. Am. Bull., 97, 396–403.

Huertas, M.J., Anchochea, E., Cantagrel, J.M., Coello, J., Fúster, J.M., Ibarrola, E., 1994. Un episódio volcánico pre-Cañadas en la Isla de Tenerife. Geogaceta, 15, 113–116.

Huertas, M.J., Arnaud, N.O., Anchochea, E., Cantagrel, J.M., Fúster, J.M., 2002. $^{40}$Ar/$^{39}$Ar stratigraphy of pyroclastic units from the Cañadas volcanic edifice (Tenerife, Canary Islands) and their bearing on the structural evolution. J. Volcanol. Geotherm. Res., 115, 351–365.

Ibarrola, E., Anchochea, E., Fúster, J.M., Cantagrel, J.M., Coello, J., Snelling, N.J., Huertas, M.J., 1993. Cronoestratigrafía del Macizo de Tigaiga: evolución de un sector del edificio Cañadas (Tenerife, Islas Canarias). Bol. R. Soc. Esp. Hist. Nat. (Sec. Geol.), 88, 57–71.

Iverson, R.M., 1997. The physics of debris flows. Rev. Geophys., 35, 245–296.

Iverson, R.M., Vallance, J.W., 2001. New views of granular mass flows. Geology, 29, 115–118.

Jiménez, M.J., García-Fernández, M., 1996. Aftershock sequence of the 9 May 1989 Canary Islands earthquake. Tectonophysics, 255, 157–162.

Jurado-Chichay, Z., Walker, G.P.L., 2001. Variability of plinian fall deposits: examples from Okataina volcanic centre, New Zealand. J. Volcanol. Geotherm. Res., 111, 239–263.

Krippner, S.J.P., Briggs, R.M., Wilson, C.J.N., Cole, J.W., 1998. Petrography and geochemistry of lithic fragments in ignimbrites from the Mangakino Volcanic Centre: implications for the composition of the subvolcanic crust in western Taupo Volcanic Zone, New Zealand. J. Geol. Geophys., 41, 187–199.

Legros, F., Kelfoun, K., Martí, J., 2000. The influence of conduit geometry on the dynamics of caldera-forming eruptions. Earth Planet. Sci. Lett., 179, 53–61.

Lindsay, J.M., de Silva, S., Trumbull, R., Emmermann, R., Wemmer, K., 2001. La Pacana caldera, N. Chile: a re-evaluation of the stratigraphy and volcanology of one of the world's largest resurgent calderas. J. Volcanol. Geotherm. Res., 106, 145–173.

Lipman, P.W., 1984. The roots of ash flow calderas in North America: windows into the tops of granitic batholiths. J. Geophys. Res., 89, 8801–8841.

López, D.L., Williams, S.N., 1993. Catastrophic volcanic collapse: relation to hydrothermal processes. Science, 260, 1794–1796.

Macedonio, G., Dobran, F., Neri, A., 1994. Erosion processes in volcanic conduits and application to the AD 79 eruption of Vesuvius. Earth Planet. Sci. Lett., 121, 137–152.

Martí, J., Ablay, G.J., Bryan, S., 1996. Comment on "The Canary Islands: an example of structural control on the growth of large oceanic-island volcanoes" by J.C. Carracedo. J. Volcanol. Geotherm. Res., 72, 143–149.

Martí, J., Gudmundsson, A., 2000. The Las Cañadas caldera (Tenerife, Canary Islands): an overlapping collapse caldera generated by magma-chamber migration. J. Volcanol. Geotherm. Res., 103, 161–173.

Martí, J., Hürlimann, M., Ablay, G.J., Gudmundsson, A., 1997. Vertical and lateral collapses on Tenerife (Canary Islands) and other volcanic ocean islands. Geology, 25, 879–882.

Martí, J., Mitjavila, J., Araña, V., 1994. Stratigraphy, structure and geochronology of the Las Cañadas caldera (Tenerife, Canary Islands). Geol. Mag., 131, 715–727.

McArthur, A.N., Cas, R.A.F., Orton, G.J., 1998. Distribution and significance of crystalline, perlitic and vesicular textures in the Ordovician Garth Tuff (Wales). Bull. Volcanol., 60, 260–285.

Mellors, R.A., Sparks, R.S.J., 1991. Spatter-rich pyroclastic flow deposits on Santorini, Greece. Bull. Volcanol., 53, 327–342.

Nairn, I.A., Wood, C.P., Bailey, R.A., 2004. The Reporoa caldera, Taupo volcanic zone: source of the Kaingaroa Ignimbrites. Bull. Volcanol., 56, 529–537.

Neumann, E.-R., Sørensen, V.B., Simonsen, S.L., Johnsen, K., 2000. Gabbroic xenoliths from La Palma, Tenerife and Lanzarote, Canary Islands: evidence for reactions between mafic alkaline Canary Islands melts and old oceanic crust. J. Volcanol. Geotherm. Res., 103, 313–342.

Nichols, H.J., 2001. Petrologic and geochemical variation of a caldera-forming ignimbrite: the Abrigo member, Diego Hernández formation, Tenerife, Canary Islands (Spain). M.Sc. Thesis, Department of Geology, Washington State University, Pullman, 123 pp.

Ortiz, R., Araña, V., Astiz, M., Garcia, A., 1986. Magnetotelluric study of the Teide (Tenerife) and Timanfaya (Lanzarote) volcanic areas. J. Volcanol. Geotherm. Res., 30, 357–377.

Palladino, D.M., Valentine, G.A., 1995. Coarse-tail vertical and lateral grading in pyroclastic flow deposits of the Latera volcanic complex (Vulsini, central Italy): origin and implications for flow dynamics. J. Volcanol. Geotherm. Res., 69, 343–364.

Papale, P., Dobran, F., 1993. Modeling of the ascent of magma during the plinian eruption of Vesuvius in A.D. 79. J. Volcanol. Geotherm. Res., 58, 101–132.

Papale, P., Dobran, F., 1994. Magma flow along the volcanic conduit during the Plinian and pyroclastic flow phases of the May 18, 1980, Mount St. Helens eruption. J. Geophys. Res., 99, 4355–4373.

Paradas Herrero, A., Fernández Santín, S., 1984. Estudio vulcanologico y geoquimico del maar de la Caldera del Rey, Tenerife (Canarias). Est. Geol., 40, 285–313.

Perrotta, A., Scarpati, C., Giacomelli, L., Capozzi, A.R., 1996. Proximal depositional facies from a caldera-forming eruption: the Parata Grande Tuff at Ventotene Island (Italy). J. Volcanol. Geotherm. Res., 71, 207–228.

Pittari, A., 2004. Eruption dynamics and emplacement processes for the climactic Abrigo member, Tenerife, Canary Islands. Ph.D. Thesis, Monash University, Clayton, 327 pp.

Pittari, A., Cas, R.A.F., 2004. Sole marks at the base of the late Pleistocene Abrigo ignimbrite, Tenerife: implications for transport and depositional processes at the base of pyroclastic flows. Bull. Volcanol., 66, 356–363.

Pittari, A., Cas, R.A.F., Edgar, C.J., Nichols, H.J., Wolff, J.A., Martí, J., 2006. The influence of palaeotopography on facies architecture and pyroclastic flow processes of a lithic-rich ignimbrite in a high gradient setting: the Abrigo ignimbrite, Tenerife, Canary Islands. J. Volcanol. Geotherm. Res., 152, 273–315.

Pous, J., Heise, W., Schnegg, P.-A., Muñoz, G., Martí, J., Soriano, C., 2002. Magnetotelluric study of the Las Cañadas caldera (Tenerife, Canary Islands): structural and hydrogeological implications. Earth Planet. Sci. Lett., 204, 249–263.

Potter, D.B., Oberthal, C.M., 1987. Vent sites and flow directions of the Otowi ash flows (lower Bandelier Tuff), New Mexico. Geol. Soc. Am. Bull., 98, 66–76.

Ridley, W.I., 1970. The abundance of rock types on Tenerife, Canary Islands, and its petrogenetic significance. Bull. Volcanol., 34, 196–204.

Roche, O., Gilbertson, M., Phillips, J.C., Sparks, R.S.J., 2002. Experiments on deaerating granular flows and implications for pyroclastic flow mobility. Geophys. Res. Lett., 29, 40-1–40-4.

Rocher, P., Westercamp, D., 1989. The Salazie Cirque Ignimbrite (Piton des Neiges volcano, Reunion Island): chronostratigraphy, description and significance of lithic fragments and eruptive mechanisms. J. Volcanol. Geotherm. Res., 36, 177–191.

Roobol, M.J., Smith, A.L., Wright, J.V., 1987. Lithic breccias in pyroclastic flow deposits on St. Kitts, West Indies. Bull. Volcanol., 49, 694–707.

Rosi, M., Vezzoli, L., Aleotti, P., De Censi, M., 1996. Interaction between caldera collapse and eruptive dynamics during the Campanian Ignimbrite eruption, Phlegraean Fields, Italy. Bull. Volcanol., 57, 541–554.

Rosi, M., Vezzoli, L., Castelmenzano, A., Grieco, G., 1999. Plinian pumice fall deposit of the Campanian Ignimbrite eruption (Phlegraean Fields, Italy). J. Volcanol. Geotherm. Res., 91, 179–198.

Scandone, R., 1990. Chaotic collapse of calderas. J. Volcanol. Geotherm. Res., 42, 285–302.

Schumacher, R., Mues-Schumacher, U., Toprak, V., 2001. The Sarikavak Tephra, Galatea, north central Turkey: a case study of a Miocene complex plinian eruption deposit. J. Volcanol. Geotherm. Res., 112, 231–245.

Scott, P.W., 1969. Pyroxenes from the Tenerife volcanic suite. Proc. Geol. Soc. Lond., 1658, 260–261.

Self, S., Goff, F., Gardner, J.N., Wright, J.V., Kite, W.M., 1986. Explosive rhyolitic volcanism in the Jemez Mountains: vent locations, caldera development and relation to regional structures. J. Geophys. Res., 91, 1779–1798.

Smith, R.T., Houghton, B.F., 1995. Vent migration and changing eruptive style during the 1800a Taupo eruption: new evidence from the Hatepe and Rotongaio phreatoplinian ashes. Bull. Volcanol., 57, 432–439.

Soriano, C., Galindo, I., Martí, J., Wolff, J., 2006. Conduit-vent structures and related proximal deposits in the Las Cañadas caldera, Tenerife, Canary Islands. Bull. Volcanol., 69, 217–231.

Soriano, C., Zafrilla, S., Martí, J., Bryan, S., Cas, R., Ablay, G., 2002. Welding and rheomorphism of phonolitic fallout deposits from the Las Cañadas caldera, Tenerife, Canary Islands. Geol. Soc. Am. Bull., 114, 883–895.

Sottili, G., Palladino, D.M., Zanon, V., 2004. Plinian activity during the early eruptive history of the Sabatini volcanic district, central Italy. J. Volcanol. Geotherm. Res., 135, 279–361.

Sparks, R.S.J., 1976. Grainsize variations in ignimbrites and implications for the transport of pyroclastic flows. Sedimentology, 23, 147–188.

Sparks, R.S.J., Self, S., Walker, G.P.L., 1973. Products of ignimbrite eruptions. Geology, 1, 115–118.

Spera, F.J., 1984. Some numerical experiments on the withdrawal of magma from crustal reservoirs. J. Geophys. Res., 89, 8222–8236.

Sulpizio, R., Mele, D., Dellino, P., La Volpe, L., 2007. Deposits and physical properties of pyroclastic density currents during complex sublinian eruptions: the AD 472 (Pollena) eruption of Somma-Vesuvius, Italy. Sedimentology, 54, 607–635, doi:10.1111/j.1365-3091.2006.00852.x.

Suzuki-Kamata, K., 1988. The ground layer of Ata pyroclastic flow deposit, southwestern Japan — evidence for the capture of lithic fragments. Bull. Volcanol., 50, 119–129.

Suzuki-Kamata, K., Kamata, H., 1990. The proximal facies of the Tosu pyroclastic-flow deposit erupted from Aso caldera, Japan. Bull. Volcanol., 52, 325–333.

Suzuki-Kamata, K., Kamata, H., Bacon, C.R., 1993. Evolution of the caldera-forming eruption at Crater Lake, Oregon, indicated by component analysis of lithic fragments. J. Geophys. Res., 98, 14059–14074.

Thirlwall, M.F., Singer, B.S., Marriner, G.F., 2000. $^{39}$Ar–$^{40}$Ar ages and geochemistry of the basaltic shield stage of Tenerife, Canary Islands, Spain. J. Volcanol. Geotherm. Res., 103, 247–297.

Thouret, J.-C., Davila, J., Eissen, J.-P., 1999. Largest explosive eruption in historical times in the Andes at Huaynaputina volcano, A.D. 1600, southern Peru. Geology, 27, 435–438.

Thouret, J.-C., Juvigné, E., Gourgaud, A., Boivin, P., Dávila, J., 2002. Reconstruction of the AD 1600 Huaynaputina eruption based on the correlation of geologic evidence with early Spanish chronicles. J. Volcanol. Geotherm. Res., 115, 529–570.

Valentin, A., Albert-Beltran, J.F., Diez, J.L., 1990. Geochemical and geothermal constraints on magma bodies associated with historic activity, Tenerife (Canary Islands). J. Volcanol. Geotherm. Res., 44, 251–264.

van den Bogaard, P., Schmincke, H.-U., 1984. The eruptive centre of the Late Quaternary Laacher See tephra. Geolog. Rundsch., 73, 933–980.

Vieira, R., Toro, C., Araña, V., 1986. Microgravimetric survey in the caldera of Teide, Tenerife, Canary Islands. Tectonophysics, 130, 249–257.

von Fritsch, K., Reiss, W., 1868. Geologische Beschreibung der Insel Tenerife. Wurster and Co., Winterthur, 496 pp.

Walker, G.P.L., 1985. Origin of coarse lithic breccias near ignimbrite source vents. J. Volcanol. Geotherm. Res., 25, 157–171.

Walker, G.P.L., Self, S., Froggatt, P.C., 1981. The ground layer of the Taupo Ignimbrite: a striking example of sedimentation from a pyroclastic flow. J. Volcanol. Geotherm. Res., 10, 1–11.

Watts, A.B., Masson, D.G., 1995. A giant landslide on the north flank of Tenerife, Canary Islands. J. Geophys. Res., 100, 24487–24498.

Watts, A.B., Masson, D.G., 2001. New sonar evidence for recent catastrophic collapses of the north flank of Tenerife, Canary Islands. Bull. Volcanol., 63, 8–19.

Wilson, C.J.N., 1980. The role of fluidisation in the emplacement of pyroclastic flows: an experimental approach. J. Volcanol. Geotherm. Res., 8, 231–249.

Wilson, C.J.N., 1984. The role of fluidisation in the emplacement of pyroclastic flows, 2: experimental results and their interpretation. J. Volcanol. Geotherm. Res., 20, 55–84.

Wilson, C.J.N., Walker, G.P.L., 1982. Ignimbrite depositional facies: the anatomy of a pyroclastic flow. J. Geol. Soc. Lond., 139, 581–592.

Wilson, L., Sparks, R.S.J., Walker, G.P.L., 1980. Explosive volcanic eruptions IV: the control of magma properties and conduit geometry on eruption column behaviour. Geophys. J. R. Astron. Soc., 63, 117–148.

Wilson, L., Walker, G.P.L., 1987. Explosive volcanic eruptions VI: ejecta dispersal in plinian eruptions: the control of eruption conditions and atmospheric properties. Geophys. J. R. Astron. Soc., 89, 657–679.

Wolff, J.A., 1985. The effect of explosive eruption processes on geochemical patterns within pyroclastic deposits. J. Volcanol. Geotherm. Res., 26, 189–201.

Wolff, J.A., 1987. Crystallisation of nepheline syenite in a subvolcanic magma system: Tenerife, Canary Islands. Lithos, 20, 207–223.

Wolff, J.A., Grandy, J.S., Larson, P.B., 2000. Interaction of mantle-derived magma with island crust? Trace element and oxygen isotope data from the Diego Hernández formation, Las Cañadas, Tenerife. J. Volcanol. Geotherm. Res., 103, 343–366.

Wolff, J.A., Toney, J.B., 1993. Trapped liquid from a nepheline syenite: a re-evaluation of Na-, Zr-, F-rich interstitial glass in a xenolith from Tenerife, Canary Islands. Lithos, 29, 285–293.

Wright, J.V., 1981. The Rio Caliente Ignimbrite: analysis of a compound intraplinian ignimbrite from a major late Quaternary Mexican eruption. Bull. Volcanol., 44, 189–212.

Wright, J.V., Walker, G.P.L., 1977. The ignimbrite source problem: Significance of a co-ignimbrite lag-fall deposit. Geology, 5, 729–732.

Yokoyama, S., 1974. Mode of movement and emplacement of the Ito pyroclastic flow from Aira Caldera, Japan. Tokyo Kyoiku Daigaku. Sci. Rep. Sect. C, 12, 1–63.

Zafrilla, S., 2001. Relationships between magmatic evolution and phonolitic volcanic activity in the Las Cañadas edifice, Tenerife, Canary Islands. Ph.D. Thesis, University of Barcelona, Barcelona, Spain, 312 pp.

# The Ignimbrite Flare-Up and Graben Calderas of the Sierra Madre Occidental, Mexico

Gerardo J. Aguirre-Díaz[1],[*], Guillermo Labarthe-Hernández[2], Margarito Tristán-González[2], Jorge Nieto-Obregón[1] *and* Isaac Gutiérrez-Palomares[1]

## Contents

## Abstract

The Sierra Madre Occidental (SMO) is the largest continuous ignimbrite province in the world. It covers the NW portion of Mexico and has a minimum estimated volcanic rock volume of about 400,000 km³. The southern part of the North American Basin and Range extensional province is in Mexico and was formed by NW- to NE-trending normal faults that bound many large grabens, which are particularly long and deep in the southern SMO. Graben formation and ignimbrite-forming pyroclastic flow eruptions coincided in space and time, particularly for the 38–23 Ma period, which has been referred to as the

[*]Corresponding author. Tel.: +52-55-56234116, Ext. 107; Fax: +52-55-56234101
*E-mail address:* ger@geociencias.unam.mx

[1] Centro de Geociencias, Universidad Nacional Autónoma de México, Campus Juriquilla, Querétaro, Qro., 76230, Mexico
[2] Instituto de Geología, Universidad Autónoma de San Luis Potosí, S.L.P., México

Ignimbrite Flare-up event. Geologic observations in the southern SMO indicate that the vents of several large-volume silicic ignimbrites were related to the graben master faults. We propose the new name "graben caldera" for this type of explosive-volcano-tectonic-collapse structure. The evidences for vent location of graben calderas include large pyroclastic dikes, co-ignimbrite lithic-lag breccias, and post-ignimbrite aligned rhyolitic domes and rhyolitic lava dikes. All these features are found along the graben caldera walls or on the graben's margins and thus were controlled by the main graben faults. Large-volume ignimbrite-forming eruptions occurred during graben collapse, usually through several vents along the graben caldera walls. Often, only part of the graben acted as a collapse caldera. In most cases, the downdropped blocks inside the collapsed segment of the graben have several distinct tilting directions, opposite to those caused by regular domino faulting (with tilting outwards from the graben's axis), indicating a chaotic collapse of blocks. This is interpreted as collapse of blocks during magma evacuation from an elongated and possibly batholith-sized magma chamber controlled by the regional extensional tectonics that existed under the collapsed segment of the graben. This collapse produced a piece-meal-like caldera confined within a graben. Generally, the pyroclastic dikes occur as discontinuous elongate lenses rather than regular tabular bodies. Usually, an elongated lava dome filled the vent and this totally covers the pre-existent pyroclastic dike, but in some cases the pyroclastic dike is exposed. Faulting and subsidence continued for several millions of years after the collapse and ignimbrite emplacement, displacing the intra-graben caldera products downward into the tectonic depression, but preserving or even intensifying the chaotic arrangement of the collapsed blocks. Fluvio-lacustrine continental deposits are generally found beneath and over the main and most voluminous ignimbrite, indicating that subsidence started before ignimbrite emplacement and graben collapse, and that continued after these events. In many cases the graben caldera vents are related to gold and silver hydrothermal mineralisation; thus understanding the relationship between ignimbrites, graben caldera vents, and fluvio-lacustrine deposits will be important for economic purposes.

# 1. Introduction

The Sierra Madre Occidental (SMO) and the Mexican Volcanic Belt are the two main volcanic provinces of Mexico. Each province developed at different times and both were related to continental margin volcanism associated with a long–term subduction of oceanic plates beneath the North American plate, at least between 100 Ma and Present (Atwater, 1989; Aguirre-Díaz and McDowell, 1991; Figure 1). The SMO was formed first, with peaks in volcanic activity in the Eocene, Oligocene, and Early Miocene, and was followed by the Mexican Volcanic Belt, which started in the Middle Miocene and continues in the Present (Ferrari et al., 1999; Figure 2). This work summarises the main characteristics of the SMO volcanic province focusing on the extraordinary Ignimbrite Flare–up event, which built most of the SMO and caused its main feature, a thick sequence of large–volume silicic ignimbrites (McDowell and Clabaugh, 1979; Aguirre-Díaz and Labarthe-Hernández, 2003; Swanson et al., 2006). Then we propose a new type of collapse caldera structure, the graben caldera, based on the geologic evidence observed in the SMO. We conclude
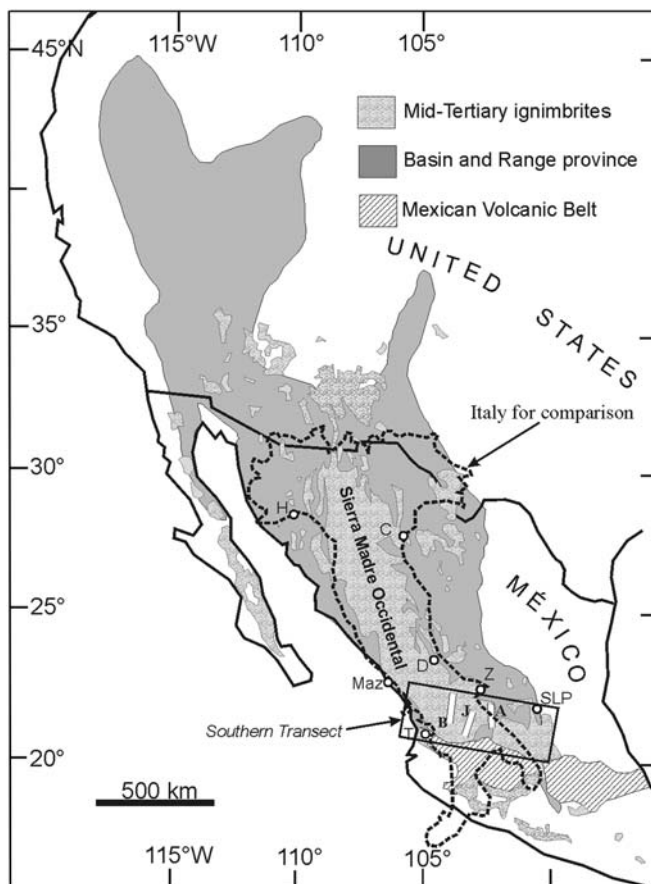
**Figure 1**   Index map of the Sierra Madre Occidental (SMO) volcanic province, the Basin and Range extensional tectonic province, and of Mid-Teriary ignimbrites in Mexico and the SW United States. Note the superimposed Italy outline for scale comparison, and the location of the Southern Transect Project. The SMO and the Basin and Range provinces overlap in space and time. Some of the most important graben related to the Basin and Range extension are shown in the figure: B, Bolaños; J, Juchipila; A, Aguascalientes. Cities: H, Hermosillo; C, Chihuahua; Maz, Mazatlán; D, Durango; T, Tepic; Z, Zacatecas; SLP, San Luis Potosí. (Modified from Aguirre-Díaz and Labarthe-Hernández (2003), with permission from Geological Society of America).

that this type of caldera structure was related to the eruption of large-volume ignimbrites of the SMO, during the Ignimbrite Flare-up.

## 2. The Sierra Madre Occidental Volcanic Province

*Sensu strictu*, the SMO is the name given to a physiographic province, a long range bordering the NW coast of mainland Mexico (Raisz, 1964). The same name
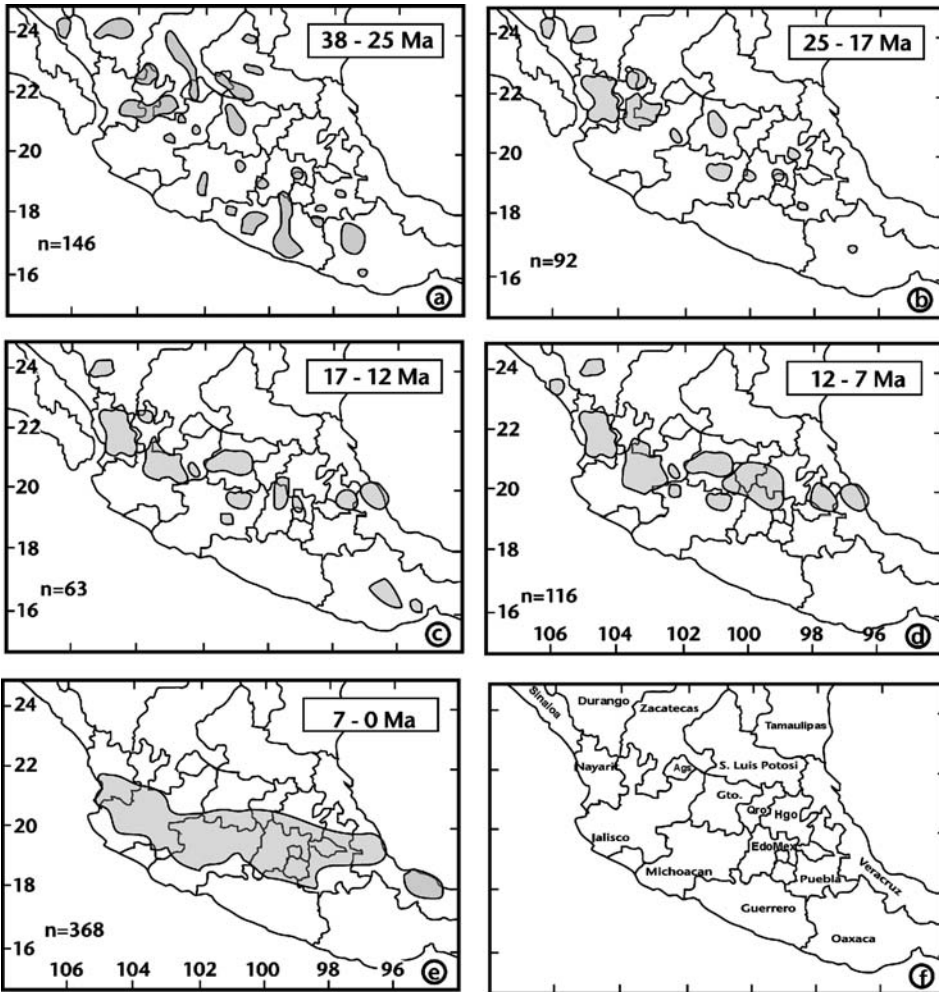
**Figure 2** Space—time patterns of volcanism in Mexico, from 38 Ma to Present representing the distribution patterns of continental margin volcanism from the SMO to the Mexican Volcanic Belt. Patterned areas represent volcanic rocks distribution for the indicated time period. States of central and southern Mexico are also shown for reference, where: Ags, Aguascalientes; Gto, Guanajuato; Qro, Querétaro; Hgo, Hidalgo; EdoMex, Estado de México. Modified from Ferrari et al. (1999).

has been used for the volcanic province (McDowell and Clabaugh, 1979). The SMO is a Cretaceous to Mid-Tertiary volcanic province that extends continuously for about 1,000 km, between 21° and 31° Lat. N along NW Mexico (Figure 1). It can be followed from the U.S.–Mexico border at the North to its intersection with the Mexican Volcanic Belt at the South. It includes three main volcanic packages, (1) a Cretaceous to Early-Tertiary lower volcano–plutonic sequence, (2) a middle thick package that is mostly composed of Mid–Tertiary high-silica rhyolitic

ignimbrites, and (3) an upper suite of Miocene basalts and basaltic–andesites that occur dispersed throughout the SMO. Because the main features of the SMO are the large-volume ignimbrites of the second package, the SMO has been restricted to the Mid–Tertiary ignimbrites occurring between the Latitudes 21° to 31° N. However, Mid–Tertiary ignimbrites similar to those of the SMO continue as discontinuous outcrops farther to the South of the Mexican Volcanic Belt, as well as to the North of the U.S.–Mexico border, extending as far as Parallel 18° Lat. N to the South, and up to Latitude 35° N, to the North, including the Mogollon–Datil volcanic field (Figure 1). The SMO changes its width from North to South; it is about 600 km wide in its northern sector, including the states of Sonora, Chihuahua, and the westernmost portion of Texas, and it narrows to about 250 km wide in the central sector, including the states of Sinaloa and Durango. It is about 550 km wide at the southern sector, including the states of Nayarit, Zacatecas, Jalisco, Aguascalientes, Guanajuato, San Luis Potosí, and Querétaro. In order to visualise the size of this volcanic province, the area that it covers is about the same size as Italy (Figure 1).

A conservative estimated volume of the SMO ignimbrites is about 400,000 km$^3$, assuming an average thickness of 1 km and the actual surface distribution of the mid–Tertiary ignimbrites between Latitudes 21° and 31° N (Table 1 — in Aguirre-Díaz and Labarthe-Hernández, 2003). The estimate of Aguirre-Díaz and Labarthe-Hernández (2003) does not consider the erosion of the ignimbrites, nor the extension caused by the Basin and Range (up to 22% according to Henry and Aranda-Gómez, 2000), and the consequent separation of Baja California from mainland Mexico. Based upon its dimensions and volume, the SMO has been catalogued as the largest ignimbrite province in the world (Swanson and McDowell, 1984; Aguirre-Díaz and Labarthe-Hernández, 2003; Swanson et al., 2006).

There have been several studies on the SMO province. These include classic regional geology studies (McDowell and Clabaugh, 1979; Gastil et al., 1979; Mauger, 1981; Labarthe-Hernández et al., 1982; Swanson and McDowell, 1984; Henry and

**Table 1** Volume of mid-Tertiary ignimbrites in Mexico.

| Province | Area (km$^2$) | Thickness (km) | Volume (km$^3$) |
| --- | --- | --- | --- |
| Sierra Madre Occidental main | 392,775 | 1 | 392,775 |
| Eastern Chihuahua | 66,583 | 1 | 66,583 |
| Sonora | 7,982 | 1 | 7,982 |
| South of Mexican volcanic belt | 35,287 | 1 | 35,287 |
| Baja California | 36,421 | 1 | 36,421 |
| Inferred beneath the Mexican volcanic belt | 32,136 | 1 | 32,136 |
| Total | 586,727 | | 586,727 |
| Total of San Juan Mountains[a] | | | 20,000 |

*Source:* modified from Aguirre-Díaz and Labarthe-Hernández (2003), with permission from Geological Society of America.

*Note:* volume is approximated and related to 17 calderas.

[a]Data from Lipman et al. (1970).

Fredrikson, 1987; Aguirre-Díaz and McDowell, 1991), petrogenetic-oriented studies (Bagby et al., 1981; Cameron et al., 1980; Cameron and Cameron, 1986; Ruiz et al., 1988; Wark et al., 1990), and many on the geology of particular areas with important Au–Ag ore deposits (Gross, 1975; Damon et al., 1981; Clark et al., 1982; Goodell, 1981; Lyons, 1988; Scheubel et al., 1988; Randall et al., 1994).

Some researchers have drawn attention to the problem of the lack of observed conventional caldera structures for the extraordinary volume of silicic ignimbrites (Swanson and McDowell, 1984; Aguirre-Díaz and Labarthe-Hernández, 2003). It has also been difficult to explain how this large volume of silicic products originated. Two models have been proposed to explain the magma genesis, one favouring crystal fractionation from mantle-derived basalt (Cameron and Cameron, 1986), and the other favouring crustal anatexis (Ruiz et al., 1988). Newer work basically focuses on either one of these two hypotheses. The former hypothesis has the problem of requiring a large volume of a basaltic magma parent, for which evidence is not abundant, and the latter requires melting of large quantities of continental crust. Wark et al. (1990) proposed a crystal fractionation evolution from an andesitic magma parent, based on their work in the Tomochic caldera, Chihuahua, a model that at least would reduce the large amounts of basaltic parental magma required, but with the problem of still needing a petrogenetic history for the parental andesite; i.e., either crystal fractionation from a basaltic parent, a magma-mixing derived andesite, or an andesite formed from crustal melting by basalt underplating of the intermediate composition batholithic roots of the SMO. Ferrari et al. (2002) propose an elaborate hypothesis involving detachment of the extinct Farallon oceanic plate beneath the North American plate, which caused basalt underplating through this slab window and assimilation of the crust. In our opinion, a plausible petrogenetic model for the origin of the large mass of rhyolitic magma that the SMO ignimbrites represent remains unsolved.

McDowell et al. (1990) referred to the "Ignimbrite Flare-up" in the SMO, in a similar way as Lipman et al. (1970, 1972) used to describe a large-volume ignimbrite event in the western U.S. More recently, Aguirre-Díaz and Labarthe-Hernández (2003) define the Ignimbrite flare-up as "a period of intense explosive volcanic activity that produced enormous volumes of silicic ignimbrite sheets, which took place mainly between 38 and 23 Ma in Mexico." Aguirre-Díaz and McDowell (1991, 1993) report that Eocene volcanism in the SMO was as extensive as that in the Oligocene, and that Basin and Range block faulting in Mexico started at least 29 Ma, coincident with peaks in volcanic activity of regional scale. McDowell and Mauger (1994) confirm this model for the northern sector of the SMO. Ferrari et al. (1999) summarise the space and time distribution patterns of the volcanism in western Mexico, since the SMO to the Mexican Volcanic Belt, on the basis of the space distribution of a compilation of radiometric ages. In summary, it is generally accepted that the SMO was formed during several volcano–tectonic episodes, in which peaks in volcanism coincided with peaks in a long-term extensional regime that includes the formation of the Basin and Range province (Aguirre-Díaz and McDowell, 1991; Henry and Aranda-Gómez, 1992; McDowell and Mauger, 1994; Aranda-Gómez et al., 2000, 2003; Ferrari et al., 2002; Aguirre-Díaz and Labarthe-Hernández, 2003).

# 3. Regional Stratigraphy of the Sierra Madre Occidental

The SMO volcanic rocks can be divided stratigraphically into three major sequences, the older one, known as the Lower Volcano-plutonic Complex, the second (younger), known as the Upper Volcanic Supergroup (McDowell and Clabaugh, 1979), and the third (youngest), named here the Miocene Mafic Lavas. The regional stratigraphy of the SMO is shown in Figure 3, which summarises the stratigraphy reported in several works (Table 2 — Aguirre-Díaz and Labarthe-Hernández, 2003). In general, the basal portion of the SMO is mainly formed by rocks of a volcanic arc complex, with a predominance of andesitic–dacitic lavas and associated volcanoes, but also with important packages of silicic domes and ignimbrites. In the most eroded portions of the SMO, either in the bottoms of deep canyons, or at the deeply eroded westernmost margin of the SMO in the northern states of Sinaloa and Sonora (and in the now separated Baja California Peninsula), the roots of this volcanic arc are exposed as batholiths, mostly of intermediate composition. In general these remain little studied (e.g., Henry and Fredrikson, 1987; McDowell et al., 1989, 2001; Albretch and Goldstein, 2000). On the other hand, at the eastern margin of the SMO, Mezosoic marine sedimentary rocks from the Mexican folded belt of Laramide age directly underlie ignimbrites of Eocene–Oligocene age of the Upper Volcanic Supergroup, with a few exposures of the lower volcanic arc (Aguirre-Díaz and McDowell, 1991, McDowell and Mauger, 1994). However, Eocene–Oligocene plutonic bodies in the form of stocks occur scattered along the central-eastern margin of the SMO (Aguirre-Díaz and McDowell, 1991), some of which could well be interpreted as the roots of silicic lava domes (porphyry-rhyolite intrusives) that commonly are related to precious metal ore deposits, such as Mapimí, Velardeña, and Guanajuato (Damon et al., 1981, 1983; Gilmer et al., 1988; Randall et al., 1994).

The Upper Volcanic Supergroup is mostly composed of rhyolitic ignimbrites and lava domes, but at some sites andesitic–dacitic lavas are also an important part of the sequence; for instance, at the San Luis Potosí volcanic field and nearby areas (Labarthe-Hernández and Tristán-González, 1978, 1980a, 1980b; Labarthe-Hernández et al., 1982). Plinian pyroclastic-fall deposits appear to be absent within the ignimbrite sequence of the SMO. Instead, pyroclastic surge-like, cross-bedded deposits are relatively common. These deposits and minor non-welded ignimbrites are generally found beneath the large-volume ignimbrites with no time-breaks (volcanic hiatus, sedimentary deposits, paleosoils) between them, indicating that this type of explosive volcanism pre-dated the emplacement of large and catastrophic pyroclastic flow that formed a major ignimbrite. An example of this situation is the Alacrán Ignimbrite at the Bolaños mining district in Jalisco State (Lyons, 1988; Gutiérrez-Palomares and Aguirre-Díaz, 2005), which is described in more detail below.

In general, the ignimbrites of the upper group are capped by basalts and basaltic andesite lava flows, that occur scattered throughout the SMO (Figure 3). In some localities this mafic volcanism consists of alkaline basalts interpreted as intra-plate magmatism (Aguirre-Díaz and McDowell, 1993), but in others they consist of
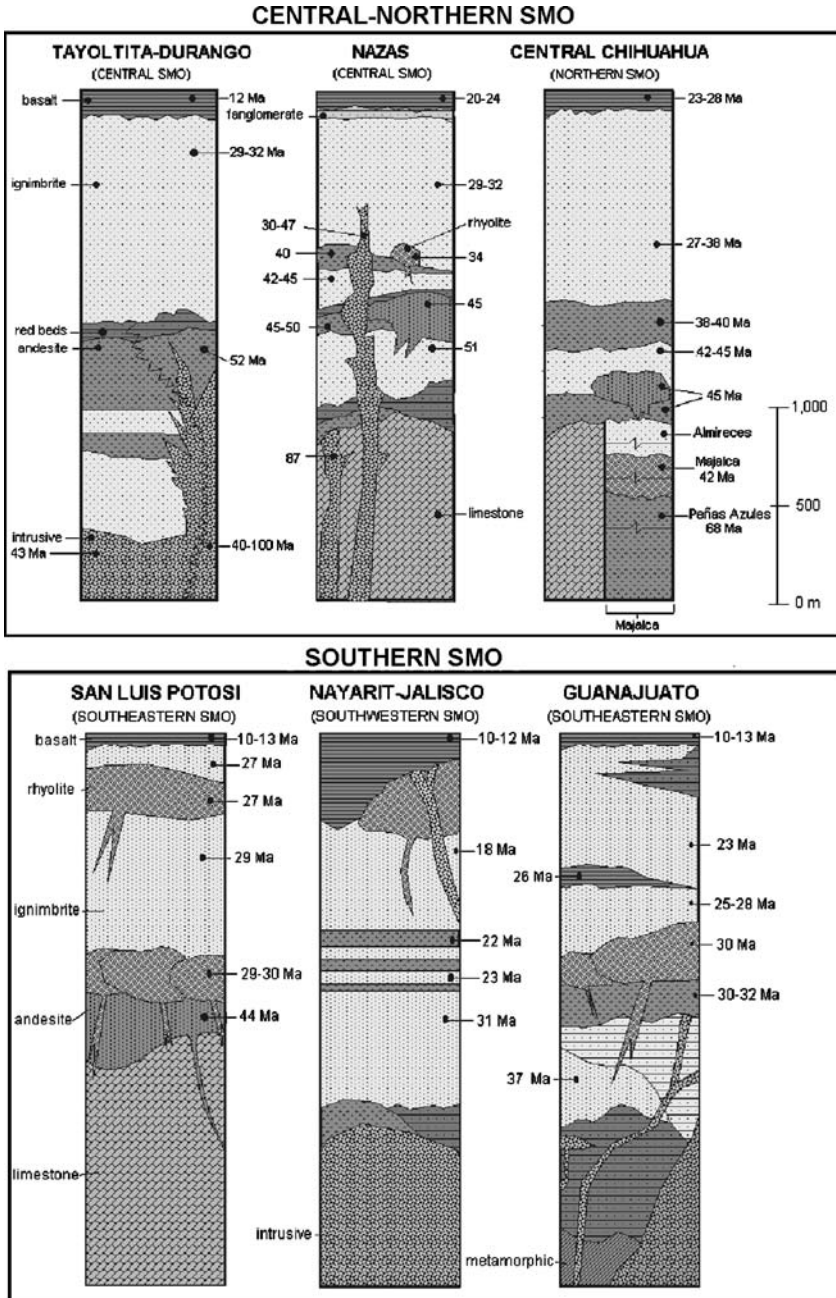
**Figure 3**  Representative schematic sections of the main stratigraphic units and lithologies of the SMO as two separate groups, one for the central–northern sectors and another for the southern sector. Each locality shows a particular stratigraphy, but it can be noticed that in general the thickest units correspond to the mid-Tertiary ignimbrite package that mostly occurred between 38 and 23 Ma. This has an average thickness of 1,000 m, which has been defined as the Ignimbrite Flare-up event (Aguirre-Díaz and Labarthe-Hernández, 2003). (Modified from Aguirre-Díaz and McDowell, 1991).

**Table 2** Representative geologic studies in the Sierra Madre Occidental.

| Northern SMO | Central SMO | Southern SMO |
|---|---|---|
| Alba and Chavez (1974) | Aguirre–Díaz and McDowell (1991) | Aguillón-Robles et al. (1996) |
| Bagby et al. (1981) | Aguirre–Díaz and McDowell (1993) | Aguirre–Díaz et al. (1997) |
| Bockoven (1981) | Aranda–Gómez et al. (1997) | Aguirre–Díaz and Labarthe–Hernández (2003) |
| Cameron and Cameron (1986) | Aranda–Gómez et al. (2000) | Aranda–Gómez and McDowell (1998) |
| Cameron et al. (1980) | Clark et al., (1980) | Aranda–Gómez et al. (2003) |
| Capps (1981) | Clark et al. (1982) | Aranda–Gómez et al. (2000) |
| Cárdenas (1983) | Clemons and McLeroy (1966) | Ban et al. (1994) |
| Clark et al. (1980) | Damon et al. (1981) | Cerca–Martínez et al. (2000) |
| Clark et al. (1982) | Enciso–De La Vega (1963) | Clark et al. (1980) |
| Cochemé and Demant (1991) | Henry and Fredrikson (1987) | Clark et al. (1981) |
| Duex (1983) | Luhr et al. (2001) | Clark et al. (1982) |
| Goodell (1981) | McDowell and Keizer (1977) | Damon and Nieto–Obregón (1979) |
| Henry and Price (1984) | McDowell and Clabaugh (1979) | Damon et al. (1981) |
| Keller et al. (1982) | McLeroy and Clemons (1965) | Echegoyén (1970) |
| Mauger (1981) | Nemeth (1976) | Edwards (1955) |
| Mauger (1983a) | Pantoja-Alor (1963) | Gross (1975) |
| Mauger (1983b) | Pantoja-Alor et al. (1967) | Lyons (1988) |
| Mauger (1983c) | Reyes-Cortés (1985) | Martínez–Reyes (1992) |
| Mauger and Dayvault (1983) | Roldán–Quintana (1968) | Nieto–Obregón et al. (1981) |
| McDowell and Mauger (1994) | Shafiqullah et al. (1980) | Nieto–Samaniego et al. (1996) |

**Table 2** (*Continued*)

| Northern SMO | Central SMO | Southern SMO |
|---|---|---|
| McDowell et al. (1989) | Swanson and McDowell (1984) | Nieto-Samaniego et al. (1999) |
| McDowell et al. (1999) | Swanson et al. (1978) | Labarthe-Hernández and De la Huerta-Cobos (1999) |
| McDowell et al. (2001) | Valencia-Moreno et al. (2001) | Labarthe-H. and Jiménez-López (1992) |
| Megaw (1981) | | Labarthe-H. and Jiménez-López (1993) |
| Megaw and McDowell (1983) | | Labarthe-Hernández and Tristán-González (1978) |
| Mora-Álvarez and McDowell (2000) | | Labarthe-Hernández and Tristán-González (1980a) |
| Roldán-Quintana (2002) | | Labarthe-Hernández and Tristán-González (1980b) |
| Shafiqullah et al. (1980) | | Labarthe-Hernández et al. (1982) |
| Spruill (1976) | | Quintero-Legorreta (1992) |
| Stimac and Wark (1983) | | Randall et al. (1994) |
| Swanson and McDowell (1984) | | Shafiqullah et al. (1980) |
| Swanson and McDowell (1985) | | Scheubel et al. (1988) |
| Swanson et al. (2006) | | Tristán-González (1986) |
| Valencia-Moreno et al. (2001) | | Tristán-González and Labarthe-Hernández (1979) |
| Wark et al. (1990) | | Valencia-Moreno et al. (2001) |
| | | Webber et al. (1994) |
| | | Zimmermann et al. (1990) |

*Source:* modified from Aguirre-Díaz and Labarthe-Hernández (2003).

subalkalic andesitic lavas, which were grouped and named as the Southern Cordillera Basaltic Andesitic Suite (SCORBA) by Cameron et al. (1989), with a subduction tectonic regime geochemical signature combined with the Basin and Range extension. These rocks range in age from 28 to 12 Ma. However, most of them occur within 24–20 Ma and are here considered as a separate volcanic group, named the Miocene Mafic Lavas of the SMO.

## 4. Graben Calderas of the Sierra Madre Occidental

Aguirre-Díaz and Labarthe-Hernández (2003) proposed that a large proportion of the ignimbrites of the SMO were related to fissure vents associated with regional fault systems and grabens of the Basin and Range province, basing their proposal on geologic observations and on the fact that the SMO volcanic province and the Basin and Range extensional province overlap in space and time (Figure 1). However, this fissural eruption style does not completely replace the vents related to classic semi-circular calderas. There is evidence for both classic calderas and for fissures as vents for the ignimbrites in the region, but we believe that most of the volume was erupted from fissure type vents related to Basin and Range grabens. Swanson et al. (2006) report new caldera sources for ignimbrites of the northern sector of the SMO, but as new mapping is done in this province, more evidence of fissure type vents related to grabens are documented. In some cases, the mapping has been done, and in a few places with great detail; for instance, in the mining districts that exist throughout the SMO, or the systematic mapping done in the State of San Luis Potosí (e.g. Labarthe-Hernández et al., 1982). However, the interpretation of the geologic maps with respect to the vents and volcanic units related to these vents was not performed until the late 1990s and early 2000s (Aguirre-Díaz et al., 1998; Aguirre-Díaz and Labarthe-Hernández, 1999, 2003). In most of the cases that we have studied, we conclude that the ignimbrites were related to fissure type vents and graben collapse volcanic structures that we have named "graben calderas" (Aguirre-Díaz et al., 2005, 2007). Thus, a graben caldera can be defined as a collapse-explosive-volcano-tectonic structure from which ignimbrite-forming pyroclastic flows were erupted through the graben's faults during collapse of the roof of a shallow magma chamber that was structurally controlled by the graben domain. In other words, a collapse caldera with the form of a graben, or a graben that collapsed as a caldera. There are several types that we have documented, including piece-meal graben calderas, single-block graben calderas, half-graben calderas (trap-door), and scattered fissure vents along regional fault systems that do not concentrate within a single part of the graben or half-graben.

Geologic observations that support the graben caldera model include five lines of evidence: (1) pyroclastic dikes that used the graben faults as conduits, (2) co-ignimbrite lithic-lag breccias that occur next to the graben faults, (3) post-collapse silicic lava domes and lava diques that occur aligned along the graben master faults,

(4) inward and/or chaotic tilting of downdropped blocks inside the graben observed only in segments of the graben that collapsed as a caldera (piece-meal collapse), (5) drastic thickness variations of the intra-graben ignimbrite (relatively much thicker) with respect the out-flow ignimbrite (relatively much thinner).

Our studies have focused on the southern SMO, in a project that we have called the Southern Transect of the SMO, a geologic transect that our group has been mapping systematically since the 1980s (Figure 1). We have also carried out studies in the central sector of the SMO, which include sites in the states of Durango and Zacatecas (e.g., Labarthe-Hernández et al., 1985; Aguirre-Díaz and McDowell, 1991, 1993; Tristán-González et al., 1994; Labarthe-Hernández et al., 1996). In the southern sector of the SMO there are a series of large grabens with a general orientation from NW to NE, with lengths of about 80–150 km by 25–40 km wide, and some about 2 km (topographically) deep (Figure 4). Faulting and subsidence continued for several millions of years after the graben caldera collapse and ignimbrite emplacement, displacing the intra-graben caldera products downward into the tectonic depression, but preserving and even enhancing the chaotic arrangement of the collapsed blocks for the case of piece-meal graben calderas. Fluvial red beds and lacustrine deposits indicate that in most cases alluvial fans and lakes existed before the graben caldera collapse, suggesting that graben subsidence started before the caldera formation and ignimbrite emplacement. Subsidence and faulting continued after caldera collapse, producing relatively thick sequences of post-ignimbrite lacustrine beds that filled the graben and were later faulted and tilted (Aguirre-Díaz and Carranza-Castañeda, 2000). These pre- and post-ignimbrite fluvio-lacustrine deposits suggest differences in the subsidence rate during graben development, with apparently fast rates during graben caldera collapse and ignimbrite emplacement, and relatively slow rates before and after graben caldera collapse. In many cases, such as Bolaños (Scheubel et al., 1988; Lyons, 1988), the graben caldera vents are related to gold and silver hydrothermal mineralisation, and thus, understanding the relationship between the graben tectonics, the graben caldera vents, the hydrothermal processes that occurs around them, and the water input from the intra-graben lakes, will be important for economic purposes.

The graben of the southern SMO are, from east to west, the Santa María del Río and the Juachín half-graben system, and the Aguascalientes, Malpaso, Calvillo, Juchipila, Tlaltenango, Bolaños, Tuxpan de Bolaños, and the Huejumic graben (Figures 4 and 5). There are also the Jerez, Atengo, and Jesús María graben, and other less well known graben in the central SMO, such as Ventanas, El Rodeo, Santiaguillo, and San Juan Papasquiaro graben. All of these are in the Durango state. Here we only describe the cases of Santa María del Río, Juachín, Malpaso, Juchipila, and Bolaños as representative examples (Figure 5).

## 4.1. Graben calderas and fissure vents of San Luis potosí

In the central-southern portion of the State of San Luis Potosí (Figure 6) there are two volcanic areas that, although have some similarities, contain different volcanic sequences; one is the San Luis Potosí volcanic field, and the other the Santa María del Río volcanic field (Labarthe-Hernández et al., 1982; Tristán-González, 1986).
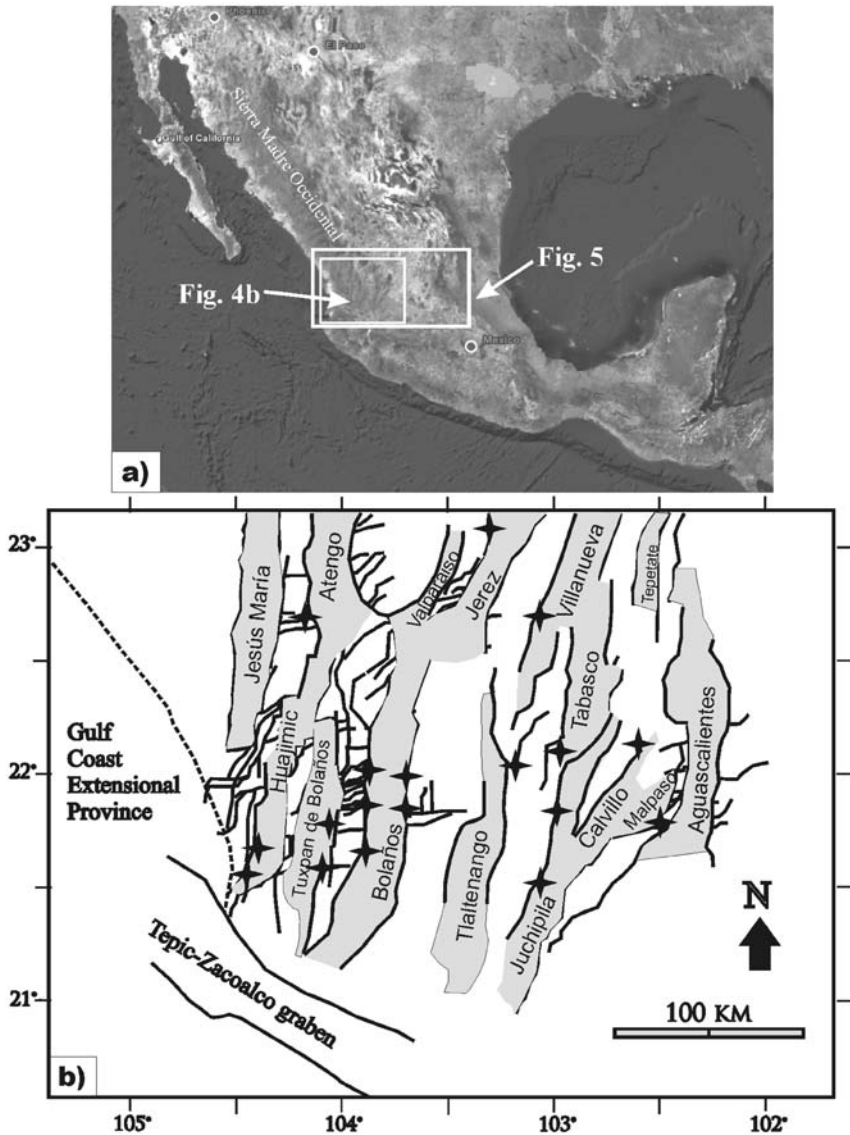
**Figure 4** Index map of Basin and Range grabens in the southern sector of the SMO; (a) regional location of the southern sector in Mexico and of Figure 5b. Location and names of the graben at the southern SMO, and of other regional structures, such as the Gulf-coast extensional province and of the Tepic–Zacoalco graben. Stars indicate sites of fissure type vents. Lines indicate major normal faults (with permission from Google).

In these two volcanic fields there are examples of graben calderas and fissure vents that were controlled by the regional extension of Basin and Range tectonics (Tristán-González et al., 2006), and both include the widespread volcanic unit called Panalillo Inferior ignimbrite, whose feeder vents are related to pyroclastic
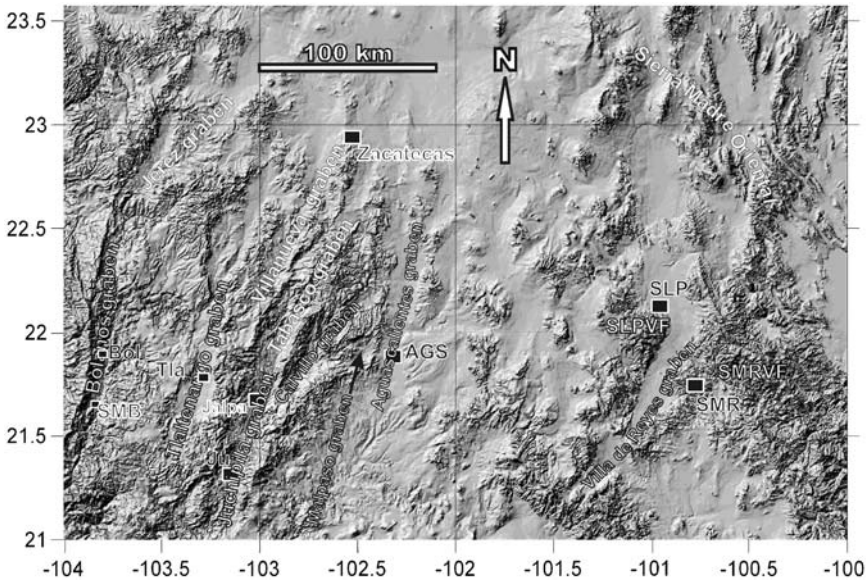
**Figure 5**    Digital shaded elevation model of the southern sector of the SMO showing the location and extent of several graben in this sector, and of the San Luis Potosí Volcanic Field (SLPVF) and the Santa María del Río Volcanic Field (SMRVF). Towns shown: Bol, Bolaños; SMB, San Martín de Bolaños; Tla, Tlaltenango; Ju, Juchipila; AGS, Aguascalientes; SLP, San Luis Potosí; SMR, Santa María del Río.

dikes (Aguirre-Díaz and Labarthe-Hernández, 2003; Torres-Hernández et al., 2006). In Santa María del Río there is a series of relatively small grabens in the range of 0.5 by 3 km to 3 by 12 km, and a cluster of half-grabens, all oriented NW-SE (Figure 7). Along the master faults of these grabens there are pyroclastic dikes, which were the vents for a major ignimbrite in the area, the Panalillo Inferior ignimbrite, which is a poorly-welded, white deposit, composed mostly of pumice shards, small pumice fragments, sanidine, quartz and biotite. This ignimbrite is dated at 27 Ma (Labarthe-Hernández et al., 1982) and is the product of the last large ignimbrite event in this region. The graben apparently collapsed as single-block graben calderas, since structurally they consist of a downdropped block (the graben) that is bounded by the corresponding horsts (Figure 8). There are also pyroclastic dikes that fed the Panalillo Inferior Ignimbrite along the faults of several small half-graben near Santa María del Río (Figure 7). The dikes and faults used as conduits generally have a high angle, in the range of 70–90° (Figure 9a and b). The dikes have lenticular shapes in plan view rather than continuous tabular shapes (Figure 9c), and range in width from a few cm to about 30 m. They have the same aspect and composition as the Panalillo Inferior ignimbrite and thus, they are mostly composed of pumice shards and phenocrysts of quartz, sanidine, and biotite, with small pumice lumps occasionally observed (Figure 9d). The dikes intruded country rock made of older, densely welded ignimbrites and dacitic lavas. The contacts with the country rock show signs of heating such as cooking and/or hydothermal alteration (Figure 9e). At the dike's margins the pyroclastic rock is
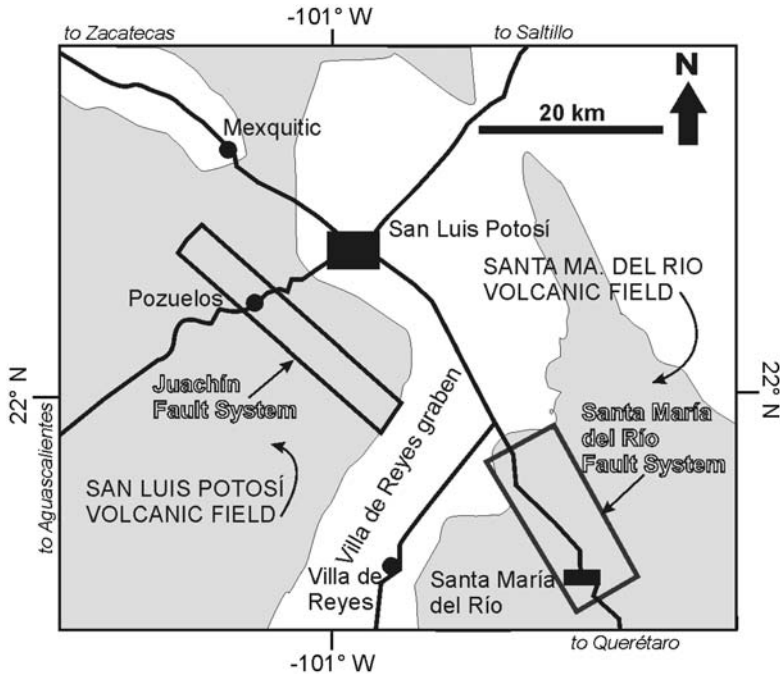
**Figure 6** Index map of the San Luis Potosí and Santa María del Río volcanic fields, showing the location of the Juachín and Santa María del Río fault systems. Shaded areas show extent of mid-Tertiary ignimbrites and lavas.

densely welded, quenched, and in many cases silicified (Figure 9f). These observations indicate that the dike contained a hot, pyroclastic material, which formed a vertically emplaced pyroclastic fill that is white and poorly welded in the dike's interior and pink to red at the densely welded and quenched margins, similar to the welded tuff dike described by Wolff (1986) in Texas.

In the San Luis Potosí Volcanic Field there are a series of pyroclastic dikes that discontinuously follow a regional fault system, named the Juachín Fault System, which is oriented NW, crosses the whole San Luis Potosí Volcanic Field for about 50 km (Figure 6), and is also related to Basin and Range extension (Aguirre-Díaz and Labarthe-Hernández, 2003). The dikes used segments of these faults as conduits to reach the surface (Figure 10a and b). As in Santa María del Río, the dikes occur as discontinuous lenses and are composed of poorly welded white pyroclastic material, with pumiceous glass shards, sparse lithics, and phenocrysts of quartz, sanidine, and biotite (Figure 10a). The pyroclastic dikes were the source of the widespread Panalillo Inferior Ignimbrite, which is more voluminous in this volcanic field than in Santa María del Río. The dikes range in width from about 50 cm to about 115 m (Figure 10c and d). The widest is found at the village of Pozuelos (Figures 6 and 10d). The dikes occur with high angles, between 75 and 85° (Figure 10a, b and e). This particular dike system can be followed for about 50 km, as discontinuous outcrops with lenticular shapes along the Juachín Fault
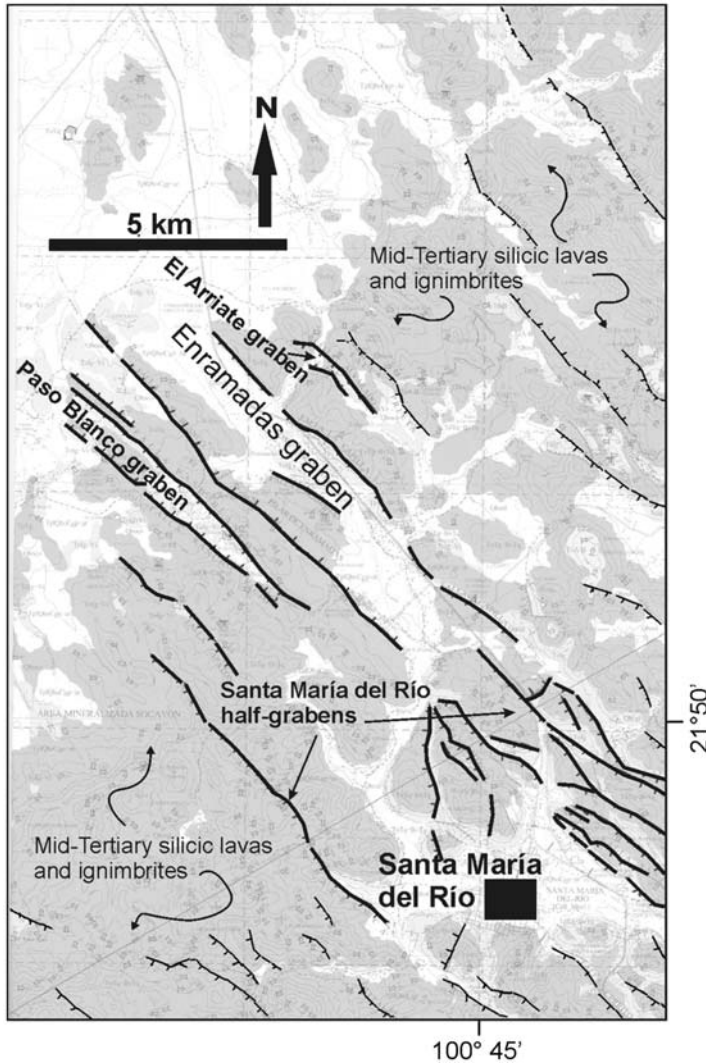
**Figure 7**    Index map of the Santa María del Río Fault System, showing faults, graben and half-graben, all with a NW—SE orientation, which were formed during the Basin and Range extension. Faults in thicker lines indicate those faults used as vents for the Panalillo Inferior Ignimbrite (27 Ma). Vents mostly occur along the master faults of graben or half-graben; for instance, at the Paso Blanco, Enramadas, and El Arriate graben, and at the master faults of the half-graben cluster in the vicinity of Santa María del Río. Shaded areas show extent of mid-Tertiary ignimbrites and lavas.

System (Figure 6). The margins of these dikes are composed of densely welded orange-brown ignimbrite-like material, with fiamme aligned vertically (Figure 10e and f). These welded margins are only a few tens of cm wide, and change to a poorly welded ignimbrite-like material inside the dike (Figure 10f). Some dikes are sheared by post-dike displacements along the fault that they occupied (Figure 10b).
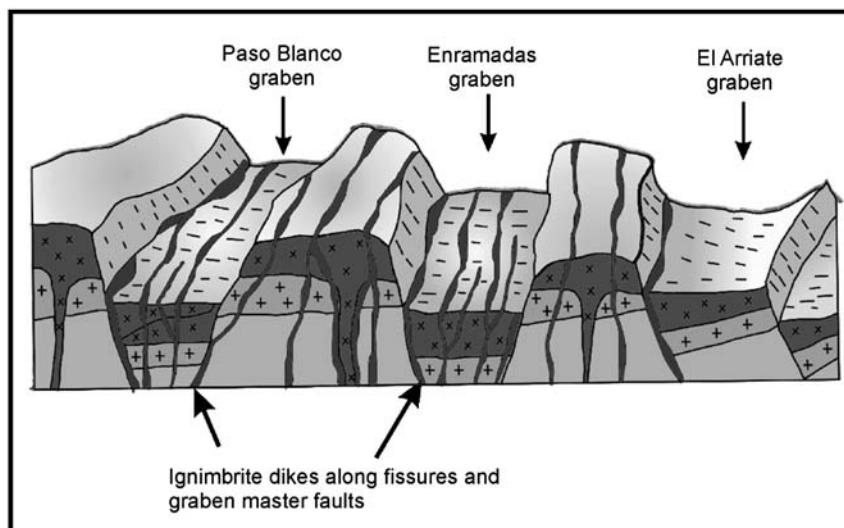
**Figure 8** Schematic cross-section of the grabens at the Santa María del Río Fault System, from which ignimbrite-forming eruptions occurred using the grabens master faults as conduits, now evident as pyroclastic dikes. These eruptions produced the single-block graben calderas of Paso Blanco, Enramadas and El Arriate.

At the Juachín Fault System we also found evidence of fault-related vents in the form of co-ignimbrite lithic-lag breccias. These breccias are found next to large normal faults of this system. The co-ignimbrite breccias are very coarse, with blocks up to 3 m in diameter of older rocks from the region at the vent facies (Figure 11), supported by a pumiceous matrix, and forming a stack of several flow units, each with an ash-rich top. At the vents, the deposit is mostly composed of lithics (mostly of rhyolitic lava), with little content of pumiceous-ash matrix, but this relationship changes with distance from the vent, where the deposit is a sequence of lithic-rich stratified ignimbrites in the proximal facies, to a sequence of ignimbrites with fewer lithics in the distal facies.

## 4.2. The piece-meal graben caldera of Malpaso

Just to the west of Aguascalientes City there is a large depression that has been interpreted as part of the Calvillo graben (Aranda-Gómez, 1989; González Arroyo et al., 1997; Nieto-Samaniego et al., 1999 — Figures 4 and 5). We have named this depression as Malpaso, from the largest town that it contains, because it is neither the Calvillo graben, nor part of the Calvillo graben as the previous works indicate. Our studies show that the Malpaso depression is an explosive-collapse-volcano-tectonic structure, thus a graben caldera. This structure occurs between two well known grabens, the N–S trending Aguascalientes graben to the East and the NE-trending Calvillo graben to the West (Figure 12). The Malpaso depression has several structural characteristics that complicate the original idea for a normal graben; for instance, the chaotic arrangement of the intra-graben downdropped
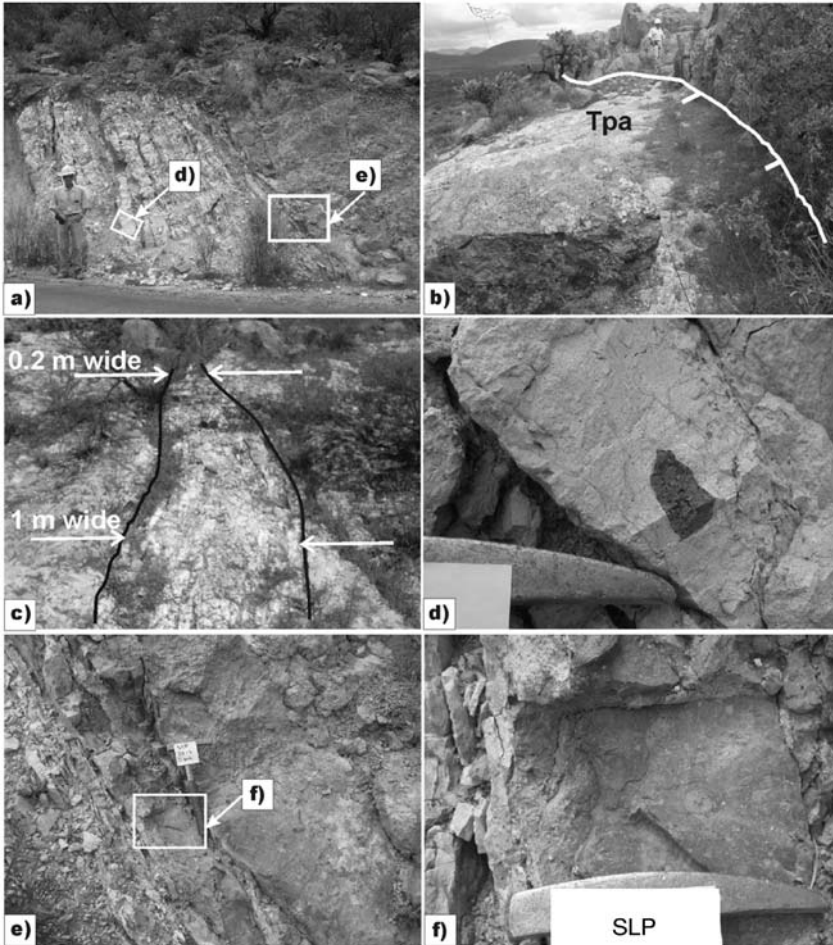
**Figure 9** Ignimbrite feeder dikes of the Panalillo Inferior ignimbrite (Tpa) at the Santa María del Río volcanic field. (a) Western part of a 30 m-wide pyroclastic dike along a half-graben master fault of the Santa María del Río Fault System intruding dacitic lava. (b) Pyroclastic dike of Panalillo Inferior ignimbrite (Tpa) along the western master fault of the Enramadas graben. (c) Pyroclastic dike of Tpa showing the discontinuos and pinching-out shape along strike that is a common feature in these dikes. (d) Close-up of photograph (a) showing a pyroclastic material, mostly composed of a white sintered pumiceous-ash, with sparse lithics. (e) Detail of the contact between the pyroclastic dike shown in photograph (a) and the dacitic lava that makes the country rock; note the darker color of the dike along the contact because of welding of pyroclastic material and the alteration of the country rock by leaching. (f) Close-up of photograph (e) showing the welded (dark) zone of the pyroclastic dike at the contact with the country rock; light-color inclusions are lithics of lava within the dike material.

blocks and the great structural complexity of the faults among these blocks, including reverse faults of the downdropped blocks within the graben, and the high-angle (over 75°) fault scarps that bound this structure to the Northwest and to the Southeast. This structural complexity contrasts with the normal aspect observed
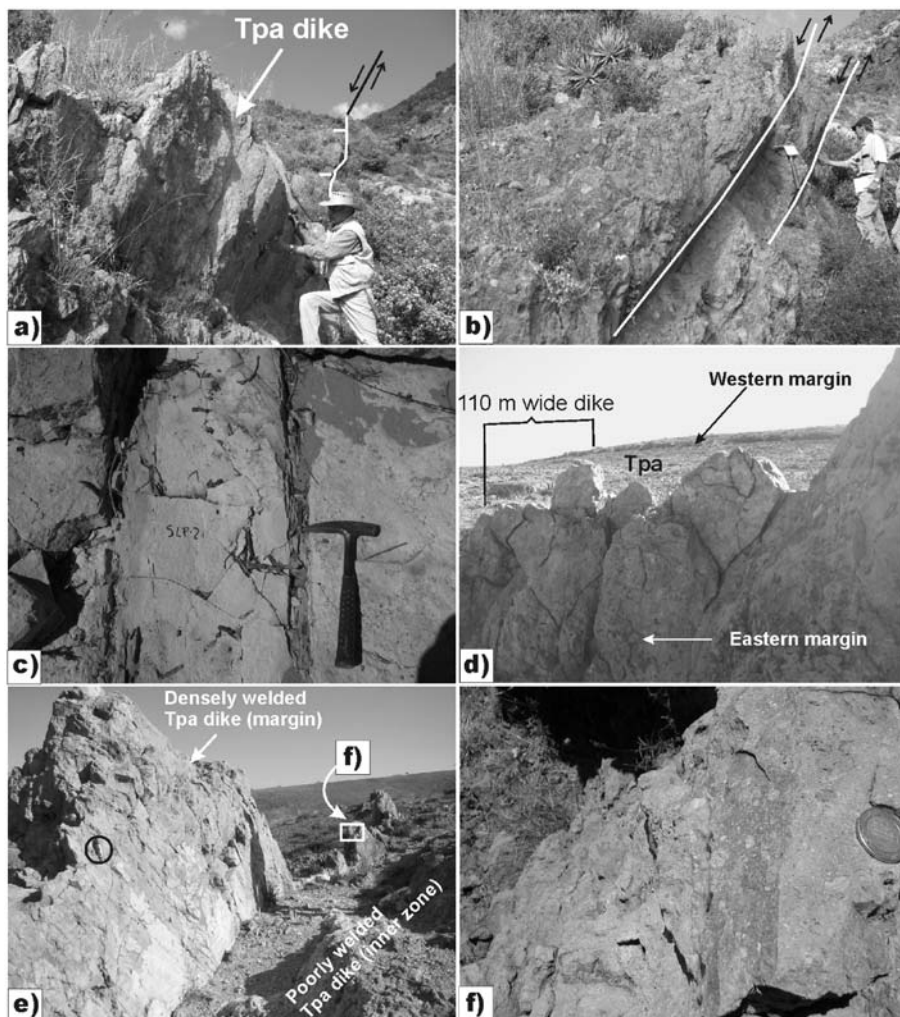
**Figure 10** Ignimbrite feeder dikes of Panalillo Inferior ignimbrite (Tpa) of the San Luis Potosí volcanic field along the NW-oriented Juachín Fault System. (a) Margin of a lithic-rich, welded, ignimbrite dike near El Peaje dam that follow the major normal fault of El Peaje; note the high-angle character of the dike. (b) Same dike margin of photograph (a) affected by normal faults (white lines) with slicken-sides with the same orientation than the dike and the El Peaje fault, indicating that after emplacement of the dike faulting continued on the same fault used as conduit. (c) Plan view of another Tpa dike only a few cm wide; note the sheared margins. (d) Dike at Pozuelos is the widest and largest associated with the Juachín Fault System. Dike is 110 m wide at this site, but it reaches up to 115 m at the widest part. Photograph shows the two welded margins of the dike, which form narrow walls, less than 1 m thick, outstanding from the ground level, which eventually join along strike forming a lense-shape dike. (e) Marginal zones of Pozuelos dike were indurated because they are formed of densely welded Tpa ignimbrite that was silicified along the margins. The internal part of the dike is composed of partly welded, white, pumiceous pyroclastic material similar to that of Tpa ignimbrite. Note pen for scale (in circle). (f) Detail of photograph (e) showing the densely welded, dark, silicified ignimbrite of the dike margin.
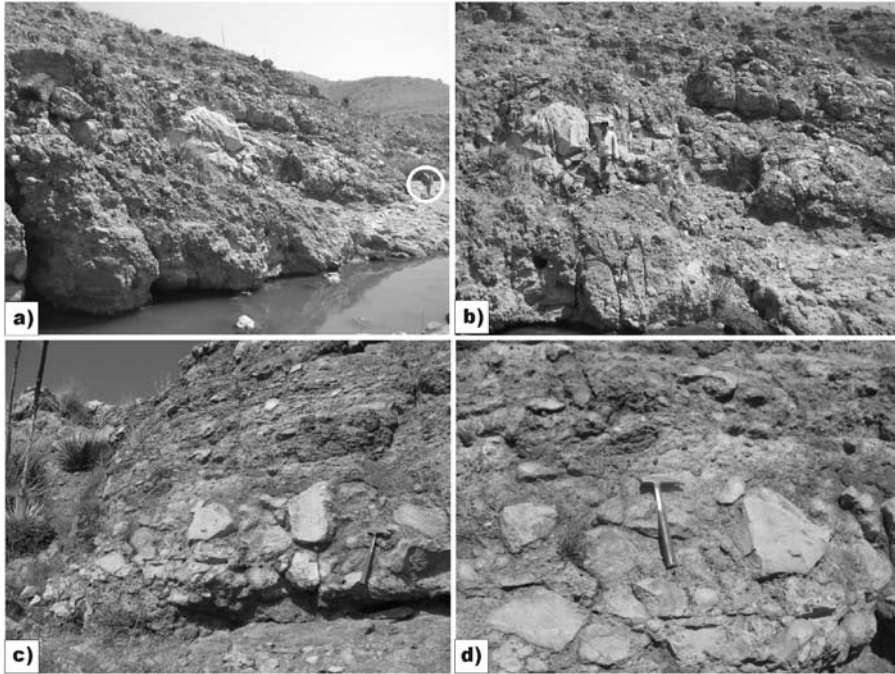
**Figure 11**    Co–ignimbrite lithic–lag breccias associated with Panalillo Inferior ignimbrite in
the Juachín Fault System. (a) Coarse lithic–lag breccias at the vent site, along a major normal
fault next to El Juachín creek. The lithics are mostly of rhyolitic and dacitic lavas of older units
in a pumiceous ash matrix. Note person for scale (in circle). (b) Lithics within breccias at (a)
can be up to 3 m in diameter, this particular one shown in photograph next to geologist is
2.5 m across. (c) Angular clasts in the near-vent facies of the lithic-lag breccias at the vent facies.
The deposit is a layered sequence of several co–ignimbrite lithic–lag breccia units indicating
that it was formed from several eruptive pulses. (d) Detail of lithic–lag breccias supported by
pumice-ash matrix.

in the two grabens that bound this depression to the East (Aguascalientes graben)
and to the West (Calvillo graben), which have more typical normal faults (in the
range of 50–70°) and blocks downdropped with a domino style. These complex
structural characteristics are reflected on the actual morphology of the Malpaso
graben caldera; thus, there is a rough and irregular topography within this
depression, and a more flat or regular morphology outside the depression, with two
well defined limits along two main scarps that bound the depression (Figure 13).
These two main scarps are slightly curved and concave towards the interior of the
depression, forming a NW scarp with a NE to ENE orientation, and a SE scarp
(Sierra El Laurel scarp) with an ENE to NNE orientation (Figure 13). These scarps
mark the limits of the graben caldera. The chaotic blocks within the depression
apparently resulted from the piece-meal collapse of these blocks during the graben
caldera formation on top of the sub-caldera magma chamber. This may explain
the chaotic arrangement of the blocks and inter-block faults, in contrast with the
non-chaotic and more regular structures outside the graben caldera.
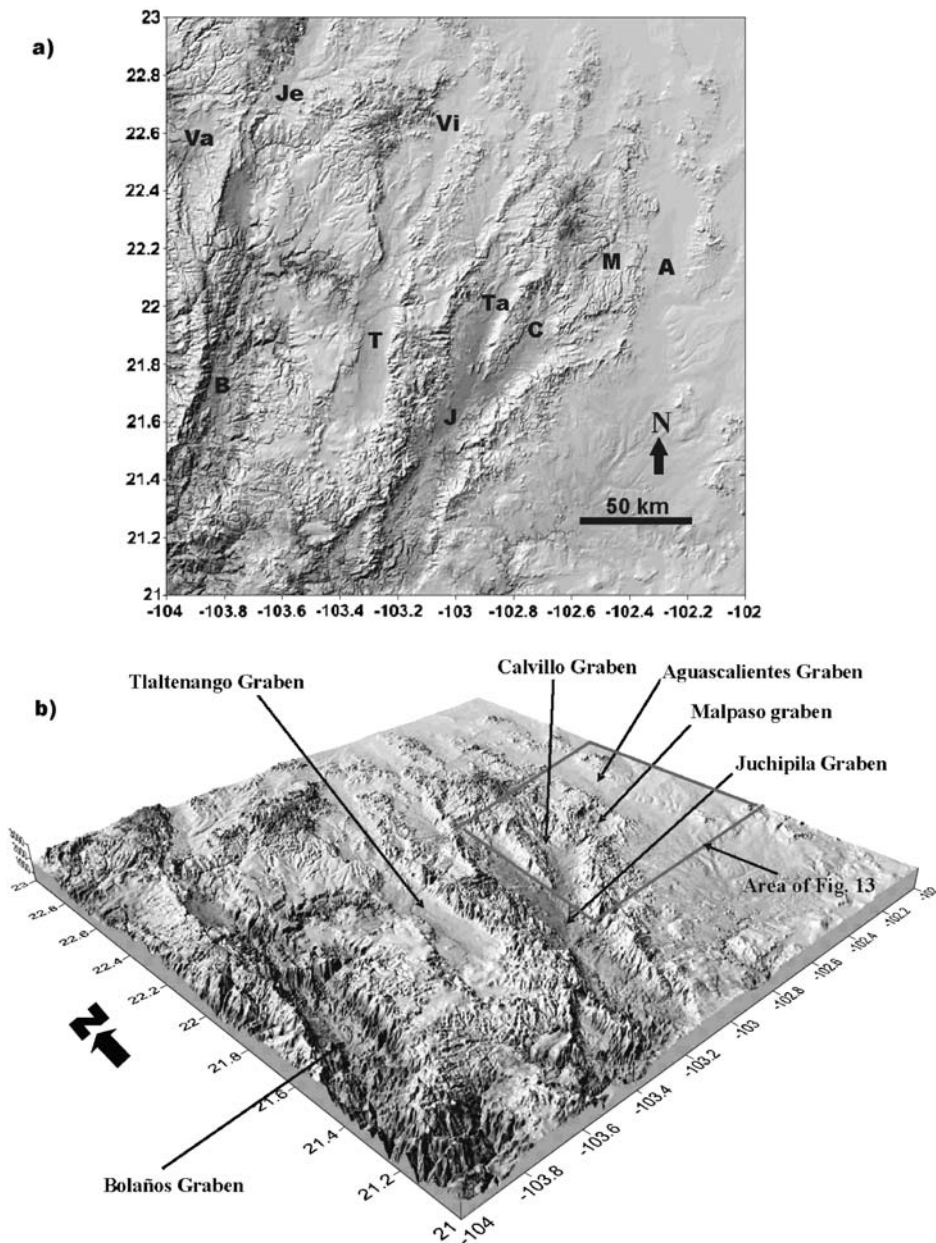
**Figure 12** Digital elevation models of the grabens at the SW sector of the SMO. (a) Plan view; the graben are: Va, Valparaiso; Je, Jerez; Vi, Villanueva; B, Bolaños; T, Tlaltenango; J, Juchipila; Ta, Tabasco; C, Calvillo; M, Malpaso; A, Aguascalientes. (b) 3D model of area shown in (a), indicating also the area covered in Figure 13a. The deepest graben is Bolaños in the segment between 21.2° and 22° Lat. N. This deep segment corresponds to the graben caldera of Bolaños.
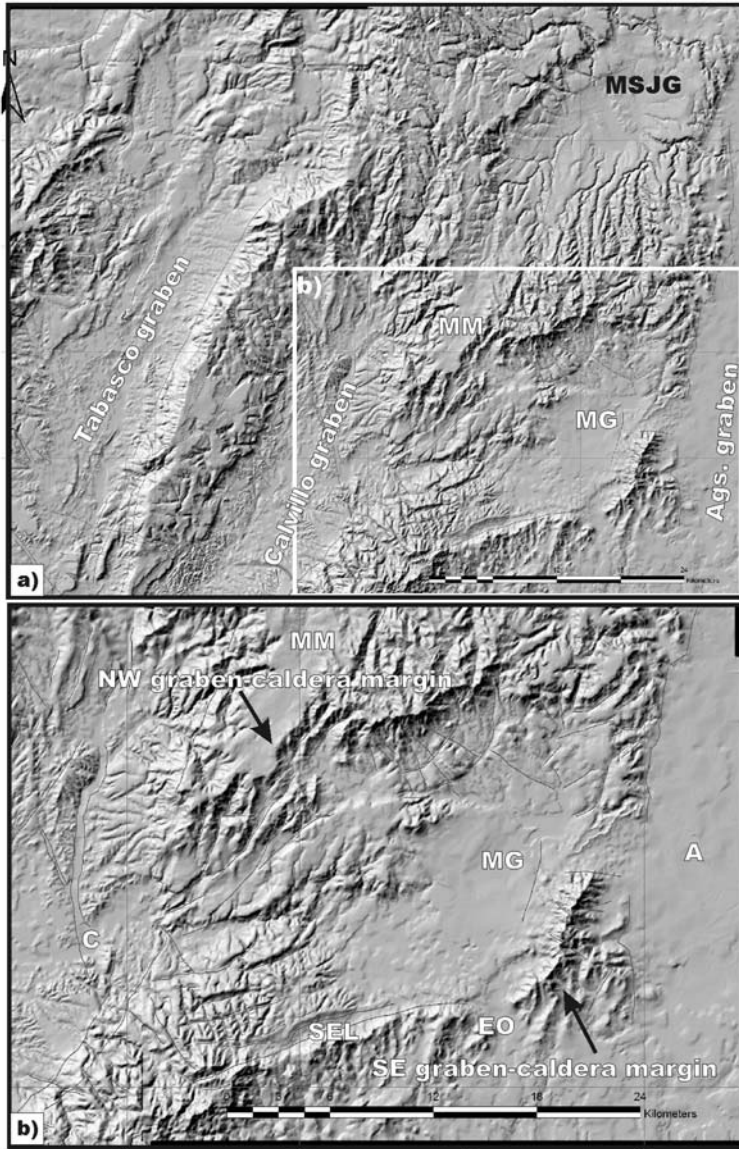
**Figure 13**  Digital elevation models of the Malpaso graben caldera and surrounding area. (a) Malpaso graben caldera (MG) is bordered by two larger graben, Aguascalientes graben to the east (Ags. Graben), and Calvillo graben to the west, farther to the west is the Tabasco graben, which is the northern continuation of the Juchipila graben. Inset shows the area covered in Figure 13b. (b) Malpaso graben caldera shown in more detail. It is a rhombohedral-shape structure oriented NE. Two main fault scarps mark the limits of the graben caldera, to the northwest is the Mesa Montoro (MM) fault scarp, and to the southeast is the Sierra El Laurel (SEL) fault scarp. The type section of the El Ocote ignimbrite is at the internal graben caldera scarp near El Ocote village (EO). A, Aguascalientes City; C, Calvillo City. Thin lines in images are normal faults.

Besides the structural characteristics briefly mentioned above, there are other features that confirm that the Malpaso depression is a graben caldera. The first is a high-grade, rheomorphic ignimbrite that we have named the El Ocote ignimbrite from the type section locality at El Ocote village on the SE margin of the Malpaso depression (Figure 13). This ignimbrite is over 400 m thick (with no base exposed) within the Malpaso depression, and only 20–60 m thick on the NW shoulder of the depression, and about 70–120 m thick on the SE shoulder along the Sierra El Laurel (Figure 14a and b). From the NW margin, the ignimbrite gradually thickens to the North, and once filled an open valley, it now forms the San José de Gracia plateau (Figure 13). This ignimbrite is easily recognised because of its extreme high-grade welding and rheomorphism that formed overturned and even sheath folds (Figure 14c and d). Rheomorphic folds only occur within the Malpaso depression, whereas outside the depression the ignimbrite only shows flat or slightly undulating flow foliation with extremely flattened pumices (Figure 14e and f). The great difference in thickness of the ignimbrite inside and outside the depression represents the intra-caldera and outflow deposits marking the boundary of the graben caldera precisely where this change occurs, that is, on the graben's shoulders or graben caldera margins. The rheomorphic ignimbrite formed folds only in the interior of the graben caldera, possibly as the piece-meal blocks foundered and accommodated during and/or after the caldera collapse.

Further evidence indicates that the vents for the El Ocote ignimbrite are precisely next to the main fault scarps that bound the graben caldera. These include co-ignimbrite collapse-breccias along the internal graben caldera wall and co-ignimbrite lithic-lag breccias within a thick sequence of intra-caldera pyroclastic flow deposits that preceded the El Ocote ignimbrite and that are part of the caldera-forming sequence (Figure 15). This sequence of lithic-rich pyroclastic flow deposits may represent the decompression phase of the sub-caldera magma chamber just before the piece-meal collapse of the graben caldera, which produced the main catastrophic explosive eruption that formed the El Ocote ignimbrite. These observations will be described in more detail in other work that is in progress and that focuses on the stratigraphy, structure, rheomorphism, and volcano-tectonic evolution of the graben caldera of Malpaso.

## 4.3. Pyroclastic dikes of the piece-meal graben caldera of Juchipila

To the west of the Malpaso graben caldera is the graben of Calvillo, which is a northern branch of the larger Juchipila graben (Figures 12 and 13). The Juchipila graben is a structure about 85 long and 20–32 km wide. To the north it branches to the Calvillo graben and the Tabasco graben, which connects to the Villanueva graben that continues farther to the north (Figure 4). Together, the Juchipila and Tabasco graben have a length of 140 km. At segments of this large graben system there are several fissure vents that used the master faults of the graben as conduits. The Juchipila graben in particular contains some of the best examples of these dikes, from which ignimbrite-forming pyroclastic flows were erupted, producing the collapse structure named here the Juchipila graben caldera, after the main town of this area. One is a lithic-rich dike near Juchipila, which is N–S oriented and dips
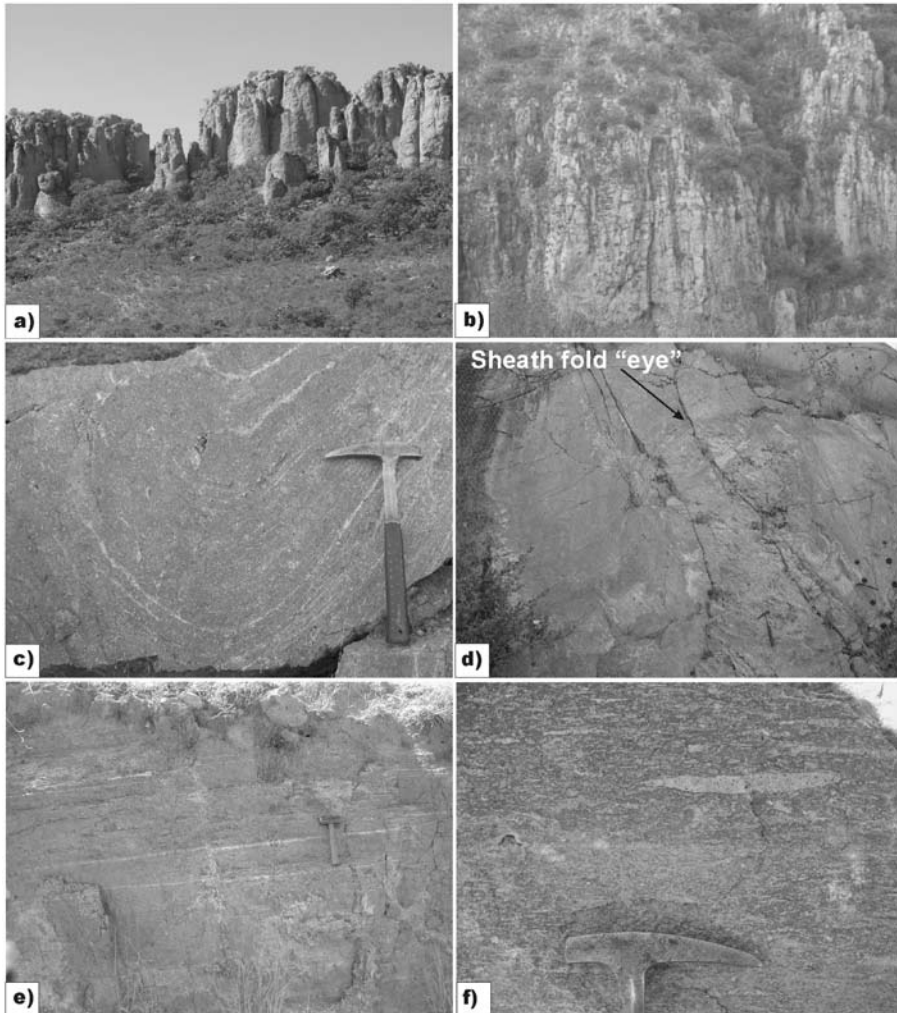
**Figure 14**    El Ocote ignimbrite at several localities. (a) Out-flow, near-vent facies of El Ocote ignimbrite at the Sierra El Laurel, close to the type locality. The ignimbrite is high-grade and forms well-developed columnar joints. Thickness at this site is 70—120 m. (b) Intra-graben caldera ignimbrite fill of El Ocote ignimbrite, near the fault scarp of Sierra El Laurel. The ignimbrite is about 400 m thick with no base exposed, and includes co-ignimbrite lithic-lag breccias (not visible in photograph). (c) Lava-like, rheomorphic fold in extremely high-grade El Ocote ignimbrite at intra-graben caldera outcrop. (d) Sheath fold (eye-structure) in lava-like, extremely rheomorphic high-grade facies of El Ocote ignimbrite in intra-graben caldera outcrop. (e) Flat-lying, lava-like, high-grade El Ocote ignimbrite at near-vent out-flow facies close to El Ocote. (f) Flat-lying, high-grade El Ocote ignimbrite at the northern out-flow facies that formed the Mesa San José de Gracia (MSJG in Figure 13a). Pumice is collapsed but not as extremely elongated as in near-vent facies (Figure 14e).
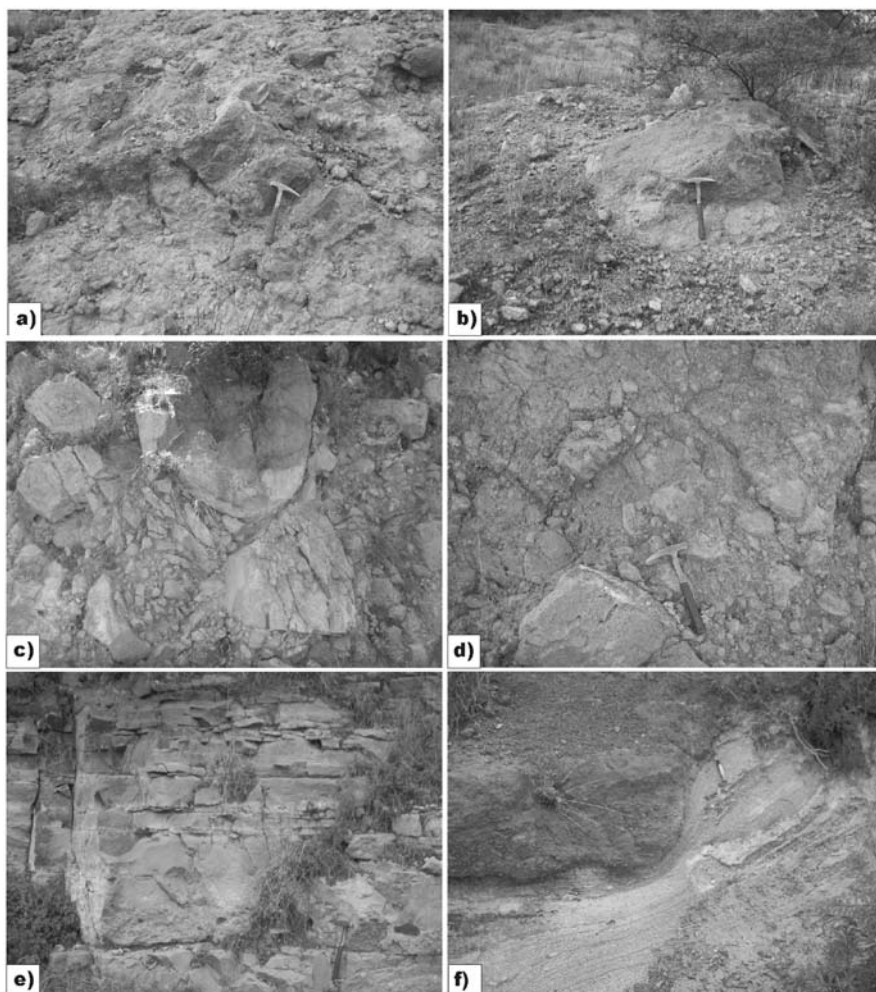
**Figure 15** Co-ignimbrite lithic-lag breccias and intra-graben caldera collapse breccias of Malpaso graben caldera and El Ocote ignimbrite. (a) Co-ignimbrite lithic-lag breccia on the northern margin of the graben caldera showing angular lithics up to 50 cm in diameter in a pumiceous brown matrix. (b) Large lithics in the co-ignimbrite lithic-lag breccia on same site as (a); lithic is 1.5 m in diameter. (c) Intra-graben caldera collapse breccia at the southern fault scarp, next to Sierra El Laurel. (d) Closer view of the collapse-breccia deposit shown in (c). (e) Pre-El Ocote ignimbrite layered sequence at the northern fault scarp composed of surge deposits and thin, non-welded ignimbrite units. (f) Surge deposits at the northern fault scarp showing pumice-rich, lithic-poor pyroclastic flow deposits overlain by a lithic-rich, lithic-lag breccia-like pyroclastic flow deposit (note pen at top of lithic-poor surge deposit).

$85°$ E, following the main trend of the graben of Juchipila. It is 10–20 m wide, intrudes welded ignimbrites, and is partly covered by white Miocene–Pliocene lacustrine deposits that filled the graben after collapse that include index vertebrate fossils of 6–3 Ma (Aguirre-Díaz and Carranza-Castañeda, 2000; Carranza-Castañeda

and Aguirre-Díaz, 2001). The dike is lithic-rich, with 30–40 vol.% of lithic content. The lithics reach up to 40 cm in diameter, and are mostly of welded ignimbrite and propilitised andesite. The pyroclastic fill material of the dike is composed of pumiceous glass shards and pumice lumps. Next to the dike there is a co-ignimbrite lithic-lag breccia with the same type of lithics and components than those of the dike, suggesting that this dike was the feeder of the flat-lying lithic-rich ignimbrite.

Another ignimbrite feeder dike of the Juchipila graben caldera is about 10 km to the west of Jalpa. This dike is unusual in the sense that it is composed of three different pyroclastic dikes that were vertically emplaced episodically using the same conduit (Figure 16). Aguirre-Díaz and Labarthe-Hernández (2003) already mention this composite dike, which is about 50 m thick and has a general orientation of N20°W and an inclination of 75° to the NE. The three pyroclastic dikes are named here as Dike A, Dike B, and Dike C (Figure 16). In all three dikes evidence can be observed for vertical emplacement of pyroclastic material, including a general vertical arrangement of components, vertical fiamme, and what appear to be degassing pipes that are also parallel to the vertical fiamme, suggesting a near surface portion of the observed dike (Figure 16c and d). The pyroclastic dike leached and cooked the country rock (flat-lying red bed deposits), or one of the previously emplaced dikes, indicating that hot pyroclastic material filled the conduit (Figure 16e and f).

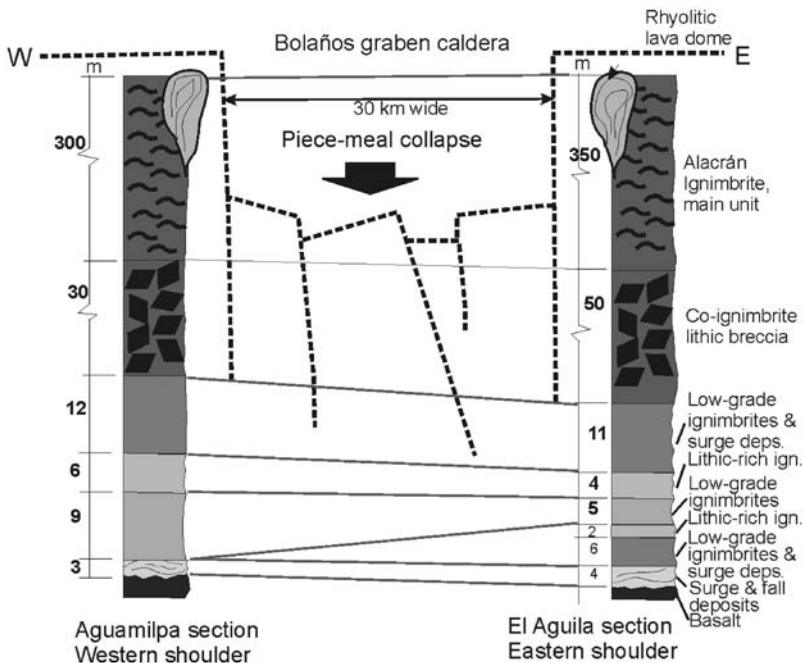## 4.4. Co-ignimbrite lithic-lag breccias of the graben caldera of Bolaños

The graben of Bolaños is located to the west of the Juchipila graben (Figure 12). It is a large graben about 110 km long and 20–30 km wide, with a general N–S orientation. It branches at the north to the Valparaiso (West branch) and Jerez graben (East branch, Figures 4 and 12), making a total length of about 180 km for the Bolaños-Jerez graben system. The Bolaños graben is the deepest of all the grabens in the southern SMO, with a topographic depth of 1,800–2,000 m. The deepest segment of this graben is about 100 km long and includes the mining towns of Bolaños and San Martín de Bolaños (Figure 5), between 21.2° and 22.0° Lat. N (Figure 12). Based on geologic evidence, we deduced that this segment of the graben is a piece-meal graben caldera. The evidence includes the following observations: co-ignimbrite lithic-lag breccias and post-collapse lava domes, both aligned along the graben caldera walls, and the chaotic collapse of blocks inside the graben caldera. A large-volume ignimbrite (possibly over 1000 km$^3$, volcanic rock volume), the Alacrán ignimbrite, resulted from the graben caldera collapse. This ignimbrite is one of the thickest and most voluminous observed in the SMO. Near vent outflows are about 350 m thick. The intra-caldera ignimbrite thickness is unknown because the available bore-hole data do not reach the bottom of the graben caldera, but at least 400 m has been measured by the mining companies. However, the intra-caldera ignimbrite should be much thicker than this minimum value.

We propose that the pyroclastic flows that produced the Alacrán ignimbrite were erupted through fissure vents controlled by the Bolaños graben master faults. This conclusion was inferred by Scheubel et al. (1988), and was confirmed more recently by Aguirre-Díaz and Labarthe-Hernández (2003). The most significant
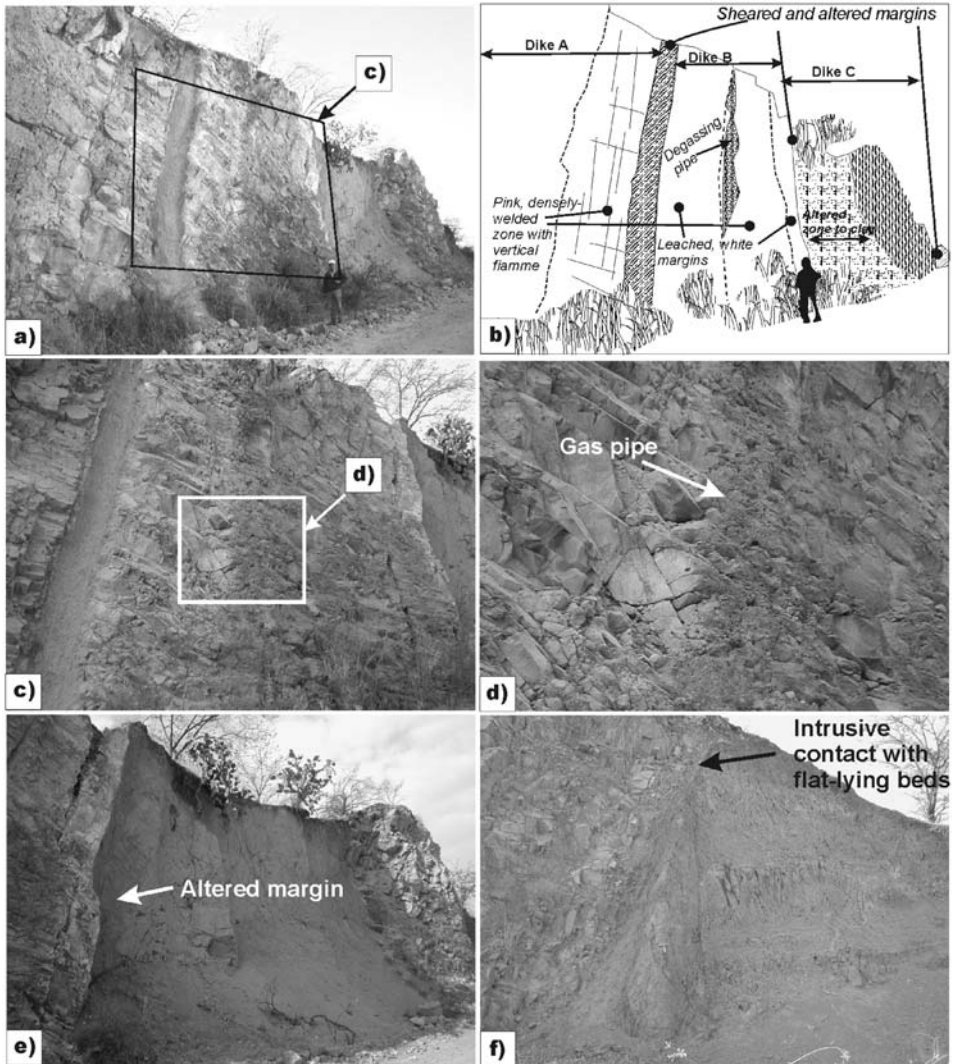
**Figure 16** Composite ignimbrite feeder dike at the western wall of Juchipila graben caldera, located west of Jalpa town (modified from Aguirre-Díaz and Labarthe-Hernández, 2003). (a) General view to the SW showing the three different pyroclastic dikes, named as Dike A, Dike B and Dike C. (b) Sketch of Figure 16a indicating the principal features observed in this composite dike. (c) General view of Dike B showing the leached, light-colour dike margins caused by hydrothermal fluids and shearing of the pyroclastic material along the borders formed during dike emplacement. (d) Detail of the vertical gas-escape pipe in Dike B; the gas pipe is parallel to the dike, indicating a vertical emplacement of the pyroclastic fill material. (e) General view of Dike C showing one of the margins cooked by the Dike B (dark-color zone); Dike C was severly altered to clay by hydrothermal fluids probably associated to Dike B. Dike C gradually changes to a less altered rock towards the opposite side (away from Dike B), where it is a densely, grey ignimbrite-like material with horizontal cooling joints (perpendicular to dike margins). (f) Intrusive contact of Dike C with the country rock, which consists of flat-lying continental deposits gravels and sands (red beds) that pre-date the Oligocene ignimbrites of the area (Modified from Aguirre-Díaz and Labarthe-Hernández, 2003).

observations for this argument are the near vent deposits related to the Alacrán ignimbrite that occur on both sides of the graben caldera of Bolaños (Figures 17–19). These deposits include a sequence of phreatomagmatic surges with ballistic lithics up to 40 cm in diameter (Figures 18c, d and 19f). The surge deposits are lithic-rich layers interbedded with lithic-poor pumiceous surge deposits and ignimbrites up to 2 m thick (Figures 18b, 19b, c, and d). These ignimbrites include lithic-lag breccias with lithics of underlying units up to 35 cm in diameter (Figures 18c, d, 19c and d). Overlying this pyroclastic sequence is the major ignimbrite of Alacrán (Figure 18b), with a co-ignimbrite lithic-lag breccia up to 50 m thick and lithics of underlying rocks up to 1.5 m in diameter (Figure 18e and f). The pre-ignimbrite lithic-rich surge sequence and the overlying co-ignimbrite lithic-lag breccias that grade upward to a major ignimbrite can be observed next to the graben caldera fault scarps, on both sides of the graben caldera (Figures 17, 18a and 19a), that is, East and West of the 20–30 km wide depression (Figure 17). The pre-ignimbrite surge sequence can be interpreted as the decompression phase of the sub-graben caldera magma chamber previous to the graben caldera collapse, similar to the case of El Ocote ignimbrite at the Malpaso graben caldera. After the collapse and ignimbrite emplacement, several rhyolitic lava domes were emplaced along the graben caldera master faults (Figures 17, 18a and 19e). These domes are thought to represent the



**Figure 17** Sketch of a cross-section of the Bolaños graben caldera showing the two type sections for the Alacrán Ignimbrite, the major volcanic event related to the graben caldera collapse, with co-ignimbrite lag-breccias at both sides of the graben. See text for details. Photographs of these two sections are shown in Figures 18 and 19.
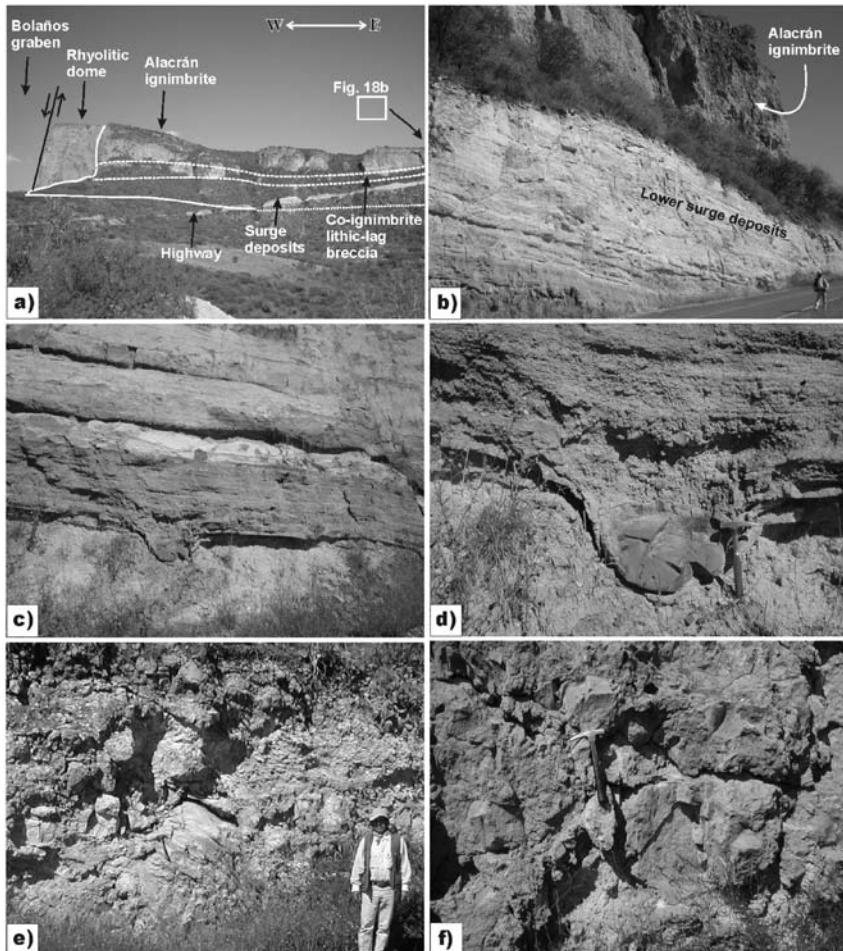
**Figure 18** Alacrán Ignimbrite type section at the eastern graben caldera margin. (a) Panoramic view to the north of the Alacrán Ignimbrite on the eastern shoulder of the graben caldera of Bolaños, indicating the two main deposits that compose this section, the lower surge deposits and the major ignimbrite with a thick basal co-ignimbrite lithic-lag breccia. Also indicated is a rhyolitic lava dome that post-dates the Alacrán Ignimbrite. (b) General view of the sequence, with the underlying surge deposits sequence (white, layered deposits), and the overlying major ignimbrite. (c) Lower surge deposits with ballistic blocks. (d) Detail of a ballistic lithic indicating a trajectory from west (left) to east (right), confirming that the graben caldera of Bolaños was the source for these deposits. (e) Coarse co-ignimbrite lithic-lag breccia at the base of Alacrán Ignimbrite with lithics of underlying lavas up to 1.5 m in diameter. (f) Closer view of co-ignimbrite lithic-lag breccia of Alacrán Ignimbrite, showing a matrix that is composed of pumice and ash (hammer for scale).

degassed magma that remained in the sub-graben caldera magma chamber after the explosive ignimbrite-forming eruptions, as occurs with the ring-lava domes in a typical caldera cycle, such as in the Valles caldera in New Mexico (Heiken et al., 1990).
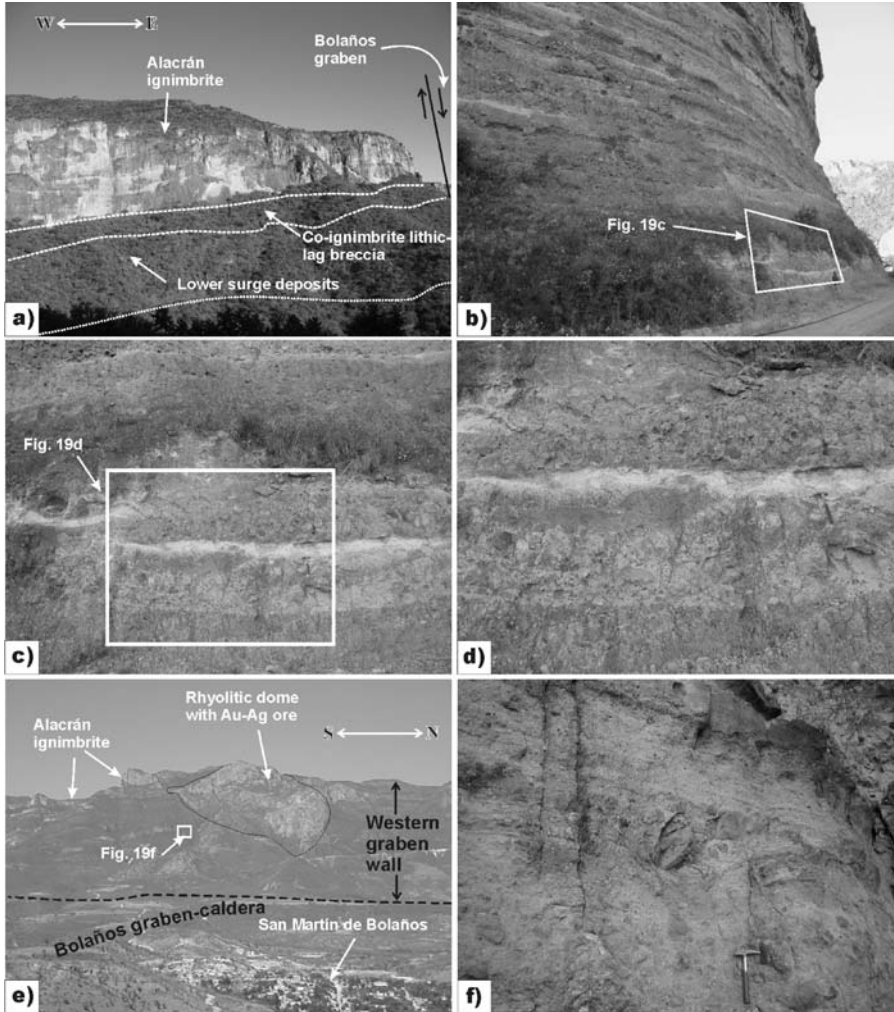
**Figure 19** Alacrán Ignimbrite type section at the western graben caldera margin and at another section to the south near San Martín de Bolaños. (a) Panoramic view to the northeast of the Alacrán Ignimbrite on the western shoulder of the graben caldera of Bolaños, showing the two main deposits that compose this section, the lower surge deposits and the upper major ignimbrite with a basal co-ignimbrite lithic-lag breccia. This sequence corresponds to a similar sequence at the opposite side of the graben shown in Figure 19. (b) Surge deposits and minor ignimbrites forming the lower layered sequence. (c) Closer view of the co-ignimbrite lithic-lag breccias shown in Figure 19b. Note the lense-shape of the deposits that produce a general cross-bedding. (d) Detail of the co-ignimbrite lithic-lag breccia shown in Figure 19c, showing a lithics-rich base that changes to an upper ash-rich deposit, which is interpreted as the co-ignimbrite ash fall deposit. (e) Panoramic view to the west of the western wall of the graben caldera of Bolaños, at San Martín de Bolaños. (f) Lithic-rich surge deposits of the lower sequence at the western graben caldera wall near San Martín de Bolaños, showing ballistic blocks and similar features as those observed at other near vent localities, such as those in Figure 18.

# 5. Conclusions

- The SMO is the largest continuous ignimbrite province in the world, with a minimum estimated rock volume of about $400,000 \, \text{km}^3$.
- The Ignimbrite Flare-up in Mexico was a period of intense explosive volcanic activity that produced enormous volumes of silicic ignimbrite sheets, which took place mainly between 38 and 23 Ma in Mexico.
- This paper summarises evidence that suggest that a large volume of the ignimbrites of the SMO were erupted from fissural vents related to grabens and fault systems associated with the Basin and Range extension.
- We propose the name of graben caldera for a volcano-tectonic explosive collapse structure from which large-volume ignimbrites were erupted through the master faults of the graben and the faults of the intra-graben collapsed blocks. This implies the existence of a sub-graben caldera magma chamber that was at least partially controlled by the regional extensional tectonics, in this case, the Basin and Range extensional regime.
- The graben calderas observed in the SMO include three types, single-block (piston equivalent), piece-meal (the most common), and half-graben caldera (trap-door equivalent).
- The succession associated with the graben calderas of the SMO in general consists of a red beds sequence followed by a pre-major ignimbrite sequence of pyroclastic surge deposits and minor ignimbrites, followed by the major ignimbrite, and then the emplacement of silicic lava domes along the main trend of the graben. This succession represents the typical graben caldera cycle in the SMO, from magma chamber depressurisation phase (surge deposits), the graben caldera collapse and ignimbrite emplacement (major ignimbrite), and the post–collapse emplacement of degassed magma as lava domes through the main faults of the collapsed structure. A Plinian fallout phase is not evident in the graben caldera volcanic eruption cycle.
- Ignimbrite-feeder pyroclastic dikes are associated with regional fault systems and graben caldera master faults, and represent the vents through which large-volume ignimbrite-forming pyroclastic flows were erupted. Pyroclastic dikes range in size from a few cm to over 100 m wide, commonly have lense-shapes, and can be welded to non-welded, lithic–rich or lithic-poor.

## ACKNOWLEDGMENTS

## REFERENCES

Aguillón-Robles, A., Rodríguez-Ríos, R., Leroy, J.L., Aranda-Gómez, J.J., Marín-Solís, J.D., 1996. Geología y Características del Centro Volcánico de Pinos, Zac. Instituto Nacional de Geoquímica, A.C., México. Actas Inageq, 2, 3–8.

Aguirre-Díaz, G.J., Carranza-Castañeda, O., 2000. Las grandes cuencas del Oligo-Mioceno del centro de México. Segunda Reunión Nacional de Ciencias de la Tierra. Geos, 20, 301.

Aguirre-Díaz, G.J., Ferrari, L., Labarthe-Hernández, G., 1998. The source paradigm of the voluminous ignimbrites of the Sierra Madre Occidental, Mexico. European Geophysical Society General Assembly 1998. Ann. Geophys., 16, 1210.

Aguirre-Díaz, G.J., Ferrari, L., Rosas-Elguera, J., Urrutia-Fucugauchi, J., 1997. The Sierra Madre Occidental Southern Transect. B&R grabens and a new caldera. General Assembly IAVCEI, Puerto Vallarta 1997. Abstracts volume 13.

Aguirre-Díaz, G.J., Labarthe-Hernández, G., 1999. Fissure-source vs. caldera-source for the voluminous ignimbrites of the Sierra Madre Occidental, Mexico. Geological Society of America Annual Meeting, Abstracts with Programs, 31, 477.

Aguirre-Díaz, G.J., Labarthe-Hernández, G., 2003. Fissure ignimbrites: fissure source origin for voluminous ignimbrites of the Sierra Madre Occidental and its relationship with Basin and Range faulting. Geology, 31, 773–776.

Aguirre-Díaz, G.J., Labarthe-Hernández, G., Carranza-Castañeda, O., Tristán-González, M., Nieto-Obregón, J., Gutiérrez-Palomares, I., 2005. Graben-calderas de la Sierra Madre Occidental, México. Reunión Anual de la Unión Geofísica Mexicana. Geos, 25, 201–202.

Aguirre-Díaz, G.J., Labarthe-Hernández, G., Tristán-González, M., Nieto-Obregón, J., Gutiérrez-Palomares, I., 2007. Graben-calderas. Volcano-tectonic explosive collapse structures of the Sierra Madre Occidental, Mexico. European Geosciences Union Annual Meeting at Viena, Geophysical Research Abstracts, 9, 04704.

Aguirre-Díaz, G.J., McDowell, F.W., 1991. The volcanic section at Nazas, Durango, Mexico, and the possibility of widespread Eocene volcanism within the Sierra Madre Occidental. J. Geophys. Res., 96, 13-373–13-388.

Aguirre-Díaz, G.J., McDowell, F.W., 1993. Nature and timing of faulting and syn-extensional magmatism in the southern basin and range, central-eastern Durango, Mexico. Bull. Geol. Soc. Am., 105, 1435–1444.

Alba, L.A., Chavez, R., 1974. K–Ar ages of volcanic rocks from central Sierra Peña Blanca, Chihuahua, Mexico. Isochron West, 10, 21–23.

Albretch, A., Goldstein, S.L., 2000. Efects of basement composition and age on silicic magmas across an accreted terrane–Precambrian crust boundary, Sierra Madre Occidental, Mexico. J. S. Am. Earth Sci., 13, 255–273.

Aranda-Gómez, J.J., 1989. Geología Preliminar del Graben de Aguascalientes. Universidad Nacional Autónoma de México. Revista del Instituto de Geología, 8, 22–32.

Aranda-Gómez, J.J., Godchaux, M.M., Aguirre-Díaz, G.J., Bonnichsen, B., Martínez-Reyes, J., 2003. Three superimposed volcanic arcs in the southern Cordillera — from the early Cretaceous to the Miocene, Guanajuato, Mexico. In: Geologic transects across Cordilleran Mexico, Guidebook for field trips of the 99th Annual Meeting of the Cordilleran Section of the Geological Society of America, Mexico, D.F., April 5–8, 2003, Universidad Nacional Autónoma de México, Instituto de Geología, Publicación Especial 1, Field trip, Vol. 6, pp. 123–168.

Aranda-Gómez, J.J., Henry, C.D., Luhr, J.F., 2000. Evolución tectonomagmática post-paleocénica de la Sierra Madre Occidental y de la porción meridional de la provincia tectónica de Cuencas y Sierras, Mexico. Boletín de la Sociedad Geológica Mexicana, 53, 59–71.

Aranda-Gómez, J.J., Henry, C.D., Luhr, J.F., McDowell, F.W., 1997. Cenozoic volcanism and tectonics in NW Mexico — a transect across the Sierra Madre Occidental volcanic field and observations on extension-related magmatism in the southern Basin and Range and Gulf of California tectonic provinces. In: Aguirre-Díaz, G.J., Aranda-Gómez, J.J., Carrasco-Núñez, G. and Ferrari, L. (Eds), Magmatism and tectonics of central and northwestern Mexico — a selection of the 1997 IAVCEI General Assembly excursions: México, D.F., Universidad Nacional Autónoma de México, Instituto de Geología, Excursión, Vol. 11, pp. 41–84.

Aranda-Gómez, J.J., McDowell, F.W., 1998. Paleogene extension in the southern basin and range province of México: syndepositional tilting of Eocene red beds and Oligocene volcanic rocks in the Guanajuato mining district. Int. Geol. Rev., 40, 116–134.

Atwater, T., 1989. Plate tectonic history of the northeast Pacific and western North America. In: Winterer, E.L., Hussong, D.M. and Decker, R.W. (Eds), The Geology of North America, Vol. N: The Eastern Pacific Ocean and Hawaii. Geological Society of America, Boulder, CO, pp. 21–72.

Bagby, W.C., Cameron, K.L., Cameron, M., 1981. Contrasting evolution of calc–alkalic volcanic and plutonic rocks of western Chihuahua, Mexico. J. Geophys. Res., 86, 10402–10410.

Ban, M., Hasenaka, T., Delgado-Granados, H., Takaoka, N., 1994. K–Ar ages of lavas from shield volcanoes in the Michoacán–Guanajuato volcanic field. Geofis. Int., 3, 467–474.

Bockoven, N.T., 1981. Tertiary stratigraphy of the Sierra Del Gallego area of Chihuahua with comparisons to the Peña Blanca uranium district. In: Goodell, P.C. and Waters, A.C. (Eds), Uranium in volcanic and volcaniclastic rocks, AAPG Studies Geol., Vol. 13, pp. 181–187.

Cameron, K.L., Cameron, M., 1986. Geochemistry of quartz-normative igneous rocks from the Chinati Mountains and Terlingua areas, west Texas: a comparison with Cenozoic volcanic rocks from Chihuahua and Baja California Sur, Mexico. In: Price, J.G., Henry, C.D., Parker, D.F. and Barker, D.S. (Eds), Igneous geology of Trans-Pecos Texas, Univ. Texas, Austin, Bureau of Economic Geology, Guidebook, Vol. 23, pp. 143–163.

Cameron, K.L., Cameron, M., Bagby, W., Moll, J.E., Drake, R., 1980. Petrologic characteristics of mid-Tertiary volcanic suites, Chihuahua, Mexico. Geology, 8, 87–91.

Cameron, K.L., Nimz, G.J., Kuentz, D., Niemeyer, S., Jun, S., 1989. Southern Cordillera Basaltic Andesite Suite, southern Chihuahua, Mexico: a link between Tertiary continental arc and flood basalt volcanism in North America. J. Geophys. Res., 94, 7817–7840.

Capps, R.C., 1981. Geology of the Rancho El Papalote area, Chihuahua, Mexico. In: Goodell, P.C. and Waters, A.C. (Eds), Uranium in volcanic and volcaniclastic rocks, AAPG Studies Geol., Vol. 13, pp. 243–264.

Cárdenas, D.F., 1983. Volcanic stratigraphy and uranium deposits of central Sierra Peña Blanca, Chihuahua, Mexico. In: Clark, K.F. and Goodell, P.C. (Eds), Geology and mineral resources of north-central Chihuahua, El Paso Geological Society Guidebook, 1983 Field Conference, 325–334.

Carranza-Castañeda, O., Aguirre-Díaz, G.J., 2001. Índices bioestratigráficos de las cuencas sedimentarias del Terciario Tardío del centro de México. Reunión Anual de la Unión Geofísica Mexicana. Geos, 21, 206.

Cerca-Martínez, M., Aguirre-Díaz, G.J., López-Martínez, M., 2000. The geologic evolution of southern Sierra de Guanajuato, Mexico: a documented example of the transition from the Sierra Madre Occidental to the Mexican volcanic belt. Int. Geol. Rev., 12, 131–151.

Clark, K.F., Damon, P.F., Schutter, S.R., Shaffiqullah, M., 1980. Magmatismo en el norte de México en relación a los yacimientos metalíferos. Geomimet, 106, 51–71.

Clark, K.F., Damon, P.E., Shafiqullah, M., Ponce, S.B.J., Cárdenas, F.D., 1981. Sección geológica-estructural a traves de la parte sur de la Sierra Madre Occidental, entre Fresnillo y la costa de Nayarit, Asociación de Ingenieros de Minas Metalurgistas y Geólogos de México, Memoria, XIV Convención Nacional, 74, 104.

Clark, K.F., Foster, C.T., Damon, P.E., 1982. Cenozoic mineral deposits and subduction-related magmatic arcs in Mexico. Geol. Soc. Am. Bull., 93, 533–544.

Clemons, R.E., McLeroy, D.F., 1966. Resumen de la geología de la Hoja Torreón, Universidad Nacional Autónoma de México, Instituto de Geología, Carta Geológica de México, Hoja Torreón, 13R-1 (1), 1:100,000.

Cochemé, J.J., Demant, A., 1991. Geology of the Yécora area, northern Sierra Madre Occidental, Mexico. In: Pérez-Segura, E. and Jacques-Ayala, C. (Eds), Studies of Sonoran geology, Geological Society of America Special Paper, 254, pp. 81–94.

Damon, P.E., Nieto-Obregón, J., 1979. Un plegamiento neogénico en Nayarit y Jalisco, y evolución geomórfica del Rio Grande de Santiago, Reporte en progreso. Asociación de Ingenieros de Minas Metalurgistas y Geólogos de México, Memoria XII Convención Nacional, 156, 191.

Damon, P.E., Shafiqullah, M., Clark, K.F., 1981. Age trends of igneous activity in relation to metallogenesis in the southern Cordillera. Relations of tectonics to ore deposits in the southern Cordillera. Arizona Geol. Soc. Digest, 14, 137–153.

Duex, T.W., 1983. Geology of the Cuauhtemoc area, central Chihuahua, Mexico. In: Clark, K.F. and Goodell, P.C. (Eds), Geology and mineral resources of north-central Chihuahua, El Paso Geological Society Guidebook, 1983 Field Conference, 213–218.

Echegoyén, J., Romero-Martínez, S., Velázquez-Silva, S., 1970. Geología y yacimientos minerales de la parte central del distrito minero de Guanajuato. Boletín Consejo de Recursos Minerales no Renovables, 75, 35.

Edwards, D.J., 1955. Studies of some early Tertiary red conglomerates of central Mexico, U.S. Geological Survey, Professional Paper, 264-H, 153–185.

Enciso-De La Vega, S., 1963. Resumen de la geología de la Hoja Nazas, estado de Durango, Universidad Nacional Autónoma de México, Instituto de Geología, Carta Geológica de México, Hoja Nazas, 13-k (6), 1:100,000.

Ferrari, L., López-Martínez, M., Aguirre-Díaz, G.J., Carrasco-Núñez, G., 1999. Space-time patterns of Cenozoic arc volcanism in Central Mexico: from Sierra Madre Occidental to Mexican Volcanic Belt. Geology, 27, 303–306.

Ferrari, L., López-Martínez, M., Rosas-Elguera, J.G., 2002. Ignimbrite flare-up and deformation in the southern Sierra Madre Occidental, western Mexico: implications for the late subduction history of the Farallon plate. Tectonics, 21, 1–24.

Gastil, R.G., Krummenacher, D., Jensky, W.E., 1979. Reconnaissance geology of west-central Nayarit, Mexico. Geological Society of America, Text to accompany Map and Chart Series Map MC-24, 8 p.

Gilmer, A.L., Clark, K.F., Conde, J., Hernández, I., Figueroa, J., Porter, E.W., 1988. Sierra de Santa María, Velardeña Minino District, Durango, Mexico. Econ. Geol., 83, 1802–1829.

González-Arroyo, A., Martínez-Tovar, M., Montañez-Castro, A., Chavez-Rangel, F., García-Ruiz, J.M., 1997. Consejo de Recursos Minerales, SECOFI, Carta Geológica Minera Zacatecas, F13–6, Escala 1:250,000.

Goodell, P.C., 1981. Geology of the Peña Blanca uranium deposits, Chihuahua, Mexico. In: Goodell, P.C. and Waters, A.C. (Eds), Uranium in volcanic and volcaniclastic rocks, AAPG Studies Geol., Vol. 13, pp. 275–291.

Gross, W.H., 1975. New ore discovery and source of silver–gold veins, Guanajuato, Mexico. Econ. Geol., 70, 1175–1189.

Gutiérrez-Palomares, I., Aguirre-Díaz, G.J., 2005. Características físicas de la Ignimbrita Alacrán, Bolaños, Jalisco. Reunión Anual de la Unión Geofísica Mexicana. Geos., 25, 209.

Heiken, G., Goff, F., Gardner, J.N., Baldridge, W.S., 1990. The Valles/Toledo Caldera Complex, Jemez Volcanic Field, New Mexico. Ann. Rev. Earth Planet. Sci., 18, 27–53.

Henry, C.D., Aranda-Gómez, J.J., 1992. The real southern basin and range: mid- to late Cenozoic extension in Mexico. Geology, 20, 701–704.

Henry, C.D., Aranda-Gómez, J.J., 2000. Plate interactions control middle–late Miocene, proto-Gulf and Basin and Range extension in the southern Basin and Range. Tectonophysics, 318, 1–26.

Henry, C.D., Fredrikson, G., 1987. Geology of part of southern Sinaloa, Mexico adjacent to the Gulf of California. Geological Society of America Map and Chart Series MCH063, 14 p.

Henry, C.D., Price, J.G., 1984. Variations in caldera development in the Tertiary volcanic field of Trans-Pecos, Texas. J. Geophys. Res., 89, 8765–8786.

Keller, P.C., Bockoven, N.T., McDowell, F.W., 1982. Tertiary volcanic history of the Sierra del Gallego area, Chihuahua, Mexico. Geol. Soc. Am. Bull., 93, 303–314.

Labarthe-Hernández, G., De la Huerta-Cobos, M.A., 1998. Geología del semi-graben de Bledos, San Luis Potosí, México, Esc. 1:20,000. Universidad Autónoma de San Luis Potosí, Instituto de Geología, Folleto Técnico 124, 33 p.

Labarthe-Hernández, G., Jiménez-López, L.S., 1992. Características físicas y estructura de lavas e ignimbritas riolíticas en la Sierra de San Miguelito, S.L.P. Universidad Autónoma de San Luis Potosí, Instituto de Geología, Folleto Técnico 114, 31 p.

Labarthe-Hernández, G., Jiménez-López, L.S., 1993. Geología del domo Cerro Grande, Sierra de San Miguelito, S.L.P. Universidad Autónoma de San Luis Potosí, Instituto de Geología Folleto Técnico 117, 22 p.

Labarthe-Hernández, G., Tristán-González, M., 1978. Cartografía geológica Hoja San Luis Potosí. Universidad Autónoma de San Luis Potosí, Instituto de Geología y Metalurgia, Folleto Técnico 69, 41 p.

Labarthe-Hernández, G., Tristán-González, M., 1980a. Cartografía Geológica, Hoja Santa María del Río, S.L.P. Universidad Autónoma de San Luis Potosí, Instituto de Geología y Metalurgia, Folleto Técnico 67, 32 p.

Labarthe-Hernández, G., Tristán-González, M., 1980b. Cartografía Geológica Hoja San Francisco, S.L.P. Universidad Autónoma de San Luis Potosí, Instituto de Geología y Metalurgia, Folleto Técnico 69, 28 p.

Labarthe-Hernández, G., Tristán-González, M., Aguillón-Robles, A., 1985. Análisis de la Geología del Yacimiento de Hierro del Cerro de Mercado Durango, Dgo. GEOMIMET XIV Época, No 151.

Labarthe-Hernández, G., Tristán-González, M., Aranda-Gómez, J.J., 1982. Revisión estratigráfica del Cenozoico de la parte central del estado de San Luis Potosí: Universidad de San Luis Potosí, Instituto de Geología y Metalurgía, Folleto Técnico 85, 208 p.

Labarthe-Hernández, G., Tristán-González, M., Barboza-Gudino, J.R., Mata-Segura, J.L., 1996. Cartografía Geológica 1:10,000 del área de La Ciénega y su correlación con otros distritos mineros de la Sierra Madre Occidental en el Estado de Durango. Universidad Autónoma de San Luis Potosí, Instituto de Geología (reporte interno inédito peparado para Compañía Minera Peñoles), 86 p.

Lipman, P.W., Prostka, H.J., Christiansen, R.L., 1972. Cenozoic volcanism and plate tectonic evolution of the western United States I, early and middle Cenozoic. Philos. Trans. R. Soc. Lond. Ser. A, 271, 217–248.

Lipman, P.W., Steven, T.A., Mehnert, H.H., 1970. Volcanic history of the San Juan Mountains, Colorado, as indicated by potassium–argon dating. Geol. Soc. Am. Bull., 81, 2329–2352.

Luhr, J.F., Henry, C.D., Housh, T.B., Aranda-Gómez, J.J., McIntosh, W.C., 2001. Early extension and associated mafic alkalic volcanism from the southern Basin and Range province: geology and petrology of the Rodeo and Nazas volcanic fields, Durango, Mexico. Geol. Soc. Am. Bull., 113, 760–773.

Lyons, J.I., 1988. Geology and ore deposits of the Bolaños silver district, Jalisco, Mexico. Econ. Geol., 83, 1560–1582.

Martínez-Reyes, J., 1992. Mapa geológico de la Sierra de Guanajuato con resumen de la geología de la Sierra de Guanajuato. Universidad Nacional Autónoma de México, Instituto de Geología, Cartas geológicas y mineras 8, escala 1:100,000.

Mauger, R.L., 1981. Geology and petrology of the central part of the Calera-Del Nido block, Chihuahua, Mexico. In: Goodell, P.C. and Waters, A.C. (Eds), Uranium in volcanic and volcaniclastic rocks, AAPG Studies Geol., Vol. 13, pp. 205–242.

Mauger, R.L., 1983a. The geology and volcanic stratigraphy of the Sierra Sacramento block near Chihuahua City, Chihuahua, Mexico. In: Clark, K.F. and Goodell, P.C. (Eds), Geology and mineral resources of north-central Chihuahua, El Paso Geological Society Guidebook, 1983 Field Conference, 137–156.

Mauger, R.L., 1983b. Geologic map of the Majalca-Punta De Agua area, central Chihuahua, Mexico. In: Clark, K.F. and Goodell, P.C. (Eds), Geology and mineral resources of north-central Chihuahua, El Paso Geological Society Guidebook, 1983 Field Conference, 169–174.

Mauger, R.L., 1983c. A geologic study of the Providencia-El Nido area, northeast flank of Sierra El Nido, central Chihuahua, Mexico. In: Clark, K.F. and Goodell, P.C. (Eds), Geology and mineral resources of north-central Chihuahua, El Paso Geological Society Guidebook, 1983 Field Conference, 187–193.

Mauger, R.L., Dayvault, R.D., 1983. The tertiary volcanic rocks in lower Santa Clara canyon, central Chihuahua, Mexico. In: Clark, K.F. and Goodell, P.C. (Eds), Geology and mineral resources of north-central Chihuahua, El Paso Geological Society Guidebook, 1983 Field Conference, 1175–186.

McDowell, F.W., Clabaugh, S.E., 1979. Ignimbrites of the Sierra Madre Occidental and their relation to the tectonic history of western Mexico. In: Chapin, C.E. and Elston, W.E. (Eds), Ash-Flow Tuffs, Geological Society of America Special Paper, 180, pp. 113–124.

McDowell, F.W., Housh, T.B., Wark, D.A., 1999. Nature of the crust beneath west-central Chihuahua, Mexico, based upon Sr, Nd, and Pb isotopic compositions at the Tomóchic volcanic center. Geol. Soc. Am. Bull., 111, 823–830.

McDowell, F.W., Keizer, R.P., 1977. Timing of mid-Tertiary volcanism in the Sierra Madre Occidental between Durango City and Mazatlán, Mexico. Geol. Soc. Am. Bull., 88, 1479–1487.

McDowell, F.W., Mauger, R.L., 1994. K–Ar and U–Pb zircon chronology of late Cretaceous and Tertiary magmatism in central Chihuahua State, Mexico. Geol. Soc. Am. Bull., 106, 118–132.

McDowell, F.W., Mauger, R.L., Walker, N.W., 1989. Geochronology of Cretaceous–Tertiary magmatic activity in central Chihuahua, Mexico, continental magmatism. New Mexico Bureau Mines Miner. Resources Bull., 131, 181.

McDowell, F.W., Roldán-Quintana, J., Connelly, J.N., 2001. Duration of late Cretaceous–early Tertiary magmatism in east-central Sonora, Mexico. Geol. Soc. Am. Bull., 113, 521–531.

McDowell, F.W., Wark, D.A., Aguirre-Diaz, G.J., 1990. The Tertiary ignimbrite flare-up in western Mexico: Geological Society of America Abstracts with Programs, Vol. 22, 66 p.

McLeroy, D.F., Clemons, R.E., 1965. Resumen de la geología de la Hoja Pedriceñas, estados de Durango y Coahuila. Universidad Nacional Autónoma de México, Instituto de Geología, Carta Geológica de México, Hoja Pedriceñas 13R-1 (4), esc. 1:100,000.

Megaw, P.K.M., 1981. Volcanic rocks of the Sierra Pastorias caldera area, Chihuahua, Mexico. In: Goodell, P.C. and Waters, A.C. (Eds), Volcanic and volcaniclastic rocks, AAPG Studies Geol., Vol. 13, pp. 189–187.

Megaw, P.K.M., McDowell, F.W., 1983. Geology and geochronology of volcanic rocks of the Sierra Pastorias area, Chihuahua, Mexico. In: Clark, K.F. and Goodell, P.C. (Eds), Geology and Mineral Resources of North-Central Chihuahua, El Paso Geological Society Guidebook, 1983 Field Conference, 195–203.

Mora-Álvarez, G., McDowell, F.W., 2000. Miocene volcanism during late subduction and early rifting in the Sierra Santa Ursula of western Sonora, Mexico. In: Delgado-Granados, H., Stock, J. and Aguirre-Díaz, G.J. (Eds), Cenozoic Tectonics and Volcanism of Mexico, Geological Society of America Special Paper, 334, pp. 123–142.

Nemeth, K. E., 1976. Petrography of the lower volcanic group Tayoltita-San Dimas district, Durango, Mexico. M.A. Thesis, University of Texas at Austin, Austin, Texas, 141 p.

Nieto-Obregón, J., Delgado-Argote, L.A, Damon, P.E., 1981. Relaciones petrológicas y geocronológicas del magmatismo de la Sierra Madre Occidental y el Eje Neovolcánico en Nayarit, Jalisco y Zacatecas. Asociación de Ingenieros de Minas Metalurgistas y Geólogos de México, Memoria XIV Convención Nacional, 327–361.

Nieto-Samaniego, A.F., Ferrari, L., Alaníz-Álvarez, S.A., Labarthe-Hernández, G., Rosas-Elguera, J., 1999. Variation of Cenozoic extension and volcanism across the southern Sierra Madre Occidental volcanic province, Mexico. Geol. Soc. Am. Bull., 111, 347–363.

Nieto-Samaniego, A.F., Macías-Romo, C., Alaniz-Alvarez, S.A., 1996. Nuevas edades isotópicas de la cubierta volcánica cenozoica de la parte meridional de la Mesa Central, México, Universidad Nacional Autónoma de México, Instituto de Geología. Revista Mexicana de Ciencias Geológicas, 13, 117–122.

Pantoja-Alor, J., 1963. Hoja San Pedro del Gallo y resumen de la geología de la Hoja San Pedro del Gallo, estado de Durango Universidad Nacional Autónoma de México, Instituto de Geología, Carta Geológica de México, Hoja San Pedro del Gallo 13R-k (3), esc. 1:100,000.

Pantoja-Alor, J., Orta-Rincón, C., Solorio, J.G., Fries, C., Jr., 1967. Edad de tres rocas intrusivas de la parte centro-septentrional de México, Universidad Nacional Autónoma de México. Instituto de Geología, Boletín, 82, 7–23.

Quintero-Legorreta, O., 1992. Geología de la Región de Comanja, estados de Guanajuato y Jalisco, Universidad Nacional Autónoma de México. Instituto de Geología Revista, 10, 6–25, Available at http://satori.geociencias.unam.mx/10-1.htm

Raisz, E., 1964. Landforms of Mexico. Geography Branch, Office of Naval Res., Cambridge Mass, 2nd Edition, Map scale: 1:300,000.

Randall, J.A., Saldaña, E., Clark, K.F., 1994. Exploration in a volcano-plutonic Center at Guanajuato, Mexico. Econ. Geol., 89, 1722–1751.

Reyes-Cortés, I.A., 1985. Geology and uraniferous mineralization in the Sierra de Coneto, Durango, Mexico. M.A. Thesis, University of Texas at El Paso, El Paso, Texas, 245 p.

Roldán-Quintana, J.S:F., 1968. Estudio geológico de reconocimiento de la región de Peñón Blanco, Estado de Durango. Boletín Sociedad Geológica Mexicana, 31, 79–105.

Roldán-Quintana, J.S.F., 2002. Caracterización geológico-geoquímica y evolución del arco magmático Mesozoico-Terciario entre San Carlos y Maycoba, sur de Sonora. Tesis Doctoral, Universidad Nacional Autónoma de México, Instituto de Geología, Posgrado en Ciencias de la Tierra, México, D.F., 185 p.

Ruiz, J., Patchett, P.J., Arculus, R.J., 1988. Nd–Sr isotope composition of lower crustal xenoliths — evidence for the origin of mid-Tertiary felsic volcanics in Mexico. Contrib. Mineral. Petrol., 99, 36–43.

Scheubel, F.R., Clark, K.F., Porter, E.W., 1988. Geology, tectonic environment, and structural controls in the San Martín de Bolaños district, Jalisco, Mexico. Econ. Geol., 83, 1703–1720.

Shafiqullah, M., Damon, P.E., Lynch, D.J., Reynolds, S.J., Rehrig, W.A., Raymond, R.H., 1980. K–Ar geochronology and geologic history of southwestern Arizona and adjacent areas. In: Jenney, J.P. and Stone, C. (Eds), Studies in western Arizona, Arizona Geological Society Digest, Vol. 12, pp. 201–260.

Spruill, R.K., 1976. The volcanic geology of the Rancho Peñas Azules area, Chihuahua, Mexico. M.S. Thesis, Greenville, North Carolina, East Carolina Univ., 99 p.

Stimac, J., Wark, D.A., 1983. Geology of the Cusihuiriachic–Buenos Aires area, Chihuahua, Mexico. In: Clark, K.F. and Goodell, P.C. (Eds), Geology and mineral resources of north-central Chihuahua, El Paso Geological Society Guidebook, 1983 Field Conference, 205–212.

Swanson, E.R., Keizer, R.P., Lyons, J.I., Clabaugh, S.E., 1978. Tertiary volcanism and caldera development near Durango City, Sierra Madre Occidental, Mexico. Geol. Soc. Am. Bull., 89, 1000–1012.

Swanson, E.R., McDowell, F.W., 1984. Calderas of the Sierra Madre Occidental volcanic field western Mexico. J. Geophys. Res., 89, 8787–8799.

Swanson, E.R., McDowell, F.W., 1985. Geology and geochronology of the Tomochic caldera, Chihuahua, Mexico. Geol. Soc. Am. Bull., 96, 1477–1482.

Torres-Hernández, J.R., Labarthe-Hernández, L., Aguillón-Robles, A., Gómez-Anguiano, M., Mata-Segura, J.L., in press. The pyroclastic dikes of the Tertiary San Luis Potosí volcanic field: implications on the emplacement of Panalillo ignimbrite. Geofís. Int., 45, 243–253.

Tristán-González, M., 1986. Estratigrafía y Tectónica del Graben de Villa de Reyes, en los estados de San Luis Potosí y Guanajuato, Universidad Autónoma de San Luis Potosí, Instituto de Geología y Metalurgia, Folleto Técnico 107, 91 p.

Tristán-González, M., Labarthe-Hernández, G., 1979. Cartografía Geológica Hoja Tepetate, S.L.P. Universidad Autónoma de San Luis Potosí, Instituto de Geología y Metalurgia, Folleto Técnico 66, 31 p.

Tristán-González, M., Labarthe-Hernández, G., Aguillón-Robles, A., Torres-Hernández, J.R., Aguirre-Díaz, G., 2006. Diques piroclásticos en fallas de extensión alimentadores de

ignimbritas en el occidente de Campo Volcánico del Río Santa María, S.L.P., Reunión Anual Unión Geofísica Mexicana. Geos, 26, 163.

Tristán-González, M., Torres-Herández, J.R., Mata-Segura, J.L., 1994. Correlación Estratigráfica de la geología de la Mina Proaño y Plateros, Zacatecas; con otras localidades del Terreno Guerrero, al suroriente del Estado de Zacatecas. Universidad Autónoma de San Luis Potosíç Instituto de Geología (reporte interno inédito para La Cía. Minera Peñoles), 97 p.

Valencia-Moreno, M., Ruiz, J., Barton, M.D., Patchett, J.P., Zürcher, L., Hodkinson, D.G., Roldán-Quintana, J., 2001. A chemical and isotopic study of the Laramide granitic belt of northwestern Mexico: Identification of the southern edge of the North American Precambrian basement. Geol. Soc. Am. Bull., 113, 1409–1422.

Wark, D.A., Kempter, K.A., McDowell, F.W., 1990. Evolution of waning subduction-related magmatism, northern Sierra Madre Occidental, Mexico. Geol. Soc. Am. Bull., 102, 1555–1564.

Webber, K.L., Fernández, L.A., Simmons, W.B., 1994. Geochemistry and mineralogy of the Eocene–Oligocene volcanic sequence, southern Sierra Madre Occidental, Juchipila, Zacatecas, Mexico. Geofis. Int., 33, 77–89.

Wolff, J.A., 1986. Welded-tuff dykes, conduit closure, and lava dome growth at the end of explosive eruptions. J. Volcanol. Geotherm. Res., 28, 379–384.

Zimmermann, J.L., Stein, G., Lapierre, H., Vidal, R., Campa, M.F., Monod, O., 1990. Données géochronologiques nouvelles sur les granites laramiens du centre et l'ouest du Mexique (Guerrero et Guanajuato). Société Géologique de France, Reunion des Sciences de la Terre 13, Grenoble, France, 127.

# Characterisation of Archean Subaqueous Calderas in Canada: Physical Volcanology, Carbonate-Rich Hydrothermal Alteration and a New Exploration Model

W.U. Mueller[1,*], J.B. Stix[2], J.D.L. White[3], P.L. Corcoran[4], B. Lafrance[5] *and* R. Daigneault[1]

## Contents

*Corresponding author. Tel.: 1-418-545-5013; Fax: 1-418-545-5012
*E-mail address:* Wulf_Mueller@uqac.ca

[1] Sciences de la terre, Université du Québec à Chicoutimi, Canada, G7H 2B1
[2] Department of Earth & Planetary Sciences, McGill University, Canada
[3] Geology Department, University of Otago, Dunedin, New Zealand
[4] Department of Earth Sciences, University of Western Ontario, London, Ontario, Canada, N6A 5B7
[5] Cogitore, 1300 Saguenay, Suite 200 Rouyn-Noranda, Québec Canada J9X 7C3

## Abstract

Ancient and modern subaqueous calderas form in deep- to shallow-marine oceanic settings and are primary sites for volcanogenic massive sulphide (VMS) deposits. Caldera structures hosting VMS deposits are concentrated in the Archean Abitibi greenstone belt and in the Wabigoon subprovince. The Hunter Mine and Normetal calderas, two little-known effusive-dominated edifices, are emphasised and Sturgeon Lake is the best known explosive-dominated caldera. Although VMS deposits are linked to calderas, their 5–30 km diameter size, poses problems in pin-pointing highly favourable sites for VMS exploration. The overall caldera geometry is readily recognised based on regional-scale mapping but detailed volcanic facies mapping is required to distinguish caldera subsettings in the Archean. Caldera subenvironments include: (1) the *caldera wall* featuring (a) chaotic breccias, (b) dyke intrusions, (c) synvolcanic faults and (d) pyroclastic debris; (2) the *intracaldera moat or floor* with (a) horst and graben structures (synvolcanic faults), (b) superposed dome-flow-hyaloclastite complexes, (c) extensive central dyke swarm and (d) small explosive volcanic edifices formed by magmatic fountaining eruptions and (3) *caldera apron deposits* showing (a) extensive volcaniclastic debris of pyroclastic and autoclastic origin and (b) local dome-flow-hyaloclastite complexes. All loci are possible sites for VMS formation, but the caldera wall favours large VMS deposits.

Based on the studied calderas, a new hydrothermal alteration model is proposed that helps explain chert—Fe carbonate assemblages in Archean volcanic sequences. The early hydrothermal silica seals the volcaniclastic-dominated rocks (cap rock) at or near the edifice–seawater interface. These silicified volcaniclastic turbidite deposits have generally been referred to as chert or exhalites but this interpretation necessitates reconsideration. Overprinting the silicification phase is a pervasive semi-conformable carbonate hydrothermal alteration zone with a discordant focussed root zone along faults. Three distinct carbonate pairings are observed: (1) proximal siderite (sideroplesite) — Fe–ankerite next to the VMS-deposit, (2) an intermediate ankerite–Fe–dolomite zone and (3) a distal calcite–dolomite zone. Transitions between zones are subtle and changes are indicated mineral assemblage overlaps. Our results shed new light on hydrothermal alteration patterns, but also resolve some of the problems associated with chert–iron carbonate formations. The chert and hydrothermal carbonates as well as the VMS deposits are of the replacement type, rather than chemical precipitants and black smoker deposits.

## 1. Introduction

Calderas are volcano–tectonic collapse structures between ca. 2 and 100 km in diameter resulting from paroxysmal explosions and effusive evacuation of high-level magma chambers (Smith and Bailey, 1968; Bailey et al., 1976, Tilling and Dvorak, 1993; Lipman, 2000; Acocella, 2007). According to White et al. (2003) ca. 85% of volcanism occurs underwater so that arc calderas should be a common feature (e.g. Yuasa and Kano, 2003). Fiske et al. (1998, 2001) and Gamble and Wright (1999) identified subaqueous calderas and noticed their explosivity, yet surprisingly the first detailed documentation of subaqueous explosive deposits originated from ancient sequences (e.g. Fiske and Matsuda, 1964; Niem, 1977). Silicic submarine calderas were recognised as favourable volcanogenic massive sulphide (VMS) sites early on (Ohmoto, 1978, 1996), but only later did Stix et al. (2003) allude to the importance of caldera ring faults in VMS genesis. The latter is corroborated by the present $9 \times 10^6$ tonne caldera wall Sunrise deposit in the Myojin Knoll (Iizasa et al., 1999; Glasby et al., 2000), as well as VMS mineralisation within the active submarine Brothers caldera (Wright et al., 1998). The Izu–Bonin arc with boninites (high Mg-andesites; Crawford et al., 1989), moderate to deep-water calderas and hydro-thermal massive sulphide mineralisation (Ishibashi and Urabe, 1995; Iizasa et al., 1999) is considered an analogue to the Archean Abitibi greenstone belt. As our knowledge of seafloor calderas is restricted to submersible dives, ancient dissected submarine calderas are prime sites to identify edifice geometry, construction and collapse.

The Abitibi greenstone belt is world class VMS metallotect with a production and reserves in excess of 480 Mt for polymetallic massive sulphide and gold-rich massive sulphides, including the past Horne and current Bousquet-LaRonde mines, Blake River caldera complex (Figure 1; Chartrand and Cattalani, 1990; Gibson and Watkinson, 1990; Hannington et al., 1999a). Our study is divided into: (1) a segment concerning the physical volcanology and geometry of the little known subaqueous Abitibi Hunter Mine and Normetal calderas, and the Sturgeon Lake caldera, Wabigoon Subprovince, and (2) a segment addressing the poorly documented hydrothermal carbonate alteration. The felsic 2,728–2,734 Ma Hunter Mine caldera is effusive dominated, as is the bimodal 2,728–2,730 Ma Normetal caldera, whereas the felsic 2,733–2,736 Ma Sturgeon Lake caldera is explosive dominated. A new volcanic hydrothermal alteration model for submarine Archean calderas is proposed, and exemplifies how detailed volcanic facies and alteration mapping with basic petrography are important tools in reconstructing volcanic edifices and VMS exploration.

## 2. Abitibi Greenstone Belt Geology

The $300 \times 700$ km Abitibi greenstone belt (Figure 1) is the best-studied greenstone belt of oceanic arc affinity in the world because of its vast economic potential. Arc-related volcanism continued for 65 m.y. (ca. 2,735–2,670 Ma), and
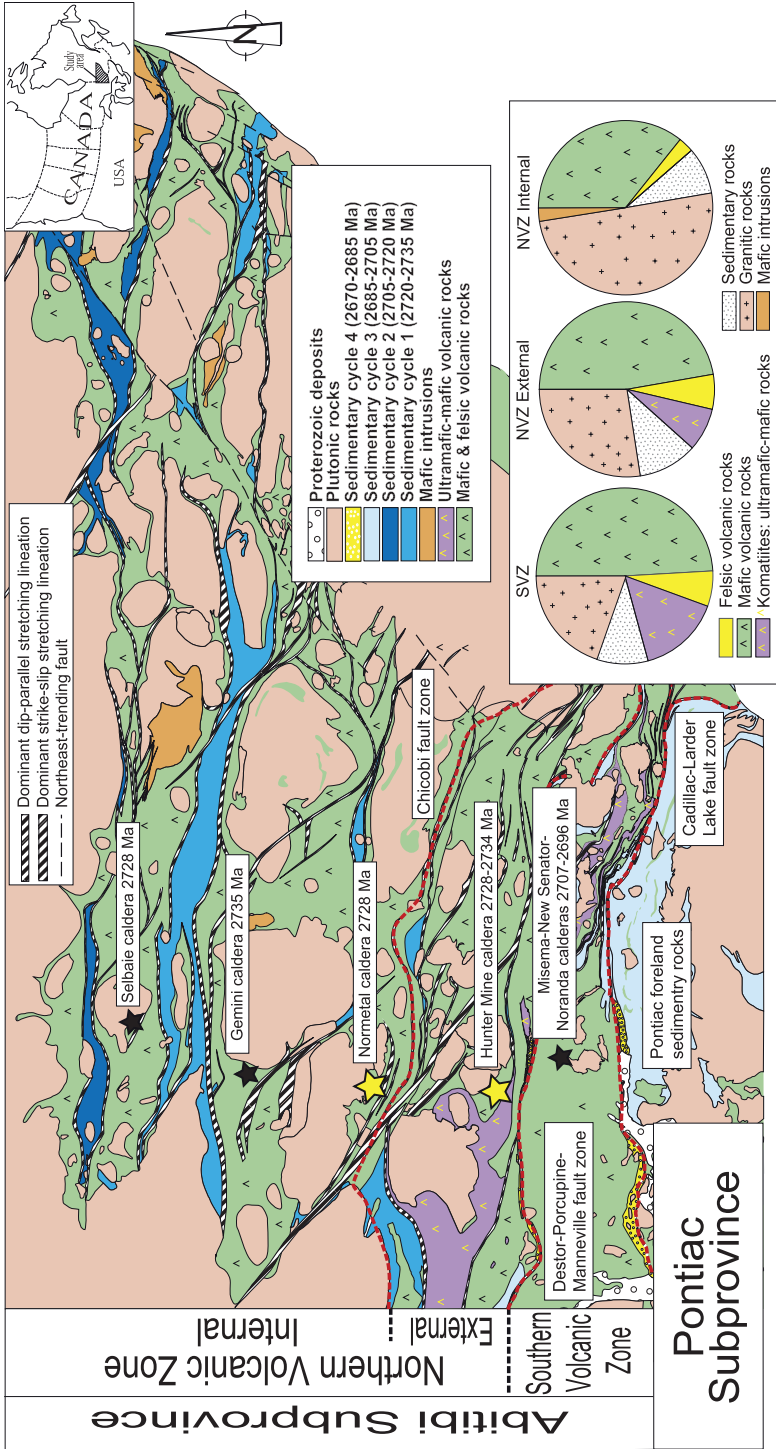
**Figure 1** (A) General geology of the 300 × 700 km Abitibi Greenstone Belt with the location of numerous calderas including the Hunter Mine and Normetal calderas. Abitibi greenstone belt divided into Northern Volcanic (NVZ) and Southern Volcanic Zones (SVZ) based on major crustal scale faults. The pie diagrams show the distribution of lithological units within zones (modified from Daigneault et al., 2004).

intrusive synvolcanic to late tectonic activity occurred over a protracted period of approximately 95 m.y. (2,735–2,640 Ma). The Abitibi supracrustal sequence displays a modern plate tectonic succession of events from arc formation, to arc evolution, to arc–arc collision and arc fragmentation (Chown et al., 1992; Mueller et al., 1996). This evolutionary sequence is based on U–Pb zircon age determinations (e.g. Ayer et al., 2002; Davis, 2002), the physical volcanology of mafic (Cousineau and Dimroth, 1982; Dimroth et al., 1978, 1985) and felsic flows (de Rosen-Spence et al., 1980), basin analyses (Mueller and Donaldson, 1992a), structural studies (Daigneault et al., 2002, 2004) and plutonic emplacement history (Chown et al., 1992, 2002). The usage of volcanic and sedimentary cycles is retained in this study (Dimroth et al., 1982; Daigneault et al., 2002, 2004) as it best expresses oceanic arc dynamics.

## 2.1. Abitibi greenstone belt divisions

The Southern (SVZ) and Northern Volcanic Zones (NVZ; Chown et al., 1992) represent a collage of two arcs, separated by the crustal-scale Destor-Porcupine Manneville Fault Zone (DPMFZ; Mueller et al., 1996). The E-trending Cadillac-Larder Lake Fault Zone (CLLFZ) separates the SVZ from the Pontiac foreland sedimentary rocks. These faults are considered arc terrane boundaries and are characterised by remnant strike–slip basins (Mueller et al., 1996; Daigneault et al., 2002, 2004). The divisions into a NVZ and a SVZ were based on the seminal work of Dimroth et al. (1982, 1983) with internal and external zones. On a large-scale geodynamic setting, the 2,735–2,705 Ma NVZ is an oceanic arc with numerous central volcanic complexes that evolved from a diffuse and submerged arc (volcanic cycle 1, ca. 2,735–2,720 Ma), to a mature and partially eroded arc, best characterised by volcanic cycle 2 (2,720–2,705 Ma) in the Chibougamau region. The subaqueous 2,734–2,728 Ma Hunter Mine and 2,728 Ma Normetal calderas are integral components of NVZ volcanic cycle 1. Commensurate with volcanic evolution are intra-arc flysch basins (sedimentary cycle 1) and clastic-dominated arc aprons (sedimentary cycle 2; Mueller and Dimroth, 1987; Mueller and Donaldson, 1992a). The sedimentary basins were initiated during arc volcanism and continued to evolve until 2,690 Ma.

The 2,714–2,696 Ma SVZ is separated from the Pontiac sedimentary rocks (an accretionary prism) to the south by the CLLFZ and the DPMFZ to the north, respectively. An extensive inter-arc sedimentary basin (sedimentary cycle 3), over 200 km in length and represented by the Porcupine Group, Kewagama Group and Caste Formation, connected the NVZ and SVZ prior to shortening and transcurrent motion as indicated by layer-parallel faults (Mueller et al., 1996; Daigneault et al., 2004). Sedimentary cycle 4 strike-slip basins were formed in the fault zones of uplifted sedimentary cycle 3 basins that feature local ultra-potassic volcanism and host abundant orogenic gold deposits (Robert, 2001).

# 3. Notion of Calderas

Stratovolcanoes, composite volcanoes or shield volcanoes are the precursor structures to calderas. The former two favour large-volume silicic-dominated, paroxysmal ash-flow calderas (e.g. Valles caldera; Smith and Bailey, 1968; Long Valley caldera, Bailey, 1989) whereas the latter is generally associated with mafic summit calderas (e.g. Kilauea, Hawaii; Tilling and Dvorak, 1993). Caldera geometry varies from central circular depressions such as the $6 \times 7$ km in diameter, submarine Myojin Knoll, (Fiske et al., 2001) to the small 9–16 km ellipsoidal Las Cañadas caldera (Martí and Gudmundsson, 2000), the medium-scale $17 \times 32$ km Long Valley Caldera (Bailey, 1989) and the large $30 \times 100$ km, Toba caldera (Lipman, 2000). Calderas are rarely isolated and occur (1) in clusters, as indicated by the Taupo volcanic zone (Cole et al., 2005) or the Minami–Aizu field (Miura and Tamai, 1998), (2) nested, as exemplified by the Campi Flegrei field (Orsi et al., 1996) or (3) as overlapping collapse calderas such as Las Cañadas caldera (Martí and Gudmundsson, 2000). In addition, complex mega-nested calderas of the Olympic Mons type on Mars may develop, as indicated by the Abitibi Blake River caldera complex (Pearson, 2005). Volcano-depressions are caused by numerous processes including: (1) the rapid explosive evacuation of magma producing hundreds of $km^3$ of pyroclastic debris (e.g. subaerial silicic arc, Taupo calderas; continental rift systems, Valles caldera), (2) continuous outpouring of magma via extensive lava flows and fountaining eruptions (some Archean arc calderas), (3) draining of magma into satellite chambers along rift zones (oceanic hot spot, e.g. Hawaii) and (4) magma migration causing a shift and overlap of calderas (oceanic hot spot, e.g. Las Cañadas caldera).

Our understanding of caldera development has advanced significantly based on recent analogue experiments (Acocella et al., 2000, 2001; Acocella, 2008; Roche et al., 2000; Walter and Troll, 2001; Kennedy et al., 2004), numerical modelling of stress regimes associated with caldera-forming eruptions (Gudmundsson, 1998, 2008), studies of collapse processes and subsidence geometry (Lipman, 1997) and direct monitoring of caldera collapse (Geshi et al., 2002). The importance of early reverse faults was recognised by Mueller and Mortensen (2002), and Stix et al. (2003) in their role during the circulation of hydrothermal fluids and formation of VMS deposits structures preceded normal ring faults. Modelling of Acocella et al. (2000, 2001) and Roche et al. (2000) confirmed the inference of Branney (1995) that during draining of a shallow magma chamber, an early set of outward-dipping faults with a reverse sense of displacement develop and encircle the subsidence centre. Ring faulting is a rapid, syneruptive phenomenon, and is associated with the formation of chaotic breccias or talus scree breccias, as newly formed caldera walls suffer large landslides. The intracaldera depression contains further syneruptive debris as a result of synthetic and antithetic fault formation, which forms complex horst and graben structures. Gudmundsson (1998) argues that the encircling normal faults are used for magma venting. The greatest displacements typically occur along the outermost set of encircling ring faults (Walker, 1984). The collapse mechanism of calderas varies with depth of magma chamber (e.g. Roche et al., 2000), its size,

evacuated magma and volume and magma composition. Piston, trapdoor piecemeal calderas are well documented whereas down sag and funnel calderas are uncommon (Lipman, 1997). Acocella (2007) gives an excellent caldera review.
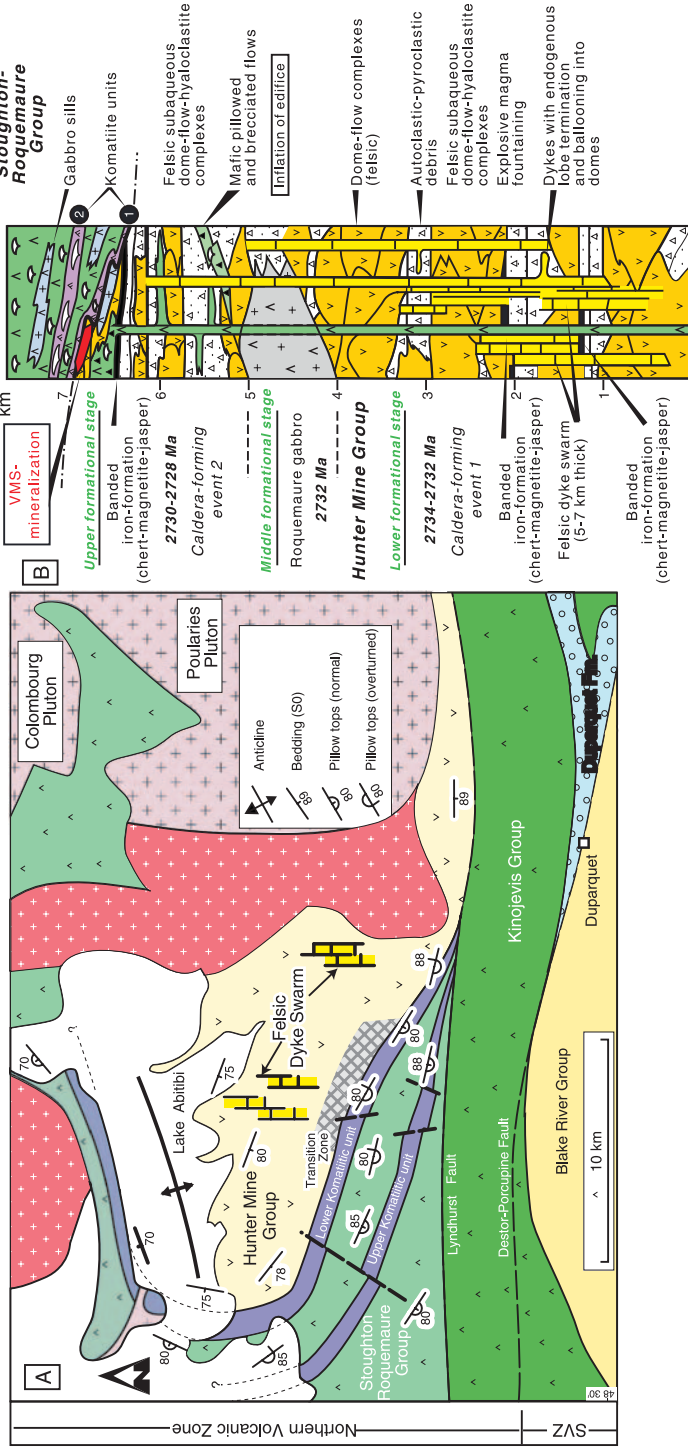
## 4. Hunter Mine Caldera

The Hunter Mine caldera (HMC) in the NVZ (Figure 1) is a complex subaqueous felsic-dominated, calc-alkaline arc edifice (Dostal and Mueller, 1996) overlain conformably by a komatiite–basalt succession (Dostal and Mueller, 1997; Mueller and Mortensen, 2002; Figure 2A, B). Initial depth of the HMC is >500 m as suggested by: (a) a silicified mudstone horizon at the top of the HMC (Chown et al., 2000; Figure 3A), (b) banded iron-formation (Figure 3B; BIF) and abundant Bouma-cycled turbiditic tuffs (Figure 3C, D) throughout the stratigraphy, (c) bedded felsic hyaloclastite deposits and (d) an upper depositional contact with pillowed komatiite–basalt flows. Evidence of shallow-water wave-induced structures or reworking is lacking.

The composite HMC stratigraphy (Figure 2B) displays a 5–6 km-thick dominantly felsic sequence characterised by an extensive 5–7 km wide felsic feeder dyke swarm (Mueller and Donaldson, 1992b). The caldera sequence is divided into *lower, middle and upper formational stages* based on U–Pb age determinations and lithology. The lower and upper stages are distinct caldera forming phases separated by a major intrusive phase, the Roquemaure sill (Table 1). The central caldera depression was at least 7 km in diameter. Numerous synvolcanic faults and fractures with local vertical displacements of up to 20 m are not uncommon. Synvolcanic structures include: (1) fluid escape structures in tuff turbidites (Figure 3E), (2) precipitation of hydrothermal fluids within fractures/faults resulting in black and white chert, chert–jasper–magnetite filling fractures and draping dyke margins (Figure 3F), (3) discrete volcanic facies changes across faults and dykes and (4) abrupt changes in the style and types of hydrothermal alteration. The high-level, TTG (tonalite–trondhjemite–granodiorite), synvolcanic Poularies pluton is characterised by widespread argillic to propylitic porphyry-type alteration associated with numerous chalcopyrite–molybdenite showings (Chown et al., 2002). The Poularies pluton and thick Roquemaure sill (Figure 2B) are considered the heat sources for caldera-hosted hydrothermal convection, as required for VMS (Galley, 2003).

### 4.1. Lower formational stage (first caldera event)

The 3–4 km thick lower formational stage (Figure 2B) represents the first caldera event with dome-flow deposits and abundant autoclastic breccias (70%), and subaqueous pyroclastic deposits and reworked equivalents (30%). Three distinct lithofacies were observed: (1) coherent and brecciated felsic lithofacies, (2) volcaniclastic and iron-formation lithofacies and (3) a felsic dyke swarm best exposed at this edifice level (Table 1).

**Figure 2**   (A) General geology of the Lake Abitibi region. (B) Composite stratigraphic column of the Hunter Mine caldera with early and late caldera–forming events separated by a major intrusive phase at 2,732 Ma Roquemaure Sill (modified from Mueller and Mortensen, 2002).
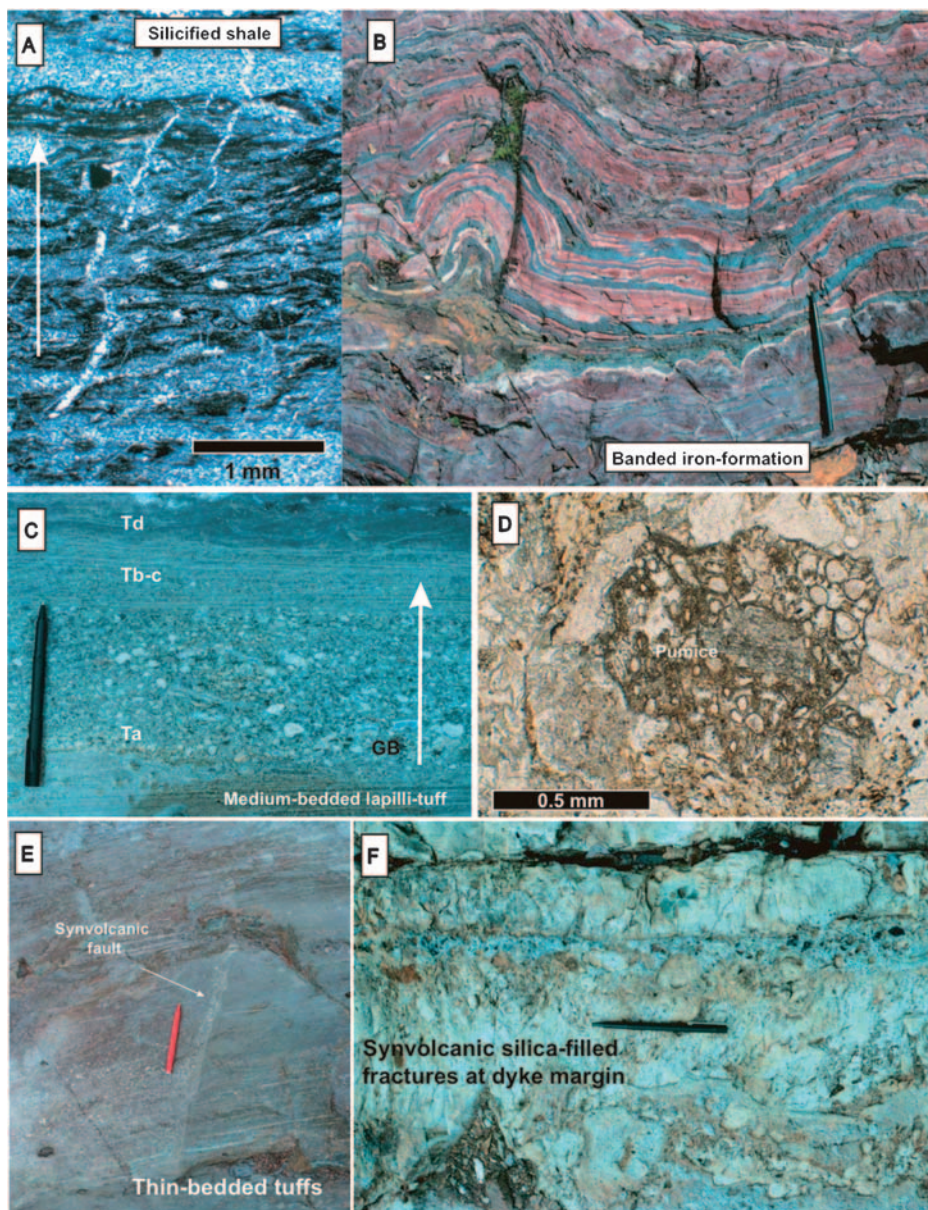
**Figure 3**   Characteristics of the subaqueous Hunter Mine caldera (HMC). Tip of pen indicates top. (A) Silicified mudstone (shale) at the interface with the komatiitic Stoughton-Roque-maure Group. (B) Jasper—magnetite raft in chaotic breccia located at inferred caldera margin wall. Scale pen 13 cm. (C) Graded bedded (GB) tuff—lapilli tuff. Scale pen 13 cm. (D) Archean pumice with feldspar phenocryst in GB tuff—lapilli tuff unit. Note quartz-filled vesicles. (E) Synvolcanic N-trending fault with fluid migration in GB tuff—lapilli tuffs. Scale pen 12 cm. (F) Margin of N-trending mafic dyke with white and black chert at brecciated margin. Location: near top of succession at inferred caldera wall margin.

**Table 1**  Subaqueous volcanic lithofacies of Hunter Mine Caldera.

| Hunter mine caldera stratigraphy | Lithofacies/lithology | Salient characteristics of volcanic and volcaniclastic rocks | Interpretation, process and locus |
|---|---|---|---|
| *Upper formational stage* 0.5–2 km-thick: 2nd caldera subsidence event | (c) Sills and dykes | (c) Aphanitic to porphyritic mafic and felsic, dykes and sills; intrusions are contemporaneous with caldera construction. Late feldspar–quartz-phyric dyke-sill (FQP <2,706 Ma) related to late Poularies pluton phases | (c) Intrusion of dykes-sills during edifice construction; feldspar–quartz-phyric dykes are associated with late plutonic suites. Extension and crustal-thinning processes. Locus: central part of volcanic edifice |
| Age: 2,728–2,730 Ma (inheritance 2,740.8 Ma) Based on dykes and felsic lava flow units. No older dykes than 2,730 Ma documented as the oldest aphanitic dykes phases did not yield zircons for age determinations, Phenocryst-rich dykes <2,730 Ma | (b) Volcaniclastic lithofacies and iron-formation lithofacies | (b-1) Volcaniclastic lithofacies: 2–20 m-thick with 2–50 cm-thick tuff and lapilli tuff turbidites ($T_a$-$S_3$ beds and $T_{ab}$, $T_{abc}$, $T_{ad}$, $T_{abcde}$ beds); beds composed of shards, wispy vitric and angular lithic volcanic fragments, pumice, and broken and euhedral crystals; cm-thick (locally silicified) black mudstone capping tuff turbidites is probably fine-grained felsic vitric tuff. M-thick mudstone beds (silicified) cap iron-formation (b-2) Iron-formation lithofacies: 0.2–5 m-thick units of chert (silicified tuff)–jasper, chert–magnetite and jasper–magnetite in thin beds and as m-thick folded rafts; 1–30 m-thick chert (silicified tuff)–iron carbonate | (b-1) Pumice in tuff and lapilli tuff beds indicates pyroclastic origin; both primary and syneruptive with limited reworking. Transport mechanism: high and low-concentration density currents. Mudstone: suspension deposits as pelagic background sedimentation and vitric fines settling through water (b-2) Iron-formation represents percolation of hydrothermal fluids and diagenesis. Locus: subaqueous intracaldera floor and caldera margin faults |

| Felsic lava flows and lobes contemporaneous with felsic dykes | (a) Felsic volcanic lithofacies and mafic volcanic lithofacies | (a-1) Felsic volcanic lithofacies: 2–30 m-thick coherent to brecciated felsic flows with lobate terminations; extensive flow banding; breccia units contain angular to subangular clasts with flow-banding; presence of m-thick massive to stratified lapilli tuff breccias and lapilli tuffs containing subordinate pumice (a-2) Mafic volcanic lithofacies: mafic tholeiitic and high Mg (10–11%), 50–80 m-thick basalt flows composed of massive, pillowed, pillow breccia and pillow fragment breccia; 2–20 m-thick massive columnar-jointed flows grade into lobate-pillowed flows and up-section into pillows and pillow breccia. Chaotic breccia facies 30–40 m-thick composed of large rafts of BIF, volcaniclastic blocks, and segments felsic and mafic flows. Heterolithic breccia facies (2–5 m-thick) silicified and dominated by mafic clasts with chert, BIF and felsic clasts | (a-1) Subaqueous massive to brecciated lava flows indicative of autoclastic and hydroclastic fragmentation processes; massive to stratified lapilli tuff suggestive of synvolcanic resedimentation by subaqueous density currents (a-2) Lateral and vertical flow changes in basalt flows characteristic of subaqueous flow processes; brecciation caused by autoclastic fragmentation and thermal granulation. Heterolithic breccia is a mass flow deposit; chaotic breccia represents a talus scree deposit. Locus: intracaldera setting adjacent to caldera faults and margin. Faults site of extensive hydrothermal silicification |

**Table 1** (*Continued*)

| Hunter mine caldera stratigraphy | Lithofacies/lithology | Salient characteristics of volcanic and volcaniclastic rocks | Interpretation, process and locus |
|---|---|---|---|
| *Middle formational stage*<br>Up to 1 km-thick: major extensional phase of caldera<br>Age: 2,732 Ma | Gabbro: Roquemaure Sill | E-trending gabbro–quartz diorite with a subophitic (±ophitic) hypidiomorphic granular texture; pods with cm-scale hornblende, pyroxene, and plagioclase with interstitial quartz; dark green to brown weathered intrusive body; geochemistry, tholeiitic ferrogabbro with FeO contents from 17 to 21%; early felsic dykes locally intruded unconsolidated phases of gabbro; late feldspar–quartz–phyric dykes cut sill (no zircons) | Early mafic intrusive phase of HMG within limits of central dyke swarm<br>Thick sill intruded caldera and caused ballooning; geochemical signature suggests tapping of mantle–derived magma formed during arc extension–crustal thinning phase Locus: central and marginal part of intracaldera setting |
| *Lower formational stage*<br>3–4 km-thick: 1st caldera subsidence event | (c) Felsic-dominated dyke swarm (<10% mafic dykes) | (c) Abundant, N-trending dykes occurring in eastern and western portions of the Hunter Mine Caldera. Dyke generations occur as multiple magma pulses. Dyke phases: D-1a, aphanitic, D-1b, feldspar-phyric; D-2, quartz–feldspar-phyric (<5% qtz); D-3, quartz–feldspar-phyric (10–25% qtz); D-4, dacitic feldspar-phyric, D-5a, b, mafic dykes. Western part well documented (ca. 2.8 km-thick; traceable 2.5 km up-section); eastern segment poorly exposed; combined thickness of 5–7 km for high-density dyke population | (c) High dyke density indicates dyke swarm and an extensive volcanic plumbing system. A 5–7 km extent of swarm suggests rifting and supports caldera formation. Dykes locally terminate as endogenous lobes and balloon into domal structures. QFP-dykes feed flows in upper formational stage. Locus: central intracaldera segment and caldera margin wall |

| | | | |
|---|---|---|---|
| Age: ca. 2,732–2,734 Ma Dykes described in Lower Formational Stage but crosscut flows and pyroclastic deposit (ages 2,728–2,730 Ma) Dykes locally terminate as endogenous lobe | (b) Volcaniclastic lithofacies and Iron-formation lithofacies | (b-1) Volcaniclastic lithofacies: (1) pyroclastic facies and (2) reworked pyroclastic & autoclastic facies. Pyroclastic facies divided into: (i) a basal 7–20 m-thick, massive lapilli tuff breccia (ii) a middle up to 51 m-thick, stratified lapilli tuff and (iii) an upper 2 m-thick turbiditic tuff-lapilli tuff. Volcaniclastic lithofacies well preserved in screens of dyke swarm. Pyroclastic deposits feature massive beds with irregular amoeboid-shaped clasts, stratified beds with blocky clasts and graded tuff beds; pyroclasts contain ca. 30–60% quartz-filled vesicles. Reworked pyroclastic and autoclastic facies: 1–5 m-thick tuff and lapilli tuff deposited in massive, graded and laminated beds (b-2) Iron-formation lithofacies: 5–100 cm-thick units of magnetite and jasper-magnetite in mm–cm–scale beds and as large rip-up clasts. BIF: banded iron-formation. | (b-1) Pyroclastic facies: directly from a magmatic fountaining eruption with insulation from water, by a steam carapace. Collapse of fountain results in water ingestion and hydroclastic fragmentation. Transport via high- and low-concentration density currents: (1) laminar mass flows and (2) turbidity flows Reworked pyroclastic and autoclastic facies resulted from slope failure or tremors; transport by turbidity currents or as pelagic rain during volcanic quiescence. Locus: intracaldera floor and caldera margin (b-2) Iron-formation lithofacies formed by pervasive subsurface percolation of hydrothermal fluids (and cold seeps) and diagenesis |

**Table 1** (*Continued*)

| Hunter mine caldera stratigraphy | Lithofacies/lithology | Salient characteristics of volcanic and volcaniclastic rocks | Interpretation, process and locus |
|---|---|---|---|
| Aphanitic felsic flows and pyroclastic debris not favourable for U–Pb age determinations, >2,732 Ma based on field relationships, as flows cut by Roquemaure Sill | (a) Coherent and brecciated felsic lithofacies | (a) Coherent and brecciated lithofacies: Aphanitic to porphyritic rhyodacites and rhyolites (SiO$_2$ contents of 68–78%); coherent to brecciated flows or segments of exogenous domes (5–150 m-thick); endogenous lobes and lobate dyke terminations intrude disorganized and massive lapilli tuff breccias; m-scale lobes may display an arcuate columnar joint array near the margins; chilled lobe and flow-banded margins prominent and perlitic cracks and spherulites common | (a) A complex association of lava flows and domes in situ and autoclastic breccia deposits. Lapilli tuff breccias may represent carapace and hyaloclastite breccias with their reworked counterparts; abundant interaction with water. Effusive flows and domes in a composite volcanic structure. Dykes balloon into lobes/domes. Locus: central part of submarine edifice |

### 4.1.1. Coherent and brecciated felsic lithofacies

The coherent and brecciated felsic lithofacies contains lava flow units, and exogenous and endogenous domes. The 5–150 m thick, massive, lobate, flow-banded to brecciated felsic lava flows are prominent indicate different volcanic facies of the flow (De Rosen-Spence et al., 1980; Yamagishi and Dimroth, 1985). Observed flow bands at the margins of felsic units are typical of endogenous domes (Goto and McPhie, 1998) and extrusive flows/lobes (Yamagishi and Dimroth, 1985). Hyaloclastite (lapilli tuff) with lobate structures are well preserved (Figure 4A) in remnant screens within the feeder dyke swarm, and represent carapace breccias. The aphyric to quartz–feldspar-phyric flows have structureless centres, which grade into in-situ breccia and flow-banded hyaloclastite margins (Figure 4B), consistent with a subaqueous setting (e.g. Yamagishi and Dimroth, 1985). Flow terminations display contorted flow banding, and in situ to disrupted autoclastic breccia. Dykes locally billow into domal-lobate structures (Mueller and Mortensen, 2002), which caused inflation of the edifice. The large m-scale lobes (Figure 4B) commonly display radial-oriented columnar joints; these joint patterns are complex due to ingress of water along fractures that result in new cooling fronts. The vesicularity in flows and clasts varies significantly (5–70%) and reflects changing volatile conditions. Phenocryst rich flow units are consistent with the formation of high-viscosity thick stubby felsic flows (Yamagishi and Dimroth, 1985), whereas aphanitic flows have a lower viscosity and hence are more extensive. Although pumice is commonly associated with violent eruptions, it is also an integral component of lava flows (Fink and Manley, 1987), as observed in the HMC carapace breccias.

### 4.1.2. Volcaniclastic lithofacies and iron-formation lithofacies

The volcaniclastic lithofacies, which includes a pyroclastic facies, and a reworked pyroclastic and autoclastic facies, is interstratified with the iron-formation lithofacies (Figure 4C). The 9–71 m-thick pyroclastic facies is a product of low viscosity, deep-water fountaining eruptions (e.g. White, 2000, 2004) and is divided into (i) a basal 7–20 m-thick, massive lapilli tuff breccia with C-shaped pumice and segregation pipes (Figure 4D, E, F), (ii) a middle up to 51 m-thick, stratified lapilli tuff (Figure 4G), and (iii), an up to 2 m-thick turbiditic tuff–lapilli tuff (Figure 4C). The massive lapilli tuff breccia contains clusters of isolated and compressed irregular vesicle-rich amoeboid- to C-shaped clasts with chilled margins, fluidal textures and vesicle trains (Figure 4F). These deposits originated from hot magmatic fountains insulated from the ambient medium, water, by a steam carapace. Segregation pipes with Fe-lining at pipe margins (Figure 4E) developed locally and support hot emplacement consistent with vapour phase streaming (Fisher, 1979). The erosive power of the hot lapilli tuff breccias is substantiated by entrained m-scale BIF rip-up clasts (Figure 4D). The stratified lapilli tuff unit (Figure 4G) reflects the change from magmatic to phreatomagmatic processes caused by the ingestion of water into the magma column (Mueller and White, 1992). Stratified units in 20–50 cm-thick couplets are composed of vesicle-rich blocky lapilli, and individual layers locally pinch out laterally and display low-angle discordances. The turbidite tuff–lapilli tuff
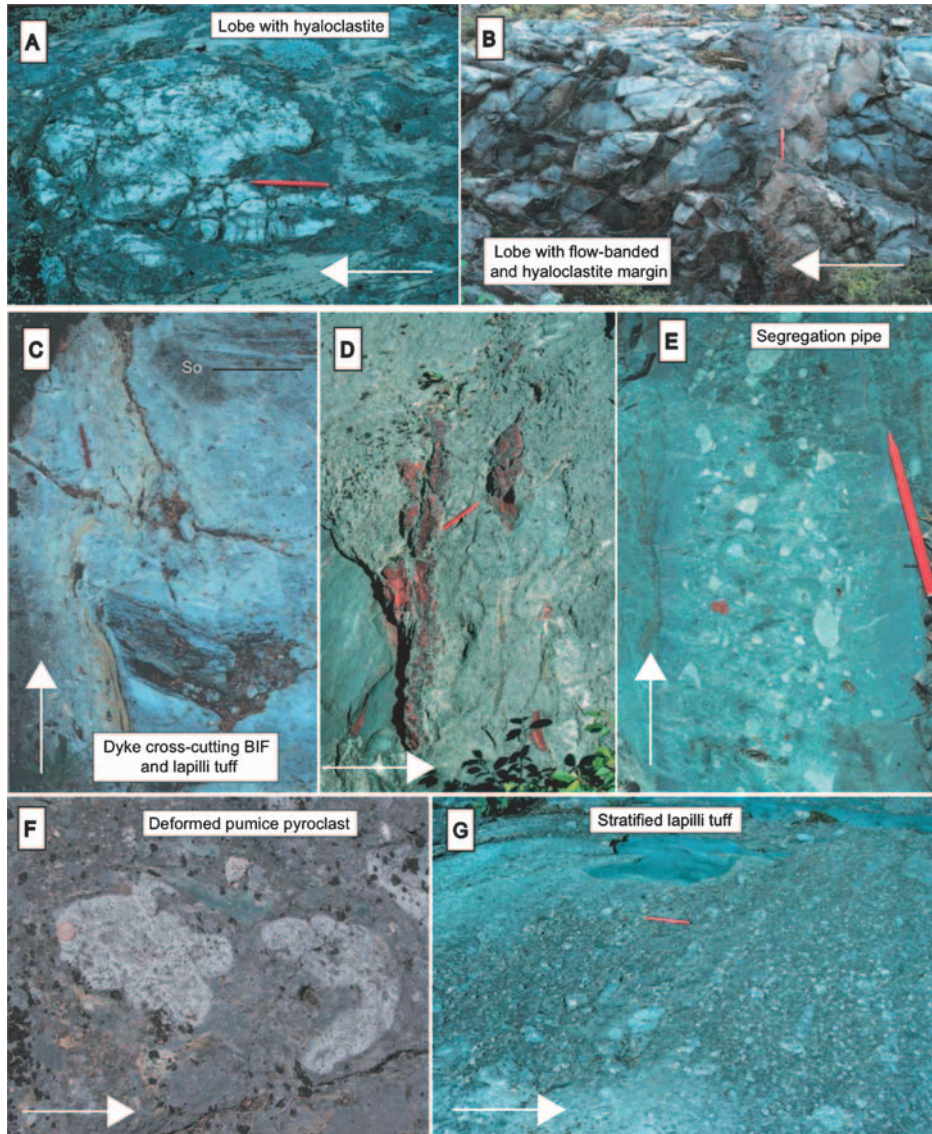
**Figure 4**   Lower formational stage of Hunter Mine caldera (HMC). Arrow indicates top in photographs. (A) Lobate structure in lapilli tuff breccia. Scale, pen 12 cm. (B) Columnar-jointed felsic lobe with altered hyaloclastite margin. Scale, pen 12 cm. (C) Felsic dyke with chilled hyaloclastite margin cross-cutting turbiditic tuff—lapilli tuff units and magnetite—jasper iron-formation. Scale, pen 12 cm. (D) Massive lapilli tuff breccia division with rip-ups clasts of jasper. Scale, pen 12 cm. (E) Hot segregation pipe in massive lapilli tuff breccia. Note delicate Fe-lining at dyke margin and largest clasts in central segment of dyke. Scale, pen 14 cm. (F) Amoeboid to C-shaped pyroclasts in massive lapilli tuff breccia. Scale, white arrow 20 cm. (G) Stratified lapilli tuff division. Scale, pen 14 cm.

unit with $T_a-T_{a-b}$ beds contains pumice, lithic fragments and vitric grains and is the result of subaqueous eruptive plume collapse. Local scours indicate turbulence during bedload transport from high-density turbidity currents. The 1–5 m-thick reworked pyroclastic and autoclastic facies consists of fine- to coarse-grained bedded tuff and lapilli tuff beds that were remobilised down-slope via density currents. The 5–20 cm-thick tuff contains graded $T_{a-b}$ beds, and 10–50 cm-thick coarse-grained tuff with 10–20% lapilli features low-angle shallow scours, suggestive of unstable density currents with pyroclasts transported under bedload conditions (Lowe, 1982; White and Busby-Spera, 1987).

The iron-formation lithofacies with magnetite, magnetite–jasper, and jasper beds (2–100 cm thick) marks the top of the tuff horizons of the tuff–lapilli tuff units (Figure 4C). This iron-formation facies developed via hydrothermal activity during periods of volcanic quiescence. Large rip-ups of jasper were observed in pyroclastic beds. Chown et al. (2002) suggested that iron-oxide formations in volcanic settings may be due to cold water seeping, but chemical precipitation is an attractive and commonly advocated alternative (Lascelles, 2007).

### 4.1.3. Felsic dyke swarm

A 5–7 km-thick, N-trending calc-alkaline rhyolite dyke swarm (Mueller and Donaldson, 1992b; Dostal and Mueller, 1996; Table 1) documents the complex evolution of the HMC. The western part of the dyke swarm can be traced 2.5 km up-section and 2.8 km along strike. Outcrop zones display a dyke density of 80% with small well-preserved remnant screens of carapace breccia. A dyke evolution from aphanitic to porphyritic phases suggests phenocryst enrichment in a high-level magma chamber. The various dyke phases based on cross-cutting relationships are: (1) D-1a aphanitic and D-1b feldspar-phyric dykes, (2) D-2, quartz–feldspar-phyric (<5% qtz), (3) D-3, quartz–feldspar-phyric (10–25% qtz), (4) D-4, dacitic feldspar-phyric and (5) D-5a, b mafic dykes. Columnar jointing is the outstanding felsic dyke feature, whereby multiple rows of columnar joints are arranged within composite dykes (up to 25 m-thick). The flow direction of the swarm is from north (base) to south (top) indicated by inverted V-shaped columnar jointed contacts (Mueller and Donaldson, 1992b). The felsic dyke swarm is similar to the distribution of mafic dykes in the rift zone of Iceland (e.g. Gudmundsson, 1983, 1984). Multiple rows of columnar joints indicate selective magma pulses (e.g. Gudmundsson, 1984). Chilled, flow-banded and hyaloclastite dyke margins are locally vesicular, have orb-like or microgranophyric textures, and contain quench spherulites. High-temperature spherulites, located in the central portions of the dyke, formed during slow cooling and nucleated preferentially around quartz phenocrysts.

## 4.2. Middle formational stage (intrusive event)

The 2,731.8+2.2/−2.0 Ma, up to 1 km-thick, E-trending Roquemaure sill, a gabbro-quartz diorite (Figure 2B; Eakins, 1972), defines the middle formational stage (Table 1; Mueller and Mortensen, 2002). Sill emplacement, like dykes,

requires a local or regional extension (Wharton et al., 1994) and extensional processes are readily accommodated in an arc setting. As the sill represents an intracaldera intrusion, it may be considered a caldera resurgence phase. The sill has been employed as a marker unit to separate lower and upper evolutionary stages (see Mueller and Mortensen, 2002 for details) and separates caldera evolution into two distinct events. Grain size differences, characterising this massive, dark green intrusive body, suggest a polyphase history. The fine- to coarse-grained gabbro contains pods with intergrowths of cm-scale hornblende, pyroxene, plagioclase and interstitial quartz. The pods yielded the age of the sill. A subophitic ($\pm$ophitic) to hypidiomorphic granular texture is prevalent: pyroxene and plagioclase are commonly uralitised and saussuritised. The sill is a tholeiitic ferrogabbro (17–21% FeO; Eakins, 1972; Mueller and Dostal, unpublished data), and felsic dykes cross-cut the sill while it was still unconsolidated, as suggested by magma mixing textures.

## 4.3. Upper formational stage (second caldera event)

A gradual up-section change from felsic- to mafic-dominated volcanism is recorded where tholeiitic, normal to Mg-rich basalts are interstratified with calc-alkaline rhyolites (Figure 2B). The lithological diversity of the second caldera event is striking. Three major lithofacies, which occur roughly in equal proportions, characterise the upper formational stage: (1) felsic and mafic volcanic lithofacies, (2) volcaniclastic and iron-formation lithofacies and (3) mafic dykes and sills (Table 1).

### 4.3.1. Felsic volcanic lithofacies and mafic volcanic lithofacies

The up to 500 m-thick felsic volcanic lithofacies displays the features of effusive lava flows with autoclastic fragmentation (e.g. Yamagishi and Dimroth, 1985; Kano et al., 1991). The coherent to brecciated felsic flows, 2–30 m-thick, have lobate terminations and flow banded margins. Brecciated upper portions of flows contain massive to stratified lapilli tuffs related to limited reworking and density current deposition (De Rosen-Spence et al., 1980; Kano et al., 1991). The 50–80 m-thick mafic volcanic lithofacies with tholeiitic and Mg–basalt (10–11% MgO) contains 2–10 m-thick massive-columnar jointed, pillowed and brecciated flow units inherent to submarine flows (Wells et al., 1979; Dimroth et al., 1985). This lithofacies includes a 30–40 m-thick chaotic breccia facies of randomly oriented rafts of magnetite–jasper iron-oxide formation (Figure 3B), segments of felsic flows, mafic flows and dismembered volcaniclastic deposits that have undergone extensive hydrothermal alteration. A collapse breccia is inferred to have formed at the caldera margin and is similar to the megabreccia at the Dorobu caldera (Miura and Tamai, 1998). Heterolithic breccias, 2–5 m-thick, are dominated by basalt clasts and minor chert, BIF fragments and felsic clasts. The massive heterolithic breccia facies with entrained pillows are debris flow deposits that formed adjacent to the caldera margin and have undergone hydrothermal silicification.

### 4.3.2. Volcaniclastic lithofacies and iron-formation lithofacies

The volcaniclastic and iron-formation lithofacies is 2–20–m–thick and composed of 2–50 cm-thick tuff–lapilli tuff (Figure 3C). The tuff–lapilli tuffs are graded $T_a$ ($S_3$–beds of Lowe, 1982), $T_{ab}$, $T_{abc}$, $T_{ad}$ and $T_{abcde}$ beds that are consistent with high- and low-concentration density current deposition. Rip-up clasts of chert and jasper are common. Pyroclast constituents include felsic shards, wispy vitric and angular lithic volcanic fragments, pumice and broken and euhedral crystals, which collectively argue for a pyroclastic deposit (Fisher and Schmincke, 1984), although they could be syneruptive with limited reworking. The black $T_d$ of the tuff turbidites and the $T_e$ mudstone represent a felsic vitric ash component (e.g. Fritz and Vanko, 1992) and background sedimentation that settled through the water column, respectively (Figure 3A). Synvolcanic faults with fluid movement (Figure 3E), water escape structures, and small-scale load casts are well preserved. The iron-carbonate horizons alternate with chert, which is either silicified tuff or diagenetically recrystallised and compacted shard-rich tuff. Even the iron-formations have been locally silicified, indicating numerous stages of hydrothermal alteration.

### 4.3.3. Mafic dykes and sills

Numerous sills and dykes intrude the upper formational stage. Tholeiitic columnar-jointed dykes intruded N-trending, synvolcanic faults and fractures, with hydrothermal black and white chert as well as laminated jasper deposited along brecciated dyke margins (Figure 3F). The gabbro sills have a well–defined subophitic texture and are massive or columnar-jointed. Columnar-jointed sills were emplaced high in the sequence, where abundant seawater may have percolated to cause rapid cooling and vesiculation due to devolatisation. In addition, aphanitic basalt and dacite bodies intrude at a shallow angle subparallel to bedding. These sills acted as local barriers for hydrothermal fluid movement, which resulted in sulphide precipitation at the volcaniclastic sediment–sill interface.
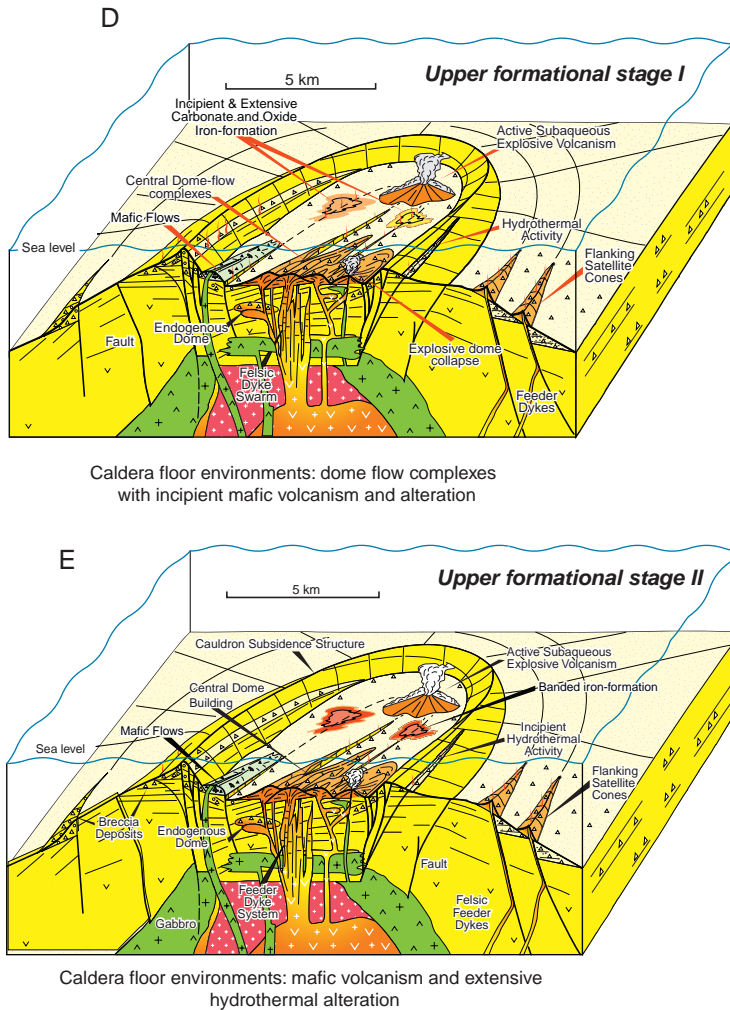
## 4.4. Evolution of hunter mine caldera

The subaqueous HMC has a polyphase history (Figure 5A–E), in which a caldera, dominated by effusive felsic volcanism evolved over ca. 6 m.y. The distribution of lithofacies and synvolcanic faults, if only at the small scale, suggest either a piston or incipient piecemeal caldera. The first caldera-forming event (lower formational stage, Figure 5A, B) exhibits both incremental fragmentation of the caldera floor into horst and graben structures and the development of a caldera margin along a major ring fault. Early reverse and subsequent normal faults formed and facilitated subsidence. Volcanism was dominated by thick dome-flow-hyaloclastite complexes and some of the vesicular clast-rich breccias may have a low-energy explosive (frothing) component, caused by devolatisation and violent water–magma interaction. Energetic fountains driven by rapid devolitisation of magma developed locally under deep-water hydrostatic pressures (Mueller and White, 1992). A period of felsic quiescence ensued as major tholeiitic sills intruded high in the sequence. The Roquemaure sill (Figure 5C) of the middle formational stage attests to a phase
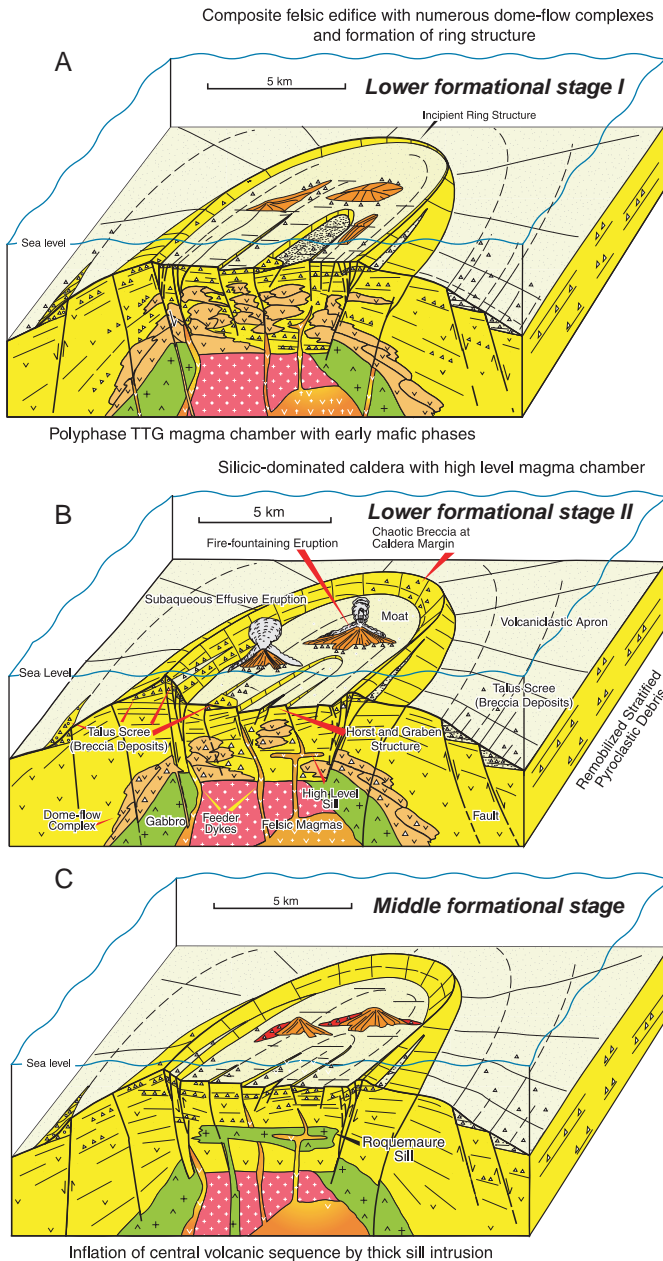
**Figure 5** Evolution of the Hunter Mine caldera based on physical volcanology, sedimentology, faults and precise U—Pb zircon ages (modified from Mueller and Mortensen, 2002). (A) Incipient submarine caldera subsidence structure with ring fractures and a central moat zone composed of felsic volcanic flows and domes. The intracaldera floor developed a horst and graben structure. (B) Continued subsidence in central portion of volcanic structure during first caldera phase with magmatic-fountaining eruptions and autoclastic dome fragmentation processes. (C) Emplacement of the Roquemaure sill and inflation of the central subsidence structure. (D) Well-developed second caldera event with a major dome–building phase and the extrusion of mafic tholeiitic pillowed flow at the caldera walls. Note formation of banded iron-formation deposits on the caldera floor. (E) Extensive hydrothermal alteration and banded iron-formation associated with VMS (modified from Mueller and Mortensen, 2002).

Caldera floor environments: dome flow complexes
with incipient mafic volcanism and alteration



Caldera floor environments: mafic volcanism and extensive
hydrothermal alteration

**Figure 5**  (*Continued*).

of extension that triggered caldera resurgence and endogenic growth, commonly referred to as ballooning of the edifice. The geometry of the sill compares favourably with a high-level laccolith. The upper formational stage (Figure 5D, E) represents the second caldera-forming event with formation of a major felsic dyke swarm related to dome-flow-hyaloclastite complexes. Explosive and effusive felsic volcanism continued, but at the caldera wall margin mafic effusive volcanism was initiated. During this stage, extensive low-temperature hydrothermal activity commenced. Hydrothermal iron-formations and a pervasive Fe-carbonate alteration pattern developed (see Section 7.1). The mineralisation is linked to the alteration and is located at the top of the sequence in the volcaniclastic deposits near the interface with komatiites.

# 5. Normetal Caldera

The Normetal volcanic complex in the NVZ (Figure 1) is a 4 km-thick volcano-sedimentary sequence, here redefined as the Normetal caldera (NC). The ca. 2,728 Ma NC is part of the north Normetal block (Figure 6A, B), which includes underlying basalt and iron-formation of the Gale Group (Latulippe, 1976). The south Normetal block contains basalt, andesite, iron formation and gabbro (Péloquin, 1994). The Patten fault separates the northern NC from Chicobi Group sedimentary rocks of the south Normetal block. Lafrance et al. (2000) divided the 4 km-thick NC (Figure 6B) into five volcanic phases and one volcaniclastic event (Table 2). Phase 1 represents a basaltic subaqueous shield volcano, in which the incipient ring fractures were established. Mafic and felsic volcanic–volcaniclastic rocks of phases 2, 3 and 4 are indicative of various caldera-forming stages. The 20–70 m-thick Normetal volcaniclastic units and shale constitutes the Normetal marker horizon (Table 2) and represents a pause in volcanism. Phase 5 is the youngest volcanic succession (Lafrance et al., 2000), which hosts the Normetal mine (11 Mt grading 5.12% Zn, 2.15% Cu, 0.549 g/t Au and 45.25 g/t Ag; Teasdale, 1993) and the satellite Normetmar deposit (160,000 t at 12.6% Zn). The overall NC geometry was based on lithofacies organisation, structural analysis, and the recognition of synvolcanic faults, and permitted the separation into western, central and eastern caldera segments (Figure 6A).

## 5.1. Normetal caldera phases 1 and 2

Phase 1 is the 1–2 km-thick precaldera mafic shield-building stage which is composed of basaltic andesite, andesite and minor dacite. Massive, pillowed and pillow breccia flows represent a typical subaqueous flow arrangement (Dimroth et al., 1978; Cousineau and Dimroth, 1982). The 4–20 m thick pillowed flows have 0.5–2 m-wide pillows that display local radial cooling joints. Pillow breccias contain 10–30 cm amoeboid-shaped pillow fragments suggesting low-viscosity. Interstratified felsic flows of dacitic composition are massive and aphanitic.

Phase 2 (Table 2) constitutes the principal constructive and complex caldera-forming phase of the NC. The 0.8–2.2 km-thick andesite–dacite and rhyolite units, are divided into (i) a basal andesite unit (phase 2a), (ii) a medial felsic volcaniclastic unit (phase 2b) and (iii) an uppermost andesite–dacite and rhyolite unit (phase 2c), which is distributed in the western (Figure 7A, B), central (Figures 7C–D and 8a–b) and eastern caldera segments (Figure 8C, D). The andesitic phase 2a in the western and central segments is a 30–640 m-thick lava flow unit displaying a lateral change from massive to pillowed flows to pillow breccia passing up-section and laterally into lapilli tuff over 2–3 km (Figure 7A, B). A subaqueous setting dominated by effusive volcanism is interpreted (Dimroth et al., 1978).

Phase 2b, represented by 5–50 m-thick felsic volcaniclastic deposits of graded bedded (GB) tuff–lapilli tuff, matrix-supported lapilli tuff breccia, and clast-supported lapilli tuff breccia, is restricted to the western and central segments. The tuff–lapilli tuff is considered a product of high- to low-concentration turbidity
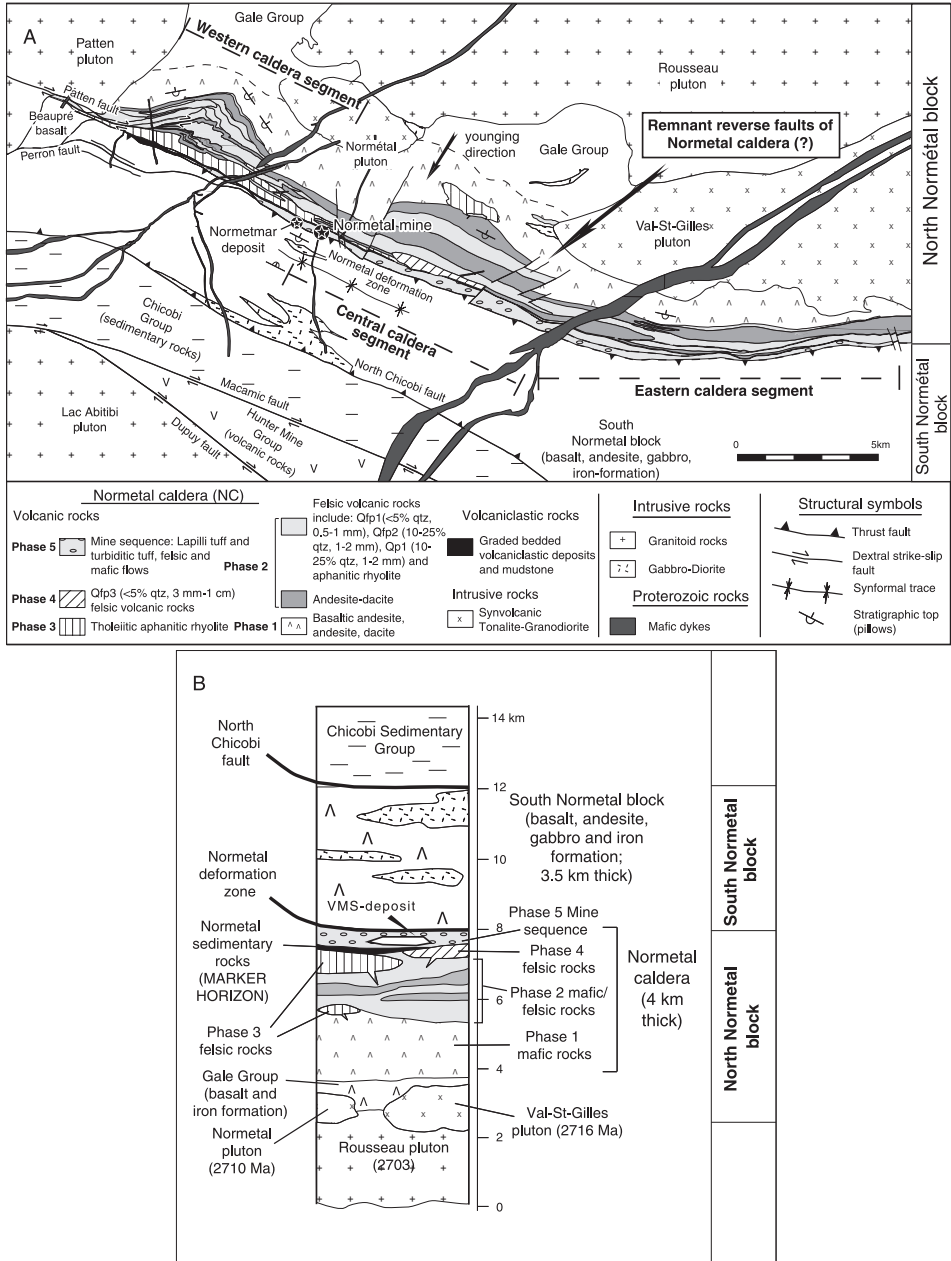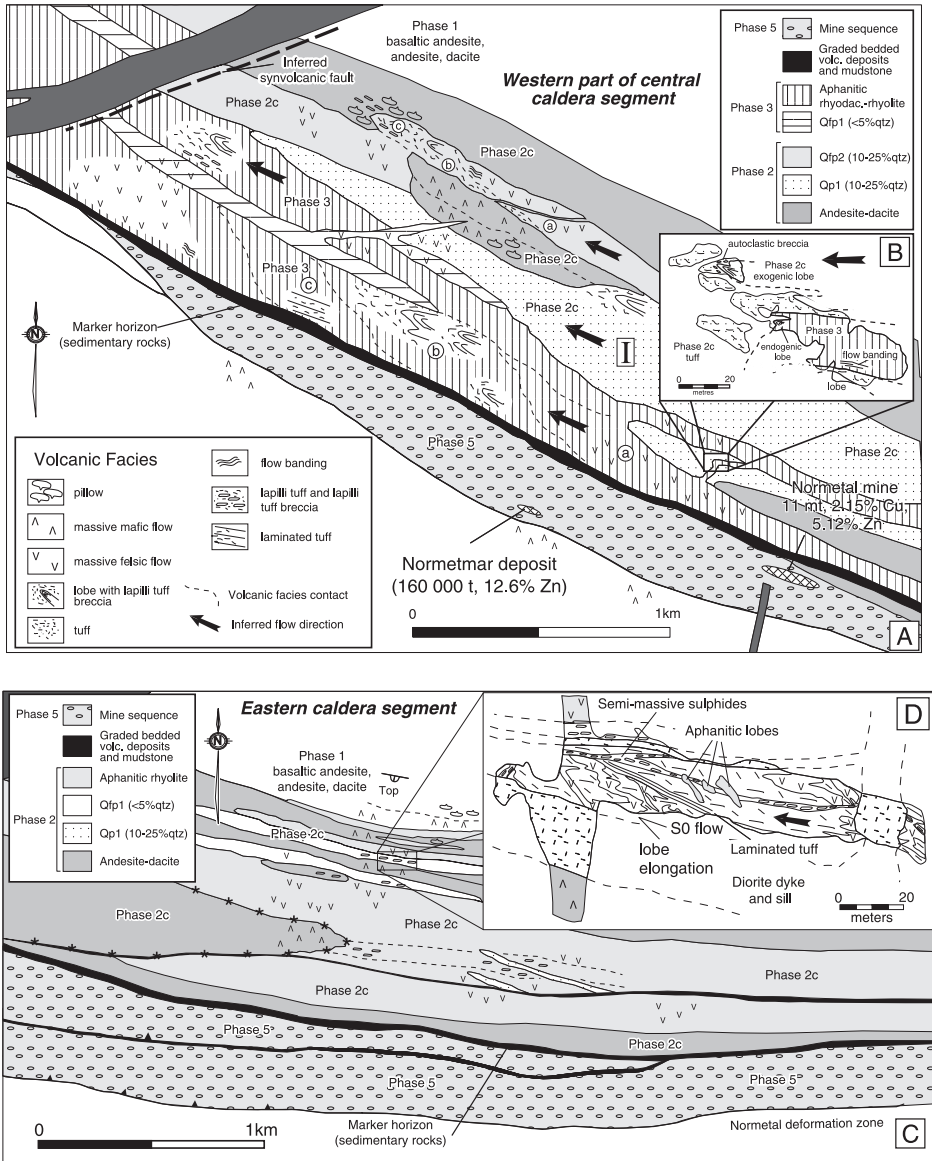
**Figure 6**   (A) Regional geology of the Normetal area. (B) Composite stratigraphy of the Normetal area (modified from Lafrance et al., 2000, with permission from Elsevier).

**Table 2**  Characteristics of the Normetal caldera.

| | Phase I | Phase II | | | Phase III | | Phase IV | Normetal Marker horizon | Phase V |
| --- | --- | --- | --- | --- | --- | --- | --- | --- | --- |
| | | Phase IIa | Phase IIb | Phase IIc | | | | | |
| Composition: $SiO_2$ vs. Zr/$TiO_2$ ratios | Basaltic andesite, andesite and dacite | Andesite | Rhyolitic volcaniclastic deposits | Andesite–dacite | Rhyolite | Rhyodacite–rhyolite | Rhyodacite and rhyolite | Volcaniclastic deposits and background sedimentation | Andesite–dacite and rhyolite |
| Phenocryst/crystal content of rhyolites/volcaniclastics | | | 10–25% qtz crystals, 1–2 mm | | Qfp1 (<5% qtz, 0.5–1 mm) Qp1 and Qfp2 (10–25% qtz, 1–2 mm) Aphanitic | Aphanitic (micro feldspar-phyric) | Qfp3 (<5% qtz 3 mm–1 cm) | 10–20% qtz crystals, 1–2 mm | Qfp1 (<5% qtz, 0.5–1 mm) Qfp2 (10–25% qtz, 1–2 mm) Aphanitic |
| Flows morphology and deposits textures | Massive and pillowed, flows with minor pillow breccias | Massive or pillowed flows with pillow breccias, block lavas, lapilli tuff | Turbiditic tuff, lapilli tuff breccia, fine-grained laminated tuff | Massive or pillowed flows with pillow breccias, lapilli tuff, sills; dacite block lava | Massive flows and lobes with lapilli tuff, flow banding and columnar joints; lapilli tuff, lapilli tuff breccia, tuff; felsic domes | Massive flows and lobes with lapilli tuff, breccia, flow banding and columnar joints, lapilli tuff, tuff, dykes, sills, felsic domes | Massive and flow banded dykes and felsic intrusions | Turbiditic $S_3$ tuff-lapilli tuff $T_{d-e}$ beds; fining- and thinning-upward sequences; reworked volcanic deposits | Mafic–felsic flows Lapilli tuff breccia, lapilli tuff and tuff; fining- and thinning-upward sequence |

| | | | | | | | | | |
|---|---|---|---|---|---|---|---|---|---|
| Stratigraphic thickness | 1–2 km | 30–640 m | 5–50 m | 90–580 m | 150–920 m | 100–600 m | 475 m | 20–70 m | 100–400 m |
| Flow/bed thickness | 4–20 m | 30–225 m | 1 cm–10 m | 35–150 m | 115–350 m | 75–275 m | | 2–40 cm fine- and coarse-grained tuff, 0.3–5 cm shale | 2–50 cm tuff, lapilli tuff; 1–3 m lapilli tuff breccia |
| Dimension of dome | | | | 1 km long and 170 m thick | 2.5 km long and 250 m thick (Qfp2) and 1 km long and 225 m thick (Qfp1) | 2.2 km long and 550 m thick | 3.5 km long and 475 m thick | | Highly deformed |
| Volcanic setting and eruptive style | Subaqueous Effusive and autoclastic | Subaqueous Effusive and autoclastic | Subaqueous Resedimented hydroclastic or autoclastic | Subaqueous Effusive and autoclastic | Subaqueous Effusive and autoclastic | Subaqueous Effusive and autoclastic Endogenic lava intrusions | Subaqueous Exogenic (?) dome | Substorm-wavebase, Deep-water sedimentation | Subaqueous hydroclastic (reworked?) and effusive volcanism |

*Note:* Qfp, quartz feldsparphyric; Qp, quartz-phyric.

**Figure 7** (A—B) Detailed facies analysis of western and (C—D) central segments of the Normetal caldera. Note lateral flow changes from massive to lobate to brecciated (labelled a—b—c) in rhyolite as well as lateral changes from massive to pillow to pillow breccia (labelled a—b—c) in the basaltic andesite. Volcanic facies organisation is used to indicate a principal flow component (modified from Lafrance et al., 2000, with permission from Elsevier).

**Figure 8** (A—B) Western and (C—D) central segments of the Normetal caldera. The VMS deposit and mineralisation is restricted to phase 5 (modified from Lafrance et al., 2000, with permission from Elsevier).

currents. The matrix-supported lapilli tuff breccia and the clast-supported lapilli tuff breccia are interpreted as cohesive debris flow deposits transported down-slope via laminar flow conditions (Lowe, 1982). These fragmental deposits may be either pyroclastic or autoclastic in origin, but considering the predominance of effusive flows in this part of the sequence, autoclastic debris triggered by tremors or dome

collapse and redistributed by sediment gravity flow processes is favoured (Mueller et al., 1994). Phase 2c (0.8–1.5 km thick) contains andesite, dacite and rhyolite flows, dykes and endogenous domes. A 90–580 m-thick massive and pillowed andesite with pillow breccia and lapilli tuffs is well exposed in the eastern part of the central segment (Figure 7C, D). Dacite flows are massive with local, angular breccia-size fragments. The 150–920 m rhyolite units are flows, dykes and endogenous domes, and are associated with tuff, lapilli tuff and lapilli tuff breccia. Columnar joints, 5–20 cm in diameter, characterise flows (Figure 9A, B) and high-level endogenous domes. Lateral flow morphology over 1–2 km includes (Figure 7A–D) changes from massive to 1–20 m-thick, west-closing lobes with massive centres and a marginal metre-thick flow-banding lapilli tuff breccia (Figure 9C) and laminated-stratified tuff. These features compare favourably to subaqueous facies models of Yamagishi and Dimroth (1985) and de Rosen-Spence et al. (1980). Large massive bodies, characterised by uniform phenocryst content, massive facies and local intrusive contacts are interpreted as endogenous domes (Goto and McPhie, 1998). Massive to lobate rhyolitic flows are products of viscous flow (Kano et al., 1991; Manley, 1992, 1996).

## 5.2. Normetal caldera phases 3 and 4

The 100–600 m-thick, aphanitic rhyodacite–rhyolite phase 3 volcanism in western and central segments (Figures 7a, d, 8a, b) contains 75–275 m-thick flow units traceable for 10 km along strike. Flow units display a change over 2–3 km, from massive to 3–30 m-thick massive or flow-banded lobes to lapilli tuff breccia, which grade up-section and laterally into massive, 1–10 m-thick lapilli tuff (2–5 cm-size) and 1–10 m-thick laminated tuff composed of 2–10 cm-thick beds. Well developed 8–15 cm-wide columnar joints are predominant in the basal parts of flows. Sills and dykes crosscut the previous phase 2 flows and feature local lobes with flow banded chilled margins. Similarly, massive to flow-banded units and lapilli tuff breccias alternate in the central segment. Metre-scale flow banding with mm to cm thick sericite-rich bands mark the contact between massive flows and lapilli tuff breccia. Collectively, these features are hallmarks of lateral volcanic facies changes in subaqueous felsic flows (de Rosen-Spence et al., 1980; Yamagishi and Dimroth, 1985; Kano et al., 1991) and domal structures. Water depths may range between 200 and 1,000 m (Kano et al., 1991). The lapilli tuffs and laminated tuffs formed from high- and low-concentration turbidity flows (Lowe, 1982), representing either reworked autoclastic debris or local explosive hydroclastic products.

A 475 m-thick rhyodacite–rhyolite unit of phase 4 (Figure 9D) in the central segment is composed of a massive unit and dykes that contain 3–10 mm large quartz and feldspar phenocrysts (Qfp3; Figure 7C, D). The 15–20 m-thick Qfp3 dykes cut phase 2 rocks. The dykes are massive with 30 cm-thick flow banded margins and have 10–15 cm-thick chilled margins at the contact with phase 2c Qp1 lapilli tuffs. The geometry, large-scale change in flow band orientation from NW–SE to NE–SW and intrusive nature of the unit favour the interpretation of a high-level endogenous dome (Burt and Sheridan, 1987; Goto and McPhie, 1998) and the dykes of similar phenocryst composition are considered feeders to the dome.
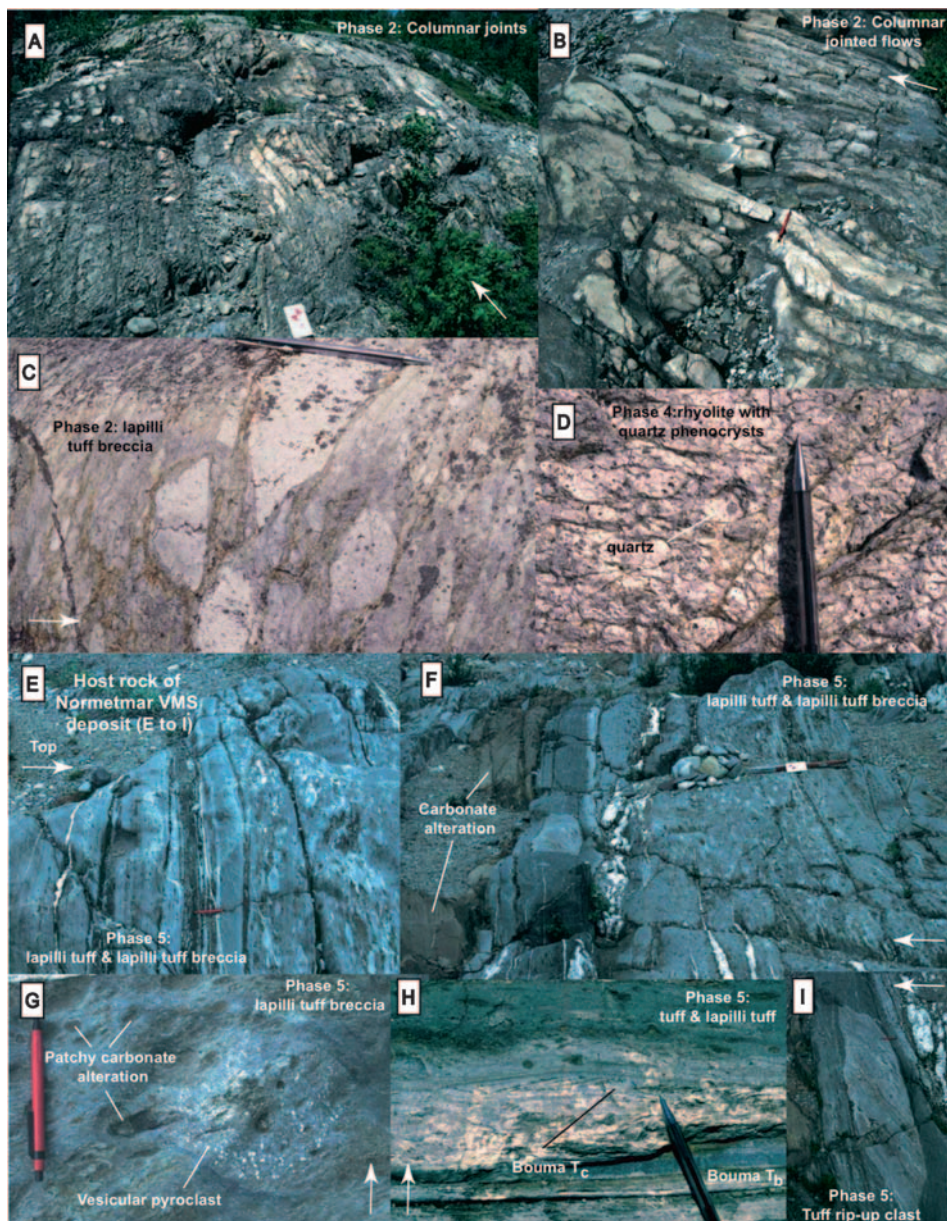
**Figure 9** Characteristics of the Normetal caldera. Arrow indicates younging direction. (A) Phase 2 rhyolite flow with 5–15 cm columnar joints. Scale: field book 17 cm. (B) Close-up of columnar-jointed flow. Scale: pen 13 cm. (C) Lapilli tuff (autoclastic) breccia of major caldera construction phase. Scale: pen 13 cm. (D) Massive quartz-phyric rhyolite of phase 4. Note the large quartz phenocrysts and the deformation. Scale: pen 6 cm. (E) Volcaniclastic deposits of phase 5 with lapilli tuff breccia, and stratified lapilli tuff. Scale: pen 13 cm. (F) Basal part of fining-upward sequence with lapilli tuff breccia and lapilli tuff. Scale: field book 17 cm. (G) Pyroclast with abundant calcite-filled vesicles. Selected pyroclasts display patchy brown carbonate alteration. Scale: pen 13 cm. (H) Thin-bedded tuff turbidites with parallel-laminated Bouma $T_b$ and crossbedded Bouma $T_c$ sedimentary structures. Scale: pen 8 cm. (I) Out-sized tuff rip-up clast in lapilli tuff bed. Scale: pen 13 cm.

## 5.3. Normetal volcaniclastic deposits (normetal marker horizon)

The 20–70 m-thick volcaniclastic rocks, traceable for ca. 35 km, represent the marker horizon from which Normetal caldera geometry can be deciphered. The volcaniclastic rocks are composed of massive and normal graded lapilli tuff and tuffs with up to 4 m-thick massive to finely laminated fine-grained tuffs and locally 1 m-thick laminated mudstone capping coarser sequences. The 2–10 m-thick fining and thinning upward sequences are locally developed. Generally, 10–40 cm-thick lapilli tuff and tuff beds contain 10–20% quartz crystals, whereas fine-grained tuff and mudstone forms 2–25 cm and 0.3–5 cm-thick beds, respectively. The broken and euhedral quartz crystals favour a pyroclastic origin (Stix, 1991), whereas the massive and normal graded lapilli tuff and tuffs are interpreted as sediment gravity flows that represent rapid fallout from high-concentration flows (Bouma $T_a$ or $S_3$-beds; Lowe, 1982; Chough and Sohn, 1990). The laminated tuff and mudstone represent Bouma $T_{de}$ divisions, in which fines were deposited from volcanic fallout and background sedimentation, respectively. Suspension sedimentation associated with turbidites suggests a depth below storm wave base ($>200$ m depth).

## 5.4. Normetal caldera mine sequence phase 5

The 100–400 m-thick Mine Sequence hosts the Normetmar and Normetal deposits. Phase 5 is a combination of massive mafic and felsic volcanic flows and volcaniclastic deposits exposed 30 km along strike discontinuously. The volcanic flows are similar to the flows of the other caldera phases. The polymetallic deposits are hosted in the fragmental rocks. The andesitic to felsic lapilli tuff breccia, lapilli tuff and tuff are best exposed at the Normetmar showing (Figure 9E, F). The volcaniclastic units contain 2–5 m-thick fining-upward sequences, and display a prominent patchy carbonate alteration (Figure 9E, F) and a subtle quartz-sericite-chloritoid alteration assemblage. The basal, 1–3 m-thick lapilli tuff breccia contains lithic, feldspar-phyric and vesicular pyroclasts (Figure 9G). The massive to GB, 2–50 cm-thick tuff and lapilli tuff beds locally contain ripples and crossbeds (Figure 9H). Numerous lapilli tuff beds have an internal stratification with upper portions of graded beds locally laminated. Outsized volcanic blocks and rip-up clasts were observed in some beds (Figure 9I). The componentry and fining- and thinning-upward sequences of the massive to graded tuff–lapilli tuff support a volcanic and possibly explosive origin (Mueller et al., 1994). Massive to graded tuff–lapilli tuff represents deposition from subaqueous density currents (Bouma $T_a$ or $S_3$-beds; Lowe, 1982), and laminated portions of graded beds (Bouma $T_b$) are consistent with reduced fallout rates and transport velocity during the same depositional event (Smellie and Hole, 1997). The stratification in planar beds and ripples/crossbeds are $S_1$-beds of Lowe (1982) and Bouma-$T_c$ subunits that indicate bedload transport and flow unsteadiness. This is common in pyroclastic deposits due to turbulence and rapidly changing particle concentrations with highly variable particle densities. The massive and in part poorly graded lapilli tuff breccia is considered a high concentration particulate density flow, possibly the equivalent of $R_3$-beds (c.f. Lowe, 1982).

## 5.5. Normetal caldera evolution

The bimodal Normetal caldera is divided into 5 volcanic phases and a sedimentary event (Figure 10A–F; Lafrance et al., 2000), with an overall geometry suggestive of a piston caldera. The early phase I construction is a broad subaqueous shield volcano composed of pillowed basalts and basaltic andesites associated with minor massive dacite flows (Figure 10A). The shield volcano evolved into three structurally controlled segments that formed volcanic centres with felsic subaqueous volcanism characterised by effusive flows and autoclastic debris. The central caldera structure formed during phase II and synvolcanic fault systems were well established (Figure 10B). The principal events of volcanic construction with overlapping of emission centres occurred during phase III. Volcanism was both andesitic and rhyolitic with abundant volcaniclastic debris of both autoclastic and possibly pyroclastic origin (Figure 10C). Phase IV is small-scale event, but important as indicated by the emplacement of endogenous and exogenous domes and the geochemistry. Instead of calc-alkaline rhyolites, distinct tholeiitic rhyolite volcanism occurred at this stage (Lafrance et al., 2000; Figure 10D). After extensive volcanic construction, a period of volcaniclastic sedimentation ensued. These deposits are volcaniclastic turbiditic deposits and background sedimentary rocks that can be traced 30 along strike, and therefore serve as the principal marker horizon for the Normetal Caldera complex (Figure 10E). Phase V represents the Mine Sequence with volcaniclastic deposits hosting the massive sulphides (Figure 10F). Subordinate (<20%) mafic and felsic flows constitute the remaining portion of this last stage. The Normetal VMS deposit and Normetmar mineralisation is constrained to the volcaniclastic lithofacies.

## 6. Sturgeon Lake Caldera, Wabigoon Subprovince

The 2,733–2,736 Ma Sturgeon Lake caldera of the Wabigoon Subprovince (Figure 11A) is composed of a 2–4 km-thick, volcanic sequence (Hudak et al., 2003; Franklin et al., 2005). The base of the caldera is intruded by high-level 2,734 Ma Beidelman Bay intrusive complex, a tonalite–diorite sill-like body at least 2 km-thick and traceable for 20 km along strike (Morton et al., 1991; Galley, 1993). The 2–4 km-thick intracaldera succession contains six past producing VMS deposits with a total of $18.7 \times 10^6$ tonnes at an ore grade of 8.5% Zn, 1.06% Cu, 0.91% Pb and 119.7 g/tonne Ag. The 11.4 Mt Mattabi deposit was the largest. The Sturgeon Lake VMS deposits are linked to the early and late phases of a 30 km wide intracaldera volcano-tectonic depression (Figure 11B; Morton et al., 1991), which is dominated by 1–2 km-thick volcaniclastic debris and subaqueous pyroclastic density flow deposits. The sequence is briefly described as this caldera is a rare Archean example of a subaqueous tephra dominated structure.

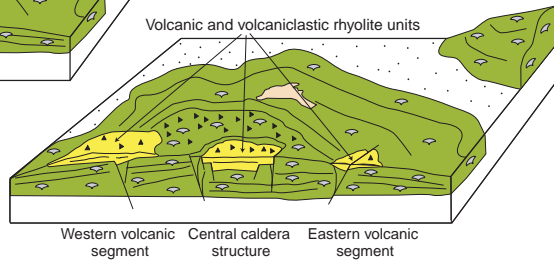## 6.1. Sturgeon lake caldera volcanic succession

The Sturgeon Lake caldera is composed of an extensive mafic shield volcano and a shoaling caldera-forming phase (Morton et al., 1991; Hudak et al., 2003), which is
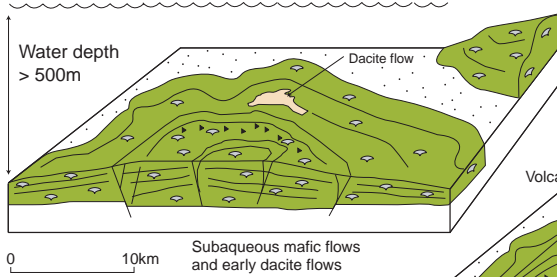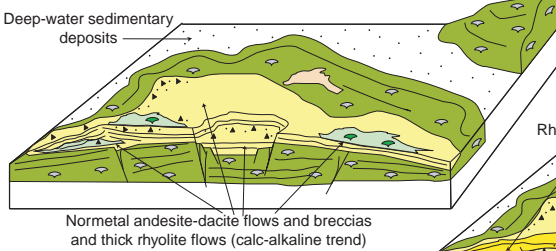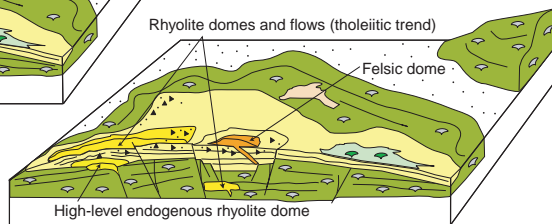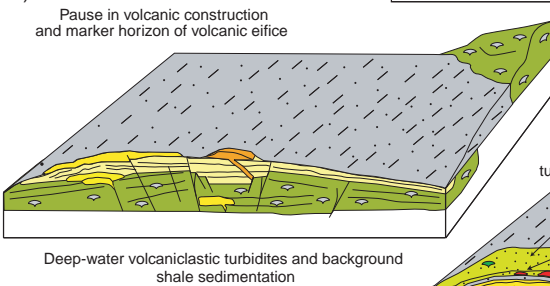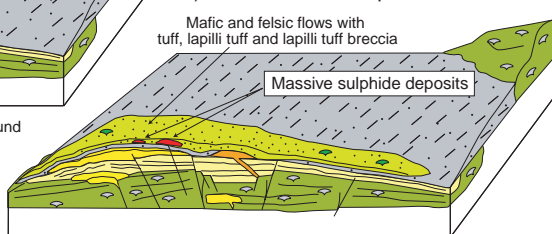
**Figure 10**    Paleogeographic reconstruction of the Normetal caldera from a mafic subaqueous shield volcano to a piston type caldera. See text for details (modified from Lafrance et al., 2000, with permission from Elsevier).

comparable to the subaqueous to subaerial shield volcano stage on Tenerife (Martí and Gudmundsson, 2000) and the subaqueous shield volcano complex of the Normetal (this study). The evolution of the caldera can be divided into: (i) a 200–2,100 m-thick, shield-forming phase composed of mafic to felsic volcanic rocks,
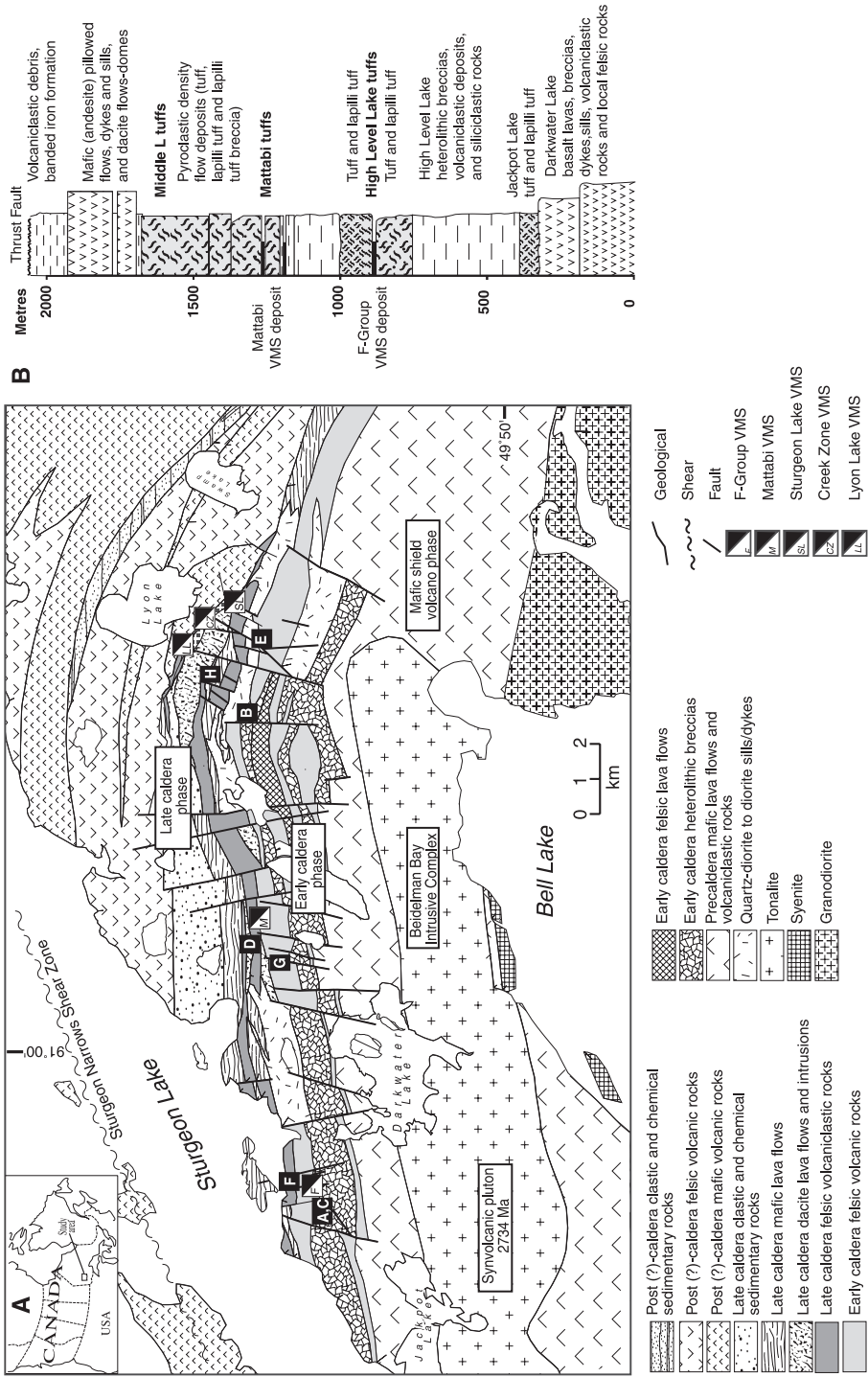
**Figure 11** (A) Sturgeon Lake caldera in the Wabigoon Subprovince divided into precaldera, early and late caldera phases (modified from Mueller et al., 2004). Note the abundance of pyroclastic debris. (B) Composite stratigraphy of the Sturgeon Lake caldera with the early and late caldera phases (modified from Franklin et al., 2005; stratigraphic section from author A. Galley).

(ii) an early, 650–1,300 m-thick, caldera stage composed of pyroclastic deposits that contains the principal Mattabi VMS deposit, (iii) a 500–1,500 m-thick, late caldera stage with andesite–dacite flows, endogenic domes, banded iron-formation and volcaniclastic debris and (iv) the poorly correlated Lyon Lake Fault succession composed of basaltic–andesitic flows and volcaniclastic rocks (Morton et al., 1991; Hudak et al., 2003).

The precaldera shield volcano, referred to as the Darkwater succession (Figure 11), was interpreted by Groves et al. (1988) as an emergent to subaqueous mafic sequence, yet volcanism must be subaqueous considering the presence of massive sulphide deposits up-section in prominent water-lain GB deposits. According to Groves et al. (1988) this lowermost succession contains four units: (1) a 600–800 m-thick unit composed of mafic massive and flow-top breccias, (2) 20–400 m-thick felsic lava flow units with individual massive to brecciated flows 3–80 m-thick, (3) 40–100 m-thick breccias and 0.5–1.5 m-thick bedded tuff–lapilli tuffs deposited by turbidity currents and (4) 100–800 m-thick bedded pyroclastic unit deposited by high- and low-concentration density currents in a subaqueous setting.

The intracaldera succession has an early and late caldera phase, and Hudak et al. (2003; Figure 12) have given a rigorous description of the pyroclastic rocks. The early basal phase of the caldera features the inferred subaerial Jackpot Lake succession and meso- to mega-breccias interpreted as caldera wall collapse deposits (Morton et al., 1991). Up-section the 16 km$^3$ High Level Lake Tuff represents the first large-scale explosive phase and the voluminous 27 km$^3$ Mattabi Tuff ends the early caldera phase. The 80–300 m-thick High Level Lake tuff contains massive, graded to well–bedded tuffs and lapilli tuff units that display marked lateral facies change along strike of the intracaldera floor. The subaqueous Mattabi tuff pyroclastic units, collectively 15–650 m-thick (Figure 12), exhibit a vertical fining-upward sequence composed of (a) a basal 10–155 m-thick massive lapilli tuff, (b) a medial 6–48 massive to graded lapilli tuff and (c) a normal to inverse graded medium bedded to laminated tuff up to 13 m-thick (Hudak et al., 2003), which Mueller et al. (2004) used to interpret as an indicator of primary deposition in a subaqueous setting.

The late caldera phase, with the exception of the explosive 7 km$^3$ Middle L tuff unit, features predominant subaqueous effusive volcanism. A thick pillowed andesitic unit covers a large portion of the intracaldera floor and felsic lava domes are common. The 15–150 m-thick Middle L tuff, thickest at the F-Group deposits, is composed of (a) 3–60 m-thick massive to normal graded quartz and feldspar-rich tuff and lapilli tuff and (b) 0.1–15 m-thick massive graded and parallel laminated tuff locally rich in quartz crystals. The Lyon Lake Fault sequence remains enigmatic. The massive sulphide deposits are located in the porous pyroclastic deposits (Figure 12).

# 7. The Link: Subaqueous Calderas with Chert–Iron Formation and Hydrothermal Carbonates

Calderas contain autoclastic and pyroclastic debris as well as caldera wall collapse deposits that have a high porosity over kilometre distances, so that
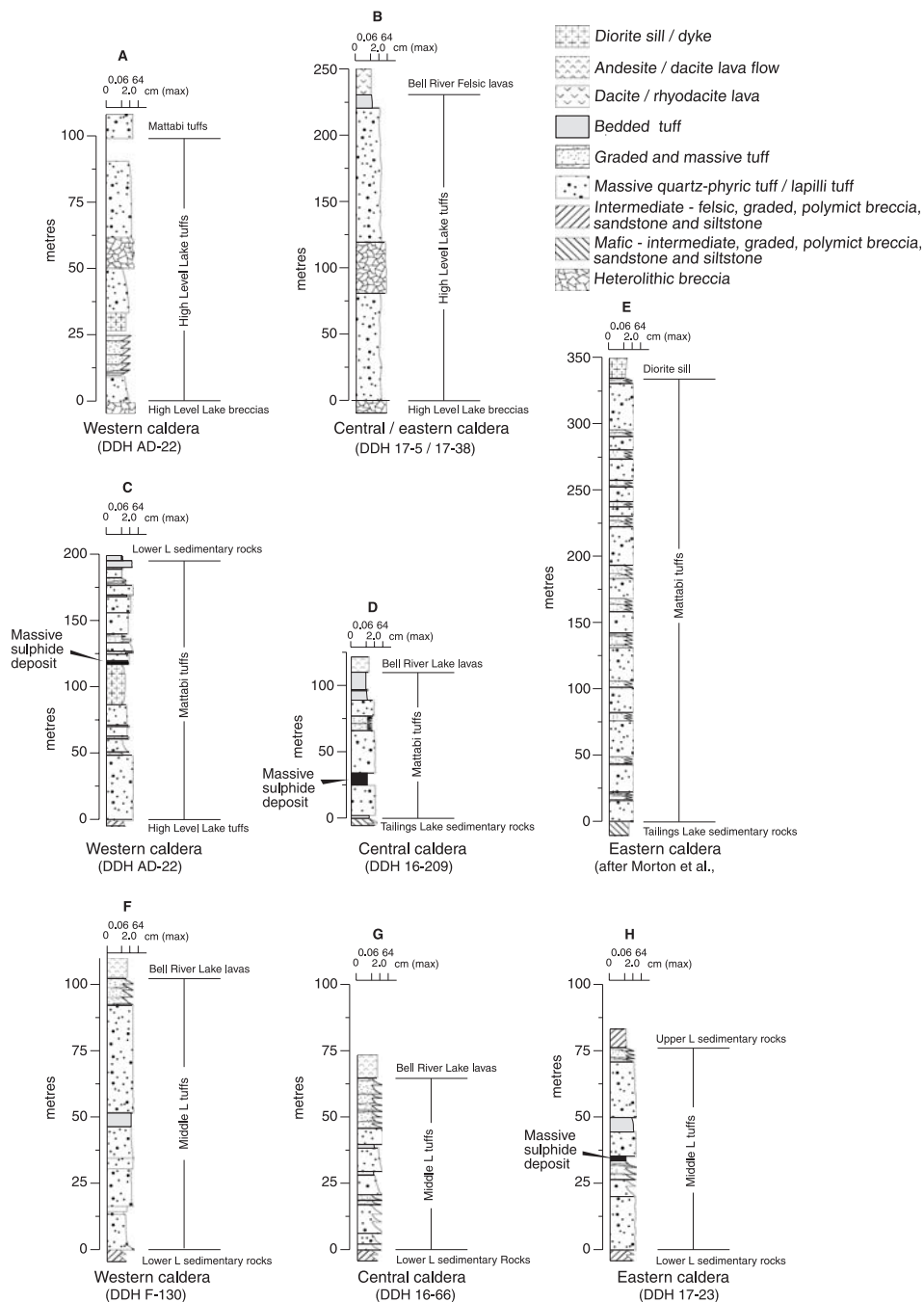
**Figure 12** Sturgeon Lake caldera with the location of massive sulphide deposits in the thick intracaldera subaqueous pyroclastic density flow deposits (from Hudak et al., 2003; Mueller et al., 2004, with permission from Elsevier).

circulation of hydrothermal and metal-bearing fluids is readily accommodated. Silica impregnation and carbonate alteration are important ingredients. Modern arc analogues show calderas are excellent hydrothermal massive sulphide sites (Ishibashi and Urabe, 1995; Iizasa et al., 1999), yet extensive carbonate alteration with VMS appears to be an Archean and Paleoproterozoic phenomenon, although it has been observed in the Paleozoic, Que River deposit, Mount Read Volcanics (Offler and Whitford, 1992). Morton and Franklin (1987) initially defined two types of alteration patterns related to hydrothermal fluid movement: (1) the Noranda type with a discordant chlorite–sericite alteration pipe, and (2) a Mattabi type with semi-conformable carbonate alteration zone. Numerous Archean silicic-dominated calderas in the Archean Superior Province display up to 50 km wide carbonate alteration zones (Chown et al., 2000; Lafrance, 2003). Franklin (1993) and Galley (1993) recognised the importance of carbonate alteration in VMS deposits but detailed studies of hydrothermal carbonate remain scarce. Exceptions are the Normetal caldera (Lafrance, 2003), the Ben Nevis area of the Blake River Group (Hannington et al., 2003) and the Hemingway property, Kidd Creek (Schandl and Wicks, 1993).

Still controversial are banded iron-formations (BIF) and related chert, as both have been generally interpreted as chemical precipitates rather than replacement deposits (Maliva et al., 2005; Lascelles, 2007). They are commonly referred to as exhalites (e.g. Tucker-Barrie et al., 2005), but the interpretation as exhalite is highly misleading and often erroneous. Precambrian iron-formations have been correlated with an early Earth $CO_2$-enriched atmosphere (Trendall, 2002). The chert–iron carbonate formation in the studied submarine volcanic centres is of hydrothermal origin (e.g. Chown et al., 2000), and represents a subset of what was originally referred to as Algoma type iron-formations or as proposed by Dimroth (1986), pelagic iron-formations. They are distinct from classical chert–magnetite oxide iron formations originally termed Superior type or platform iron-formations (Dimroth, 1986). Iron-formations of the pelagic iron-formation type and associated chert horizons are key elements in VMS exploration.

Silicification associated with carbonates represents an early stage of hydro-thermal alteration (Galley, 1993; Chown et al., 2000), and is located near or at the surface (Skirrow and Franklin, 1994; this study) or at a depth of 1–2 km close to synvolcanic plutons (Galley, 1993; Skirrow and Franklin, 1994; Lafrance, 2003). The silica is derived from (1) low-temperature 50–150°C seawater rock inter-actions (element leaching) of the volcanic rocks (Galley, 1993) and (2) deuteric (autohydrothermal) fluids from felsic volcanics and synvolcanic plutons that subsequently precipitated as amorphous silica in porous rocks of the discharge zone. In contrast to the Normetal caldera silicification at depth, the HMC displays an impermeable silica cap rock close to or at seafloor surface as suggested by silicified shale (Figure 3A) and overlying unaltered basalt–komatiite sequence. The silica-rich fluids migrated along synvolcanic fractures and dyke margins (Figure 3F). Rather than being a silica gel deposited on the Archean seafloor or exhalative, the laminated cherts are felsic turbiditic tuffs (Figure 3C, D) produced by a combination of percolating silica-rich fluids along bed boundaries, bed compaction and diagenesis of felsic glass shards. Silicification is also observed in basalt breccias that show a silicified matrix (Figure 13A, B). The fragments were subsequently
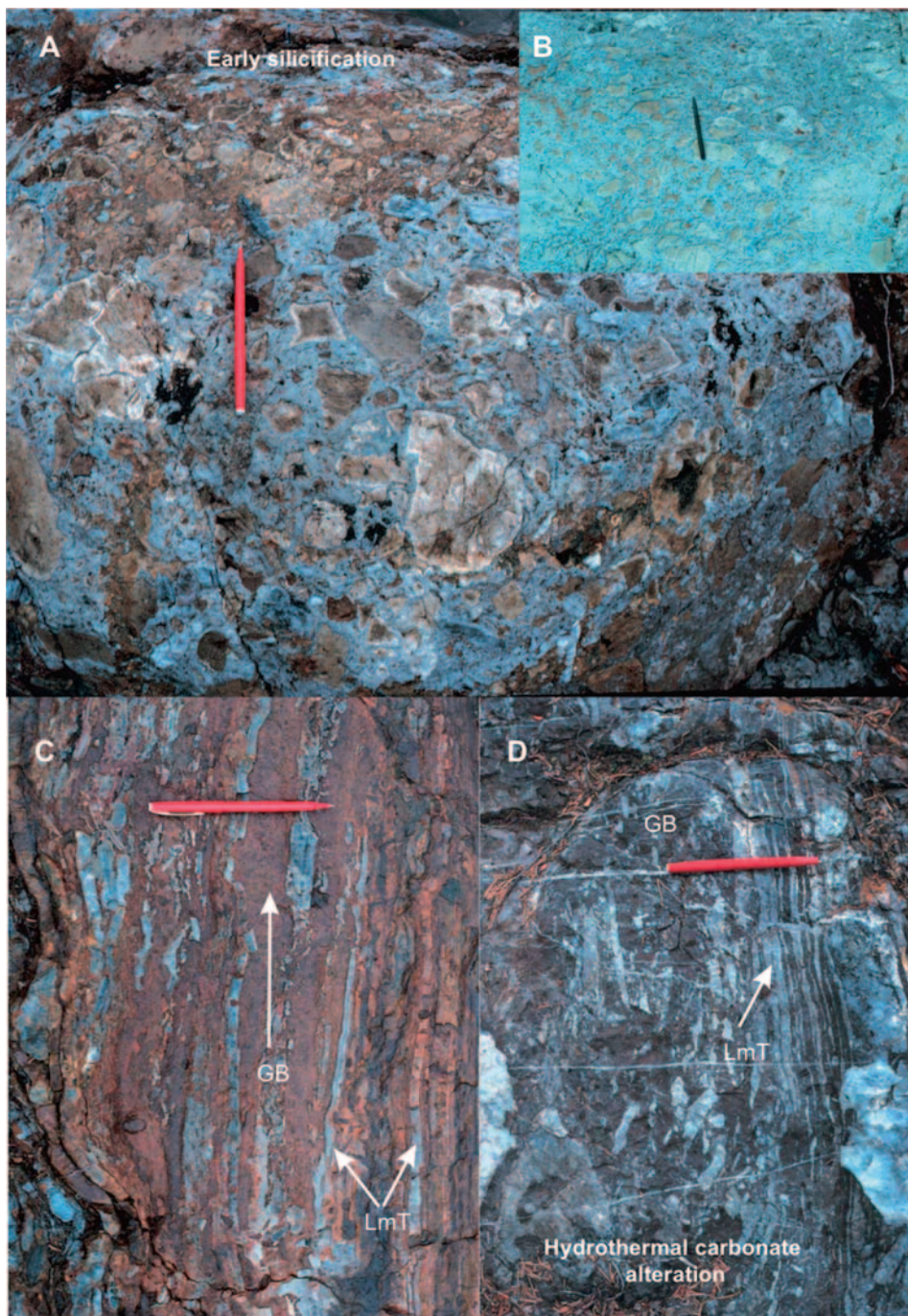
**Figure 13** Characteristics of early hydrothermal silicification and late carbonate alteration. Scale in all photographs 13 cm (pen). (A) Mafic breccia matrix pervasively replaced by silica-rich fluids. Note carbonate altered basalt clasts. (B) Network style silicified matrix in basalt breccia. (C) Turbiditic tuff: white chert is laminated portion of tuff bed (LmT) and brown carbonate is GB portion of tuff bed (moderate carbonate alteration). D) Intensely carbonate altered GB tuff and white laminated tuff (LmT).

altered to carbonate. The turbiditic tuffs have cherty Bouma $T_b$ and $T_d$ divisions with moderately (Figure 13C) to intense carbonate altered $T_a$-divisions (Figure 13D). Amorphous silica mounds at the seafloor interface and volcanic sands cemented by amorphous silica are components of the modern Okinawa Trough sites (Glasby and Notsu, 2003).

Extensive carbonate alteration is characteristic of subaqueous Archean volcanic centres. The Archean atmosphere is inferred to have contained high levels of $CO_2$ (Kasting, 1993), thus necessitating one or more significant $CO_2$ sinks. Silicate weathering on continents represented one important sink for $CO_2$, as this process was further intensified by humid Archean conditions (des Marais, 1994). A second important $CO_2$ sink was the ocean, where dissolution and precipitation of carbonate species occurs. Archean carbonate precipitation has been attributed to the influence of faults and seafloor hydrothermal activity (Nakamura and Kato, 2004). The latter applies to the present study. The apparent increase in carbonate alteration in Archean caldera–hosted VMS systems could be attributed to an elevated carbon flux into oceanic crust, due to seafloor hydrothermal alteration (Nakamura and Kato, 2004). High level synvolcanic plutons and inferred seawater temperatures of $55-85°C$ (Knauth and Lowe, 2003) facilitated the leaching of host rocks by percolating fluids. Additional sources for $CO_2$ are magmatic, especially with VMS deposits (Glasby and Notsu, 2003).

## 7.1. Results of hydrothermal carbonate species

The hydrothermal carbonate (Figure 14A, B) in the Hunter Mine and Normetal calderas ranges in composition from calcite, dolomite, ankerite to siderite. Based on field relationships the carbonates indicate distal to proximal settings with respect to zones of focused, higher temperature, high Fe, hydrothermal discharge to the massive sulphide deposit or mineralisation. Microprobe analysis of hydrothermal carbonates in the studied felsic-dominated calderas identified several Fe- Mg- and Ca-rich species. Samples (n-71) from the Normetal caldera show a distinct distribution of hydrothermal carbonate with the Fe-rich varieties proximal and Ca-rich varieties distal to the deposit or mineralisation (Figure 14A). The organisation of carbonate species occurs in couples so that distal calcite — (Fe-) dolomite grades into medial-proximal Fe–dolomite — ankerite, which in turn changes into proximal siderite (sideroplesite) — Fe–ankerite. The dolomite to ankerite trend is readily observed (Figure 14A) in a felsic-dominated sequence (this study), whereas a pronounced siderite–magnesite distribution is favoured in ultramafic rocks (Kidd Creek; Schandl and Wicks, 1993; Figure 14B). The studied carbonate alteration in HMC (Figure 14B) was restricted to the massive sulphide showing. As can be seen, of the 92 analysed carbonates Fe–ankerite and siderite (sideroplesite) were prevalent. Even though this seems straightforward the overall hydrothermal zonation pattern is far more complex than previously perceived as fluids evolve and carbonate species may overprint previous lower temperature or less focused phases (Mueller et al., 2005).
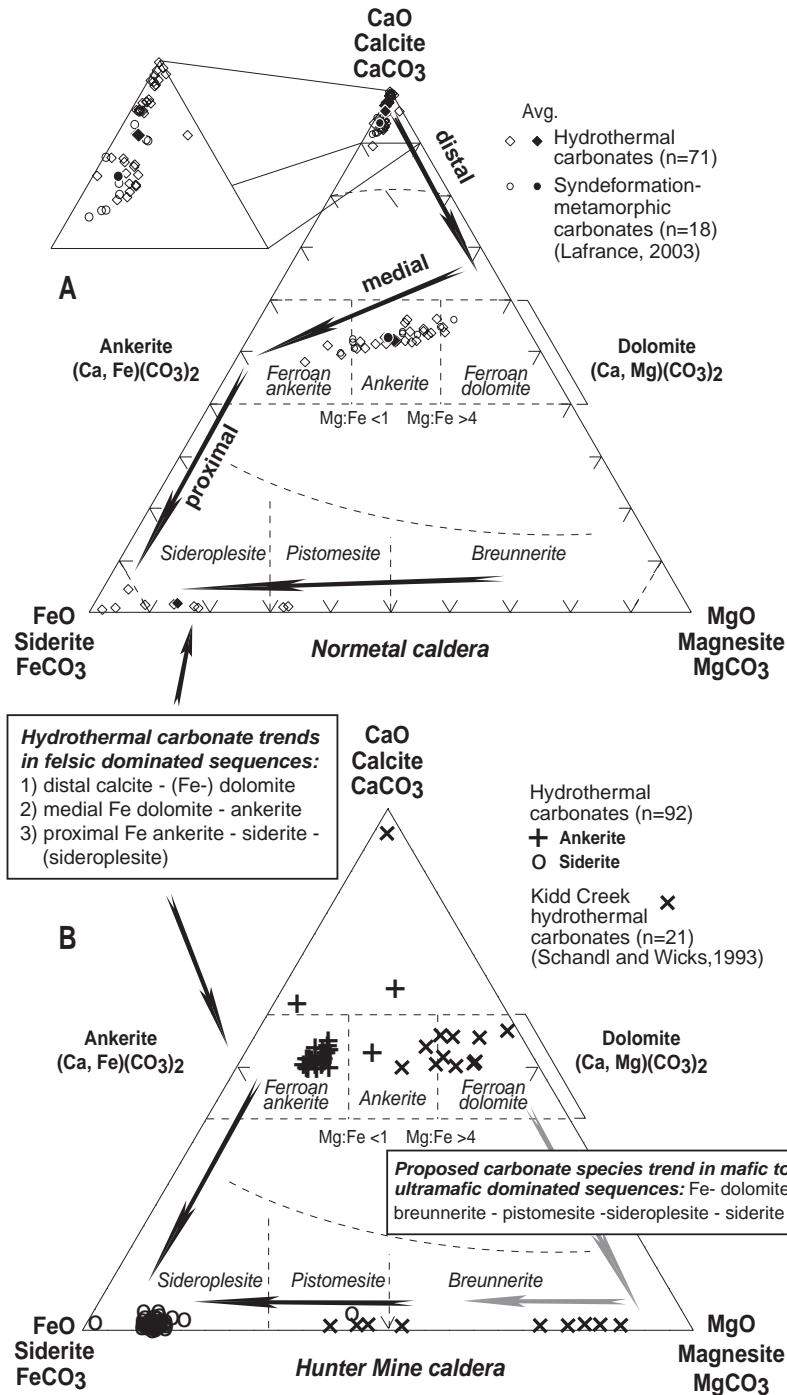
**Figure 14** Carbonate species associated with massive sulphide deposits. (A) Normetal caldera (modified with permission from Lafrance, 2003), and (B) Hunter Mine caldera (modified from Chown et al., 2000, with permission from Elsevier) and carbonate analyses from Kidd Creek (data from Schandl and Wicks, 1993).

## 8. Discussion

Subaqueous calderas are significant structures with varying geometries, complex evolutionary histories and different types of processes responsible for volcano-tectonic caldera subsidence. The three studied calderas give a spectrum of caldera types from the effusive felsic Hunter Mine to explosive felsic Sturgeon Lake type. The effusive but bimodal Normetal caldera adds to the complexity of subaqueous calderas, so that it becomes very important to understand the physical volcanology of such systems. Identifying an Archean caldera remains problematic as numerous observations must be conducted to warrant such an interpretation. Prime criteria are recognising: (1) synvolcanic fault systems, (2) volcanic facies or thickness changes across faults or dykes, (3) felsic dyke swarms and (4) primary pyroclastic deposits, but also considering (5) the map-scale geometry and (6) hydrothermal alteration patterns. The numerous subaqueous emission centres in calderas can be located by tracing lateral volcanic facies changes in mafic and felsic flows. Proximal flow segments are massive, often columnar-jointed, that grade either into lobate (felsic) or pillowed portions (mafic), and finally grade into brecciated flows that commonly terminate with stratified hyaloclastite density flow deposits. Abundant flows and domes characterise both Abitibi edifices. Extensive large-scale subaqueous pyroclastic deposits are lacking in both study areas, so that caldera subsidence driven by the continuous extrusion of thick lava flow units is compelling (Mueller et al., 2004). The process controlling caldera subsidence is also similar to mafic summit calderas in which the magma chamber evacuates and migrates along the rift zone (Tilling and Dvorak, 1993).

Fracture systems, filled with chert or jasper, are synvolcanic and related to migration of hydrothermal/magmatic fluids during edifice construction. As shown for the Normetal area, the geometry and distribution of volcanic rocks and their facies organisation (Figures 7 and 8) is consistent with a subsidence structure bordered by faults. The HMC contains a major dyke swarm, chaotic breccias near faults (megablock slumps; e.g. Geshi et al., 2002), chert–jasper filled fractures and small-volume fountaining eruption deposits. Incremental caldera collapse may be due to low-volume eruptions (Skilling, 1993), but an absence of large-scale vertical movement along synvolcanic faults precludes a piecemeal interpretation. Further work is required, whereas the map geometry of the Normetal caldera supports a classic piston type (Figures 6 and 10).

In contrast, the Sturgeon Lake caldera with three large explosive events during the early and late caldera stage, displays the attributes of the explosive-dominated Myojin Knoll silicic caldera (Fiske et al., 2001). The geometry of the volcanic edifice and lithofacies distribution, the large high-level sill, the Beidelman Bay intrusion, and a thick volcanic succession parcelled into blocks via synthetic and antithetic faults, argue for a piecemeal caldera (Mueller et al., 2004; Figure 11).

## 8.1. Hydrothermal carbonate species distribution

The distribution of hydrothermal carbonate occurs in carbonate couplets, in which the Ca-rich varieties are distal and the Fe-rich varieties are proximal to the massive

sulphide deposit. Although the Mattabi–type is used as the classic area for semi–conformable carbonate alteration detailed studies have yet been conducted, so that our study focuses on the available data. The general carbonate distribution is best exemplified by the Normetal caldera (Figure 15A, B) as samples were collected over 30 km along strike so that a representative set of proximal and distal hydrothermal carbonates is given (Figures 14a and 15b). Results show that close to the massive deposits Fe–(Mg) carbonate species are prominent. The siderite–(sideroplesite)–Fe ankerite occurs adjacent to the Normetal and Normetmar deposits whereas the calcite–dolomite pairing is in the footwall well below the major subsurface discharge zone. Fe–ankerite, ankerite to Fe–dolomite represents the intermediate stage of alteration, whereby Fe–ankerite may also be part of the proximal carbonate assemblage, suggesting a transitional overlap. As hydrothermal carbonate assemblages are laterally pervasive identifying distinct varieties is significant so that
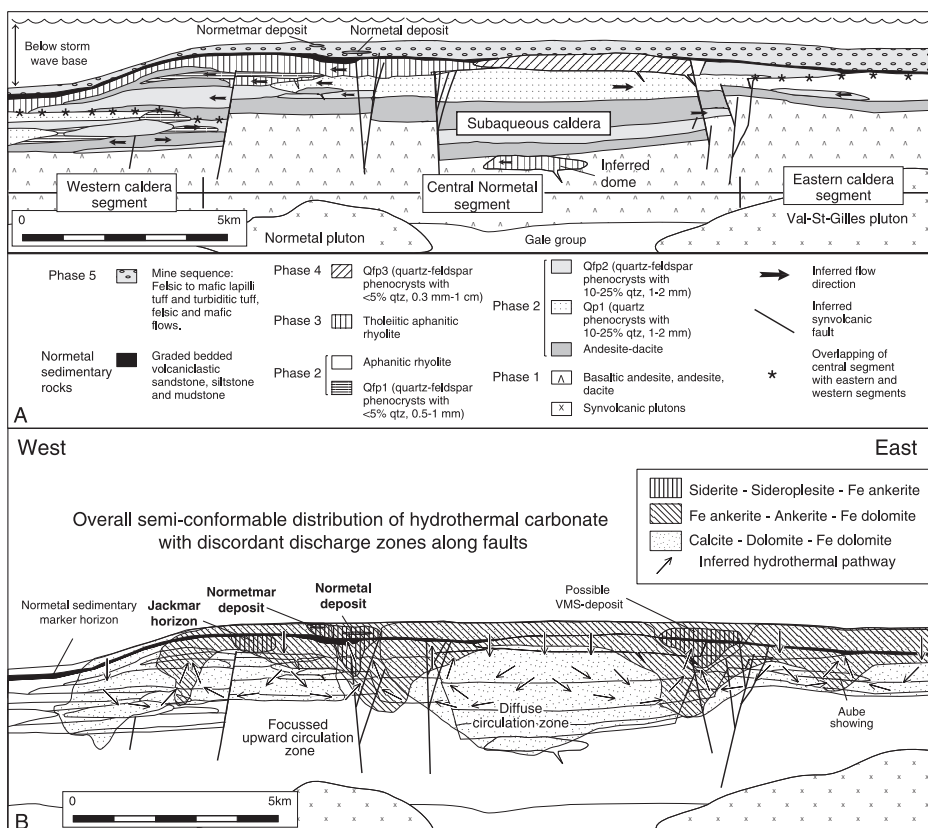


**Figure 15** Distribution of the carbonate alteration in the Normetal caldera. (A) Cross–section of the Normetal caldera with western, central and eastern segments and bordering normal to reverse faults. (B) Hydrothermal alteration pattern superposed on the caldera. Note the discordant root zone along the synvolcanic faults and the km–scale proximal to distal carbonate alteration pattern (modified with permission from Lafrance, 2003).

the proximal series has a range of 0–2 km, the ankerite–dolomite series is 2–5 km and the calcite–dolomite zone is generally > 3 km from the site of mineralisation at Normetal. The proximal carbonate assemblage (0–1 km) at the HMC contains siderite (sideroplesite) and Fe–ankerite (Figure 14B). Just as seafloor chimneys and ore zones evolve due to increasing temperatures from sphalerite to pyrrhotite–chalcopyrite (e.g. Ansil deposit; Galley et al., 1995), hydrothermal carbonate alteration systems may evolve Fe–ankerite to siderite–sideroplesite as fluids become more focused. Overprinting of carbonate alteration patterns (Mueller et al., 2005; this study) as well as metal mineral species is common (Galley et al., 2000) and can be explained by evolving hydrothermal systems. On the large-scale the alteration halo is semi-concordant, but next to the discharge zone along synvolcanic faults a discordant alteration pipe develops. It is interesting to note that known carbonate alteration patterns have a precursor silicification stage that seal the system sufficiently for carbonate precipitation and subsequent mineralisation. The sealing permits temperature increase as sulphide bearing fluids are constrained and focused, rather than dissipated throughout the complex. Hydrothermal massive sulphide deposits and their alteration patterns are complex systems governed by high-level plutons, their intrusive phases (Galley, 2003; Chown et al., 2002) and caldera geometry (Roche et al., 2000; Kennedy et al., 2004), all of which control sub-seafloor fluid convection.

## 8.2. Proposed Archean massive sulphide model in calderas

As calderas are large-scale volcano-tectonic subsidence structures, discovering the location of VMS in ancient sequences is difficult. The combination of physical volcanology and hydrothermal alteration indicators is important. Numerous subenvironments are dispersed on the intracaldera floor (moat), the caldera margin and volcaniclastic apron. Each of these can host massive sulphide deposits but all are linked to synvolcanic faults and magma conduits. Pin-pointing these subsettings are of economic importance. Favourable intracaldera sites are (1) dome-flow complexes, and (2) small volume explosive fountaining edifices as both contain abundant porous and permeable volcaniclastic debris of pyroclastic or autoclastic origin (Figure 5B, D). The presence of fine-grained tuff should not deter exploration as it can be proximal to the mineralised zone. The grain-size of volcaniclastic debris is not a criterion for either proximal or distal within the moat setting. It is the eruption and transport process that controls grain-size distribution. Sound criteria for finding emission centres are: (1) dykes or dyke swarms as these intrude synvolcanic faults, (2) tracing laterally flows and their facies changes, and (3) hydrothermal alteration patterns. Smaller VMS deposits should develop in the sub-surface of the intracaldera moat.

In contrast, the most voluminous massive sulphide deposits should form at the caldera margin (e.g. 16 Mt Quemont Breccia; Gibson and Watkinson, 1990; 50 Mt Horne Mine, Kerr and Gibson, 1993; 62 Mt Flin Flon deposit; Syme and Bailes, 1993) between the outer normal faults and inner inverse faults as the highest heat and fluid flow is registered here. The caldera margin, km-thick, is a tectonically active area with no coherent stratigraphy that is generally composed of large

mega–blocks and volcanic rubble breccias. The high porosity volcanic debris makes it a prime site for metal–rich fluid discharge. Identification of the marginal annular caldera wall in the ancient rock record is difficult but a predominance of chaotic breccias, dyke intrusions and silica-filled fractures would be strong arguments. The gold-rich VMS Sunrise deposit of the Myojin Knoll volcano, located at the foot of the caldera wall at 1,210–1,360 m depth (Iizasa et al., 1999; Fiske et al., 2001), underlines the importance of active margin faults. The volcanic apron zone, outside of the major subsidence structures, displays a prevalence of volcaniclastic debris with local effusive satellites. The massive sulphide deposits are probably smaller and have lower temperature Zn-rich zones, as they are off axis from the principal hydrothermal discharge sites. In the studied cases, the alteration and mineralisation is of the replacement type and depths below the water–sediment–volcanic rock interface are generally between 10 and 200 m (e.g. Galley et al., 1995; Doyle and Allen, 2003). Our observations suggest sub-seafloor replacement close to or at the rock–seawater interface.
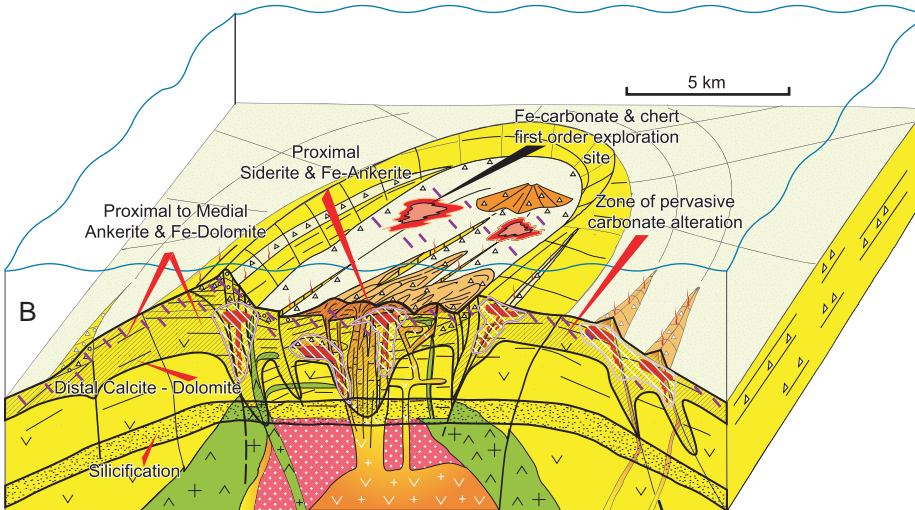
The proposed model combines the physical geology of the Hunter Mine, Normetal and Sturgeon Lake calderas. The model emphasises the volcanology of effusive flow-dominated calderas, but considers the horst and graben structures of piecemeal calderas. Hydrothermal alteration ensues with early silicification and subsequent carbonate alteration. The studied calderas have an early massive to locally network style silica cap either at depth (Lafrance, 2003) or close to the surface (Mueller and Mortensen, 2002). Intense silicification has been identified at Sturgeon Lake (Galley, 1993), at Snow Lake (Skirrow and Franklin, 1993), at Kidd Creek (Hannington et al., 1999b), in the Noranda caldera (Gibson and Watkinson, 1990) and at the modern TAG deposit (You and Bickle, 1998). Silicification is cherty in the volcaniclastic (Figure 13C, D) and background sedimentary rocks (e.g. silicified shale; Figure 3A) and displays network veining structures in basaltic breccias (Figure 13A, B). The silicified rocks are replaced by hydrothermal carbonate (Figure 13C, D). Silica-rich fluids precipitate near the seafloor (Figure 16A), but may form at depth as an impermeable barrier (Figure 16B).

The semi-conformable carbonate alteration halo contains both a lateral and a discordant (focused) carbonate zonation (Figure 16A, B). Detailed studies of the Normetal and HMCs reveal a carbonate alteration assemblage that is pervasive along the extent of the edifice and discordant along synvolcanic faults (Figure 15B). The focused alteration next to the massive sulphide deposits displays a rather consistent alteration assemblage of siderite–(sideroplesite)–Fe–ankerite, (Figure 16B) and is analogous to that of the Gemini area (Figure 1; Mueller et al., 2005). The change from proximal siderite–Fe–ankerite to ankerite–Fe–dolomite is subtle. The ankerite–Fe–dolomite assemblage may be kilometres from the mineralised zone (Figure 15B) and the distal dolomite–calcite assemblage > 10 km. There appears to be a transitional hydrothermal carbonate from one zone to another, but the overall pairings of siderite–Fe–ankerite to ankerite–Fe–dolomite and finally to dolomite–calcite are representative of a proximal–distal carbonate alteration pattern. The Kidd Creek alteration displays a different pattern as mafic to ultramafic rocks favour an Mg-rich carbonate trend from dolomite to breunnerite to siderite
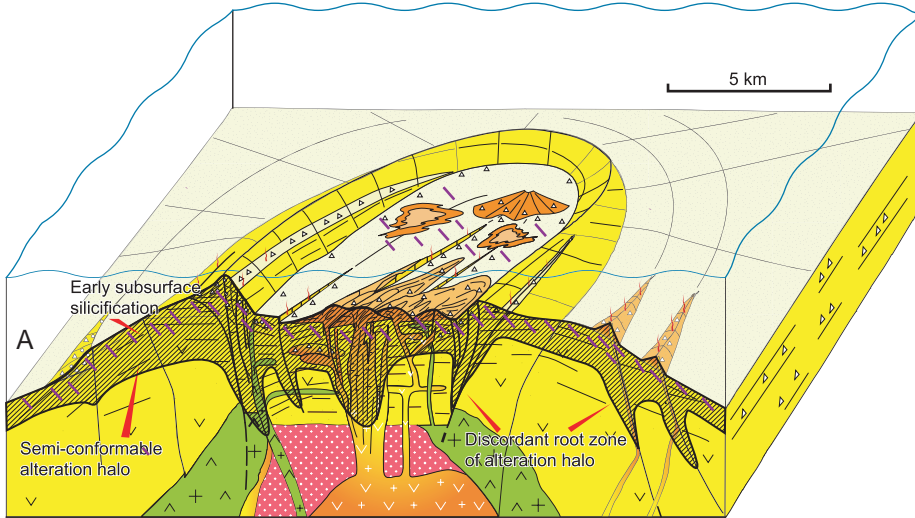
**Figure 16**   Hydrothermal carbonate alteration model of a submarine caldera is primarily based on the Hunter Mine caldera with attributes of the Normetal and Sturgeon Lake calderas. (A) General alteration patterns with an early phase of near surface silicification and an extensive semi–conformable alteration zone which discordant at discharge zones. (B) Carbonate altera–tion pairings indicate lateral change across strike of the caldera from focused to more distal reaches. Silicification at depth is shown in this diagram but is contemporaneous with the near–surface silicification shown in A. Note the importance of the subenvironments and the polymetallic deposits in the volcaniclastic deposits, wherein the largest VMS deposits are favoured at the caldera wall.

(Figure 15B). Hydrothermal carbonates associated with Kidd Creek felsic rocks have the Normetal dolomite–ankerite–siderite trend.

The pervasive nature of this type of alteration halo yields a semi–conformable distribution but it is decidedly discordant along fluid pathways or discharge zones (Figure 16B). As noted from numerous massive sulphide mining camps such as Matagami and Rouyn-Noranda of the Abitibi greenstone belt, massive sulphide deposits occur in clusters within a volcanic structure, and Figure 16B provides a survey of favourable sites. The caldera wall favours large VMS deposits, whereas the central moat and volcaniclastic apron subsettings generally contain smaller VMS deposits probably 5 Mt and less.

## 9. Conclusions

Submarine calderas are highly favourable loci for volcanic massive sulphide deposition, but recognising a VMS site on the intracaldera floor, the caldera margin, and volcaniclastic apron requires a more systematic approach because caldera dimensions are highly variable. This is especially true of ancient systems. Calderas have a complex diachronous emplacement history with respect to dome-flow complexes, dykes-sills, and subvolcanic intrusions. The overall geometry and evolution of studied Archean calderas compares favourably with modern oceanic arc and island arc analogues, such as Tenerife-Las Cañadas and the subaqueous Myojin Knoll caldera, with a shield-building phase, a dome-building stage or stratovolcano construction and a caldera volcano-tectonic collapse event. The overall evolution of calderas requires approximately 6–13 m.y. as shown for the (1) Valles Caldera, (2) Tenerife-Las Cañadas and (3) HMC sequences, whereby the most devastating events generally occur in the last 1 m.y. This timeframe shows that calderas evolve and require a prolonged construction period prior to catastrophic subsidence.

The basal shield-forming succession, a fundamental precaldera constructional stage, involves a broad subaqueous to subaerial shield volcano, in which individual shield volcanoes coalescence (e.g. Hawaii and Tenerife). The basal sequence in ancient subaqueous successions comprises thick units of basaltic to andesitic lava flows, breccias and stratified hyaloclastites (tuff, lapilli tuff and lapilli tuff breccia). Minor felsic (dacite) dome-building volcanism may develop locally during the shield-building event. Subsequently, numerous individual felsic constructional phases develop on the shield volcano. The major subaqueous constructional phase in the effusive dominated calderas features large and small felsic dome-flow-hyaloclastite complexes formed along synvolcanic fault systems. Small explosive fountaining eruptions develop locally. The caldera subsidence structure is controlled by abundant effusive volcanism and possibly magma chamber migration. Mafic volcanism can be contemporaneous with felsic volcanic activity, as in the Normetal caldera and during the late Hunter Mine caldera event. Fragmental volcanic debris, commonly heterolithic, is mainly of autoclastic origin but chaotic collapse breccias are prevalent at the caldera wall. In the subaqueous setting, fragmental debris is far more prominent in dome-building phases.

In contrast, at Sturgeon Lake caldera the shield structure grades rapidly into an explosive succession with explosive and extensive ignimbrite-forming events similar to the Valles Caldera. The three large pyroclastic events are only disrupted by minor felsic dome-forming phases, but the major mafic pillowed flow event at the top of the sequence attests to a submerged edifice. Identifying the type of caldera in an Archean succession remains problematic, but from the apparent geometry, the Hunter Mine caldera may be part of a nested caldera sequence, the Normetal caldera has the salient attributes of a piston type and the Sturgeon Lake caldera best qualifies as a piecemeal type.

With detailed volcanic facies and regional mapping, the overall structure of a caldera sequence is readily identified, even in the Archean, but targeting VMS sites remains problematic. Our model predicts mineralisation sites by using physical volcanology and hydrothermal alteration processes. In Archean terranes, subaqueous caldera subsettings require detailed volcanic facies mapping of intracaldera settings so that individual domes or small explosive volcanic centres can be identified. Volcanic massive sulphide sites are linked to synvolcanic fracture systems and growth faults that form at the caldera wall and on the fragmented caldera floor. In ancient systems, synvolcanic faults and associated blocks or segments may be difficult to recognise, but they are extremely important. It is along these extensional fractures that intracaldera subenvironments form. If synvolcanic faults cannot be directly recognised in the subsettings, then indirect indictors such as numerous dyke intrusions, abrupt volcano-sedimentary facies changes, synsedimentary or synvolcanic deformation or chaotic breccia assemblages may be used to suggest fault proximity. Intense hydrothermal alteration commonly overprints vent facies assemblages.

Our carbonate alteration study shows a chronological alteration pattern from proximal, focused, to distal, less focused, fluid movement with carbonate species occurring in pairs. A systematic alteration process is recorded from proximal siderite–Fe–ankerite to intermediate ankerite–Fe–dolomite to distal calcite–dolomite. The type of carbonate alteration pattern varies according to host rock, as felsic-dominated successions show the dolomite–ankerite–siderite trend, whereas ultramafic rocks favour the dolomite–magnesite–siderite trend.

## *ACKNOWLEDGEMENTS*

# REFERENCES

Acocella, V., 2007. Understanding caldera structure and development: an overview of analogue models compared to natural calderas. Earth-Sci. Rev., 85, 125–160.

Acocella, V., 2008. Structural development of calderas: a synthesis from analogue experiments — this volume.

Acocella, V., Cifelli, F., Funiciello, R., 2001. The control of overburden thickness on resurgent domes: insights from analogue models. J. Volcanol. Geotherm. Res., 111, 137–153.

Acocella, V., Cifelli, F., Funiciello, R., 2000. Analogue models of collapse calderas and resurgent domes. J. Volcanol. Geotherm. Res., 104, 81–96.

Ayer, J., Amelin, Y., Corfu, F., Kamo, S., Ketchum, J., Kwok, K., Trowell, N., 2002. Evolution of the Abitibi greenstone belt based on U–Pb geochronology: autochthonous volcanic construction followed by plutonism, regional deformation and sedimentation. Precambrian Res., 115, 63–95.

Bailey, R.A., 1989. Geologic map of the Long Valley caldera, Mono-Inyo craters volcanic chain, and vicinity, Eastern California. Misc. Investigation Series, US Geol. Surv., Map I-1933 (with 11 page report).

Bailey, R.A., Dalrymple, G.B., Lanphere, M.A., 1976. Volcanism, structure and geochronology of Long Valley Caldera, Mono County, California. J. Geophys. Res., 81, 725–744.

Barrie, C.T., Taylor, C., Ames, D., 2005. Geology and metal contents of the Ruttan volcanogenic massive sulfide deposit, northern Manitoba, Canada. Mineral. Deposita, 39, 795–812.

Branney, M.J., 1995. Downsag and extension at calderas: new perspectives on collapse geometries from ice-melt, mining, and volcanic subsidence. Bull. Volcanol., 57, 303–318.

Burt, D.M., Sheridan, M.F., 1987. Types of mineralization related to fluorine-rich silicic lava flows and domes. Geol. Soc. Am. Spec. Pap., 212, 103–109.

Chartrand, F., Cattalani, S., 1990. Massive sulfide deposits in Northwestern Quebec. In: Rive, M., Verpaelst, P., Gagnon, Y., Lulin, J.-M., Riverin, G., Simard, A., Lulin, J.M. and Gagnon, Y. (Eds.), The northwestern Quebec polymetallic belt: A summary of 60 years of mining exploration. Can. Inst. Min. Metal., Spec. Vol. 43, pp. 77–92.

Chough, S.K., Sohn, Y.K., 1990. Depositional mechanics and sequence of base surges, Songaksan tuff ring, Cheju Island, Korea. Sedimentology, 37, 1115–1135.

Chown, E.H., Daigneault, R., Mueller, W., Mortensen, J., 1992. Tectonic evolution of the Northern Volcanic Zone, Abitibi belt, Quebec. Can. J. Earth Sci., 29, 2211–2225.

Chown, E.H., Harrap, R., Moukhsil, A., 2002. The role of granitic intrusions in the evolution of the Abitibi Belt, Canada. Precambrian Res., 115, 291–310.

Chown, E.H., N'Dah, E., Mueller, W.U., 2000. The relation between iron-formation and low temperature hydrothermal alteration in an Archean volcanic environment. Precambrian Res., 101, 263–275.

Cole, J.W., Milner, D.M., Spinks, K.D., 2005. Calderas and caldera structures: a review. Earth Sci. Rev., 69, 1–26.

Cousineau, P., Dimroth, E., 1982. Interpretation of relations between massive, pillowed and brecciated facies in an Archean submarine andesite volcano — Amulate andesite, Ropuyn-Noranda. J. Volcanol. Geotherm. Res., 13, 83–102.

Crawford, A.J., Falloon, T.J., Green, D.H., 1989. Classification, petrogenesis, and tectonic setting of boninites. In: Crawford, A.J. (Ed.), Boninites and Related Rocks. Unwin and Hyman, London, England, pp. 2–44.

Daigneault, R., Mueller, W.U., Chown, E.H., 2002. Oblique Archean subduction: accretion and exhumation of an oceanic arc during dextral transpression, Southern Volcanic Zone, Abitibi Greenstone Belt, Canada. Precambrian Res., 115, 261–290.

Daigneault, R., Mueller, W.U., Chown, E.H., 2004. Abitibi greenstone belt plate tectonics: the diachronous history of arc development, accretion and collision. In: Eriksson, P., Altermann, W., Nelson, D., Mueller, W.U., Catuneanu, O. (Eds), The Precambrian Earth: Tempos and Events. Dev. Precambrian Geol., Elsevier, Vol. 12, pp. 88–103.

Davis, D.W., 2002. U–Pb geochronology of Archean metasedimentary rocks in the Pontiac and Abitibi subprovinces, Quebec, constraints on timing, provenance and regional tectonics. Precambrian Res., 115, 97–117.

Des Marais, D.J., 1994. The Archean atmosphere: its composition and fate. In: Condie, K.C. (Ed.), Archean Crustal Evolution: Dev. Precambrian Geol. 11. Elsevier, Amsterdam, pp. 505–519.

de Rosen-Spence, A.F., Provost, G., Dimroth, E., Gochnauer, K., Owen, V., 1980. Archean subaqueous felsic flows, Rouyn-Noranda, Quebec, Canada, and their Quarternary equivalents. Precambrian Res., 12, 43–77.

Dimroth, E., 1986. Depositional environment and tectonic settings of the cherty iron-formations of the Canadian Shield. Geol. Soc. India, 28, 239–250.

Dimroth, E., Cousineau, P., Leduc, M., Sanschagrin, Y., 1978. Structure and organization of Archean subaqueous basalt flows, Rouyn-Noranda area, Quebec, Canada. Can. J. Earth Sci., 15, 902–918.

Dimroth, E., Imreh, L., Cousineau, P., Leduc, M., Sanschagrin, Y., 1985. Paleogeographic analysis of mafic submarine flows and its use in the exploration for massive sulfide deposits. In: Ayres, L.D., Thurston, P.C., Card, K.D., Weber W. (Eds), Evolution of Archean Supracrustal Sequences. Geol. Assoc. Canada, Spec. Pap., Vol. 28, pp. 203–222.

Dimroth, E., Imreh, L., Goulet, N., Rocheleau, M., 1983. Evolution of the south-central part of the Archean Abitibi Belt, Quebec; Part III, Plutonic and metamoprhic evolution and geotectonic model. Can. J. Earth Sci., 20, 1374–1388.

Dimroth, E., Imreh, L., Rocheleau, M., Goulet, N., 1982. Evolution of the south-central part of the Archean Abitibi Belt, Quebec; Part I, Stratigraphy and paleogeographic model. Can. J. Earth Sci., 19, 1729–1758.

Dostal, J., Mueller, W., 1996. An Archean oceanic felsic dyke swarm in a nascent arc; the Hunter Mine Group, Abitibi greenstone belt, Canada. J. Volcanol. Geotherm. Res., 72, 37–57.

Dostal, J., Mueller, W., 1997. Komatiite-flooding of a rifted rhyolitic arc complex: geochemical signature and tectonic implications, Stoughton-Roquemaure Group, Abitibi greenstone belt, Canada. J. Geol., 105, 545–563.

Doyle, M.G., Allen, R.L., 2003. Subsea-floor replacement in volcanic-hosted massive sulfide deposits. Ore Geol. Rev., 23, 183–222.

Eakins, P.R., 1972. Canton de Roquemaure: comté d'Abitibi-ouest. Ministère des Ressources Naturelles, Québec, RG-150, 72 pp.

Fink, J.H., Manley, C.R., 1987. Origin of pumiceous and glassy textures in rhyolite flows and domes. Geol. Soc. Am. Spec. Paper, 212, 77–88.

Fisher, R.V., 1979. Models for pyroclastic surges and pyroclastic flows. J. Volcanol. Geotherm. Res., 6, 305–318.

Fisher, R.V., Schmincke, H.-U., 1984. Pyroclastic Rocks. Springer-Verlag, Berlin, 472 pp.

Fiske, R.S., Cashman, C.V., Shibata, A., Watanabe, K., 1998. Tephra dispersal from Myojinsho, Japan, during its shallow submarine eruption of 1952–1953. Bull. Volcanol., 59, 262–275.

Fiske, R.S., Matsuda, T., 1964. Submarine equivalents of ash flows in the Tokiwa Formation, Japan. Am. J. Sci., 262, 76–106.

Fiske, R.S., Naka, J., Iizasa, K., Yuasa, M., Klaus, A., 2001. Submarine silicic caldera at the front of the Izu-Bonin Arc, Japan: voluminous seafloor eruptions of rhyolite pumice. Geol. Soc. Am. Bull., 113, 813–824.

Franklin, J.M., 1993. Volcanic-associated massive sulfide deposits. In: Kirkham, R.V., Sinclair, W.D., Thorpe, R.I. and Duke, J.M. (Eds), Mineral Deposit Modelling. Geol. Assoc. Canada, Spec. Pap., Vol. 40, pp. 315–334.

Franklin, J.M, Gibson, H.L., Jonasson, I.R. and Galley, A.G., 2005. Volcanogenic massive sulphide deposits. In: Hedenquist, J.W., Thompson, J.F.H., Goldfarb, R.J., Richards, J.P. (Eds), Economic Geology, 100th Anniversary Volume, Economic Geology Pub., pp. 523–560.

Fritz, W.J., Vanko, D.A., 1992. Geochemistry and origin of a black mudstone in a volcaniclastic environment, Ordovician Lower Rhyolitic Tuff Formation, North Wales, UK. Sedimentology, 39, 663–674.

Galley, A.G., 1993. Characteristics of semi-conformable alteration zones associated with volcanogenic massive sulphide districts. J. Geochem. Explor., 48, 175–200.

Galley, A.G., 2003. Composite synvolcanic intrusions associated with Precambrian VMS-related hydrothermal systems. Mineral. Deposita, 38, 443–473.

Galley, A.G., Jonasson, I.R., Watkinson, D.H., 2000. Magnetite-rich calc-slicate alteration in relation to synvolcanic intrusion at the Ansil volcanogenic massive sulfide deposit, Rouyn-Noranda, Quebec, Canada. Mineral. Deposita, 35, 619–637.

Galley, A.G., Watkinson, D.H., Jonasson, I.R., Riverin, G., 1995. The subsea-floor formation of volcanic-hosted massive sulfide: evidence from the Ansil deposit, Rouyn-Noranda, Canada. Econ. Geol., 90, 2006–2017.

Geshi, N., Shimano, T., Chiba, T., Nakada, S., 2002. Caldera collapse during the 2000 eruption of Miyakejima Volcano, Japan. Bull. Volcanol., 64, 55–68.

Gibson, H.L., Watkinson, D.H., 1990. Volcanogenic massive sulphide deposits of the Noranda cauldron and shield volcano, Quebec. The northwestern Quebec polymetallic belt; a summary of 60 years of mining exploration; proceedings of the Rouyn-Noranda 1990 symposium-La Ceinture polymétallique du Nord-Ouest québecois; synthèse de 60 ans d'exploration minière; conferences, données lors du symposium de Rouyn-Noranda 1990, 43; Montreal, PQ, Canada, Can. Inst. Min. Metal., pp. 119–132.

Glasby, G.P., Iizasa, K., Yuasa, M., Usui, A., 2000. Submarine hydrothermal mineralization on the Izu-Bonin arc, south of Japan: an overview. Mar. Georesources Geotech., 18, 141–176.

Glasby, G.P., Notsu, K., 2003. Submarine hydrothermal mineralization in the Okinawa Trough, SW of Japan: an overview. Ore Geol. Rev., 23, 299–339.

Goto, Y., McPhie, J., 1998. Endogenous growth of a Miocene submarine dacite cryptodome, Rebun Island, Hokkaido, Japan. J. Volcanol. Geotherm. Res., 84, 273–286.

Groves, D.A., Morton, R.L., Franklin, J.M., 1988. Physical volcanology of the footwall rocks near the Mattabi massive sulfide deposit, Sturgeon Lake, nortwestern Ontario. Can. J. Earth Sci., 25, 280–291.

Gudmundsson, A., 1983. Form and dimensions of dykes in eastern Iceland. Tectonophysics, 95, 295–307.

Gudmundsson, A., 1984. Formation of dykes, feeder-dykes, and the intrusion of dykes from magma chambers. Bull. Volcanol., 47, 537–550.

Gudmundsson, A., 1998. Formation and development of normal-fault calderas and the initiation of large explosive eruptions. Bull. Volcanol., 60, 160–170.

Gudmundsson, A., 2008. Magma-chamber geometry, fluid transport, local stresses, and rock behaviour during collapse-caldera formation — this volume.

Hannington, M.D., Barrie, C.T., Bleeker, W., 1999a. The giant Kidd Creek volcanogenic massive sulfide deposit, western Abitibi subprovince, Canada: Preface and introduction. In: Hannington, M.D. and Barrie, C.T. (Eds), The giant Kidd Creek volcanogenic massive sulfide deposit, western Abitibi subprovince, Canada. Econ. Geol. Monograph, Vol. 10, pp. 1–30.

Hannington, M.D., Bleeker, W., Kjarsgaard, I., 1999b. Sulfide mineralogy, geochemistry and ore genesis of the Kidd Creek deposit: Part I. north, central, and south orebodies. In: Hannington, M.D. and Barrie, C.T. (Eds), The giant Kidd Creek volcanogenic massive sulfide deposit, western Abitibi subprovince, Canada. Econ. Geol. Monograph, Vol. 10, pp. 163–224.

Hannington, M.D., Santaguida, F., Kjarsgaard, I.M., Cathles, L.M., Bleeker, W., 2003. Regional-scale hydrothermal alteration in the Central Blake River Group, western Abitibi Subprovince, Canada: implications for VMS prospectivity. Mineral. Deposita, 38, 393–422.

Hudak, G.J., Morton, R.L., Franklin, J.M., Peterson, D.M., 2003. Morphology, distribution, and estimated eruption volumes for intracaldera tuffs associated with volcanoic-hosted massive sulfide deposits in the Archean Sturgeon Lake caldera complex, Northwestern Ontario. In: Explosive subaqueous volcanism. In: White, J., Smellie, J. and Clague, D. (Eds), Geophys. Mono. Series, Vol. 140, pp. 345–360.

Iizasa, K., Fiske, R.S., Ishizuka, O., Yuasa, M., Hashimoto, J., Ishibashi, J., Naka, J., Horii, Y., Fujiwara, Y., Imai, A., Koyama, S., 1999. A Kuroko-type polymetallic sulfide deposit in a submarine silicic caldera. Science, 283, 975–977.

Ishibashi, J.-I., Urabe, T., 1995. Hydrothermal activity related to arc–backarc magmatism in the western Pacific. In: Taylor, B. (Ed.), Backarc Basins: Tectonics and Magmatism. Plenum Press, New York, pp. 451–495.

Kano, K., Takeuchi, K., Yamamoto, T., Hoshizumi, H., 1991. Subaqueous rhyolite block lavas in the Miocene Ushikiri Formation, Shimane Peninsula, SW Japan. J. Volcanol. Geotherm. Res., 46, 241–253.

Kasting, J.F., 1993. Earth's early atmosphere. Science, 259, 920–926.

Kerr, D.J., Gibson, H.L., 1993. A comparison between the volcanology and geochemistry of volcanic successions hosting the Horne mine deposit and smaller intra-cauldron deposits of the mine sequence. Econ. Geol., 88, 1419–1443.

Kennedy, B., Stix, J., Vallance, J.W., Lavallée, Y., Longpré, M.-A., 2004. Controls on caldera structure: results from analogue sandbox modeling. Geol. Soc. Am. Bull., 116, 515–524.

Knauth, L.P., Lowe, D.R., 2003. High Archean climatic temperature inferred from oxygen isotope geochemistry of cherts in the 3.5Ga Swaziland Supergroup, South Africa. Geol. Soc. Am. Bull., 115, 566–580.

Lafrance, B., 2003. Reconstruction d'un environnement de sulfures massifs volcanogènes déformés: exemple archeen de Normétal, Abitibi. Unpublished PhD thesis, Université du Québec à Chicoutimi, Canada, 362 pp.

Lafrance, B., Mueller, W.U., Daigneault, R., Dupras, N., 2000. Evolution of a submerged composite arc volcano: volcanology and geochemistry of the Normetal volcanic complex, Abitibi greenstone belt, Quebec, Canada. Precambrian Res., 101, 277–311.

Lascelles, D.F., 2007. Black smokers and density currents: a uniformitarian model for the genesis of banded iron-formations. Ore Geol. Rev., 32, 381–411.

Latulippe, M., 1976. Excursion géologique, Val d'Or, Malartic. Ministère des Richesses naturelles du Québec, DP-367, 124 pp.

Lipman, P.W., 1997. Subsidence of ash-flow calderas — relation to caldera size and magma chamber geometry. Bull. Volcanol., 59, 198–218.

Lipman, P.W., 2000. Calderas. In: Sigurdsson, H., Houghton, B., McNutt, S., Rymer, H. Stix, J. (Eds), Encyclopedia of Volcanoes. Academic Press, New York, pp. 643–662.

Lowe, D.R., 1982. Sediment gravity flows: II. Depositional models with special reference to the deposits of high-density turbidity currents. J. Sediment. Petrol., 52, 279–297.

Maliva, R.G., Knoll, A.H., Simonson, B.M., 2005. Secular change in the Precambrian silica cycle: insights from chert petrology. Geol. Soc. Am. Bull., 117, 835–845.

Manley, C.R., 1992. Extended cooling and viscous flow of large, hot rhyolite lavas: implications of numerical modeling results. J. Volcanol. Geotherm. Res., 53, 27–46.

Manley, C.R., 1996. Physical volcanology of a voluminous rhyolite lava flow: the Badlands lava, Owyhee Plateau, southwestern Idaho. J. Volcanol. Geotherm. Res., 71, 129–153.

Martí, J., Gudmundsson, A., 2000. The Las Cañadas caldera (Tenerife, Canary Islands): an overlapping collapse caldera generated by magma-chamber migration. J. Volcanol. Geotherm. Res., 103, 161–173.

Miura, D., Tamai, M., 1998. Intracaldera structure and megabreccias at Dorobau caldera, northeastern Honshu, Japan. J. Volcanol. Geotherm. Res., 80, 195–215.

Morton, R.L., Franklin, J.M., 1987. Two-fold classification of Archean volcanic-associated massive sulfide deposits. Econ. Geology, 82, 1057–1063.

Morton, R.L., Walker, J.S., Hudak, G.J., Franklin, J.M., 1991. The early development of an Archean submarine caldera complex with emphasis on the Mattabi ash-flow tuff and its relationship to the Mattabi massive sulfide deposit. Econ. Geol., 86, 1002–1011.

Mueller, W., Bédard, P., Gauthier-Ross, A., Lemieux-Claveau, E., 2005. The Gémini-Turgeon Project, Abitibi greenstone belt. Evaluation of hydrothermal carbonates associated with massive sulfides: a case history of subseafloor alteration and hydrothermal fluids. Internal report, Cambior Inc., 125 pp.

Mueller, W., Chown, E.H., Potvin, R., 1994. Substorm wave base felsic hydroclastic deposits in the Archean Lac des Vents volcanic complex, Abitibi belt, Canada. J. Volcanol. Geotherm. Res., 60, 273–300.

Mueller, W., Dimroth, E., 1987. A terrestrial–shallow marine transition in the Archean Opemisca Group east of Chapais, Quebec. Precambrian Res., 37, 29–55.

Mueller, W., Donaldson, J.A., 1992a. Development of sedimentary basins in the Abitibi belt: an overview. Can. J. Earth Sci., 29, 2249–2265.

Mueller, W., Donaldson, J.A., 1992b. A felsic feeder dyke swarm formed under the sea: the Archean Hunter Mine Group, south-central Abitibi belt, Quebec, Canada. Bull. Volcanol., 54, 602–610.

Mueller, W., White, J.D.L., 1992. Felsic fire-fountaining beneath Archean seas: pyroclastic deposits of the 2730 MA Hunter Mine Group, Quebec, Canada. J. Volcanol. Geotherm. Res., 54, 117–134.

Mueller, W.U., Daigneault, R., Mortensen, J.K., Chown, E.H., 1996. Archean terrane docking: Upper crust collision tectonics, Abitibi greenstone belt, Quebec, Canada. Tectonophysics, 265, 127–150.

Mueller, W.U., Mortensen, J., 2002. Age constraints and characteristics of subaqueous volcanic construction, the Archean Hunter Mine Group, Abitibi greenstone belt. Precambrian Res., 115, 119–152.

Mueller, W.U., Stix, J., White, J.D.L., Hudak, G., 2004. Archaean calderas. In: Eriksson, P., Altermann, W., Nelson, D., Mueller, W.U.Catuneanu, O. (Eds), The Precambrian Earth: tempos and events in Dev. Precambrian Geol., Elsevier, Vol. 12, pp. 345–356.

Nakamura, K., Kato, Y., 2004. Carbonatization of oceanic crust by seafloor hydrothermal activity and its significance as a $CO_2$ sink in the Early Archean. Geochim. Cosmochim. Acta, 68, 4595–4618.

Niem, A.R., 1977. Mississippian pyroclastic flow and ash-fall deposits in the deep-marine Ouachita flysch basin, Oklahoma and Arkansas. Geol. Soc. Am. Bull., 88, 49–61.

Offler, R., Whitford, D.J., 1992. Wall-rock and metamorphism of a volcanic-hosted massive sulfide at Que River, Tasmania: petrology and mineralogy. Econ. Geol., 87, 686–705.

Ohmoto, H., 1978. Submarine calderas: a key to the formation of volcanogenic massive sulfide deposits. Mining Geol., 89, 1687–1696.

Ohmoto, H., 1996. Formation of volcanogenic massive sulfide deposits: the Kuroko perspective. Ore Geol. Rev., 10, 135–177.

Orsi, G., De Vita, S., di Vito, M., 1996. The restless, resurgent Campi Flegrei nested caldera (Italy): constraints on its evolution and configuration. J. Volcanol. Geotherm. Res., 74, 179–214.

Pearson, V., 2005. Le Groupe de Blake River: revisité. Géosciences Abitibi, Recueil des résumées, Forum Technologique, Consorem, pp. 25–27.

Péloquin, S., 1994. Summary report of the 1994 geological mapping on the Normétal properties. NTS: 32D/14, 32E/3. Internal report, Falconbridge Limited.

Roche, O., Druitt, T.H., Merle, O., 2000. Experimental study of caldera formation. J. Geophys. Res., 105, 395–416.

Robert, F., 2001. Syenite-associated disseminated gold deposits in the Abitibi greenstone belt, Canada. Mineral. Deposita, 36, 503–516.

Schandl, E.A., Wicks, F.J., 1993. Carbonate and associated alteration of ultramafic and rhyolitic rocks at the Hemingway Property, Kidd Creek volcanic complex, Timmins, Ontario. Econ. Geol., 88, 1615–1635.

Skilling, I.P., 1993. Incremental caldera collapse of Suswa volcano, Gregory Rift Valley, Kenya. J. Geol. Soc. Lond., 150, 885–896.

Skirrow, R.G., Franklin, J.M., 1994. Silicification and metal leaching in semiconformable alteration beneath the Chisel Lake massive sulfide deposit, Snow Lake, Manitoba. Econ. Geol., 89, 31–50.

Smellie, J.L., Hole, M.J., 1997. Products and processes in Pliocene — recent, subaqueous to emergent volcanism in the Antarctic Peninsula: examples of englacial Surtseyan volcano construction. Bull. Volcanol., 58, 628–646.

Smith, R.L., Bailey, R.A., 1968. Resurgent cauldrons. In: Coats, R.R., Hay, R.L. and Anderson, C.A. (Eds), Studies in Volcanology 116. Geol. Soc. America Mem., pp. 613–662.

Stix, J., 1991. Subaqueous, intermediate to silicic-composition explosive volcanism; a review. Earth Sci. Rev., 31, 21–53.

Stix, J., Kennedy, B., Hannington, M., Gibson, H., Fiske, R., Mueller, W., Franklin, J., 2003. Caldera-forming processes and origin of submarine volcanogenic massive sulfide deposits. Geology, 31, 375–378.

Syme, E.C., Bailes, A.H., 1993. Stratigraphic and tectonic setting of Early Proterozoic volcanogenic massive sulfide deposits, Flin Flon, Manitoba. Econ. Geol., 88, 566–589.

Teasdale, N., 1993. Regional study of geochemical alteration associated with the Normétal deposit Abitibi greenstone belt, Québec. MSc-thesis, École Polytechnique, Montréal, 102 pp.

Tilling, R.I., Dvorak, J.J., 1993. Anatomy of a basaltic volcano. Nature, 363, 125–133.

Trendall, A.F., 2002. The significance of iron-formation in the Precambrian stratigraphic record. In: Altermann, W. and Corcoran, P.L. (Eds), Precambrian sedimentary environments: modern approach to ancient depositional systems. Spec. Publ. Int. Assoc. Sediment., Vol. 33, pp. 33–66.

Walker, G.P.L., 1984. Downsag calderas, ring faults, caldera sizes, and incremental caldera growth. J. Geophys. Res., 89, 8407–8416.

Walter, T.R., Troll, V.R., 2001. Formation of caldera periphery faults: an experimental study. Bull. Volcanol., 63, 191–203.

Wells, G., Bryan, W.B., Pearce, T.H., 1979. Comparative morphology of ancient and modern pillow lavas. J. Geol., 87, 427–440.

Wharton, M.R., Hathway, B., Colley, H., 1994. Volcanism associated with extension in an Oligocene–Miocene arc, southwestern Viji Levu, Fiji. In: Smellie, J.L. (Ed). Volcanism Associated with Extension at Consuming Plate Margins. Geol. Soc. London, Spec. Publ., Vol. 81, pp. 95–114.

White, J.D.L., 2000. Subaqueous eruption-fed density currents and their deposits. Precambrian Res., 101, 87–109.

White, J.D.L., 2004. Subaqueous explosive volcanism In: Eriksson, P., Altermann, W., Nelson, D., Mueller, W.U., Catuneanu, O. (Eds), The Precambrian Earth: tempos and events in Dev. Precambrian Geol. 12, Elsevier, pp. 334–345.

White, J.D.L., Busby-Spera, C.J., 1987. Deep marine arc apron deposits and syndepositional magmatism in the Alisitos Group at Punta Cono, Baja California, Mexico. Sedimentology, 34, 911–928.

White, J.D.L., Smellie, J.L., Clague, D.A., 2003. Introduction: a deductive outline and topic overview of subaqueous explosive volcanism. In: White, J., Smellie, J. and Clague, D. (Eds), Explosive subaqueous volcanism, Geophys. Mono. Series 140, pp. 1–23.

Wright, I.C., Gamble, J.A., 1999. Southern Kermadec submarine caldera arc volcanoes (SW Pacific); caldera formation by effusive and pyroclastic eruption. Marine Geol., 161, 209–229.

Wright, I.C., de Ronde, C.E.J., Faure, K., Gamble, J.A., 1998. Discovery of hydrothermal sulfide mineralization from southern Kermadec arc volcanoes (SW Pacific). Earth Planet. Sci. Lett., 164, 335–343.

Yamagishi, H., Dimroth, E., 1985. A comparison of Miocene and Archean rhyolite hyaloclastites: evidence for a hot and fluid rhyolite lava. J. Volcanol. Geotherm. Res., 23, 337–355.

You, C.-F., Bickle, M.J., 1998. Evolution of an active sea-floor massive sulfide deposit. Nature, 394, 668–671.

Yuasa, M., Kano, K., 2003. Submarine Silicic calderas on the northern Shichito-Iwojima Ridge, Izu-Ogsawara (Bonin). Western Pacific. In: White, J., Smellie, J. and Clague, D. (Eds). Explosive subaqueous volcanism, Geophys. Mono. Series 140, pp. 231–243.

# A Review on Collapse Caldera Modelling

J. Martí[1,*], A. Geyer[1], A. Folch[2] *and* J. Gottsmann[3]

## Contents

## Abstract

A complete study of collapse caldera formation should ideally involve multiple aspects such as regional tectonics, system geometry, magma and host rock properties, fluid-structure interaction, pre-existing structural discontinuities, and deformation history. Due to the complexity of such a comprehensive analysis, studies so far have centred on

*Corresponding author. Tel.: +34934095410; Fax: +34934110012
*E-mail address:* joan.marti@ija.csic.es

[1] Institute of Earth Sciences 'Jaume Almera', CSIC, c/Lluis Sole Sabaris s/n, 08028 Barcelona, Spain
[2] Osservatorio Vesuviano (OV-INGV), Napoli, Italy
[3] Department of Earth Sciences, University of Bristol, Wills Memorial Building, Queens Road, Bristol BS8 1RJ, UK

relevant but atomised topics. From a methodological point of view, and in addition to essential field and petrological studies, collapse calderas have also been investigated through analogue and theoretical models and geophysical imaging. Each approach presents advantages and disadvantages. We review the most significant contributions, summarise the relevant outcomes, and highlight the strong points and weaknesses of each approach. Analogue models enable a qualitative study of the structural evolution of a collapse process and allow us to infer which geometric factors play a relevant role. Differences among employed models lie in the applied experimental devices, the host rock analogue material (dry quartz sand, flour, etc.), and the magma chamber analogue (water or air-filled balloons, silicone reservoirs, etc.). However, the results obtained from different experimental setups are not substantially different if basic input parameters are kept similar in the experiments. Discrepancies in results mainly stem from restrictions of experimental designs. Theoretical (mathematical) models have grown in importance during the past decades, in combination with the development of computational resources. Nowadays, these models constitute a significant source of information on caldera-forming processes and can predict semi-quantitatively general conditions for fault formation and propagation. Theoretical studies can be classified in two groups according to their objectives. One group focuses on the evolution of pressure within the magmatic reservoir during a caldera-forming eruption. The second looks more into the structural conditions for caldera collapse and hence relate to analogue models. Both analogue and theoretical models are employed to gain a fundamental understanding of caldera processes and their resulting structures. Additionally, geophysical imaging helps to construct a regional image of the subsurface at active calderas, thus imposing constraints on the structural investigations based on analogue and mathematical modelling. A revision of each of these three complementary approaches to the study of collapse calderas is given in this paper, together with a combined analysis of their main findings and restrictions.

## 1. Introduction

Collapse calderas form by subsidence of the magma chamber roof during magma removal from a reservoir primarily in the form of a volcanic eruption but also by lateral magma migration. They represent one of the most enigmatic geological structures we can recognise on Earth and other terrestrial planets (Francis, 2003; Lipman, 2000). Their tremendous destructive potential, commonly implying significant atmospheric impacts, as well as their association with ore deposits and geothermal resources, have made calderas one of the main subjects of interest of modern and traditional volcanology.

Like any other volcanic phenomena, caldera-forming eruptions represent the culmination of a long-lived geological process involving the generation of magma at depth, its ascent and differentiation, and finally its eruption on the Earth surface. They occur in nearly all volcanic environments and are associated with most magma types including basalts and more evolved compositions. However, caldera-forming eruptions are rare compared to volcanic eruptions without caldera formation, as they require very specific stress and thermodynamic conditions for collapse to occur (Druitt and Sparks, 1984; Gudmundsson, 1998; Gudmundsson et al., 1997; Martí

et al., 2000; Jellinek and De Paolo, 2003; Folch and Martí, 2004; Lavallée et al., 2006). It is generally assumed that collapse calderas form after a significant decompression of the associated magma chamber following a central vent eruption (Druitt and Sparks, 1984; Martí et al., 2000), but conditions for caldera formation may also develop under overpressure in the magma chamber (Gudmundsson et al., 1997; Gudmundsson, 1998).

Traditionally, our knowledge on collapse calderas has been based on field studies (Williams, 1941; Williams and McBirney, 1979; Lipman, 1984, 1997, 2000; Walker, 1984), which allow us to identify the caldera-forming products and the resulting caldera structure. However, the different degree of preservation of calderas precludes, in most cases, a complete view of its internal structure and the corresponding caldera-forming deposits. Young calderas tend to have good exposures of extra-caldera deposits but do not show the caldera interior, while in old calderas erosion and, occasionally, tectonism, expose to some extent the internal caldera structure (see Mueller et al., 2008) but may not preserve the whole sequence of caldera products or the original caldera wall. We must appreciate that field studies can provide vital insights into the final stage of caldera formation and thus enable an indirect way to infer the caldera-forming process mostly through the analysis of the succession of caldera deposits. However, active calderas field studies are not capable of deducing the structural evolution of calderas, their deep structure, or the conditions that lead to caldera formation.

A significant advance in the understanding of caldera formation has been provided in recent years by the application of experimental (analogue and scale) and theoretical (mathematical) modelling. These studies offer an easy way to infer and visualise the structural evolution of a caldera and to predict the mechanical and thermodynamic conditions that control its formation. Also, geophysical sounding is progressively providing improved images of the interior structure of some calderas and their associated subvolcanic systems. In combination with field studies, experimental, theoretical and geophysical imaging is required to capture the full complexity of caldera-forming processes. This multidisciplinary approach is particularly vital in order to obtain a reliable image of caldera structures, not only for prospecting mineral deposits or geothermal exploitation, but also for the forecasting of future behaviour of calderas at unrest or to analyse the potential for caldera-forming eruptions in active volcanic systems.

The main goal of this paper is to revise the existing experimental, theoretical, and geophysical studies of collapse calderas, comparing their results and analysing their advantages and limitations, and to list the main advances that the application of such models has provided on our understanding of this type of volcanic structures.
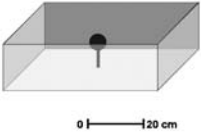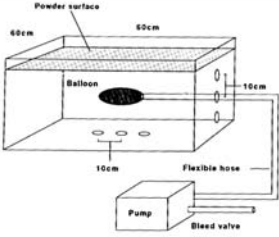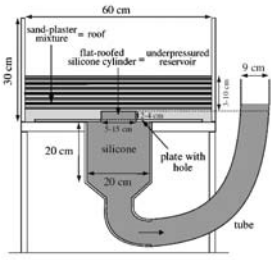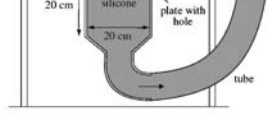
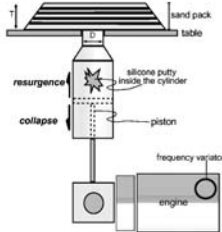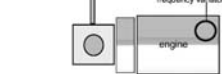## 2. The Role of Experimental Models in Caldera Studies

During recent years, analogue and scale modelling has become a useful tool to study volcanic processes, in particular those related to the dynamics of shallow magma chambers, eruption mechanisms, dynamics of volcanic plumes and

pyroclastic flows, or volcano instability (Martí and Folch, 2005). Analogue and scale experiments can simulate volcanic processes in the laboratory under conditions that are comparable or similar to those in nature. Such experiments have the advantage that they help to visualise phenomena that cannot be directly observed in natural systems. In comparison with field studies, experimental modelling, together with theoretical modelling (see later in this paper), helps to understand the processes that give rise to the products found in the geological record. Experimental models, together with field observations and laboratory data, are necessary to validate theoretical models.

   Analogue and scale experiments have been developed to investigate the internal structure of collapse calderas, but also their dynamics and structural controls (Komuro et al., 1984; Komuro, 1987; Martí et al., 1994; Roche et al., 2000; Acocella et al., 2000, 2001, 2004; Roche and Druitt, 2001; Walter and Troll, 2001; Kennedy et al., 2004; Lavallée et al., 2004; Holohan et al., 2005; Geyer et al., 2006). These experiments need to reproduce permanent deformation structures such as fractures and faults so that the experimental design for most cases includes cohesive, dry, powder mixtures (sand, fused alumina, flour, etc) simulating the crust, and silicone, air or water into an elastic balloon to simulate magma and magma chambers (Figure 1). As a result, analogue and scale experiments allow us to reproduce different caldera structures depending on the geometry (depth, shape, and size of the experimental chamber) and initial conditions (existence or not of previous doming, regional tectonics, etc.) of each experiment. Moreover, they provide relevant information on the structural evolution of the caldera process as they allow to trace the evolution of fractures and faults that control caldera subsidence (Geyer et al., 2006).

   However, analogue and scale experiments also expose some significant limitations. The principal drawback is the problem of scale. Volcanic systems involve processes that operate over a much wider larger space and longer timescales than those reproducible in the laboratory. The correct scaling is of utmost importance to assess dynamics, since they may be directly dependent on processes on different scales. In many cases, the appropriate scaling relationships are unknown. However, rigorous scaling almost always involves scaling of both the physical properties of the materials used and the dimensions of the system. Therefore, fully scaled dynamical simulations will usually require the use of appropriate analogue materials. If analogue experiments are not fully scaled, their 'simulation' of natural processes is unlikely to reproduce the entire spectra of dynamic behaviour. The role of not-for-scale experiments is primarily to offer a tool for the investigation and visualisation of caldera–collapse processes in order to deduce which geometrical relationships between the magma chamber and its surrounding medium may control the final results.

   A detailed revision of the different experimental designs and results from caldera studies is given in another contribution to this volume (Acocella, 2008). Here, we briefly summarise some significant aspects of experimental modelling of collapse calderas in order to provide a basis for a general discussion of collapse caldera modelling.

| Author | Year | Experimental Device | Materials |
|---|---|---|---|
| Komuro et al. | 1984 |  Box with dimensions 12 × 45 × 55 cm. Hole of 1 cm at the bottom. Through this hole a shaft is passed with a mounted rigid globe. The shaft, which is controlled by a motor, rises with an uniform speed. The box is filled with the analogue material, once the shaft has been adjusted to the desired depth. <br> 0 ⊢——⊣ 20 cm <br> Scale 1:200.000 | **Material I:** dry sand + clay powder <br> ρ=1.25 g/cm³ <br> φ= 26° <br> c=1.3·10³ Pa <br> **Material II:** clay powder <br> ρ=1.12 g/cm³ <br> φ= 28 <br> c=5.2·10³ Pa |
| Komuro, H. | 1987 | A ball of ice is introduced in a rectangular container and covered with the analogue material. Evaporation of ice imitates the outpouring or effusion of magma. <br> Scale 1:200.000 | dry sand + clay powder <br> ρ=1.25 g/cm³ <br> φ= 26° <br> c=1.3·10³ Pa |
| Martí et al. | 1994 |  Glass tank with dimensions 60 × 60 cm filled with alumina powder. A latex balloon is connected via a flexible hose through a pressure gauge to a small pump. <br> Scale 1:100.000 | fused alumina powder <br> ρ=3.1 g/cm³ <br> φ= 38° <br> c=200 Pa <br> φ=0.054 mm |
| Roche et al. | 2000 |  Experiments carried out in 2-D and 3-D. <br><br> 2-D apparatus: 60 ×10 ×30 cm <br> 3-D apparatus:60 × 60 ×30 cm <br><br> The silicone layer representing the magma chamber is underlain by a large volume of silicone connected to an outflow tube, which is blocked during the preparation phase. The experiments are initiated by opening the outflow tube. The silicone is free to leave the reservoir as the roof subsides. <br> Scale 1:100.000 | **Material I:** dry sand <br> ρ=1.5 g/cm³ <br> φ= 33.5°±0.8° <br> φ_mean=200 μm <br> **Material II:** silicone putty <br> ρ=1.15 g/cm³ <br> v= 2.4·10⁴Pa s |
| Roche & Druitt | 2001 | | **Material I:** dry sand <br> ρ=1.36 g/cm³ <br> φ= 29° <br> c = 40-60 Pa <br> **Material II:** silicone putty <br> ρ=1.15 g/cm³ <br> v= 2.4·10⁴ s |
| Acocella et al. | 2000 |  Piston within a cylinder at the base of a table. Horizontal layers of sand are placed on the table covering the output hole of the cylinder. The piston's vertical movement is controlled by an engine. Upward and downward movements of piston simulate doming and collapse, respectively. <br> Scale 1:100.000 | **Material I:** dry quartz sand <br> ρ=1.5 g/cm³ <br> φ= 35° <br> c=200-500 Pa <br> **Material II:** silicone putty <br> ρ=1.14g/cm³ <br> v=10⁴ Pa s |
| Acocella et al. | 2001 | | |

ρ → density   φ→ internal friction angle   c→ cohesion   ν → viscosity   φ → particle diameter

**Figure 1**   List of existing studies of analogue models of caldera collapse. A short description and sketch of the experimental device is included, along with the physical properties of the analogue materials ($\rho$, density; $\phi$, internal friction angle; $c$, cohesion; $v$, viscosity; $\varphi$, particle diameter).

## 2.1. Mining subsidence: an analogue for caldera collapse

An important contribution to the experimental modelling applied to the under–standing of collapse calderas stems from mining subsidence studies and scaled experimental models of ground subsidence (Sanford, 1959; Whittaker and Reddish, 1989). A 2-D analysis of mining subsidence allows these authors to define the *roof aspect ratio*, the ratio between roof width and roof thickness (Figure 2). They distinguish between three cases of mining subsidence: subcritical, critical, and supercritical. The critical aspect ratio is given by:

$$\tan\theta = \frac{(w/2)}{h} = \frac{1}{2R} \qquad (1)$$

where $\theta$ ($\sim 35°$) is the angle of draw, localised between the vertical and the lines that draw from the edges of the cavity and delimit the collapse depression at surface; $w$ the roof width and $h$ the roof thickness (depth). For $\theta = 35°$, the critical value of $R$ is 0.7. Therefore, the three different cases are: *subcritical case* ($R > 0.7$) in which there is a single point of maximum compression located at the centre of the depression; *critical case* ($R = 0.7$) in which there are two points of maximum compression and a single point of no deformation at the centre; and *supercritical case* ($R < 0.7$) in which there are two points of maximum compression and an undeformed zone of finite width in between. The model distinguishes between three different areas: extensional, compressional, and non–deformed (Figure 2). The width of the marginal deformed zone (extensional and compressional) is constant for a given $\theta$ and $h$, and does not depend on $w$. For low values of $R$, there is a central non–deformed zone bounded by marginal deformed zones. By contrast, for high values of $R$ the entire depression is affected by surface deformation.

Branney (1995) and Roche et al. (2000) suggested that caldera collapse is strongly controlled by the relationship between the geometry of the magma chamber and the thickness of the overlying roof (magma chamber depth), so that caldera collapse and the resulting caldera structures behave in a similar way to mining subsidence. Therefore, they propose to apply the concept of *roof aspect ratio*, defined as the ratio between magma chamber depth and magma chamber width, to collapse calderas. The *roof aspect ratio* concept can be applied to classify caldera subsidence and, therefore, to interpret the morphological characteristics and structural features of the different collapse processes reproduced by analogue and scale models (Acocella, 2008, and references therein). The idea that caldera collapse and the resulting caldera depressions are strongly controlled by the relationship between the geometry of the magma chamber and the thickness of the overlaying roof (magma chamber depth) is also supported by theoretical models (e.g. Folch and Martí, 2004), as we will see later in this paper.

## 2.2. Main observations

As described in Acocella (2008), experimental models on collapse calderas may differ depending on the main feature they seek to simulate (Figure 1). Hence, there are experiments (i) simulating the development of collapse calderas, as a
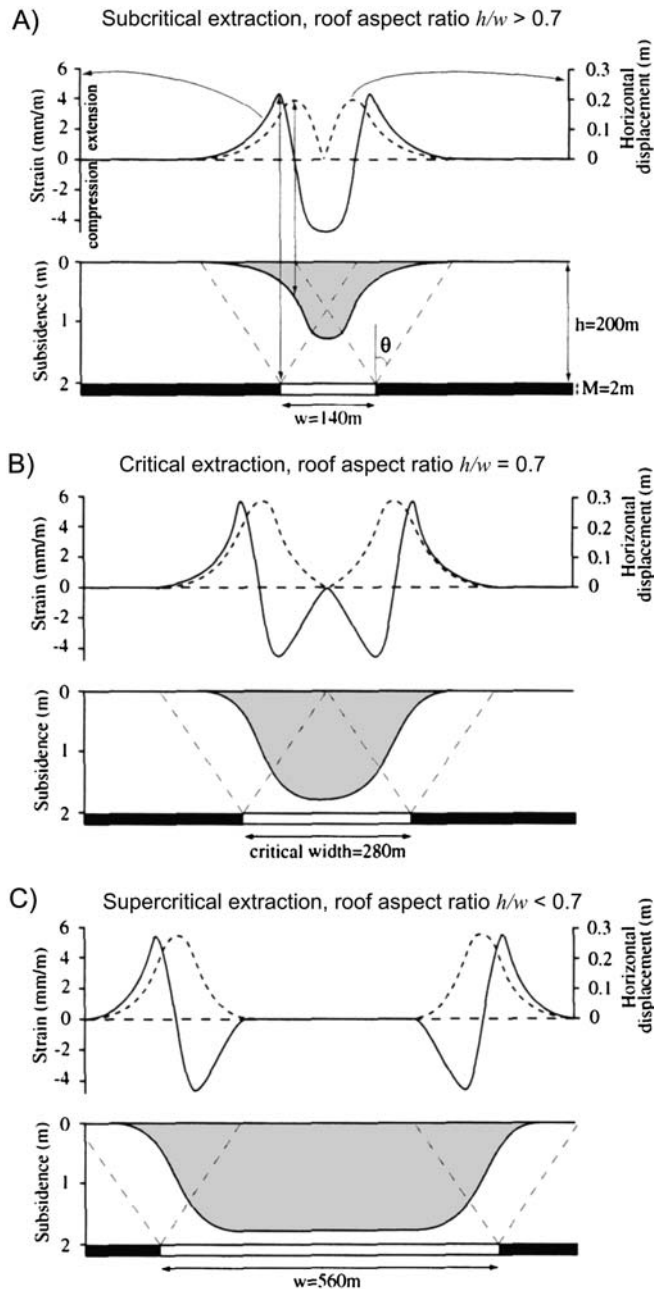
**Figure 2** Model for subsidence, horizontal displacement, and strain at the surface caused by a rectangular cavity 2 m high and 200 m deep. (A) subcritical case, (B) critical case, and (C) supercritical case. The angle of draw $\theta$ is 35° (modified after Whittaker and Reddish, 1989).

consequence of a pressure decrease within the chamber; (ii) simulating the development of caldera collapse at the summit of a doming structure caused by a pressure increase inside a magma chamber; (iii) simulating the effect of the superposition of inflation (doming) and deflation episodes on the development of collapse calderas; (iv) simulating the development of a collapse caldera, considering the topographic loading of a volcanic edifice; and finally (v) those simulating pure collapse due to magma chamber decompression, considering the role of pre-existing structures and the effect of superimposing a regional tectonic regime (deviatoric stress) on the local stress field.

The most common case reproduced experimentally corresponds to the pure caldera collapse (i.e. subsidence takes place as a consequence of a pressure decrease within the chamber without previous inflation) (Komuro, 1987; Martí et al., 1994; Roche et al., 2000; Acocella et al., 2000, 2001; Roche and Druitt, 2001; Walter and Troll, 2001; Kennedy et al., 2004; Lavallée et al., 2004; Geyer et al., 2006). In this case, experimental results show that this type of collapse entirely depends on the roof aspect ratio $R$. For low values of $R$ (i.e. when $R < 0.7$–$0.85$) the caldera collapse is piston-like, whereas for higher roof aspect ratios ($R > 0.7$–$0.85$) the collapse tends to be of incoherent or funnel type (Geyer et al., 2006). In the first case, the subsiding block is coherent and collapse is controlled by a combination of outward dipping reverse faults and vertical or subvertical ring faults (Figure 3A). In the second case, collapse occurs along multiple reverse faults. At first, a pair of faults nucleates at the top of the magma chamber and propagates upwards triggering the formation of a second pair, and so on until the structures arrive at surface (Figure 3B). No peripheral faults are generated, and subsidence is greater at depth than at the surface. Collapse begins in both cases with downward flexuring of the roof ('down sagging'); however, this effect is more marked for low values of $R$. Also, the percentage of extensional area in relation to the total collapse area increases with $R$.

We can also observe in these experiments that the resulting caldera is characterised by two depressions (Figure 3). The inner one is bordered by outward-dipping,
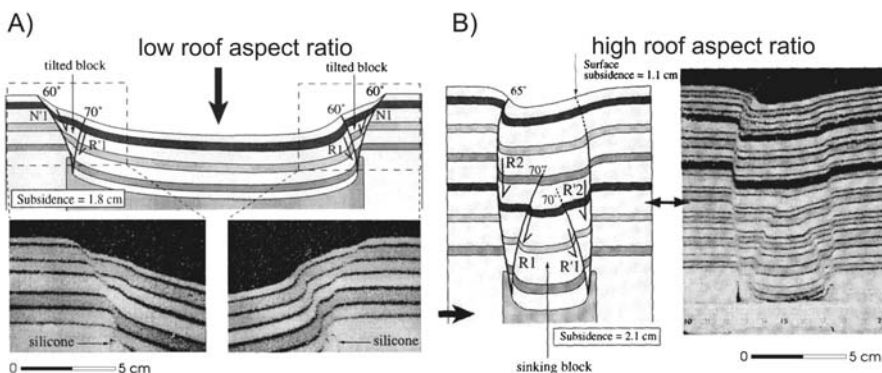


**Figure 3** Photographs and sketches of two of the experiments conducted by Roche et al. (2000). (A) $R = 0.2$ and (B) $R = 2$. $R$, reverse fault; $N$, normal fault (modified after Roche et al., 2000).

high-angle reverse ring faults. The outer depression is defined by inward-dipping normal ring faults. During the collapse, the caldera walls break down causing the caldera rim to propagate outwards.

The structural pattern controlling caldera collapse inferred from these experiments can be considered as the most common one, and it is generally believed to represent the same structural sequence that would control the formation of natural calderas (Acocella, 2008). However, some changes in this general behaviour can be observed as soon as other aspects are taken into account including previous doming, topographic loading, or deviatoric tectonic stresses.

Most caldera-collapse experiments are concerned with the final stage in the formation of a collapse caldera or with the structural evolution of such a volcanic process, but ignore its relationship with the magma chamber decompression. Recently, Geyer et al. (2006) have determined experimentally and semi-quantitatively the fraction of magma ($f$) necessary to be removed in order to form the different structural features that lead to caldera subsidence. They performed analogue experiments to correlate the structural evolution of a collapse with the erupted magma chamber volume fraction. The experimental device is similar to the one used by Martí et al. (1994) but water was used instead of air to inflate the balloon (see Figure 1). This setup enables the temporal evolution of the collapse to be recorded and the tracking of the evolution of fractures and faults. Geyer et al. (2006) study the appearance and development of specific brittle structures, such as surface fractures or internal reverse faults, and correlate each brittle structure with the corresponding magma volume fraction removed from the chamber (Figure 4). Geyer et al. (2006) also determine the critical conditions for the onset of caldera formation.

Experimental results show that, at any characteristic structural event (e.g. first appearance of surface fractures), the experimental relationship between volume fraction ($f$) and chamber roof aspect ratio ($R$) fits a logarithmic curve (Figure 5). This implies that volume fractions required to trigger collapse are lower for chambers with low aspect ratios (shallow and wide) than for chambers with high aspect ratios (deep and small). These results are in agreement with natural examples and theoretical studies.

## 2.3. Restrictions of the experimental modelling

Before discussing any experimental results and their geological implications for the study of collapse calderas, it is necessary to determine the restrictions of the experimental setup and, if possible, try to minimise their effects for future analogue models. In this section, we describe the restrictions and limitations imposed by individual experimental setups (Figure 1). Analogue materials used to mimic the host rocks and the magma chamber analogue pose major limitations on experimental results. The main restrictions include (1) unrealistic deformation of the experimental magma chamber, (2) existence of grain-flow processes, (3) impossibility of dyke injection, and (4) homogeneous magma chamber roof.

The choice of the magma chamber analogue is an important part of the experimental design. Its physical properties, as well as its deformation pattern, have
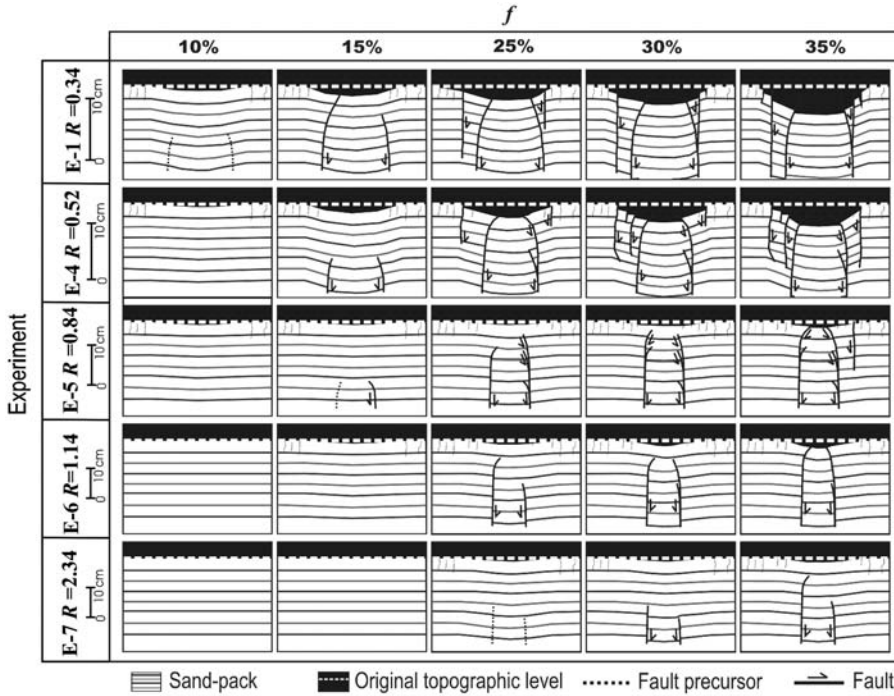
**Figure 4**  Sketches showing different stages in the structural evolution of the collapse process. Notice that, for constant values of *f*, structural development is strongly dependent on the roof aspect ratio *R* (modified after Geyer et al., 2006).

a significant bearing on ground subsidence and the resulting structures, which eventually determine whether results are deemed realistic. The most widespread magma chamber analogues are latex balloons (filled with either air or water) and silicone reservoirs. Other analogue materials such as a rigid ball (Komuro et al., 1984) or a dry ice ball (Komuro, 1987) were used on one occasion, but their use was subsequently abandoned.

The use of a latex balloon as a magma chamber analogue imposes several restrictions. The main limitations are wall effects of the elastic material. The balloon can be deflated almost indefinitely, allowing the system to steadily pass through different stages of collapse. This is certainly not the case in natural systems, where the withdrawal process from the chamber can be interrupted as soon as magma is unable to flow out, for example, when the eruption conduit is blocked (Martí et al., 2000). Furthermore, during doming processes, the elastic walls permit an almost infinite expansion to geologically improbable levels (Martí et al., 1994). In natural systems, once expansion reaches a certain level, the tensile strength of the country rock is exceeded, fracturing is induced, and an eruption can ensue (Tait et al., 1989). Collapse and doming structures can be overstated compared to natural cases. Some authors (Lavallée et al., 2004; Geyer et al., 2006) avoid these edge effects by stopping the experiment while the induced ground deformation is within realistic limits.
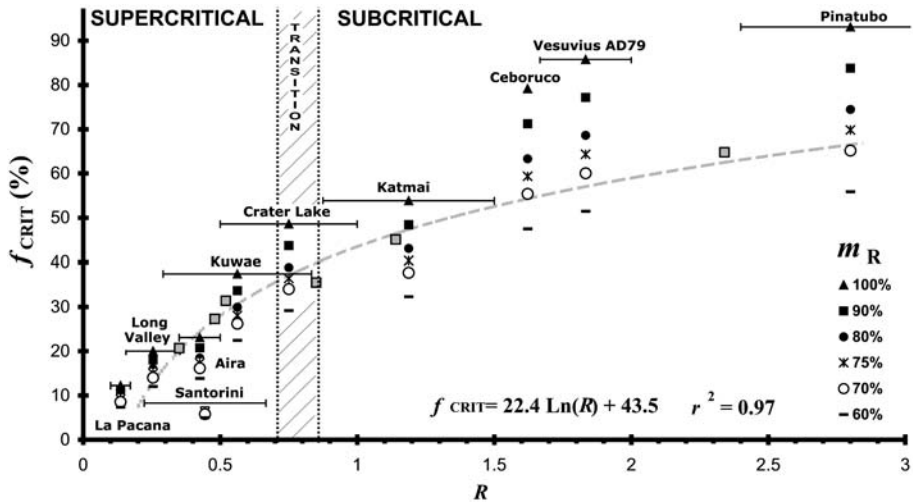
**Figure 5** Erupted volume fraction at the caldera onset, as a function of $R$. Grey squares indicate experimental $f_{CRIT}$ values ( $f$ values at the caldera-collapse onset). A discontinuous line shows the log-fit to experimental values. Values of $f_{CRIT}$ for natural examples are calculated considering different percentages (100–60%) of erupted magma (see Geyer et al., 2006 for details). Horizontal lines in triangles ( $f_{CRIT}$ values considering that the magma chamber is completely emptied) are the error bars due to the roof aspect ratio uncertainty. The vertical line marks the transition from subcritical to supercritical collapses (modified after Geyer et al., 2006).

During the deflation process, a water-filled balloon creates surface deformation in two different ways. First, filled to its maximum capacity it deflates elastically and contracts due to overpressure decrease (see figures in Lavallée et al., 2004 for more details). Second, by contrast, at lower water capacities, the roof subsides vertically as the water is evacuated. Lavallée et al. (2004) proposed that these two mechanisms of analogue chamber deformation represent initially elastic behaviour of the crust and the crystal mush around the chamber during contraction as the pressure in the magma chamber decreases, followed by brittle failure of the roof when the deviatoric stress reaches the Mohr–Coulomb criterion curve.

The elastic walls of the balloon generate forces that do not have a counterpart in natural systems and, in consequence, violate the principles of scaling. Lavallée et al. (2004) argued that the elastic walls can be interpreted as the boundary between the water and the sand and may represent the crystal–mush transition between the magma and the rock. However, the same authors admit that this boundary is not scaled and prevents physical processes such as intrusion and the collapse of blocks into the analogue magma chamber. In nature, such processes may affect the magmatic pressure and could play a vital role during the process of caldera formation.

Finally, some authors (e.g. Martí et al., 1994; Walter and Troll, 2001; Geyer et al., 2006) bury the balloon close to one of the walls of the experimental tank. This layout is useful to observe the temporal evolution of the collapse but may alter the structures developed during the collapse process. Martí et al. (1994) evaluated

the importance of this perturbation and considered that these edge effects did not significantly affect the experimental results.

The use of silicone as a magma chamber analogue circumvents the restrictions imposed by elastic balloon walls, but introduces other limitations such as an inappropriate geometry of the silicone container to simulate a magma chamber.

With regard to the simulation of the host rock, all analogue experiments use granular materials (e.g. dry quartz sand, flour). Although these materials have the ability to deform in a brittle manner and do expose a Mohr–Coulomb behaviour alike natural rocks, they are also susceptible to slump and readjustments by small-scale grain flow. These processes lead to structures that may not have an analogy in natural systems and must be regarded as permanent plastic deformation (Martí et al., 1994). This effect can be reduced by decreasing the grain size and increasing the cohesion of the material.

None of the experimental devices and setups used, at the time of this writing, succeeds in simulating dyke injection during tumescence or collapse. The high viscosity of silicone and the granular nature of sand prohibit intrusion of silicone and the formation of 'ring dikes' during experiments (Roche et al., 2000). Dyke injection is likely to be important during the evolution of shallow magmatic system, as dykes may regulate the thermodynamic equilibrium inside the magma chamber. For example, in situations of overpressure, repeated dyke intrusions can decrease the magma chamber pressure and may avoid the initiation of an eruptive event. Also, dyke injection will change the strength of the host rock, one of the key parameters in controlling the structural evolution of the whole system and, therefore, possible caldera-collapse events.

Before concluding this section, it is also important to mention that the studied experimental models have been carried out with homogenous roofs above the magma chamber analogue. This is not a correct approximation to natural system, since country rocks around magma chambers are normally heterogeneous in composition and mechanical behaviour. Previous volcanic eruptions or sedimentation processes create a roof composed of materials with very different physical properties such as pyroclasts and lavas. Compositional heterogeneities can influence the stress field and consequently fracture propagation and structure development (Gudmundsson, 2008). Therefore, it is important to introduce compositional heterogeneities in order to mimic realistic phenomena.

## 3. Theoretical Models on Collapse Calderas Formation

Theoretical models based on solid and fluid mechanics are a valuable tool for understanding the physics behind many volcanic processes and, in particular, those during collapse caldera formation (Martí and Folch, 2005). The governing equations behind the models can be quite complex and often do not have analytical solutions. As a consequence, numerical techniques are needed to solve such problems. For this reason, the terms 'numerical model' or 'computational model' have become, by abuse of language, synonymous with 'theoretical model'. In this

section, we review the contribution of current numerical models to caldera–collapse studies (see Table 1 for a short description).

Ideally, the modelling of collapse calderas formation should be performed considering physical processes that occur both inside and outside the magma reservoir. Our understanding of this 'fluid-structure' interaction is, however, far from complete. For simplification, models deal, in practice, with only a part of the problem (chamber or surrounding rocks) at a time, i.e. focus on one domain and incorporate simplistically the effect of the other. In this sense, theoretical models on collapse calderas formation can be classified into two groups:

(i)  models based on thermodynamics and fluid mechanics that aim to quantify processes occurring inside the chamber prior to and during collapse (hereafter termed magma chamber models), i.e. they analyse aspects such as the evolution of pressure within a magma reservoir; and

(ii)  models based on solid mechanics, exploring processes outside the chamber (hereafter termed host rock models), i.e. they deal with aspects such as stress conditions for the formation of fractures and faults in the host rocks.

## 3.1. Magma chamber models

This family of models is based on equations of state of magma combined with a simple criterion for collapse, which is commonly defined as an underpressure threshold (Druitt and Sparks, 1984; Bower and Woods, 1997, 1998; Martí et al., 2000; Roche and Druitt, 2001; Macedonio et al., 2005). Imposing mass conservation, these models track pressure variations within the magma reservoir as a function of erupted mass. They enable prediction of eruptive conditions that satisfy the criteria for collapse based on parameters such as magma composition, volatile content, host rock mechanics, or magma chamber geometry (mainly dimensions and depth). It is important to note that this group of models simulate implicitly the 'classical' caldera scenario, in which collapse results from critical decompression of the magma reservoir. As such, these models simulate the following succession: (i) a chamber pressure increase until $P_M > P_L + \Delta P_{START}$ (where $P_M$, $P_L$, and $\Delta P_{START}$ stand for magma pressure, lithostatic pressure, and critical overpressure respectively, see Figure 6); followed by (ii) eruption, during which the conduit is enlarged by sidewall erosion (an open conduit is maintained against lithostatic forces); and finally (iii) the onset of a piston–like collapse as soon as the failure criteria is satisfied, i.e. when the chamber pressure drops below the lithostatic value by a certain amount (Figure 6).

The main deliverable of these models is $f$, the percentage of magma volume that must be erupted in order to reach critical underpressure. It is important to understand that the removal of magma does not imply the creation of a 'void cavity'. In fact, since the magma's bulk density decreases during decompression, due to further exsolution of volatiles, the remaining magma reservoir can be envisaged as a pressurised porous media which always fills its cavity as the eruption proceeds due to its increasing void fraction (the exsolved gas volume fraction). For a given chamber roof aspect ratio, the value of $f$ depends on the volatile content, the

**Table 1** List of the existing studies of numerical models related to caldera collapse; a short description of the models as well as the applied rheology (AR) and the values for the principal parameters are indicated.

| Authors | Type of models | AR | Values for the principal parameters | |
|---|---|---|---|---|
| | | | Chamber/magma | Host rock |
| *Models focused on the pressure evolution inside the chamber and the erupted magma fraction* | | | | |
| Druitt and Sparks (1984) | Analysis of magma chamber pressure during an eruption. Estimate of erupted magma chamber volume fraction | – | Chamber: $d = 2.5$–$10$ km Magma: zoned chamber *silicic magma* $T$: 900°C $B$: 30 GPa $\Delta P+$: 25 MPa wc: 4.5–7.5% *mafic magma* $B$: 10–100 GPa | CT: 35–40 km TR: extensional HF: 60 mW m$^{-2}$ fc: 0.6 $\rho$: 2,700 kg m$^{-3}$ $E$: 100 GPa $v$: 0.25 |
| Bower and Woods (1997) | Model to expose some of the fundamental controls on the mass, which may erupt from a chamber during the caldera-forming eruption until the critical underpressure at which the walls fail under compression | – | Chamber $d$: 2–7 km ve: 3 km vol: 10 km$^3$ $\Delta P+$: 1–45 Mpa $\Delta P-$: 0–30 Mpa Magma $\rho$: 2,700 kg m$^{-3}$ $T$: 922°C $B$: 10–100 GPa vc: 3–7% mcc: 0–0.4 | – |
| Martí et al. (2000) | Pressure evolution model during explosive caldera-forming eruptions. Description of the pressure variation throughout the whole central vent eruption–caldera collapse cycle | EL | Chamber $d$: 3–6 km he: 1–5 km ve: 1–5 km $\Delta P+$: 10–30 Mpa $\Delta P_{COLL}$:30–60 MPa Magma $T$: 850°C $\rho$: 2,500 kg m$^{-3}$ wc: 3.5–6 % | ss: 40 MPa |

| Roche and Druitt (2001) | (A) Scaling analysis: failure criterion for piston collapse along reverse ring fault. Comparison with experimental results (B) Calculation of volume fraction required to trigger caldera collapse | MC | Chamber $d$: 2.5–10 km $ve$: 0.5–3 km $\Delta P+$: 0.1–1 MPa $ec$: 1–2.5 | Magma: silicic $T$: 895°C $B$: 30 GPa $\rho$: 2,200 kg m$^{-3}$ wc: 3–7 wt% | fc: 0.5–0.7 $\theta$: 70–90° $c$: 0.1–5 MPa $\rho$: 2,700 kg m$^{-3}$ sc: 0.6 |
|---|---|---|---|---|---|
| *Models to determine stress conditions for normal-fault caldera initiation (incl. caldera morphology)* | | | | | |
| Komuro et al. (1984) | Apical caldera collapse as a consequence of domal deformation | ELP-VM | – | – | $v$: 0.25 |
| Chery, et al. (1991) | (1) Quasi-static evolution of thermally stratified continental crust near an: –Inflating magma chamber –Relaxing magma chamber (2) Caldera collapse (3) Resurgence of a central dome | ELPV | Chamber: he: >gt;10 km $d$: 5 km vol: 2,000 km$^3$ $\Delta P+$: 30–60 MPa | Magma: Rhyolitic $T$: 1,150°C | CT: 35–40 km TR: extensional HF: 60 mW m$^{-2}$ fc: 0.6 $\rho$: 2,800 kg m$^{-3}$ $E$: 100 GPa $v$: 0.25 |
| Gudmundsson et al. (1997) Gudmundsson (1998) | Magma chamber under: Lithostatic equilibrium Overpressure Underpressure Horizontal tensile stresses Vertical compressive stresses | EL-GCTS | Chamber: he: 2a–4a $\Delta P+$: 1–5 Mpa $\Delta P-$: 10MPa | | $E$: 40 GPa $v$: 0.25 ts: 5 MPa |
| Folch and Martí (2004) | Coupled thermomechanical model to explore conditions for caldera collapse due to magma chamber underpressure | TEL-GCTS MC | Chamber: $d$: 3.5 km | Magma: $T$: 950°C | Crust: $E$: 60 GPa $v$: 0.25 ts: 15 MPa ss: 50 GPa |

**Table 1** (*Continued*)

| Authors | Type of models | AR | Values for the principal parameters | |
|---|---|---|---|---|
| | | | Chamber/magma | Host rock |
| Kusumoto and Takemura (2005) | Quantitative discussion of the relationship between caldera geometry and magma chamber depth | ELP-MC | Chamber: 2$d$/he: 1–8 km | Basaltic crust: $E$: 40 GPa fa: 30° $v$: 0.25 cs: 15 MPa Ss: 50 GPa $\theta$: 0–40° |
| *Models predicting fault location using non-elastic rheology* | | | | |
| Burov and Guillou–Frottier (1999) | Thermomechanical numerical model (1) stationary temperature field (rapid caldera collapses) No regional compression/extension Regional extension (2) Time-dependent thermal conduction and advection (caldera collapse and long-term post-collapse activity) Influence of: heat diffusion from the hot magma body and thermal blanketing by the ignimbrite cover | ELPD -MC -NV | Chamber: ve: 5–10 km he: $d$—25$d$ $d$: 2–5 km | Upper crust: $\rho$: 2,650 kg m$^{-3}$ Lower crust: $\rho$: 2,900 kg m$^{-3}$ Both crusts: CT: 10 km fa: 30° $E$:0.8 GPa $v$: 0.25 $V$: 10$^{19}$–10$^{21}$ Pa s |

Magma: $T$: 800°C $B$: 30 GPa $\rho$: 2,200 kg m$^{-3}$ $v$: 10$^{16}$ Pa s

| Guillou–Frottier et al. (2000) | Caldera collapse over pre-defined rectangular magma chamber. Steady-state geotherm and no heat transport during the collapse | ELPD -MC -NV | Chamber: $d$: 2.5 km he: 10–15 km ve: 2d $\Delta P+$: 10 MPa | C: 10 km fa: 30° $\rho$: 2,900 kg m$^{-3}$ $E$: 0.8 GPa $V$: 0.25 C: 0–20 MPa $V$: 10$^{19}$–10$^{21}$ Pa s |
| Gray and Monaghan (2004) | Numerical simulations of formation of cracks under tensional stresses or increasing magma chamber pressure. It includes a fracture model that allows following the growth of fractures under stress | EL P-VM DM GCTS | Chamber: $d$: 3.5 km he: 3.5 km ve: 1.6 km | – |

*Note*: $\rho$, density; $\nu$, Poisson's ratio; $\Delta P+$, magma chamber overpressure; $\Delta P-$, magma chamber underpressure; $\Delta P_{COLL}$, collapse trigger underpressure; $\theta$, ring–fault dip angle; $B$, bulk modulus; $c$, cohesion; cs, compression strength; CT, crust thickness; $d$, magma chamber depth; $E$, Young modulus; ec, ellipticity coefficient; EL, elasticity; ELP, elastoplastic; ELPD, elastic–plastic–ductile; ELPV, elastic–visco–plastic; fa, friction angle; fc, friction coefficient; GCTS, Griffith criterion under tensile strength; he, magma chamber horizontal extension; HF, heat flow; mcc, magma crystal content; NV, non–linear viscous; P, plasticity; VM, Von Mises failure criterion; $T$, temperature; TEL, thermoelasticity; TR, tectonic regime; ts, tensile strength; $v$, viscosity; vc, volatile content; ve, magma chamber vertical extension; vol, magma chamber volume; wc, water content.

: Caldera collapse through magma chamber overpressure.

: Caldera collapse through magma chamber underpressure.

: Caldera collapse through magma chamber over- and underpressure.
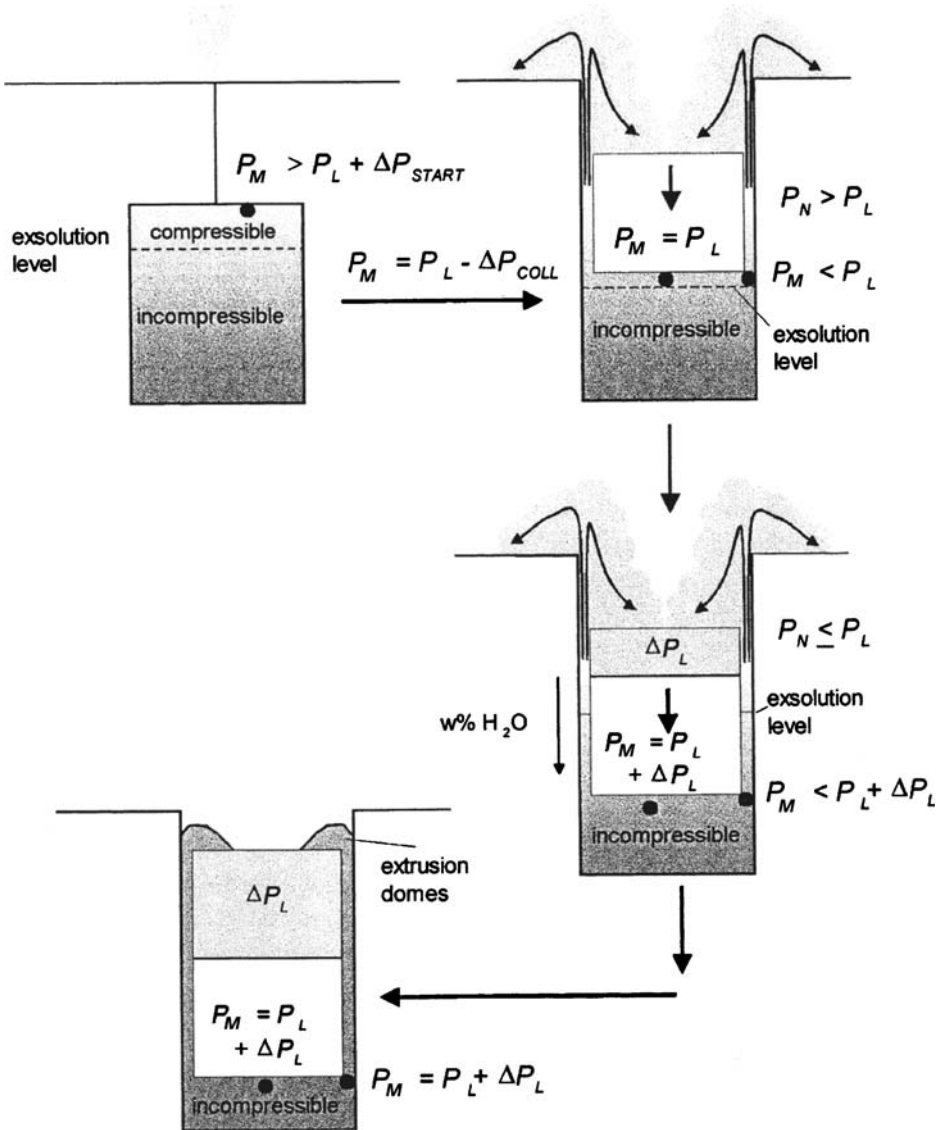
**Figure 6** Schematic representation of an explosive caldera–collapse process. The central vent eruption progressively decompresses the overpressurised ($P_L+\Delta P_{START}$) magma chamber. The chamber pressure decreases well below the lithostatic pressure. Caldera collapse starts when chamber decompression reaches a critical value ($P_L-\Delta P_{COLL}$) at which the chamber roof fails under shear. Caldera collapse brings the magma pressure at the chamber roof to lithostatic pressure. Subsidence of the chamber roof will continue either until the pressure at the base of the magma column occupying the ring fault is equal to the lithostatic pressure of the chamber ($P_L+\Delta P_L$), or until all magma has been erupted. Solid dots indicate points inside the magma chamber for which $P_M$ is indicated. $P_M$, magmatic pressure; $P_L$, lithostatic pressure; $\Delta P_{START}$, overpressure required to fracture the country rock and to form a conduit to the surface; $\Delta P_{COLL}$, shear strength of the rock, i.e. the underpressure necessary to initiate caldera collapse (modified after Martí et al., 2000).

cohesion and internal friction coefficient of the chamber roof, the ring-fault dip angle, the magma chamber's thickness, and on the depth at which the magma chamber is located (Figure 7). Values predicted for *f* are quite variable, depending on the model and on the parameters above, and may vary from a few to as much as 60–70 vol.%. In shallow silicic reservoirs, for instance, most magma is expected to be oversaturated with volatiles, and hence the fraction of compressible magma (above the exsolution level) is larger. It follows that, the rest being equal, in order to achieve a certain pressure drop more magma needs to be withdrawn from shallower reservoirs than from deeper reservoirs. For the same reason, a magma chamber with a vertical gradient in volatile contents has a lower value of *f* compared to that of a homogeneous chamber. The influence of the chamber vertical extent (thickness) is also relevant, as pressure decreases faster with increasing thickness. Sill-like chambers, therefore, have a value of *f* lower than that of dyke-like chambers if the rest of the parameters remain the same. Magma chambers with the same aspect ratio but different geometries (cylindrical or ellipsoidal) present similar results.

An obvious important limitation of these models is their assumption that collapse occurs after critical decompression, without considering the evolution of the stress field around the chamber. This evolution dictates if collapse faults can form or reactivate for a particular chamber geometry and ambient conditions. A second less evident drawback is that these models assume implicitly that magma can continue to flow out even if the chamber pressure decreases below lithostatic value by several megapascals. In the case of volatile-rich magma, this can be justified by the presence of gas bubbles, which drive the ascent of magma through the conduit, such that the bulk density of the rising magma column may become much lower than the bulk density of the surrounding medium. As a result, parts of the chamber can have a pressure exceeding the pressure caused by the magma
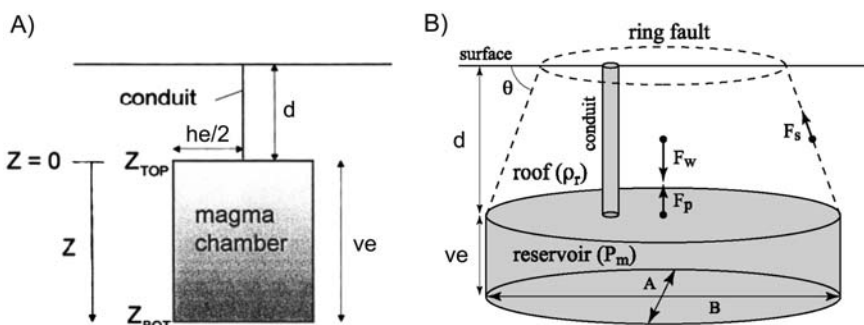


**Figure 7** Examples of model geometries applied to numerical models. (A) 2-D rectangular magma chamber used by Martí et al. (2000) for the eruptive phase. (B) System considered by Roche and Druitt (2001). $\rho_r$, country rock of density; $\theta$, potential vertical or outward-dipping ring fault of angle; A, B, magma chamber axis; $d$, magma chamber depth; $F_w$, weight of the roof; $F_p$, upward force on the roof exerted by the magma; $F_s$, resisting upward shear force on the potential ring fault; he, magma chamber horizontal extent; $P_m$, fluid reservoir pressure; ve, magma chamber vertical extent; Z, displacement.

column's weight (i.e. a positive pressure gradient with depth; otherwise magma in the conduit would not flow out), yet at the same time there is a negative pressure gradient with respect to the host rock, i.e. the lithostatic load. The presence of volatiles and their effect on magma density can thus, in part, justify the application of such models. However, what remains unexplained is the fact that during the vast majority of volatile-rich eruptions conduit closure occurs before the underpressure condition is reached and consequently caldera formation is avoided. This phenomenon indicates that geometric and/or dynamic conditions required to keep a conduit open are only achieved occasionally. The question as to why and how this is achieved remains unanswered. The timescales of magma ascent and host rock response to pressure variations are, in our opinion, key aspects that should draw further attention.

## 3.2. Host rock models

This group of models (Komuro et al., 1984; Chery et al., 1991; Gudmundsson et al., 1997; Gudmundsson, 1998; Burov and Guillou-Frottier, 1999; Guillou-Frottier et al., 2000; Roche and Druitt, 2001; Folch and Martí, 2004; Gray and Monaghan, 2004; Gudmundsson, 2008) focus on the conditions necessary for the initiation of ring faults. A ring fault is essentially a subvertical normal fault that requires specific stress conditions to form or slip (e.g. Gudmundsson et al., 1997, 2008). A ring fault may initiate at any depth between the margins of the chamber and the surface. If failure initiates at the margin of the chamber, the resulting dykes would relax the stress difference and may hinder the development of a ring fault. Furthermore, ring faults may extend to considerable depth, but calderas are surface features and do not form unless the stress field at surface favours ring-fault formation. The stress field in the vicinity of the surface is thus a controlling factor for caldera formation. Existing numerical results suggest that faults controlling caldera collapse commonly develop from tension fractures at the surface of the associated volcano and propagate to greater depths, towards the boundary of the associated magma chamber (Gudmundsson, 1988a, 1988b). At a certain depth, these tensional ring fractures change into normal-fault ring fractures. In general, models assume that for this to occur the maximum shear stress must concentrate at the lateral margins of the magma chamber and, simultaneously, the maximum tensile stress must peak both at the surface and at a radial distance close to the surface projection of the chamber walls. The latter condition is supported by field evidence which suggests that ring faults are nearly vertical, and by analogue experiments which show a correlation between the area of collapse and the cross-sectional area of the reservoir (see previous sections).

In addition to the definition of the appropriate stress field, models also need to specify a fracture criterion. Rocks behave as brittle materials at rapid loads, low confining pressures, and low temperatures, whereas they tend to be ductile at high confining pressures and temperatures (Rutter, 1974). Consequently, it seems reasonable to assume both brittle and ductile fracture criteria near the magma chamber walls. One possible choice (Gudmundsson, 1988b, 1998; Folch and Martí,

2004) is to assume that tensional fractures are produced when:

$$\sigma_3 \leq -T_0 \tag{2}$$

whereas shear fractures occur if:

$$\sigma_1 - \sigma_3 \geq S_0 \tag{3}$$

where $T_0$ and $S_0$ represent the tensile and the shear strength of the embedding crust, respectively. Equation (2) is the Griffith failure criteria for brittle materials under a tensional regime ($\sigma_1 + 3\sigma_3 < 0$), whereas Equation (3) reflects a limit of the Mohr–Coulomb shear failure criteria near the brittle-ductile transition. Hence, the above expressions can be considered as end-members of the combined Griffith/Mohr–Coulomb failure criteria for brittle materials. Using these criteria, tensional fractures are produced in a plane perpendicular to $\sigma_3$, whereas a conjugate pair of shear fractures occurs in the plane $\sigma_1 - \sigma_3$ forming angles of $\pm 45°$ with respect the $\sigma_1$ direction.

Once a fracture criteria and a crustal rheology is defined, we can use models to assess the likelihood of a collapse formation depending on load conditions, magma chamber geometry, and crustal properties (homogeneous, horizontal layering, etc.). Thus, in contrast to magma chamber models, host rock models are based on stress-field computations to analyse distinct collapse scenarios defined by different load conditions such as magma chamber overpressure (e.g. Komuro et al., 1984; Chery et al., 1991; Gudmundsson et al., 1997; Gudmundsson, 1998; Burov and Guillou-Frottier, 1999; Guillou-Frottier et al., 2000; Gray and Monaghan, 2004; Gudmundsson, 2008), underpressure (e.g. Druitt and Sparks, 1984; Folch and Martí, 2004; Gudmundsson 2008), or the existence of regional tectonic stress such as horizontal tension or regional doming (e.g. Gudmundsson, 1998; Gudmundsson et al., 1997; Gudmundsson, 2008). Figure 8 shows the general sketch of the scenario contemplated by this group of models. The main findings of models can be summarised as follows:

(1) Formation of ring faults considering underpressure load conditions.

   All results from models employing purely elastic and homogeneous rheology agree that spherical magma chambers are unlikely to generate ring faults because the maximum tensile stress at the ground surface is much lower than the chamber's underpressure, and the maximum shear stress occurs at the centre of the chamber rather than at its margins. However, for a fixed underpressure, increasing the chamber's eccentricity entails an increase of tensional stresses at surface and a progressive shift of the maximum shear stress towards the chamber margins. This suggests that sill-like chambers having a certain eccentricity and subjected to sufficient underpressure can induce dyke injection (Gudmundsson, 2008), ring-fault formation (Gudmundsson, 1998; Folch and Martí, 2004), or a combination of both. Thus, Folch and Martí (2004) propose that the formation of calderas by underpressure may be governed by two different mechanisms strongly controlled by the chamber geometry (Figure 9). For very eccentric geometries, ring faults would form as a consequence of the flexural bending of the chamber roof. This would be the mechanism related to the formation of
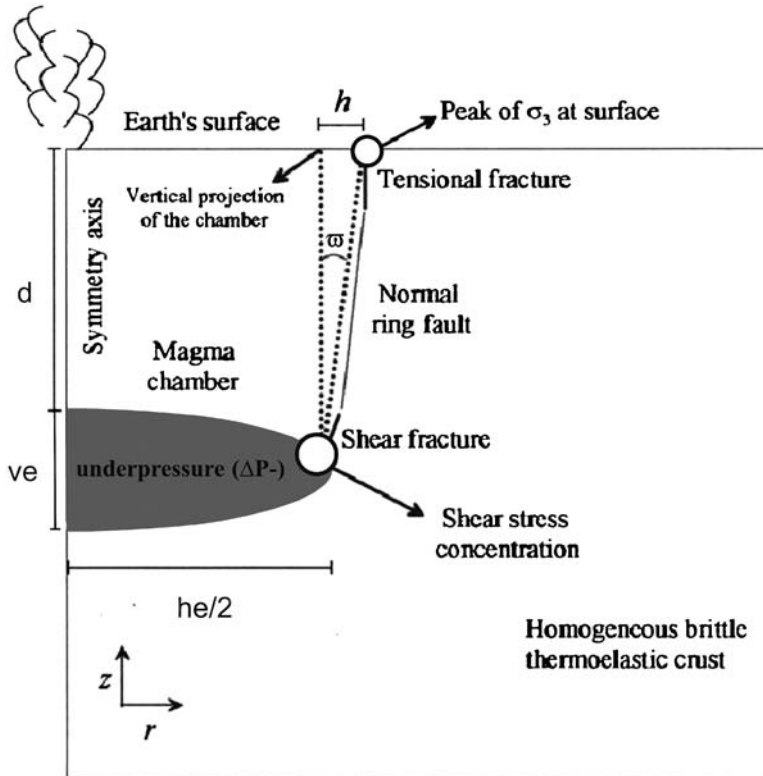
**Figure 8** Example of the model geometry applied by Folch and Martí (2004). *d*, magma chamber depth; he, magma chamber horizontal extent; ve, magma chamber vertical extent; α, fault dip angle; ΔP, pressure difference (modified after Folch and Martí, 2004).

large plate-subsidence calderas, without the necessity for previous inflation–deflation cycles. Here, low chamber underpressures would trigger collapse, yet only a relatively small fraction of the magma chamber volume would be extruded before the onset of collapse. In contrast, the formation of ring faults for less eccentric geometries would be more complex, similar to that found in analogue models, and probably dependent on the previous history of deformation. This scenario would be associated with small to moderately sized collapse calderas, commonly associated with the growth and destruction of large stratovolcanoes and multiple episodes of chamber inflation and deflation. In this scenario, a higher chamber decompression is necessary to induce the collapse, implying the extrusion of a considerable fraction of the chamber volume before the onset of collapse.

(2) Formation of ring faults considering overpressure load conditions.

Overpressure, combined with extensional load conditions, has been investigated by several models assuming either elastic or non-elastic crustal rheology (Table 1 and Figure 10). The advantage of time-dependent non-elastic
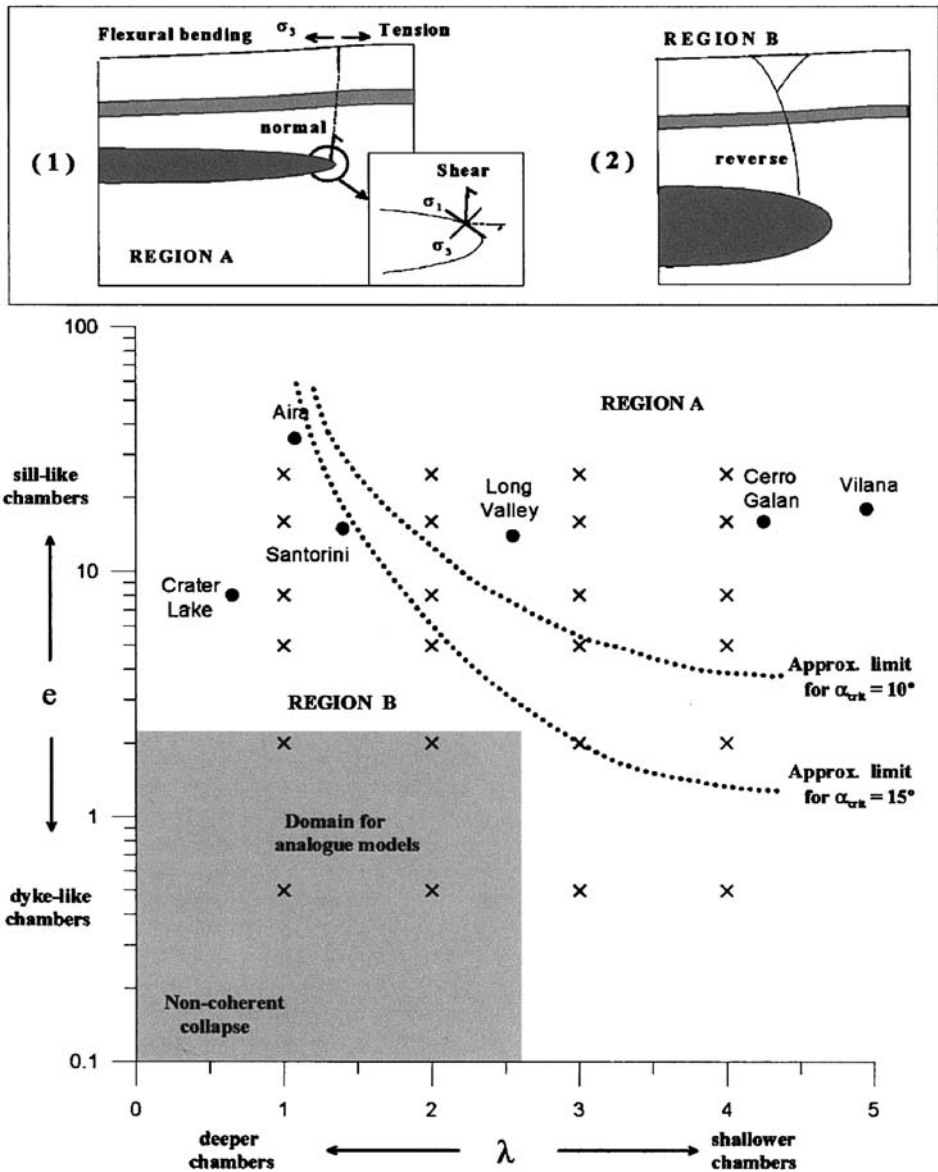
**Figure 9** Summary of simulation performed by Folch and Martí (2004). Chamber configurations are plotted using a small cross in terms of the dimensionless parameters $\lambda$ (he/2d) and e (he/ve) (the latter in logarithmic scale). Cases that verify the conditions for ring-fault formation lay in the region A, whereas the rest lay in the region B. The approximate critical limit that separates these two regions is marked using a dotted line for two different values of fault dip angle $\alpha_{CRIT}$. The domain for which results of analogue models exist is indicated in grey. The position in the diagram of some documented collapse calderas is also shown using black dots. Top inset: schematic representation, not at scale, of the ring-fault structure suggested by: (1) numerical experiments for region A and (2) experimental models for region B (modified after Folch and Martí, 2004).
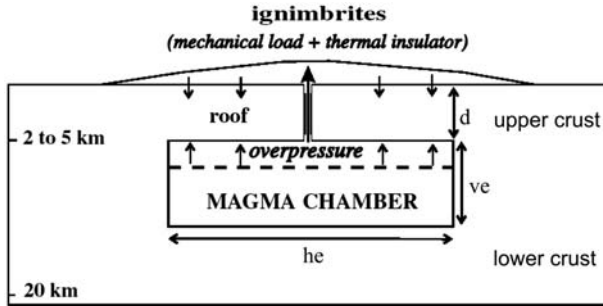
**Figure 10**   Sketch of the thermo-mechanical model showing initial and boundary conditions (modified after Guillou-Frottier et al., 2000).

models (e.g. Gray and Monaghan, 2004) is that one can track the nucleation and growth of fractures. Alternatively, the influence of thermal effects on the stress field can be explored (Burov and Guillou-Frottier, 1999; Guillou-Frottier et al., 2000), since these effects can alter crustal rheology and hence influence the formation and subsequent development of fractures. In general, non-elastic models dealing with overpressure load condition divide the collapse process into two different stages. First, the chamber's overpressure triggers ground uplift, roof bending, fracturing, and magma extrusion, and second, erupted materials accumulate. When the sum of chamber excess pressure and roof strength can no longer balance the load of the erupted products, the chamber roof starts to flex down and subsides. Some models cover both stages of the collapse (e.g. Burov and Guillou-Frottier, 1999) while others simply focus on the development of fractures during the second phase (e.g. Gray and Monaghan, 2004). The calculations provide stress and thermal regimes versus time around the magma chamber and predict fault location. For example, Burov and Guillou-Frottier (1999) find that during uplift, overpressure results in flexural uplift of the roof causing bending and eventually failure at the borders and initiation of normal inclined border faults. The area affected by posterior subsidence of the roof is thus limited to the inward-dipping cover. A later snapping of the roof triggers a piston-like subsidence. Consequently, this model predicts two groups of faults: inclined primary (initiated during the bending stage) and subvertical secondary (initiated during overloading and subsidence). Inclined normal faults may be initialised either at the surface during the subsidence phase or at depth during the possible uplift phase (in this case, they first appear as inverse faults) and propagate upward to the surface. Again, magma chamber geometry is a key parameter because the number and location of faults depend on the chamber aspect ratio. For large aspect ratio chambers ($>3$), the flexural stress concentrates at the upper corners of the magma chamber resulting in the formation of inverse inclined border faults with an inclination controlled by the friction angle. More eccentric geometries can, in addition, create internal embedded faults.
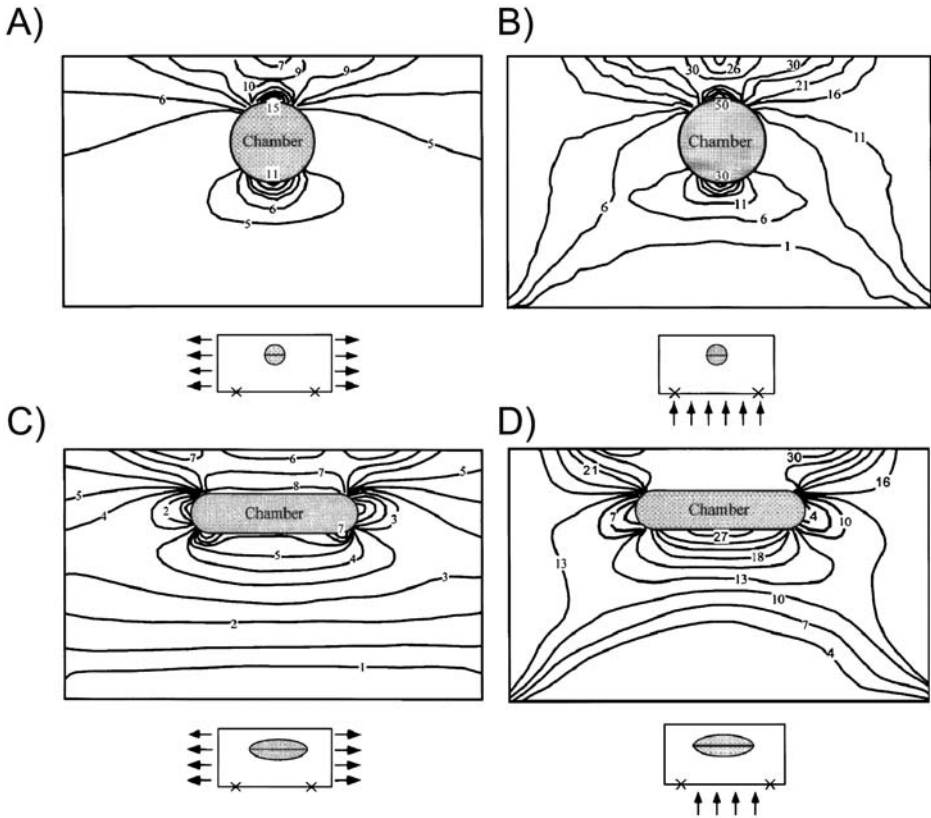
**Figure 11**   Boundary-element results showing the contours of the maximum principal tensile stress in megapascals. Models simulate a magma chamber subject to remote horizontal tensile stress of 5 MPa. Two chamber reservoir shapes have been considered: (A) spherical shape and (C) sill-like. The other two sketches show the results of models emulating a magma chamber under the effects of a magmatic overpressure (10 MPa) in a reservoir located at the base (underplating) of the volcanic field containing the magma chamber. Two different chamber reservoir shapes have been considered: (B) spherical shape and (D) sill-like (modified after Gudmundsson, 1998).

(3) Formation of ring faults considering regional extension or doming.

Elastic models indicate that sill-like chamber geometries subjected to regional doming or extension may generate a stress field adequate for ring-fault formation (Figure 11) even if the chamber overpressure is low (Gudmundsson, 1998; Gudmundsson et al., 1997) or inexistent (Gudmundsson, 2008). In the case of doming, the area of the volcanic field subject to doming must, however, be much larger than the cross-sectional area of the chamber, otherwise the surface stresses peak above the centre of the chamber and do not favour the initiation of a ring fault. Other geometries such as spherical magma chambers are not suitable for ring-fault formation. Regional extension has also been investigated by some time-dependent non-elastic models (e.g. Burov and

Guillou-Frottier, 1999). Their conclusion is that the presence of far-field stresses can significantly modify the distribution and geometry of faulting. Regional extensional stresses shift the locations of the zones of minimal and maximal bending stresses, leading to both the formation of multiple faults and favouring the occurrence of deep faulting centred over the magma chamber roof. As long as the extension continues, fractures develop at a more vertical angle and propagate from the centre to the borders to create a wider dispersed fault zone.

In conclusion, results from the available models agree that magma chamber geometry and load conditions are the two main controlling factors for ring-fault formation and, hence, the generation of collapse calderas. With few exceptions, models concur in predicting that sill-like chamber geometries are a necessary requirement. In addition, only the satisfaction of specific conditions seems to generate a favourable stress field for collapse: tension, regional doming, chamber overpressure combined with load increase by erupted products, and chamber underpressure.

## 3.3. Restrictions and limitations of theoretical models

Theoretical models contribute important semi-quantitative information complementing experimental models and field studies. However, as with all models, they also have restrictions and limitations that we discuss in this section.

Similar to the analogue models, numerical models assume, with few exceptions, a homogenous crust. It is certainly a gross approximation to nature because country rocks are normally heterogeneous in composition and properties. Lithological heterogeneities can influence the stress field and the rock strength profile and, consequently, the development and propagation of fractures (e.g. Gudmundsson and Brenner, 2005).

One of the main problems of existing models on caldera-collapse-formation processes is that fluid dynamics and rock mechanics are, in all cases, uncoupled. As mentioned above, in an ideal case, all physical processes should be simulated simultaneously, as processes occurring inside the chamber may affect those taking place in the country rock and vice versa.

None of the discussed models succeeds in simulating dyke injection neither during collapse nor during tumescence. However, as mentioned before, the possibility of dyke injection is important during pre-caldera episodes as it can regulate (dis)equilibrium conditions inside the magma chamber. The impossibility of simulating dyke injection has further consequences: (i) dyke intrusions may significantly modify the physical properties of country rock, for example, its tensile or shear strengths, evidently affecting fault nucleation and propagation; and (ii) some interpretation of results obtained may be misinterpreted. Whereas some authors claim that ring fault or other collapse-controlling structures develop from the top of the magma chamber to the surface (e.g. Gray and Monaghan, 2004), others state that ring-fault nucleation at depth is not possible as any magma chamber rupture would lead to a dyke intrusion (e.g. Gudmundsson, 1998). Of course, these

controversies will last until the application of a model, which also considers dyke injection, will be available (see also Walter, 2008).

The stress field around a magma chamber is the most important controlling factor of caldera-collapse-formation processes. In natural systems, this stress field has contributions from three main sources: the stress perturbation associated with the magma chamber itself (over- or underpressure), the regional or far-field stress, and finally the topography loading stresses. In fact, at some volcanic complexes, the topographic load may constitute the principal upper-crustal stress field and is able to modify the regional fault patterns, increase the fault throw, and induce extension (Lavallée et al., 2004, and references therein). Despite this fact, most numerical models use a flat horizontal topography, although calderas usually form in volcanic fields with significant topographic relief. There are only a few studies on the effect of a volcanic edifice on magma chamber emplacement and dyke propagation (e.g. Pinel and Jaupart, 2000, 2003, 2004).

Another important restriction of existing models is that they are unable to introduce regional faults or previously formed structures. Thus numerical models are unable to simulate multi-cycling processes of inflation and deflation, although in some of them (e.g. Burov and Guillou-Frottier, 1999) it is possible to observe the reactivation of structures formed during the uplift stages. Clearly, the existence of regional faults or previously formed structures strongly affects the morphology and, in some cases, the mechanism of caldera collapse (Acocella et al., 2001) as well as the post-collapse behaviour (Folch and Gottsmann, 2006; Gottsmann and Battaglia, 2008).

Finally, it is important to remark that there is still no consensus on the most adequate rheology for the magmas and host rock, and models dealing with different rheologies may give rise to markedly different results.

## 4. Geophysical Imaging and Its Value for Caldera Studies

As we have seen in the previous sections, mathematical and analogue models of processes leading to caldera formation and post-collapse evolution provide generalised insights into the evolution of volcanoes. These studies certainly have implications in their own right as described earlier, but in order to validate their applicability modelling results need to be critically assessed against the results obtained from other studies such as field observations. The investigation of deeply eroded caldera complexes can reveal information on the shape, depth, and dynamics of regional magma reservoirs (preserved as plutons or batholiths) as well as on the geometry of bounding faults (Lipman, 2000). The analysis of ancient successions thus provides a critical validation of such models.

Obtaining information on the subsurface structure at modern active calderas is less straightforward, as direct large-scale probing of the subsurface is impossible. Petrological investigations of erupted materials as well as the chemical analysis of volcanic gases help constraining an image of the caldera subsurface (Todesco, 2008).

Such information can play important roles in the assessment of the physico-chemical state of a magmatic system. However these tools are inappropriate in constructing a 3-D image of the subsurface.

Geophysical investigations can currently be regarded as the unique tool for constructing a regional image of the subsurface at an active caldera. Geophysical images beneath volcanoes are generally constructed from data obtained by seismic, gravimetric, magnetic, or electrical investigations. Instrumentation is usually deployed on the ground surface as well as in boreholes, although both air- and space-borne potential measurements may become important for the analysis of volcanic systems in the future (CHAMP and GRACE missions, Thompson et al., 2004; Wahr et al., 2004). Geophysical imaging is the result of collection of geophysical data and their evaluation in order to obtain a spatial image of the substructure. These measurements are performed in static mode and, hence, aim to resolve the substructure in the space domain. In contrast, dynamic geophysical investigations aim at identifying changes in the subsurface over time, and information on the substructure are hence obtained in the time domain. Recent investigation have also successfully explored a 4-D approach to geophysical imaging (Foulger et al., 2003).

In addition to their undisputable value for economic exploration in volcanic environments, results from (static) geophysical imaging serve three important scientific aspects in analysing dynamic processes at active caldera volcanoes: (i) subsurface images help validate results from analogue and mathematical modelling of processes accompanying caldera reactivation; (ii) subsurface images play a major role in the interpretation of results from dynamic geophysical investigations; and (iii) subsurface images are hence critical for the assessment of hazards associated with caldera unrest and for the mitigation of risks.

Information from geophysical imaging of depth and shape of magmatic reservoirs, for example, are crucial for the validation of mathematical or analogue models aiming at investigating the dynamics of post-collapse processes such as resurgence or active faulting (Acocella et al., 2000; Walter and Troll, 2001; Roche et al., 2000; Folch and Martí, 2004). The identification of magmatic bodies at depth is also of great importance for the validation of causative bodies inferred from geodetic and gravimetric dynamic investigations (Battaglia et al., 2003; Beauducel et al., 2004; Gottsmann et al., 2006b; Gottsmann and Battaglia, 2008). Due to the non-unique nature of results from inversion of time-series data obtained during caldera unrest, geophysical images provide critical constraints on the plausibility of inversion results. In assessing subsurface dynamics at active calderas, geophysical imaging not only facilitates the interpretation of results from other investigations but also provides information against which other results can be critically assessed. As a direct consequence, hazard assessment during periods of unrest at active calderas is improved via a combination of space- and time-domain investigations (Gottsmann and Battaglia, 2008).

The aim of this section is not to provide a comprehensive review on individual imaging techniques and their application. Detailed information can be found in general geophysical literature: seismic imaging (e.g. Scales, 1994; Sheriff and Geldart, 1982a, 1982b), gravimetric and magnetic imaging (Blakely, 1996; Wahr,

1996), and electric and electromagnetic imaging (Wait, 1982; Parasnis, 1996). Here, we aim at reviewing existing work from geophysical imaging and to assess the value of geophysical information to provide insights into the evolution of collapse calderas including key issues such as magma generation, storage, and the distribution of subsurface discontinuities. We restrict this evaluation to relatively well-studied calderas that either showed historic eruptions or are currently undergoing unrest.

We particularly assess published work to analyse its potential for providing answers to the two most controversially discussed issues at active calderas. First, the question of shape, size, and depth of underlying magmatic bodies (see previous sections), and second, the question of faults and their role in the evolution of calderas (Acocella, 2008; Gudmundsson, 2008; and previous sections). The first question has two important implications for the dynamics at active calderas:

(i)  A widely accepted hypothesis to explain that the generation of a collapse caldera is a considerable emptying of a horizontally elongated (sill-shaped) magma body, which results in the formation of a surface depression with a diameter approximately equal to the diameter of the reservoir. The identification of magmatic systems at depth using geophysical imaging provides essential constraints on their geometry and thermodynamic state. This information is critical for the assessment of potential caldera collapse when such volcanoes eventually undergo magmatic reactivation.

(ii) Magma reservoirs identified by geophysical imaging can be assessed if they qualify as candidates of causative bodies (magmatic or hydrothermal) responsible for periods of unrest inferred from dynamic investigations as explained above.

The second question relates directly to the issue of bounding fault geometry (inclination, length, strike). The vertical collapse of crustal roof rocks along bounding faults into an emptying magma reservoir is widely regarded as the prime mechanism for the generation of a volcanic caldera as outline in the previous sections. Faults determine the style of collapse as well as the structure of the resulting depression (Acocella, 2008; Gudmundsson, 2008; and previous sections). Post–caldera eruptions and resurgence are also attributed to activity along bounding faults (Saunders, 2001, 2004). Other studies emphasise the influence of bounding faults on ground deformation during caldera unrest (De Natale et al., 1997; Folch and Gottsmann, 2006). Geophysical information on fault geometries at calderas not only provide insights into the stress regime leading to collapse but also provide important constraints for the evaluation of signals during caldera unrest.

We review the work published on the calderas of Rabaul (Papua New Guinea), Campi Flegrei (Italy), Taupo (New Zealand), Toba (Indonesia), Las Cañadas de Tenerife (Spain), Valles (USA), and Long Valley (USA). We have selected these calderas predominantly because of the availability of a relative wealth of geophysical data from multi-parametric imaging and their spread of geotectonic settings. Table 2 provides an overview of geophysical techniques applied at the selected calderas as well as key results on their subsurface structure. Note that we focus on information that provides insights into subsurface reservoirs and faults.

**Table 2** Compilation of results from geophysical investigations at selected calderas.

| Location | Geophysical investigation | Main results | Source |
|---|---|---|---|
| Taupo caldera, New Zealand | Gravity | Negative Bouguer anomaly in northern part of Lake Taupo | Davy (1993), Davy and Caldwell (1998), Ingham (2005), Bibby et al. (1995), Soengkono (1995) |
| | Seismic | Positive magnetic anomaly at western edge of collapse structure | |
| | Electric | ca. 3 km thick volcaniclastic caldera fill (ca. 420 km$^3$) | |
| | Magnetic | Steep inward-inclined faults coincide with southern and northern boundaries of caldera | |
| Campi Flegrei, Italy | Seismic | Negative Bouguer anomaly centred within the caldera depression near Pozzuoli | Vanorio et al. (2005), Aster and Meyer (1988), Bruno (2004), Orsi et al. (1999), de Lorenzo et al. (2001a, 2001b); Guidarelli et al. (2002) |
| | Gravity | Flat and low Vp/Vs anomaly up to 4 km depth | |
| | Magnetic | Under the city of Pozzuoli may represent overpressured gas-bearing formation | |
| | | $V_p \star V_s$ horseshoe-shaped anomaly located at 2 km depth, consistent with gravity data and well data, might represent on-land remainder of caldera rim | |
| | | Top of magma reservoir between 4–5 km depth | |
| Toba, Indonesia | Seismic | Two separate horizontally adjacent reservoirs | Masturyono et al. (2001), Nishimura et al. (1984) |
| | Gravity | One low-velocity zone coincides with gravity low and can be traced into the uppermost mantle | |
| Valles caldera, USA | Seismic | Multiple, low-velocity zones extending into the upper mantle | Bruce and Keller (1993), Lutter et al. (1995), Steck et al. (1998), Wannamaker (1997), Aprea et al. (2002), Heiken et al. (1990) |
| | Gravity | Multiple fracture and fault zones | |
| | Magnetotelluric | Central gravity low: | |
| | Borehole data | Upper 200 m of relatively low resistivity corresponding to unconsolidated land-slide and debris flows | |
| | | Beneath Bandelier Tuff higher but variable resistivities because of alteration controlled by local faulting | |
| | | Substantial change in structural relief | |

| | | | |
|---|---|---|---|
| Long Valley caldera, USA | Seismic<br>Gravity<br>Magnetotelluric<br>Borehole data | Major normal fault to the southeast is located under Freelove canyon<br>Rejuvenated magma chamber and basaltic underplating at the crust/mantle interface at ca. 37 km<br>Low-velocity zone beginning at ca 6 km depth with 13 km diameter may indicate magma body<br>Low $v_p/v_s$ anomaly extending from near the surface to ca. 1 km bmsl. beneath Mammoth Mountain may represent a $CO_2$ reservoir<br>Significant temporal changes in both $v_p$ and $v_s$ indicate migration of $CO_2$<br>Heavily dissected and faulted sub-surface<br>2 km thick post-caldera fill at moat<br>Easterly deepening of the base of the seismogenic layer beneath the resurgent dome from 5 to 8 km<br>Gravity data indicates thickening of caldera-fill towards east<br>Low $v_p/v_s$ anomaly adjacent to the Casa Diablo hot springs geothermal area from near the surface to 2 km bmsl<br>No indication of recent magma intrusion to within 2 km depth<br>High electrical conductivity within western half of caldera<br>Resistive and gravitational feature of a basement structural 'high' may be related to the structural evolution of the resurgent dome<br>Two gravity highs at south moat may indicate magmatic intrusions near base of caldera fill Caldera<br>15–30% low-velocity zone at ca 11.5 km depth<br>15% LVZ at ca 24 km | Foulger et al. (2003); Ponko and Sanders (1994), Sanders (1993), Steck and Prothero (1994), Hermance et al. (1988), Rundle and Hill (1988), Prejean et al. (2002), Weiland et al. (1995), Carle (1988) |

**Table 2** (*Continued*)

| Location | Geophysical investigation | Main results | Source |
|---|---|---|---|
| Las Canadas caldera, Spain | Gravity Magnetic Borehole data | Positive gravity anomaly at southern edge of caldera (Boca Tauce structure)<br>>500 m post-caldera fill<br>Conductive layer at around 700 m depth may indicate water-saturated caldera fill<br>Highest electric conductivity along caldera wall, due to hydrothermal alteration and extension of aquifers<br>NE and N of Pico–Teide large and deep conductive layer<br>Some gravity and magnetic lows consistent with caldera fill<br>Low-density areas at Teide-Pico Viejo complex connected with recent volcanism; hydrothermal alteration is assumed to be the cause of a short-wavelength magnetic low over Teide volcano<br>Highly magnetic sources may represent gabbro–ultramafic cumulates<br>Possible magma chamber represented by magnetic horizon at 6 km depth | Ablay and Kearey (2000), Araña et al. (2000), Ortiz et al. (1986), Pous et al. (2002), Camacho et al. (1991) |
| Rabaul, PNG | Seismic | Depth-dependent outward and inward dipping caldera ring faults<br>Ellipsoidal geometry of hypocentres delineating active zones<br>A 30–35 km³ low-velocity region (?magma reservoir) at 3–6 km depth<br>Heterogeneity in P-wave velocity both laterally and vertically within the Rabaul caldera, significant complexity within quite a small area<br>High-velocity rock units around the caldera rims may indicate large volumes of mafic intrusive rock at shallow (4 km) depths | Mori and McKee (1987), Saunders (2001), Jones and Stewart (1997), Finlayson et al. (2003), Bai and Greenhalgh (2005) |

## 4.1. Results from geophysical imaging of caldera structures

Despite the significant differences in imaging techniques, measurement protocols, and resulting image resolution, in addition to different tectonic settings, ages, and evolution of calderas, a number of striking similarities in their subsurface structural arrangement are evident:

(i)   A central negative gravity anomaly inside the collapse structure indicating the presence of less dense material compared to its surroundings.
(ii)  Isolated gravity highs as well as positive magnetic anomalies within the periphery of the collapse structure, suggesting shallow high-density crystalline bodies.
(iii) A complex arrangement of subsurface structures including:
    – Substantial changes in the subsurface relief.
    – Vertical and horizontal asymmetries, including structural discontinuities.
    – Large- and small-scale anomalous bodies.
    – Seismic anomalies occurring at different lithospheric levels (there is usually a central anomalous body within 4–10 km below ground surface).
    – Some degree of magmatic underplating at the interface of the subcalderan lithosphere and asthenosphere, as well as indications of deep (mantle-based) roots of central plumbing systems.
(iv)  Structural complexities induced by caldera resurgence.

### 4.1.1. The size, shape, and depth of magma reservoirs
In recent years, seismic imaging in particular has provided a number of clues on the shape and geometries of magmatic reservoirs beneath active calderas. Seismic waves are reflected, refracted, or diffracted by subsurface heterogeneities enabling the mapping of such bodies. P-wave velocity contrasts can also be evaluated as a mean to assess the liquid fraction in a subsurface reservoir. The resolvable wavelength of an anomaly is directly proportional to the spacing of seismometers operational during the survey (Finlayson et al., 2003).

*Shallow-seated reservoirs.*    Shallow (ground surface to a depth of few kilometers) low-velocity zones were imaged, for example, beneath Campi Flegrei, Rabaul, Valles, and Long Valley. Their low $v_p/v_s$ ratios are generally interpreted to result from a high proportion of pressurised fluid-bearing rock formations. At Campi Flegrei, the combination of seismic attenuation tomography and borehole data enabled the discrimination of the reduction in P-wave velocities by hydrothermal activity from that of conductive cooling of a deeper magma reservoir (de Lorenzo et al., 2001a, 2001b). Marked changes in $v_p/v_s$ velocity ratios (with values up to 2.5 km/s in the first 2–3 km, and lower values (1.6–1.7 km/s) at larger depth were interpreted as highly fractured layers saturated with water (high $v_p/v_s$) at shallow depth, and with gas (low $v_p/v_s$) at larger depth (Vanorio et al., 2005). At Long Valley, a low $v_p/v_s$ area extending from the surface to ca. 3 km depth is interpreted as a $CO_2$ reservoir that is supplying $CO_2$-rich springs, venting at the surface, and killing trees (Foulger et al., 2003). Shallow hydrothermal reservoirs were detected by magnetotelluric studies at the Las Cañadas caldera which also coincide with
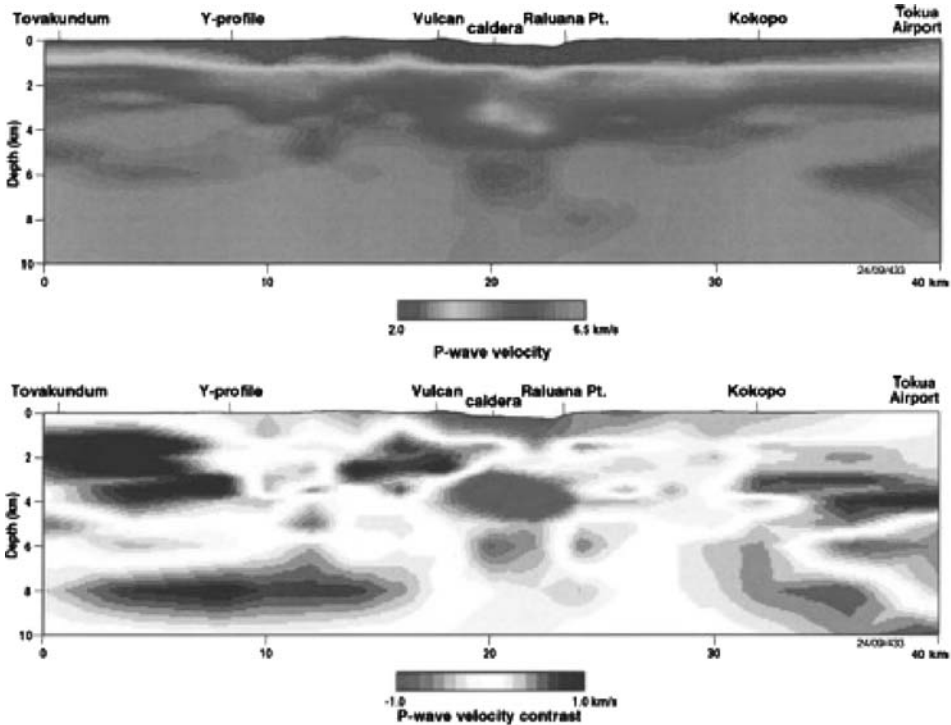
**Figure 12** Tomographic images of P-wave velocity beneath the Rabaul caldera. (a) P-wave velocity and (b) residual velocity difference after subtracting the regional 1-D velocity from data shown in (a). The significant low-velocity region under the centre of the caldera is inter-preted to be a region of high-temperature magma accumulation (reproduced with permission from Finlayson et al., 2003).

short-wavelength magnetic anomalies within the central part of the caldera as well as along the caldera periphery (Araña et al., 2000).

*Mid-crustal reservoirs.*    Seismic studies at the calderas of Rabaul and Long Valley have revealed the presence of central magma reservoirs (Finlayson et al., 2003; Steck and Prothero, 1994). These central reservoirs appear to be located at mid-crustal levels and exhibit a horizontally elongated shape. Their geometry can be best approximated by a sill-like body or an oblate spheroid. At Rabaul, the diameter of an oblate body approximates the diameter of the collapse structure measured at the ground surface (Figure 12). For the Valles caldera, the combination of teleseismic tomography (Steck et al., 1998) and Kirchhoff wavefield migration (Aprea et al., 2002) has succeeded in identifying a rather complex arrangement of sills at different lithospheric levels, as well as a large prolate ellipsoid body around 12 km beneath the northwest quadrant of the caldera (Figure 13).

P-wave velocity in each of the three calderas varies significantly both vertically and horizontally attesting to the complexities of the subsurface. The Rabaul anomaly exhibits an up to 10% decrease in P-wave velocities for a anomalous
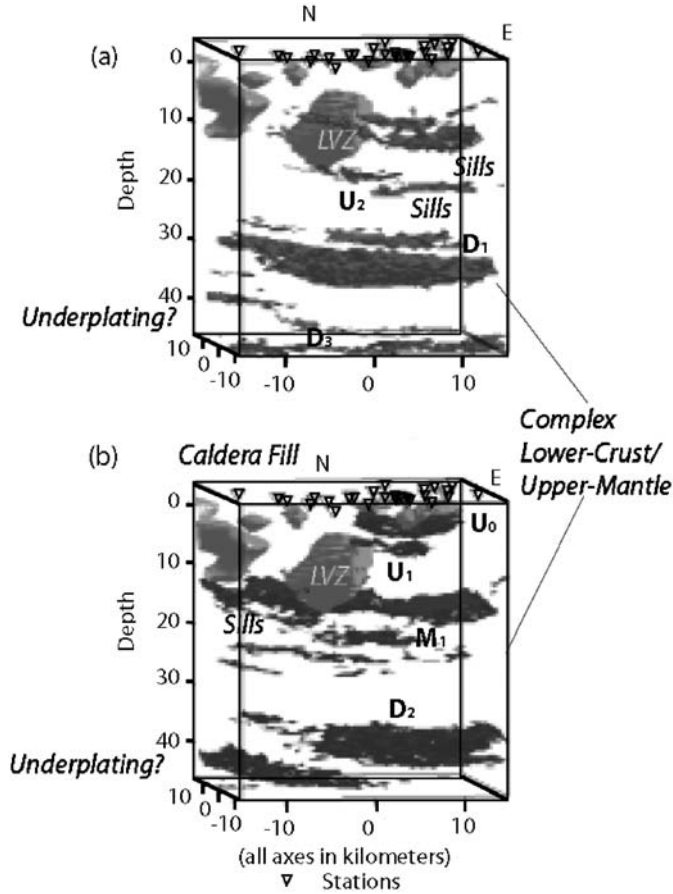
**Figure 13**   The superposition of the 3-D views of different polarity reflectors of the Kirchoff migrated image, where all absolute values of the reflectivity function $I < 0.35$ are made transparent, over the low-velocity anomaly (LVZ) associated with the magma chamber (absolute anomaly larger than 12%) reported in Steck et al. (1998) (a) Reflectors U0, U1, and D2 are labelled. (b) Reflectors U2, D1, and D3 are labelled. The interpretation of the reflectors is depicted with bold labels (modified after Aprea et al., 2002).

volume of between 30 and $35\,km^3$ (Finlayson et al., 2003) and approximately $100\,km^3$ (Bai and Greenhalgh, 2005) at a depth of about 4 km. At Long Valley, the sill-like anomaly exhibits up to 30% reduction in P-wave velocity about 8–12 km beneath Mammoth Mountain (Steck and Prothero, 1994). This body forms the upper part of an asymmetric diapir-like low-velocity zone. Likewise, the ellipsoidal body beneath Valles caldera shows a reduction in P-wave velocities of about 23% (Steck et al., 1998). A magnetic anomaly located at 6 km bsl beneath the centre of the Las Cañadas caldera is interpreted as representing the top of a magma reservoir, which also coincides with a marked density low (Araña et al., 2000).

At Toba, seismic tomography revealed two adjacent oblate magmatic bodies extending from the ground surface to ca. 10 km depth (Masturyono et al., 2001).

Their combined horizontal extent matches the long axis of the $30 \times 100\,km$ wide caldera. The location of a pronounced gravity low within the collapse structure coincides with one of these reservoirs. The combined results suggest the presence of, as yet, the world's largest magmatic reservoir at mid-crustal levels beneath Toba (Masturyono et al., 2001).

*Deep-seated reservoirs (or deep extension of magmatic bodies).*   In addition to the two large mid-crustal reservoirs, the seismic image at Toba also reveals a low-velocity column with a reduction in P-wave velocities similar to those of the mid-crustal reservoirs which can be traced from one of the reservoirs into the uppermost mantle (Masturyono et al., 2001). The extent of this low-velocity zone is matched by the planar distribution of low-frequency earthquakes in the range of $20–40\,km$ depth. A picture of a deep root of magma replenishment also emerges from Valles, where a large planar zone of reduced P-wave velocities ($-15\%$) can be mapped out in the lower crust or upper mantle (Aprea et al., 2002). This zone is interpreted to represent melt formation in the upper mantle and subsequent basaltic underplating. At Long Valley, the tabular mid-crustal reservoir may represent the top of a diapir-like ridge rising up from the migmatized lower crust of the Basin and Range province (Steck and Prothero, 1994). At Las Cañadas, the magnetic anomaly appears to be rooted in a dyke complex down to ca. $16\,km$ bsl (Araña et al., 2000).

*The nature of reservoirs.*   While shallow-level low-velocity zones are generally regarded to represent hydrothermal reservoirs, deeper-seated anomalies are usually associated with the presence of a melt phase. However, the upper crust around a volcano is composed of rocks, which are expected to show large variations of seismic wave velocity due to significant variations of composition, fluid content, porosity, and temperature. As a consequence, ray paths are undoubtedly 3-D, adding a high degree of non-linearity to the relationship of ray path and velocity. Thus, assessing the melt fraction within a low-velocity zone is challenging and potentially associated with large errors. Weiland et al. (1995) give a short discussion on the ambiguities involved in estimating melt percentage in low-velocity zones and compare results obtained from different models. For example, the tabular $-30\%$ low-velocity zone at Long Valley is regarded as containing a melt fraction anywhere between 7 and 100%. At Valles, 100% melt is attributed to the central ellipsoidal $-30\%$ velocity (Figure 13). Masturyono et al. (2001) infer melt-dominated reservoirs with $<10\,km$ thickness in the mid-crust and a 0.1 melt fraction in the deep root of the plumbing system.

## 4.1.2. Caldera bounding faults

Geophysical information on the geometry of bounding faults is scarce and stems predominantly from seismic investigations. One of the key questions regarding bounding faults and their role in caldera evolution concerns their dip angle as well as their dip direction: vertical, inward, or outward dipping with respect to the centre of the caldera.

Based on experimental results, the activity of both reverse and normal faults constitutes a possible solution to the so-called space problem (see previous sections) during major collapses or resurgences (Acocella et al., 2000). Mori and McKee (1987) in their seminal paper highlight the presence of outward-dipping (away from the depression) bounding faults at Rabaul caldera and provided a straightforward solution to the space problem during caldera collapse. Relocation of earthquake hypocenters at Rabaul (1971–1992) including seismic data employed by Mori and McKee (1987) were presented in Saunders (2001). In this paper, the subsurface distribution of hypocenters draws a complex picture of seismic zones particularly for depths shallower than 2 km (Figure 14), with a pronounced spread of seismicity at less than $\sim$1,000 m. Saunders (2001) interprets this spread of seismicity as shallow structures consisting of antithetic normal faults. At greater depth, the seismic pattern may be a approximated by two arcuate faults delineating an elliptical ring fault with a ellipticity of about two, whereas at depths less than 2 km the epicentre pattern displays a more circular appearance.

At Campi Flegrei, a circular caldera geometry was recently invoked by the joint inversion of seismic and gravity data (Capuano and Achauer, 2003), which is in very good agreement with the symmetry and extension of the area affected by ground deformation during recent unrest periods (De Natale et al., 2006; Troise et al., 2007, 2008). Furthermore, seismic activity clusters around the deeper part of the ring-fault system, with focal mechanisms in agreement with a slightly inward-dipping geometry of the system (Troise et al., 2003). Studies of local seismicity (Troise et al., 2003), volcano-tectonic trends imaged by seismic reflection data (Bruno, 2004) and magnetic data (Cassano and La Torre, 1987) highlight the influence of the regional stress regime (NE-SW trending regional faults), both on the caldera geometry as well as on post-caldera processes.

At Campi Flegrei, the geometry of the eastern caldera wall and the alignment of several monogenetic volcanoes along regional NE–SW trending regional faults imaged by seismic reflection data highlights the influence of the regional stress field, both on caldera formation as well as on post-caldera processes (Bruno, 2004). Gravity and magnetic anomalies are also aligned along the same strike direction (Cassano and La Torre, 1987).

At Taupo, seismic reflection data indicate the presence of slightly inward-dipping (towards the caldera centre) faults marking the southern and northern caldera boundary (Davy and Caldwell, 1998). These faults border the gravity low situated in the northern part of Lake Taupo.

High-resolution hypocentres for earthquakes that occurred between 1980 and 2000 in the Long Valley caldera area reveal discrete fault planes in the southern part of the caldera (Prejean et al., 2002) (Figure 15). One of these most active structures within the caldera (labelled WSMZ1 in Figure 15) is a near-vertical slightly inward-dipping fault, which may be related to the caldera ring-fracture system. Seismicity in this zone does not lie along a simple plane but rather along an up to 1 km wide fault zone. Focal mechanisms indicate that this zone is composed of a series of many small faults of varying orientations, which are active over a depth range of 3–9 km. Other fault zones subparallel to WSMZ1 along the southern resurgent dome dip towards the caldera centre at a significantly lower angle.
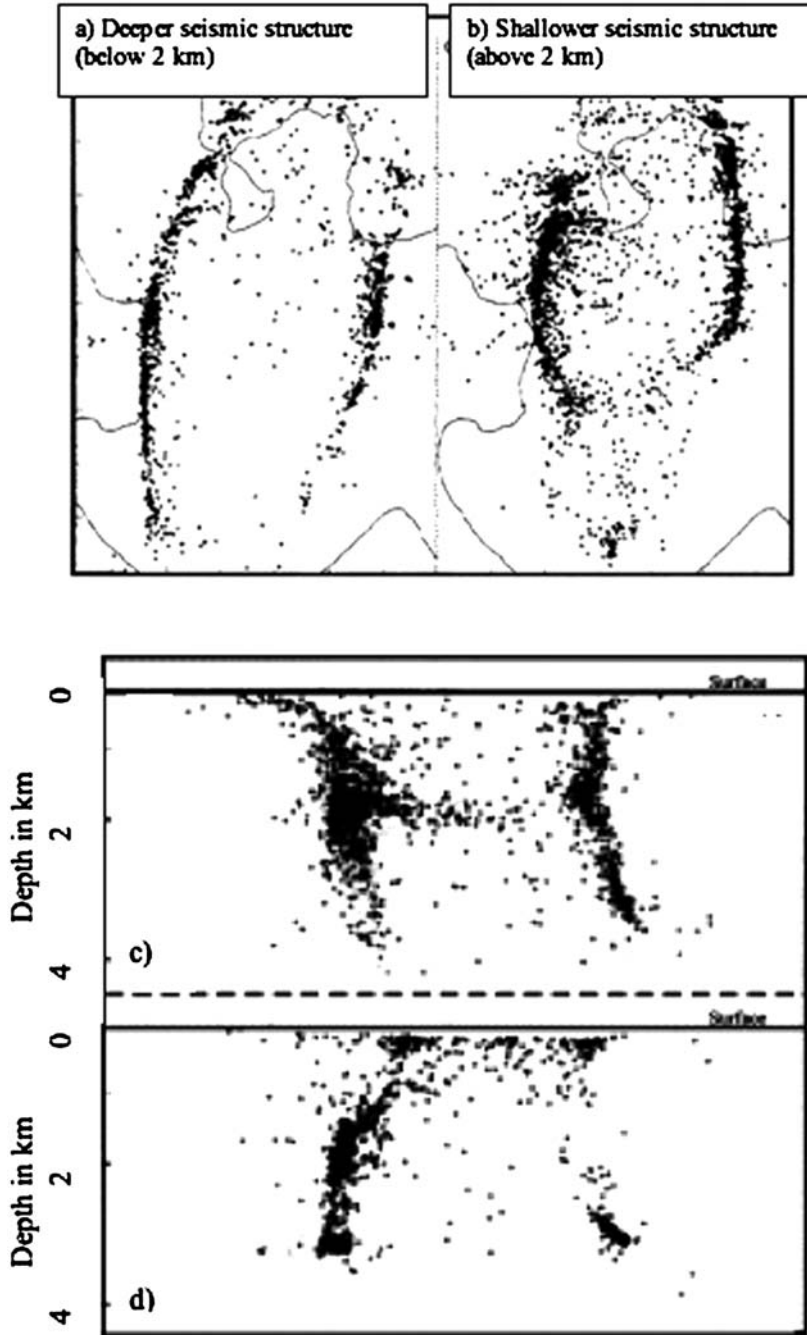
**Figure 14**  Plane view of hypocentre location of earthquakes recorded at Rabaul between 1971 and early 1992: (a) below 2 km and (b) above 2 km, (c) and (d) Two WNW–ESE sectional views $A$--$A'$ and $B$--$B'$ through the centre and a few kilometres to the south of the centre of the seismic annulus, respectively. North is up. Note in (c) a 'complexity' at $\sim 2$ km depth, coinciding with the area where the deeper structure overlaps or merges with the shallower structure (modified after Saunders, 2001).
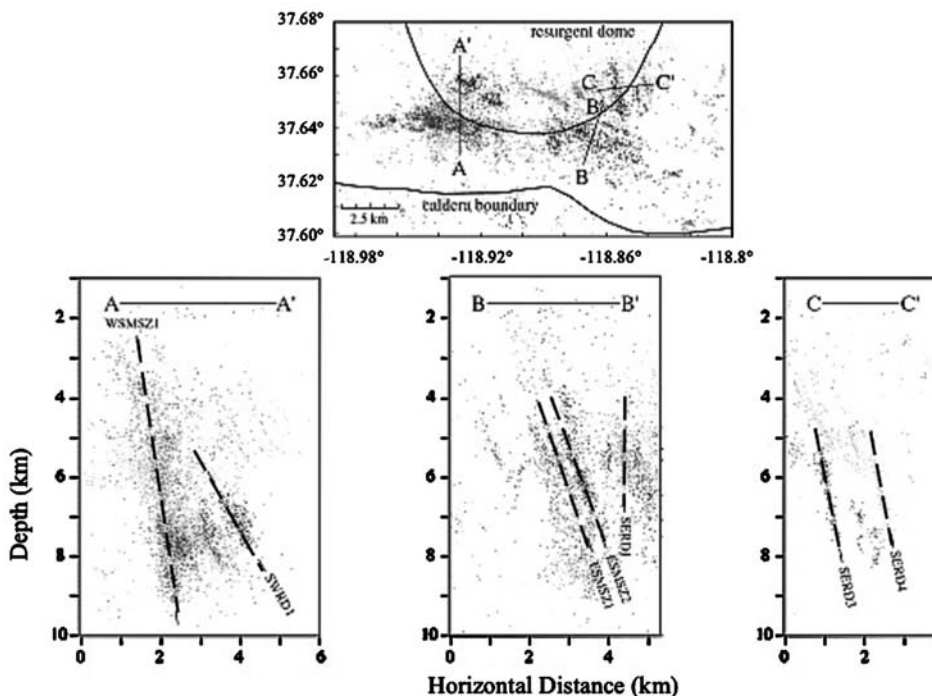
**Figure 15** Relocated hypocenters of July 1997 to January 1998 Long Valley caldera seismicity in map view (top) and three cross sections (bottom). Cross sections A—A′, B—B′, and C—C′ show hypocentres along the transect line shown in map view. Main faults are marked by straight lines (modified after Prejean et al., 2002).

## 4.2. Limitations of geophysical imaging

When evaluating information obtained from geophysical data to validate results from other studies, we must not forget to also assess the limitations associated with geophysical investigations and data processing. The first limitation is the problem of scale and concerns the limitation in spatial resolution of geophysical images, which inherently depends on the spacing between deployed instruments (array size) as well as on the distribution of nodes in inversion models. In contrast to, for example, geochemical studies which achieve to resolve minute changes in chemical parameters in minerals on the submillimetre scale, geophysical imaging beneath volcanoes generally targets large-wavelength (usually $\gg 1$ km in horizontal extent) anomalies and is hence better suited to resolve small wavenumber-sized, deep-seated structures. Depending on seismic tomography experiments, the resolution limit for anomalous bodies is generally between 1 and 3 km within the first few kilometres depth. At greater (mid- to lower crustal) depth, the resolution limit readily increases by a factor of 2–3. Gravimetric mapping, as well as magnetic and electrical imaging suffer from similar resolution limits.

Second, there are a number of inherent ambiguities in interpreting geophysical data:

(i)   Uncertainties in physicochemical properties of subsurface materials (e.g. temperature, pressure, chemical composition, porosity, permeability, elastic moduli, structural relaxation times, viscosity, density, fluid content, and composition) have a strong effect on the emerging subsurface image. For example, seismic wave speeds are strongly dependent on viscosity and temperature, whereas the identification of density anomalies is biased on the assumed density contrasts at depth. Physico–chemical property values of melts are more commonly determined (see Spera, 2000 for a recent review), and they should be incorporated in the analysis.

(ii)  Parameterisation, for example, of the regional velocity model employed during seismic investigation is crucial to the interpretation of velocity contrasts.

(iii) Computational restrictions play an important role for multi-parameter inversion when comparing modern results to those obtained decades ago as increased CPU power has enabled more elaborate modelling techniques.

(iv)  Modelling and mathematical frameworks pronouncedly bias geophysical results, for example, when comparing forward modelling results to inversion results from gravimetric or magnetic investigations. The same applies to differences in results between 1.5-D, 2-D, or 3-D modelling. When evaluating compressive wave speed decrease, the assumed shape melt is contained in strongly affects the inferred melt fraction (Weiland et al., 1995).

(v)   The non-uniqueness of results is one of the major limitations for geophysical investigations to provide realistic images of the subsurface, and this remains a major challenge. For example, results from gravimetric inversions are ambiguous due to the fact that different density distributions at depth can cause the same gravitational perturbation at the surface.

In summary, geophysical imaging reveals a complex arrangement of subsurface reservoirs beneath active calderas. At shallow level (surface to a few kilometres depth), hydrothermal reservoirs and altered rock appear to cause a reduction in wave velocities as well as negative magnetic anomalies. Caldera bounding faults also represent zones of increased hydrothermal activity and must be regarded as important pathways for fluid flow from depth (Todesco, 2008; Gottsmann and Battaglia, 2008). Magma reservoirs can undoubtedly be associated with low velocities at mid-crustal depth. However, the question still remaining concerns the melt fraction in these anomalous bodies. Current estimates from P-wave contrasts or $v_p/v_s$ ratios in these zones can be regarded merely as rough proxies and are less suitable to assess the eruptability of a large subcaldera magma reservoir. Moreover, due to the resolution limit of geophysical images, smaller-sized magma pockets are very difficult to recognise, if at all. Assuming that small (monogenetic) eruptions may be fed by the interaction of fluid-filled cracks (Takada, 1989, 1994), information from geophysical images are of only limited value for the assessment of hazards during periods of increased unrest. In assessing the melt fraction in large anomalous bodies, there is a high degree of uncertainty regarding their relative 'age'. It is obviously impossible to assess whether the melt phase is a remnant of a crystallising magma reservoir that

may have been active during previous eruptions, including the formation of the caldera itself, or whether this melt has been recently replenished from greater depth through deep-rooted plumbing systems. As a general picture, we can infer the existence of multiple reservoirs situated at different depths beneath active calderas: a deep lower crust/upper mantle magma reservoir is tapped by a plumbing system which channels melt upwards to form mid-crustal magma reservoirs. Most of these reservoirs appear to have flat sill-like tops with diameters matching the diameter of the superficial collapse structure. What is important to note is that low-velocity zones overlying these mid-crustal reservoirs indicate the coupling effects of magma reservoirs into a third level of reservoirs, shallow-seated hydrothermal systems. These coupling effects have recently been inferred as the predominant source of recent unrest at some of the investigated calderas here (Battaglia et al., 2006; Foulger et al., 2003; Gottsmann et al., 2006a, 2006b; Todesco, 2008; Gottsmann and Battaglia, 2008).

The available information on caldera bounding faults and their geometry from geophysical studies can be regarded as inconclusive at best. While fault planes of active regional faults can be imaged rather accurately, for example, at Long Valley (Prejean et al., 2002) (Figure 15), images of lateral discontinuities associated with bounding faults are blurred, particularly at shallow levels. This could be due to two factors: explosive calderas are systems with activities spanning over tens to hundreds of thousands of years. Experimental work shows that resurgence over collapse (and vice versa) is characterised by the complete reactivation, with opposite kinematics, of all the pre-existing ring faults during inversion (Acocella et al., 2000). Continual kinematic movement along bounding faults over the lifespan of an explosive caldera is likely to initiate strong weakening of the bounding rocks as well as the creation of secondary faults. Second, bounding faults are important escape routes for magmatic fluids from the reservoir to the ground surface as evidenced by intense hydrothermal activity, alteration and magnetic lows along the walls at many active calderas. Prolonged corrosion of fault walls and the presence of fluids within the fault system significantly affect the mechanical properties of the surrounding rocks as well as their coupling to seismic waves.

The available data suggest that bounding faults are, averaged over their entire imaged length, subvertical with a trend to a slight inward dip towards the caldera centre. Assuming that these faults are representative of the faults active during the collapse event, the data do not provide a solution to the space problem. However, bearing in mind the complexities at shallow depths (as imaged, for example, at Rabaul in Figure 12) and results of fault alignment in analogue models (at systems of both inward- and outward-dipping faults), the same faults may be active during the formation of a caldera as well as throughout its post-collapse evolution.

# 5. Discussion and Implications

## 5.1. On the use of experimental models

Experimental models on collapse calderas enable a qualitative study of the structural evolution of a collapse process and suggest which factors play a more relevant role.

Analogue and scale models have verified that caldera-collapse formation is influenced by multiple aspects such as regional tectonics, system geometry, magma and host rock properties, pre-existing structural discontinuities, deformation history, etc.

Differences among the existing analogue models lie on the applied experimental setup, the host rock analogue materials (dry quartz sand, flour, etc.), and the magma chamber analogue (water or air-filled balloons, silicone reservoirs, etc.). Although the results obtained are generally similar, there are some marked differences. A subsequent comparison of the experimental results with field data and theoretical models may help to infer which discrepancies stem from experimental restrictions.

Experimental models are useful to offer a 'semi-quantitative' approach to the understanding of caldera collapse. In some cases, experimental results are important to crosscheck analytical results. In other cases, experimental results lay the foundations for more elaborate future numerical analyses. Three types of semi-quantitative analyses can be performed with the results from revised experimental models: (i) the quantification of the erupted magma chamber volume fraction $f$ required to achieve each step of a collapse process (and the dependence $f(R)$); (ii) the analysis of the subsidence pattern and its spatial extent; and (iii) the study of the influence of the roof aspect ratio on the extent of the collapsed zone at both surface and depth.

In contrast to inferences from scaled models and mining subsidence, there is a significant difference between these analogues and natural calderas. Caldera processes, to some extent, are often related to overpressure in an associated magma chamber, which induces a ground deformation pattern that may later be reused during collapse. In addition, caldera collapse appears to occur despite a still significant pressurisation of the chamber, a phenomenon absent during mining subsidence where collapse occurs into an empty cavity. This apparent discrepancy raises an interesting observation as to the possibility of caldera subsidence in some cases taking place at the end of an eruption, when most magma has already been evacuated from the chamber, rather than during the eruption. In the latter case, mostly applicable to large caldera eruptions, a great proportion of the caldera products would be deposited into the depression. In the former case, caldera-forming products would not be deposited inside the ensued depression.

It is also important to mention that experimental results reveal that the apparent diversity of caldera morphologies and collapse mechanisms inferred from field studies (Lipman, 1997, 2000) may just result from the effect of different combinations of magma chamber geometries, magma chamber roof aspect ratios, and regional faults, or may simply correspond to different stages of a single collapse process. Therefore, based on the results from scaled experimental models, it may be prudent to revise the classification of collapse calderas based on their morphology or their inferred collapse mechanism. This classification may just result or correspond to an artefact due to different degrees of exposure of natural examples.

Finally, experimental models also enable the examination of the effect of regional faulting and/or tumescence (due to local uplift produced by the inflation of a shallow magma chamber or regional doming resulting from underplating or compressional tectonics) on the formation of collapse calderas.

However, there are also some important limitations to the application of experimental models. First, they do not provide a means to quantify important variables such as stress or pressure. They also offer little flexibility in establishing chamber geometries and in varying mechanical properties of the host rock analogues. Finally, there is until now no link between solid and fluid mechanics (the physical properties of magma). We are thus restricted in our knowledge on magma chamber pressure and the amount of magma withdrawal before collapse. We must be aware that experimental models offer a good approach to gain a basic understanding of caldera–collapse processes, yet these models only provide answers to parts of the entire spectra of dynamics.

## 5.2. On the use of theoretical models

In contrast to experimental models, theoretical models offer the possibility of parameterising the variables in each model. They also permit the definition semi-quantitatively of the general conditions for fracture and faults formation. Moreover, they can provide a link to incorporate magma properties into simulations of collapse and are sufficiently flexible so that a parametric study should be straightforward. However, there are still some important limitations: insofar as there is lack of knowledge about the system under consideration (rock and magma rheology, geometry, boundary conditions), theoretical models may provide results, which may lead to erroneous conclusions. Increasingly complex theoretical models require operators to not only use the software but also users with the necessary background knowledge to distinguish between realistic or unrealistic results. However, theoretical models are still not able to simulate fracture and fault propagation, which still represents a serious numerical challenge.

Despite their limitations, theoretical models offer the unique possibility to understand when and why caldera collapse occurs. This complements the information obtained from experimental models referring to how caldera subsidence takes place. Theoretical models on collapse calderas provide the necessary information to determine the stress conditions that favour collapse and also those in which such catastrophic events will not occur. In agreement with experimental results, numerical models also show that the occurrence of caldera collapse is strongly dependent on the geometry of the subvolcanic system (shape and volume of the magma chamber, chamber depth) and on the physical properties of the host rock and magma. One of the main results from theoretical models is that only very particular stress configuration around a magma chamber will favour collapse. We must hence conclude that collapse will only rarely occur over the whole history of a volcanic system. Theoretical models also indicate that ring faults controlling caldera subsidence will form at the margins of the magma chamber. As a consequence, the area covered by the resulting caldera depression will be of the same order as the surface projection of the underlying magma reservoir. This excludes, in agreement with experimental results, the formation of wide calderas from relatively narrow magma chambers and vice versa.

Theoretical models demonstrate that ring faults controlling caldera collapse may originate from magma chambers with either overpressure or underpressure. Nature exhibits calderas which may have formed by either condition: (i) there are examples of large calderas, usually located in continental settings, where the analysis of the caldera deposits supports the idea of a rapid accumulation of caldera-forming deposits without any preceding central vent eruption that could have resulted in an *a priori* chamber decompression (Sparks et al., 1985; Martí, 1991; Petrinovic, 1999; Aguirre-Díaz and Labharte-Hernández, 2003). (ii) There are also numerous examples of caldera collapses preceded by plinian central vent eruptions that account for a significant decompression of the magma chamber prior to the initiation of caldera subsidence (Williams, 1941; Mahood, 1980; Bacon, 1983; Heiken and McCoy, 1984; Heiken et al., 1990; Hildreth and Fierstein, 2000).

There are still some aspects that need to be studied in more detail in order to confirm the validity of the numerical models. One of the main uncertainties corresponds to the rheological behaviour of the host rock. Most of the existing theoretical models assume a purely elastic behaviour for the magma chamber walls. This is clearly an oversimplification, particularly in long-standing volcanic systems with a series of inflation and deflation episodes and ensuing thermal effects of magma replenishment on host rocks. Development of theoretical models using more realistic rheologies is definitively needed in order to better constrain the mechanics of caldera formation.

## 5.3. Implications of geophysical images on the assessment of caldera processes

Despite their limitations as outline above, geophysical images provide invaluable insights into the interior of calderas and, thus, represent an important contribution to our understanding of subsurface dynamics. While geophysical imaging is a universal and widely applied tool for assessing the structure of and dynamics in oil or gas reservoirs, images of the interior of collapse calderas are however still rare, given the fact that more than 100 calderas have shown signs of unrest in the past decades (Newhall and Dzurisin, 1988). As a result, our knowledge on the subsurface is far from complete, and many questions remain regarding the timescale and amount of magma replenishment beneath active calderas. Other questions pertaining to short-wavelength anomalies, for example, the extent of fault zones or hydrothermal systems or the existence of fluid (?magma)-filled pockets, are difficult to answer with a caldera-wide distribution of recording devices but could be answered by dedicated high-precision surveys at selected areas that have proven to show marked anomalies during conventional surveys. Recent archaeological studies may serve as an example (Cardarelli and de Nardis, 2001).

Another key implication of geophysical imaging concerns the question of the origin of calderas. A current subsurface image of an active caldera rarely mirrors the subsurface structure prior to the formation of a collapse caldera. Although it is tempting to adopt a geophysical image of a caldera-wide magmatic reservoir of given shape and depth as a mirror image of the magma chamber causative for the collapse, in order to validate results from other investigations, we have to be

conscious that such an image is not a reconstruction of the subsurface prior to the collapse.

## 6. Conclusions

Despite the existence of important limitations, the application of experimental, theoretical, and geophysical modelling has represented a significant advance in the understanding of caldera-collapse processes. In combination with traditional field studies, the development of experimental and theoretical models has allowed us to determine the causes and mechanisms controlling caldera collapse. They provide a clear idea on how and when caldera collapse will occur and on what the resulting structure will look like. Similarly, geophysical modelling helps to visualise the internal structure of collapse calderas and can provide clues as to sources of unrest in active systems.

The combination of field studies with experimental, theoretical, and geophysical modelling enables identification and quantification of the main controlling factors of collapse caldera formation. These factors include magma chamber size and shape, magma chamber depth, host rock rheology, previous history of deformation, topography, regional tectonics, temperature field around the magma chamber, and magma composition and rheology. In the same way, the critical role of the magma chamber shape, roof aspect ratio, and volume fraction of erupted magma on the resulting caldera structure have also been determined using experimental and theoretical modelling. It has also been possible to prove that fractures and faults controlling caldera subsidence may nucleate both at the free surface and at depth. Conditions for caldera collapse may be achieved in magma chambers subjected to both overpressure and underpressure.

However, there are some critical aspects that need to be improved in future models in order to make them more realistic and reliable. For example, new models should consider host rock mechanical heterogeneities and the pre-existing deformation history of the volcanic systems, assuming fracture and fatigue of host rock, as well as considering the effect of a gradual loading of a growing volcanic edifice. Similarly, future models should be able to include the presence of fluids (possibility of dyke injection) and to allow coupling between magma chamber thermodynamics and rock mechanics.

Finally, in order to better understand the dynamic processes at caldera volcanoes, cross-boundary interaction across many disciplines of Earth sciences is of utmost importance. Only then can the benefit of each individual technique for providing answers to the most striking questions on caldera volcanism be addressed.

# REFERENCES

Ablay, G., Kearey, P., 2000. Gravity constraints on the structure and volcanic evolution of Tenerife, Canary Islands. J. Geophys. Res., 105, 5783–5796.

Acocella, V., 2008. Structural development of calderas: a synthesis from analogue experiments (this volume).

Acocella, V., Cifelli, F., Funiciello, R., 2000. Analogue models of collapse calderas and resurgent domes. J. Volcanol. Geotherm. Res., 104, 81–96.

Acocella, V., Cifelli, F., Funiciello, R., 2001. Formation of nonintersecting nested calderas: insights from analogue models. Terra Nova, 13, 58–63.

Acocella, V., Funiciello, R., Marotta, E., Orsi, G., de Vita, S., 2004. The role of extensional structures on experimental calderas and resurgence. J. Volcanol. Geotherm. Res., 129, 199–217.

Aguirre-Díaz, G.J., Labharte-Hernández, G., 2003. Fissure ignimbrites: fissure-source origin for voluminous ignimbrites from the Sierra Madre Occidental, México and its relationship with basin and range faulting. Geology, 31(9), 773–776.

Aprea, C.M., Hildebrand, S., Fehler, M., Steck, L., Baldridge, W., Roberts, P., Thurber, C.H., Lutter, W.J, 2002. Three-dimensional Kirchhoff migration: imaging of the Jemez volcanic field using teleseismic data. J. Geophys. Res. B, Solid Earth Planets, 107(10), 15.

Araña, V., Camacho, A.G., Garcia, A., Montesinos, F.G., Blanco, I., Vieira, R., Felpeto, A., 2000. Internal structure of Tenerife (Canary Islands) based on gravity, aeromagnetic and volcanological data. J. Volcanol. Geotherm. Res., 103(1–4), 43–64.

Aster, R.C., Meyer, R.P., 1988. Three-dimensional velocity structure and hypocenter distribution in the Campi Flegrei caldera, Italy. Tectonophysics, 149(3–4), 195–218.

Bacon, C.R., 1983. Eruptive history of Mount Mazama and Crater Lake caldera, Cascade Range, U.S.A. J. Volcanol. Geotherm. Res., 18, 57–115.

Bai, C.-Y., Greenhalgh, S., 2005. 3D multi-step travel time tomography: imaging the local, deep velocity structure of Rabaul volcano, Papua New Guinea. Phys. Earth Planet. Inter., 151(3–4), 259–275.

Battaglia, M., Segall, P., Roberts, C., 2003. The mechanics of unrest at Long Valley caldera, California. 2. Constraining the nature of the source using geodetic and micro-gravity data. J. Volcanol. Geotherm. Res., 127(3–4), 219–245.

Battaglia, M., Troise, C., Obrizzo, F., Pingue, F., De Natale, G., 2006. Evidence for fluid migration as the cause of unrest at Campi Flegrei caldera (Italy). Geophys. Res. Lett. Res. Lett., 33, L01307.

Beauducel, F., de Natale, G., Obrizzo, F., Pingue, F., 2004. 3-D modelling of Campi Flegrei ground deformations: role of caldera boundary discontinuities. Pure Appl. Geophys., 161, 1329–1344.

Bibby, H.M., Caldwell, T.G., Davey, F.J., Webb, T.H., 1995. Geophysical evidence on the structure of the Taupo volcanic zone and its hydrothermal circulation. J. Volcanol. Geotherm. Res., 68(1–3), 29–58.

Blakely, R.J., 1996. Potential theory in Gravity and Magnetic Applications. Cambridge University Press, New York, 441 pp.

Bower, S.M., Woods, A.W., 1997. Control of magma volatile content and chamber depth on the mass erupted during explosive volcanic eruptions. J. Geophys. Res., 102, 10273–10290.

Bower, S.M., Woods, A.W., 1998. On the influence of magma chambers in controlling the evolution of explosive volcanic eruptions. J. Volcanol. Geotherm. Res., 86, 67–78.

Branney, M.J., 1995. Downsag and extension at calderas: new perspectives on collapse geometries from ice-melt, mining, and volcanic subsidence. Bull. Volcanol., 57, 303–318.

Bruce, A.I., Keller, G.R., 1993. Upper crustal structure of the Valles Caldera; an interpretation of the gravity anomaly field in the Jemez Mountain volcanic field. EOS Trans. Am. Geophys. Union, 74, 549 pp.

Bruno, P., 2004. Structure and evolution of the Bay of Pozzuoli (Italy) using marine seismic reflection data: implications for collapse of the Campi Flegrei caldera. Bull. Volcanol., 66(4), 342–355.

Burov, E.B., Guillou-Frottier, L., 1999. Thermomechanical behaviour of large ash flow calderas. J. Geophys. Res., 104(B10), 23081–23109.

Camacho, A.G., Vieira, R., Del Toro, C., 1991. Microgravimetric model of the Las Canadas caldera (Tenerife). J. Volcanol. Geotherm. Res., 47, 75–88.

Capuano, P., Achauer, U., 2003. Gravity field modeling in the Vesuvius and Campanian area. In: Zollo, A., Bobbio, A., Gasparini, P., Casale, R. and Yeroyanni, M. (Eds), The TOMOVES Project: Looking Inside Mt. Vesuvius. CUEN, Napoli E-book.

Cardarelli, E., de Nardis, R., 2001. Seismic refraction, isotropic and anisotropic seismic tomography on an ancient monument. Geophys. Prospect., 49(2), 228–240.

Carle, S.F., 1988. Three-dimensional gravity modeling of the geologic structure of Long Valley caldera. J. Geophys. Res. B, Solid Earth Planets, 93(11), 13,237–13,250.

Cassano, E., La Torre, P., 1987. Geophysics. In: Rosi, M. and Sbrana, A. (Eds), Phlegrean Fields, Quaderni de la Ricerca Scientifica, Roma, Vol. 114, pp. 103–131.

Chery, J., Bonneville, A., Villote, J.P., Yuen, D., 1991. Numerical modelling of caldera dynamical behaviour. Geophys. J. Int., 105, 365–379.

Davy, B., 1993. Seismic reflection profiling of the Taupo caldera, New Zealand. Explor. Geophys., 24(3–4), 443–454.

Davy, B.W., Caldwell, T.G., 1998. Gravity, magnetic and seismic surveys of the caldera complex, Lake Taupo, North Island, New Zealand. J. Volcanol. Geotherm. Res., 81(1–2), 69–89.

de Lorenzo, S., Gasparini, P., Mongelli, F., Zollo, A., 2001a. Thermal state of the Campi Flegrei caldera inferred from seismic attenuation tomography. J. Geodyn., 32(4–5), 467–486.

de Lorenzo, S., Zollo, A., Mongelli, F., 2001b. Source parameters and three-dimensional attenuation structure from the inversion of microearthquake pulse width data: Qp imaging and inferences of the thermal state of the Campi Flegrei caldera (southern Italy). J. Geophys. Res. B, Solid Earth Planets, 106(8), 16,265–16,286.

De Natale, G., Petrazzuoli, S.M., Pingue, F., 1997. The effect of collapse structures on ground deformation in calderas. Geophys. Res. Lett., 24, 1555–1558.

De Natale, G., Troise, C., Pingue, F., Mastrolorenzo, G., Pappalardo, L., Battaglia, M., Boschi, E., 2006. The Campi Flegrei caldera: unrest mechanisms and hazards. In: Troise, C., De Natale, G.Kilburn, C.R.J. (Eds), Mechanisms of activity and unrest at large calderas. Geological Society, Special Publications, London, Vol. 269, pp. 25–45.

Druitt, T.H., Sparks, R.S.J., 1984. On the formation of calderas during ignimbrite eruptions. Nature, 310, 679–681.

Finlayson, D.M., Gudmundsson, O., Itikarai, I., Nishimura, Y., Shimamura, H., 2003. Rabaul Volcano, Papua New Guinea: seismic tomographic imaging of an active caldera. J. Volcanol. Geotherm. Res., 124(3–4), 153–171.

Folch, A., Gottsmann, J., 2006. Faults and ground uplift at active calderas. In: Troise, C., De Natale, G., Kilburn, C.R.J. (Eds), Mechanisms of activity and unrest at large calderas. Geological Society, Special Publications, London, Vol. 269, pp. 109–120.

Folch, A., Martí, J., 2004. Geometrical and mechanical constraints on the formation of ring-fault calderas. Earth Planet. Sci. Lett., 221, 215–225.

Foulger, G.R., Julian, B.R., Pitt, A.M., Hill, D.P., Malin, P.E., Shalev, E., 2003. Three-dimensional crustal structure of Long Valley caldera, California, and evidence for the migration of $CO_2$ under Mammoth Mountain. J. Geophys. Res. B, Solid Earth Planets, 108(3), 16.

Francis, P., 2003. Volcanoes. A planetary perspective. Oxford University Press, Oxford, 443 pp.

Geyer, A., Folch, A., Martí, J., 2006. Relationship between caldera collapse and magma chamber withdrawal: an experimental approach. J. Volcanol. Geotherm. Res., 157, 375–386.

Gottsmann, J., Folch, A., Rymer, H., 2006a. Caldera unrest at Campi Flegrei: a contribution to the magmatic vs. hydrothermal debate from inverse and finite element modeling. J. Geophys. Res., 111(B07203), doi: 10.1029/2005JB003745.

Gottsmann, J., Rymer, H., Berrino, G., 2006b. Caldera unrest at the Campi Flegrei: a critical evaluation of source parameters from geodetic data inversion. J. Volcanol. Geotherm. Res., 150, 132–145.

Gottsmann, J., Battaglia, M., 2008. Deciphering causes of unrest at explosive collapse calderas: recent advances and future challenges of joint time-lapse gravimetric and ground deformation studies (this volume).

Gray, J.P., Monaghan, J.J., 2004. Numerical modelling of stress fields and fracture around magma chambers. J. Volcanol. Geotherm. Res., 135, 259–283.

Gudmundsson, A., 1988a. Effect of tensile stress concentration around magma chambers on intrusion and extrusion frequencies. J. Volcanol. Geotherm. Res., 35, 179–194.

Gudmundsson, A., 1988b. Formation of collapse calderas. Geology, 16, 808–810.

Gudmundsson, A., 1998. Formation and development of normal-fault calderas and the initiation of large explosive eruptions. Bull. Volcanol., 60, 160–171.

Gudmundsson, A., 2008, Magma-chamber geometry, fluid transport, local stresses, and rock behaviour during collapse caldera formation (this volume).

Gudmundsson, A., Brenner, S.L., 2005. On the conditions of sheet injections and eruptions in stratovolcanoes. Bull. Volcanol., 67, 768–782.

Gudmundsson, A., Martí, J., Turón, E., 1997. Stress fields generating ring faults in volcanoes. Geophys. Res. Lett., 24, 1559–1562.

Guidarelli, M., Sarao, A., Panza, G.F., 2002. Surface wave tomography and seismic source studies at Campi Flegrei (Italy). Phys. Earth Planet. Inter., 134(3–4), 157–173.

Guillou-Frottier, L., Burov, E.B., Milési, J.-P., 2000. Genetic links between ash-flow calderas and associated ore deposits as revealed by large-scale thermo-mechanical modeling. J. Volcanol. Geotherm. Res., 102, 339–361.

Heiken, G., McCoy, F., Jr., 1984. Caldera development during the Minoan eruption, Thira, Cyclades, Greece. J. Geophys. Res., 89, 8441–8462.

Heiken, G., Goff, F., Gardner, J.N., Baldridge, W.S., 1990. The Valles/Toledo caldera complex, Jemez Volcanic field, New Mexico. Annu. Rev. Earth Planet. Sci., 18, 27–53.

Hermance, J.P., Neumann, G.A., Slocum, W., 1988. The regional subsurface structure of Long Valley (California) caldera fill from gravity and magnetotelluric data. Geol. Soc. Am. Bull., 100(11), 1819–1823.

Hildreth, W., Fierstein, J., 2000. Overview: Katmai volcanic cluster and the great eruption of 1912. Bull. Geol. Soc. Am., 112(10), 1594–1620.

Holohan, E.P., Troll, V.R., Walter, T.R., Münn, S., McDonnell, S., Shipton, Z.K., 2005. Elliptical calderas in active tectonic settings: an experimental approach. J. Volcanol. Geotherm. Res., 144, 119–136.

Ingham, M., 2005. Deep electrical structure of the central volcanic region and Taupo volcanic zone, New Zealand. Earth, Planets, Space, 57(7), 591–603.

Jellinek, A.M., De Paolo, G.J., 2003. A model for the origin of large silicic magma chambers: precursors of caldera-forming eruptions. Bull. Volcanol., 65, 363–381.

Jones, R.H., Stewart, R.C., 1997. A method for determining significant structures in a cloud of earthquakes. J. Geophys. Res. B, Solid Earth Planets, 102(4), 8245–8254.

Kennedy, B., Stix, J., Vallance, J.W., Lavalleé, Y., Longpré, M.-A., 2004. Controls on caldera structure: results from analogue sandbox modeling. GSA Bull., 116, 515–524.

Komuro, H., 1987. Experiments on cauldron formation: a polygonal cauldron and ring fractures. J. Volcanol. Geotherm. Res., 31, 139–149.

Komuro, H., Fujita, Y., Kodama, K., 1984. Numerical and experimental models on the formation mechanism of collapse basins during the Green Tuff orogenesis of Japan. Bull. Volcanol., 47, 649–666.

Lavallée, Y., Stix, J., Kennedy, B., Richer, M., Longpré, M.-A., 2004. Caldera subsidence in areas of variable topographic relief: results from analogue modeling. J. Volcanol. Geotherm. Res., 129, 219–236.

Lavallée, Y., De Silva, S.L., Salas, G., Byrnes, J.M., 2006. Explosive volcanism (VEI6) without caldera formation: insight from Huaynaputina volcano, southern Perú. Bull. Volcanol., 68, 333–348.

Lipman, P., 2000. Calderas. In: Sigurdsson, H., Houghton, B.F., McNutt, S.R., Rymer, H.Stix, J. (Eds), Encyclopedia of Volcanoes. Academic Press, San Diego, CA, pp. 643–662.

Lipman, P.W., 1984. The roots of ash flow calderas in western North America: windows into the tops of granitic batholiths. J. Geophys. Res., 89(B10), 8801–8841.

Lipman, P.W., 1997. Subsidence of ash-flow calderas: relation to caldera size and magma-chamber geometry. Bull. Volcanol., 59, 198–218.

Lutter, W.J., Roberts, P.M., Thurber, C.H., Steck, L., Fehler, M.C., Stafford, D.G., Baldridge, W.S., Zeichert, T.A., 1995. Teleseismic P-wave image of crust and upper mantle structure beneath the Valles Caldera, New Mexico: initial results from the 1993 JTEX passive array. Geophys. Res. Lett., 22(4), 505–508.

Macedonio, G., Neri, A., Martí, J., Folch, A., 2005. Temporal evolution of flow conditions in sustained magmatic explosive eruptions. J. Volcanol. Geotherm. Res., 143, 153–172.

Mahood, G., 1980. The geological evolution of a Pleistocene volcanic center Sierra La Primavera, Jalisco, New Mexico. J. Volcanol. Geotherm. Res., 8, 199–203.

Martí, J., 1991. Caldera-like structures related to Permo-Carboniferous volcanism of the Catalan Pyrenees (NE of Spain). J. Volcanol. Geotherm. Res., 45, 173–186.

Martí, J., Ablay, G.J., Redshaw, L.T., Sparks, R.S.J., 1994. Experimental studies of collapse calderas. J. Geol. Soc. Lond., 151, 919–929.

Martí, J., Folch, A., 2005. Anticipating volcanic eruptions. In: Marti, J. and Ernst, G.J. (Eds), Volcanism and the Environment. Cambridge University Press, Cambridge, pp. 90–120.

Martí, J., Folch, A., Macedonio, G., Neri, A., 2000. Pressure evolution during caldera forming eruptions. Earth Planet. Sci. Lett., 175, 275–287.

Masturyono, McCaffrey, R., Wark, D.A., Roecker, S.W., Fauzi, Ibrahim, G., Sukhyar, 2001. Distribution of magma beneath Toba caldera complex, north Sumatra, Indonesia, constrained by three-dimensional P wave velocities, seismicity, and gravity. Geochem. Geophys. Geosyst., 2, doi:2000GC000096.

Mori, J., McKee, C., 1987. Outward-dipping ring-fault structure at Rabaul caldera as shown by earthquake locations. Science, 235, 193–195.

Mueller, W.U., Stix, J.B., White, J.D.L., Corcoran, P.L., Lafrance, B., Daigneault, R., 2008. Characterisation of Archean Subaqueous Calderas in Canada: physical volcanology, carbonate-rich hydrothermal alteration and a new exploration model (this issue).

Newhall, C.G., Dzurisin, D., 1988. Historical unrest at large calderas of the world, U.S. Geological Survey Bulletin. U.S. Geological Survey, Reston, VA, 1108 pp.

Nishimura, S., Abe, E., Nishida, J., Yokoyama, T., Dharma, A., Hehansua, P., Hehuwat, F., 1984. A gravity and volcanostratigraphic interpretation of Lake Toba region, North Sumatra, Indonesia. Tectonophysics, 109, 253–272.

Orsi, G., Patella, D., Piochi, M., Tramacere, A., 1999. Magnetic modeling of the Phlegraean volcanic district with extension to the Ponza archipelago, Italy. J. Volcanol. Geotherm. Res., 91(2–4), 345–360.

Ortiz, R., Arana, V., Astiz, M., Garcia, A., 1986. Magnetotelluric study of the Teide (Tenerife) and Timanfaya (Lanzarote) volcanic areas. J. Volcanol. Geotherm. Res., 30(3–4), 357–377.

Parasnis, D.S., 1996. Principles of Applied Geophysics. Chapman & Hall, London & New York, 402 pp.

Petrinovic, I., 1999. La caldera de colapso del Cerro Aguas Calientes, Salta, Argentina: evoluación y esquema estructural. Acta Geológica Hispánica, 34(2–3), 243–253.

Pinel, V., Jaupart, C., 2000. The effect of edifice load on magma ascent beneath a volcano. Philos. Trans. R Soc. Lond., 358, 1515–1532.

Pinel, V., Jaupart, C., 2003. Magma chamber behavior beneath a volcanic edifice. J. Geophys. Res., 108(B2), 4-1/4–17.

Pinel, V., Jaupart, C., 2004. Magma storage and horizontal dyke injection beneath a volcanic edifice. Earth Planet. Sci. Lett., 221(1–4), 245–262.

Ponko, S.C., Sanders, C.O., 1994. Inversion for P and S wave attenuation structure, Long Valley caldera, California. J. Geophys. Res. B, Solid Earth Planets, 99(2), 2619–2635.

Pous, J., Heise, W., Schnegg, P.-A., Munoz, G., Marti, J., Soriano, C., 2002. Magnetotelluric study of the Las Canadas caldera (Tenerife, Canary Islands): structural and hydrogeological implications. Earth Planet. Sci. Lett., 204(1–2), 249–263.

Prejean, S., Ellsworth, W., Zoback, M., Waldhauser, F., 2002. Fault structure and kinematics of the Long Valley caldera region, California, revealed by high-accuracy earthquake hypocenters and focal mechanism stress inversions. J. Geophys. Res. B, Solid Earth Planets, 107(12), 19.

Roche, O., Druitt, T.H., 2001. Onset of caldera collapse during ignimbrite eruptions. Earth Planet. Sci. Lett., 191, 191–202.

Roche, O., Druitt, T.H., Merle, O., 2000. Experimental study of caldera formation. J. Geophys. Res. B, Solid Earth Planets, 105(1), 395–416.

Rundle, J.B., Hill, D.P., 1988. The geophysics of a restless Caldera Long Valley, California. Annu. Rev. Earth Planet. Sci., 16, 251–271.

Rutter, E.H., 1974. The influence of temperature, strain rate and intersticial water in the experimental deformation of calcite rocks. Tectonophysics, 22, 311–334.

Sanders, C.O., 1993. Reanalysis of S-to-P amplitude ratios for gross attenuation structure, Long Valley caldera, California. J. Geophys. Res. B, Solid Earth Planets, 98(12), 22069–22079.

Sanford, A.L., 1959. Analytical and experimental study of simple geologic structures. Bull. Geol. Soc. Am., 70, 19–52.

Saunders, S.J., 2001. The shallow plumbing system of Rabaul caldera: a partially intruded ring fault? Bull. Volcanol., 63, 406–420.

Saunders, S.J., 2004. The possible contribution of circumferential fault intrusion to caldera resurgence. Bull. Volcanol., 67, 57–71.

Scales, J.A., 1994. Theory of Seismic Imaging. Samizdat Press, Golden, 297 pp. http://www.samizdat.mines.edu

Sheriff, R.E., Geldart, L.P., 1982a. Exploration Seismology Vol. 1: History, Theory and Data Acquisition. Cambridge University Press, Cambridge.

Sheriff, R.E., Geldart, L.P., 1982b. Exploration Seismology Vol. 2: Data Processing and Interpretation. Cambridge University Press, Cambridge.

Soengkono, S., 1995. A magnetic model for deep plutonic bodies beneath the central Taupo volcanic zone, North Island, New Zealand. J. Volcanol. Geotherm. Res., 68(1–3), 193–207.

Sparks, R.J.S., Francis, P.W., Hamer, R.D., Pankhurst, R.J., O'Callahan, L.O., Thorpe, R.S., Page, R., 1985. Ignimbrites of the Cerro Galán caldera, NW Argentina. J. Volcanol. Geotherm. Res., 24, 205–248.

Spera, F., 2000. Physical properties of magma. In: Sigurðsson, H. (Ed.), Encyclopedia of Volcanoes. Academic Press, San Diego, pp. 171–190.

Steck, L.K., Prothero, W.A., Jr., 1994. Crustal structure beneath Long Valley caldera from modeling of teleseismic P wave polarizations and Ps converted waves. J. Geophys. Res. B, Solid Earth Planets, 99(4), 6881–6898.

Steck, L.K., Thurber, C.H., Fehler, M.C., Lutter, W.J., Roberts, P.M., Baldridge, W.S., Stafford, D.G., Sessions, R., 1998. Crust and upper mantle P wave velocity structure beneath Valles caldera, New Mexico: results from the Jemez teleseismic tomography experiment. J. Geophys. Res. B, Solid Earth Planets, 103(10), 24,301–24,320.

Tait, S., Jaupart, C., Vergniolle, S., 1989. Pressure, gas content and eruption periodicity of a shallow crystallizing magma chamber. Earth Planet. Sci. Lett., 92, 107–123.

Takada, A., 1989. Magma transport and reservoir formation by a system of propagating cracks. Bull. Volcanol., 52, 118–126.

Takada, A., 1994. Development of a subvolcanic structure by the interaction of liquid-filled cracks. J. Volcanol. Geotherm. Res., 61, 207–222.

Thompson, P.F., Bettadpur, S.V., Tapley, B.D., 2004. Impact of short period, non-tidal, temporal mass variability on GRACE gravity estimates. Geophys. Res. Lett., 31(L06619), doi: 10.1029/2003GL01928S.

Todesco, M., 2008. Hydrothermal fluid circulation and its effect on caldera unrest (this volume).

Troise, C., Pingue, F., De Natale, G., 2003. Coulomb stress changes at calderas: modeling the seismicity of Campi Flegrei (southern Italy). J. Geophys. Res., 108(B6), 2292.

Troise, C., De Natale, G., Pingue, F., Obrizzo, F., De Martino, P., Tammaro, U., Boschi, E., 2007. Renewed ground uplift at Campi Flegrei caldera (Italy): new insight on magmatic processes and forecast. Geophys. Res. Lett., 34, L03301, doi: 10.1029/2006GL028545.

Troise, C., De Natale, G., Pingue, F., Tammaro, U., De Martino, P., Obrizzo, F., Boschi, E., 2008. A new uplift episode at Campi Flegrei caldera (southern Italy): implications for unrest interpretation and eruption hazard evaluation (this volume).

Vanorio, T., Virieux, J., Capuano, P., Russo, G., 2005. Three-dimensional seismic tomography from P wave and S wave microearthquake travel times and rock physics characterization of the Campi Flegrei caldera. J. Geophys. Res., 110, doi: 10.1029/2004JB003102.

Wahr, J., 1996. Geodesy and Gravity. Samizdat Press, Golden, 304 pp. http://www.samizdat.mines.edu

Wahr, J., Swenson, S., Zlotnicki, V., Velicogna, I., 2004. Time-variable gravity from GRACE: first results. Geophys. Res. Lett., 31(L11501), doi: 10.1029/2004GL019779.

Wait, J.R., 1982. Geo-Electromagnetism. Acadamic Press, New York.

Walker, G.P.L., 1984. Downsag calderas, ring faults, caldera sizes and incremental caldera growth. J. Geophys. Res., 89, 8407–8416.

Walter, T., 2008. Facilitating dyke intrusion into ring faults (this volume).

Walter, T.R., Troll, V.R., 2001. Formation of caldera periphery faults: an experimental study. Bull. Volcanol., 63, 191–203.

Wannamaker, P.E., 1997. Tensor CSAMT survey over the sulphur springs thermal area, Valles caldera, New Mexico, U.S.A. Part 1, Implications for structure of the western caldera. Geophysics, 62(2), 451–465.

Weiland, C.M., Steck, L.K., Dawson, P.B., Korneev, V.A., 1995. Nonlinear teleseismic tomography at Long Valley caldera, using three-dimensional minimum travel time ray tracing. J. Geophys. Res. B, Solid Earth Planets, 100(10), 20379–20390.

Whittaker, B.N., Reddish, D., 1989. Subsidence: Occurrence, Prediction and Control. Elsevier Science, New York, 528 pp.

Williams, H., 1941. Calderas and their origin. Geol. Soc. Am. Bull., 25(6), 239–346.

Williams, H., McBirney, A.R., 1979. Volcanology. Freeman, Cooper and Co. San Francisco, CA, 397 pp.

This page intentionally left blank

CHAPTER 7

# STRUCTURAL DEVELOPMENT OF CALDERAS: A SYNTHESIS FROM ANALOGUE EXPERIMENTS

Valerio Acocella[*]

## Contents

## Abstract

A number of analogue models studying caldera architecture and development have been recently performed under different conditions (apparatus, materials, scaling parameters, stress conditions). An overview of the experiments reveals a consistent scenario for caldera structure and development, regardless of imposed boundary condition. In fact, a complete collapse can be summarised through four main stages, proportional to the amount of subsidence, progressively characterised by a: (1) downsag; (2) reverse ring fault; (3) peripheral downsag and (4) peripheral normal ring fault. A brief comparison to natural cases shows that all these experimental

[*]Corresponding author. Tel:. 0039-06-57338043; Fax: 0039-06-54888201
*E-mail address:* acocella@uniroma3.it

Dip. Scienze Geologiche Roma Tre, Roma, Italy

structures, as well as their development, are commonly observed, even at various scales. Such a consistency between models and nature suggests a general applicability of experimental results. The four evolutionary stages adequately explain the architecture and development of the established caldera end-members (downsag, piston, funnel, piecemeal, trapdoor) along a continuum, where one or more end-members may correspond to a specific stage. While such a continuum is controlled by progressive subsidence, specific collapse geometries result from secondary contributory factors (roof aspect ratio, collapse symmetry, pre-existing faults). The proposed evolutionary scheme incorporates not only the geometric features of calderas, but more importantly, also their genetic features.

## 1. Introduction

Collapse calderas are subcircular collapses formed during volcanic eruptions, whose diameter is larger than that of explosive vents and craters (Williams, 1941). Accordingly, only those volcanic depressions wider than $\sim 1$ km should be considered as calderas. Calderas may be characterised by significant variations in diameter (km to tens of km), subsidence (m to km), shape (circular, elliptic or polygonal, nested, overlapping), composition of erupted products (mafic to felsic) and tectonic setting (extensional, strike-slip or compressional) (Gudmundsson and Nilsen, 2006, and references therein).

Calderas are usually considered as the surface expression of the emptying of the magma chamber during effusive or explosive eruptions. As a result of an underpressure within the magma chamber, the roof of the reservoir collapses, forming a depression at surface (Williams, 1941; Druitt and Sparks, 1984; Branney, 1995; Lipman, 1984, 1997; Martì et al., 2000). The common association between caldera formation and eruption is one of the main motivations to study their structure and development; in fact, predicting the possible structural control on the behaviour of calderas during periods of unrest may prove crucial. In addition, understanding the structure of calderas is important in geothermal and ore exploration (Stix et al., 2003).

One approach toward systematic analysis of calderas has been to define discrete end-member types with distinct geometric, evolutionary and eruptive character-istics (Walker, 1984; Lipman, 1997; Kennedy and Styx, 2003; Cole et al., 2005). Primarily based on field data, five end-member caldera geometries or styles (piston, piecemeal, trapdoor, downsag, funnel) have been proposed (Figure 1; e.g. Lipman, 1997) and commonly referred to in the literature (e.g. Cole et al., 2005, and references therein). However, such an end-member classification may be too restrictive and not as useful in documenting a collapse style, which may correspond to different morphologies at the surface (Cole et al., 2005). In addition, there is still fragmented or very poor information on the main subsurface structures and how these develop (Figure 1). Currently unanswered major structural questions include the: (a) relationships between caldera morphology and caldera structure; (b) resolution of the "room problem", that is how the subsidence of the
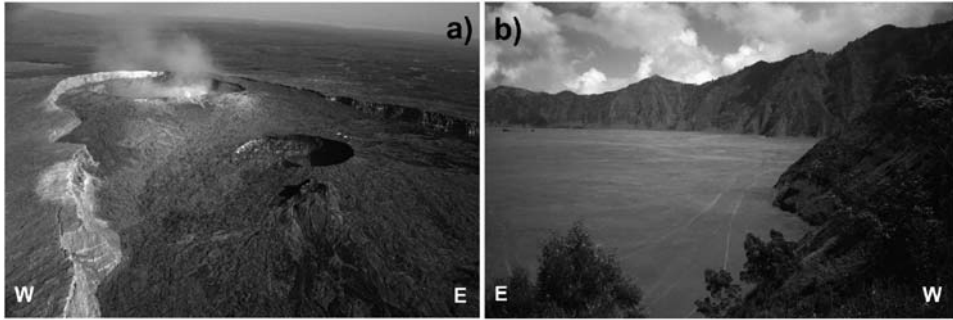
**Figure 1**   Surface structure of exceptionally exposed calderas: (a) n rim of Erta Ale caldera, Afar, Ethiopia; (b) W rim of Bromo caldera, Indonesia. Even in these favourable cases, it is still not possible to define the deeper structure and how and why this developed.

central block is accommodated at crustal depths and (c) nature (geometry and kinematics) of the caldera's bounding faults.

This study tries to put constraints on the structure and development of calderas through an overview of previously performed analogue experiments. Several sets of analogue models have been performed, in the last years, to simulate calderas. These have been run under different conditions, providing an invaluable amount of data to understand the deeper structure and the development of calderas. Most of these studies have focused mainly on the experimental results themselves, rather than on the comparison to similar models and to nature; for this reason, these experiments appear yet under-acknowledged within the volcanological community. Within this framework, this study aims to: (a) give an overview of the experiments, highlighting similarities and differences; (b) propose a consistent structural evolutionary model; (c) reconcile this model with the available geological and geophysical data; and (d) propose, from the comparison between models and nature, an updated genetic caldera classification.

## 2. ANALOGUE MODELLING

### 2.1. General features

Analogue modelling consists of a scaled simulation of natural processes. Simulating calderas, analogue models allow an understanding of the mechanism of collapse, defining the mode of deformation and the role of the different parameters in controlling the deformation. This is obtained through a systematic change in the value of each parameter, while keeping the others fixed. This procedure allows consideration of the general mechanism of deformation, potentially applicable to a wide range of cases.

The main advantage of the analogue models is the possibility to directly observe the deformation process in 3D, at an accessible laboratory scale (mm to m), within a reasonable time span (minutes to days). Moreover, analogue models, conversely to

most numerical models, permit the study of discontinuous solutions, (i.e. the development of faults) during the deformation process. Therefore, they are particularly suitable to reconstruct mechanisms of deformation and associated structural patterns. Another advantage is that the modelling does not require any advanced analytical approach.

The greatest limitation concerns the current difficulty in simulating temperature gradients. This may become relevant when dealing with magma-related processes, such as caldera collapse, implying that a fundamental assumption in all the performed experiments is the lack of a temperature control. Caldera collapse is therefore studied simulating a system with two components, a magma chamber and a brittle upper crust; the presence of a ductile crust overlying the magma chamber is neglected. Another common assumption is that the simulated contraction of the magma chamber, even though related to the extrusion of magma at surface, is not simulated as such. In fact, rather than reproducing the development of a conduit feeding a vent responsible for magma extrusion, these experiments are simply focused on its effect.

## 2.2. Materials and scaling

The modelling is achieved through the attainment of the geometric, kinematic and dynamic similarity with nature (Hubbert, 1937; Ramberg, 1981). This is obtained through the definition of precise scaling proportions between model and nature, which influence the choice of both the analogue materials and the apparatus.

The brittle crust in the caldera experiments is usually simulated by sand, flour or clay. The choice of any of these materials depends upon the imposed length ratio between model and nature $L^*$ (Merle and Vendeville, 1995, and references therein); in fact, this ratio affects the cohesion of the crustal analogue to be chosen for modelling. In most experiments, for practical reasons, $L^* \sim 10^{-5}$; moreover, the density ratio between rocks and most experimental materials is $\rho^* \sim 0.5$ and the gravity ratio between model and nature is $g^* = 1$. Therefore, the corresponding stress ratio between model and nature is $\sigma^* = \rho^* g^* z^* \sim 5 \times 10^{-6}$ (Table 1). As the cohesion $c^*$ has the dimensions of stress, assuming a Mohr–Coulomb criterion and a cohesion $c \sim 10^7$ Pa for the rocks, a material with $c \sim 50$ Pa is required to simulate the brittle crust. Therefore, the most suitable material to reproduce the behaviour of the brittle crust is dry quartz sand, with a negligible cohesion (in the order of a few Pa). In addition, dry sand has a Mohr–Coulomb failure criterion similar to the rocks in the brittle crust, with an angle of internal friction $\phi \sim 30°$. Flour and clay have slightly larger cohesion (1–3 orders of magnitude) and therefore are not ideal crust analogues, at least with the imposed ratios. Nevertheless, if added in small quantities ($\leq 10\%$) to sand, they may be useful in enhancing the resolution and details of the structural features at surface (including the formation of subvertical scarps and extension fractures).

The magma chamber responsible for collapse has been simulated by air (e.g. Marti et al., 1994), water (e.g. Kennedy et al., 2004) and silicone (e.g. Roche et al., 2000) in the various experimental sets. The main difference in these materials lies in

**Table 1** Parameters scaled to simulate the brittle crust and the ductile magma chamber during caldera-collapse (modified after Merle and Vendeville, 1995).

| Parameter | Model/nature ratio |
|---|---|
| Brittle crust | |
|    Length | $L^*$ |
|    Density | $\rho^*$ |
|    Gravity | $g^*$ |
|    Stress | $\sigma^* = \rho^* g^* L^*$ |
|    Cohesion | $c^* = \sigma^*$ |
| Magma | |
|    Viscosity | $\mu^*$ |
|    Strain rate | $\varepsilon^* = \sigma/\mu$ |
|    Time | $t^* = 1/\varepsilon^*$ |
|    Velocity | $v^* = e^* L^*$ |

their viscosity $\mu$, ranging from $10^{-5}$ (air) to $10^{-3}$ (water) and $10^{4}$ (silicone) Pa s. The viscosity of magma can vary over 12 orders of magnitude, depending on its composition and temperature (Talbot, 1999). Ideally, using a certain analogue with a given viscosity, it is possible to experimentally simulate a wide range of magma viscosities, by controlling the related strain rates $\varepsilon^*(\varepsilon^* = \sigma^*/\mu^*)$, times $t^*$ $(t^* = 1/\varepsilon^*)$ and velocities of deformation $v^*(v^* = \varepsilon^* L^*)$ (Table 1; Merle and Vendeville, 1995). In practice, all the used magma analogues have some advantage and limitation. While silicone may be used to simulate very viscous magmas $(\mu \sim 10^{10}\,\mathrm{Pa\,s})$ under ordinary laboratory times (hours), the lower viscosity of air and, mostly, water remains more suitable to simulate basaltic magmas. However, unlike silicone, their common confinement within an elastic balloon limits their flow, mobility and attitude to intrude.

## 3. Experimental Studies on Calderas

### 3.1. General features

This section considers the experiments on calderas where collapse is achieved simulating an underpressure within the analogue magma chamber (Komuro, 1987; Marti et al., 1994; Acocella et al., 2000, 2001; Roche et al., 2000; Walter and Troll, 2001; Troll et al., 2002; Kennedy et al., 2004; Lavallèe et al., 2004; Belousov et al., 2005; Geyer et al., 2006), including the influence of a regional stress field (Cailleau et al., 2003; Acocella et al., 2004; Holohan et al., 2005). However, as part of these 13 experimental sets share common research groups, materials, apparati and stress conditions, this review will consider only the following eight key papers: Komuro (1987), Marti et al. (1994), Acocella et al. (2000, 2004), Roche et al. (2000), Walter and Troll (2001), Kennedy et al. (2004) and Holohan et al. (2005) (Table 2).

**Table 2**   List of the performed experiments on collapse calderas.

| Experiment | Materials and Apparatus | Main structural achievements |
|---|---|---|
| Komuro (1987) | Dry ice evaporating in powder | Outward dipping reverse faults |
| Marti et al. (1994) | Balloon deflating in powder | Outward dipping reverse faults and subvertical faults |
| Acocella et al. (2000) | Silicone sinking in sand | Outward dipping reverse faults and inward dipping normal faults |
| | | Definition of room problem |
| Roche et al. (2000) | Silicone sinking in sand | Outward dipping reverse faults and inward dipping normal faults |
| | | Role of roof aspect ratio |
| | | Structure independent from the reservoir shape |
| Acocella et al. (2001) | Silicone sinking in sand | Constant architecture of nested pairs of calderas |
| Walter and Troll (2001) | Balloon deflating in flour | Outward dipping reverse faults and inward dipping normal faults |
| Troll et al. (2002) | Balloon deflating in flour | Inflation and deflation cycles form piecemeal collapses |
| Cailleau et al. (2003) | Balloon deflating in flour (under regional stress) | Outward dipping reverse faults and inward dipping normal faults |
| | | Caldera elongated accordingly with regional stress |
| Acocella et al. (2004) | Silicone sinking in sand (regional pre-existing faults) | Caldera elongation may depend on regional fault reactivation |
| | | No piecemeal collapses |
| Kennedy et al. (2004) | Balloon deflating in sand | Reverse and normal faults controlled by the shape of chamber roof |
| Lavallèe et al. (2004) | Balloon deflating in sand (with topography-cones) | Outward dipping reverse faults and inward dipping normal faults |
| | | Topography may locally vary the shape of calderas |
| Holohan et al. (2005) | Balloon deflating in sand (under regional stress) | Outward dipping reverse faults and inward dipping normal faults |
| | | Calderas elongated parallel to minimum compression |
| Geyer et al. (2005) | Balloon deflating in sand | Roof aspect ratio and magma chamber withdrawal |

## 3.2. Caldera collapse without regional stress field

Komuro (1987) is the first attempt to specifically simulate a collapse caldera. This is achieved using dry ice evaporating beneath a mixture of sand and clay. The spherical dry ice simulates a contracting reservoir extruding magma at surface, whereas the sand–clay mixture simulates the upper crust. The length ratio between model and nature is $L^* \sim 10^{-5}$. As stated by the author, because of the cohesive clay, this mixture probably has a strength one order of magnitude larger than required to simulate the upper crust. Evaporation of dry ice results in the overburden collapse, which propagates upwards to surface, where subcircular ring fractures are observed (Figure 2). These are outward dipping in the central part, formed at early stages, and subvertical at the periphery of the collapse, formed at later stages. The outward dip of the ring faults may permit the intrusion of magma during collapse (Figure 2b). No radial fractures are observed.

Marti et al. (1994) simulate caldera collapse by deflating an elastic balloon (magma chamber analogue) within fused alumina powder (upper crust analogue) (Figure 3a). Different balloon shapes (spherical, cylindrical, flat, penny-shaped) are used to reproduce a wide range of magma chambers. The length ratio between model and nature is $L^* \sim 10^{-5}$. To simulate collapse, air is removed from the balloon. The resulting subsidence is mainly achieved by means of subvertical faults, which confine an area characterised by several concentric collapsing blocks; these are all bordered by outward dipping reverse faults, each accommodating a minor amount of displacement and dying out towards the subvertical faults (Figure 3b). Given these concentric ring faults at surface, the authors suggest that nested calderas may result from the activity of a single magma chamber. The area of collapse increases with the size of the balloon and decreases with its depth.

Roche et al. (2000) is probably the most detailed and comprehensive experimental study focused on collapse calderas so far. Collapses are achieved by sinking Newtonian silicone putty (magma analogue) at the base of a sand-pack (brittle crust analogue). The sand–silicone interface is flat. Sinking is obtained by
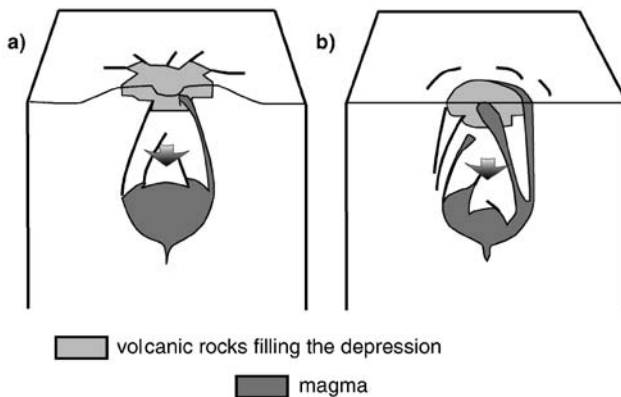


**Figure 2** Experiments from Komuro (1987). (a) Inflation+deflation; (b) deflation only (modified after Komuro, 1987).

AU :1
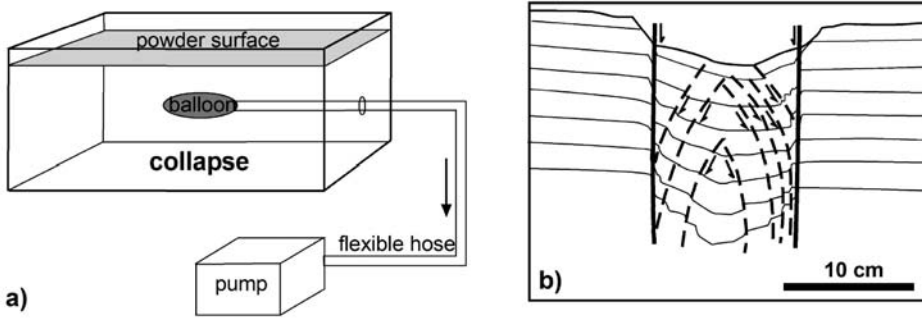
**Figure 3** Experiments from Marti et al., 1994. (a) Adopted apparatus; (b) section view of a collapse experiment, characterised by subvertical normal faults and outward dipping reverse faults (modified after Marti et al., 1994).
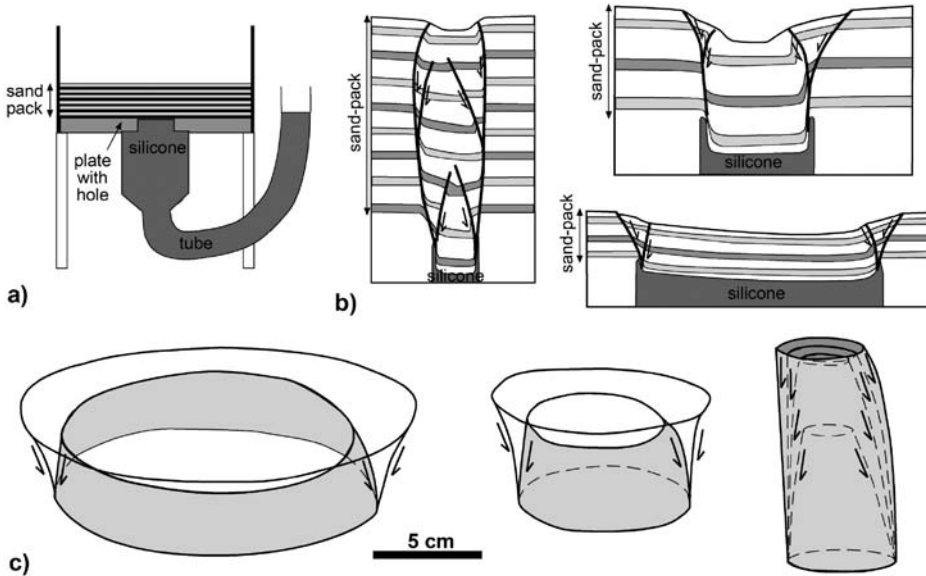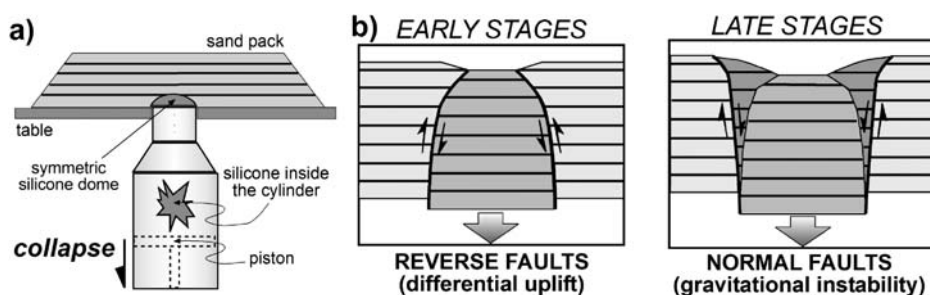


**Figure 4** Experiments from Roche et al., 2000. (a) Adopted apparatus, section view; (b) section view of three experiments characterised by different aspect ratios of the chamber roof; (c) 3D structure of the experimental collapses with different roof aspect ratios (modified after Roche et al., 2000).

lowering the height of the top-level of silicone in a tube connected to the main reservoir (Figure 4a). The length ratio between model and nature is $L^* \sim 10^{-5}$ and the experiments last hours to days. Several tens of experiments were performed in 2D and 3D, using a wide range of roof aspect ratios (thickness/width 0.2–4.5) (Figure 4b). For low roof aspect ratios ($\leq 1$, type A), subsidence occurs through a broad flexure at surface and the subsequent formation of outward dipping reverse faults (Figure 4c). When these reach a certain threshold of displacement, peripheral

inward dipping normal faults form. Inward tilted wedges at surface are bordered by the reverse and normal faults. Both the normal and reverse faults nucleate at the periphery of the silicone layer, along the point of maximum curvature of the sand–silicone interface. Subsidence usually occurs asymmetrically. This set of experiments may explain the development of coherent piston-like calderas delimited by reverse faults, whereas the gravity-driven normal faults are interpreted to border an outer zone, source of large landslides. For high aspect ratios ($\geq 1$, type B), multiple sets of reverse faults propagate upwards concentrically, forming a series of nested cones (Figure 4c). Normal faults, if present, are restricted to the periphery of the upper cone, where the reverse faults reach surface. Accordingly with the authors, this set of experiments may explain the development of funnel-like calderas with minor explosive activity.

Acocella et al. (2000) use Newtonian silicone putty (same type as Roche et al., 2000) sinking below a sand-pack through a descending piston (Figure 5a). The length ratio is $L^* \sim 10^{-5}$ and the experiments last a few hours. Various shapes of the sand–silicone interface (flat, symmetric dome, asymmetric dome) are considered. All the experiments have roof aspect ratios falling in the A type of Roche et al. (2000). The evolution of collapse is consistent with that observed by Roche et al. (2000). Two sets of concentric ring faults form, the former being reverse and the latter normal. Before the propagation at surface of each fault, the surface undergoes a diffuse deformation with an inward tilt at surface. When faulting reaches the surface, this turns into localised deformation. While the reverse faults are the straightforward consequence of differential uplift (Sanford, 1959; Mandl, 1988), the normal faults form as a gravitational response to the instability given by the slip along the reverse faults. The activity of both the reverse and normal faults may solve the room problem during large collapses (Figure 5b). The same structures also form during the reactivation of the pre-collapse doming structures. Significant asymmetric depressions (trapdoor calderas) are not common, unlike Roche et al. (2000) and form only imposing asymmetric domes along the sand–silicone interface. These silicone domes influence the position of nucleation of the faults, which show differential slip and generate asymmetric collapses (Acocella et al., 2001). The development of two concentric depressions may explain pairs of nested calderas in nature (Acocella et al., 2001).



**Figure 5**   Experiments from Acocella et al., 2000. (a) Adopted apparatus; (b) evolution of an experimental caldera (modified after Acocella et al., 2000).
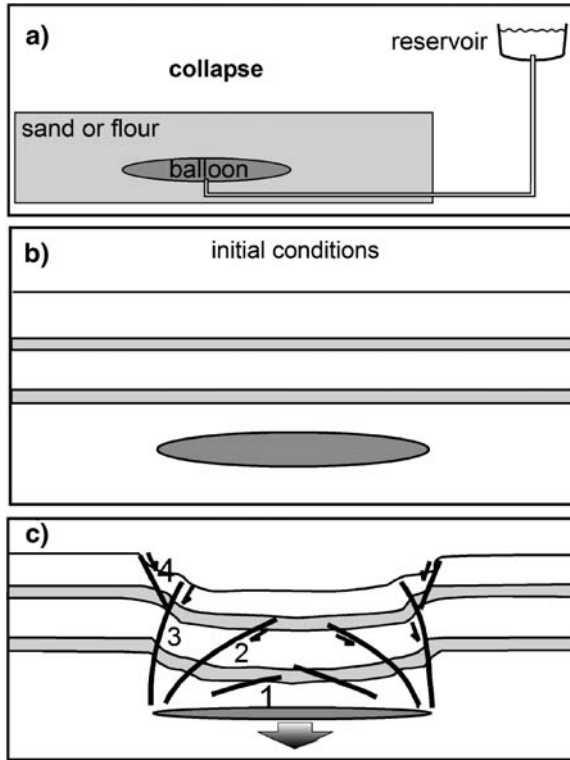
**Figure 6**   Experiments from Walter and Troll, 2001. (a) Adopted apparatus; (b) undeformed stage; (c) final stage of collapse (modified after Walter and Troll, 2001).

Walter and Troll (2001) use a deflating sill-like shaped balloon, containing air or water (magma chamber analogue) within a sand or flour box (upper crust analogue) (Figure 6a). The length ratio between model and nature is $L^* \sim 10^{-5}$. The role of a conical volcanic edifice, added to the top of the sand pack, is also tested. The evolution of the collapse (pure evacuation) experiments is consistent with the one of Roche et al. (2000) and Acocella et al. (2000). This is given by the development of one or more outward dipping reverse faults and, subsequently, by peripheric inward dipping normal faults (Figure 6c). In some cases, the normal faults do not nucleate directly from the top of the chamber, but in a shallower position. In general, increasing the depth to the balloon increases the subsidence rate of the ring faults and decreases their diameter. With a pre-existing volcanic edifice, the distribution of the reverse and normal faults is influenced by the initial morphology of the edifice: steep and irregular initial flanks result in a tilted and more structurally complex caldera floor. Nevertheless, the overall deformation pattern is totally consistent with the one observed without volcanic edifices. The same experiments also suggest that repeated inflation and deflation cycles may explain the development of piecemeal collapses, formed by radial and concentric structures, as observed at Gran Canaria (Troll et al., 2002).

Kennedy et al. (2004) used a rubber bladder containing water (magma chamber analogue) placed within sand (brittle crust analogue) to simulate collapse calderas (Figure 7a). The length ratio between model and nature is $L^* \sim 10^{-5}$ and the experiments last a few minutes. These models are characterised by a larger apparatus than the previous ones ($\sim 1\,m$ wide bladder). Consistently with what previously observed (Roche et al., 2000; Acocella et al., 2000; Walter and Troll, 2001), after flexure at surface, an inner outward dipping set of concentric reverse faults forms.
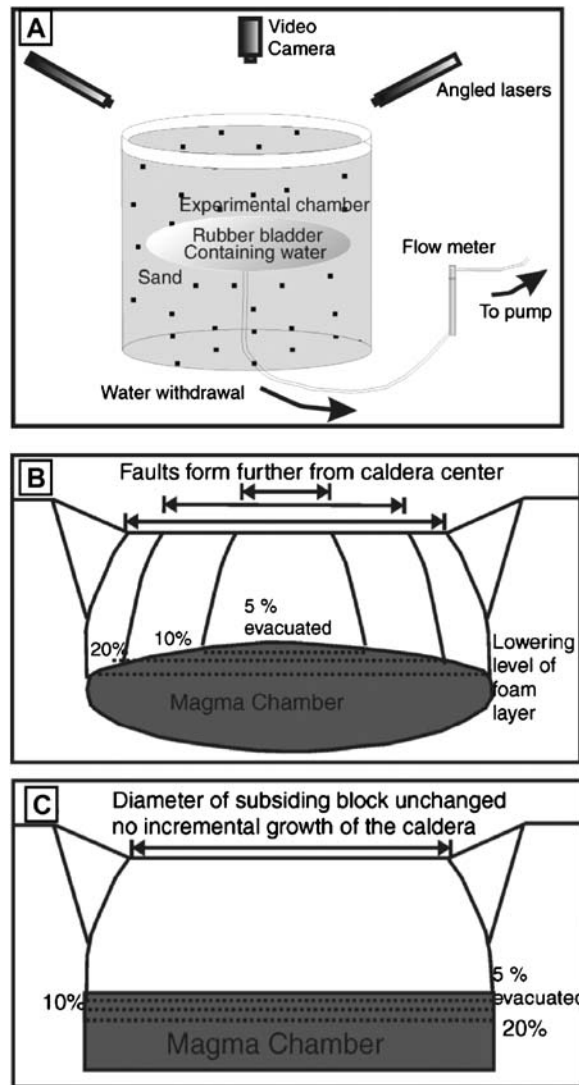


**Figure 7** Experiments from Kennedy et al., 2004. (A) Adopted apparatus; (B) and (C) modalities of collapse as a consequence of the different shape of the chamber—roof interface (modified after Kennedy et al., 2004).

These nucleate from the centre of the reservoir towards its periphery, as a result of the progressive enlargement of the evacuated area at the top of the dome-shaped bladder. This results in an outward incremental caldera growth (Figure 7b). Subsequently, a peripheral outer set of inward-dipping normal faults develops. Increasing the depth to the bladder decreases the width of the collapsed area, its symmetry and coherence. Despite the overall similarity and consistency of the deformation pattern with regard to previous models, minor differences exist. These mainly concern the outward incremental growth of the caldera, conversely to what observed in experiments with flat roof, where the width of the caldera is constant from the beginning (Figure 7c; Acocella et al., 2000; Roche et al., 2000). Also, here both the inner and outer set of faults show a polygonal shape (in map view), very seldom previously observed. Finally, conversely to Acocella et al. (2001), trapdoor subsidence is larger where the reservoir is deeper; this results from the larger amount of local subsidence within the reservoir.

## 3.3. Caldera collapse under a regional stress field

Acocella et al. (2004) use the same apparatus and materials as Acocella et al. (2000). However, here the sand-pack undergoes "regional extension" (achieved by the lateral sliding of a basal sheet) only before the collapse starts. As the strain rates during caldera collapse ($\varepsilon \sim 10^{-10}\,\mathrm{s}^{-1}$) are much faster than those induced by regional tectonics ($\varepsilon \sim 10^{-15}\,\mathrm{s}^{-1}$), regional extension during collapse may be neglected in the models. Therefore, these experiments simulate only the effect of pre-existing regional normal faults on collapse, not of a coeval regional stress field. However, they are useful to recognise the effect of the existing regional stress field in controlling the geometry of the magma chamber at depth. The regional faults are subparallel, mainly with similar dip and plunge (inward dipping at $\sim 60^{\circ}$), bordering a graben or half-graben structure. The main effect of the pre-existing structures on collapse is their partial reactivation during the development of the outward dipping reverse faults. This occurs only when the reverse fault is nearby and subparallel to any regional normal fault (Figure 8). The reactivation forms a wider caldera along the direction perpendicular to the normal faults, resulting in an elliptical depression at surface. Its major axis is therefore parallel to the former extension direction. The reactivation may account for the formation of elliptic calderas, with eccentricity $> 0.8$, elongated perpendicular to the rift axis. Moreover, this reactivation may suggest an explanation for the presence of subsidiary depressions around the borders of the calderas, influenced by both caldera collapse and regional tectonics (e.g., Spinks et al., 2005).

Holohan et al. (2005) use the same apparatus as Walter and Troll (2001). However, the brittle material undergoes regional extension or contraction (achieved by the sliding of a side wall) during collapse (Figure 9a). Therefore, these models, conversely to Acocella et al. (2004), simulate any possible effect of a regional stress field coeval to collapse. The main result is the variation in the dip angle of the outward dipping reverse faults bordering the caldera (Figure 9). In fact, under regional extension, along a section parallel to the maximum extension, the reverse faults are subvertical, rather than dipping at $\sim 70^{\circ}$ (Figure 9c).
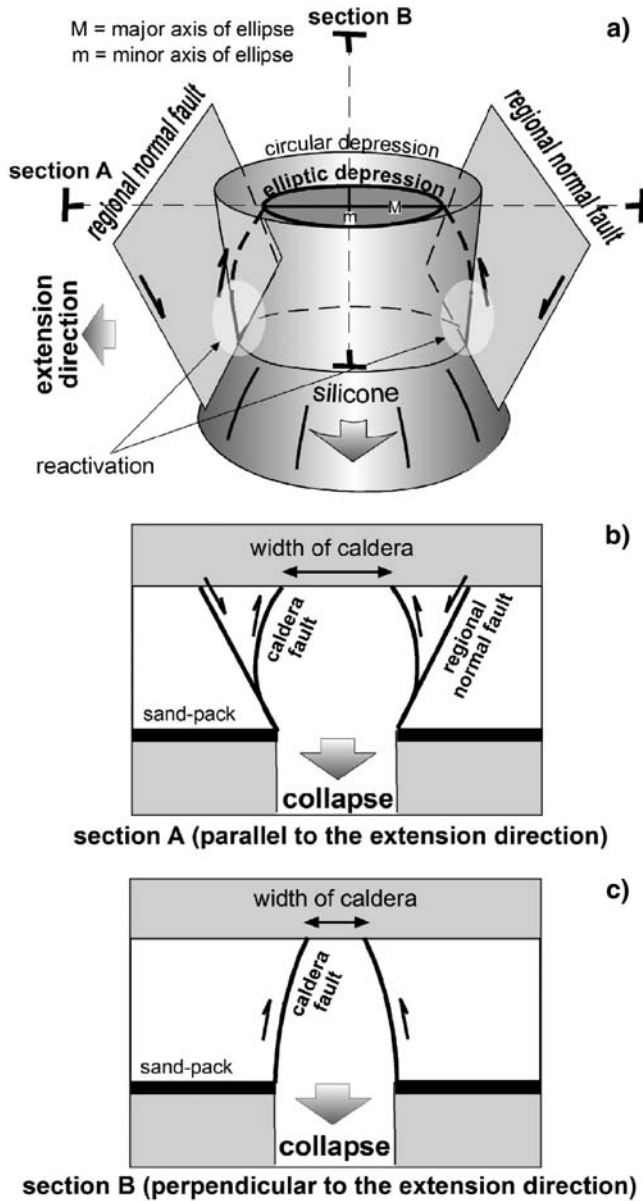
**Figure 8** Experiments with regional stress: Acocella et al., 2004. (a) Explanation for the ellipticity of the caldera considering the deformation pattern across two orthogonal sections (b and c) (modified after Acocella et al., 2004).

This variation is induced by the imposed regional extension, which increases the dip of the maximum direction of compression $\sigma 1$. The opposite occurs under regional compression, where the mean dip of the reverse faults lowers to $\sim 50°$, as due to the increase in the dip of the minimum direction of compression $\sigma 3$ (Figure 9d).
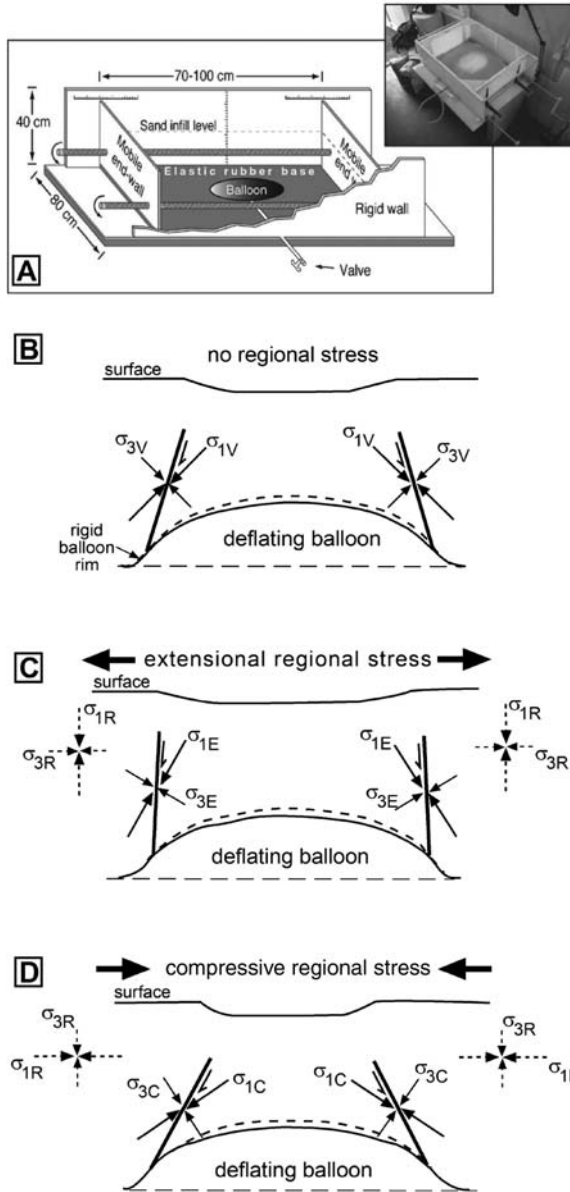
**Figure 9** Experiments with regional stress: Holohan et al., 2005. (A) Adopted apparatus; section view of the caldera reverse ring faults with neutral (B), extensional (C) and compressional (D) stress field (modified after Holohan et al., 2005).

Since these variations are observed only along a direction parallel to $\sigma 3$ (regional extension) or $\sigma 1$ (regional compression), the overall result is the development of an elliptic caldera, elongated parallel to $\sigma 3$ (during extension) or perpendicular to $\sigma 1$ (during compression). Its minimum eccentricity is $\sim 0.8$.

Regional tectonics may also affect the shape of the reservoir, forming elliptic magma chambers (e.g. Bosworth et al., 2003). The role of the shape of the magma chamber on caldera development was previously tested, with results consistent with those previously described (Roche et al., 2000). Therefore, the shape of the chamber (possibly) resulting from regional tectonics does not play an important role in controlling the structure and development of experimental calderas.

## 4. Discussion

### 4.1. Consistency of the experiments

The most important similarities within this category lie in the structural development of the calderas and the related final deformation pattern. In fact, a complete collapse consistently gives two ring structures. The inner outward dipping reverse ring fault develops first. The outer inward dipping to subvertical normal ring fault develops at later stages, after a certain amount of slip of the inner ring. Each ring may be formed by a single continuous fault, accommodating all the displacement or, more often, by multiple, closely spaced systems of concentric ring faults or portions of them. The amount of faults forming a ring structure may depend upon the reservoir shape. With a flat shape, the strain accumulates at the tips of the reservoir, enhancing the nucleation of a single pair (reverse+normal) of ring faults (Acocella et al., 2000; Roche et al., 2000). With a domed shape, strain may accumulate also at the points of maximum curvature of the reservoir (Mandl, 1988), generating additional ring faults (Acocella et al., 2001). Moreover, if the contraction of the domed–shaped reservoir is not homogeneous and migrates outwards, multiple sets of concentric reverse ring faults may form (Marti et al., 1994; Walter and Troll, 2001; Kennedy et al., 2004). Whether consisting of a single fault or a multiple set, the central volume delimited by the reverse faults constitutes the sinking piston of the caldera. The inward dipping normal faults form at the periphery of this volume, accommodating the gravitational deformation. Similarly to the reverse faults, multiple sets of concentric ring faults may also form (Walter and Troll, 2001; Kennedy et al., 2004). A consistent deformation pattern, given by outward dipping reverse faults and inward dipping normal faults, has been observed also in the experiments under a regional stress field, with elliptical calderas (Acocella et al., 2004; Holohan et al., 2005); the only difference lies in the variation of the dip of the reverse faults.

Another important similarity among the underpressure experiments is the transition from diffuse to localised strain before and during the development of a ring fault. Since the collapse is imposed at depth in the experiments, all the ring faults nucleate at the top of the chamber analogue and propagate towards surface. In their upward propagation, the diffuse deformation beyond the fault tip results in an inward tilt at surface. Increased upward propagation of the fault localises the deformation. Therefore, the presence of an inward tilt along the caldera sides suggests a partially developed collapse, controlled by a limited subsidence.

Roche et al. (2000) suggest that the deformation pattern during collapse is controlled by the roof aspect ratio. Lower ratios (type A; Section 3.2) are associated

with one set of reverse and normal faults; higher ratios (type B; Section 3.2) are associated with multiple sets of reverse faults and eventually, by a set of normal faults on top (Figure 4). However, this discrepancy is purely apparent. In fact, in type B experiments, multiple reverse faults are required to propagate the collapse upwards in a thicker crust analogue. Normal faults, as resulting from the gravitational collapse of the wedges above the upper reverse ring fault at surface, form only if the displacement along this upper fault reaches a certain threshold. This is exactly what is observed with type A experiments. Therefore, independently from the roof aspect ratio, all the collapses may display one or more set of reverse faults; if the displacement on the upper ring fault at surface reaches a certain threshold, a normal ring fault may also form.

In synthesis, despite minor variations in the amount and location of the ring faults, the evolution of all the experimental collapses is characterised by outward dipping reverse ring faults and, after a certain amount of slip, inward dipping normal ring faults at the periphery; both ring faults replace former inward tilts. This behaviour is observed with different apparatus and materials (sand, flour or clay as brittle crust analogue and air, water and silicone as magma analogue), scaling (times, strain rates and lengths), topography (with or without volcanic edifices, with various slope dips), stress conditions (neutral, compressional, extensional) and caldera elongation. Interestingly, the same structures were also obtained in previous experiments investigating differential uplift (Sanford, 1959) and the depletion of reservoirs (Odonne et al., 1999). Such a general consistency indicates that the overall deformation pattern during collapse is, in the experiments, independent from the strength of the used brittle crust analogues, the viscosity of the magma analogue, the duration and size of the experiment and the presence of a regional stress field or the load of any edifice. Moreover, this consistency indicates a precise and constant structural behaviour in accommodating the room problem during collapse, inferring a wide applicability of the analogue results.

Despite this general agreement among the various experimental data, some minor discrepancies do exist. Possibly, the most relevant regards the development of trapdoor collapses. Trapdoor collapses were common in Roche et al. (2000), Walter and Troll (2001) and Kennedy et al. (2004), and rare in Acocella et al. (2000). Some of the obtained trapdoor structures were expectable from the imposed conditions, as the shape of the chamber analogue (Acocella et al., 2001) or the distribution of the roof load (Kennedy et al., 2004). Other trapdoors were unexpected, and may have occurred as a result of heterogeneities in the system, often difficult to control a priori (Roche et al., 2000). Moreover, in Acocella et al. (2000), the most subsided part of the trapdoor is always located above the top of the asymmetric domed reservoir. Conversely, in Kennedy et al. (2004), the most subsided part of the trapdoor collapse is above the most depressed area of the reservoir. This apparent discrepancy can be explained by the fact that, when the subsidence is homogeneous, the faults form along the points of maximum curvature of the top of the reservoir; these are usually located in the most uplifted part of the reservoir. As a consequence, the maximum subsidence is observed above the most uplifted part of the reservoir (Acocella et al., 2001). Conversely, when the subsidence within the reservoir is differential (as when deflating a balloon), the most

collapsed area at surface coincides with the most emptied area within the reservoir (Kennedy et al., 2004).

## 4.2. Towards a consistent experimental model

The consistency among the experiments simulating underpressure, under different boundary conditions, permits to propose a comprehensive model describing the evolution of experimental collapses. This can be adequately summarised through four main stages, representing discrete moments within an evolutionary continuum controlled by the amount of subsidence (Figure 10; Acocella, 2007).

Stage 1 is characterised by a broad depression, with inward tilted margins, at the surface. This usually occurs with a subsidence of very few mm (in a caldera a few cm wide), corresponding to several tens to few hundreds of m in nature. At the same time, the upward propagation of the reverse ring fault starts at depth; as long as the fault remains buried, the diffuse strain forms the inward tilt at surface. At this stage, an experimental downsag caldera is formed (Figure 10a).

At Stage 2, the reverse ring fault reaches surface, replacing the downsag. This usually occurs with a subsidence of several mm (in a caldera a few cm wide), corresponding to several hundreds of m in nature. The structural boundary of the caldera is completely defined, exhibiting a clear rim or scarp, above the reverse ring fault. While the reverse fault is always outward dipping, the caldera rim above, due to rapid decay of the overhanging reverse fault scarp, is subvertical or inward dipping and may be located in an outer position. Additional reverse ring faults may be present within the rim, accordingly with the above-mentioned mode of outward incremental growth (Kennedy et al., 2004). At this stage, the basic structure of the experimental caldera resembles a piston-type (with lower aspect ratios of the caldera roof) or funnel-type (with higher aspect ratios) (Figure 10b; Roche et al., 2000).

Stage 3 results from the further increase in subsidence, usually in the order of $\sim 1$ cm (in a caldera a few cm wide), corresponding to $\sim 1$ km in nature. This stage develops an inward tilt on the outer periphery of the reverse ring fault. This is the surface accommodation of the incipient, upward-propagating outer normal ring fault. At this stage, a peripheral downsag forms (Figure 10c).
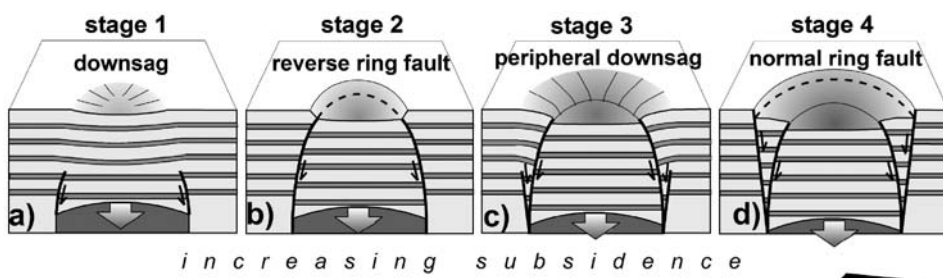


**Figure 10**    Schematic representation of the four stages of evolution of caldera collapse, obtained in all the experiments, as a function of the amount of subsidence.

Stage 4 results from a subsidence usually in the order of 1 cm or more (in a caldera a few cm wide), corresponding to $\geq 1$ km in nature. This develops an outer normal ring fault, replacing the former peripheral downsag. The fault reaches surface forming an additional rim, or scarp; the caldera rim is inward dipping, as the underlying fault. Even though this stage is characterised by the development of the normal fault, slip along the inner reverse fault still continues; therefore, the overall collapse structure consists of a pair of nested calderas (Figure 10d). No variation in the deformation pattern is observed in the experiments with larger subsidence.

The above estimates of the amount of collapse required to reach a certain stage vary as a function of the diameter of the caldera and the thickness of the brittle crust analogue. In particular, it is expected that wider calderas require higher subsidence to develop ring faults.

## 5. COMPARISON TO NATURE: GUIDELINES

The main structural features of the experiments are the downsags (Stages 1 and 3) and the ring faults (Stages 2 and 4). Both are visible at well-studied natural calderas (Newhall and Dzurisin, 1988).

The sagged floor may be the only structure accommodating subsidence, as at Bracciano (Italy; Di Filippo, 1993) or Buckhorn (Texas; Henry and Price, 1984), or may be accompanied by a ring structure within, as at Bolsena (Italy; Walker, 1984; Nappi et al., 1991), Rotorua and Reporoa (Figure 11a; New Zealand; Milner et al., 2002; Spinks et al., 2005). Many downsags have later turned into ring faults, as Sabaloka (Sudan; Almond, 1977), Ishizuchi (Japan; Yoshida, 1984) and Grizzly Peak (Colorado; Fridrich and Mahood, 1984; Fridrich et al., 1991), consistently with the experimental evolution.

Regarding ring faults, while the presence of a ring fault at surface may be highlighted by the caldera rim, at depth its location is more uncertain. This has generated a debate over the fault's nature, variously described as normal inward dipping, reverse outward dipping or vertical (Kennedy and Styx, 2003). Despite the common expectation that calderas are bordered by normal faults (Newhall and Dzurisin, 1988, and references therein), there is widespread, scale-invariant evidence for outward dipping reverse faults. At the 10–100 m scale, subcircular collapses and pit craters are bordered by outward dipping reverse faults, as at Taupo Volcanic Zone (New Zealand; Figure 11b) and Masaya volcano (Nicaragua; Figure 11c; Roche et al., 2001). At larger scales (several km), outward dipping ring faults border Rabaul (Figure 11d; Mori and Mckee, 1987; Saunders, 2001), Ishizuchi (Yoshida, 1984) and Glencoe calderas. Peripheral normal ring faults may be present as well, as at Miyakejima (Figure 11; Geshi et al., 2002) or Rabaul (Saunders, 2001), forming pairs of concentric ring faults, as observed in Stage 4 experiments. Such nested pairs of concentric calderas are common, as at Campi Flegrei (Figure 11e), Latera, Pantelleria (Italy), Tavua (Fiji), Batur (Indonesia), Fantale (Ethiopia), Taupo (New Zealand), Suswa (Kenya), Guayabo (Costa Rica), Daisetsu (Japan), the Archean Hunter Mine Group (Canada) and Karkar and
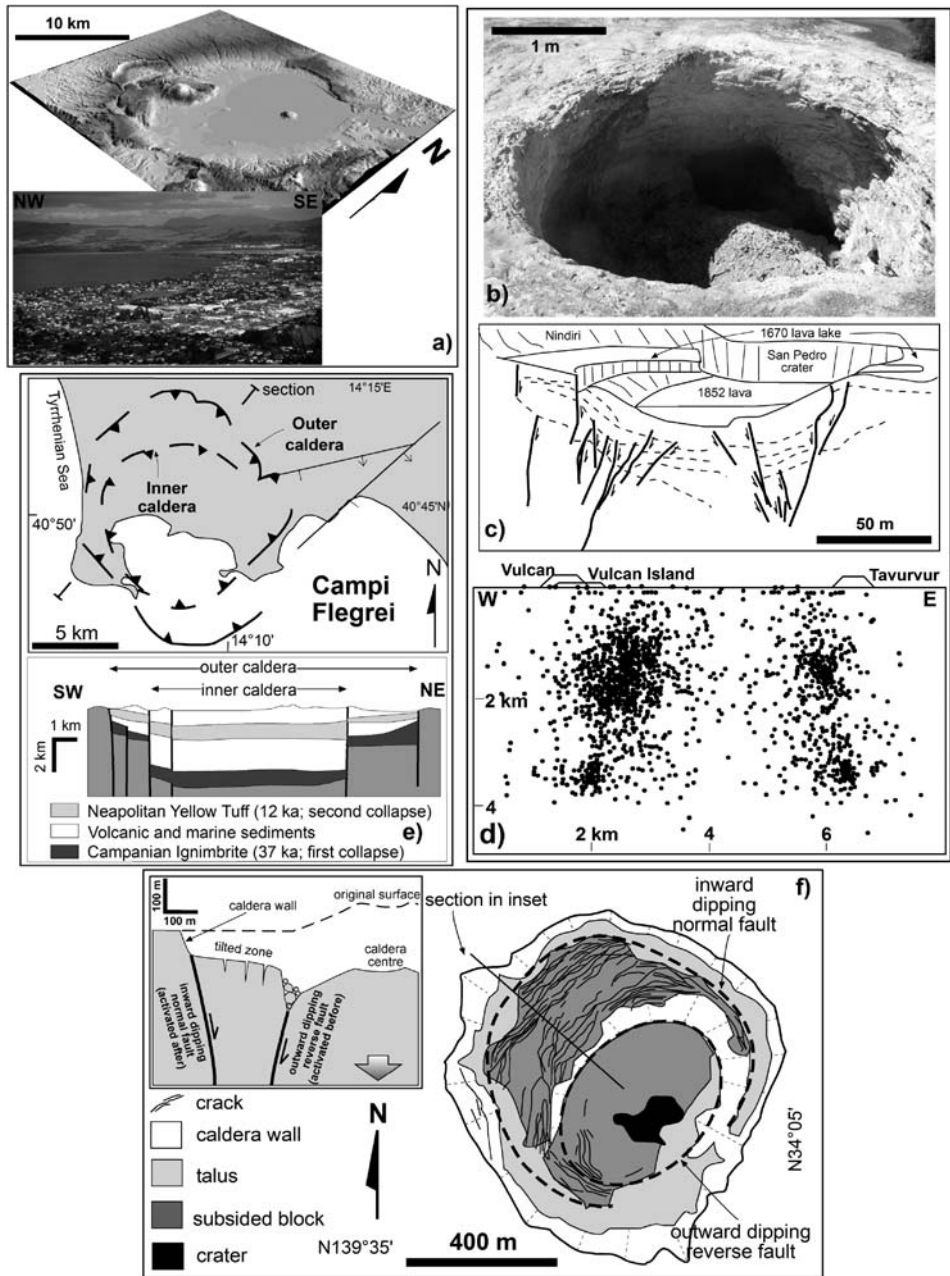
**Figure 11**    (a) Downsag caldera at Rotorua, Taupo Volcanic Zone, New Zealand (courtesy of Karl Spinks); (b) collapse structure bordered by outward dipping reverse faults in hydrothermal deposits, Taupo Volcanic Zone, New Zealand; (c) pit crater bordered by outward dipping reverse faults at Masaya, Nicaragua (scale is approximate; modified after Roche et al., 2001); (d) outward dipping faults highlighted by the distribution of seismicity at Rabaul (section view; modified after Mori and Mckee, 1987); (e) map and section view of Campi Flegrei nested caldera, Italy (modified after Orsi et al., 1996); (f) map and section view of Miyakejima caldera, Japan, formed in 2000, bordered by reverse faults (formed first) and normal faults (formed later) (modified after Geshi et al., 2002).

Rabaul (Papua New Guinea) (Newhall and Dzurisin, 1988; Hallinan, 1993; Skilling, 1993; Acocella et al., 2001, and references therein; Acocella et al., 2002; Mueller and Mortensen, 2002). In particular, the Miyakejima collapse in 2000 is possibly the most significant caldera–collapse episode (with subsidence of several hundreds of m and fracturing) observed so far: the authors clearly describe the development of an inner outward dipping reverse ring fault, formed first, and a subsequent outer inward dipping normal fault, with an architecture and evolution identical to that in the experiments (Figure 11f; Geshi et al., 2002).

The experimental results suggest that these concentric pairs of nested calderas may be related to the same eruptive episode (Marti et al., 1994; Acocella et al., 2001), not necessarily to two distinct eruptions, as often believed (e.g. Newhall and Dzurisin, 1988, and references therein). In these cases, one can only discriminate between the two possibilities constraining the relative timing of development of the two collapses, considering not only surface data. In fact, at natural nested calderas, surface data can only indicate that the outer caldera is older, as otherwise the inner one would have been covered by the activity and deposits of the outer. For example, surface data suggest that several pairs of nested calderas are characterised by an inner younger structure, as Campi Flegrei, Latera, Tavua (Orsi et al., 1996; Capaccioni et al., 1987; Setterfield et al., 1991). Interestingly, available subsurface data at these same calderas indicate that the inner depression coincides with an older buried collapse, later reactivated. This is shown, for instance, by the deep section of Campi Flegrei, obtained from borehole and geophysical data (Figure 11; modified after Orsi et al., 1996); the dips of the faults are approximate. The different thickness of the syn-collapse deposits within the two nested structures suggests that the inner, deeper depression formed before the outer one. Moreover, the presence of syn-collapse deposits in both depressions suggests that there has been interaction between the depressions during the same collapse event. These features are in close agreement with the evolution and timing of formation of the experimental collapses. These examples suggest that surface geology alone is not sufficient to evaluate the relative timing of development of the depressions and, when such an age is inferred only from surface data, it is not sufficient to define whether a pair of nested calderas is consistent with Stage 4 or results from two distinct collapses.

Several large calderas in nature, characterised by a low aspect ratio of the chamber roof ($t/d < 0.5$) and significant subsidence ($> 2,000$ m), have only one major ring fault visible at their borders. Notable examples include Long Valley (Carle, 1988), Valles (Self et al., 1986), La Garita and Creede (Lipman, 1997, 2003), Western United States and Okueyama (Japan; Aramaki et al., 1977). In the light of the experiments, these calderas, characterised by an advanced subsidence, can be interpreted as being bordered by two ring faults lying next to each other. Their proximity makes it difficult to resolve each structure, resembling, at the caldera scale, a single ring system. A very similar deformation pattern, with almost coincident ring faults, is shown in the experiments with $t/d < 0.5$ and significant subsidence (Figure 4b; Roche et al., 2000).

Asymmetries in the development of these structures may result in trapdoor collapses, commonly observed in the experiments and in nature, as at Grizzly Peak (Colorado; Fridrich et al., 1991), Bolsena, Latera (Italy; Nappi et al., 1991) and

Kumano (Japan; Miura, 2005). These collapses show a differential subsidence, accommodated by ring faults (deeper part) and flexures (shallower part).

Therefore, the experimental structures are commonly observed in nature. Moreover, their progression is also commonly found at several well-studied calderas (as for example, Sabaloka, Ishizuchi, Grizzly Peak, Miyakejima, Bolsena, Guayabo). At many calderas, these structural features may easily overlap. This may occur with advanced subsidence, when older structures remain preserved, or with asymmetric collapse, developing structures only apparently corresponding to different collapse stages along the caldera.

This overview highlights the importance of defining the structure of a caldera beyond its overall morphological expression, especially at young calderas. In fact, only the precise assessment of certain structural features (ring faults, downsags) should be employed as a diagnostic feature of collapse types.

# 6. Towards a New Caldera Evolution Scheme

The experiments and their matching to nature suggest an original revision of the structure, mechanism of development and relationships of the established caldera types described in the literature: downsag, piston-type, funnel, trapdoor and piecemeal. In fact, the consistency among experiments and nature suggests that the architecture and development of the caldera end-members described in the literature may be contextualised within a subsidence continuum (Figure 12; Acocella, 2006a, 2007). Along such a continuum, the exact geometry and style of the established caldera types may be related to contributory factors, as roof aspect ratio, symmetries, reactivation of pre-existing faults.

Downsag calderas, corresponding to experimental Stage 1 form under limited subsidence and are the starting architecture to develop any other collapse. Most collapses will pass through the downsag phase, explaining the moderate number of downsag calderas in nature. Likely candidates are Buckhorn and Bracciano (Henry and Price, 1984; Di Filippo, 1993).

The increase in subsidence results in the partial or full development of a high angle reverse ring fault (Stage 2), whose surface expression in nature is a rim scarp. In these calderas, the rapid decay of the overhanging reverse fault scarp develops subvertical to inward dipping caldera rims, towards the outer border of the ring fault. Therefore, the structural boundary of Stage 2 calderas lies in an inner position with regard to the morphological rim. The fault may bound piston or funnel collapses, with roof aspect ratios $A < 1$ or $A > 1$, respectively (Roche et al., 2000; Figure 12). Likely candidates of Stage 2 calderas are Erta Ale, Kilauea, Krafla and Sierra Negra (Newhall and Dzurisin, 1988; Munro and Rowland, 1996; Acocella, 2006b; Gudmundsson and Nilsen, 2006).

Increasing the subsidence further forms an external downsag bordering the reverse fault (Stage 3). This downsag is distinguished from that of Stage 1 by the presence of the inner ring fault, formed at Stage 2. Likely candidates are Rotorua and Bolsena (Barberi et al., 1994; Milner et al., 2002).
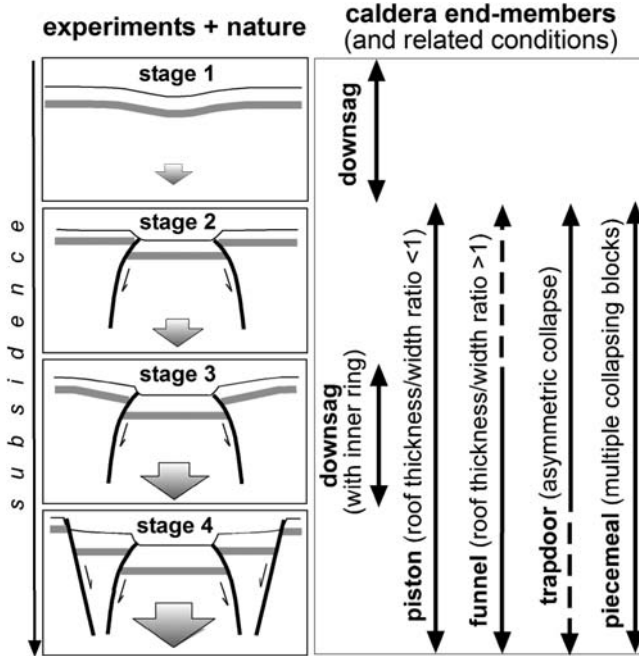
**Figure 12** Evolution of natural calderas geometries, summarized in four stages, which derives from the merging of the experimental and natural data. To the right, the classic caldera end-members (Lipman, 1997; Cole et al., 2005) and related conditions to form.

When the normal ring fault, peripheral and concentric to the reverse fault, reaches surface, it forms two nested collapses (Stage 4). Such caldera pairs, common in nature, may relate to the same collapse episode, not necessarily to two distinct collapse events (Marti et al., 1994; Acocella et al., 2001). Likely candidates are Campi Flegrei, Latera, Long Valley, Valles, Miyakejima, La Garita, Fernandina and Rabaul (Self et al., 1986; Carle, 1988; Barberi et al., 1994; Munro and Rowland, 1996; Orsi et al., 1996; Lipman, 1997; Geshi et al., 2002; Bai and Greenlangh, 2005).

In this evolutionary frame, additional remarks concern the trapdoor and piecemeal end-members. The experiments suggests that trapdoors may develop as a result of asymmetries in the chamber analogue (Acocella et al., 2001), in the roof load (Kennedy et al., 2004) or of small other heterogeneities (Roche et al., 2000). In general, they may be associated with very small roof aspect ratios (thin crust compared to chamber width), where their formation may be enhanced by an asymmetric load distribution above the magma chamber. Trapdoor calderas show, in addition to a portion of ring fault, a downsagged side. Trapdoors may therefore represent specific asymmetries during Stages 2 to 4. With lower subsidence, a downsag structure forms on one side and a (reverse) fault on the opposite (Stage 2 caldera). Higher subsidence may induce (reverse) faulting on the flexured side and form an additional (normal) fault at the periphery of the reverse fault (Stage 4 caldera). However, fully developed Stage 4 calderas should not be trapdoor, as the downsag should be completely replaced by the outer ring fault.

Piecemeal collapse is the only established caldera end–member that has probably not been satisfactorily simulated experimentally. In fact, experimental piecemeals have been obtained during inflation–deflation cycles (Troll et al., 2002), but not during the reactivation of pre–existing regional structures (Acocella et al., 2004), as suggested by field data (Moore and Kokelaar, 1998). The poor evidence for experimental piecemeal collapses is also mirrored by field studies: (a) there is only a small number of observed piecemeal calderas (Lipman, 1997) and (b) even at type locality of piecemeal calderas (Glencoe, Scafell), collapse was mainly achieved by downsag and, only to a lesser extent, by faulting (Branney and Kokelaar, 1994; Moore and Kokelaar, 1998). These facts suggest that the occurrence of piecemeal collapse is a minor mechanism during caldera formation. As piecemeal calderas require pre–existing faulting, they may, in principle, belong to any of the last three evolutionary stages (Figure 12).

The possible domains for the established caldera end–members show that more than one end–member may correspond to a certain evolutionary stage (Figure 12). This means that, while a caldera evolution stage is precisely defined by its structural features (Figure 10), elements from multiple caldera end–members (Figure 12, right portion) may be present as well, even though not being diagnostic of the collapse stage.

It thus appears that the five established caldera end–members classically described in the literature can be easily reconciled with the four experimental stages of caldera evolution, accordingly with the evolutionary scheme proposed in Figure 12 (Acocella, 2006a, 2007). This relies on the evolution, amount of subsidence and diameter of the calderas and identifies a caldera accordingly with its overall surface structure, mechanism of formation and evolution. It therefore not only incorporates the geometric features, but more importantly, also the genetic features of calderas.

# 7. Conclusions

The overview of the analogue models of calderas permits to define the following aspects on their structure and evolution:

(1) All the experiments simulating caldera collapse point out to a consistent scenario defining the evolution and structure of calderas, regardless of any experimental boundary condition (materials, apparatus, scaling, volcanic edifices and regional stresses).
(2) In these experiments, a complete cycle of caldera collapse develops in four main stages, proportional to the amount of subsidence, progressively characterised by: (a) a downsag, (b) a reverse ring fault; (c) a peripheral downsag, (d) a peripheral normal ring fault.
(3) Most of the available surface and subsurface geological and geophysical data at known worldwide calderas are consistent with the experimental structural features, as well as with their progression.
(4) The evolutionary stages explain the architecture and development of the established caldera end–members along a continuum, where one or more

end-members may correspond to a specific stage. While such a continuum is defined by precise structural features and controlled by progressive subsidence, specific geometries result from secondary factors (roof aspect ratio, collapse symmetry, pre-existing faults), not diagnostic of the collapse stage.

## ACKNOWLEDGEMENTS

## REFERENCES

Acocella, V., 2006a. Caldera types: how end-members relate to evolutionary stages of collapse. Geophys. Res. Lett., 33, L18314, doi: 10.1029/2006GL0274340.

Acocella, V., 2006b. Regional and local tectonics at Erta Ale caldera, Afar (Ethiopia). J. Struct. Geol., 28, 1808–1820.

Acocella, V., 2007. Understanding caldera structure and development: an overview of analogue models compared to nature. Earth Sci. Rev., 85, 125–160.

Acocella, V., Cifelli, F., Funiciello, R., 2000. Analogue models of collapse calderas and resurgent domes. J. Volcanol. Geotherm. Res., 104, 81–96.

Acocella, V., Cifelli, F., Funiciello, R., 2001. Formation and architecture of nested collapse calderas: insights from analogue models. Terra Nova, 13, 58–63.

Acocella, V., Funiciello, R., Marotta, E., Orsi, G., de Vita, S., 2004. The role of extensional structures on experimental calderas and resurgence. J. Volcanol. Geotherm. Res., 129, 199–217.

Acocella, V., Korme, T., Salvini, F., Funiciello, R., 2002. Elliptic calderas in the Ethiopian Rift: control of pre-existing structures. J. Volcanol. Geotherm. Res., 119, 189–203.

Almond, D.C., 1977. Sabaloka igneous complex, Sudan. Philos. Trans. R. Soc. Lond. Series A, 287(1348), 595–633.

Aramaki, S., Takahashi, M., Nozawa, T., 1977. Kumano acidic rocks and Okueyama complex: two examples of granitic rocks in the outer zone of southwestern Japan. In: Yamada, N. (Ed.), Plutonism in Relation to Volcanism and Metamorphism, Proceedings of the 7th Circum-Pacific Plutonism Project Meeting, International Geological Correlation Program, UNESCO, Toyama, Japan, pp. 127–147.

Bai, C., Greenlangh, S., 2005. 3D multi-step travel time tomography: imaging the local, deep velocity structure of Rabaul volcano, Papua New Guinea. Phys. Earth Planet. Inter., 151, 259–275.

Barberi, F., Buonasorte, G., Cioni, R., Fiordalisi, A., Foresi, L., Iaccarino, S., Laurenzi, M.A., Sbrana, A., Vernia, L., Villa, I.M., 1994. Plio-Pleistocene geological evolution of the geothermal area of Tuscany and Latium. Mem. Descr. Carta Geol. d'It., XLIX, 77–134.

Belousov, A., Walter, T.R., Troll, V.R., 2005. Large scale failures on domes and stratocones situated on caldera ring faults: san-box modelling of natural examples from kamchatka, Russia. Bull. Volcanol., 67, 457–468.

Bosworth, W., Burke, K., Strecker, M., 2003. Effect of stress fields on magma chamber stability and the formation of collapse calderas. Tectonics, 22(4), 1042, doi: 10.1029/2002TC001369.

Branney, M.J., 1995. Downsag and extension at calderas: new perspectives on collapse geometries from ice-melt, mining, and volcanic subsidence. Bull. Volcanol., 57, 303–318.

Branney, M.J., Kokelaar, P., 1994. Volcanotectonic faulting, soft-state deformation and rheomorphism of tuffs during development of a piecemeal caldera, English Lake District. Geol. Soc. Am. Bull., 106, 507–530.

Cailleau, B., Walter, T.R., Janle, P., Hauber, E., 2003. Modeling volcanic deformation in a regional stress field: implications for the formation of graben structures on Alba Patera, Mars. J. Geophys. Res., 108, E12, 5141, doi: 10.1029/2003JE002135.

Capaccioni, B., Nappi, G., Renzulli, A., Santi, P., 1987. The eruptive history of Vepe Caldera (Latera volcano): a model inferred from structural and geochemical data. Periodico Mineralogia, 56, 269–283.

Carle, S.F., 1988. Three-dimensional gravity modelling of the geologic structure of Long Valley caldera. J. Geophys. Res., 93, 13237–13250.

Cole, J.W., Milner, D.M., Spinks, K.D., 2005. Calderas and caldera structures: a review. Earth Sci. Rev., 69, 1–96.

Di Filippo, M., 1993. Sabatini Volcanic Complex. C.N.R., Roma, 109 pp.

Druitt, T.H., Sparks, R.S., 1984. On the formation of calderas during ignimbrite eruptions. Nature, 310, 679–681.

Fridrich, C.J., Mahood, G.A., 1984. Reverse zoning in the resurgent intrusions of the Grizzly Peak cauldron, Sawatch Range, Colorado. Geol. Soc. Am. Bull., 95, 779–787.

Fridrich, C.J., Smith, R.P., De Witte, E., McKee, E.H., 1991. Structural, eruptive, and intrusive history of the Grizzly Peak caldera, Sawatch range, Colorado. Geol. Soc. Am. Bull., 103, 1160–1177.

Geshi, N., Shimano, T., Chiba, T., Nakada, S., 2002. Caldera collapse during the 2000 eruption of Miyakejima volcano, Japan. Bull. Volcanol., 64, 55–68.

Geyer, A., Folch, A., Martì, J., 2006. Relationship between caldera collapse and magma chamber withdrawl: an experimental approach. J. Volcanol. Geotherm. Res., 157, 375–386.

Gudmundsson, A., Nilsen, K., 2006. Ring faults in composite volcanoes: structures, models, and stress fields associated with their formation. J. Geol. Soc. Lond., 269, 83–108.

Hallinan, S., 1993. Nonchaotic collapse at funnel calderas: gravity study of the ring fractures at Guayabo caldera, Costa Rica. Geology, 21, 367–370.

Henry, C.H., Price, J.G., 1984. Variations in caldera development in the Tertiary volcanic field of Trans-Pecos Texas. J. Geophys. Res., 89, 8765–8786.

Holohan, E.P., Troll, V.R., Walter, T.R., Munn, S., McDonnell, S., Shipton, Z.K., 2005. Elliptical calderas in active tectonic settings: an experimental approach. J. Volcanol. Geotherm. Res., 144, 119–135.

Hubbert, M.K., 1937. Theory of scale models as applied to the study of geologic structures. Bull. Geol. Soc. Am., 48, 1459–1520.

Kennedy, B., Styx, J., 2003. Igneous rock associations of Canada 2. Stages in the temporal evolution of calderas. Geosci. Can., 30, 129–140.

Kennedy, B., Styx, J., Vallance, J.W., Lavallèe, Y., Longprè, M.A., 2004. Controls on caldera structure: results from analogue sandbox modelling. Geol. Soc. Am. Bull., 106, 515–524.

Komuro, H., 1987. Experiments on cauldron formation: a polygonal cauldron and ring fractures. J. Volcanol. Geotherm. Res., 31, 139–149.

Lavallèe, Y., Stix, J., Kennedy, B., Richer, M., Longprè, M.A., 2004. Caldera subsidence in areas of variable topographic relief: results from analogue modelling. J. Volcanol. Geotherm. Res., 129, 219–236.

Lipman, P.W., 1984. The roots of ash flow calderas in western North America: windows into the tops of granitic batholiths. J. Geophys. Res., 89, 8801–8841.

Lipman, P.W., 1997. Subsidence of ash-flow calderas: relation to caldera size and magma-chamber geometry. Bull. Volcanol., 59, 198–218.

Lipman, P.W., 2003. Geometrically Complex Calderas and Underlying Magma Chambers in the western USA. Proceedings of the IUGG XXIII Assembly, Sapporo, Japan, pp. 526–527.

Mandl, G., 1988. Mechanics of Tectonic Faulting: Models and Basic Concepts. Elsevier, Amsterdam, 401pp.

Marti, J., Ablay, G.J., Redshaw, L.T., Sparks, R.S.J., 1994. Experimental studies of collapse calderas. J. Geol. Soc. Lond., 151, 919–929.

Martì, J., Folch, A., Neri, A., Macedonio, G., 2000. Pressure evolution during explosive caldera-forming eruptions. Earth Planet. Sci. Lett., 175, 275–287.

Merle, O., Vendeville, B., 1995. Experimental modelling of thin-skinned shortening around magmatic intrusions. Bull. Volcanol., 57, 33–43.

Milner, D.M., Cole, J.W., Wood, C.P., 2002. Asymmetric, multiple block collapse at Rotorua caldera, Taupo Volcanic Zone, New Zealand. Bull. Volcanol., 64, 134–149.

Miura, D., 2005. Effects of changing stress states on the development of caldera-bounding faults: geological evidence from Kumano caldera, Japan. J. Volcanol. Geotherm. Res., 144, 89–103.

Moore, I., Kokelaar, P., 1998. Tectonically controlled piecemeal caldera collapse: a case study of Glencoe volcano, Scotland. Geol. Soc. Am. Bull., 110, 1448–1466.

Mori, J., Mckee, C., 1987. Outward-dipping ring-fault structure at Rabaul Caldera as shown by earthquake locations. Science, 235, 193–195.

Mueller, W.U., Mortensen, J.K., 2002. Age constraints and characteristics of subaqueous volcanic construction, the Archean Hunter Mine Group, Abitibi greenstone belt. Precamb. Res., 115, 119–152.

Munro, D.C., Rowland, S.K., 1996. Caldera morphology in the western Galapagos and implications for volcano eruptive behaviour and mechanism of caldera formation. J. Volcanol. Geotherm. Res., 72, 85–100.

Nappi, G., Renzulli, A., Santi, P., 1991. Evidence of incremental growth in the Vulsinian calderas (central Italy). J. Volcanol. Geotherm. Res., 47, 13–31.

Newhall, C.G., Dzurisin, D., 1988. Historical Unrest at Large Calderas of the World. U.S. Geol. Sur. 1109 pp.

Odonne, F., Ménard, I., Massonnat, G.J., Rolando, J.P., 1999. Abnormal reverse faulting above a depleting reservoir. Geology, 27, 111–114.

Orsi, G., De Vita, S., di Vito, M., 1996. The restless, resurgent Campi Flegrei nested caldera (Italy): constrains on its evolution and configuration. J. Volcanol. Geotherm. Res., 74, 179–214.

Ramberg, H., 1981. Gravity, Deformation and the Earth's Crust, 2nd edn. Academic Press, London, 452 pp.

Roche, O., Druitt, T.H., Merle, O., 2000. Experimental study of caldera formation. J. Geophys. Res., 105, 395–416.

Roche, O., van Wyk de Vries, B., Druitt, T.H., 2001. Sub-surface structures and collapse mechanisms of summit pit craters. J. Volcanol. Geotherm. Res., 105, 1–18.

Sanford, A.R., 1959. Analytical and experimental study of simple geological structures. Bull. Geol. Soc. Am., 70, 19–52.

Saunders, S.J., 2001. The shallow plumbing system of Rabaul caldera: a partially intruded ring fault? Bull. Volcanol., 63, 406–420.

Self, S., Goff, F., Gardner, J.N., Wright, J.V., Kite, W.M., 1986. Explosive rhyolitic volcanism in the Jemez Mountains: vent locations, caldera development and relation to regional structure. J. Geophys. Res., 91, 1779–1798.

Setterfield, T.N., Eaton, P.C., Rose, W.J., Sparks, S.J., 1991. The Tavua caldera, Fiji: a complex shoshonitic caldera formed by concurrent faulting and downsagging. J. Geol. Soc. Lond., 148, 115–127.

Skilling, I.P., 1993. Incremental caldera collapse of Suswa volcano, Gregory Rift Valley, Kenya. J. Geol. Soc. Lond., 150, 885–896.

Spinks, K., Acocella, V., Cole, J., Bassett, K., 2005. Structural control of volcanism and caldera development in the transtensional Taupo Volcanic Zone, New Zealand. J. Volcanol. Geotherm. Res., 144, 7–22.

Stix, J., Kennedy, B., Hannington, M., Gibson, H., Fiske, R., Mueller, W., Franklin, J., 2003. Caldera-forming processes and the origin of submarine volcanogenic massive sulfide deposits. Geology, 31, 375–378.

Talbot, C.J., 1999. Can field data constrain rock viscosities? J. Struct. Geol., 21, 949–957.

Troll, V.R., Walter, T.R., Schmincke, H.U., 2002. Cyclic caldera collapse: piston or piecemeal subsidence? Field and experimental evidence. Geology, 30, 135–138.

Walker, G.P.L., 1984. Downsag calderas, ring faults, caldera sizes, and incremental caldera growth. J. Geophys. Res., 89, 8407–8416.

Walter, T.R., Troll, V.R., 2001. Formation of caldera periphery faults: an experimental study. Bull. Volcanol., 63, 191–203.

Williams, H., 1941. Calderas and their origin. Calif. Univ. Publ. Geol. Sci. Bull., 21, 239–346.

Yoshida, T., 1984. Tertiary Ishizuchi Cauldron, southwestern Japan Arc: formation by ring fracture subsidence. J. Geophys. Res., 89, 8502–8510.

This page intentionally left blank

# Magma-Chamber Geometry, Fluid Transport, Local Stresses and Rock Behaviour During Collapse Caldera Formation

Agust Gudmundsson*

## Contents

## Abstract

Collapse calderas are common on Earth and some other solid planetary bodies, particularly on Io (a satellite of Jupiter), Mars and Venus. Caldera structures are generally similar on all these bodies but the sizes vary considerably. Here I present numerical models of caldera-fault formation in volcanoes with shallow, spherical or sill-like magma chambers. In all the anisotropic models, the crustal segment (including the volcano) above the shallow chamber is composed of 30 comparatively thin layers with stiffnesses (Young's moduli) alternating between 1 and 100 GPa. The chamber itself

*Corresponding author. Tel.: 44 (0) 1784-443581; Fax: 44 (0) 1784-471780
*E-mail address:* a.gudmundsson@gl.rhul.ac.uk

Department of Structural Geology and Geodynamics, GZG, University of Göttingen, Germany; Department of Earth Sciences, Royal Holloway, University of London, Queens Building, Egham, Surrey, TW20 0EX, UK

is located in a single, thick layer with stiffness different from that of the other layers. The crustal segment hosting the chamber is either 20 or 40 km wide but has a constant thickness of 20 km. The loading conditions considered are crustal segments subject to: (a) underpressure (lack of magmatic support) of 5 MPa; (b) tensile stress of 5 MPa; (c) excess magmatic pressure of 10 MPa at the bottom of the crustal segment (doming of the volcanic field containing the chamber) and (d) combination of tension and doming. In all the models, the magma-chamber top is at 3 km depth; the diameter of the sill-like chamber is 8 km (its thickness is 2 km) while that of the spherical chamber is 4 km.

The main results are as follows: (1) Underpressure and excess pressure in a shallow, crustal chamber normally result in dyke injection rather than caldera formation. (2) For doming or tension, a spherical magma chamber normally favours dyke injection rather than ring-fault initiation. However, when the spherical chamber is located in a very soft (10 GPa) layer, the local stress field may be suitable for caldera-fault formation. (3) For a sill-like chamber in a 20-km-wide volcanic field, a ring fault may be initiated either during horizontal tension or a combination of tension and doming. (4) For a sill-like chamber in a 40-km-wide volcanic field, doming alone is sufficient to initiate a caldera fault. The results indicate that the local stresses in composite volcanoes most likely to initiate caldera faults are associated with sill-like chambers subject to tension, doming or both.

## 1. INTRODUCTION

In the last few decades it has become generally realised that collapse calderas are not confined to volcanic regions on Earth; they are common structures on several other solid planets and satellites. Known calderas in the solar system range in diameter from about 1.6 km to nearly 300 km and have been observed on Earth, Venus, Mars and Io (a satellite of Jupiter). Calderas may exist on many other planetary bodies, for example the Moon and Mercury, where most of the circular structures, however, are impact craters.

Traditionally, collapse calderas have been defined as circular or elliptical volcanic depression with a maximum diameter similar to or larger than about 1 mile or 1.6 km (Macdonald, 1972). When this lower limit is used, pit craters on Earth, which rarely exceed 1 km in diameter, can be distinguished from calderas (Okubo and Martel, 2001). While most calderas are actually elliptical in plan view, and many have rectangular margins along parts of, or the entire, periphery, the slip plane along which the main caldera subsidence takes place will here be referred to as a ring fault (Figure 1).

Clearly, the ring fault of a collapse caldera is a fracture; more specifically it is a shear fracture, that is, a fault. And as such it can only form under certain special stress conditions. Thus, to be able to forecast the likelihood of caldera formation or slip during an unrest period, we must understand the stress conditions that favour ring–fault formation. These stress conditions are still poorly understood and remain the main unsolved problem regarding collapse calderas.

Since ring faults are faults, we might expect that their formation could be understood within the general framework of earthquake mechanics. But there appear
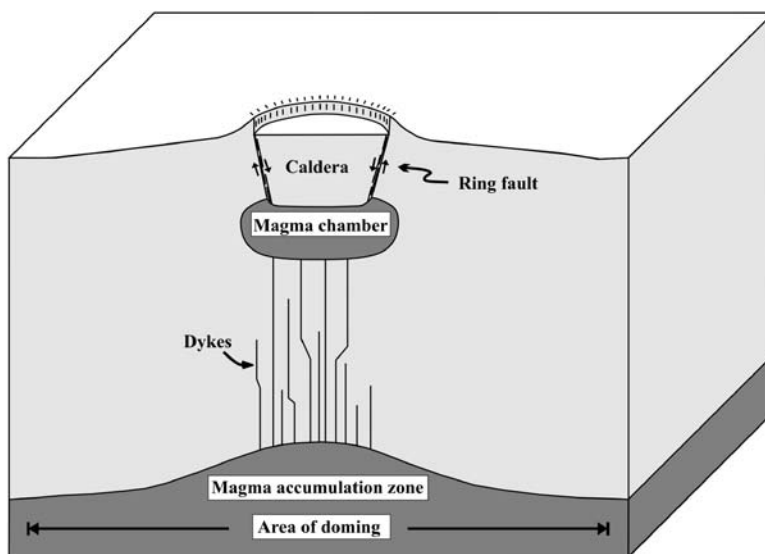
**Figure 1** Collapse caldera is normally associated with a magma chamber of a cross–sectional geometry similar to the caldera fault itself. While most collapse caldera faults are dip slip, some may be outward–dipping reverse faults whereas others are inward–dipping normal faults, like the one shown here. Many calderas occur in volcanic fields located above large magma–accumulation zones. The crustal segment hosting the field may, occasionally, be subject to magmatic pressure that gives rise to slight doming (uplift) of the field.

to be significant mechanical and geometric differences between ring faults and most earthquake faults. The first difference is that the calderas faults normally form closed — or near to closed — rings or ellipses. By contrast, earthquake faults are comparatively straight, if often composed of offset segments, and do not form closed loops.

A second difference is that the displacement during a single caldera-collapse event is normally much larger than the displacement during a single earthquake. In both cases, the fracture is primarily a shear fracture and the displacement is driven by shear stress concentration at the fault plane. In a very intense earthquake, the displacement (slip) may reach a maximum of 10–20 m. By contrast, many ring-fault displacements during a single caldera collapse reach hundreds of metres and some several kilometres.

The third difference concerns the fault dip. Ring faults are dip–slip faults (Figures 1 and 2). Dip-slip earthquake faults normally dip 45–75° (and less for thrust faults). By contrast, most ring faults are close to vertical (Figure 2). Since the mean angle between the direction of the maximum principal stress, $\sigma_1$, and the fault plane is unlikely to be different between caldera faults and earthquake faults, these observations indicate that there is a fundamental difference between the local stress fields controlling earthquake faulting and caldera faulting as regards orientation of the principal stresses at the time of fault formation or slip.

Many models and mechanisms have been proposed to explain ring-fault formation and caldera collapses (Anderson, 1936; Williams, 1941; Druitt and Sparks, 1984; Walker, 1984; Scandone, 1990; Chery et al., 1991; Marti et al., 1994;
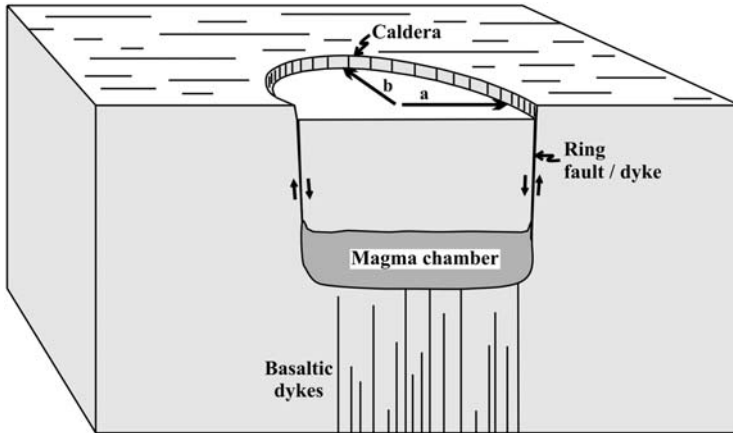
**Figure 2**  Caldera faults are commonly referred to as ring faults, as is done in this paper. Most caldera faults, however, are not perfect circles but rather ellipses where the radius or semi–major axis *a* is larger than the semi–minor axis *b*. Most measured caldera faults appear to dip close to vertical, as is indicated here.

Branney, 1995; Lipman, 1997; Gudmundsson, 1998a; Burov and Guillou–Frottier, 1999; Roche et al., 2000; Acocella et al., 2000, 2003, 2004; Newman et al., 2001; Walter and Troll, 2001; Saunders, 2001, 2004; Jellinek and DePaolo, 2003; Folch and Marti, 2004; Gray and Monaghan, 2004; Cole et al., 2005). All these models agree that the displacement along a ring fault is somehow related to the existence of a crustal magma chamber into which the caldera block, sometimes referred to as a 'piston', subsides. Before the subsidence takes place, however, the ring fault must form, and at present there is no consensus as to its mechanics of formation.

One principal aim of this paper is to put constraints on the mechanical conditions and processes that are likely to take place during ring-fault initiation and subsequent caldera collapse. These conditions and processes include the shape and local stress field of the associated magma chamber as well as the fluid transport out of the chamber prior to and during collapse. The focus is on ring-fault formation on Earth because this has been best studied and actually observed. Furthermore, ring faults on Earth are exposed not only at the surface but also in deeply eroded sections, thereby providing a three-dimensional view of the faults. Data on calderas on some other planets and satellites, however, are mentioned to emphasise the point that ring-fault formation is a universal feature of volcanism. The implication is that general models of caldera formation on Earth should, with suitable modifications, be equally applicable to calderas on other planetary bodies. In the section on caldera structure, there is thus a brief review of the geometries of extraterrestrial calderas. Any general discussion of calderas, however, refers to calderas on Earth.

A second principal aim is to present conceptual and numerical models of the most likely conditions for ring-fault formation and slip. The conceptual models aim at clarifying the issues of general ring-fault dip and caldera stability. Thus, the purpose of these models is to help clarify, first, whether ring faults are generally outward dipping or inward dipping and, second, how the dip relates to the process

of subsidence and general caldera stability. For example, it is known that many calderas have, subsequent to their formation, been filled with eruptive materials without slipping. The conceptual models help explain the conditions under which this is possible.

The principal aim of the numerical models is to clarify the stress conditions for ring-fault initiation so as to help forecast the likelihood of caldera collapse during future unrest periods. Various loading conditions and magma-chamber geometries are considered. In particular, I consider circular and sill-like chambers in layered crustal segments where the layers have widely different mechanical properties. The loading conditions in the models include magma-chamber underpressure and horizontal tension and slight doming of the segment hosting the chamber.

## 2. COLLAPSE CALDERA STRUCTURES

A collapse caldera is characterised by a ring fault (Figures 1 and 2). The ring fault is concentric and normally steeply inward dipping (Figure 2). Most ring faults are not perfect circles in plan view but rather elliptical, that is, radius $a$ in Figure 2 is larger than radius $b$. For example, in Iceland the average $a/b$ radius of collapse calderas in the active volcanic zones is about 1.4 (Gudmundsson and Nilsen, 2006). Acocella et al. (2003) discuss elliptical calderas in the Ethiopian Rift in Africa, and Holohan et al. (2005) provide a general review of elliptical calderas in various tectonic settings. Some calderas have rectangular margins, many of which are described by Spinks et al. (2005), for calderas on Earth, and by McEwen et al. (2000), Radebaugh et al. (2000, 2001) and Leutwyler (2003) for calderas on Io.

In the following paragraphs, I give a brief description of the caldera structures on Io, Mars and Venus, and compare them with calderas on Earth. A general outline of volcanic activity and landforms on the solid planetary bodies, however, is beyond the scope of the present paper. Fortunately, there are many recent reviews on extraterrestrial volcanism, including the relevant chapters in Sigurdsson (2000) and Lopes and Gregg (2004). Much general information is also provided by Frankel (2005). Physical data on the planetary bodies discussed here, as well as maps and photographs of many volcanoes and calderas, can be obtained from Lodders and Fegley (1998), Greeley and Batson (2001), Leutwyler (2003) and Miller and Hartmann (2005), as well as from the books and papers cited above and below.

There is a significant difference in caldera sizes on Earth and other planetary bodies (Figure 3). Since many calderas are multiple or form clusters, deciding the (maximum) diameter of a caldera may not be as straightforward as it might seem. This is, no doubt, the main reason for the different maximum sizes for calderas quoted by various authors. Nevertheless, Radebaugh et al. (2000, 2001) have analysed the sizes of calderas on Venus, Earth, Mars and Io. The size (diameter) distributions are negative exponential laws rather than normal (Gaussian) laws. The authors found that the mean diameter of calderas on Venus is about 68 km, on Mars 48 km and that on Io 41 km. Calderas on Venus reach up to 225 km in diameter (Frankel, 2005), and those on Io (the multiple caldera Tvashtar Catena) up to
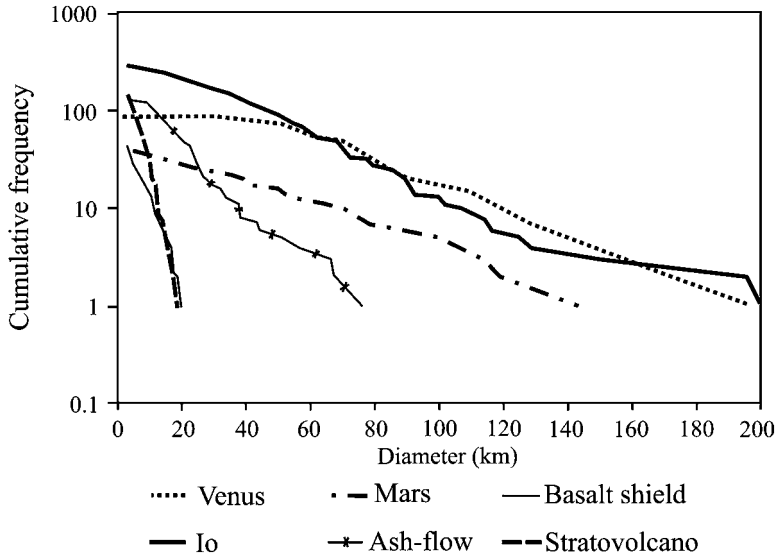
**Figure 3**    Calderas are not confined to the Earth but occur on several of the solid planets and satellites. The calderas on Mars, Venus and Io (a satellite of Jupiter) tend to be considerably larger than most calderas on Earth. Many, perhaps most, extraterrestrial calderas are not related to explosive eruptions but rather to a mechanism similar to that which generates shield–volcano calderas such as on the islands of Hawaii and Galapagos (modified from Radebaugh et al., 2000).

290 km (Leutwyler, 2003). Since many of the large calderas are multiple, and some large calderas, particularly on Venus, contain extensive sets of concentric fracture systems, the maximum diameter of the largest calderas is partly a matter of definition. There is no doubt, however, that many caldera diameters on Io and Venus exceed 200 km and the largest ones approach 300 km (Figure 3; Radebaugh et al., 2000; Leone and Wilson, 2000; Wilson, personal communication, 2006).

In a study of 97 calderas on Venus, Krassilnikov and Head (2004) found the average diameter to be about 68 km. Other studies indicate that the calderas are commonly 40–80 km in diameter (Head et al., 1992; Crumpler and Aubele, 2000; Pace and Krassilnikov, 2003). Most of the calderas are: (1) simple depressions, rather than located at the top of major volcanic edifices; (2) comparatively shallow, with depths of a few hundred metres to a maximum of 1.5 km; (3) unrelated to major rift zones and (4) if volcanically active then the activity followed (rather than being prior to) the collapse (Pace and Krassilnikov, 2003; Krassilnikov and Head, 2004).

Analysis of 292 calderas on Io gave a range in diameter from 2.5 to 203 km (Radebaugh et al., 2000). Although the mean caldera diameter is about 40 km, the mode (most common) diameter is close to 6 km. As indicated above, at the multiple caldera Tvashtar Catena is presumably the largest on Io and has a maximum diameter of at least 290 km (Leutwyler, 2003; Wilson, personal communication, 2006). Many calderas on Io have one or more comparatively straight sides and are thus clearly controlled by tectonic structures; some calderas on Io in fact appear to be related to regions of pull–apart (McEwen et al., 2000; Radebaugh et al., 2000).

When referred to as 'paterae' rather than calderas, as is common for Io, about 42% of the calderas have straight or irregular margins (Radebaugh et al., 2001).

The mean diameter of calderas on Mars is somewhat smaller than on Venus, or 48 km compared with 68 km on Venus, but larger than the mean diameter (41 km) of calderas on Io (Radebaugh et al., 2000, 2001). Perhaps the best known caldera on Mars is the multiple and nested caldera on Olympus Mons (Mouginis-Mark and Rowland, 2001), but many other calderas have been studied in detail (Crumpler et al., 1996; Scott and Wilson, 2000). Most of the calderas on Mars appear to have inward-dipping fault scarps (Scott and Wilson, 2000).

Calderas on Earth are much smaller than those on Venus, Mars and Io. Earth calderas vary in maximum diameter from about 1.6 km to about 80 km, the largest one being multiple or geometrically complex (Lipman, 2000) like the largest calderas on other planetary bodies. Calderas on Earth can be classified in various ways according to the types of volcanoes to which they belong (Francis, 1993; Lipman, 2000; Radebaugh et al., 2001; Krassilnikov and Head, 2004; Cole et al., 2005). Generally, however, calderas associated with basaltic shield volcanoes (Hawaii, Galapagos) tend to be smaller than those associated with composite volcanoes (including 'ash flow' calderas). Thus, the mean maximum diameter of active calderas associated with shield volcanoes is 6–7 km, whereas that of calderas associated with composite volcanoes is 18–19 km (Radebaugh et al., 2001). Similarly, maximum diameters of Quaternary calderas range from about 1.6 to 50 km, with about 94% of them having maximum diameters of less than 20 km (Lipman, 1997; Krassilnikov and Head, 2004).

Many calderas on Earth have been filled with lava flows to their rims. For example, the Mokouaweoweo caldera at the Mauna Loa volcano, Hawaii, shows clear evidence of lava flows having flowed out of the present caldera rims, suggesting that when lava flowed the caldera was full. Similar results have been obtained from the Kilauea caldera, suggesting that both calderas have been filled to overflow during the past 1,000 years (Mouginis-Mark and Rowland, 2001). Also, the Galapagos calderas are all of similar diameters (average 6 km) but the depths vary from about 200 m (Sierra Negra) to about 920 m (Fernandina). These calderas show clear evidence of having varied in depth over time, presumably partly as a function of the degree of lava filling. Furthermore, there is evidence that some calderas on Mars and Venus have become partly or completely filled with lava flows (Mouginis-Mark and Rowland, 2001).

Partial and complete filling of calderas has implications for their mechanical strength and stability and, therefore, for the dips of the ring faults. There is no doubt that most ring faults are subvertical dip-slip faults (Figures 1, 2 and 4–9). While it is likely that the dips of ring-fault segments vary depending on the local stresses in individual layers, particularly in composite volcanoes (Figure 4 and 9), the average dip is an important factor in any model of ring-fault formation (Gudmundsson and Nilsen, 2006). Some studies indicate that the general dip of the ring fault is outward from the centre of the caldera (Williams et al., 1970; Branney, 1995; Cole et al., 2005); other studies indicate that the ring fault is generally steeply inward-dipping (Macdonald, 1972; Filson et al., 1973; Aramaki, 1984; Lipman, 1984, 1997, 2000; Newhall and Dzurisin, 1988; Gudmundsson, 1998a;
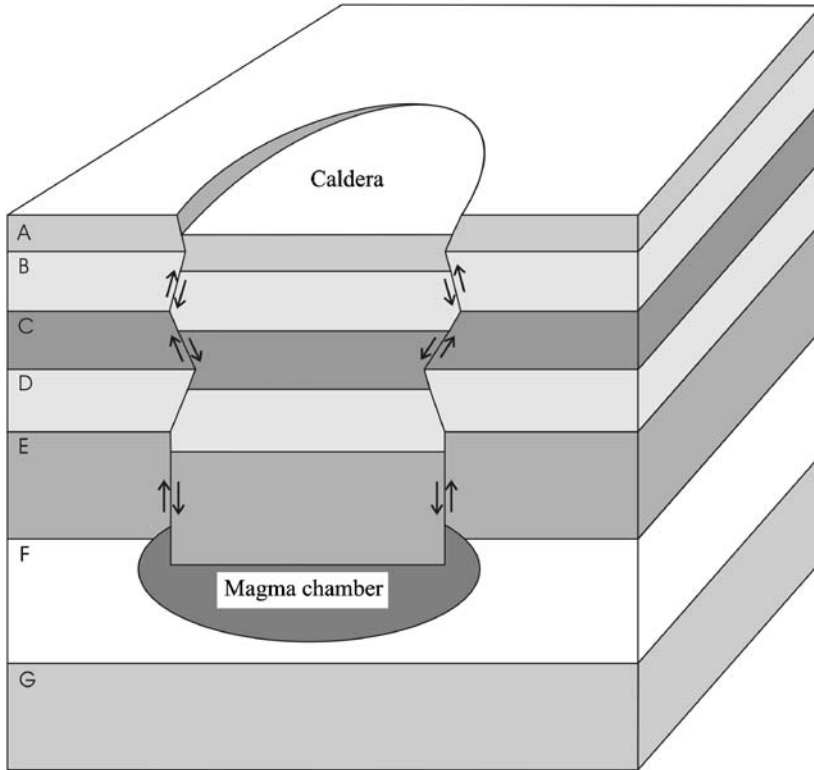
**Figure 4**  When the mechanical properties (particularly Young's modulus) of the layers that constitute a composite volcano change abruptly from one layer to another, the local stresses in the layers may be very different. Consequently, the local stresses that favour outward-dipping ring-fault segments in some layers may favour vertical or inward-dipping segments in other layers (Gudmundsson, 2007).

Geshi et al., 2002). It should be noted that Glencoe in Scotland is often taken as an example of an outward-dipping ring fault but is actually a tilted ring fault — part of the fault dips outward and part inward — that was originally with a dip close to vertical (Anderson, 1936).

The conceptual model of a steeply inward-dipping ring fault is supported by the well-documented collapse of the Fernandina caldera in the Galapagos Islands in 1968; the collapse occurred on a ring-fault dipping inward at about 80° (Simkin and Howard, 1970). More recently, the collapse of the Miyakejima caldera in Japan in 2000 was primarily on an inward-dipping ring fault (Geshi et al., 2002). Also, many ring faults are occupied by dykes, most of which are vertical or steeply inward dipping (Oftedahl, 1953; Almond, 1977).

Lava flows that erupt on the floor of a caldera indicate, first, that there is an active (that is, at least partly fluid) magma chamber beneath the caldera (Figure 5). Clearly, if there was no magma chamber beneath the caldera there would be no source for the lava flows to be erupted inside the caldera. In fact, eruptions inside calderas are very common, both on Earth (Newhall and Dzurisin, 1988) and
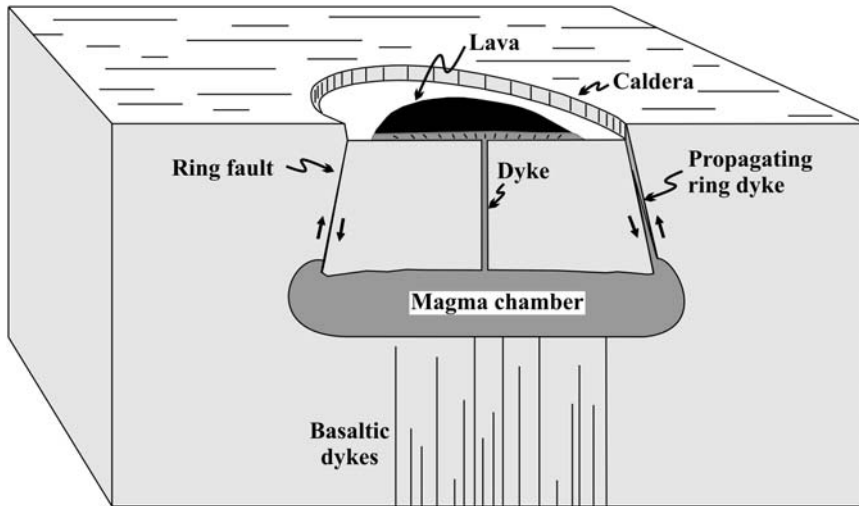
**Figure 5**   Many calderas become filled with eruptive materials, mainly lava flows, without slipping. Active volcanism inside a caldera indicates that there must be a fluid magma chamber beneath the caldera. If the caldera fault were outward dipping, one would expect slip to occur due to the extra loading from the lava flows inside the caldera (Figure 6). Dyke-fed eruptions inside a reverse-fault caldera would encourage slip since the overpressure associated with a dyke generates horizontal compressive stress on part of the ring fault, and this stress favours reverse movement along the fault (cf. Figure 8).
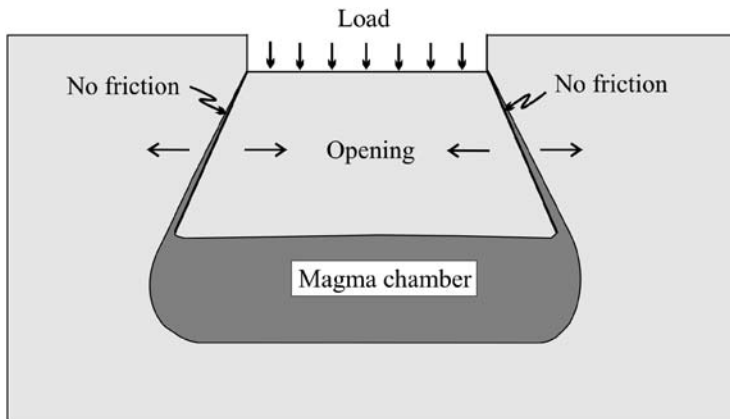


**Figure 6**   Eruptive material that accumulates on the floor of an existing caldera generates load (Figure 5). For an outward-dipping ring fault, the vertical load has the effect of opening up the fault, resulting in very little friction along the fault walls, particularly if there forms or exists a non-solidified ring dyke along the fault. It is thus not clear, for an outward-dipping fault, how new lava flows can pile up in the caldera without ring-fault slip.

elsewhere in the solar system (Scott and Wilson, 2000; Mouginis-Mark and Rowland, 2001). Second, when lava flows fill the caldera and overflows its rims the indication is that the caldera is able to sustain the extra load without a corresponding slip on the existing ring fault. The present Fernandina caldera is

as deep as 900 m. If it became filled with lava flows, as has occurred on many of the Galapagos calderas, the extra load on the caldera floor would be 20–25 MPa (Figure 6). That the caldera is able to sustain this load without slip has implications for the likely dip of the ring fault.
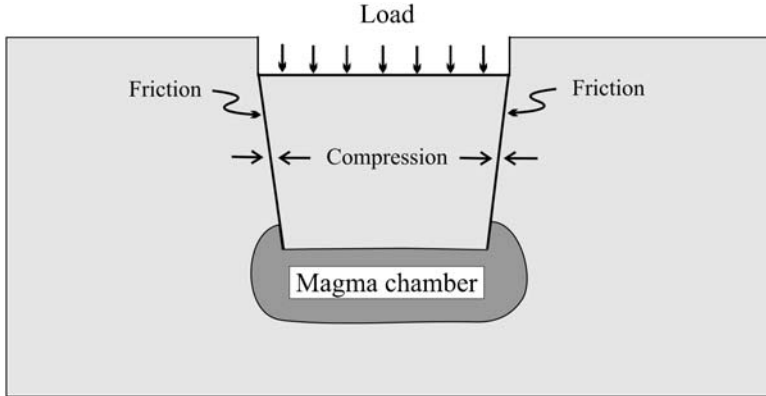


**Figure 7** Vertical loading of a caldera floor by eruptive material such as lava flows need not cause slip on an inward-dipping ring fault, anymore than on graben faults. Because of the inward dip, the vertical load generates compressive stresses across the ring fault, resulting in resistance to vertical slip. Calderas associated with inward-dipping ring faults can thus be filled with eruptive materials without slipping.
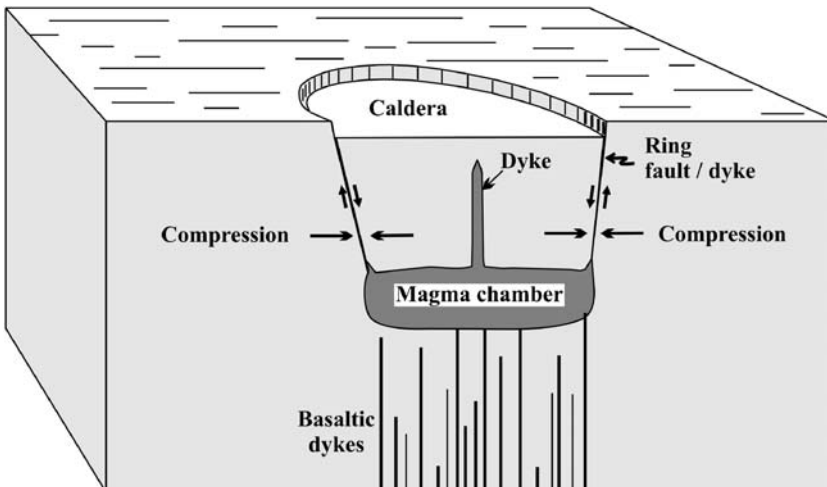


**Figure 8** Many caldera-floor eruptions are fed by dykes, the overpressure of which generates additional compressive stress on parts of the ring fault. For an inward-dipping fault, the compressive stress would encourage reverse movements on an otherwise normal fault and thus tend to lock the fault and make it non-slipping. By contrast, overpressured dykes would tend to encourage slip on an outward-dipping ring fault (Figure 5).
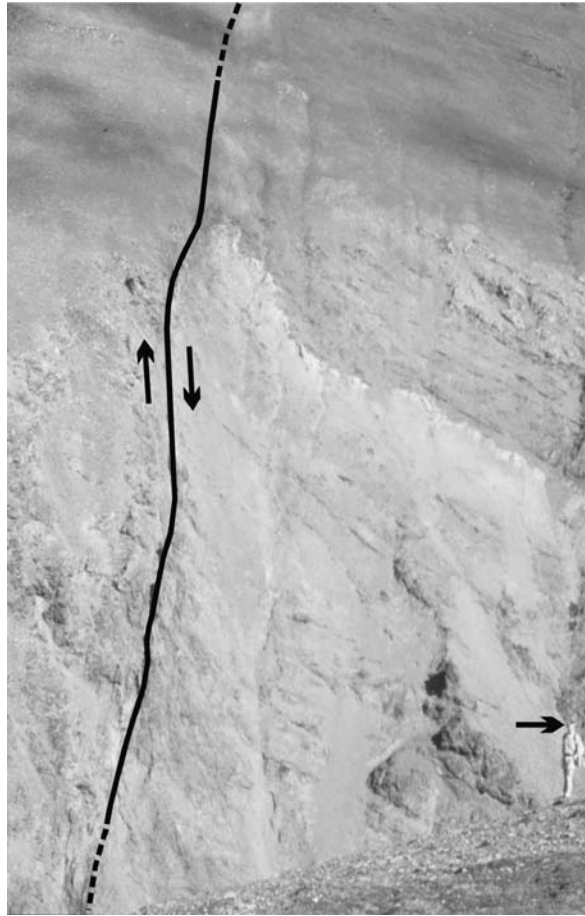
**Figure 9** Ring faults tend to be subvertical, but are often with somewhat variable dip. Here is a part of the ring fault (indicated) of the Tertiary Hafnarfjall central volcano in West Iceland. The vertical displacement across the fault is estimated at several hundred metres. A person (indicated by a white arrow) provides a scale.

There have been many discussions about the overall dip of collapse calderas (Figures 4–9); the main data are summarised by Gudmundsson and Nilsen (2006). Clearly, an outward-dipping fault that extends into a shallow magma chamber, as it must do when the chamber is the source for new lava flows erupted at the bottom of the caldera, would tend to slip as soon as the lava pile inside the caldera reached a moderate thickness. This follows from the load generated by the lava pile and the extension (and thus lack of friction) between the subsiding caldera block and the ring-fault wall resulting from the load-generated displacement (Figure 6).

For an inward-dipping ring fault, by contrast, the load-generated vertical displacement does not result in any extension across the ring fault (Figure 7). But there is, of course, extension across the fault due to the tensile stress concentration (because of doming, horizontal tension or both) as discussed below. Also, when

eruptions onto the caldera floor are supplied with magma through dykes (Figure 8), the compressive stresses generated by the dykes would encourage reverse slip on an otherwise normal ring fault and, thus, tend to lock the fault. Because of friction along the fault plane (Figures 7 and 9), ring-fault slip is much more easily stopped on an inward-dipping fault, after a certain displacement, than on an outward-dipping fault (Figure 6).

## 3. Geometry of the Magma Chamber

Most ring faults are generated by the local stresses around crustal magma chambers (Figures 1, 2 and 4–8). Field studies of plutons in deeply eroded palaeovolcanic zones suggest that many crustal chambers, at least during the end stages of their evolution, have shapes not far from ideal ellipsoids (Gudmundsson, 2006; Gudmundsson and Nilsen, 2006).

In Iceland, for example, there are many well-exposed crustal magma chambers (plutons) at 1.5–2 km depth of erosion in extinct composite volcanoes (central volcanoes, stratovolcanoes). Most of these plutons, representing the uppermost parts of extinct shallow crustal magma chambers, are of gabbro (Gudmundsson, 2000a, 2006). But there are also many felsic plutons in deeply eroded roots of extinct composite volcanoes in Iceland. Similarly, extinct crustal magma chambers of various sizes and depths of exposure occur in other deeply eroded volcanic regions on Earth, such as in Scotland (Upton, 2004).

Commonly, there are ring faults and ring dykes associated with the extinct chambers. The caldera fault in the Tertiary Hafnarfjall Volcano in West Iceland (Figure 9), for example, can be traced to a shallow gabbro pluton, the uppermost part of an extinct magma chamber (Gautneb et al., 1989). Extinct, well-exposed crustal magma chambers of this type, as well as geophysical studies of active magma chambers, indicate that chamber geometries are commonly approximately similar to ideal ellipsoidal bodies (Figure 10; Gudmundsson, 1998b, 2002, 2006). Shallow chambers are normally located in crustal segments, which, during most unrest
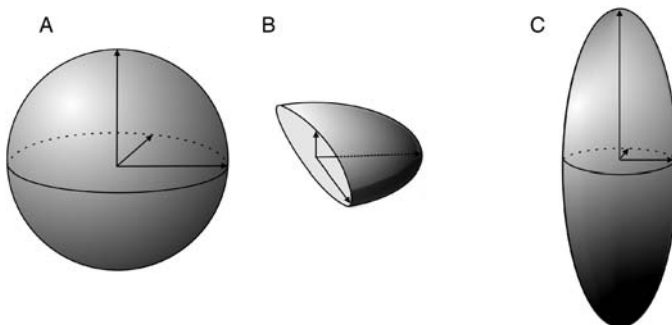


**Figure 10**   Ideal magma chambers are ellipsoidal. Three main ellipsoidal geometries of magma chambers are (A) a sphere, (B) an oblate ellipsoid, that is, a sill-like chamber, only half of which is shown here and (C) a prolate ellipsoid (modified from Gudmundsson and Nilsen, 2006).

periods, behave as elastic. Such a crustal magma chamber may thus be modelled as a finite-size cavity or, for a two-dimensional model, a hole in an elastic host rock when fluid, and as an elastic inclusion when solidified. These lead to different stress concentrations since the fluid in the cavity may have zero Young's modulus (stiffness) whereas the inclusion stiffness is non-zero.

On solidification, the stiffness of the magma in the chamber increases until the chamber rock and the host rock reach similar temperatures. If the chamber rock and the host rock have similar composition, the stiffness of the solidified magma in the chamber may then approach that of the host rock. The chamber (pluton) is then mechanically an elastic inclusion (Eshelby, 1957). All cavities (Savin, 1961; Yu, 2000) and inclusions with stiffnesses different from that of the host rock (Eshelby, 1957; Lekhnitskii, 1968) and subject to loading concentrate stress and generate a local stress field (Gudmundsson, 2006). This local stress field controls the formation and slip of ring faults.

Magma chambers with volumes as great as hundreds or thousands of cubic kilometres, and even larger for some of the volcanoes on Venus, Mars and Io, are clearly formed over considerable periods of time. The exact mechanism by which magma chambers form is not known, but some kind of magma traps must be generated in order to arrest the magma and form the chamber. One possibility of generating chambers is through stress barriers that lead to the formation of thick sills that subsequently absorb the magma of the dykes that enter them and evolve into chambers (Gudmundsson, 2006). The protochamber is obviously much smaller than the mature chamber, so that it must somehow generate space for itself. The problem of space for large plutons (or magma chambers) is an old one, but it is clear that the space is partly generated by elastic–plastic expansion of the crust, partly by partial melting of the crust, and partly by stoping.

During its growth, the magma chamber not only becomes larger but may also change its shape. These two factors, that is, increase in size relative to depth below the surface and change in shape, have strong effects on the local stress field around the chamber and, hence, on the probability of generating collapse calderas (Gudmundsson and Nilsen, 2006). Certain shapes of magma chambers, particularly sill-like (oblate ellipsoidal), favour the formation of collapse calderas whereas other shapes such as prolate ellipsoidal, do not (Figure 10).

During its evolution, and associated changes in shape and size, a particular magma chamber may from time to time have a shape that is favourable to caldera formation, whereas during the main part of its lifetime it may have shapes that are unfavourable to caldera formation (Gudmundsson, 2006; Gudmundsson and Nilsen, 2006). The evolution of a magma chamber partly explains, first, why caldera formation or slip on an existing ring fault is such a rare event in evolution of a volcano in comparison with the number of eruptions (Walker, 1984; Newhall and Dzurisin, 1988) and sheet and dyke injections (Gudmundsson, 2002, 2006; Gudmundsson and Nilsen, 2006). Second, why caldera collapse can occur repeatedly at the same volcano while its magma chamber may change its location, shape or both. In fact, multiple and nested calderas are very common on Earth (Figures 11 and 12) as well as on Venus, Mars and Io (Scott and Wilson, 2000; Mouginis-Mark and Rowland, 2001; Lopes and Gregg, 2004; Frankel, 2005), and imply changes with time in magma chamber shape, size and, possibly, location.
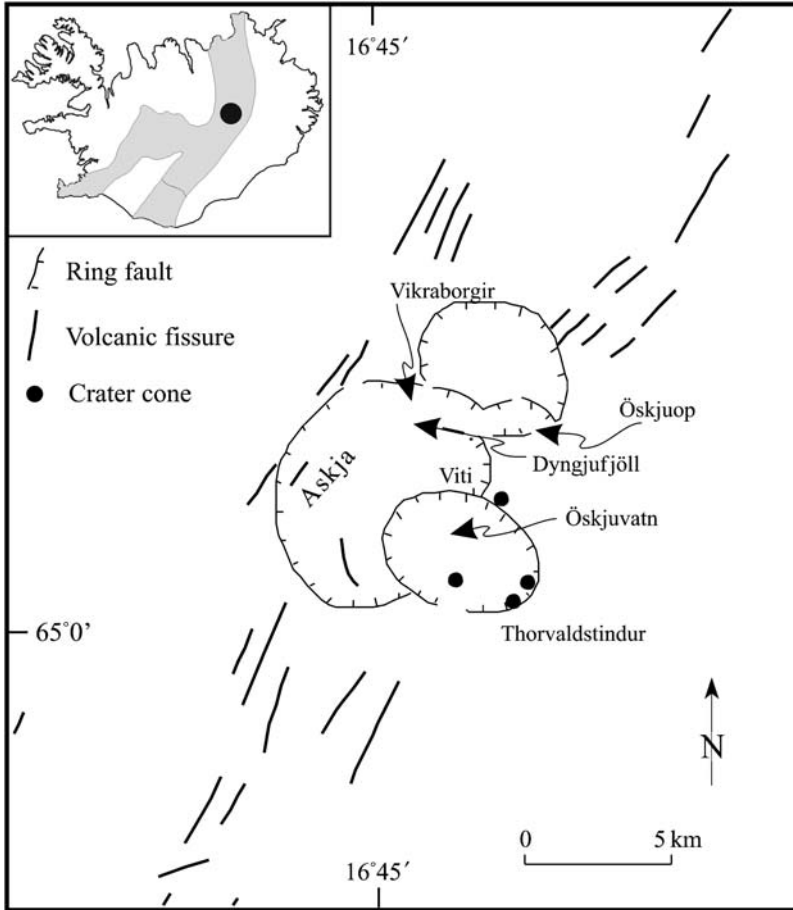
**Figure 11**  Multiple and nested calderas are common in many volcanic regions. Here is the triple caldera of the Dyngjufjöll-Askja central volcano in central Iceland. The northernmost caldera has no name and is of unknown age, but the other two are the Askja caldera formed at 5000–6000 BP, and the Lake Öskuvatn caldera, which formed following the AD 1875 Askja eruption. The vertical displacement along the ring fault of the Askja caldera is at least 180 m, while that on the ring fault of the Lake Öskuvatn caldera is 250 m (modified from Thorarinsson, 1963).

And, third, why many calderas remain inactive during the subsequent evolution of the associated magma chamber. This last point, elaborated below, follows from the shape of the chamber becoming unfavourable to ring-fault slip while being favourable to dyke and sheet injections and eruptions.

## 4. Behaviour of Crustal Rocks

The mechanical behaviour of crustal rocks in the laboratory has been studied extensively and is now comparatively well known (Jaeger and Cook, 1979;
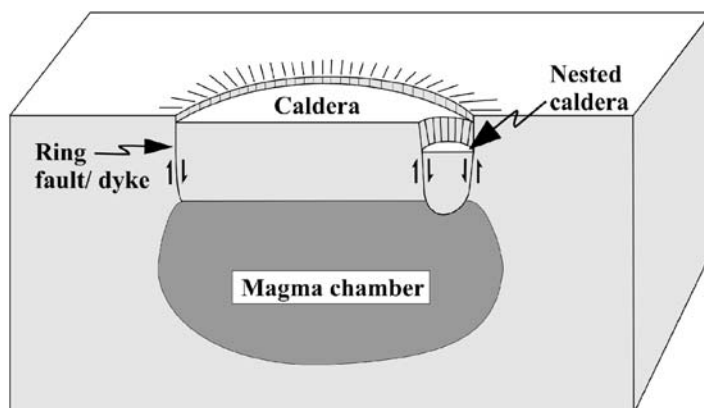
**Figure 12**    Schematic illustration of a nested collapse caldera similar to the pair Askja–Lake Öskuvatn in central Iceland (Figure 11).

Farmer, 1983; Hudson and Harrison, 1997; Bell, 2000; Schön, 2004). At low temperature and pressure and reasonably high strain rates, most solid rocks behave as approximately linear elastic up to about 1% strain. For a completely anisotropic (triclinic) linear elastic material, there are 21 independent elastic constants to be considered (Love, 1927; Nye, 1957; Hudson and Harrison, 1997).

It is not feasible to model rocks as completely anisotropic, but quite a few numerical solutions have been obtained from models where the rock body is regarded as transversely isotropic (layered), in which case three independent constants must be specified (Hudson and Harrison, 1997). The most common approach for layered rocks, however, is to regard each individual layer as homogeneous and isotropic, for which two independent constants are needed, and then introduce the anisotropy through layers, contacts and discontinuities with different mechanical properties.

The two elastic constants or moduli most commonly used in rock physics are Young's modulus and Poisson's ratio. Young's modulus is a measure of the rock stiffness, and is often referred to as stiffness. When determining which Young's moduli to use for rock layers in a numerical model, there are certain aspects as to its measurements and values that must be taken into account. First, for a given rock body, particularly at shallow depths in a composite volcano or rift zone, the dynamic modulus is normally much higher than the static modulus (Goodman, 1989; Schön, 2004). For a highly fractured and porous rock at shallow depths, the dynamic modulus may be as much as 10–15 times higher than the static modulus of the same rock.

Second, small-sample laboratory measurements, dynamic and static, yield stiffness values that are commonly 1.5–5 times greater than those of the field modulus of the same rock (Heuze, 1980). For igneous and metamorphic rocks, the laboratory modulus is commonly three times the field modulus.

Third, with increasing depth or mean stress Young's modulus generally increases (Heuze, 1980). Fourth, with increasing temperature, porosity and water content, or a combination of these, Young's modulus decreases.

At shallow crustal depths in tectonically active areas, the field Young's modulus of a rock unit depends strongly on the fracture frequency of that unit (Priest, 1993). It is well known that Young's modulus of a rock mass is normally less than that of a laboratory sample of the same type of rock. This difference is mainly attributed to fractures and pores in the rock mass, which do not occur in small laboratory samples (Farmer, 1983; Priest, 1993). With increasing number of fractures, in particular in a direction perpendicular to loading, the ratio $E_{is}/E_{la}$ ($E$ in situ/$E$ laboratory) shows a rapid decay. Similar results are obtained for elastic materials in general (Sadd, 2005). Thus, as the fracture frequency and porosity increase in a rock unit, its Young's modulus normally decreases.

Another parameter of great importance for collapse caldera formation is rock strength. Usually, one distinguishes between three types of rock strengths: tensile strength, shear strength and compressive strength. Theoretically, the shear strength should be about twice the tensile strength, and the compressive strength about 10 times the tensile strength (Jaeger and Cook, 1979). These theoretical predictions are generally supported by observations. Laboratory tensile strengths range up to a few tens of megapascals (Jumikis, 1979; Myrvang, 2001), compressive strengths up to a few hundred megapascals and shear strengths are somewhere in between these extremes, mostly close to twice the tensile strengths (Jumikis, 1979; Bell, 2000; Nilsen and Palmström, 2000; Myrvang, 2001). For ring-fault formation, tensile and shear strengths are the most important.

The field or in situ values of these strengths, however, are normally much lower than the laboratory values. Perhaps, the best-studied field strength is the tensile strength. It has been estimated from numerous hydraulic fracturing experiments in solid rocks worldwide. This method of testing is very suitable for magma chambers and dyke emplacement since the in situ tensile strength is estimated from the fluid pressure (in excess of the minimum compressive stress) that is needed to fracture open the rock (Amadei and Stephansson, 1997). The results indicate that the tensile strength of solid rocks has a comparatively narrow range, that is, 0.5–6 MPa and most commonly 2–3 MPa (Haimson and Rummel, 1982; Schultz, 1995; Amadei and Stephansson, 1997). For comparison, the driving shear stress (estimated from the stress drop) of earthquakes generally ranges between 1 and 10 MPa and is most commonly 3–6 MPa (Kanamori and Anderson, 1975; Scholz, 1990), or roughly twice the tensile strength. At the high temperatures close to the margin of a fluid magma chamber, the tensile (and thus the shear) strength is likely to decrease somewhat, but still be within the ranges indicated above.

In some numerical models in this paper, I use the laboratory rock stiffnesses but scale them down to reasonable field values using the information above. The highest stiffness used in the models, 100 GPa, may occur in nature, but is here used mainly to emphasise the stress-field effects of the contrast with the soft layers. In none of the models, however, do I use the most extreme stiffnesses one might encounter in composite volcanoes. For example, laboratory measurements of volcanic tuffs yield stiffnesses as low as 0.05–0.1 GPa (Afrouz, 1992; Bell, 2000), in which case the field stiffnesses could be even lower. Similarly, laboratory measurements of some rocks yield stiffnesses as high as 150–200 GPa (Myrvang, 2001). In the models, all the stiffness values used are within the range of 1–100 GPa.

Many authors have suggested that surrounding the magma chamber there is a shell of rock that behaves as elastic–plastic or viscoelastic (e.g., Bonafede et al., 1986; Chery et al., 1991; Burov and Guillou-Frottier, 1999; Newman et al., 2001; Jellinek and DePaolo, 2003). It is of course quite possible that the rocks in such a shell behave as, for example, elastic–plastic, and in the numerical models below the von Mises shear stress (Jaeger and Cook, 1979) is used to indicate the likely location of ring faults. Most dykes in the roofs and envelopes of shallow magma chambers studied in Iceland, however, are extension fractures that seem to propagate primarily as elastic cracks during volcanic unrest periods (Gudmundsson, 2006). In this paper, the rock properties prior to failure are assumed elastic.

## 5. Magma-Chamber Rupture and Fluid Transport Along a Dyke

For magma to be transported out of a magma chamber, a sheet or a dyke must be initiated at the margin of the chamber and be able to propagate into the host rock. For an eruption to occur, the sheet or dyke must be able to propagate through all the rock layers and contacts between the point of rupture at the margin of the chamber and the free surface of the associated volcano. Based on the Griffith crack theory, and supported by analogy with the results of numerous hydraulic–fracture experiments worldwide (Valko and Economides, 1995; Yew, 1997), a magma-filled chamber ruptures and initiates a sheet or dyke when the following condition is satisfied:

$$p_1 + p_e = \sigma_3 + T_0 \tag{1}$$

Here $p_1$ denotes the lithostatic stress (or pressure) at the depth of the chamber; $p_e = p_t - p_l$, the excess magmatic pressure, is the difference between the total magma pressure, $P_t$, in the chamber at the time of its rupture and the lithostatic stress or pressure; and $\sigma_3$ and $T_0$ denote the minimum principal stress and the in situ tensile strength, respectively, at the site of rupture of the chamber. Here and elsewhere in this paper, compressive stress is considered positive. Therefore, when there is an absolute tension, $\sigma_3$ is negative (but is here given by its absolute value), whereas the maximum compressive principal stress, $\sigma_1$, is always positive.

The local $\sigma_3$ and $T_0$ are the relevant parameters in Equation (1). It follows that sheet injection occurs when the condition of Equation (1) is reached at any point at the margin of the chamber, irrespective of the chamber shape and depth below the surface. The condition of Equation (1) is reached by increasing $p_e$, decreasing $\sigma_3$ or both (Gudmundsson, 2002, 2006). Since Equation (1) refers to the local $\sigma_3$ stress concentration, effects due to the shape of the magma chamber, including irregularities at its boundary, are automatically taken into account. Thus, Equation (1) does not represent the condition for the rupture of a fluid-filled cavity in terms of maximum and minimum compressive regional stresses ($\sigma_H, \sigma_h$), as is normal when dealing with hydraulic fractures initiated from boreholes (Valko and Economides, 1995; Amadei and Stephansson, 1997; Yew, 1997; Charlez, 1997).

In contrast to a newly drilled borehole, a magma chamber is a long-lived fluid-filled structure that is presumably in lithostatic equilibrium with its surroundings for most of its lifetime. Thus, in Equation (1), the normal condition everywhere along the margin of the chamber is $p_1 = \sigma_3(= \sigma_1)$. During short periods, that is unrest periods, the situation may be $p_e > 0$, either because of added volume of magma (absolute increase in the chamber excess pressure) or reduction in $\sigma_3$. It is during these periods that the condition of Equation (1) may be satisfied, resulting in rupture and sheet or dyke initiation.

The initiated sheet may propagate for only a short distance from the chamber, and then become arrested (Gudmundsson, 2002; Gudmundsson and Brenner, 2005). Alternatively, the sheet may propagate to the surface and supply magma to an eruption. Consider a chamber located in a host rock that behaves as elastic and a sheet inclined (dipping) at an angle of $\alpha$ to the surface (Figure 13), where the vertical co-ordinate $z$ is positive upwards. Then it follows from the Navier–Stokes equation (Lamb, 1932; Milne-Thompson, 1996) that the volumetric flow rate $Q_L^e$ through an ideal, parallel-wall sheet (a magma-filled fracture) is (Gudmundsson and Brenner, 2005):

$$Q_L^e = \frac{\Delta u^3 W}{12\mu} \left[ (\rho_r - \rho_m)g \, \sin\alpha - \frac{\partial p_e}{\partial L} \right] \tag{2}$$

In the symbol for the volumetric flow rate $Q_L^e$, the superscript $e$ is used to indicate that the fracture occurs in an elastic rock and the subscript $L$ denotes the dip-dimension (distance of magma transport) of the sheet. Here, $\Delta u$ is the aperture (opening) of the fracture (similar to the thickness of the inclined sheet after
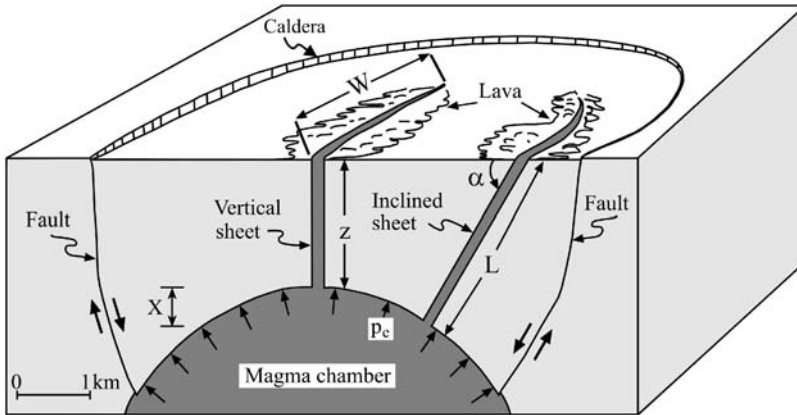


**Figure 13** Flow of magma through a dyke or an inclined sheet to the surface of a caldera (cf. Figures 5 and 8; modified from Gudmundsson and Brenner, 2005). The volumetric flow rate $Q$ depends on the dip and dip dimension of the feeder. A vertical dyke has a dip dimension $z$. An inclined sheet with a dip $\alpha$ has a dip dimension $L$. For the dyke and the sheet, the surface trace length (outcrop length) perpendicular to the magma-flow direction is denoted by $W$. The excess magmatic pressure in the chamber is $p_e$, and the difference is depth between the point of initiation of the vertical and the inclined sheet is denoted by $X$ (cf. Equation (2)).

solidification), $W$ the fracture width in a direction perpendicular to the flow direction (assuming $W \gg \Delta u$, the fracture cross-sectional area perpendicular to the flow is $A = \Delta u W$), $\mu$ the dynamic (absolute) viscosity of the magma, $\rho_r$ the host-rock density, $\rho_m$ the magma density (assumed constant), $g$ the acceleration due to gravity, and $\partial p_e / \partial L$ the pressure gradient in the direction of the flow. This equation ignores possible stress gradients in the host rock, for example, due to variation in mechanical properties and thus local stresses, topography of the volcano or both.

When the flow is vertical, that is, along a vertical dyke, the dip $\alpha = 90°$ so that $\sin \alpha = 1$, and substituting $z$ for $L$ (Figure 13), we get:

$$Q_z^e = \frac{\Delta u^3 W}{12\mu} \left[ (\rho_r - \rho_m)g - \frac{\partial p_e}{\partial z} \right] \tag{3}$$

Similarly, when the magma flow is horizontal, either along a sill or a laterally propagating dyke, then the dip $\alpha = 0°$ and $\sin \alpha = 0$. Consequently, the first term in the brackets in Equation (2) drops out. For a sill in the horizontal $xy$-plane, the width $W$ is measured along the $y$-axis; for or a laterally propagating dyke in the vertical $xz$-plane, the width $W$ is measured along the $z$-axis. In either case, if the magma flow is assumed to be along a mechanical layer with a density equal to that of the magma (the assumption of a 'neutral buoyancy') and the length $L$ is measured along the $x$-axis, then we may substitute $x$ for $L$ in Equation (2) to obtain volumetric magma flow rate $Q_x^e$:

$$Q_x^e = -\frac{\Delta u^3 W}{12\mu} \frac{\partial p_e}{\partial x} \tag{4}$$

Thus, in the absence of a stress gradient, the only pressure gradient for driving magma flow through a dyke (or a sill) emplaced laterally along a neutral buoyancy layer is due to the excess pressure $p_e$ in the magma chamber.

In terms of mechanics of collapse caldera formation, Equation (4) indicates that for fluid to be driven out of a chamber there must be excess pressure $p_e > 0$ in the chamber. If this excess pressure falls to zero, there is no pressure gradient available to drive the magma out of the chamber, and the magma flow should stop. It follows that for the underpressure models or 'withdrawal of magmatic support' for explaining ring-fault formation, which commonly assume that underpressure is generated because of flow of magma out of the chamber along a laterally propagating dyke, it must be shown that somehow Equation (4) is not valid during caldera collapse.

One suggested reason for Equation (4) not being valid is that once a conduit has opened to the surface during an eruption, the static pressure in a magma column may be less than that in a similar and adjacent column of host rock (Folch, personal communication, 2007). The magmastatic pressure is $p_m = \rho_m g h$, where $h$ is depth and all the symbols are as defined above. For comparison, the lithostatic pressure in a rock column would be $p_l = \rho_r g h$, where all the symbols are defined above. When $\rho_r > \rho_m$, it follows that $p_m < p_l$ and the possibility may exist that $p_m + p_e < p_l = \sigma_3$ even if $p_e > 0$. If this were correct, there could be a positive excess pressure so that

$p_e > 0$ which could drive out the magma even if the magmastatic pressure $p_m$ plus the excess pressure were less than the minimum principal compressive stress $\sigma_3$.

   This possibility, as well as the dynamic effects, certainly needs to be explored. Ring-fault slips may also result in explosive build up of gas pressure in the associated chamber, by which means the excess pressure is maintained as positive, that is, $p_e > 0$ during the collapse (Gudmundsson, 1998a). The present suggestion that $p_m + p_e < p_l = \sigma_3$ and $p_e > 0$, however, seems to imply a rigid rather than elastic crust, that is, one with an infinite Young's modulus. Since the shallow crust is known to behave, to a first approximation, as elastic, the proposal in its present form does not seem very likely. While further work is definitely needed on this important topic, current understanding indicates that Equation (4) is approximately valid for magma flow from a chamber during ring-fault formation or slip.

## 6. Stress Fields Triggering Ring-Fault Initiation

   Field observations show that most ring faults and ring dykes originate near the lateral ends of the associated magma chambers (Figures 1, 2 and 4). A necessary condition for a ring fault to form, or an existing one to slip, is thus that the shear stress and the near-surface tensile stress favouring dip-slip faults must peak above the lateral ends of the associated magma chamber. Therefore, the stresses must peak above the 'equator' of a spherical chamber and the 'vertices' of an oblate ellipsoidal (sill-like) chamber. This is because ring faults are primarily shear fractures and thus cannot form or slip unless the local shear stress satisfies the condition for failure. This condition is normally represented by the Navier–Coulomb criterion, von Mises criterion and other similar criteria (Jaeger and Cook, 1979).

   Unrest periods and eruptions are much more common in collapse calderas than slips on existing ring faults (Newhall and Dzurisin, 1988). The local stress field around a shallow magma chamber may trigger tens of thousands of sheet injections during its lifetime, resulting in hundreds or thousands of eruptions, while caldera collapses remain very infrequent. The local stress field, in turn, depends primarily on the shape of the magma chamber, the loading conditions and the mechanical properties of the host rock (Gudmundsson, 1998a, 1998b; Gudmundsson and Brenner, 2005). As indicated above, there are three ideal shapes that a magma chamber can have: prolate ellipsoidal, oblate ellipsoidal and spherical (Figure 10). A prolate ellipsoidal magma chamber has a vertical, long axis and is normally unlikely to generate local stresses suitable for ring-fault formation (Tsuchida and Nakahara, 1970; Tsuchida et al., 1982; Gudmundsson, 1998a, b). The focus here is therefore on circular (spherical) and sill-like (oblate ellipsoidal) magma chambers.

   Based on the magma-chamber geometries and earlier results as to likely stress states for initiating ring faults (Gudmundsson, 1998a, 2007; Gudmundsson and Nilsen, 2006), four types of loading conditions are used in the present numerical models. The loadings are: (1) internal magmatic excess pressure in the chamber (that is, pressure in excess of the lithostatic stress or overburden pressure at the margin of the chamber); (2) external horizontal tensile stress applied to the crustal segment hosting the chamber; (3) magma accumulation and excess pressure at the

base of the crustal segment, resulting in a very small (centimetres) upward (concave) bending or doming of the crustal segment hosting the chamber and (4) magmatic underpressure, that is, negative excess pressure in the chamber. All the models are two-dimensional, so that a spherical chamber is modelled as a circle and a sill-like chamber as a flat 'tunnel-shaped' through crack (Gudmundsson, 2000b). The two-dimensional model results, however, have been compared with three-dimensional analytical (Tsuchida and Nakahara, 1970; Tsuchida et al., 1982) and numerical models. While the magnitudes of the stresses differ between the two- and three-dimensional models, the geometries of the local stress fields are generally similar.

The numerical models in this paper derive from recent studies using the finite-element programme ANSYS (Gudmundsson, 2007; Gudmundsson and Nilsen, 2006). The finite-element method is described by Zienkiewicz (1977), the ANSYS programme by Logan (2002) and the ANSYS homepage (www.ansys.com). The finite-element method is also discussed in the context of rock-mechanics problems by Jing and Hudson (2002).

In some of the numerical models, the rock stiffnesses used are from laboratory tests (Carmichael, 1989; Afrouz, 1992; Bell, 2000; Myrvang, 2001); in other models, the stiffnesses are modified from laboratory tests using information on in situ rock properties (Farmer, 1983; Priest, 1993; Schön, 2004). The boundary conditions used are derived from geological and geophysical field studies (cf. Gudmundsson, 2006). I consider first magma chambers of circular (spherical) shape and then of sill-like (oblate ellipsoidal) shape.

The stress field around a circular magma chamber in a homogeneous, isotropic crust and subject to various types of loading is unlikely to trigger ring-fault initiation (Gudmundsson, 1998a; Gudmundsson and Nilsen, 2006). When the loading is internal excess magmatic pressure (in excess of the lithostatic stress or pressure), the maximum surface tensile and shear stresses occur at the point directly above the centre of the chamber. When the chamber is subject to underpressure, that is, negative excess pressure, the surface shear stress peaks above the centre of the chamber. Neither stress field is suitable for ring-fault formation. Similarly, when the crustal segment hosting the chamber is subject to either external horizontal tension or doming pressure at its lower margin (due to magma accumulation), the maximum tensile and shear stress at the margin of the chamber occur at the point next to the free surface and thus not at a suitable location for ring-fault or ring-dyke formation.

In all these models, magma-chamber rupture is most likely to result in dyke or sheet injection (Figure 13) rather than ring-fault formation. The models assume, however, that the crustal segment hosting the chamber is homogeneous and isotropic, an assumption that is normally unrealistic for composite volcanoes and rift zones. Circular magma chambers located in layered crustal segments generate different stress fields, some of which may be suitable for ring-fault formation.

In order to test this possibility, many numerical models were made of a circular chamber in a layered crustal segment, a volcanic zone, 20 km thick and 40 km wide, the chamber itself supplying magma to the associated composite volcano. The upper part of the crustal segment is composed of 30 layers, each 100 m thick and

alternating in stiffness (Young's modulus) between 1 GPa (soft layers) and 100 GPa (stiff layers). Many sedimentary and pyroclastic layers in Iceland and other volcanic areas have thicknesses of about 100 m, and so do many pahoehoe lava flows (Gudmundsson, 2006). The circular chamber itself, 4 km in diameter and with a top at 3 km depth, is located in a soft layer with a stiffness of 10 GPa. The rest of the crustal segment, down to its bottom, is a moderately stiff layer of 40 GPa, typical for many rift-zone segments (Gudmundsson, 2006). At the bottom of the rift zone, there is a magma reservoir, that is, a dome-shaped 'notch', with a width of 16 km and thus similar to the width of a typical volcanic system in Iceland (Gudmundsson, 2000a). The reservoir has an 'amplitude' or height (vertical dimension) of 2 km.

In the models below, when the loading is 'doming', it means that the deep-seated reservoir is subject to magmatic excess pressure of 10 MPa. But when the loading is through horizontal tension, there is no excess pressure in the deep-seated reservoir (the reservoir being in lithostatic equilibrium with its host rock). Then the applied horizontal tensile stress is 5 MPa, a figure that is similar to the maximum in situ tensile strength of most solid rocks (Haimson and Rummel, 1982; Schultz, 1995; Amadei and Stephansson, 1997).

Horizontal tension (Figure 14) and doming (Figure 15) generally yield similar results. For horizontal tension (Figure 14), the maximum tensile stress $\sigma_3$ at the margin of the magma chamber is about 5 MPa, whereas at the free surface above the chamber $\sigma_3$ shows two peaks of 15 MPa. Similarly, the von Mises (octahedral) shear stress $\tau$ at the margin of the chamber reaches about 4 MPa, but at the free surface above the chamber $\tau$ shows two peaks of about 13 MPa.

Doming stress (pressure) at the base of the crustal segment generates tensile $\sigma_3$ and shear $\tau$ stresses at the surface that both peak above the margins of the chamber; $\sigma_3$ reaches about 25 MPa and $\tau$ about 22 MPa (Figure 15). At the margin of the chamber, these same stresses reach maximum values of about 14 and 12 MPa, respectively.

In both models (Figures 14 and 15), the conditions for ring-fault formation at the free surface and at shallow depths are thus likely to be reached before the condition of rupture of the chamber itself. Tensile surface stresses of 15–25 MPa would normally not be reached in nature. However, because they are so much higher than the tensile stresses at the chamber margin, ring-fault formation rather than dyke injection from the chamber is favoured.

The results for a circular chamber in a layered crustal segment indicate that when the chamber is located in a soft layer, such as a soft sedimentary or pyroclastic unit, horizontal tensile stress or doming pressure may trigger ring-fault formation. For other loading conditions and layering, however, a circular chamber is normally unlikely to trigger ring-fault formation. Numerous numerical models indicate that the magma-chamber geometry most likely to initiate ring faults is sill-like (oblate ellipsoidal) (Gudmundsson, 1998a; Gudmundsson and Nilsen, 2006).

The results for a sill-like magma chamber in a homogeneous, isotropic crust are well known and may be summarised as follows (Gudmundsson, 1998a, 2007; Gudmundsson and Nilsen, 2006). A chamber that is subject to internal magmatic excess pressure as the only loading is unlikely to trigger ring-fault formation
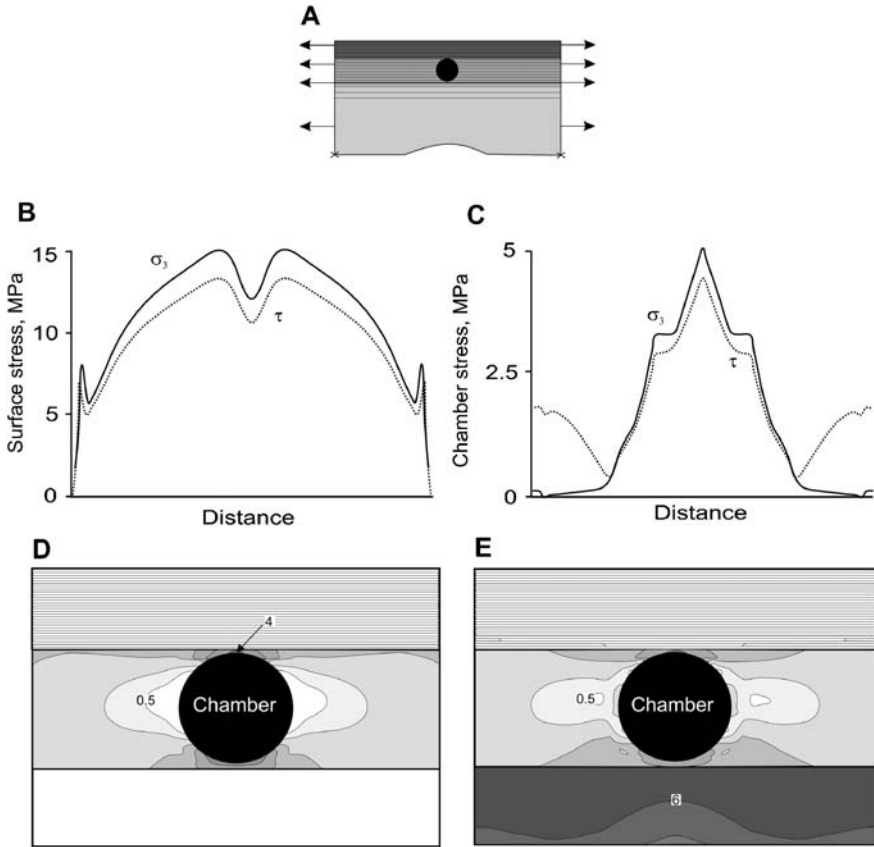
**Figure 14** Circular magma chamber located in a layered crustal segment, 20 km thick and 40 km wide, subject to horizontal tensile stress of 5 MPa. Below the chamber, itself with a top at 3 km depth and located in a comparatively soft layer (stiffness 10 GPa), there is a layer with a uniform stiffness of 40 GPa. Above the chamber there are 30 layers alternating in stiffness between 1 and 100 GPa. (A) Configuration of the model; (B) maximum principal tensile stress $\sigma_3$ and von Mises shear stress $\tau$ at the free surface; (C) tensile stress $\sigma_3$ and the shear stress $\tau$ at the upper boundary of the magma chamber; (D) contours of the tensile stress $\sigma_3$ around the magma chamber and (E) contours of shear stress $\tau$ around the magma chamber. In this and subsequent numerical models, the distance along the horizontal axis indicated in the figures marked (B) are from one end to the other of the surface in figures (D) and (E). In the figures marked (C), the distance along the horizontal axis is from one lateral end to the other of the upper half (margin) of the chamber.

since both the maximum tensile and shear stresses at the free surface occur at the point directly above the centre of the chamber. When the crustal segment hosting the chamber is subject to either horizontal tensile stress or doming pressure, the resulting stress field is likely to trigger ring-fault formation. This follows since both the free-surface tensile and shear stresses peak at a certain radial distance from the free-surface point (the epicentre) above the centre of the chamber and may connect with stress–concentration regions at the upper surface of the chamber itself.
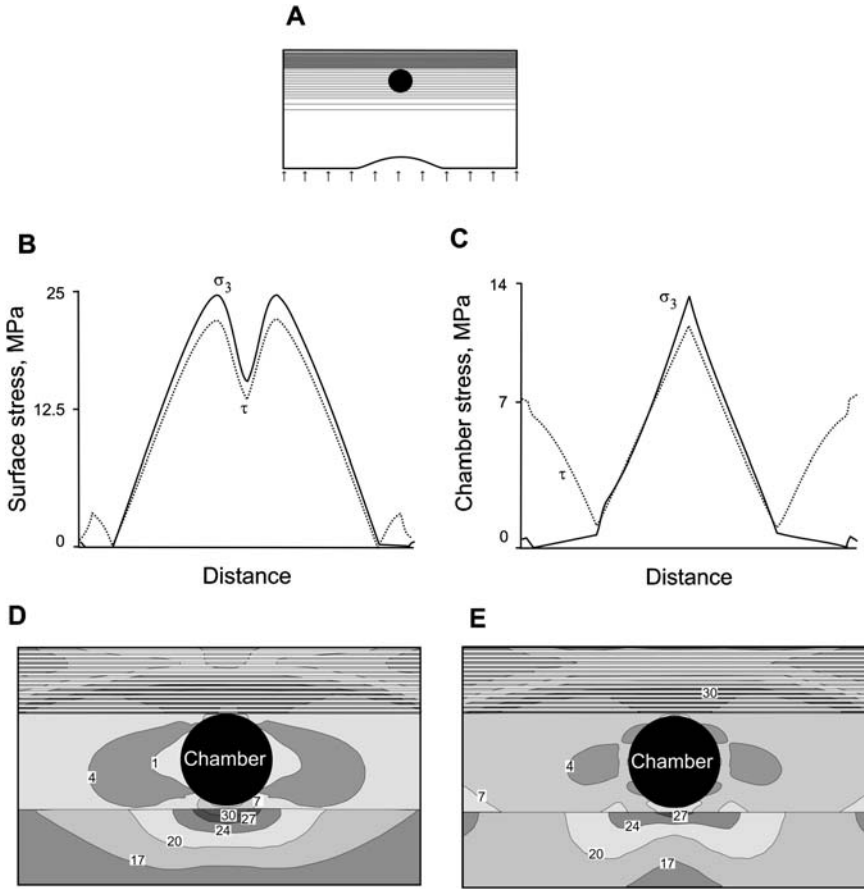
**Figure 15**   Same circular magma chamber and crustal segment as in Figure 14 but here subject to a doming stress (pressure) of 10 MPa at the bottom of the segment. (A) Configuration of the model; (B) maximum principal tensile stress $\sigma_3$ and von Mises shear stress $\tau$ at the free surface; (C) tensile stress $\sigma_3$ and the shear stress $\tau$ at the upper boundary of the magma chamber; (D) contours of the tensile stress $\sigma_3$ around the magma chamber and (E) contours of shear stress $\tau$ around the magma chamber.

If a sill-like chamber is subject to underpressure as the only loading, however, the resulting stress field is unlikely to initiate a typical, single ring fault (Figure 16) because: (1) the maximum tensile stress at the upper margin of the chamber occurs at its centre and would encourage dyke injection rather than ring-fault initiation; (2) the maximum free-surface shear stress occurs above the centre of the chamber; and (3) the regions of high shear stress and high tensile stress between the upper margin of the chamber and the free surface do not coincide. Thus, if the shear stress gave rise to any ring fault at all, it would be an outward-dipping reverse fault. By contrast, the tensile stress would tend to generate, if any fault at all, an inward–dipping normal fault. Such systems of faults are also developed during underpressure analogue modelling (Marti et al., 1994; Acocella et al., 2000; Roche et al., 2000).
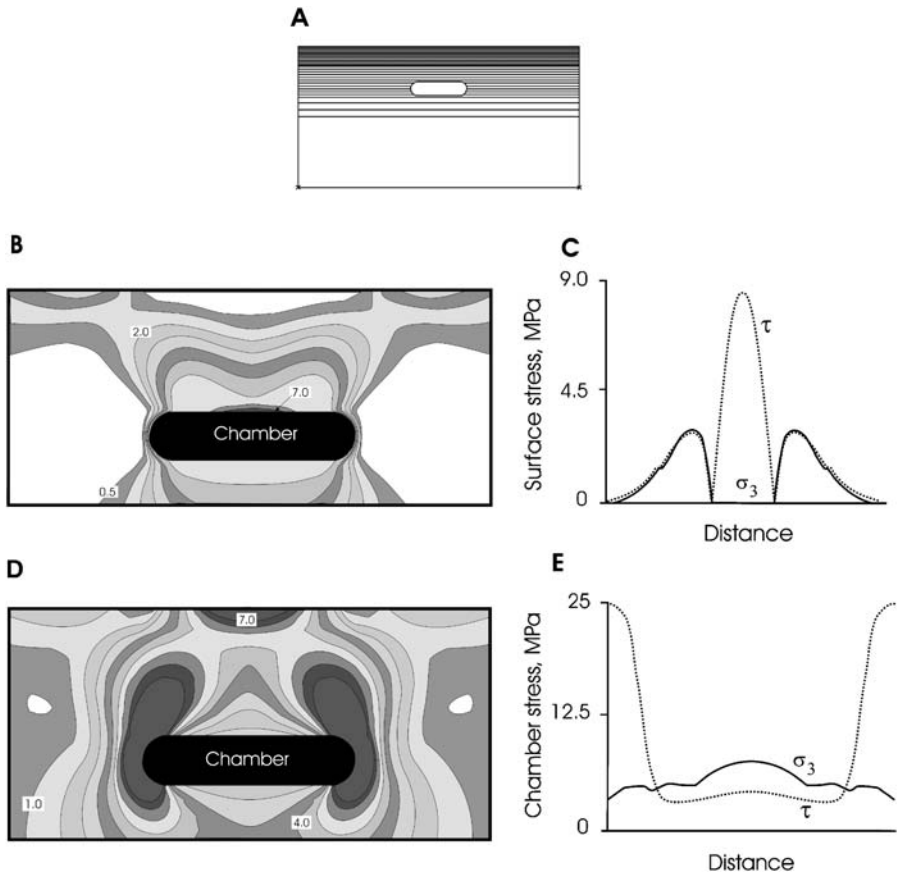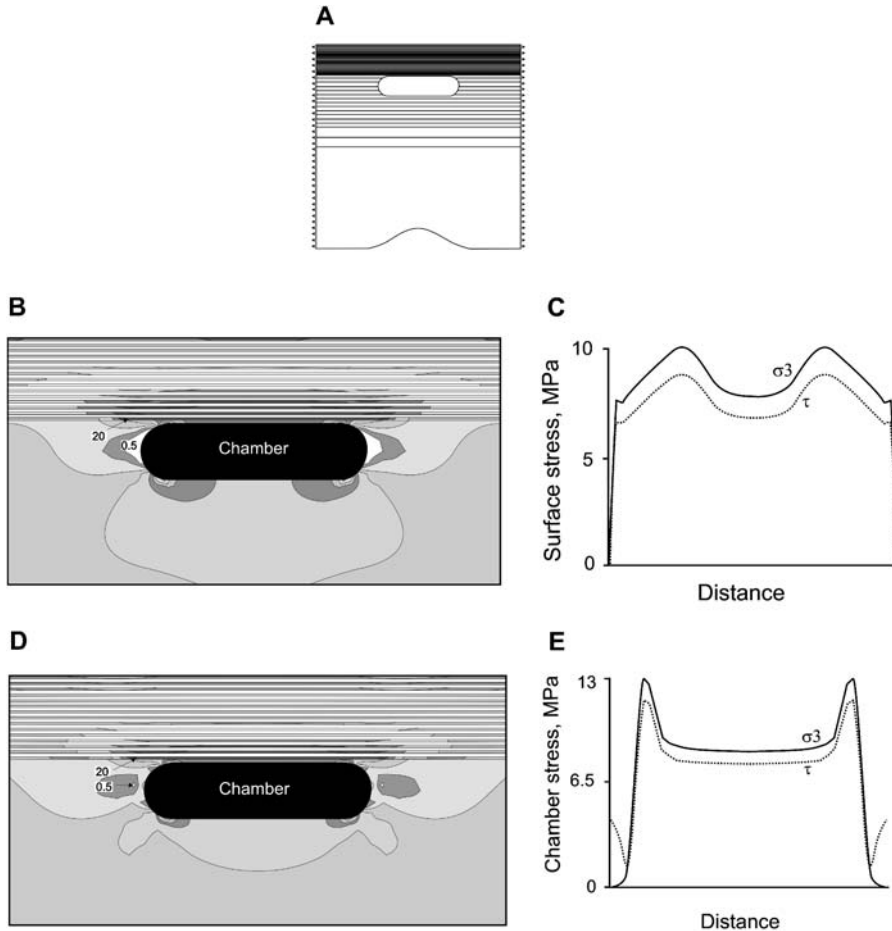
**Figure 16**    Sill–like magma chamber subject to an underpressure of 5 MPa. The chamber is 8 km wide and 2 km thick; it is located at 5 km depth in a homogeneous, isotropic crustal segment, 20 km thick and 40 km wide, with a stiffness of 40 GPa. (A) Configuration of the model; (B) contours of tensile stress $\sigma_3$ around the magma chamber; (C) maximum principal tensile stress $\sigma_3$ and von Mises shear stress $\tau$ at the free surface; (D) contours of shear stress $\tau$ around the magma chamber and (E) tensile $\sigma_3$ and shear $\tau$ stress at the upper boundary of the magma chamber.

I know of no well–documented field observations of such double–fault systems being associated with collapse calderas; however, if such a system is observed, then it might be explained in terms of this model or a similar one.

To show the effects of mechanical layering on the local stress fields and the likelihood of ring–fault formation, I present several models of a sill–like chamber in a layered crustal segment. In all the models, the chamber is 8 km wide (horizontal diameter), 2 km thick and with a top at 3 km below the free surface. The crustal segment hosting the chamber is 20 km thick and 40 km wide. The segment's upper part is composed of 30 layers, each 100 m thick and alternating in stiffness between 1 and 100 GPa, whereas the layer hosting the chamber, and the remainder of the crustal segment, has a stiffness of 40 GPa. Underlying the crustal segment is a

magma reservoir with a width of 16 km and a height of 2 km, as in the circular magma–chamber models. When the loading is doming, the deep-seated reservoir is subject to magmatic excess pressure of 10 MPa.

In the first model, the chamber is located in a crustal segment subject to horizontal tension of 5 MPa as the only loading. Here, the maximum tensile stress $\sigma_3$ and the Mises shear stress $\tau$ peak at the appropriate locations for the initiation of a ring fault (Figure 17). Since the stresses at the upper boundary of the chamber are
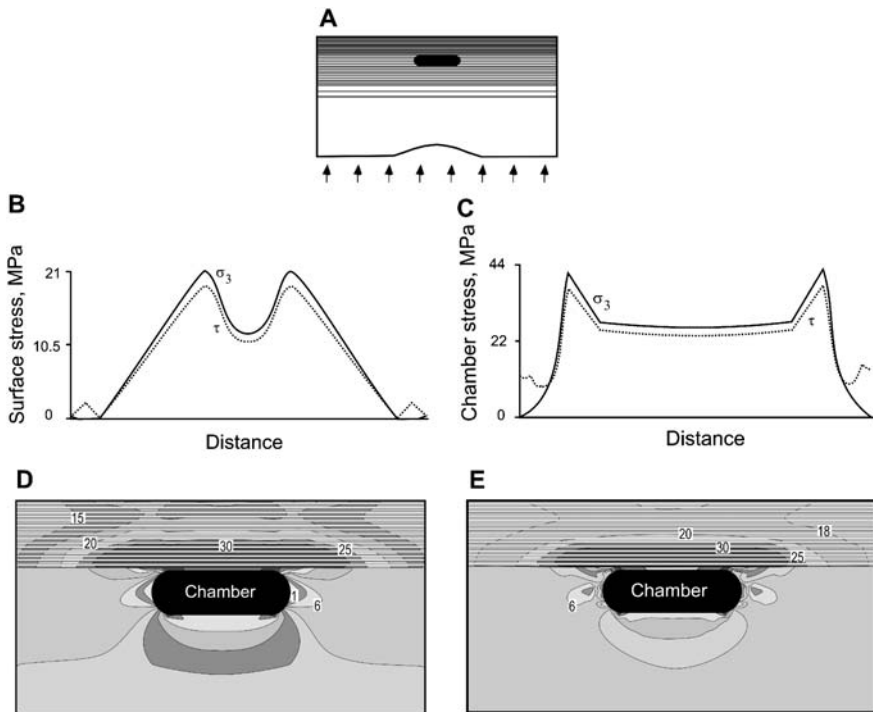


**Figure 17**   Sill–like magma chamber, 8 km wide and 2 km thick. The chamber is located at 3 km depth in a 20 km thick and 20 km wide layered crustal segment subject to horizontal tensile stress of 5 MPa. The lower part of the segment (hosting the chamber) has a stiffness of 40 GPa, whereas the uppermost 3 km above the chamber consists of 30 layers alternating in stiffness between 1 and 100 GPa. (A) Configuration of the model; (B) contours of tensile stress $\sigma_3$ around the magma chamber; (C) maximum principal tensile stress $\sigma_3$ and von Mises shear stress $\tau$ at the free surface; (D) contours of shear stress $\tau$ around the magma chamber and (E) tensile $\sigma_3$ and shear $\tau$ stress at the upper boundary of the magma chamber.

somewhat higher than those at the free surface, a ring dyke would also be expected to form.

In the second model, that chamber is subject to a 10 MPa doming stress (pressure) as the only loading. Here, the tensile $\sigma_3$ and shear $\tau$ stresses at the surface reach their maximum values above the margins of the chamber, and the stresses at the upper margin of the chamber peak near the lateral ends (Figure 18). The theoretical maximums of the tensile $\sigma_3$ and shear $\tau$ stresses, close to 20 MPa at the free surface and 40 MPa at the upper margin of the chamber, are much higher than either the tensile or shear strengths of ordinary rocks (Haimson and Rummel, 1982; Schultz, 1995; Amadei and Stephansson, 1997; Bell, 2000; Myrvang, 2001). It follows that a ring fault is likely to form, and since the theoretical stresses are higher at the chamber boundary than at the free surface, a ring dyke would also be expected to form.

In the third model, the chamber is simultaneously subject to doming pressure of 10 MPa and horizontal tensile stress of 5 MPa (Figure 19). Here, the tensile $\sigma_3$ and



**Figure 18** Sill–like magma chamber, 8 km wide and 2 km thick. The chamber is located at 3 km depth in a 20 km thick and 40 km wide layered crustal segment subject to doming stress (pressure) of 10 MPa at the segment bottom. The lower part of the segment (hosting the chamber) has a stiffness of 40 GPa, whereas the uppermost 3 km above the chamber consists of 30 layers alternating in stiffness between 1 and 100 GPa. (A) Configuration of the model; (B) maximum principal tensile stress $\sigma_3$ and von Mises shear stress $\tau$ at the free surface; (C) tensile stress $\sigma_3$ and the shear stress $\tau$ at the upper boundary of the magma chamber; (D) contours of tensile stress $\sigma_3$ around the magma chamber and (E) contours of shear stress $\tau$ around the magma chamber.
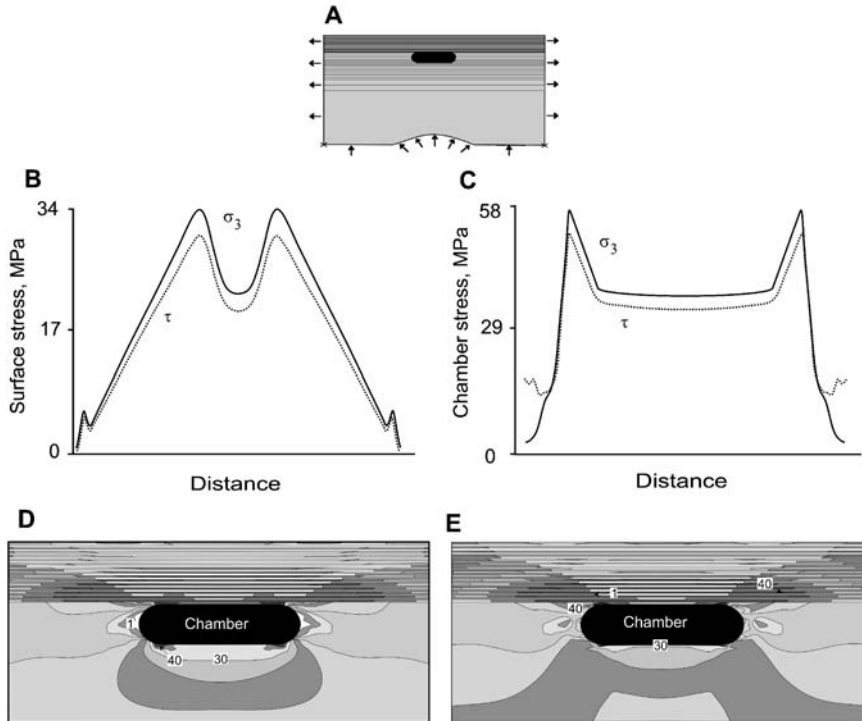
**Figure 19**   Sill–like magma chamber, 8 km wide and 2 km thick. The chamber is located at 3 km depth in a 20 km thick and 40 km wide layered crustal segment subject to doming stress (pressure) of 10 MPa at the segment bottom as well as horizontal stress of 5 MPa. The lower part of the segment (hosting the chamber) has a stiffness of 40 GPa, whereas the uppermost 3 km above the chamber consists of 30 layers alternating in stiffness between 1 and 100 GPa. (A) Configuration of the model; (B) maximum principal tensile stress $\sigma_3$ and von Mises shear stress $\tau$ at the free surface; (C) tensile stress $\sigma_3$ and the shear stress $\tau$ at the upper boundary of the magma chamber; (D) contours of tensile stress $\sigma_3$ around the magma chamber and (E) contours of shear stress $\tau$ around the magma chamber.

shear $\tau$ stresses at the free surface peak above, and the upper margin stress of the chamber at, the lateral ends. Since the theoretical peak stresses are close to 57 MPa at the chamber margin and 33 MPa at the free surface, they are likely to initiate a ring fault and a ring dyke.

# 7. Discussion

Collapse calderas are common on the Earth and on several of the rocky planets and their satellites (Figure 3). While many extraterrestrial calderas as well as calderas in basaltic edifices on Earth may form and slip without significant eruptions, most large calderas on Earth are related to large explosive eruptions (Newhall and Dzurisin, 1988). In fact, the largest and most devastating explosive eruptions on Earth are

associated with large caldera collapses. It follows that it is of fundamental importance to understand the processes that lead to ring-fault formation and caldera subsidence.

The general mechanics of formation of the ring faults of collapse calderas is as yet poorly understood. Nevertheless, certain aspects are clear. For example, it is known that the ring faults are primarily shear fractures, so that their initiation and development must depend on the state of stress in the host rock. The state of stress in a volcano is partly controlled by the mechanical properties of its rock units and structures such as existing contacts, faults and joints (Figure 4). Partly, however, the volcano stresses are controlled by the loading conditions to which the volcano is subject, in particular, the geometry of and magma pressure in the associated chamber and the tectonic regime (external tension, doming etc.) within which the chamber is located. The initiation of a ring fault is thus essentially a problem in rock physics, whereas the commonly associated fluid transport out of the magma chamber during the subsidence of the caldera floor is a problem in geological fluid dynamics.

## 7.1. The underpressure model

One mechanism of the formation of collapse calderas that has been widely discussed for many decades is underpressure in the magma chamber into which the caldera floor eventually subsides. This mechanism, also referred to as 'withdrawal of magmatic support', represents the earliest attempt to account for caldera formation (Anderson, 1936). In Anderson's model, the underpressure is modelled as a centre-of-compression strain nucleus. In the extreme version of the underpressure model, it is assumed that following an eruption there is an empty cavity, a void, that forms a part of or perhaps the entire magma chamber into which the chamber roof and, therefore, the caldera subsides (Williams, 1941; Scandone, 1990; Branney, 1995; Lavallee et al., 2006). The volume of the void, and thus of the subsequently formed caldera, is then supposed to correspond to that of the erupted and intruded materials during the caldera-forming eruption.

This model is, of course, very appealing in its simplicity and implies that caldera collapses are analogous to many ground subsidences, such as sink holes and pit craters. There is, of course, little doubt that if a magma chamber could suddenly be partly or totally emptied so as to leave a cavity in the ground, there would be surface subsidence and, depending on the size and shape of the chamber in relation to its depth and associated stress field, some sort of collapse. However, sink holes and pit craters are small structures that normally reach only very shallow depths. Sink holes, for example, are on average about 50 m in diameter and 10 m deep and are clearly related to collapse of the roof of underground cavities such as caves (Esterbrook, 1993). Similarly, most pit craters are related to tension fractures and normal faults at shallow depths where absolute tension occurs; these pit craters are not related to magma chambers (Okubo and Martel, 2001). In contrast, the magma chambers to which most collapse calderas are related occur at depths as great as many kilometres, that is, too great depths for absolute tension to occur except next to the chamber itself.

Several difficulties with the underpressure model of ring-fault formation are discussed by Gudmundsson and Nilsen (2006). One problem is already discussed, namely, how the fluid in the chamber is supposed to be driven out if the excess

pressure becomes zero or, in fact, in the underpressure model negative. This problem follows from Equations (1)–(4) and was discussed in the context of these equations. When dealing with petroleum reservoirs and hydraulic fractures injected from drill holes, it is normally assumed that the fluid must have pressure in excess of the minimum principal compressive stress to keep the hydraulic fracture open at its contact with the drill hole (Valko and Economides, 1995; Charlez, 1997; Yew, 1997). By contrast, in the underpressure model, the dyke fractures are supposed to remain open when the magma pressure is less than the minimum principal compressive stress. It remains to be explained how magma chambers can behave in this way and under what conditions.

A second problem, not mentioned by Gudmundsson and Nilsen (2006), is the shear stress generated in the roof of a supposed-to-be empty magma chamber. For a chamber with a top at the depth of 4–5 km, for example, an empty cavity at the chamber top would result in a shear stress of at least 50–60 MPa. By contrast, the in situ shear strength, twice the tensile strength, is likely to be about 10 MPa or less. In fact, driving shear stresses (stress drops) in most earthquakes are 1–10 MPa (Scholz, 1990). So the following question must be answered: how can the rocks sustain the shear stresses necessary for an empty cavity to form at many kilometres depth?

Perhaps, the most serious problem for the underpressure model, from a general volcanological point of view, is the poor correlation between collapse (caldera) volume and combined volumes of extrusive and intrusive material leaving the chamber during the caldera eruption. For calderas in basaltic edifices the volume correspondence is normally poor (Walker, 1988). In fact, the two best-documented large caldera collapses in recent decades, that of Fernandina in Galapagos in 1968 (Filson et al., 1973; Munro and Rowland, 1996) and that of Miyakejima in Japan in 2000 (Geshi et al., 2002) had hardly any eruptions at all. And even if dykes were associated with the volcano-tectonic events leading to these collapses, realistic dyke-volume estimates are only fractions of the collapse volumes.

There exist many other careful estimates showing similar lack of volume correspondence (Smith, 1979; Williams and McBirney, 1979). An interesting aspect of the lack of volume correspondence is that not only do many calderas subside without significant eruption or intrusion, but there are also several large-volume explosive eruptions that show no major ring-fault slip at the eruption site (Lavallee et al., 2006). For example, an explosive eruption at 1600 AD of the Huaynaputina volcano in Peru produced about 11 km$^3$ DRE of eruptive materials and unspecified volume of intrusive materials. This large explosive eruption was associated with two small collapse structures, one about 1 km and the other about 0.6 km in diameter (and thus too small to be really classified as calderas), with a combined volume of 0.043 km$^3$ or about 0.4% of the eruptive volume (Lavallee et al., 2006).

The examples of lack of volume correspondence serve to illustrate the point that there is clearly no critical eruptive/intrusive volume depending on the size of the chamber that can be regarded as a threshold for ring-fault formation or slip. Hundreds of eruptions and dyke injections occur in volcanoes worldwide every century, and of greatly varying volumes, but very few result in ring-fault formation or slip on existing ring faults. In terms of purely empirical theories of caldera formation, such as the underpressure model, it is not easy to account for the rarity

of caldera slip. In the underpressure model, it is also difficult to explain why collapses, even if rare, are so much more frequent in basaltic edifices than in stratovolcanoes (Gudmundsson and Nilsen, 2006). Thus, in basaltic edifices such as those on Hawaii and the Galapagos Islands, slip on existing calderas, often with very small or no eruptions, is comparatively common.

## 7.2. Ring-fault structure and slip

One of the main conclusions of this paper is that purely empirical models, such as the underpressure model, are unlikely to help us forecast whether ring-fault formation or slip is likely to occur during an unrest period. In the paper, I argue that to understand how and when a ring fault develops and why an existing ring fault slips so infrequently, we must know the state of stress in the host volcano. This implies the knowledge of the properties of the rock layers and structures that constitute the volcano. Furthermore, to forecast whether a ring fault is likely to form or slip during a particular unrest period, we must have a rough idea of the geometry of the associated magma chamber. Ring-fault formation and slip are mechanical processes that cannot be forecasted solely on the basis of empirical criteria; to develop viable models to assess the probability of ring-fault formation or slip, these processes must be understood in mechanical terms.

While the ring-fault structure is likely to be commonly complex in detail (Figure 4), it is very important when assessing the probability of slip during unrest periods to know if the ring fault is generally outward or inward dipping (Figures 5–9). Many authors have proposed that the dip is primarily outward (Williams et al., 1970; Branney, 1995; Cole et al., 2005), but observations of ring faults that are subvertical to inward dipping have a long history (Kuno et al., 1964; Smith et al., 1961; Filson et al., 1973; Aramaki, 1984; Lipman, 1984, 1997, 2000; Newhall and Dzurisin, 1988; Gudmundsson, 1998a; Geshi et al., 2002; Lavallee et al., 2006). As indicated above, the well-documented collapse of the Fernandina caldera in the Galapagos Islands in 1968 occurred on a ring fault dipping about $80°$ inwards (Simkin and Howard, 1970). Similarly, the collapse of the Miyakejima caldera in 2000 was primarily on inward-dipping faults (Geshi et al., 2002). And the inferred small collapse structures associated with the 1600 AD explosive eruption of the Huaynaputina volcano in Peru was on vertical or steeply inward-dipping faults (Lavallee et al., 2006). Also, by definition, all funnel-shaped calderas must dip inwards (Aramaki, 1984; Lipman, 1997; Cole et al., 2005). All ring faults studied in Iceland are either vertical or dip inwards (Gudmundsson and Nilsen, 2006). Similarly, ring dykes are commonly vertical or dip steeply inwards (Oftedahl, 1953; Almond, 1977). Thus, although one cannot rule out possible outward-dipping ring faults, formed under special stress conditions (reverse faults are occasionally found in extensional tectonic environments), the general field evidence seems to favour most ring faults being vertical or inward-dipping normal faults (Gudmundsson, 1998a).

This conclusion is also in agreement with the conceptual and numerical models presented in this paper. As regards the conceptual models, they indicate that there would normally be very little friction to stop the vertical subsidence along an

outward–dipping ring fault (Figures 5 and 6). Consequently, slip on outward–dipping faults and the associated eruptions would be expected to be very large because the rock block bounded by the ring fault (the piston) would tend to subside to the bottom of the chamber and thus drive out much of, or all, its magma. But we know that many terrestrial caldera slips and associated eruptions are small, and it is thought that many, perhaps most, collapse calderas on the planets and satellites are not associated with large eruptions.

These results are also in agreement with the numerical models (Figures 14–19). In these models, slight doming of the crustal segment hosting the chamber, horizontal tension of that crustal segment or both can initiate ring faults. By contrast, underpressure does not really generate a stress field that is likely to initiate typical ring faults (Figure 16).

Ring dykes are associated with many ring faults (Figures 5, 6, 8 and 12). This relationship obviously needs further exploration, since the timing of the ring-dyke emplacement may be crucial in reducing the friction along the fault plane and, thus, to allow slip more freely. For most caldera collapses, the sequence of events is also unclear. One possibility is that the ring dyke initiates at the surface of the magma chamber and then meets with a downward-propagating ring fault. Another possibility is that the ring fault propagates, either from the free surface or from some layers in the roof of the chamber, down to the top part of the magma chamber and, on meeting the chamber, is injected by magma to form a ring dyke.

# 8. Conclusions

1. Although the details of the mechanics of formation of ring faults are still not fully understood, it is known that most ring faults of collapse calderas are primarily shear fractures, the initiation and development of which depend on the state of stress in the host rock. Also, it is known that the state of stress in a volcano is primarily controlled by the mechanical properties of its rock units and structures (such as existing contacts, faults and joints), as well as by the loading conditions, in particular, the geometry and magma pressure of the associated chamber. Field studies of active and extinct calderas show that ring faults are generally dip-slip faults, although many are partly faults (shear fractures) and partly ring dykes (extension fractures). While slip on existing ring faults is much more common in basaltic edifices (shield volcanoes) than in true composite volcanoes, in both types of volcanoes most caldera unrest periods do not result in ring-fault slip.

2. The paper provides a review of some popular models of ring-fault formation, in particular, the underpressure (lack of magmatic support) model. While this model is very appealing in its simplicity (the erupted magma leaves an empty cavity into which the roof subsides, forming a caldera), there are several difficulties with this explanation (Gudmundsson and Nilsen, 2006). Apart from lack of volume correspondence between the magma leaving the chamber and the volume of the collapse, perhaps the main mechanical problem is to explain how

magma can be driven out of the chamber when its excess pressure is supposed to be zero or even negative (Equations (3) and (4)). Theoretical and experimental results indicate that it is unlikely that the excess pressure in the chamber can become negative while magma continues to be driven out of the chamber.

3. Several new conceptual models as to ring-fault initiation and development are presented in the paper. These indicate that most ring faults are likely to be of somewhat irregular dips (Figure 4), but that the general fault plane is mostly vertical or steeply inward dipping (Figures 1, 2 and 7–9). While outward-dipping ring faults may exist, calderas associated with such faults are likely to be mechanically very unstable and unlikely to become filled with lava flows without slip, as is common in many calderas on Earth and other planets (Figure 5). Formation of outward-dipping ring faults would normally result in emptying of the associated magma chamber and, therefore, in very large eruptions. Many, perhaps most, caldera slips and associated eruptions, however, are small.

4. The main results of numerical models of ring-fault formation (Figures 14–19) are as follows: (a) Excess pressure and underpressure in a shallow chamber normally favour dyke injection rather than ring-fault formation. (b) For doming or tension, a spherical magma chamber favours dyke injection except when the layer hosting the chamber is soft (10 GPa) or one with recent dyke injections, in which case the surface stress field favours ring-fault formation. (c) For an oblate chamber in a 20 km wide crustal segment, a ring fault can be generated either by tension or tension and doming; for a 40 km wide segment, doming alone is sufficient to generate a ring fault. (d) The individual layers in a volcano may develop different local stresses; it follows that stress-field homogenisation through all the layers between the chamber and the surface is a necessary condition for ring-fault formation. (d) Because the mechanical properties of the layers that constitute basaltic edifices are more uniform than those that constitute composite volcanoes, stress-field homogenisation and, thus, ring-fault formation or slip is more commonly reached in basaltic edifices than in composite volcanoes. (e) The stress fields most likely to initiate ring faults in all volcano types are those generated around oblate ellipsoidal chambers subject to tension, doming or both.

## ACKNOWLEDGEMENTS

## REFERENCES

Acocella, V., Cifelli, F., Funiciello, R., 2000. Analogue models of collapse calderas and resurgent domes. J. Volcanol. Geotherm. Res., 104, 81–96.

Acocella, V., Funiciello, R., Marotta, E., Orsi, G., de Vita, S., 2004. The role of extensional structures in experimental calderas and resurgence. J. Volcanol. Geotherm. Res., 129, 199–217.

Acocella, V., Korme, T., Salvini, F., Funiciello, R., 2003. Elliptic calderas in the Ethiopian rift: control of pre-existing structures. J. Volcanol. Geotherm. Res., 119, 189–203.

Afrouz, A.A., 1992. Practical Handbook of Rock Mass Classification Systems and Modes of Ground Failure. CRC Press, Boca Raton.

Almond, D.C., 1977. The Sabaloka igneous complex, Sudan. Phil. Trans. R. Soc. Lond. A, 287, 595–633.

Amadei, B., Stephansson, O., 1997. Rock Stress and its Measurement. Chapman & Hall, London.

Anderson, E.M., 1936. The dynamics of formation of cone-sheets, ring-dykes, and caldron-subsidences. Proc. R. Soc. Edinb., 56, 128–163.

Aramaki, S., 1984. Formation of the Aira caldera, southern Kryushu, $\sim$22,000 years ago. J. Geophys. Res., 89, 8484–8501.

Bell, F.G., 2000. Engineering Properties of Soils and Rocks, 4th edn. Blackwell, Oxford.

Bonafede, M., Dragoni, M., Quareni, F., 1986. Displacement and stress fields produced by a center of dilation and by a pressure source in a viscoelastic half-space: application to the study of ground deformation and seismic activity at Campi Flegrei, Italy. Geophys. J. R. Astron. Soc., 87, 455–485.

Branney, M.J., 1995. Downsag and extension at calderas: new perspectives on collapse geometries from ice-melt, mining, and volcanic subsidence. Bull. Volcanol., 57, 303–318.

Burov, E.B., Guillou-Frottier, L., 1999. Thermomechanical behavior of large ash flow calderas. J. Geophys. Res., 104, 23081–23109.

Carmichael, R.S., 1989. Practical Handbook of Physical Properties of Rocks and Minerals. CRC Press, Boca Raton.

Charlez, P.A., 1997. Rock Mechanics Vol. 2. Petroleum Applications. Editions Technip, Paris.

Chery, J., Bonneville, A., Vilotte, J.P., Yuen, D., 1991. Numerical modeling of caldera dynamic behavior. Geophys. J. Int., 105, 365–379.

Cole, J.W., Milner, D.M., Spinks, K.D., 2005. Calderas and caldera structures: a review. Earth Sci. Rev., 69, 1–26.

Crumpler, L.S., Aubele, J.C., 2000. Volcanism on Venus. In: Sigurdsson, H. (Ed.), Encyclopedia of Volcanoes. Academic Press, New York, pp. 727–769.

Crumpler, L.S., Head, J.W., Aubele, J.C., 1996. Calderas on Mars: characteristics, structure and associated flank deformation. In: McGuire, W.J., Jones, A.P.Neuberg, J. (Eds), Volcano Instability on the Earth and Other Planets. Geological Society, London Special Publications, Vol. 110, pp. 307–348.

Druitt, T.H., Sparks, R.S.J., 1984. On the formation of calderas during ignimbrite eruptions. Nature, 310, 679–681.

Eshelby, J.D., 1957. The determination of the elastic field of an ellipsoidal inclusion, and related problems. Proc. R. Soc. Lond., A241, 376–396.

Esterbrook, D.J., 1993. Surface Processes and Landforms. Macmillan, New York.

Farmer, I., 1983. Engineering Behaviour of Rocks, 2nd edn. Chapman and Hall, London.

Filson, J., Simkin, T., Leu, L., 1973. Seismicity of a caldera collapse: Galapagos Islands 1968. J. Geophys. Res., 78, 8591–8622.

Folch, A., Marti, J., 2004. Geometrical and mechanical constraints on the formation of ring-fault calderas. Earth Planet. Sci. Lett., 221, 215–225.

Francis, P., 1993. Volcanoes: A Planetary Perspective. Oxford University Press, Oxford.

Frankel, C., 2005. Worlds on Fire: Volcanoes on the Earth, the Moon, Mars, Venus and Io. Cambridge University Press, Cambridge.

Gautneb, H., Gudmundsson, A., Oskarsson, N., 1989. Structure, petrochemistry, and evolution of a sheet swarm in an Icelandic central volcano. Geol. Mag., 126, 659–673.

Geshi, N., Shimano, T., Chiba, T., Nakada, S., 2002. Caldera collapse during the 2000 eruption of Miyakejima volcano, Japan. Bull. Volcanol., 64, 55–58.

Goodman, R.E., 1989. Introduction to Rock Mechanics, 2nd edn. Wiley, New York, NY.

Gray, J.P., Monaghan, J.J., 2004. Numerical modelling of stress fields and fracture around magma chambers. J. Volcanol. Geotherm. Res., 135, 259–283.

Greeley, R., Batson, R., 2001. The Compact NASA Atlas of the Solar System. Cambridge University Press, Cambridge.

Gudmundsson, A., 1998a. Formation and development of normal-fault calderas and the initiation of large explosive eruptions. Bull. Volcanol., 60, 160–170.

Gudmundsson, A., 1998b. Magma chambers modeled as cavities explain the formation of rift zone central volcanoes and their eruption and intrusion statistics. J. Geophys. Res., 103, 7401–7412.

Gudmundsson, A., 2000a. Dynamics of volcanic systems in Iceland: example of tectonism and volcanism at juxtaposed hot spot and mid-ocean ridge system. Annu. Rev. Earth Planet. Sci., 28, 107–140.

Gudmundsson, A., 2000b. Fracture dimensions, displacements and fluid transport. J. Struct. Geol., 22, 1221–1231.

Gudmundsson, A., 2002. Emplacement and arrest of sheets and dykes in central volcanoes. J. Volcanol. Geotherm. Res., 116, 279–298.

Gudmundsson, A., 2006. How local stresses control magma-chamber ruptures, dyke-injections, and eruptions in composite volcanoes. Earth Sci. Rev., 79, 1–31.

Gudmundsson, A., 2007. Conceptual and numerical models of ring-fault formation. J. Volcanol. Geotherm. Res., 164, 142–160.

Gudmundsson, A., Brenner, S.L., 2005. On the conditions of sheet injections and eruptions in stratovolcanoes. Bull. Volcanol., 67, 768–782.

Gudmundsson, A., Nilsen, K., 2006. Ring faults in composite volcanoes: structures, models, and stress fields associated with their formation. In: De Natale, G., Kilburn, C.Troise, C. (Eds), Mechanisms of Activity and Unrest at Large Calderas. Geological Society, London Special Publications, Vol. 269, pp. 83–108.

Haimson, B.C., Rummel, F., 1982. Hydrofracturing stress measurements in the Iceland research drilling project drill hole at Reydarfjordur, Iceland. J. Geophys. Res., 87, 6631–6649.

Head, J.W., Crumpler, L.S., Aubele, J.C., Guest, J.E., Saunders, R.S., 1992. Venus volcanism: classification of volcanic features and structures, associations, and global distribution from Magellan data. J. Geophys. Res., 97, 13153–13197.

Heuze, F.E., 1980. Scale effects in the determination of rock mass strength and deformability. Rock Mech., 12, 167–192.

Holohan, E.P., Troll, V.R., Walter, T.R., Munn, S., McDonnell, S., Shipton, Z.K., 2005. Elliptical calderas in active tectonic settings: an experimental approach. J. Volcanol. Geotherm. Res., 144, 119–136.

Hudson, J.A., Harrison, J.P., 1997. Engineering Rock Mechanics: An Introduction to the Principles. Pergamon, Oxford.

Jaeger, J.C., Cook, N.G.W., 1979. Fundamentals of Rock Mechanics. Chapman and Hall, London.

Jellinek, A.M., DePaolo, D.J., 2003. A model for the origin of large silicic magma chambers: precursors of caldera-forming eruptions. Bull. Volcanol., 65, 363–381.

Jing, L., Hudson, J.A., 2002. Numerical models in rock mechanics. Int. J. Rock Mech. Min. Sci., 39, 409–427.

Jumikis, A.R., 1979. Rock Mechanics. Trans Tech Publications, Clausthal.

Kanamori, H., Anderson, D.L., 1975. Theoretical basis for some empirical relations in seismology. Bull. Seismol. Soc. Am., 65, 1073–1095.

Krassilnikov, A.S., Head, J.W., 2004. Calderas on Venus and Earth: comparison and models of formation. Lunar Planet. Sci., 35, 1531.

Kuno, H., Ishikawa, T., Katsui, Y., Yagi, K., Yamasaki, M., Taneda, S., 1964. Jpn. J. Geol. Geog., 35, 223–238.

Lamb, H., 1932. Hydrodynamics, 6th edn. Cambridge University Press, Cambridge.

Lavallee, Y., de Silva, S.L., Salas, G., Byrnes, J.M., 2006. Explosive volcanism (VEI6) without caldera formation: insight from Huaynaputina volcano, southern Peru. Bull. Volcanol., 68, 333–348.

Lekhnitskii, S.G., 1968. Anisotropic Plates. Gordon and Breach Science Publishers, New York.

Leone, G., Wilson, L., 2000. Lava flow field areas and caldera volumes on Io: their correlation with magma reservoir size and collapse events. Lunar Planet. Sci., 31, 1651.

Leutwyler, K., 2003. The Moons of Jupiter. W.W. Norton, New York.

Lipman, P.W., 1984. The roots of ash flow calderas in western North America: windows into the tops of granitic batholiths. J. Geophys. Res., 89, 8801–8841.

Lipman, P.W., 1997. Subsidence of ash-flow calderas: relation to caldera size and magma chamber geometry. Bull. Volcanol., 59, 198–218.

Lipman, P.W., 2000. Calderas. In: Sigurdsson, H. (Ed.), Encyclopedia of Volcanoes. Academic Press, San Francisco, CA, pp. 643–662.

Lodders, K., Fegley, B., 1998. The Planetary Scientist's Companion. Cambridge University Press, Cambridge.

Logan, D.L., 2002. A First Course in the Finite Element Method. Brooks/Cole, Pacific Grove, CA.

Lopes, R.M.C. and Gregg, T.K.P. (Eds), Volcanic Worlds: Exploring the Solar System's Volcanoes. Springer-Verlag, Berlin.

Love, A.E.H., 1927. A Treatise on the Mathematical Theory of Elasticity. Dover, New York, NY.

Macdonald, G.A., 1972. Volcanoes. Prentice-Hall, Englefield Cliffs, NJ.

Marti, J., Ablay, G.J., Reshaw, L.T., Sparks, R.S.J., 1994. Experimental studies of collapse calderas. J. Geol. Soc. Lond., 151, 919–929.

McEwen, A.S., et al., 2000. Galileo at Io: results from high-resolution imaging. Science, 288, 1193–1198.

Miller, R., Hartmann, W.K., 2005. The Grand Tour: A Traveller's Guide to the Solar System. Workman Publishing, New York, NY.

Milne-Thompson, L.M., 1996. Theoretical Hydrodynamics, 5th edn. Dover, New York, NY.

Mouginis-Mark, P.J., Rowland, S.K., 2001. The geomorphology of planetary calderas. Geomorphology, 37, 201–223.

Munro, D.C., Rowland, S.K., 1996. Caldera morphology in the western Galapagos and implications for volcano eruptive behaviour and mechanisms of caldera formation. J. Volcanol. Geotherm. Res., 72, 85–100.

Myrvang, A., 2001. Rock Mechanics. Norway University of Technology (NTNU), Trondheim, in Norwegian.

Newhall, C.G., Dzurisin, D., 1988. Historical Unrest of Large Calderas of the World. US Geological Survey Bulletin, Vol. 1855, Reston, VA.

Newman, A.V., Dixon, T.H., Ofoegbu, G.I., Dixon, J.E., 2001. Geodetic and seismic constraints on recent activity at Long Valley caldera, California: evidence for viscoelastic rheology. J. Volcanol. Geotherm. Res., 105, 183–206.

Nilsen, B., Palmström, A., 2000. Engineering Geology and Rock Engineering. Norwegian Soil and Rock Engineering Association, Oslo.

Nye, J.F., 1957. Physical Properties of Crystals. Oxford University Press, Oxford.

Oftedahl, C, 1953. The igneous rock complex of the Oslo region: XIII. The cauldrons, Skrifter Det Norske Videnskaps-Akademi i Oslo, 3, 1–108.

Okubo, C.H., Martel, S.J., 2001. Pit crater formation on Kilauea volcano, Hawaii. J. Volcanol. Geotherm. Res., 86, 1–18.

Pace, K.R., Krassilnikov, A.S., 2003. Calderas on Venus: tectonics, volcanism and relationship with regional plains. Lunar Planet. Sci., 34, 1309.

Priest, S.D., 1993. Discontinuity Analysis for Rock Engineering. Chapman and Hall, London.

Radebaugh, J., et al., 2000. Characteristics of calderas on Io: surface morphology, sizes, and distribution. Lunar Planet. Sci., 31, 1983.

Radebaugh, J., Keszthelyi, L.P., McEwen, A.S., Turtle, E.P., Jaeger, W., Milazzo, M., 2001. Paterae on Io: a new type of volcanic caldera? J. Geophys. Res., 106, 33005–33020.

Roche, O., Druitt, T.H., Merle, O., 2000. Experimental study of caldera formation. J. Geophys. Res., 105, 395–416.

Sadd, M.H., 2005. Elasticity: Theory, Applications, and Numerics. Elsevier, Amsterdam.

Saunders, S.J., 2001. The shallow plumbing system of Rabaul caldera: a partially intruded ring fault? Bull. Volcanol., 63, 406–420.

Saunders, S.J., 2004. The possible contribution of circumferential fault intrusion to caldera resurgence. Bull. Volcanol., 67, 57–71.

Savin, G.N., 1961. Stress Concentration Around Holes. Pergamon, New York, NY.

Scandone, R., 1990. Chaotic collapse of calderas. J. Volcanol. Geotherm. Res., 42, 285–302.

Scholz, C.H., 1990. The Mechanics of Earthquakes and Faulting. Cambridge University Press, Cambridge.

Schön, J.H., 2004. Physical Properties of Rocks: Fundamentals and Principles of Petrophysics. Elsevier, Oxford.

Schultz, R.A., 1995. Limits on strength and deformation properties of jointed basaltic rock masses. Rock Mech. Rock Eng., 28, 1–15.

Scott, E.D., Wilson, L., 2000. Cyclical summit collapse events at Ascraeus Mons, Mars. J. Geol. Soc. Lond., 157, 1101–1106.

Sigurdsson, H. (Ed.), Encyclopedia of Volcanoes, . Academic Press, New York, NY.

Simkin, T., Howard, K.A., 1970. Caldera collapse in the Galapagos Islands, 1968. Science, 169, 429–437.

Smith, R.L., 1979. Ash-flow magmatism. In: Chapin, C.E. and Elson, W.E. (Eds), Ash-Flow Tuffs. Geol. Soc. Am. Mem., Vol. 116, pp. 613–662.

Smith, R.L., Bailey, R.A., Ross, C.S., 1961. Structural evolution of the Valles caldera, New Mexico, and its bearing on the emplacement of ring dikes. US Geological Survey Professional Paper 424-D, pp. 145–149.

Spinks, K.D., Acocella, V., Cole, J.W., Bassett, K.N., 2005. Structural control of volcanism and caldera development in the transtensional Taupo volcanic zone, New Zealand. J. Volcanol. Geotherm. Res., 144, 7–22.

Thorarinsson, S., 1963. Askja on Fire. Almenna bokafelagid, Reykjavik.

Tsuchida, E., Nakahara, I., 1970. Three-dimensional stress concentration around a spherical cavity in a semi-infinite elastic body. Jpn. Soc. Mech. Eng. Bull., 13, 499–508.

Tsuchida, E., Saito, Y., Nakamura, I., Kodama, M., 1982. Stresses in a semi-infinite elastic body containing a provate spheroidal cavity subject to axisymmetric pressure. Jpn. Soc. Mech. Eng. Bull., 25, 891–897.

Upton, B., 2004. Volcanoes and the Making of Scotland. Dunedin Acad. Press, Edinburgh.

Valko, P., Economides, M.J., 1995. Hydraulic Fracture Mechanics. Wiley, New York, NY.

Walker, G.P.L., 1984. Downsag calderas, ring faults, caldera sizes, and incremental caldera growth. J. Geophys. Res., 89, 8407–8416.

Walker, G.P.L., 1988. Three Hawaiian calderas: an origin through loading by shallow intrusions. J. Geophys. Res., 93, 14773–14784.

Walter, T.R., Troll, V.R., 2001. Formation of caldera periphery faults: an experimental study. Bull. Volcanol., 63, 191–203.

Williams, H., 1941. Calderas and their origin. Bull. Dep. Geol. Sci. Univ. Calif., 25, 239–346.

Williams, H., McBirney, A.R., 1979. Volcanology. W.H. Freeman, New York, NY.

Williams, H., McBirney, A.R., Lorenz, V., 1970. An Investigation of Volcanic Depressions. Part I. Calderas. Manned Spacecraft Center, Houston, TX.

Yew, C.H., 1997. Mechanics of Hydraulic Fracturing. Gulf Publishing, Houston, TX.

Yu, H.S., 2000. Cavity Expansion Methods in Geomechanics. Kluwer, London.

Zienkiewicz, O.C., 1977. The Finite Element Method. McGraw-Hill, New York, NY.

This page intentionally left blank

# Facilitating Dike Intrusions into Ring-Faults

Thomas R. Walter*

## Contents

## Abstract

Most caldera volcanoes are associated with circular dike intrusions. Ring-dikes form during complete or partial subsidence of the caldera floor and may be responsible for eruption locations that surround a structural basin. Through a systematic set of numerical models, this paper summarizes a variety of types, mechanisms, and patterns of caldera ring-dikes that can be observed in nature. Caldera subsidence is simulated by magma chamber depressurization; three main sets of models are distinguished. First, local linear and circular faults are included in order to understand their effect on caldera-related displacements. Second, passive opening at a ring-fault is studied in order to understand where ring-dike intrusions may occur. Third, models are designed to exemplify how processes external to the caldera, such as a tectonic earthquake or an eccentric intrusion, may affect the location of a ring-dike intrusion. These models suggest that ring-dikes commonly form "incompletely," i.e. only part of a ring can be intruded because of the nonuniform displacement field around the ring-fault. As described in the discussion, these models help explain the locations of ring-dikes in various volcanic regions.

*Corresponding author. Tel.: +49 (0)331 288 1253; Fax: +49 (0)331 288 1204
*E-mail address:* twalter@gfz-potsdam.de

GFZ Potsdam, Telegrafenberg, 14473 Potsdam, Germany

## 1. Introduction

Large-volume ash-flow eruptions and sporadic cones typically align along the circumference of a caldera basin (e.g., Walker, 1984; Lipman, 1997; Cole et al., 2005). Studies of caldera structures show that groups of eruption feeder pathways form discordant intrusive bodies with near-circular geometries in map view. Intrusions along a circle around a volcanic center were described in detail in the early twentieth century (Clough et al., 1909); these intrusions are referred to as *ring-complexes*. Ring-complexes are very common for volcanoes with surface expressed calderas (Richey, 1935; Smith and Bailey, 1968; Lipman, 1984), and different types are distinguished. The geometry of ring-complexes comprise circular or angular, inwardly dipping, vertical, and outwardly dipping dikes of variable thickness. These can be singular intrusion events or multiple dikes, forming basaltic or silicic sheets. Intrusion dynamics of ring-complexes include those that generate their own propagating fractures or those that reactivate existing fracture zones. In the latter case, the dike may follow predefined faults of regional tectonic and/or volcano-tectonic origin.

In association with collapsed calderas, two main types of ring-complexes can be distinguished (see Table 1): inwardly dipping (often 30–45°) concentric dikes, referred to as cone sheets (Bailey et al., 1924), and near-vertical or often outwardly dipping concentric dikes intruded parallel to (or into) the ring-faults, referred to as ring-dikes (Anderson, 1936; Billings, 1943). In the mid-1930s, E.M. Anderson developed the first mathematical theory for the development of ring-complexes (Anderson, 1936); a fluctuating pressure within a deep parabolic magma chamber is thought to be responsible for the formation of ring-complexes. The two different types of ring-complexes are therefore defined geometrically as well as genetically; while cone sheets are thought to form during stages of caldera floor uplift (inflation), ring-dikes form during stages of caldera floor subsidence (deflation). This work focuses on the different conditions and geometries of ring-dike formation related to caldera subsidence.

Ring-dikes ideally intrude along the ring-fault and form a closed ring; more commonly, they only partially intrude into a ring-fracture to form curved or segmented dikes (Billings, 1943; Bonin, 1986). Ring-dikes are often only a few centimeters or meters thick. However, old eroded caldera system ring-dikes can reach massive dimensions, wider than 10 km and more than 0.5 km thick. Classic ring-dikes were described for volcanic systems in Scotland; for instance, at Glencoe caldera, a deeply eroded caldera with inverted relief, caldera subsidence affects an oval-shaped area and activated boundary faults (Clough et al., 1909). Although similar mechanisms were applied to most intrusive complexes in the British Volcanic Tertiary Province (Richey, 1935), newer studies suggest that some of these ring-complexes are lopolithic intrusions associated with inflation and doming (O'Driscoll et al., 2006).

A major difficulty in ring-dike studies is that exposures are usually poor and often obscured by sedimentary caldera infill or other intrusive bodies (O'Driscoll et al., 2006; Kennedy and Stix, 2007). It has been shown that the geometry of a

**Table 1** Classification of ring-complexes into cone sheets and ring dykes.

| Domain | Class | Geometry | | | Number | Genetics | Composition | Timing | Structural control |
|---|---|---|---|---|---|---|---|---|---|
| | | Dip | Strike | Width | | | | | |
| Ring complex | Cone sheets | Inward dip, 30–45° multiple sheets | Mainly circular or elliptical | Scale cm to m | Multiple intrusions, sheets | Forceful dyke intrusion from an over-pressurised reservoir | Mainly evolved magmas | Late stages, resurgence | Little |
| | Ring dykes | Vertical to outward dip, >90° often single event only | Circular, elliptical, angular, polygonal | Scale m to km | Often individual dykes | May also intrude passively into opening (ring) faults | All kinds, primitive to evolved magmas | All stages, before, during, or after caldera formation | Major |

ring-fault is important for ring-dikes. Based on studies using field constraints (Newhall and Dzurisin, 1988), laboratory work (Komuro, 1987; Roche et al., 2000; Acocella et al., 2001; Walter and Troll, 2001; Kennedy and Stix, 2003; Geyer et al., 2006) and numerical modeling (Komuro et al., 1984; Gudmundsson, 1988; Burov and Guillou Frottier, 1999; Kusumoto and Takemura, 2003, 2005), it now appears that ring-fault location, dip, and slip are mainly controlled by the depth and geometry of the magma chamber. The depth of a magma chamber is usually between 2 and 15 km. For example, an intrusive body is suspected to be 2 km beneath the Yellowstone caldera, 4–7 km beneath the Long Valley caldera, and 5–15 km beneath the Valles caldera (Lipman, 1997). Calderas are often elliptical, for instance the 35 × 73 km Garita caldera, and the presently active Rabaul caldera, which is 5 × 10 km. Besides such geometrical difficulties, combinations of stress fields, for instance, those due to a second deep magma chamber or regional tectonics, may influence the geometries of ring-complexes near the surface (Marti et al., 1996; Gudmundsson, 1998). In order to understand the general formation and appearance of ring-faults, the reader is referred to other papers within this volume detailing the structural development of caldera-related fault structures.

Ring-faults are often described as pure dip-slip structures; however, as shown by the conceptual model of Figure 1 and by the abundance of intrusive dikes along these faults, ring-faults (re)activate as opening mode fractures (Anderson, 1936). The necessary space for ring-dike intrusion can be generated during caldera floor subsidence. In fact, many former ring-faults are used as dike propagation paths, such that outcrops of ring-dikes appear to be more common than outcrops of ring-faults. A caldera ring-fault may become active during magma pressure changes associated with, for example, input of fresh magma from deeper sources (Sparks et al., 1984) or magma evacuation (Druitt and Sparks, 1984). Also, caldera ring-faults may slip or open due to tectonic activity, a remote stress field, or pre-existing strain history (Gudmundsson, 1988; Newhall and Dzurisin, 1988; Marti et al., 2000;



**Figure 1**    Sketch of ring-dike formation. During deflation of a large magma chamber (decrease of magma pressure), the chamber roof subsides (white arrow) to form subvertical or outwardly dipping ring-faults. A ring-dike (shown in dark gray) intrudes into such ring-faults. The ring-dike may reach the surface, as shown here, or may occur only underground and develop a bell-jar geometry and the surface flexure above (this geometry is shown by the dashed lines).

Bosworth et al., 2003), and thereby influence ring-dike intrusions. This means that ring-dikes may be emplaced in association with both magma chamber pressure changes and extrinsic processes. In this paper, the conditions under which ring-fractures may open to facilitate ring-dikes will be further explored and summarized. This work uses a set of boundary element models that address the question of where and under which circumstances a ring-fracture is subject to opening, and thus examines the geometric possibility of ring-dikes. The first models are simple, using spherical magma chambers and cylindrical ring-fractures. More complex models are then designed in order to understand the effects of ellipsoidal and sill-shaped chambers, and to test how extrinsic activities, such as peripheral radial dikes or earthquakes, can affect the locations and patterns of subsequent ring-dikes. Natural ring-dikes strongly compare to the patterns described herein (see Section 4). This paper intends to provide a general overview of ring-dike formation using numerical models, with the goal of stimulating successive studies at key locations elsewhere.

## 2. MODELING METHOD

Numerical models are performed in a three-dimensional linear elastic half-space medium, using a boundary element code (Crouch and Starfield, 1983; Becker, 1992; Thomas, 1993). The modeling method is based on the analytical solutions for angular dislocations in isotropic half- and full space (Comninou and Dundurs, 1975), and has already been used in various studies concerning the development of stress in volcanoes (e.g., Walter et al., 2005; Walter and Amelung, 2006). Using combinations of angular dislocations, polygonal (triangular) boundary elements are made that together can describe complex three-dimensional objects. This allows finite magma chambers and ring-faults of various dimensions to be considered. Boundary conditions are defined as tractions or displacements at the center of each element. Linear equations are solved in order to calculate displacement distributions along faults, dikes, and magma chambers. For a more detailed description, see Thomas (1993).

This study considers (i) a deflating magma chamber of various geometries (spherical, oblate spheroid, ellipsoid), (ii) a subvertical ring-fault surrounding the magma chamber (spherical, elliptical), (iii) freely slipping faults that may be reactivated during magma chamber evacuation, and (iv) dike intrusion and faulting in the periphery of the ring-fault.

The boundary element method was validated by comparing it with the analytical solution of a spheroid source (Yang et al., 1988); results agree within a few percentage for the studied range of geometries. The type of loading as shown in this paper is pressure change at the magma chamber by $-10$ MPa (depressurization). If other types of loading were applied, they are specified below. A Young's modulus of $E = 70$ GPa and a Poisson's ratio of $\nu = 0.25$ were assigned that were typical values for the shallow crust (Turcotte and Schubert, 2002). Varying these material properties can affect the magnitude of the results, but the patterns remain similar.

Various model geometries were considered, and tests were conducted for reservoir radii of 5 and 10 km, yielding very similar results. For spherical chambers, a radius of 5 km was used, while for elliptical chambers, $10 \times 5$ km was chosen. These diameters agree with most known calderas (Newhall and Dzurisin, 1988). The depth chosen for the chambers was 10 km to the reservoir center, thus between 5 and 7.5 km to the reservoir roof. Although realistic loading conditions and geometries were applied for all models, the results are used mainly in a qualitative way. The main goal of these model simulations is to emphasize the geometric complexities of ring-dikes at various caldera systems.

## 3. RESULTS

Three main sets of results are distinguished. First, deformation around a depressurized magma chamber is described together with how local structures can affect deformation. Second, the amount a ring-fault surrounding the depressurized magma chamber opens is described in order to examine the potential locations of dike intrusions. Third, models are designed to exemplify how processes external to the caldera, such as an earthquake or intrusion, can affect the location of a ring-dike intrusion. The results are shown in map view, cross-section, and side views as displacement vectors and contour plots. A coordinate system is indicated in each of the figures for orientation; $x$–$y$ is used for the horizontal plane and $z$ denotes the vertical direction, so a view in the $x$–$z$ plane is a side view.

## 3.1. Deformation around a depressurized magma chamber

### 3.1.1. Deflating spherical magma chamber

First, a simple scenario with a deflating magma chamber embedded in a uniform elastic material is considered. The magma chamber is spherical, with a radius $r = 5$ km, located at a depth $d = 10$ km below the surface (i.e. the depth of the roof of the chamber is 5 km). The magma chamber is subjected to a pressure drop of 10 MPa; this is the only type of loading in these models. The model setup is shown in Figure 2A, and results are shown in map view (Figure 2B) and along a cross-section west to east ($x$–$x'$, Figure 2C, D). The horizontal displacement field, shown by displacement vectors, indicates movement of the material towards the deflating source. Contours in Figure 2B indicate the amount of vertical displacement ($U_z$), which is negative and thus defines subsidence. The cross-sections indicate the horizontal displacement field ($U_x$, Figure 2C), showing that the material on the west side of the chamber is displaced to the east, while the material on the east of the chamber is displaced to the west (Figure 2D). At the surface, the maximum horizontal displacement occurs at a slightly eccentric location above the edge of the chamber. The vertical displacement field ($U_z$) shows that the material above the chamber sinks downward (Figure 2D); maximum subsidence occurs in a bell-shaped area just above the magma chamber. Below the chamber, a slight upward

**Deflating spherical magma reservoir**
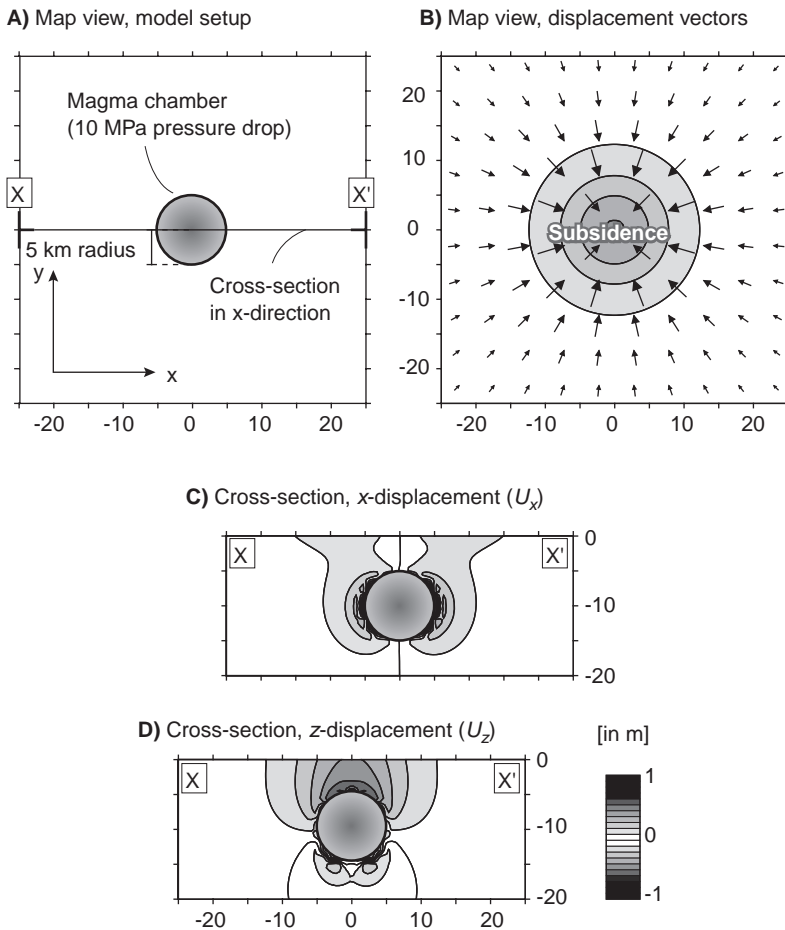


**Figure 2**  Deflation of a spherical magma chamber. (A) Map view of model setup (*x—y* plane). The magma chamber (5 km radius) is emplaced at (*x*, *y*) coordinates (0, 0) at 10 km depth, and is subject to a pressure drop of 10 MPa. (B) Map view of displacement vectors at the surface (*x—y* plane). The vectors converge toward the deflating source. Contours indicate negative vertical displacement (subsidence). (C) Cross-section *x—x′*. The displacement field in the horizontal direction (*U_x*) shows peak values near the chamber and at two locations at the surface. (D) Cross-section *x—x′*. The displacement field in the vertical direction (*U_z*) shows a bell–shaped subsidence area.

displacement can be observed (Figure 2D). Similar models have been studied by other researchers in order to simulate, for example, caldera formation, elastic flexure due to (under) pressurized sources, and related surface deformation (Gudmundsson, 1988, 1999; Bosworth et al., 2003; Kusumoto and Takemura, 2003; Pinel and Jaupart, 2005; Dzurisin, 2007).

### 3.1.2. Deflating spherical magma chamber with a nearby reactivated fault

Caldera systems are often located in tectonic areas already faulted by previous geological processes. In this set of models, a fault is introduced that is passively allowed to slip in the along-strike and dip-slip direction. All other model parameters, magma chamber shape and position, loading and output, are the same as described in the previous model. The fault is vertical and oriented south to north, 5 km from the magma chamber (Figure 3A). Displacements are calculated in map view (Figure 3B) and along cross-section x–x′, perpendicular to the fault (Figure 3C, D). The pattern of subsidence above the evacuating magma chamber

**Deflating spherical magma reservoir nearby reactivated fault**

**A)** Map view, model setup
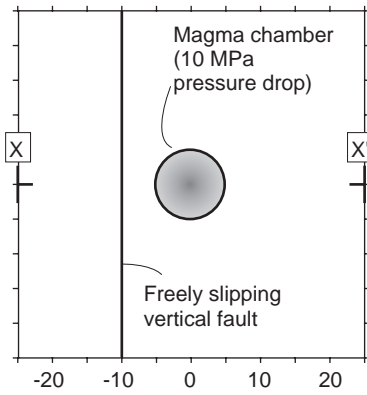
**B)** Map view, displacement vectors
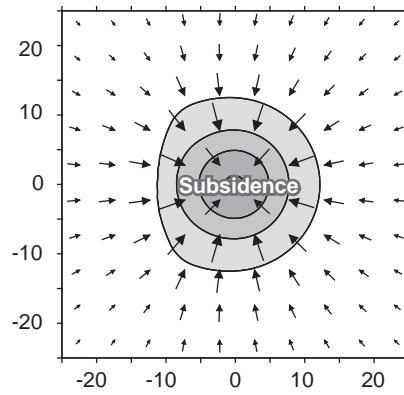
**C)** Cross-section, x-displacement ($U_x$)
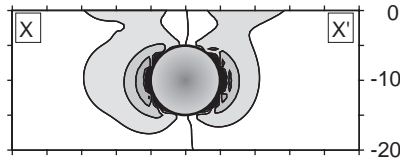
**D)** Cross-section, z-displacement ($U_z$)
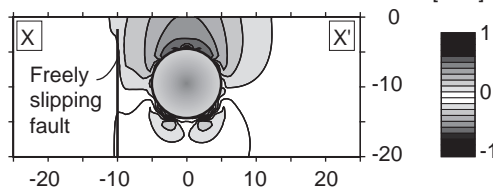
**Figure 3** Deflation of a spherical magma chamber near a reactivated fault. (A) Model setup (x–y plane). A linear vertical fault is defined 10 km from the magma chamber, from 2 to 20 km depth. The magma chamber is subject to a pressure drop of 10 MPa. As a result, the fault can be reactivated and slip in dip-slip and strike-slip motion. (B–D) Same as in Figure 2; the fault is shown only in D. Note that displacement vectors and fields are influenced by the fault.

(contours in Figure 2B) is influenced by the reactivated fault, with larger displacement vectors near the fault. The cross-sections show that evacuating the magma chamber results in higher horizontal ($U_x$) and vertical ($U_z$) displacements near the fault. The vertical displacement field $U_z$ shows a maximum downward displacement centered above the chamber. Similarly, previous researchers have discussed the effect of freely slipping faults near magma chambers subject to pressure changes (Gargani et al., 2006). Some other studies considered circular faults around a magma chamber, as detailed below.

### 3.1.3. Deflating spherical magma chamber enclosed by a reactivated ring-fault

A caldera ring-fault can be considered a zone of weakness that may accumulate volcano-tectonic strain. In the end-member scenario, caldera ring-faults are free to slip, considerably affecting deformation at the surface. Figure 4 shows a circular fault at a radius of 10 km circumscribing the deflating magma chamber. The fault can be considered a ring-fault peripheral to the active magma system, and can be reactivated in dip-slip and strike-slip. All other model parameters are the same as described above. The horizontal displacement vectors show material convergence towards the reservoir (Figure 4B). In cross-section, the displacement $U_x$ shows slightly smaller values near the surface (Figure 4C). In contrast, vertical displacement $U_z$ shows a broad area of subsidence (Figure 4D). The bell-shaped area of peak subsidence is less expressed, meaning that subsidence would most likely occur as a uniform block, limited by the reactivated ring-fault. There is more subsidence than in models lacking such a ring-fault, although the pressure drop within the magma chamber is the same (cf. Figure 2). Several previous studies have considered the effect of reactivated ring-faults surrounding a magma chamber subject to pressure changes, for instance, at the caldera of Campi Flegrei, Italy. These studies analyze the extent of deformation due to magmatic or hydrothermal activity influenced by fault reactivation (Troise et al., 1997, 2003, 2004; Petrazzuoli et al., 1999; Beauducel et al., 2004). It must be noted that the pattern of displacement fields can vary depending on the type and geometry of the reactivated ring-fault.

### 3.2. Predicting the location of ring-dike intrusions

The following models consider an evacuating magma chamber and a passively opening ring-fault. Results are shown in map view and in side views, displaying the contoured amount of ring-fault opening. In these calculations, the displacement perpendicular to each element of the ring-fault is determined; a positive displacement means that ring-dike intrusion is facilitated, while a negative displacement signifies areas where ring-dike intrusions are hindered. These models are designed to predict the most likely location and direction of a ring-dike intrusion, based on the assumption that a ring-dike intrusion may preferentially occur where the ring-fault is opened.

**Deflating spherical magma reservoir enclosed by reactivated ring-fault**

**A)** Map view, model setup



Magma chamber
(10 MPa
pressure drop)

Freely slipping
ring-fault

**B)** Map view, displacement vectors



Subsidence

**C)** Cross-section, *x*-displacement ($U_x$)



**D)** Cross-section, *z*-displacement ($U_z$)

[in m]



Freely
slipping
ring-fault
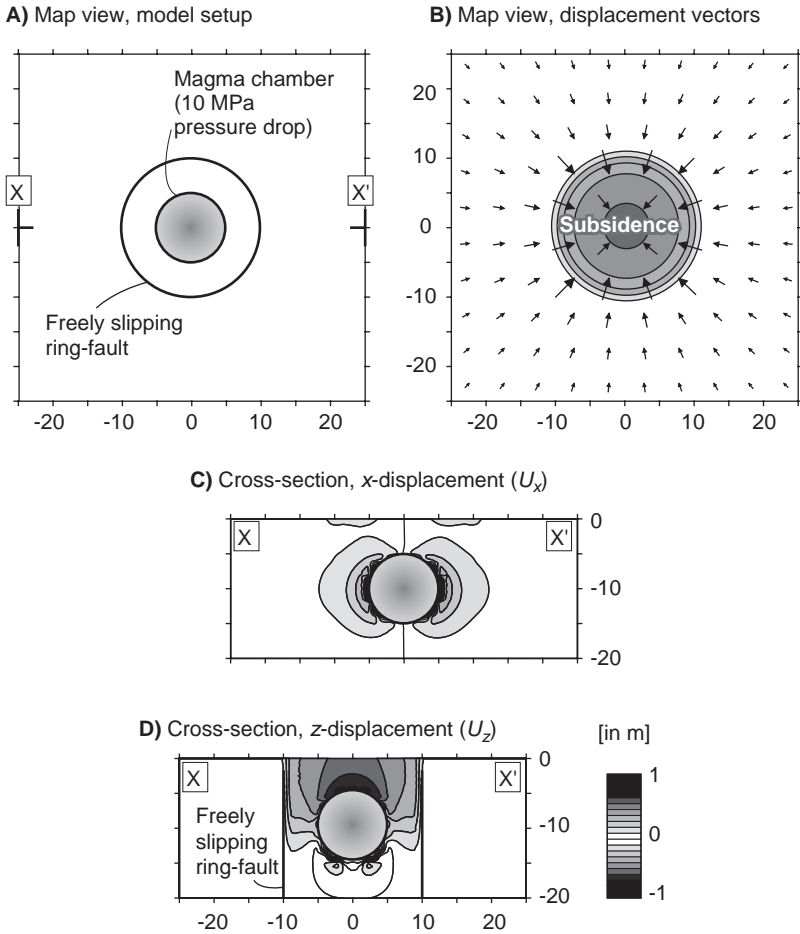
**Figure 4**    Deflation of a spherical magma chamber enclosed by a ring-fault. (A) Model setup
(*x*–*y* plane). A ring-fault is defined surrounding the magma chamber, with a radius of 10 km
at 2–20 km depth. The magma chamber is subject to a pressure drop of 10 MPa. As a result,
the ring-fault may be reactivated and slip in dip-slip and strike-slip. (B)–(D) Same as in
Figure 2. Displacement abruptly stops at the ring-fault, while $U_z$ deformation is amplified
inside the "caldera."

### 3.2.1. Deflating spherical magma chamber
In this model, a deflating magma chamber is encircled by a ring-fault, which
reaches from the base of the magma chamber to the surface (Figure 5).
Displacement vectors and displacement contours suggest piston-type subsidence
with the largest horizontal displacement in the periphery (Figure 5B). The side
views onto the opening ring-dike (Figure 5C) show that the displacement at the
ring-fault is largest at depth near the magma chamber and is radially uniform,

**Deflating spherical magma reservoir, opening at ring-fault**

**A)** Map view, model setup



**B)** Map view, displacement vectors



**C)** Side views on opening ring-dike      [in m]
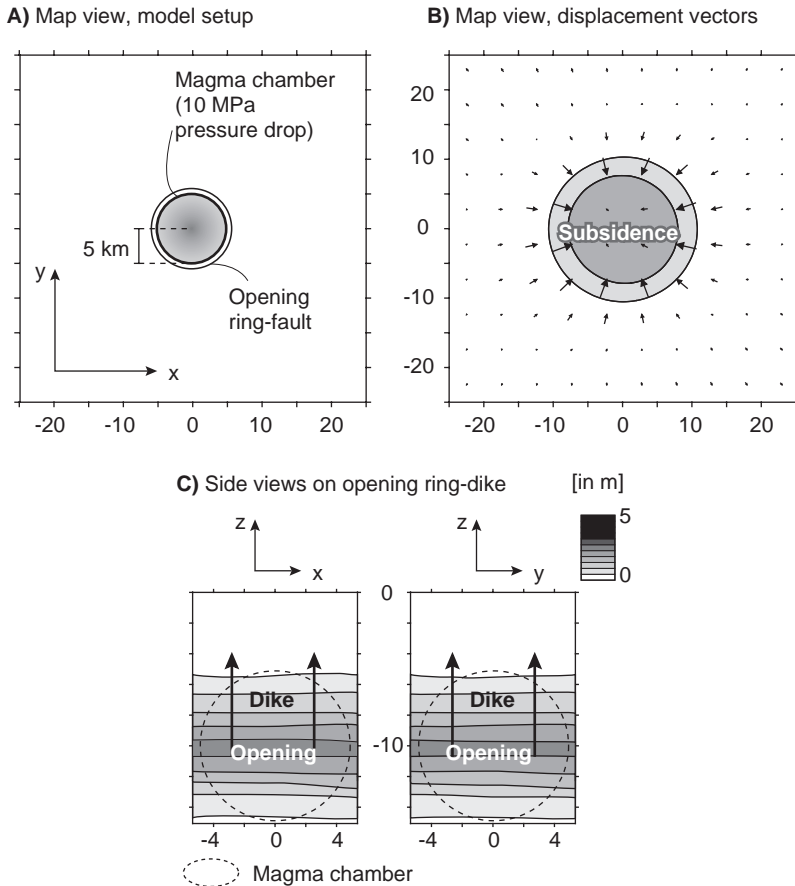


**Figure 5**   Deflation of a spherical magma chamber causes opening at a circumferential ring-fault. (A) Model setup ($x$—$y$ plane). The magma chamber (5 km radius) is emplaced at ($x, y$) coordinates (0, 0) at 10 km depth, and is subject to a pressure drop of 10 MPa. A ring-fault is defined surrounding the magma chamber, with a radius of 5 km at 0—20 km depth. Boundary conditions are set so that the ring-fault is allowed to open. (B) A map view of horizontal displacement vectors at the surface ($x$—$y$ plane) shows convergence toward the deflating source. Vector magnitudes are largest at the periphery and tend to become zero inside the caldera (piston subsidence). (C) Side views on opening ring-fault (left showing $x$—$z$ plane, right $y$—$z$ plane). The projection of the spherical magma chamber enclosed by the ring-fault in (C) is indicated as a dashed ring centered at 10 km depth. Maximum opening occurs near the magma chamber. The pattern is radially symmetric, so dike intrusion (shown by black arrow) may occur as a complete ring.

implying that a dike intrusion could occur anywhere along the ring-fault and in a complete circle around the magma chamber. Separate tests were done to study the effect of a ring-fault dipping in or out (not shown in figures), which affects the amount of opening in the sense that a larger amount of opening is found

for outwardly dipping ring-faults. However, a more complex shape of the ring-fault or magma chamber or a variably dipping ring-fault may yield variable amounts of opening, thus also affecting the geometry and completeness of a ring-dike.

### 3.2.2. Deflating sill-shaped magma chamber

Because magma chambers are typically flattened rather than spherical (Marsh, 2000), a sill-shaped (oblate spheroid) geometry must be considered, as it may significantly affect the distribution of ring-fault opening. In this model, a deflating sill-shaped magma chamber is encircled by a ring-fault, and the setup of the model is similar to the scenario described above with the only exception that the magma chamber is flat: 10 km wide and 5 km high (Figure 6). Depressurizing the sill-shaped magma chamber causes the most pronounced ring-fault opening along a narrow band around the magma chamber (Figure 6C). However, the amount of opening is smaller than for the spherical magma chamber model (note the different color scale in Figures 5 and 6). The most likely upward propagation path of a dike cannot be determined in this scenario, because the pressure source is perfectly radially symmetric; therefore, any location around the ring-fault may be used. This pattern significantly changes if the magma chamber is elliptical, as shown below.

### 3.2.3. Deflating an elliptical magma chamber

Most actual calderas and their associated ring-faults are not circular, but elliptical (Holohan et al., 2005). As a consequence, the pattern of ring-fault opening and intrusion differs significantly from the radially symmetric scenario. In this model, a sill-shaped deflating magma chamber elongated in the east-west direction is used (ellipsoid shaped). The magma chamber is 20 km long, 10 km wide, and 5 km high (elongated in the $x$-direction), and is encircled by a ring-fault (Figure 7A). The magma chamber center is 10 km below the surface and is subject to a pressure drop of 10 MPa (Figure 7B). The model predicts a maximum in ring-fault opening at magma chamber depths. The $x$–$z$ and $y$–$z$ side views onto the ring-fault show the regions subject to opening. The largest amount of opening occurs at the short-axis side of the elliptical ring-fault (Figure 7C left) and drops to zero along the long-axis side of the elliptical ring-fault (Figure 7C right). The model results can thus be interpreted in such a way that dike intrusions are more likely to occur and to propagate upward along the short-axis side of the elliptical ring-fault. It may also be possible that ring-dike intrusions change their intrusion direction and migrate laterally into the short-axis side, as indicated in Figure 7C. The caldera that formed the Bishop Tuff eruption at Long Valley, for instance, is thought to have initiated at the short-axis side, as suggested also by recent analog experiments (Holohan et al., in press).

**Deflating sill-shaped magma reservoir, opening at ring-fault**

**A)** Map view, model setup

**B)** Map view, displacement vectors



**C)** Side views on opening ring-fault
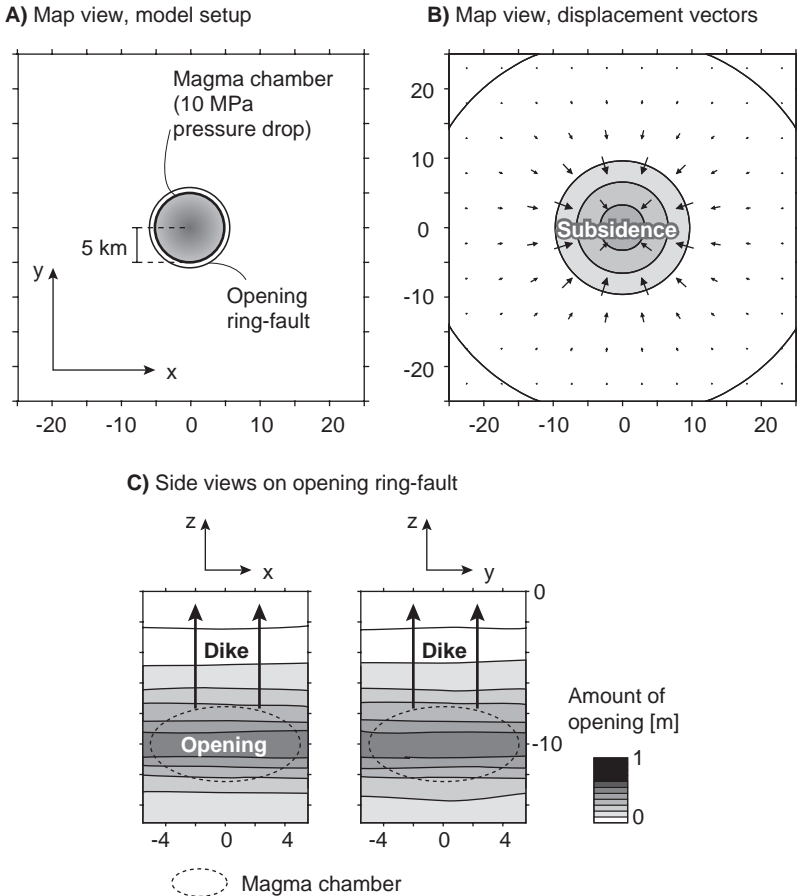


**Figure 6** Deflation of a sill–shaped magma chamber causes opening at a circumferential ring-fault. The magma chamber is vertically flattened (5 km radius in $x$ and $y$ directions, 2.5 km in $z$ direction, aspect ratio 2:1), emplaced at $(x, y)$ coordinates $(0, 0)$ at 10 km depth, and is subject to a pressure drop of 10 MPa. All other parameters and subfigure explanations (A–C) are the same as in Figure 5. This model suggests that the zone of maximum opening is restricted to very close to the sill–shaped magma chamber. The pattern is radially symmetric, so dike intrusion (shown by black arrow) may occur as a complete ring.

## 3.3. How processes external to the caldera system may affect the location of ring-dike intrusions

### 3.3.1. Tectonic earthquake at a distance

Many calderas systems are located in highly active tectonic regions where large earthquakes can occur and affect the activity of the volcano magma system. In this

**Deflating elliptical magma reservoir, opening at ring-fault**

**A)** Map view, model setup
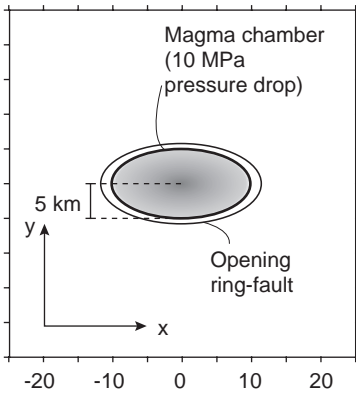
**B)** Map view, displacement vectors
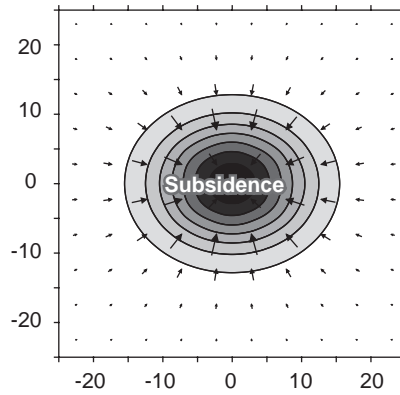
**C)** Side views on opening ring-fault, amount of opening
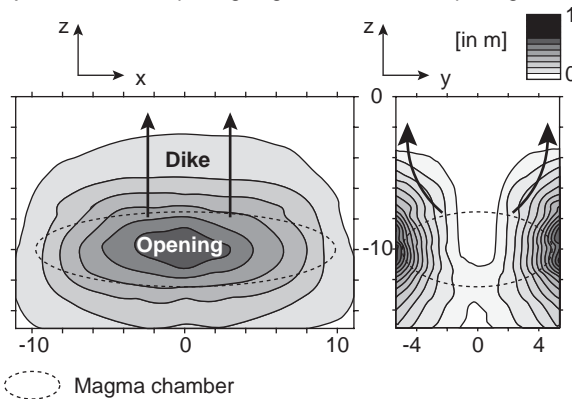
**Figure 7** Deflation of an elliptical magma chamber causes opening at a circumferential ring fault. The magma chamber is elongated in the *x*-direction and vertically flattened (10 km radius in *x*, 5 km in *y*, and 2.5 km in *z*), emplaced at (*x, y*) coordinates (0, 0) at 10 km depth, and is subject to a pressure drop of 10 MPa. All other parameters and subfigure explanations (A–C) are the same as in Figure 5. The displacement computed at the ring–fault suggests opening should occur at the short–axis side of the ring-fault. A potential dike intrusion would intrude as shown by the black arrow in (C).

model, the effect of a tectonic earthquake distant from the ring–fault is considered. The earthquake is simulated by 5 m uniform slip on a $20 \times 20$ km fault, 100 km from the ring-fault (Figure 8A). A low-angle thrust earthquake is simulated, as if in a subduction zone. As in the models described above, the amount of opening is calculated at the ring-fault in order to predict the location of a ring-dike. Map view shows displacement vectors directed to the west towards the earthquake zone and slight subsidence due to the reactivated (opened) ring-fault (Figure 8B). The model predicts maximum opening at two opposite sides of the ring-fracture, with slightly

**Tectonic earthquake at distance to ring-fault**

**A)** Side view, model setup



**B)** Map view, displacement vectors     **C)** Side views on opening ring-fault
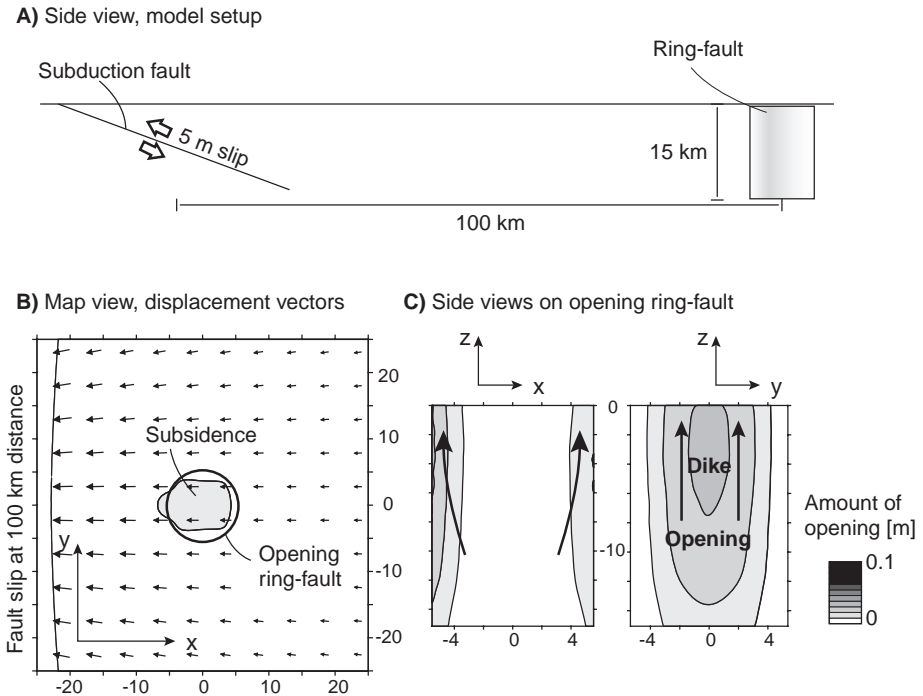


**Figure 8** Remote tectonic deformation acting on a ring-fault. (A) Model setup ($x$—$z$ plane). An earthquake was simulated 100 km from the ring-fault, its characteristics resembling a subduction earthquake. A ring-fault is defined with a radius of 5 km at 0—20 km depth. Boundary conditions are set so that the ring-fault is allowed to open due to the earthquake. (B) A map view of horizontal displacement vectors at the surface ($x$—$y$ plane) shows displacement of the hanging wall toward the earthquake source. Note small subsidence caused by reactivation of the ring-fault. (C) Side views on opening ring-fault (left showing $x$—$z$ plane, right showing $y$—$z$ plane). Maximum opening occurs at two regions of the ring-fault. Dike intrusions into the ring-fault are encouraged perpendicular to the slip direction of the earthquake (potential dike paths shown by black arrow). A similar displacement pattern is expected for ring-faults subject to rifting episodes.

more on the side closer to the earthquake (Figure 8C). The model thus suggests that a dike intrusion is encouraged in these two zones, while complete ring-fault reactivation and ring-dike formation appears unlikely. A similar effect can be expected for zones subject to tectonic rifting. The models imply that tectonic deformation may have a large effect on the ring-dike intrusion pattern and thus also affect the location of an eruption.

### 3.3.2. Radial dike intrusion outside the ring-fault
Some systems are known for a pattern of radial dikes and fractures outside the caldera basin (e.g., Galapagos Islands, Chadwick and Howard, 1991; Gran Canaria,

Troll et al., 2002). In this model, an intrusion of a radial dike outside a caldera ring-fault is considered (Figure 9A). The radial dike is 15 km long and deep, and subject to 1 m of uniform opening. This induces a displacement at the adjacent ring-fault. Similar to the models described before, the ring-fault is allowed to open. The map-view displacement vectors show extension perpendicular to the dike and two lobes of uplift (Figure 9B), typical for shallow dike intrusions (Dzurisin, 2007). The side

**Radial dike intrusion, opening at ring-fault**
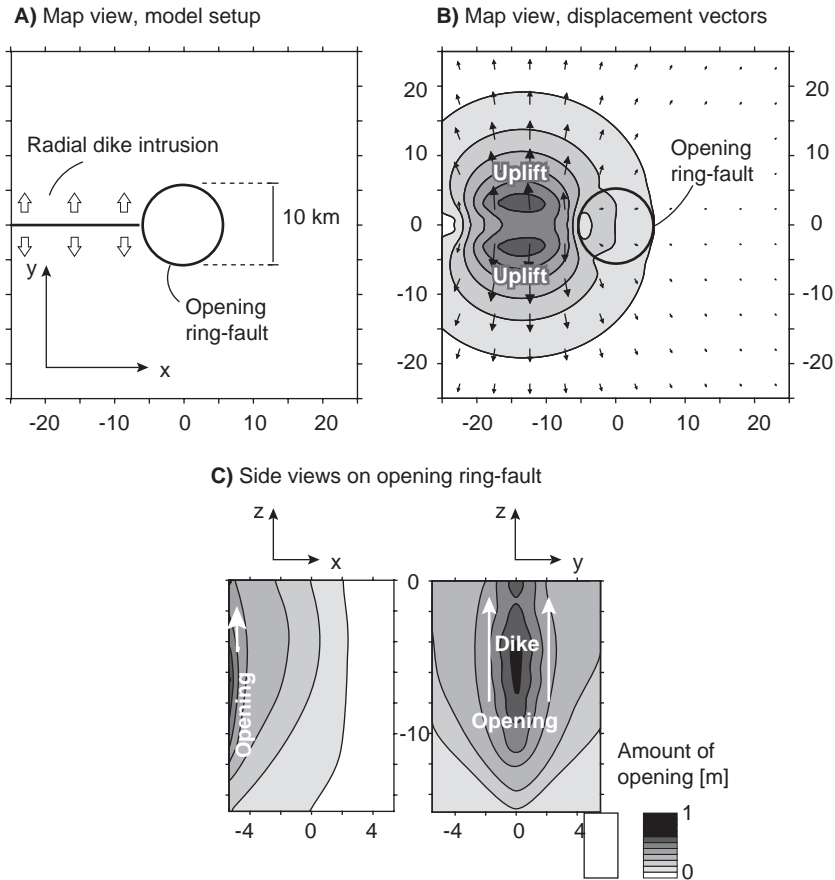


**Figure 9** Radial dike intrusion causes opening of caldera ring-fault. (A) Model setup (x–y plane). A radial dike with an area of 15 × 15 km is subject to 1 m uniform opening. The dike is located outside a ring-fault. Boundary conditions are set so that the ring-fault is allowed to open. (B) A map view of horizontal displacement vectors at the surface (x–y plane) shows displacement perpendicular to the dike, with two lobes of maximum uplift in the periphery. $U_z$ displacement contours are locally influenced by the opening ring-fault. (C) Side views shows opening of ring-fault (left shows x–z plane, right y–z plane) in the region facing the radial dike. The zones of opening can be more easily intruded by ring-dikes, so a radial dike may control the intrusion of an ensuing partial ring-dike.

views show that maximum opening occurs at the part of the ring-fault that is closest to the dike (Figure 9C). This suggests that ring–dike intrusion might occur at the segment of the ring-fault that is closest to the radial dike intrusion in the periphery of the caldera. Accordingly, a dipping dike would lead to ring–dike formation that obliquely propagates upwards.

## 4. Discussion

This paper uses numerical models to (i) describe deformation around a depressurized magma chamber and test how local structures can affect this displacement, (ii) describe the potential of opening a ring-fault in order to examine the location at which potential dike intrusions occur, and (iii) describe how processes external to the caldera, such as an earthquake or radial intrusion, affect the location of a ring–dike intrusion.

The models are simplified and assume a homogeneous elastic material. Volcanoes, especially caldera volcanoes that experience a high degree of fracturing and hydrothermal weakening, may have a time-dependent viscoelastic rheology (Newman et al., 2001) and rock-strength values that vary by as much as several orders of magnitude (Watters et al., 2000). The variations in material may be lateral (due to fracturing, dikes, alteration) or vertical (due to lithologic layering, increasing confining pressure). Thus, the development of a stress field and the deformation pattern may be influenced by such heterogeneities (e.g., Manconi et al., 2007; Gudmundsson, 2006). One may speculate, for instance, that the amount of ground displacement in a deflating or inflating caldera basin can be amplified by rock types that have a lower modulus of elasticity. Likewise, the effect of external processes, such as earthquakes or dike intrusion in the periphery of the volcano, may have an effect on caldera systems. The models used in this study assume that the intrusion of ring-dikes as subvertical extensional fractures (mode I) is governed by opening perpendicular to a ring-fault. This generally agrees with historical caldera activity, where displacement often occurs along near-vertical ring-faults (Newhall and Dzurisin, 1988). However, it must be noted that this is a simplification of more complex geometries, as some historical caldera ring-faults have shear fractures that dip slightly inward (Darwin caldera) or outward (Rabaul caldera), the latter also approximating the findings of previous seminal work (Anderson, 1936, 1937). Some (probably most) dike intrusions intrude in a mixed-mode mechanism, including opening (mode I) but also strike-slip shear (mode II) and dip-slip shear (mode III) dislocation, which is not considered in the models presented here. Nevertheless, important conclusions can be drawn from these models, as shown by comparisons to natural caldera systems.

The models imply that a ring–dike forms in a uniform circular way only when the magma chamber is uniform, perfectly spherical, and not influenced by regional or external structures or deformation fields. Most other numerical models suggest that a potential ring–dike is more likely to intrude only partially into a ring-fault. Likewise, typical ring-dikes found in nature show such complexities, where in combination with the models summarized here, external influences can be assessed.

Surface eruptions circumscribing a caldera center have occurred at several locations, for instance, on Deception Island (1967–1969) and Niuafoou (1853, 1867) (Newhall and Dzurisin, 1988). While some historical caldera activity may have been related entirely to ring-dikes, others have been due to a dike that was partially reactivated and intruded a pre-existing fault. At Rabaul, a caldera system with a strongly elliptical outline, eruptive activity simultaneously occurred on opposite sides in 1878 and 1937 (Mori and McKee, 1987; Nairn et al., 1995; Saunders, 2004). At some caldera systems, ring-dike intrusions and eruptive activity occurred at two or more ring vents, as for example at the $20 \times 30$ km wide Tondano caldera in 1952 and 1971 (Lecuyer et al., 1997).

Several examples of calderas and their ring-dike structures are shown in Figure 10. The first image shows a downsag caldera, lacking prominent ring–fractures and ring-dikes. The Gross Brukkaros system in Namibia (Figure 10a) has not formed zones of major concentric structural weakness. The 10 km wide structure was first subject to shallow magma inflation at about 4 km depth (Komuro et al., 1984) and intense surface doming, bending the surface stratigraphy (Stachel et al., 1994). The doming phase was followed by depletion of up to $5 \text{ km}^3$, but no major ring-dike or ring-fault structure was formed. This example illustrates that large magma evacuation and downsag caldera subsidence is possible without major structural fracturing and dike injection visible at the surface.

Intrusion around a caldera basin is the most comprehensible representation of a ring-dike. Some of the ring-dike intrusions occur along a single ring-fault, while others occur along several subparallel faults that form a near-concentric pattern at the surface. Ring-dikes are described in the Peninsular Range Batholiths of Baja California, Mexico, and southern California (Johnson et al., 2002). The formation of the Ramona ring-dike (Figure 10b) is thought to have been associated with a phase of subsidence of the caldera floor (Mirriam, 1941). Another elliptical ring structure is shown, from the El Pinal complex (Figure 10c), which is interpreted as a ring-dike that causes a well-developed contact zone (Duffield, 1968).

Ring-dike structures that develop in a region tectonically predisposed or subject to a tectonic stress field may develop very complex shapes. An intruding ring-dike may follow pre-existing faults or discontinuities and thus abruptly stop or change its direction, conditioned by various parameters such as material property, fault friction coefficient, pore pressure, and state of stress. A simple scenario was simulated here to illustrate the significance of pre-existing discontinuities. The numerical model showed that caldera subsidence close to a linear fault is highly asymmetrical, being focused at one side of the fault structure. The Erongo complex is one of the largest of the Damaraland complexes in Namibia, and shows a central 30 km wide massif with silicic intrusions, partly encircled by a tholeiitic ring-dike with a 50 km diameter (Figure 10d). The ring-dike half formed only on the north-western side of a SW–NE oriented regional fault that was thought to have been reactivated during intrusion (Wigand et al., 2004). It was suggested that the ring-dike formed after a caldera collapse (Wigand et al., 2004). The absence of a ring-dike on the segment opposing the fault implies that circular dike intrusion was hindered. The models shown in this study suggest that a reactivated tectonic fault may act as a barrier to deformation; so a change in magma chamber pressure leads to significant
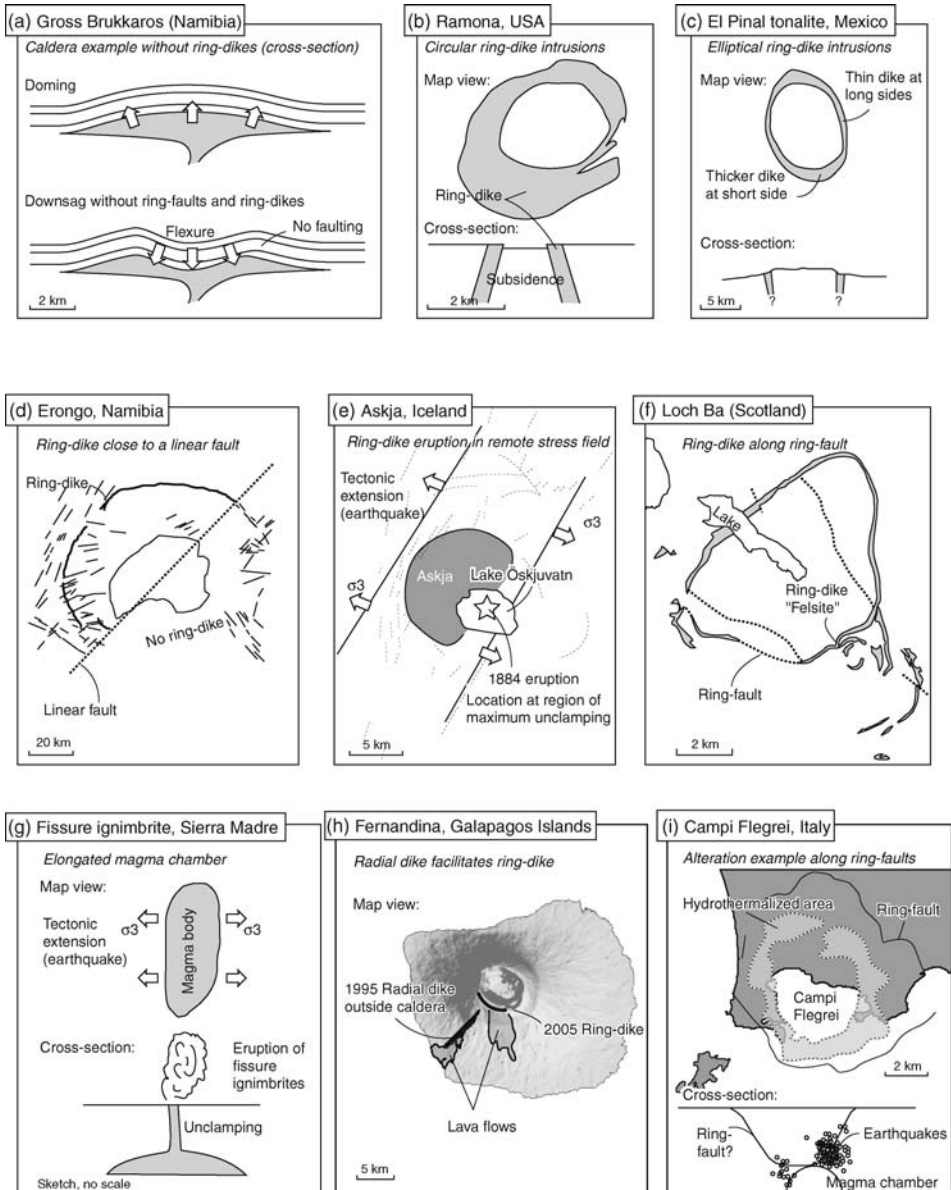
**Figure 10** Examples of ring structures and ring–dikes. (a) After Stachel et al. (1994). (b) After Johnson et al. (2002). (c) After Johnson et al. (2002). (d) After Wigand et al. (2004). (e) After Sturkell and Sigmundsson (2000). (f) After Aguirre Diaz and Labarthe Hernandez (2003). (g) After Jonsson et al. (1999) and GVP (2005). (h) After Beauducel et al. (2004). (i) After (a). See discussion text for details.

deformation only on one side of the fault. Thus, dike intrusion occurs only on one part of the circle: the numerical models support the evolutionary hypothesis and structural development proposed for the Erongo complex (compare Figures 3 and 4).

Many caldera systems and ring-dikes form in areas that are subject to tectonic deformation. The Askja volcanic complex is located at the divergent plate boundary in northern Iceland and hosts the 8 km wide Askja caldera (Sturkell and Sigmundsson, 2000). In 1875, dike intrusion occurred in the south-eastern margin of the Askja caldera, associated with a Plinian eruption and a parasitic 4.5 km wide caldera that is now filled by Lake Öskjuvatn. The dike was part of a larger rifting event, and reactivated the south-eastern flank of the Askja caldera ring-fault. The models presented in this paper show that these parts of the ring-fault are subject to opening if a remote extensional deformation source is applied, for example, a tectonic earthquake or rifting. Dike opening due to tectonic extension is also proposed for large-scale eruptions in Mexico (Aguirre Diaz and Labarthe Hernandez, 2003). The so-called fissure ignimbrites are probably not directly related to caldera collapse, but may be related to tectonic unclamping of a main dike (Figure 10g).

A well-exposed ring-dike is known from Loch Ba at the igneous center of Mull, in northwestern Scotland (Figure 10f). Ring-dike emplacement occurred during the last major intrusive event of the volcanic center, intruded directly into a ring-fault. The dike is rhyolitic and contains up to 20% mafic inclusions, implying significant magma mixing (Walker and Skelhorn, 1966; Sparks, 1988). The ring-dike is thought to have intruded the ring-fault during a rapid caldera collapse associated with the violent eruption of a welded tuff from a strongly zoned magma chamber (Sparks, 1988). The dike is mostly vertical and dips 70–80° outward in the north-western segment (Bailey et al., 1924). However, the ring-dike does not form a complete ring; instead, it intrudes with a variable thickness from 0 to 400 m along a ring 8 km in diameter. In areas where the dike did not intrude, a ring-fault is exposed. This suggests that the ring-dike intruded an existing ring-fault where variable opening of the ring-fault may be related to small variations in its orientation (strike and/or dip) or magma chamber geometry.

Volcanic activity outside of a caldera system may affect the location and timing of ring-dike intrusions. The Galapagos volcanoes are case examples for ring-dike intrusions that are surrounded by radial dikes in the periphery (Chadwick and Howard, 1991). Due to alternating radial and circumferential dikes, the Galapagos volcanoes developed a typical morphology, reminiscent of an "inverted soup bowl" (Chadwick and Dieterich, 1995). In 1995, a radial dike intrusion occurred on the south-west flank of Fernandina volcano (Figure 10h, just outside of the 5 km-wide caldera (Jonsson et al., 1999). The volcano did not erupt until an eruptive dike intruded the ring-fault in the south-western part of the caldera in 2005. The 2005 dike is a ring-dike, and its location matches the location of maximum opening as suggested by the numerical models in this study (compare Figure 9).

The locations of ring-dike intrusions are probably consistent with areas of hydrothermal activity, alteration, and ore deposition (Stix et al., 2003). For the caldera of Campi Flegrei, uplift was suggested to be largely influenced by

reactivated ring-faults (Troise et al., 1997, 2003, 2004; Petrazzuoli et al., 1999; Beauducel et al., 2004; De Natale et al., 2006). In summary, the mechanical processes that reactivate ring-fractures by dikes may also be of major importance for hydrothermal activity that follows the same trend (Beauducel et al., 2004). Thus, understanding the formation and reactivation of ring-faults and their susceptibility to intruding ring-dikes is of major interest to earth scientists of various disciplines.

## 5. Conclusion

Periods of caldera unrest mainly reflect tectonic and magmatic processes. This paper focuses on potential intrusion patterns along caldera ring-faults. A systematic set of numerical models suggests that caldera deformation may be affected by pre-existing and reactivated tectonic faults and ring-fractures, and that sites of ring-dike intrusions are controlled by various tectonic and magmatic loading processes. A tectonic event like an earthquake may lead to localized displacements at caldera systems and affect the locations of ring-dike intrusions. The shape of a deflating magma chamber of ring-fault may also affect the locations of ring-dikes. In view of this the formation of complete ring-dikes appears to be difficult. Many natural calderas have ring-dikes that can be better understood by examining the local volcano–tectonic environment and considering the models summarized in this paper. The locations and patterns of ring-dike intrusions at caldera volcanoes can also be applied to the distribution of hydrothermal activity and ore deposition elsewhere.

## REFERENCES

Acocella, V., Cifelli, F., Funiciello, R., 2001. Analogue models of collapse calderas and resurgent domes. J. Volcanol. Geotherm. Res., 104(1–4), 81–96.

Aguirre Diaz, G.J., Labarthe Hernandez, G., 2003. Fissure ignimbrites: Fissure-source origin for voluminous ignimbrites of the Sierra Madre Occidental and its relationship with Basin and Range faulting. Geology, 31(9), 773–776.

Anderson, E.M., 1936. The dynamics of the formation of cone sheets, ring dykes, and cauldron subsidence. Proc. Indian Acad. Sci., Earth Planet. Sci., 56, 128–163.

Anderson, E.M., 1937. Cone sheets and ring dikes: the dynamical explanation. Bull. Volcanol., 2(1), 35–40.

Bailey, E.M., Clough, C.T., Wright, W.B., Richey, J.E., Wilson, G.V., 1924. The tertiary and post-tertiary geology of Mull, Loch Aline, and Oban. Mem. Geol. Surv. Scotland, 1–445.

Beauducel, F., De Natale, G., Obrizzo, F., Pingue, F., 2004. 3-D modelling of Campi Flegrei ground deformations: role of caldera boundary discontinuities. Pure Appl. Geophys., 161(7), 1329–1344.

Becker, A.A., 1992. The Boundary Element Method in Engineering. McGraw-Hill, New York, NY.

Billings, M.P., 1943. Ring-dikes and their origin. Trans N. Y. Acad. Sci., Series II, 5, 131–144.

Bonin, B., 1986. Ring Complex Granites and Anorogenic Magmatism. North Oxford Academic Publishers Ltd., London.

Bosworth, W., Burke, K., Strecker, M., 2003. Effect of stress fields on magma chamber stability and the formation of collapse calderas. Tectonics, 22(4), 16-1–16-21.

Burov, E.B., Guillou Frottier, L., 1999. Thermomechanical behavior of large ash flow calderas. J. Geophys. Res., 104(10), 23081–23109.

Chadwick, W.W., Jr., Dieterich, J.H., 1995. Mechanical modeling of circumferential and radial dike intrusion on Galapagos volcanoes. J. Volcanol. Geotherm. Res., 66(1–4), 37–52.

Chadwick, W.W., Jr., Howard, K.A., 1991. The pattern of circumferential and radial eruptive fissures on the volcanoes of Fernandina and Isabela islands, Galapagos. Bull. Volcanol., 53(4), 259–275.

Clough, C.T., Maufe, H.B., Bailey, E.B., 1909. The cauldron-subsidence of Glen Coe, and the associated igneous phenomena. Q. J. Soc. Lond., 65, 611–678.

Cole, J.W., Milner, D.M., Spinks, K.D., 2005. Calderas and caldera structures: a review. Earth Sci. Rev., 69(1–2), 1–26.

Comninou, M., Dundurs, J., 1975. The angular dislocations in a half space. J. Elast., 5(3–4), 203–216.

Crouch, S.L., Starfield, A.M., 1983. Boundary Element Methods in Solid Mechanics. George Allen and Unwin, London.

De Natale, G., Troise, C., Pingue, F., Mastrolorenzo, G., Pappalardo, L., Battaglia, M., Boschi, E., 2006. The Campi Flegrei Caldera: unrest mechanisms and hazards. In: Troise, C., De Natale, G., Kilburn, C. (Eds), Mechanisms of Activity and Unrest at Large Calderas. Geological Society, London Special Publications, Vol. 269, pp. 25–45.

Druitt, T.H., Sparks, R.S.J., 1984. On the formation of calderas during ignimbrite eruptions. Nature, 310(5979), 679–681.

Duffield, W., 1968. The petrology and structure of the El Pinal tonalite, Baja California, Mexico. Geol. Soc. Am. Bull., 79, 1351–1374.

Dzurisin, D., 2007. Volcano Deformation. Springer, Chichester.

Gargani, J., Geoffrey, L., Gac, S., Cravoisier, S., 2006. Fault slip and Coulomb stress variations around a pressured magma reservoir: consequences on seismicity and magma intrusion. Terra Nova, 18, 403–411.

Geyer, A., Folch, A., Marti, J., 2006. Relationship between caldera collapse and magma chamber withdrawal: an experimental approach. J. Volcanol. Geotherm. Res., 157(4), 375–386.

Gudmundsson, A., 1988. Formation of collapse calderas. Geology, 16(9), 808–810.

Gudmundsson, A., 1998. Formation and development of normal-fault calderas and the initiation of large explosive eruptions. Bull. Volcanol., 60(3), 160–170.

Gudmundsson, A., 1999. Explosive eruptions triggered by dip–slip on caldera faults. Volcanol. Seismol., 20(2), 239–254.

Gudmundsson, A., 2006. How local stresses control magma-chamber ruptures, dyke injections, and eruptions in composite volcanoes. Earth-Sci. Rev., 79(1–2), doi: 10. 1016/j.earscirev.2006.06.006.

GVP, 2005. Global Volcanism Program. Smithsonian Institution, http://www.volcano.si.edu/

Holohan, E.P., Troll, V.R., van Wyk de Vries, B., Walsh, J.J., Walter, T.R., in press. Unzipping Long Valley: an explanation for vent migration patterns during an elliptical ring-fracture eruption. Geology G24329AR.

Holohan, E.P., Troll, V.R., Walter, T.R., Muenn, S., McDonnell, S., Shipton, Z.K., 2005. Elliptical calderas in active tectonic settings: an experimental approach. J. Volcanol. Geotherm. Res., 144(1–4), 119–136.

Johnson, S.E., Schmidt, K.L., Tate, M.C., 2002. Ring complexes in the Peninsular Ranges Batholith, Mexico and the USA: magma plumbing systems in the middle and upper crust. Lithos, 61(3–4), 187–208.

Jonsson, S., Zebker, H., Cervelli, P., Segall, P., Garbeil, H., Mouginis Mark, P., Rowland, S., 1999. A shallow-dipping dike fed the 1995 flank eruption at Fernandina volcano, Galapagos, observed by satellite radar interferometry. Geophys. Res. Lett., 26(8), 1077–1080.

Kennedy, B., Stix, J., 2003. Igneous rock associations of Canada 2. Stages in the temporal evolution of calderas. Geosci. Canada, 30(3), 129–140.

Kennedy, B., Stix, J., 2007. Magmatic processes associated with caldera collapse at Ossipee ring dyke, New Hampshire. Geol. Soc. Am. Bull., 119(1), 3–17.

Komuro, H., 1987. Experiments on cauldron formation: a polygonal cauldron and ring fractures. J. Volcanol. Geotherm. Res., 31(1–2), 139–149.

Komuro, H., Fujita, Y., Kodama, K., 1984. Numerical and experimental models on the formation mechanism of collapse basins during the Green Tuff orogenesis of Japan. Bull. Volcanol., 47, 649–666.

Kusumoto, S., Takemura, K., 2003. Numerical simulation of caldera formation due to collapse of a magma chamber. Geophys. Res. Lett., 30(24), 2278, doi:10.1029/2003GL018380.

Kusumoto, S., Takemura, K., 2005. Caldera geometry determined by the depth of the magma chamber. Earth Planets Space, 57(12), 17–20.

Lecuyer, F., Bellier, O., Gourgaud, A., Vincent, P.M., 1997. Tectonique active du Nord-Est de Sulawesi (Indonésie) et contrôle structural de la caldeira de Tondano. C.R. Acad. Sci. Paris, 325(8), 607–613.

Lipman, P.W., 1984. The roots of ash flow calderas in western North America: windows into the tops of granitic batholiths. J. Geophys. Res., 89(B10), 8801–8841.

Lipman, P.W., 1997. Subsidence of ash-flow calderas: relation to caldera size and magma-chamber geometry. Bull. Volcanol., 59(3), 198–218.

Manconi, A., Walter, T.R., Amelung, F., 2007. Effects of mechanical layering on volcano deformation. Geophys. J. Int., 170(2), 952–958.

Marsh, B.D., 2000. Magma chambers. In: Encyclopedia of Volcanoes 1. Academic Press, San Diego, CA, pp. 191–206.

Marti, J., Folch, A., Neri, A., Macedonio, G., 2000. Pressure evolution during explosive caldera-forming eruptions. Earth Planet. Sci. Lett., 175(3–4), 275–287.

Marti, J., Vila, J., Rey, J., 1996. Deception Island (Bransfield Strait, Antarctica): an example of a volcanic caldera developed by extensional tectonics. In: McGuire, W.J., Jones, A.P. Neuberg, J. (Eds), Volcano Instability on the Earth and Other Planets, Geological Society, London Special Publications, Vol. 110, pp. 253–265.

Mirriam, R.H., 1941. A southern California ring-dike. Am. J. Sci., 239, 365–371.

Mori, J., McKee, C.O., 1987. Outward-dipping ring-fault structure at Rabaul caldera as shown by earthquake locations. Science, 235(4785), 193–195.

Nairn, I.A., McKee, C.O., Talai, B., Wood, C.P., 1995. Geology and eruptive history of the Rabaul caldera area, Papua New Guinea. J. Volcanol. Geotherm. Res., 69(3–4), 255–284.

Newhall, C.G., Dzurisin, D., 1988. Historical unrest at large calderas of the world. US Geological Survey, Reston, VA, 1108 pp.

Newman, A.V., Dixon, T.H., Ofoegbu, G.I., Dixon, J.E., 2001. Geodetic and seismic constraints on recent activity at Long Valley caldera, California: evidence for viscoelastic rheology. J. Volcanol. Geotherm. Res., 105(3), 183–206.

O'Driscoll, B., Troll, V.R., Reavy, R.J., Turner, P., 2006. The great eucrite intrusion of Ardnamurchan, Scotland: reevaluating the ring-dike concept. Geology, 34(3), 189–192.

Petrazzuoli, S.M., Troise, C., Pingue, F., De Natale, G., 1999. The mechanics of Campi Flegrei unrests as related to plastic behaviour of the caldera borders. Annali di Geofisica, 42(3), 529–544.

Pinel, V., Jaupart, C., 2005. Caldera formation by magma withdrawal from a reservoir beneath a volcanic edifice. Earth Planet. Sci. Lett., 230(3–4), 273–287.

Richey, J.E., 1935. British Regional Geology. Scotland: The Tertiary Volcanic Districts. Edinburgh: HMSO for the Department of Scientific and Industrial Research Geological Survey and Museum, 1st edition. 8vo. vii[i], 115pp.

Roche, O., Druitt, T.H., Merle, O., 2000. Experimental study of caldera formation. J. Geophys. Res., 105(1), 395–416.

Saunders, S.J., 2004. The possible contribution of circumferential fault intrusion to caldera resurgence. Bull. Volcanol., 67(1), 57–71.

Smith, R.L., Bailey, R.A., 1968. Resurgent cauldrons. In: Studies in Volcanology. Geological Society of America (GSA), Boulder, CO, pp. 613–662.

Sparks, R.S.J., 1988. Petrology and geochemistry of the Loch Ba ring-dyke, Mull (N.W. Scotland): an example of the extreme differentiation of tholeiitic magmas. Contrib. Min. Petrol., 100(4), 446–461.

Sparks, R.S.J., Huppert, H.E., Turner, J.S., 1984. The fluid dynamics of evolving magma chambers. Philos. Trans. R. Soc. Lond., 310(1514), 511–534.

Stachel, T., Brey, G., Stanistreet, I.G., 1994. Gross Brukkaros — the unusual intracaldera sediments and their magmatic components. Commun. Geol. Surv. Namibia, 9, 23–41.

Stix, J., Kennedy, B., Hannington, M., Gibson, H., Fiske, R., Mueller, W., Franklin, J., 2003. Caldera-forming processes and the origin of submarine volcanogenic massive sulfide deposits. Geology, 31(4), 375–378.

Sturkell, E., Sigmundsson, F., 2000. Continuous deflation of the Askja caldera, Iceland, during the 1983–1998 noneruptive period. J. Geophys. Res., 105(11), 25671–25684.

Thomas, A.L., 1993. Poly3D: a three-dimensional, polygonal element, displacement discontinuity boundary element computer program with applications to fractures, faults, and cavities in the earth's crust. M.S. Thesis, Stanford University, Stanford, CA, pp. 1–221.

Troise, C., De Natale, G., Pingue, F., 2004. Non-linear effects in ground deformation at calderas due to the presence of structural discontinuities. Ann. Geophys., 47(4), 1513–1520.

Troise, C., De Natale, G., Pingue, F., Zollo, A., 1997. A model for earthquake generation during unrest episodes at Campi Flegrei and Rabaul calderas. Geophys. Res. Lett., 24(13), 1575–1578.

Troise, C., Pingue, F., De Natale, G., 2003. Coulomb stress changes at calderas: modeling the seismicity of Campi Flegrei (southern Italy). J. Geophys. Res., 108(6), 2292, doi:10.1029/2002JB002006.

Troll, V.R., Walter, T.R., Schmincke, H.U., 2002. Cyclic caldera collapse: piston or piecemeal subsidence? Field and experimental evidence. Geology, 30(2), 135–138.

Turcotte, D.L., Schubert, G., 2002. Geodynamics, 2nd edn. Cambridge University Press, Cambridge.

Walker, G.P.L., 1984. Downsag calderas, ring faults, caldera sizes, and incremental caldera growth. J. Geophys. Res., 89(B10), 8407–8416.

Walker, G.P.L., Skelhorn, R.R., 1966. Some associations of acid and basic igneous rocks. Earth Sci. Rev., 2(2), 93–109.

Walter, T.R., Acocella, V., Neri, M., Amelung, F., 2005. Feedback processes between magmatic events and flank movement at Mount Etna (Italy) during the 2002–2003 eruption. J. Geophys. Res., 110(B10205), 1–12.

Walter, T.R., Amelung, F., 2006. Volcano–earthquake interaction at Mauna Loa volcano, Hawaii. J. Geophys. Res., 111(B05204), 1–17. doi:10.1029/2005JB003861.

Walter, T.R., Troll, V.R., 2001. Formation of caldera periphery faults: an experimental study. Bull. Volcanol., 63(2–3), 191–203.

Watters, R.J., Zimbelman, D.R., Bowman, S.D., Crowley, J.K., 2000. Rock mass strength assessment and significance to edifice stability, Mount Rainier and Mount Hood, Cascade Range volcanoes. Pure Appl. Geophys., 157(6–8), 957–976.

Wigand, M., Schmitt, A.K., Trumbull, R.B., Villa, I.M., Emmermann, R., 2004. Short-lived magmatic activity in an anorogenic subvolcanic complex: 40Ar/39Ar and ion microprobe U–Pb zircon dating of the Erongo, Damaraland, Namibia. J. Volcanol. Geotherm. Res., 130(3–4), 285–305.

Yang, X.M., Davis, P.M., Dieterich, J.H., 1988. Deformation from inflation of a dipping finite prolate spheroid in an elastic half-space as a model for volcanic stressing. J. Geophys. Res., 93(5), 4249–4257.

# A New Uplift Episode at Campi Flegrei Caldera (Southern Italy): Implications for Unrest Interpretation and Eruption Hazard Evaluation

Claudia Troise*, Giuseppe De Natale, Folco Pingue, Umberto Tammaro, Prospero De Martino, Francesco Obrizzo *and* Enzo Boschi

## Contents

## Abstract

Campi Flegrei caldera, which includes the highly urbanized city of Naples, is the most dangerous volcanic area in the world as it represents a serious threat to around two million people. During the last four decades it has experienced a huge uplift phase, which reached about 3.5 m in 1985 when a subsidence phase started. Recent geodetic data demonstrates that such a subsidence phase has terminated, and a new uplift episode started in November 2004 has so far resulted in about 0.04 m of uplift (October 2006). Here we show that the present episode, which appears slower but longer than previous small uplifts, sheds light both on the origin of small and large unrests, and on the conditions to evolve toward large unrests. Our simple but robust method is based on continuous GPS measurements and compares the ratio between maximum horizontal to vertical displacements. Results show that such unrests are due to overpressure in a deeper source of fluids of magmatic origin. When the resulting

*Corresponding author. Tel.: +39-0816108314; Fax: +39-0816100811
*E-mail address:* troise@ov.ingv.it

stress increase causes fracturing of the overlying rocks, magmatic fluids are injected in shallower aquifers and generate large uplifts. This means that, given the common magmatic origin, both small and large unrests contribute to the increase in pressure of the magma chamber which, given sufficient magnitude, can cause fracturing of the overburden and produce an eruption. In this paper, we show that the maximum horizontal to vertical displacement ratio can be a powerful indicator of source changes, and can give important information for volcanic eruption forecast.

## 1. Introduction

Campi Flegrei caldera (Figure 1) is a volcanic field located in the western sector of larger Naples, and includes part of the city. About two million people are heavily exposed to volcanic hazards from this area, and this makes hazard estimation and eruption forecast crucial.

Campi Flegrei represents one of the most interesting examples of resurgent caldera, having triggered the most intense episodes of caldera uplift observed in recent times (Barberi et al., 1984). It is considered by several authors to be a nested
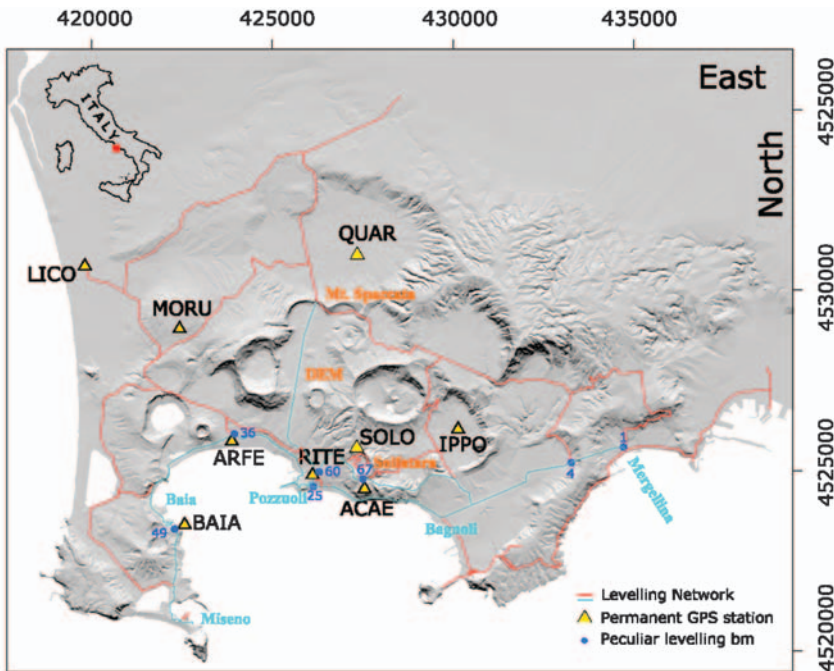


**Figure 1** Sketch map of Campi Flegrei showing the main volcanological features, the permanent GPS stations (yellow triangles), leveling network (red lines), and some peculiar leveling benchmarks (blue closed circles). Leveling lines measured in the period May 2004—September 2006 are also shown (cyan lines).

caldera formed by subsequent collapse episodes (Rosi and Sbrana, 1987; Orsi et al., 1996). However, only the innermost caldera, with a radius of about 3 km, is clearly visible by geophysical data including gravity Bouguer anomalies (Rosi and Sbrana, 1987; Capuano and Achauer, 2003) and seismic tomography (Judenherc and Zollo, 2004). This caldera was formed about 15,000 years ago by the "Neapolitan Yellow Tuff" eruption. A larger caldera, with a radius of about 6 km, can be identified by geological limits, but does not have a deep geophysical signature. Some literature ascribes this larger caldera to an ignimbrite eruption that occurred about 37,000 years BP and produced the Campanian gray tuff deposits (Rosi and Sbrana, 1987; Orsi et al., 1996); however, there is no global consensus on such a model (see, for instance, Rolandi et al., 2003). The volcanic edifices in Campi Flegrei caldera are mainly monogenetic tuff cones and tuff rings, produced by hydromagmatic eruptions with alkali-trachitic magma (Rosi et al., 1983).

The history of crustal movements at Campi Flegrei has been reconstructed for the last 2,000 years by the integration of different data: geological, archeological and, for the last 40 years, precise geodetic measurements (Parascandola, 1947; Dvorak and Mastrolorenzo, 1991; Morhange et al., 1999; Del Gaudio et al., 2005; Gottsmann et al., 2006; Morhange et al., 2006; Pingue et al., 2006) (see Figure 2). The secular trend of ground deformation is characterized by subsidence at a rate of about 1.5 cm/year. Superimposed on such a long-term trend are at least two episodes of large uplift which occurred around 600 and 1500 AD; each lasted 50–60 years, and the last eruption culminated in the only historical eruption of 1538 (Morhange et al., 1999, 2006; Bellucci et al., 2006) (Figure 2a).

Two unrest episodes (called bradisisma, from the Greek word for "slow earthquake") occurred from 1969 to 1972 and from mid-1982 to December 1984 (Barberi et al., 1984) (Figure 2b). The first event produced a net uplift of about 1.7 m. The pattern of ground deformation was a nearly circular lens centered near Pozzuoli. Only weak seismic activity was recorded during this phase. The second event presented a similar uplift pattern, but compared to the previous event this episode was accompanied by more seismicity, both in the number of earthquakes and their magnitude (Dvorak and Gasparini, 1991; De Natale et al., 1995; Troise et al., 1997). Shallow earthquake hypocenters (depth from 1 to 4 km) occurred from mid-1983 to December 1984 and damaged buildings in Pozzuoli. A magnitude 4.2 earthquake with epicenter in Pozzuoli occurred on October 4, 1983. In 1984, the town was almost completely evacuated and about 40,000 people were relocated. The total uplift recorded between January 1982 and December 1984 amounted to 1.8 m. The most deformed area had a radius of about 3 km around Pozzuoli, at the center of the caldera. Since the end of 1984, the ground has started to subside with a peak subsidence rate of about 7–8 cm/year in 1985 and at a progressively smaller rate until 2001–2002, when the subsidence ended and about 0.9 m of the total uplift was recovered (De Natale et al., 2006). Superimposed on the subsidence phase were some small and fast uplift episodes which occurred in 1989, 1994, and 2000, i.e. with an apparent period of about 5–6 years (Gaeta et al., 2003; Lanari et al., 2004). These smaller uplift episodes reached a maximum uplift of about 1–8 cm, lasted 4–10 months, and were accompanied by seismic swarms of micro-earthquakes (ML < 2) lasting from few days to 1–2 months.
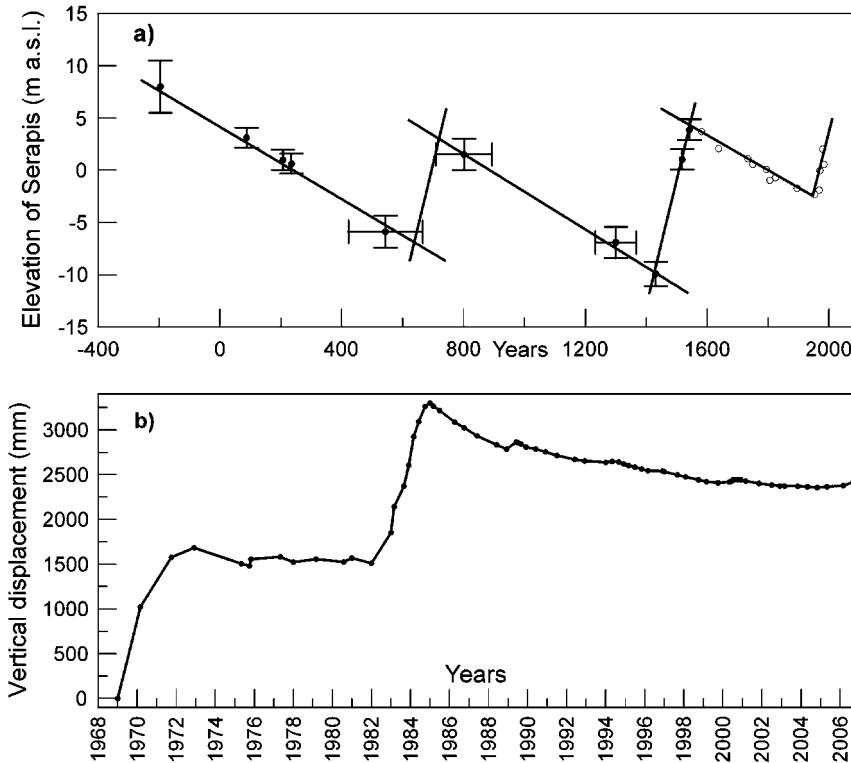
**Figure 2**    (a) Sketch of vertical movements history at Macellum in Pozzuoli, known as Serapis Temple (after Bellucci et al., 2006). Black circles represent the constraints found from radiocarbon and archeological measurements by Morhange et al. (1999); white circles (post-1538) represent inference from Dvorak and Mastrolorenzo (1991); (b) Vertical ground displacements as recorded at the benchmark in Pozzuoli harbor by leveling data in the period 1969–2006 (Macedonio and Tammaro, 2005; Del Gaudio et al., 2005; Pingue et al., 2006).

This paper analyzes precise leveling and GPS data in the area from mid–2004 to October 2006, and shows that a new episode of uplift has started in the area with an apparent rate lower than the previous mini–uplift episodes (almost 4 cm in the last year, compared to the 0.5–1.5 cm/month of the previous episodes since 1989). The similarity of the present long-term uplift episode, lasting since 1969, with past events, and in particular that which culminated in the 1538 eruption, makes it particularly important to study in detail any resuming of uplift. As hypothesized in the most recent literature (De Natale et al., 2001, 2006; Battaglia et al., 2006; Bellucci et al., 2006), eruptions at this and similar calderas can occur suddenly in the initial part of new uplift phases. This paper then tries to discriminate the source of the present uplift phase, in terms of the identification of a new magmatic and/or geothermal perturbation, and to highlight its consequence on eruption hazard assessment. We show that data from this episode help to discriminate the nature of uplift episodes and to establish their connections with magmatic phenomena.

## 2. Recent Ground Deformation Data at Campi Flegrei Caldera

The recent vertical ground deformation at Campi Flegrei has been measured by precision leveling since 1969, and by GPS since 2000. The present leveling network is made by 330 benchmarks over a total length of about 135 km in 14 circuits; in addition, nine continuous GPS stations operate in the area. The location of GPS benchmarks (Figure 1) has been determined taking into account previous evidence in the area, which shows remarkably constant displacement patterns (De Natale et al., 1997). Such consistency allowed the location of station RITE to be chosen as the expected point of maximum vertical displacement, whereas ACAE, ARFE, and BAIA should give a good sampling of the range of expected maximum horizontal displacement; the remaining points are meant to sample larger distances. During the whole period of CGPS operation, the maximum horizontal displacement has always been recorded at ACAE, thus confirming the high stability of the source axis. Figure 3 summarizes vertical displacements measured from precise leveling in the campaigns from May 2004 to September 2006 at the three common and most significant subnetworks (Solfatara circuit, Coast line and South–North line). The leveling measurements have been carried out using automatic optic levels Leica NA2 with parallel–plate micrometer (0.01 mm resolution) and using invar rods, calibrated before the survey. The double-run field procedures were utilized, with a maximum closure between forward and backward running of each section of less than $2.5 \times (L_{km})^{1/2}$ mm, where $L$ represents the length of the leg in kilometers. For leveling loops, it has been assumed that the closure error resulted in less than $2.0 \times (C_{km})^{1/2}$ mm, where $C$ represents the length (in kilometers) of the circuit. After such control, the observed height differences have been adjusted by the least squares method, deriving for every benchmark the most probable quota and its standard error.

In May 2004, a measurement of the whole leveling network was performed. The field measurements have been compensated by least squares, showing a standard deviation per unit weight $\sigma_0 = 1.02$ mm, confirming good quality data (Pingue et al., 2006). The compensated heights have been referred to the benchmark located in Naples-Mergellina, also shown in Figure 1. Compared to the May and November 2003 data, the May 2004 data show that very minor subsidence (less than 1 cm/year, almost within the errors) is still present in the area (Del Gaudio et al., 2005). In November 2004 another measurement was performed, but only on part of the network (circuits in cyan, Figure 1). This campaign still shows very slight subsidence, with a maximum of less than 1 cm at Solfatara crater, which is very close to the $2\sigma$ error limits (Pingue et al., 2006). Two further field measurement campaigns were performed in 2005 (one each in May and October) showing a slight uplift with respect to the 2004 measurements (maximum uplift of 1 cm in Pozzuoli harbor), although still in the limits of $2\sigma$ errors. A new leveling measurement was conducted in March 2006, with a $\sigma_0 = 0.63$ mm, showing a clear uplift of up to 2 cm at Pozzuoli harbor with respect to May 2004 (yellow curves in Figure 3). The last partial leveling survey was conducted in September 2006 (with a standard deviation per unit weight $\sigma_0 = 0.40$ mm), which has underlined an uplift increase of almost 4 cm (green curve in
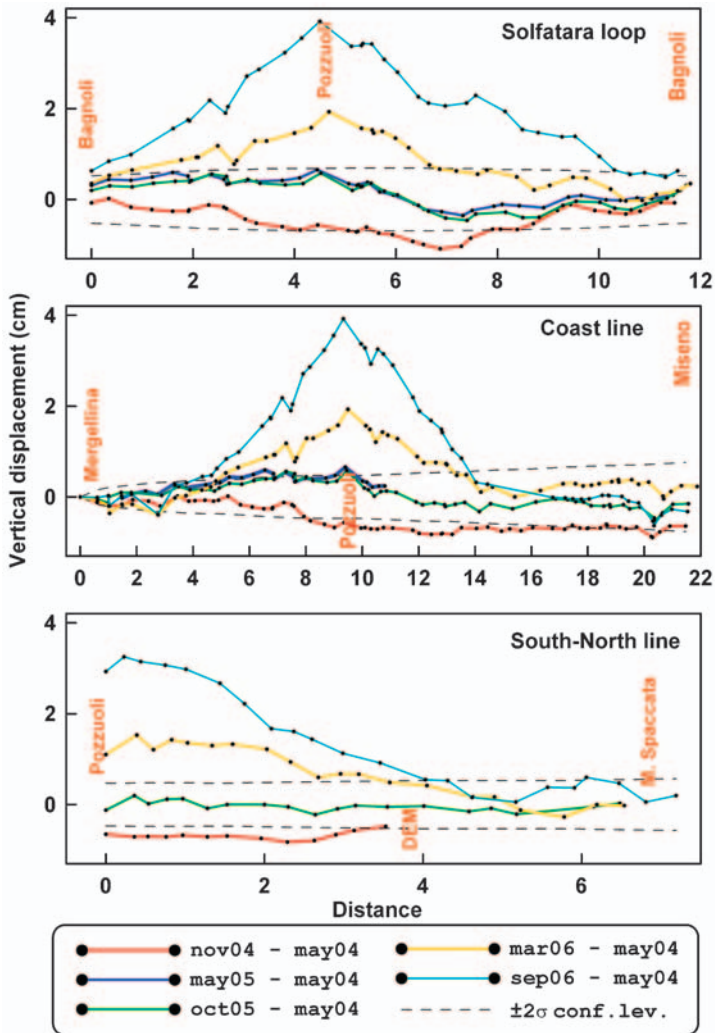
**Figure 3**   Vertical displacements measured from May 2004 to September 2006 along three leveling lines (see Figure 1) at different periods as indicated. Displacements are all referred to the benchmark of Naples–Mergellina (see Figure 1). Confidence levels of 2σ are indicated. The total maximum ground uplift between November 2004 and September 2006 (last leveling data) amounts to about 4.5 cm.

Figure 3); the uplift is now strongly significant. An accurate description of the on-going uplift is given by continuous GPS data (Figures 4 and 5). Some continuous GPS were already operating during the previous mini–uplift in 2000; for such sites the whole recording period is shown in Figure 4. GPS data at all the continuous stations from May 2004 to October 2006 are shown in Figure 5, displaying the whole evolution of the on-going uplift until now. The GPS data were processed using Bernese software version 4.2 (Beutler et al., 2001); IGS precise orbits and consistent
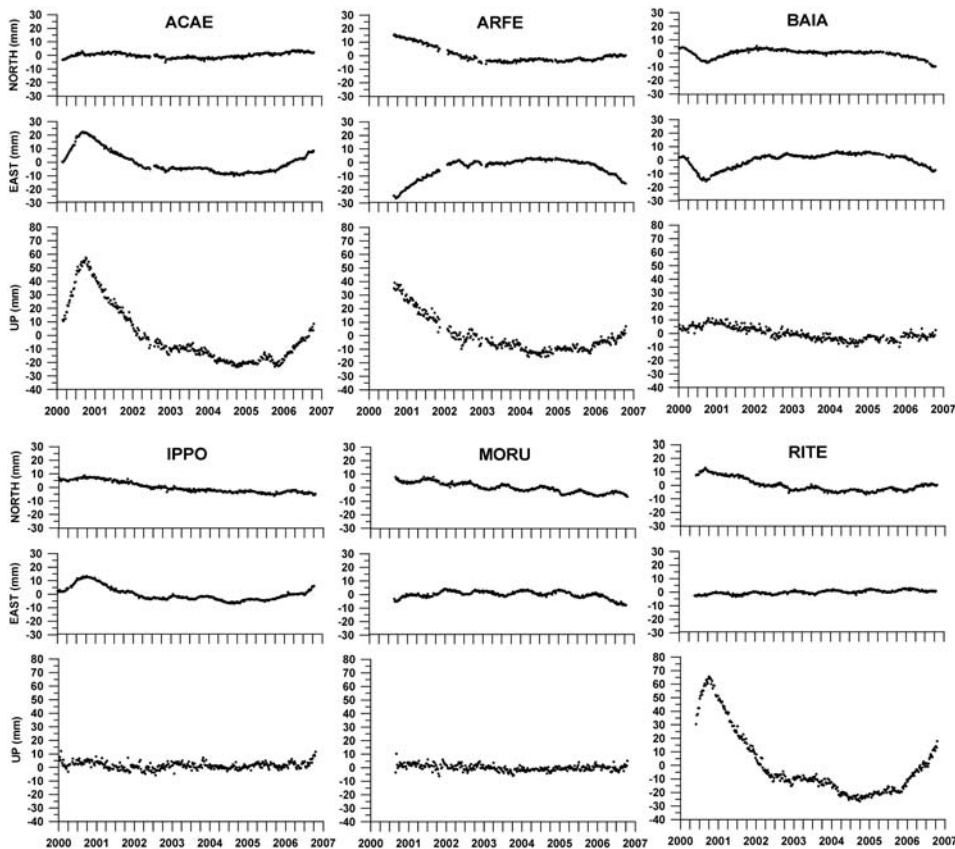
**Figure 4** GPS time series of weekly coordinate variations (North, East, and Up components) in the period January 2000—October 2006 for ACAE, ARFE, BAIA, IPPO, MORU, and RITE stations relative to QUAR (see Figure 1). SOLO has recently started operating; so the relative data are not shown. For clarity, confidence levels are not represented; they are instead reported in Figure 5 for a shorter time period.

ERP files, satellite clock corrections, antenna height phases center variations PHASE_IGS.01, and other general files were included in the computation. The ambiguities were resolved using the QIF strategy and subsequently were introduced into the final L3 (ionosphere free) fixed solution. TZD parameters were estimated every 2 h with "dry Niell" mapping function and without a prior model. The station RITE, located at the center of Pozzuoli (see Figure 1), has the largest associated uplift, of about 4 cm. The stations ACAE, ARFE, and BAIA, located within about 3.5 km from RITE, have smaller vertical displacements (up to 3 cm at ACAE) and larger horizontal displacement (up to 1.7–1.9 in modulus at ACAE and ARFE stations) (Figures 5 and 6). As a final summarizing sketch of the on-going uplift, Figure 7 shows an interpolated plot of the ground uplift measured at the GPS station in Pozzuoli (RITE) from May 2004 to October 2006. Leveling measurements at benchmark LCF/060 (close to RITE) are also superposed (stars).
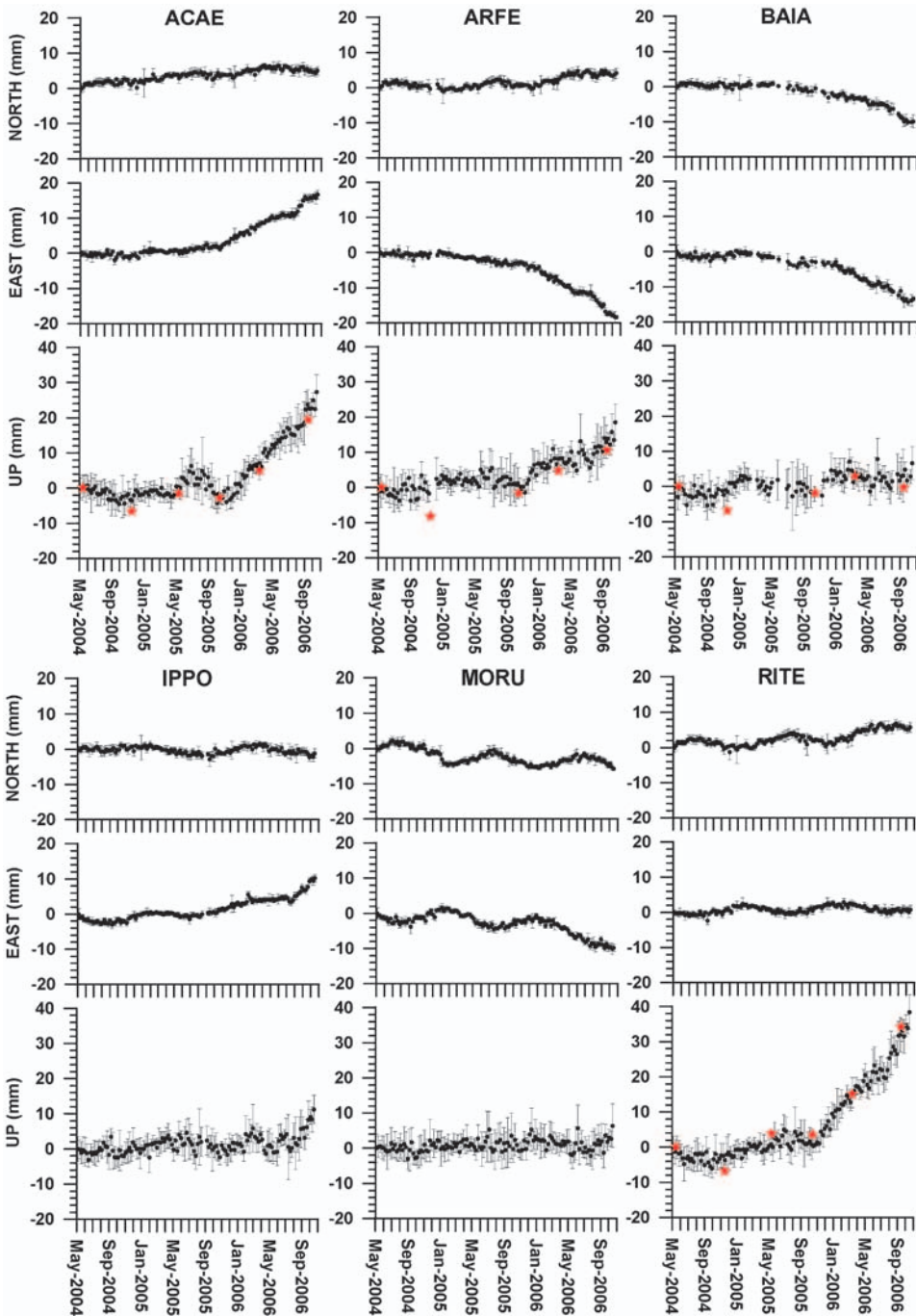
**Figure 5**  Details of the GPS time series reported in Figure 4, showing only the period of on-going uplift until now (May 2004—October 2006). Confidence levels at 1σ are indicated. Comparison with leveling data, at benchmarks very close to leveling points, is also shown (stars).
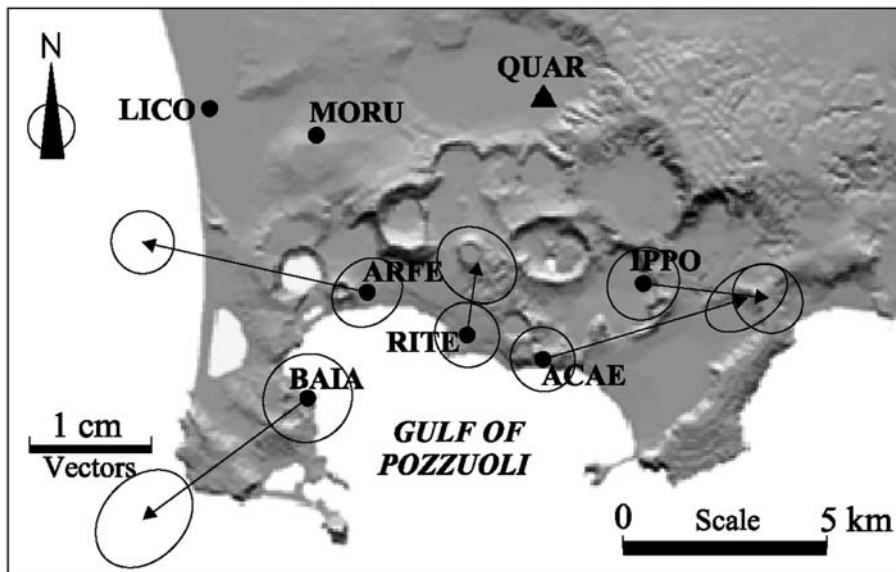
**Figure 6**  Sketch of Campi Flegrei caldera with GPS points and inferred horizontal displacement vectors in the period May 2004—October 2006, with QUAR as reference, for the five stations next to the deformed area. The 2-D error ellipses at 95% confidence level (factor=2.447) are also shown.
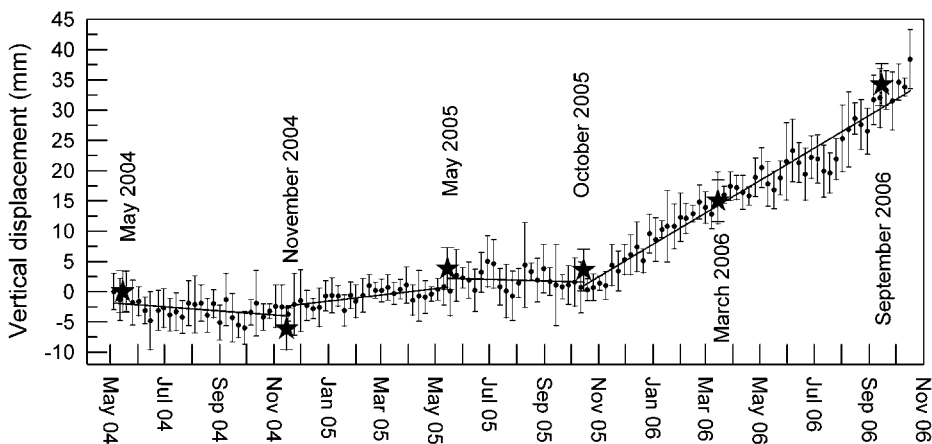


**Figure 7**  Detail of vertical displacements from May 2004 to October 2006 as recorded from continuous GPS at station RITE (dots) and precision levelings at the benchmark in Pozzuoli harbor (stars). The two benchmarks are very close (Figure 1). Errors on continuous GPS and leveling data (1σ) are also shown.

## 3. DISPLACEMENT SHAPES AND MAXIMUM VERTICAL TO HORIZONTAL RATIOS

As noted in several papers (e.g. De Natale and Pingue, 1993; De Natale et al., 1997) the shape of vertical ground deformation pattern at Campi Flegrei is remarkably constant, independent from the total amount of displacement (during both uplift and subsidence episodes) which share the same shape apart from the sign. This feature has been interpreted as the strong effect of ring faults, which represent displacement discontinuities at the caldera borders, and act to stabilize the location of the pressure source axis (De Natale et al., 1997). Recently, Battaglia et al. (2006) noted a marked difference in the ratio between horizontal and vertical displacements associated with the first phase of large uplift (1982–1983) and the subsequent subsidence episode (1985–1995) respectively, thus demonstrating that different source depth and geometry are involved and reflect different mechanisms. In order to understand the nature of the present uplift episode, it is then crucial to compare it to previous episodes.

It is well known that surface deformations cannot uniquely constrain the source (De Natale and Pingue, 1996). However, inferences on source properties can be extracted from geodetic data, provided simple geometries and mechanisms are preassigned to the source. In volcanic areas, ellipsoidal sources of homogeneous pressure changes are most often hypothesized, sometimes degenerating into penny–shaped cracks (Gudmundsson, 2006). It is also well known that using only vertical displacement data and simple homogeneous pressure sources cannot be uniquely constrained, whereas the joint use of vertical and horizontal displacements is generally able to uniquely constrain the depth and mechanism of such predefined sources. The most powerful way to monitor both vertical and horizontal displacements at the same time is to make use of GPS data. Although the precise modeling of displacement sources generally requires a dense geodetic data sampling, it is possible to use continuous GPS measurements to extract (from the ratio between horizontal and vertical data) basic information about source geometry and depth, and to detect possible changes of the ratio which would indicate modifications in the depth and/or shape of the intrusion, for example, during intrusions.

We have computed, using an FEM program (DIANA), the ratios of maximum horizontal to maximum vertical surface displacement for different ellipsoidal sources in a homogeneous elastic medium with ring faults defined as conical surfaces on which shear stress is null and opening is via normal strain (see Troise et al., 2003). An axial-symmetric scheme has been used. The dip of the ring faults is $75°$, and an average size of $50\,m$ for the smallest elements in the central part of the model has been used. The scheme has a total size of $20\,km \times 20\,km$ to avoid border effects (Troise et al., 2003). Resulting curves of displacement ratios versus depth for three kinds of ellipsoidal sources are shown in Figure 8a. Maximum displacement ratios are strongly constrained on source geometry, and particularly in the case of shallow depth sources. Monitoring displacement ratios by continuous GPS should be then be a very effective method to constrain source geometry and detect intrusive episodes that cause a significant increase in the ratio of maximum
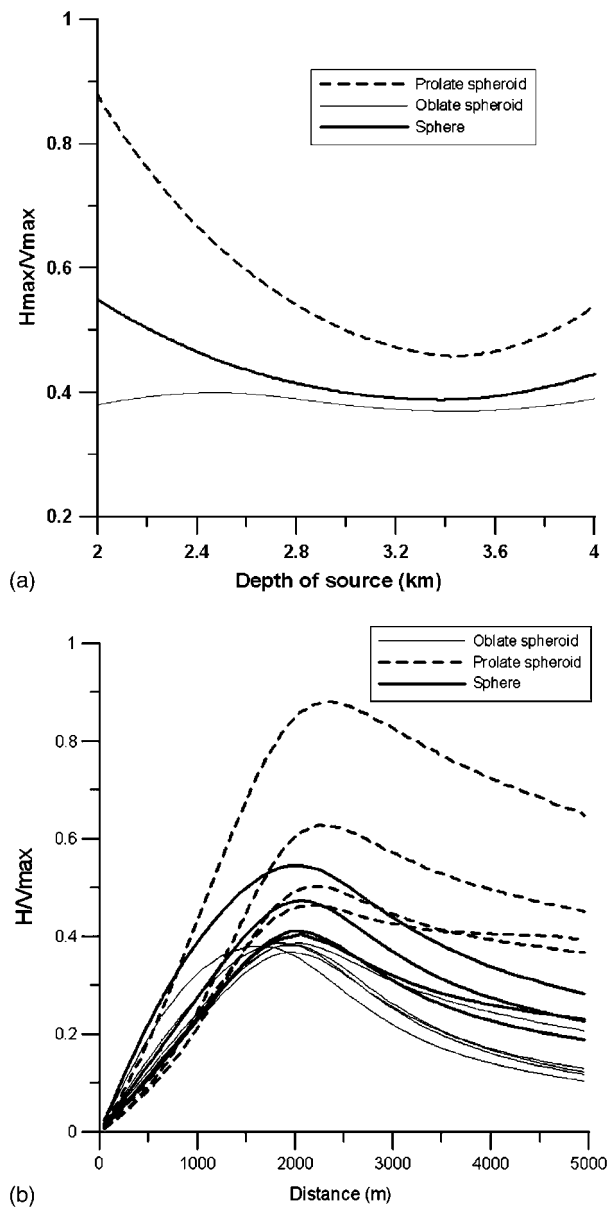
**Figure 8** (a) Theoretical curves of maximum horizontal/vertical ratios versus depth source in the case of three ellipsoidal sources with different aspect ratio $r$ (prolate ellipsoid, $r = 0.5$; sphere, $r = 1$; oblate ellipsoid, $r = 2.0$) embedded in an elastic half space with ring faults simulating the geometry of Campi Flegrei caldera borders. Curves are obtained by an axial-symmetric boundary element method, in which ring faults are described as conical surfaces on which shear stress is null (Troise et al., 2003). The geometry and depth of ring faults is taken by Beauducel et al. (2004), the radius is 2.7 km. From the figure, it is apparent that ratios larger than about 0.55 are only attained with prolate and very shallow sources. Values of 0.30−0.35, as evidenced in this study, are compatible with oblate sources, whose dependence on the depth is negligible. (b) Expected maximum horizontal displacement as a function of distance from the source calculated in the same cases shown in (a).

horizontal to vertical displacements. In order to compare the present uplift episode with previous ones, and in particular to constrain the source depth, two elements are considered:

1. the shape of vertical displacement pattern, which is well constrained by precision leveling;
2. the ratio between horizontal and vertical displacements ($\Delta H_{max}/\Delta V_{max}$), which can be obtained from GPS continuous measurements and tentatively compared with previous uplift and subsidence episodes.

In order to monitor $\Delta H_{max}/\Delta V_{max}$ with a limited number of GPS points, it is useful to determine theoretically the range in distance from the maximum elevation point at which the maximum horizontal displacement can be recorded as a function of source depth and shape. Accordingly, we have used the FEM procedure to plot horizontal displacements as a function of distance, normalized to the maximum vertical displacement, for the same source shapes and depths as Figure 8a. Resulting curves are shown in Figure 8b. We note that the range in which maximum horizontal displacements are expected is very narrow, and that this corresponds to an average distance from the maximum elevation point of $2.1 \pm 0.2$ km. This stability is partially due to the effect of ring faults, and clearly shows that for sources with constant axis location the point of maximum measured horizontal displacement is expected to vary over a very narrow distance for any depth or source shape.

The shape of the vertical displacement pattern can be computed by normalizing the leveling data with respect to the maximum, and by comparing different episodes among them. We have accordingly normalized the leveling data along the line Naples–Pozzuoli–Baia–Miseno with respect to the maximum of the 1982–1985 unrest (Pozzuoli harbor), and compared the May 2004–March 2006 and May 2004–September 2006 to 1982–1985 and 1999–2000 previous uplift episodes. As the four episodes refer to very different displacement amounts (1.768 m for 1982–1985 to 0.021 m for 2004–March 2006) the confidence limits in the normalized plots are also very different, and must be considered. Figure 9a shows the normalized vertical displacements of the four periods, with relative confidence intervals of $1\sigma$. Confidence intervals for the 1982–1985 data are generally negligible in the plot (given the large amount of displacement) except at the borders where the uplift is very small, and they have been neglected in the plot accordingly. It is clear that the shape appears constant for all the episodes, although 2004–2006 data show a higher scatter at some localized zones (explained by larger relative errors). In particular, at some points between Naples and Pozzuoli, and at most of the points between Baia and Miseno, May 2004–March 2006 relative uplift seems slightly but somewhat systematically larger than in 1982–1985. However, when considering the last data (May 2004–September 2006) uplift at the same points is very slightly lower, but much closer to 1982–1985 data. No measurements are available along the Baia–Miseno line for 1999–2000 uplift, which at the other benchmarks seem very consistent with the 1982–1985 period.

However, the similarity of normalized vertical displacements is not necessarily indicative of equal source mechanisms, due to the effect of bordering caldera-collapse
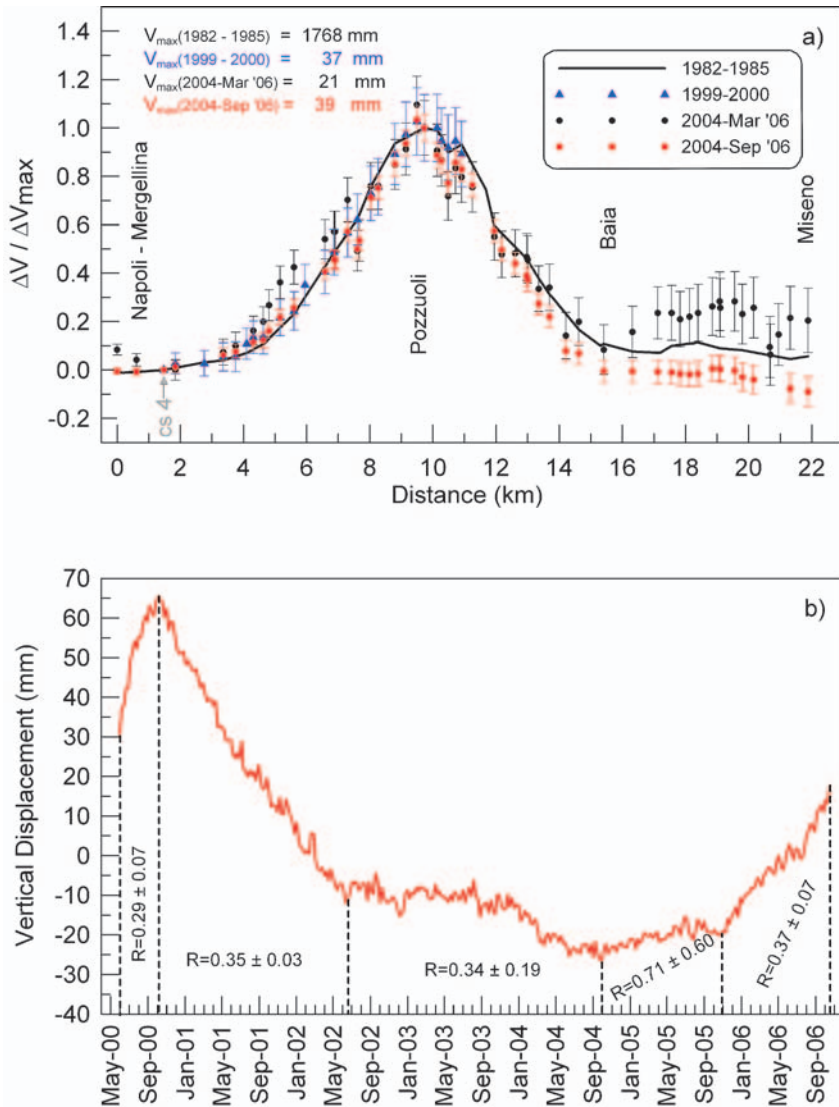
**Figure 9** Comparing ground uplift patterns at various periods. (a) Normalized vertical displacements along the Naples—Pozzuoli—Baia—Miseno leveling line (see Figure 3) in four different periods: 1982—1985, 1999—2000, 2004—March 2006, and 2004—September 2006. Displacement errors (1σ) are also shown. Normalization factors indicated in figure are the vertical displacements recorded at the benchmark in Pozzuoli harbor in the respective periods, referred to the common benchmark LCF/004, also indicated. (b) Sketch of $H/V$ values in periods of approximately constant uplift or subsidence rate, as indicated.

discontinuities that act in the same sense and appear to be very effective here. Nevertheless, it is unequivocal that the location of the axis of the pressure source is remarkably constantly, although the source depth and shape can change (see also De Natale and Pingue, 1993; De Natale et al., 1997). This strongly constrained

observation allows us to assume that any change in the ratio between maximum horizontal and vertical ground displacements is due to a change in source depth and geometry.

In order to make a homogeneous comparison of the horizontal/vertical displacement ratio, we must consider that the actual continuous GPS points are in place only since January 2000, so that we can compare GPS data only with 2000 uplift. Figure 9b shows the average $\Delta H_{max}/\Delta V_{max}$ ratios computed in periods with an almost constant positive or negative vertical displacement rate, as recorded at the RITE and ACAE stations, where vertical and horizontal displacements are maximum. In the following, we assume for simplicity that the source location is just below the point of maximum vertical uplift (RITE). If, for example, the real location were more South in the Gulf (about 1 km, see Beauducel et al., 2004), the real value of $\Delta H_{max}/\Delta V_{max}$ could be smaller. It is noteworthy that, within the errors, the average $\Delta H_{max}/\Delta V_{max}$ ratio is very similar in the whole period, ranging on average between 0.29 and 0.37, except in the period October 2004–November 2005, where the negligible amount of displacement makes the error so large that the inferred ratios are meaningless.

## 4. DISCUSSION AND CONCLUSION

The new uplift at Campi Flegrei caldera is characterized by a slow deformation rate, at least in the initial phase, but in the last few months the rate has been increasing (peak in September 2006: about 1 cm/month; Troise et al., 2007). At first glance, the slower initial rate seems to distinguish it from the episodes of small uplift that have occurred since 1989 (Gaeta et al., 2003; Lanari et al., 2004). However, as the previous mini-uplift episodes occurred in periods of general subsidence trend, a first lower rate phase could have easily gone undetected, mainly because no continuous GPS measurements existed before 2000. The shape of vertical ground deformation matches well with that from the large uplift of 1982–1984 and the small uplift of 2000. Furthermore, the ratio among maximum horizontal and maximum vertical displacement is equivalent, at the same continuous GPS points, to that observed during the small uplift of 2000. These observations suggest that, besides the apparent differences in initial deformation rates and duration, the last uplift and the previous small uplift episodes share the same source geometry and mechanism. A formal comparison with the 1982–1984 large uplift can only be made with the shape of vertical displacement, which appears very similar. Horizontal to vertical ratios cannot really be compared because continuous GPS are in place only since 2000, and horizontal data pertaining to the last large uplift episode consist of EDM measurements, which are not directly comparable. Battaglia et al. (2006) showed that the horizontal to vertical displacement ratios are significantly smaller (about one half) during the large uplift with respect to the 1990–1995 subsidence. Such data are interpreted as two different source geometries and depths for the large uplift. The first part of the uplift is interpreted to be due to overpressures within a penny-shaped crack which

contains magma or fluids of magmatic origin and is located at 3 km depth (see also De Natale et al., 2006; Troise et al., 2007). Such overpressures subsequently involved the shallower aquifers (for instance, after fracturing of the rock volume between the magmatic fluids and the aquifer). The subsidence is therefore interpreted as water deflation toward the external rocks from a prolate ellipsoidal aquifer, located at depths between 1.5 and 2.5 km. The presence of continuous GPS measurements in the area since 2000 makes, for the first time, a detailed comparison of horizontal to vertical displacement ratios between two uplift periods possible. The observed $\Delta H_{max}/\Delta V_{max}$ ratio for the 2000 and the 2004–2006 uplifts is slightly less than 0.35 and seems indicative of an oblate spheroidal source. However, since the maximum elevation point is likely to be located in the Gulf of Pozzuoli (see Beauducel et al., 2004), where no measurements exist, this ratio is best regarded as an upper limit. These observations allow the formulation of a model for the occurrence of small uplift episodes, and more generally for the fast ground deformation episodes at Campi Flegrei. In fact, in the light of the previously mentioned models, the rather small ratio between horizontal and vertical displacements observed during the small uplift episodes is indicative of over-pressures in the deeper source of fluids of magmatic origin, evidenced by Battaglia et al. (2006), with only limited or no involvement of the shallower aquifers.

A large uplift episode could then occur when the initial pulse of overpressure, causing significant fracturing of the upper rocks, migrates into the shallower aquifers. Such interpretation is consistent with the observations of Chiodini et al. (2003) that similar peaks of $CO_2$ follow both large and small uplift episodes, with a time lag of several months, thus indicating that uplift episodes are associated with a significant input of $CO_2$ from below, almost independently from the size of uplift. This is in agreement with a model in which all the uplift episodes start with an overpressure in a deep $CO_2$ rich source that is filled with magma or fluids of magmatic origin and is injected into shallower layers by the overpressure. In the last few months, the present uplift episode has been also accompanied by a consistent increase in $CO_2$ flux and other magmatic indicators (Chiodini, personal communication), and by a peak in microseismicity in October (maximum magnitude around 1) which consisted of swarms of low-frequency (around 1 Hz) events, with peak rates of several events per hour (Del Pezzo, personal communication). The increase in $CO_2$ flux is consistent with an increased supply of magmatic fluids from below, whereas the occurrence of low-frequency seismicity seems to be new at Campi Flegrei, where this kind of earthquakes has never been noted before, at least not with similar high rates of occurrence. This low-frequency seismicity can reflect magmatic gas or water overpressure in fractures. If the evolution of this phenomenon follows the previous mini-uplift episodes, we should expect the phenomenon to stop within 1–2 months. On the contrary, if the $\Delta H_{max}/\Delta V_{max}$ ratio increases (indicating an involvement of the shallower levels), we should expect a new large unrest, similar to what occurred in 1969–1972 and 1982–1984.

The model of activity has important implications on how hazardous an eruption could be. In fact, if the deeper source of overpressure evidenced in this paper directly represents the magma chamber, or the increase of magmatic fluid pressure is

anyway related to arrival of the new magma in the chamber (as also the $CO_2$ increase suggests), then each overpressure pulse adds up to increase the magma chamber total pressure bringing the system progressively closer to the critical point for rock failure and eruption (see De Natale et al., 2006).

The present results suggest that continuous monitoring of horizontal to vertical displacement ratios with CGPS should be considered one of the best methods to detect intrusive phenomena at volcanoes. At Campi Flegrei caldera, we have shown that this method is easily applicable with relatively few continuous monitoring points, due to the remarkable stability of the source axis as revealed by the constancy of the vertical ground deformation pattern. However, in general, CGPS sampling should be dense enough to detect all possible changes in source location. Furthermore, the new frontier of volcanic surveillance and forecast should be continuous monitoring of different strain components with directional strain meters in deep wells, where noise is drastically lower and measurements are generally sensitive enough to allow detection of the smallest signals of volcanic unrest and magma migration.

## ACKNOWLEDGMENTS

## REFERENCES

Barberi, F., Hill, D.P., Innocenti, F., Luongo, G., Treuil, M., 1984. The 1982–1984 bradyseismic crisis at Phlegrean Fields (Italy). Bull. Volcanol., 47, 173–411.

Battaglia, M., Troise, C., Obrizzo, F., Pingue, F., De Natale, G., 2006. Evidence for fluid migration as the source of deformation at Campi Flegrei caldera (Italy). Geophys. Res. Lett., 33(L01307-10), doi:10.1029/2005GL024904.

Beauducel, F., De Natale, G., Obrizzo, F., Pingue, F., 2004. 3-D modelling of Campi Flegrei ground deformations: role of caldera boundary discontinuities. Pageoph, 161, L01307, doi:10.1007/s00024-004-2507-4.

Bellucci, F., Woo, J., Kilburn, C.R.J., Rolandi, G., 2006. Ground deformation at Campi Flegrei, Italy: implications for hazard assessment. In: Troise, C., De Natale, G.Kilburn, C.R.J. (Eds), Mechanisms of Activity and Unrest at Large Calderas. Geological Society, London Special Publication, Vol. 269, pp. 141–157.

Beutler, G., Bock, H., Brockmann, E., Dach, R., Fridez, P., Gurtner, W., Hugentobler, U., Ineichen, D., Johnson, J., Meindl, M., Mervart, L., Rotacher, M., Schaer, S., Springer, T., Weber, R., 2001. Bernese GPS Software Version 4.2, AIUB, University of Berne.

Capuano, P., Achauer, U., 2003. Gravity field modelling in the Vesuvius and Campanian area. In: Zollo, A., Bobbio, A., Gasparini, P., Casale, R.Yeroyanni, M. (Eds), TomoVes Seismic Project: Looking Inside Mt. Vesuvius. Cuen, Napoli, under sponsorship of European Commission, project ENV4-980698, e-book.

Chiodini, G., Todesco, M., Caliro, S., Del Gaudio, C., Macedonio, G., Russo, M., 2003. Magma degassing as a trigger of bradyseismic events: the case of Phlegrean Fields (Italy). Geophys. Res. Lett., 30(8), 1434, doi:10.1029/2002GL016790.

Del Gaudio, C., Ricco, C., Aquino, I., Brandi, G., Serio, C., Siniscalchi, V., 2005. Misure di livellazione di precisione e dati tiltmetrici per il controllo delle deformazioni del suolo ai Campi Flegrei. Open File Report no. 4, INGV-OV (in Italian).

De Natale, G., Petrazzuoli, S.M., Pingue, F., 1997. The effect of collapse structures on ground deformations in calderas. Geophys. Res. Lett., 24(13), 1555–1558, doi:10.1029/97GL01600.

De Natale, G., Pingue, F., 1993. Ground deformations in collapsed caldera structures. J. Volcanol. Geotherm. Res., 57, 19–38.

De Natale, G., Pingue, F., 1996. Ground deformation modelling in volcanic areas. In: Scarpa, R. and Tilling, R.I. (Eds), Monitoring and Mitigation of Volcanic Hazard. Springer-Verlag, Berlin, pp. 365–388.

De Natale, G., Troise, C., Pingue, F., 2001. A mechanical fluid-dynamical model for ground movements at Campi Flegrei caldera. J. Geodyn., 32(4–5), 487–517.

De Natale, G., Troise, C., Pingue, F., Mastrolorenzo, G., Pappalardo, L., Boschi, E., 2006. The Campi Flegrei caldera: unrest mechanisms and hazards. In: Troise, C., De Natale, G.Kilburn, C.R.J. (Eds), Mechanisms of Activity and Unrest at Large Calderas. Geological Society, London Special Publications, Vol. 269, pp. 25–45.

De Natale, G., Zollo, A., Ferraro, A., Virieux, J., 1995. Accurate fault mechanism determinations for a 1984 earthquake swarm at Campi Flegrei caldera (Italy) during an unrest episode: implications for volcanological research. J. Geophys. Res., 100, 24167–24185.

Dvorak, J.J., Gasparini, P., 1991. History of earthquakes and vertical ground movement in Campi Flegrei caldera, Southern Italy: comparison of precursory events to the A.D. 1538 eruption of Monte Nuovo and of activity since 1968. J. Volcanol. Geotherm. Res., 48, 77–92.

Dvorak, J.J., Mastrolorenzo, G., 1991. The mechanisms of recent vertical crustal movements in Campi Flegrei caldera, southern Italy. USGS Spec. Pap., 263, 1–47.

Gaeta, F.S., Peluso, F., Arienzo, I., Castagnolo, D., De Natale, G., Milano, G., Albanese, C., Mita, D.G., 2003. A physical appraisal of a new aspect of bradyseism: the miniuplifts. J. Geophys. Res., 108(B8), 2363, doi:10.1029/2002JB001913.

Gottsmann, J., Rymer, H., Berrino, G., 2006. Unrest at the Campi Flegrei caldera (Italy): a critical evaluation of source parameters from geodetic data inversion. J. Volcanol. Geotherm. Res., 150(1–3), 132–145.

Gudmundsson, A., 2006. How local stresses control magma-chamber ruptures, dyke injections, and eruptions in composite volcanoes. Earth Sci. Rev., 79, 1–31.

Judenherc, S., Zollo, A., 2004. The Bay of Naples (southern Italy): constraints on the volcanic structures inferred from a dense seismic survey. J. Geophys. Res., 109, B10312, doi:10.1029/2004JB002876.

Lanari, R., Berardino, P., Borgstroem, S., Del Gaudio, C., De Martino, P., Fornaro, G., Guarino, S., Ricciardi, G., Sansosti, E., Lundgren, P., 2004. The use of IFSAR and classical geodetic technique for caldera unrest episodes: application to the Campi Flegrei uplift event of 2000. J. Volcanol. Geotherm. Res., 133, 247–260.

Macedonio, G., Tammaro, U. (Eds), 2005. Attività di Sorveglianza dell'Osservatorio Vesuviano. Rendiconto anno 2003. INGV-OV Report (in Italian).

Morhange, C., Bourcier, M., Laborel, J., Gialanella, C., Goiran, J.P., Crimaco, L., Vecchi, L., 1999. Phys. Chem. Earth A, 24(4), 349–354.

Morhange, C., Marriner, N., Laborel, J., Todesco, M., Oberlin, C., 2006. Rapid sea-level movements and non-eruptive crustal deformation in the Phlegrean Fields caldera, Italy. Geology, 34, 93–96.

Orsi, G., de Vita, S., Di Vito, M., 1996. The restless, resurgent Campi Flegrei nested caldera (Italy): constraints on its evolution and configuration. J. Volcanol. Geotherm. Res., 74, 179–214.

Parascandola, A., 1947. I Fenomeni Bradisismici del Serapeo di Pozzuoli. Stabilimento Tipografico G. Genovese, Naples.

Pingue, F., De Martino, P., Obrizzo, F., Serio, C., Tammaro, U., 2006. Stima del campo di spostamento ai Campi Flegrei da dati CGPS e di livellazione di precisione nel periodo maggio 2004–marzo 2006. Open File Report no. 5, INGV-OV (in Italian).

Rolandi, G., Bellucci, F., Heizler, M.T., Belkin, H.E., De Vivo, B., 2003. Tectonic controls on the genesis of ignimbrites from the Campanian volcanic zone, southern Italy. Min. Petrol., 79, 3–31.

Rosi, M., Sbrana, A., 1987. Phlegraean Fields, Quaderni de "La Ricerca Scientifica", 114 CNR, Roma, pp. 114–175.

Rosi, M., Sbrana, A., Principe, C., 1983. The Phlegraean Fields: structural evolution, volcanic history and eruptive mechanisms. J. Volcanol. Geotherm. Res., 17, 273–288.

Troise, C., De Natale, G., Pingue, F., Obrizzo, F., De Martino, P., Tammaro, U., Boschi, E., 2007. Renewed ground uplift at Campi Flegrei caldera (Italy): new insight on magmatic processes and forecast. Geophys. Res. Lett., 34, L03301, doi:10.1029/2006GL028545.

Troise, C., De Natale, G., Pingue, F., Zollo, A., 1997. A model for earthquake generation during unrest episodes at Campi Flegrei and Rabaul calderas. Geophys. Res. Lett., 24(13), 1575–1578, doi:10.1029/97GL01477.

Troise, C., Pingue, F., De Natale, G., 2003. Coulomb stress changes at calderas: modeling the seismicity of Campi Flegrei (southern Italy). J. Geophys. Res., 108(B6), 2292, doi:10.1029/2002JB002006.

CHAPTER 11

# Hydrothermal Fluid Circulation and its Effect on Caldera Unrest

Micol Todesco[*]

## Contents

## Abstract

This paper focuses on the role that hydrothermal systems may play in caldera unrest. Changes in the fluid chemistry, temperature and discharge rate of hydrothermal systems are commonly detected at the surface during volcanic unrest, as hydrothermal fluids adjust to changing subsurface conditions. Geochemical monitoring is carried out to observe the evolving system conditions. Circulating fluids can also generate signals that affect geophysical parameters monitored at the surface. Effective hazard evaluation requires a proper understanding of unrest phenomena and correct interpretation of their causes. Physical modelling of fluid circulation allows quantification of the evolution of a hydrothermal system, and hence evaluation of the potential role of hydrothermal fluids during caldera unrest. Modelling results can be compared with monitoring data, and then contribute to the interpretation of the recent caldera evolution. This paper: (1) describes the main features of hydrothermal systems; (2) briefly reviews numerical modelling of heat and fluid flow through porous media; (3) highlights the effects of

[*]Corresponding author. Tel.: +39 051 4151 468; Fax: +39 051 4151 499
*E-mail address:* todesco@bo.ingv.it

Istituto Nazionale di Geofisica e Vulcanologia, Sezione di Bologna, via Donato Creti, 12, 40128 Bologna, Italy

hydrothermal fluids on unrest processes and (4) describes some model applications to the Phlegrean Fields caldera. Simultaneous modelling of different independent parameters has proved to be a powerful tool for understanding caldera unrest. The results highlight the importance of comprehensive conceptual models that incorporate all the available geochemical and geophysical information, and they also stress the need for high-quality, multi-parameter monitoring and modelling of volcanic activity.

# 1. Introduction

Many active calderas are densely populated and thus require effective evaluation of volcanic hazards. However, the quantification of volcanic hazards in active calderas is a difficult task. This is because a large variety of eruptive styles and intensities are possible and in addition the opening of new vents can potentially affect wide areas, but the number and location of these is uncertain. To add to this complexity, non-eruptive unrest is typical of caldera volcanic systems (Newhall and Dzurisin, 1988; Hon and Pallister, 1995; Cole et al., 2005). Unrest crises commonly involve ground deformation, gravity changes and seismic activity, in addition to changes in composition, temperature or discharge rate of hydrothermal fluids, regardless of the eruptive or non-eruptive nature of the crisis. Yet eruptions may occur at calderas without significant warning. Unrest episodes have been recorded at Long Valley since 1980 (Sorey et al., 2003, and references therein), and at Phlegrean Fields since 1969 (Troise et al., 2008, this volume) without major consequences during the following twenty years. At Rabaul (New Guinea) an important unrest phase in 1983–1985 (McKee et al., 1984, 1985; Mori et al., 1989) was followed by a relatively quiet period, whereas limited warning preceded the onset of the 1994 eruption (Smithsonian Institution-GVN, 1994). Similar pattern of unrest may lead to very different eruptive and non-eruptive scenarios; therefore the identification of possible precursors of eruptive activity is difficult. Unrest phenomena may occur as magma stored at depth approaches eruptive conditions, i.e. when the ascent or intrusion of magma at shallow crustal levels modifies the local stress field, affects temperature gradients, and is accompanied by exsolution of magmatic volatiles. These processes are known to trigger typical unrest phenomena that we can monitor at the surface, such as seismicity, ground deformation or changes in geochemical and other geophysical parameters. During a volcanic crisis the mitigation measures may involve partial or total evacuation of the population, especially if a large explosive eruption is expected. In these cases crisis management decisions rely to some extent on monitoring parameters likely to signal the onset of eruptive. In the case of calderas chances of a false alarm are very high. The occurrence of non-eruptive unrest crises, observed at several calderas in the world, implies that the relationship between the magmatic system and unrest phenomena may not be straightforward and that unrest crises are not necessarily synchronous with magma ascent and evolution. Discrimination between eruptive and non-eruptive crises is often possible only right before the onset of an eruption, and evacuation may require significant time, depending on the number of people and

on the region involved. More research is needed to completely understand volcanic unrest, and to provide tools for the early recognition of eruptive crises.

A common characteristic of active calderas is the presence of hydrothermal systems, which can play an important role during unrest crises. The presence of a hydrothermal system may affect the eruptive style of a volcano, favouring the occurrence of phreatic or phreatomagmatic events, but it also controls heat and fluid transport within the volcanic edifice during both quiescent and unrest periods. A hydrothermal system represents the complex interface between the magma chamber and the surface. Geochemical or geophysical signals originating at the magma chamber level can be distorted, magnified or reduced by the presence of hydrothermal fluids. Hydrothermal systems may themselves generate additional measurable signals in response to changing conditions.

Physical modelling of hydrothermal systems is an important tool for studying the role of hydrothermal fluids during caldera unrest. Once an appropriate conceptual model is identified, physical modelling of heat and fluid circulation in the caldera then allows the quantification of relevant geochemical and geophysical signals generated by the hydrothermal system. This is a first step toward identifying the relationship between magmatic and hydrothermal systems, and hence toward the interpretation of volcanic unrest at calderas.

This paper focuses on illustrating the role of hydrothermal systems during caldera unrest. After describing the main features of hydrothermal circulation (see Section 2), Section 3 focuses on the governing equations and physical models which describe fluid circulation through porous media. The role of hydrothermal fluids during volcanic unrest is reviewed in Section 4, while the final section describes results from numerical modelling of hydrothermal fluid circulation at Solfatara (Phlegrean Fields caldera, Italy).

## 2. The Hydrothermal Fluid Circulation

Hydrothermal fluid circulation develops where a thermal anomaly heats pore fluids (i.e.: groundwater, meteoric water or seawater). In volcanic areas, the heat source is commonly a shallow magma reservoir which releases not only heat but also exsolved magmatic gases, such as water, carbon dioxide and sulphur compounds, with minor HCl and HF. Hydrothermal features detect-able at the surface depend on several parameters which include the size and geometry of the magmatic source, the properties of fluid components and the characteristics of subsurface rocks. Calderas are commonly characterised by wide heat anomalies and host larger and longer-lived hydrothermal system than stratovolcanoes.

Although magmatic volatiles are commonly identified in hydrothermal systems, mechanisms of fluid transfer from the magma chamber to the surroundings are not completely understood. It is generally assumed that a transition zone exists between the molten magma and the brittle host rock, where partially molten rock acts as a ductile medium deforming plastically, and heat is mainly transferred by conduction. Across this transition zone, porosity tends to vanish, because of high temperatures

(favouring a ductile rock behaviour), lithostatic pressures and abundant mineral deposition at temperatures in excess of 350–400°C (Fournier, 1987). However, petrological studies of contact metamorphism provide clear evidence of fluid transfer across this transition region. Upward and outward fluid migration from cooling plutons has been shown to occur at temperatures in excess of 500°C and pressures up to 220 MPa, preferentially along bedding or lithological contacts (Ferry et al., 2002; Buick and Cartwright, 2002). The presence of fluids, and of considerable mass transport via fluid phases, is known to take place through the deep crust, at depths greater than 15 km and under granulite facies conditions (Ague, 2003). Hydrofracturing may occur through the transition zone as pressure of exsolved volatiles increases above the tensile strength of the surrounding rocks (Tait et al., 1989; Jamtveit et al., 1997). This may lead to transient high flux across the transition region, lasting as long as the source is capable of sustaining it. Metamorphic devolatilisation reactions can also intervene and reduce the total solid volume, generating secondary porosity (Jamtveit et al., 1997).

Once hot magmatic gases escape the magma chamber, buoyancy forces prompt natural convection, provided that rock permeability is high enough (Ingebritsen and Sanford, 1998). Hot fluids then propagate through pores and/or fractures, interact with shallow groundwater and eventually reach the surface generating fumaroles, hot springs or geysers. Hydrothermal circulation depends on fluid properties, which in turn change as a function of system conditions. Hydrothermal systems encompass a wide range of physical conditions, spanning from almost magmatic to surface settings. As a consequence hydrothermal fluids may exist as single-phase, two-phases or supercritical fluids depending on their pressure and temperature. Physical and transport properties may change accordingly, favouring or hindering fluid motion and heat transport. If gas and liquid coexist, the mobility of each phase is reduced by the presence of the other. In this case, the gas phase tends to occupy larger pores and fractures, whereas liquid water is preferentially held into smaller pores, due to capillary pressure and surface effects (Corey et al., 1956; Elder, 1981). Above the critical point (374.15°C and 22 MPa for pure water) gas and liquid phases become indistinguishable and the resulting supercritical fluid is characterised by very high compressibility, thermal expansion and heat capacity and by low viscosity. Strong buoyancy forces and low viscous resistance favour fluid motion and greatly enhance convective heat transport as the critical transition is approached. High pore pressure is easily generated across the critical transition and, in general, the entire hydrothermal circulation is affected (Elder, 1981; Norton, 1984). The composition of circulating fluids, as well as the presence and nature of dissolved salts, also affect fluid properties and modify the temperature and pressure (and hence depth) at which phase transitions occur (Elder, 1981; Bowers and Hegelson, 1983a, 1983b; Bishoff and Pitzer, 1984; Bishoff et al., 1986; Pitzer and Pabalan, 1986; Bishoff, 1991). Highly saline fluids (or brine) are known to evolve from crystallising magma bodies, together with exsolved volatiles (Fournier, 1987). Denser brine tends to concentrate in the deeper region of hydrothermal systems and separates from the dilute gas phase that rises buoyantly. Double diffusive effects, driven by temperature, density and salinity gradients may develop between the dense and dilute convective systems (Elder, 1981; Bishoff and Pitzer, 1984;

Bishoff et al., 1986; Pitzer and Pabalan, 1986; Fournier, 1987; Bishoff, 1991). At shallower depths density differences may drive separation of hot rising gases from the denser liquid phase. As a result hot acid–sulfate springs and fumaroles, fed by $CO_2$- and $H_2S$-rich gases, tend to dominate at higher elevation, whereas neutral–chloride waters will dominate at greater depths within the volcanic edifice and feed springs at lower elevation and at the periphery of the main upflow region (White et al., 1971; Ingebritsen and Sorey, 1988). Such zonation of discharge features may not exist in wide calderas, which are commonly characterised by a rather flat ground surface (Ingebritsen and Sanford, 1998; Goff and Janik, 2000).

Rock properties also greatly affect the onset and evolution of fluid circulation. Rock permeability expresses the resistance offered by a porous medium to fluid flow. It depends on lithology, varying by several orders of magnitude among different rock types. It also varies with the degree of rock fracturing or alteration. Within the same rock formation permeability may change at different locations and can be anisotropic. Stratigraphic discontinuities, faults or fractures may act as channelways for fluid propagation, focusing the flow along preferential directions (Ingebritsen and Sanford, 1998). Where fractures are present fluid flow can be relatively fast, and thermal disequilibrium between rock and fluid may exist. If more than one phase is present fractures can also affect phase distribution, as the liquid phase is preferentially held into the smaller pores while gas occupies the fractures (Helmig, 1997). Rock permeability tends to decrease with depth as higher confining pressure, diagenetic and metamorphic processes reduce pore size (Ingebritsen and Sanford, 1998).

Rock permeability can be modified via several processes and at different spatial scales, and this affects the fluid flow pattern through time. Some of these processes are intimately associated with chemical and physical interactions between fluids and host rocks: dissolution or precipitation of mineral phases changes pore size and connectivity, whilst modifying fluid composition and properties (Norton and Knight, 1977; Fournier, 1987; Verma and Pruess, 1988; Ingebritsen and Sanford, 1998). Permeability may also increase in response to hydro–fracturing induced by high pore pressure (Norton and Knight, 1977; Burnham, 1985; Gudmundsson et al., 2002). As rock permeability within the hydrothermal system changes through time, surface features associated with fluid circulation change accordingly as the system adjusts to new flow rates and directions.

## 3. Modelling of Hydrothermal Fluid Circulation

Physical modelling of fluid flow problems is based on the solution of the fundamental equations that govern fluid motion. However, in the case of porous media flow the classical approaches of fluid mechanics, such as those based on the solution of the Navier–Stokes equations, are not immediately applicable as the details of the microscopic pore geometry are not known and flow variables and parameters cannot be defined everywhere. In this case, it is necessary to work on a macroscopic scale, where each quantity is defined as an average over an appropriate volume of material (representative elementary volume). Within this volume it is

possible to neglect the details of local variations and to assume that averaged quantities are representative of the overall macroscopic behaviour over that volume. The macroscopic approach to porous media flow is based on Darcy's law, an empirical equation derived experimentally in 1856, which describes the steady flow of liquid water through a vertical column of sand. Darcy's law relates the specific water discharge (also known as filtration or Darcy velocity) to the pressure gradients across the sand's column through a coefficient known as hydraulic conductivity [m/s], which depends on both fluid and rock properties. Darcy's law has been tested over a wide range of conditions and in most cases theoretical results are consistent with experimental data. Exceptions are found under extreme conditions, in case of very high (or very low) flow velocity when inertial (or interfacial) forces that are neglected in the empirical formulation become relevant. These extreme conditions are very rare in natural systems and Darcy's law has been successfully used to set up the water mass balance equation in countless hydrological applications. Detailed discussion of Darcy's law, its limitations and its derivation from the Navier–Stokes equation can be found in de Marsily (1986), Dullien (1992), Helmig (1997), Ingebritsen and Sanford (1998). Here we shall only briefly overview some of its basic aspects, following Helmig (1997).

Hydrothermal fluid circulation requires a slightly more complex formulation than common groundwater problems. Complexities mostly arise from the wide range of temperatures characterising hydrothermal systems, where water can exist as a liquid, a gas, a two-phase mixture or a supercritical fluid. Liquid water and steam are characterised by very different thermal and transport properties, and as the fluid propagates through different regions its properties may change considerably, affecting fluid motion. At the same time fluid flow contributes significantly to heat transport, affecting temperature distribution. Physical models of hydrothermal circulation therefore need to solve the fully coupled equations of both mass and energy balance.

For multi-phase flow problems, Darcy's law can be rewritten to explicitly state the dependence of the filtration velocity, $\mathbf{u}_\beta$ [m/s] on fluid properties:

$$\mathbf{u}_\beta = -\mathbf{k}\frac{k_\beta}{\mu_\beta}(\nabla p_\beta + \rho_\beta \mathbf{g}) \tag{1}$$

where $\mathbf{k}$ is the intrinsic rock permeability [m$^2$] and expresses the resistance opposed by porous media to fluid flow along different directions. It depends on rock porosity and pore connectivity. $k_\beta$ is the relative permeability of phase $\beta$; it expresses the interference between phases and it ranges from 0 to 1 as a function of gas saturation. $\mu_\beta$ is viscosity [Pa s]; $p_\beta$ pressure [Pa] (accounting for the effects of capillary force) and $\rho_\beta$ density [kg/m$^3$] (where subscript $\beta$ refers to fluid phase). $\mathbf{g}$ is the gravitational acceleration [m/s$^2$].

Based on the above multi-phase version of Darcy's law, the mass balance equation for phase $\beta$ can be written in differential form as:

$$\frac{\partial(S_\beta \phi \rho_\beta)}{\partial t} + \nabla \cdot (\rho_\beta \mathbf{u}_\beta) - \rho_\beta q_\beta = 0 \tag{2}$$

where $S_\beta$ is phase saturation (volumetric fraction occupied by phase $\beta$), $\phi$ rock porosity and $q_\beta$ a sink or source (if negative) of phase $\beta$. Equation (2) is non-linear due to the non-linear relations linking phase saturation, capillary pressure and relative permeability (Helmig, 1997). If more than one component is present (i.e. volcanic gases, such as carbon dioxide or dissolved solid phases), Equation (2) is appropriately modified, expressing the fluid mass per unit volume as $\rho_\beta X_\beta^\kappa$, where $X_\beta^\kappa$ represents the mass fraction of component $\kappa$ in phase $\beta$. As mentioned above, fluid properties that explicitly appear in the mass and energy balance equations may change significantly within hydrothermal systems. As a consequence, modelling of hydrothermal fluid circulation also requires the definition of appropriate equations of state which describe fluid properties at the conditions of interest. In some cases it is possible to approximate the behaviour of fluid properties as linear function of pressure and temperature. In other cases this is not feasible and more accurate non-linear equations of state are required, increasing the complexity of the numerical problem.

The energy balance equation (for phase $\beta$) is written assuming local thermal equilibrium between solid rock and fluid. It accounts for heat transport by fluid convection and by conduction through the porous matrix:

$$(1 - \phi)\rho_R c_R \frac{\partial T}{\partial t} + \phi \sum_\beta \frac{\partial(U_\beta \rho_\beta S_\beta)}{\partial t} + \nabla \cdot \left( \sum_\beta \mathbf{u}_\beta \rho_\beta h_\beta \right) + \nabla \cdot \{\lambda_R \nabla T\} - q_E = 0 \quad (3)$$

where $\rho_R$ is rock density [kg/m$^3$] (subscript R refers to rock properties); $c_R$ is specific heat of the rock [J/Kg $^\circ$K]; $T$ is temperature [$^\circ$K]; $U_\beta$ and $h_\beta$ are the internal energy and enthalpy of phase $\beta$, respectively; $\lambda_R$ is rock thermal conductivity [W/m$^\circ$K] (which depends not only on the rock, but also on thermal properties of the permeating fluid and on its saturation), and $q_E$ represents any energy sink or source within the system.

Due to the difficulty in the simultaneous solution of these highly non-linear and fully coupled equations, early models were limited to simple systems (often isothermal) with a single-phase fluid of constant properties flowing through a homogeneous porous medium (Elder, 1967a, b). Better computational capabilities and improved numerical techniques have since allowed solution of the coupled energy and mass transport equations. Pioneering studies focused on hydrothermal fluid circulation nearby cooling plutons (Cathles, 1977; Norton and Knight, 1977; Delaney, 1982), and considered fluid density to be constant everywhere except in the evaluation of buoyancy forces (Boussinesq approximation). Subsequent improvement in numerical models has been supported by the geothermal industry. A detailed overview of geothermal reservoir modelling and its development through time is given by Pruess (1990) and O'Sullivan et al. (2001). Modelling of heat and fluid flow through porous media is now a well-developed and highly sophisticated research field. At present, geothermal simulators include realistic descriptions of fluid properties and account for phase transitions and associated latent heat effects (Pruess, 1990, 1991; Hayba and Ingebritsen, 1997). Different features may characterise specific models, features such as the presence of additional fluid components (non-condensable gases or dissolved salt) or sophisticated rock

descriptions, including heterogeneous, anisotropic or time-dependent rock properties. Different strategies have been used to describe flow through fractures: considering a single, fracture-dominated continuum; accounting for discrete fracture networks; defining an equivalent (fracture and matrix) continuum; or through a dual porosity approach in which fracture and matrix are considered separately (Evans et al., 2001). More recent advances involve coupling of non-isothermal fluid flow and chemical reactions (Xu and Pruess, 2001; Xu et al., 2001; Kiryukhin et al., 2004) or hydrothermal circulation and deformation of the porous medium (Rutqvist et al., 2002). These modelling techniques are now widely applied to a variety of problems that involve underground flows ranging from site testing for nuclear waste storage to mining engineering, environmental restoration, vadose zone hydrology and more recently for investigating carbon dioxide sequestration (O'Sullivan et al., 2001).

Despite such development, applications to volcanological problems are not common. Volcanological applications face the complexity of volcanic settings and involve extreme and highly transient physical conditions, as well as the lack of appropriate modelling-oriented data sets required to constrain subsurface properties and conditions. Surface measurements of geochemical and geophysical parameters are usually carried out as a part of surveillance programs, but do not necessarily involve the definition of hydraulic properties of subsurface rocks. Although these surface data can be integrated with subsurface data from few sparse deep drill holes, large uncertainties commonly remain in the definition of the conceptual model. In spite of these difficulties, numerical modelling has been performed to study hydrothermal fluid circulation in volcanic areas (Ingebritsen and Sorey, 1985, 1988; Bonafede, 1991; Ingebritsen and Rojstaczer, 1993, 1996; Todesco, 1995, 1997; Gaeta et al., 1998, 2003; Kissling, 1999; Hurwitz et al., 2002, 2003; Chiodini et al., 2003; Todesco et al., 2003a, b, 2004; Reid, 2004; Todesco and Berrino, 2005; Villemant et al., 2005). Early studies mostly focused on the description of the natural state and were aimed at the study of some theoretical aspects of fluid flow in volcanic regions. When long-term, high-quality data sets are available it is possible to set up reliable conceptual models for the evolution of the entire volcanic system. This in turn allows implementation of more sophisticated numerical models designed to elucidate site-specific features and details of case histories. When sophisticated modelling tools and high-quality data are both available, the ideal condition of being able to compare and constrain modelling results with observations becomes possible.

## 4. Hydrothermal Systems and Volcano Monitoring

Hydrothermal fluid circulation plays a significant role during both eruptive and non-eruptive unrest events. Volcanic monitoring around the world commonly records changes in geochemical and geophysical parameters, many of which can be directly or indirectly related to the activity of hydrothermal fluids. In some cases these changes result from the evolution of the magmatic system at depth. In other cases the observed variations only reflect the natural evolution of the hydrothermal system or

its reaction to external controls, such as tectonic events. Physical models of hydrothermal fluid circulation allow the simulation of unrest phenomena related to the hydrothermal system, and elucidate what controls observed changes in the system.

## 4.1. Geochemical monitoring

Surveillance programs on active volcanoes commonly involve geochemical monitoring of hot springs, fumaroles and thermal waters. Hydrothermal fluids reveal important information about subsurface conditions, and unrest phenomena are often accompanied by changes in the temperature, composition and discharge rates of hydrothermal waters (Newhall et al., 2001).

Geochemical monitoring is based on the concept that volcanic gas emissions are fed by magma degassing and thus reflects to some extent the conditions under which degassing takes place. The composition of gases exsolving from a magma chamber will depend on magma composition, the solubility of different gas components and on the depth and temperature of the magma reservoir. Less soluble gases, such as nitrogen or carbon dioxide, exsolve first and as degassing proceeds more soluble species (such as sulphur compounds, water or halogens) will be progressively released. The ratio of less soluble to soluble components is therefore expected to change through time, as magma looses its volatiles (Carroll and Webster, 1994; Delmelle and Stix, 2000). Departure from the expected trends may indicate a change in the magmatic source, for example by the arrival of a new, gas-rich magma batch or by the ascent of the degassing magma to shallower depths. An increase in gas flow rate is also expected if a larger amount of magma is available. Discharge rate at hot springs increased dramatically before eruptions at Sakurajima (Japan) in 1914, and at Monte Nuovo (Phlegrean Fields, Italy) in 1538 (Newhall and Dzurisin, 1988). Mount Usu (Japan) eruption in 2000 was preceded by an increase in carbon dioxide degassing within the summit caldera (Hernández et al., 2001). Major diffuse degassing of carbon dioxide, killing trees in Mammoth Mountain area, was also observed during unrest at Long Valley caldera, California (Pribnow et al., 2003; Bergfeld et al., 2006). Seismicity and ground deformation have been recorded there since 1980, and this has been accompanied by a recorded increase of well fluid pressure and by a higher flow rate of magmatic gases (Sorey et al., 2003, and reference therein). The interpretation of monitoring data is, however, not always straightforward. Volcanic gas emissions do not simply reflect the process of magma degassing. As magmatic gases rise toward the surface they are affected by cooling, decompression, oxidation and reactions with host rock and groundwaters. Fluids sampled at the surface result from complex interactions between the deep, magmatic contributions and shallower components of the hydrothermal system. As hot fluids interact with shallow water bodies, heat exchange, phase transition and chemical reactions may take place: ascending fluids may gain or loose water vapour, depending on whether condensation or evaporation prevails. In addition, reactive and soluble components, such as sulphur dioxide or halogens, may be lost in groundwaters and appear substantially depleted in volcanic gas emissions. Sulphur compounds are particularly sensitive to secondary processes and redox conditions, which ultimately control the $SO_2/H_2S$ ratio; deposition (or revolatilisation) of

elemental sulphur may also occur upon cooling (heating) (Giggenbach, 1996; Delmelle and Stix, 2000; Symonds et al., 2001; Oppenheimer, 2003, and references therein). Surface hydrothermal features will therefore depend on the relative proportion of magmatic volatiles with respect to shallower fluids, and on whether or not thermal and chemical equilibrium among different components has been achieved. This in turn may depend on rock permeability, which controls fluid mobility and determines the extent and duration of the interaction between different fluid components. Temperature, discharge rate and composition of surface hydrothermal features may change as any element of these complex systems changes, either at the magma chamber level, in the groundwater system or in rocks hosting them both. As a consequence, interpretation of geochemical data can be highly controversial. Sophisticated theoretical tools are needed to estimate the conditions at which chemical equilibrium was attained, or to quantify the departure from such equilibrium conditions (Giggenbach, 1996; Chiodini and Marini, 1998; Oppenheimer, 2003).

## 4.2. Geophysical monitoring

The role of hydrothermal fluids in volcanic surveillance goes beyond the information we can obtain through geochemistry. The presence of hot fluids alters rock properties and affects the response of the entire volcanic edifice to thermal and mechanical changes. Seismic wave velocity is known to depend on the presence of pore fluids, and different degrees of seismic attenuation are expected in gas- and liquid-dominated regions. Anisotropy associated with fluid-filled microcracks is known to generate shear wave splitting. Shear wave splitting parameters (polarisation and time delay between split waves) change with stress distribution, and these are increasingly adopted as a tool in volcano monitoring (Miller and Savage, 2001; Crampin and Chastin, 2003; Bianco et al., 2004). Although volcanological applications mostly focus on stress changes induced by magma intrusion, changes in polarisation of the faster split shear wave may also arise as a consequence of increased pore pressure, as observed during injections in hot, dry-rock geothermal reservoirs or in oil fields (Cramping and Booth, 1989; Angerer et al., 2002; Crampin and Chastin, 2003).

Hydrothermal fluids can also trigger shallow seismicity. Elevated pore pressure reduces the effective normal stress, favouring focused stress release. Where rocks are close to failure, pore pressure perturbations may drive seismicity, even in non-volcanic areas (Shapiro et al., 2003; Miller et al., 2004). Microseismicity is commonly observed at geothermal fields during fluid injection in boreholes (Maillot et al., 1999). In volcanic areas, hydrothermal fluids can trigger, or participate to the generation of, long- and very-long-period seismic events and volcanic tremor (Newhall and Dzurisin, 1988; Chouet, 1996; Hellweg, 2000; Konstantinou and Schlindwein, 2002; Bianco et al., 2004; De Angelis and McNutt, 2005). Banded tremor correlated with hydrothermal and geyser activity has been observed at Yellowstone and at other locations (Newhall and Dzurisin, 1988, and reference therein). Pressurisation of hydrothermal fluids, possibly associated with shallow magma intrusion, has been invoked as a possible source for long-period

seismic events and volcanic tremor at Redoubt, Alaska (Chouet, 1996); Aso volcano, Japan (Kaneshima et al., 1996; Yamamoto et al., 1999; Kawakatsu et al., 2000); Phlegrean Fields, Italy (Bianco et al., 2004); Rabaul, Papua New Guinea (Blong and McKee, 1995; Gudmundsson et al., 2004) and Mt. Spurr, Alaska (De Angelis and McNutt, 2005). A connection between seismic swarms and long-term pulsating degassing of a shallow magma body was also proposed for La Soufrière, Guadaloupe, Lesser Antilles (Villemant et al., 2005). At Long Valley, California, the ascent of deep, $CO_2$-rich fluids (later responsible for tree-killing) was recently indicated as the possible trigger for the long seismic swarm recorded in 1989 (Hill and Prejean, 2005). Evidence of hydro-fracturing, associated with the ascent of hydrothermal fluids, was also recognised in the focal mechanism of small micro-earthquakes recorded in 1997 (Foulger et al., 2004).

Hydrothermal fluids also generate a variety of geophysical signals that can be detected at the surface. This is well known in the geothermal industry, where such signals are collected to monitor reservoir properties during exploitation. Circulating fluids induce changes in electrical potential as they move with respect to the host rock (electro-kinetic effect). Thermo-electric and electro-chemical effects are also known to arise from thermal and chemical gradients (Zlotnicki and Nishida, 2003). Self-potential (SP) anomalies are commonly identified upon fluid injection or production in geothermal reservoirs (Darnet et al., 2004). In active volcanic systems, anomalies up to several hundreds of mV are commonly associated with thermal and hydrothermal features, and their temporal evolution is known to reflect the evolution of the volcanic system (Zlotnicki and Nishida, 2003).

Phase transition or displacement of liquid water can occur within the hydro-thermal system and modify the subsurface density distribution. The resulting gravity change can be detected at the surface by accurate microgravity measurements. Gravity changes are recorded in geothermal fields to monitor reservoir properties during fluid production and to constrain numerical modelling of reservoir exploitation (Hunt and Kissling, 1994; Nortquist et al., 2004). Gravity changes are also commonly observed in active calderas during episodes of ground deformation (Brown et al., 1991; Berrino et al., 1992; Rymer, 1994; Murray et al., 2000; Battaglia et al., 2003; Battaglia and Segall, 2004; Gottsmann and Battaglia, 2008–this volume). Even though such changes are also caused by ground displacement, in some cases they can be ascribed to the motion of aqueous fluids (Berrino et al, 1992; Gottsmann and Rymer, 2002; Gottsmann et al., 2003; Todesco and Berrino, 2005).

To some extent, hydrothermal fluids can also drive ground deformation. Coupling of thermal gradients, fluid flows and mechanical deformation of rocks have been widely recognised, and complex thermo–hydro–mechanical (THM) interactions are known to occur in many geological contexts and applications (Tsang, 1999). Prolonged fluid extraction at the Wairakei geothermal field, New Zealand, was shown to have caused up to 14 m of ground subsidence, over almost 40 years of production (1950–1997) (Allis, 2000). Localised subsidence as a consequence of fluid production was also recorded in Long Valley near the Casa Diablo power plants (Howle et al., 2003). Similarly, ground uplift may follow pore pressure increase and rock thermal expansion, associated with the circulation

of hot fluids. This mechanism is particularly suited to explain ground deformation during non-eruptive unrest, when ground uplift is followed by a subsidence phase that cannot be ascribed to magma withdrawal. If uplift is generated by an increase in pore pressure, subsidence may occur as fluids propagate and eventually discharge at the surface and gradually dissipate the initial overpressure. In the case of Phlegrean Fields caldera, a long scientific tradition has suggested the involvement of hydrothermal fluids in the two recent episodes of non-eruptive unrest, each of which was accompanied by remarkable ground uplift (bradyseism) (Olivieri del Castillo and Quagliariello, 1969; Casertano et al., 1976; Bonafede, 1991; Gaeta et al., 1998; Orsi et al., 1999; De Natale et al., 1991, 2001; Castagnolo et al., 2001). Recent findings substantiate the concept and emphasise the role of hydrothermal system during recent unrest events (Chiodini et al., 2003; Todesco et al., 2004; Todesco and Berrino, 2005; Battaglia et al., 2006).

## 5. An Example of Assessing the Role of Hydrothermal Processes During Unrest: Solfatara (Phlegrean Fields Caldera, Italy)

The Phlegrean Fields caldera (Figure 1) represents an optimal site for modelling hydrothermal fluid circulation. Volcanic surveillance was started here in the early 1980s and long data series are now available to describe the caldera's recent evolution. The last major unrest took place between 1982 and 1984 and involved seismic activity, ground deformation (with ground uplift up to 1.8 m), positive
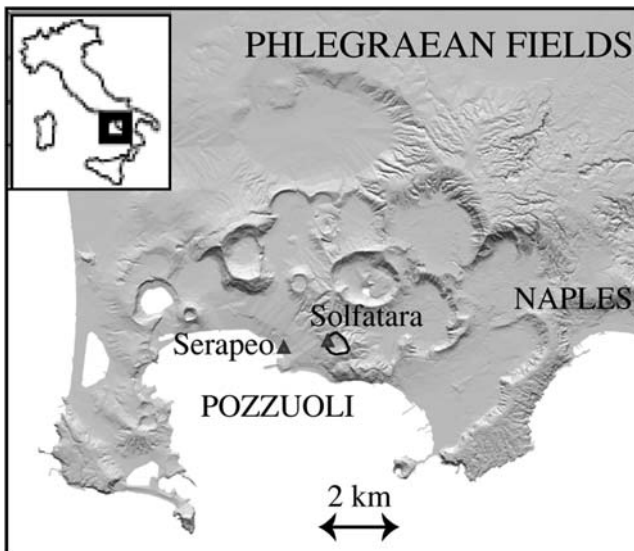


**Figure 1**    The Phlegrean Fields caldera, and the Solfatara crater, where fumaroles and diffuse degassing are concentrated. Locations of two gravity stations (Solfatara and Serapeo) are also shown (modified after Todesco and Berrino, 2005).

gravity residuals and significant changes in the composition of gases discharged at Solfatara crater. A slow subsidence begun in 1985, periodically interrupted by minor uplift (few cm each), accompanied by significant changes in gas composition and occasional minor seismic activity (see Troise et al., 2008–this volume, and references therein). As mentioned above, several authors highlight the role of hydrothermal fluid circulation in governing the recent evolution of the Phlegrean Fields caldera (Bonafede, 1991; Gaeta et al., 1998; Orsi et al., 1999; De Natale et al., 1991, 2001; Castagnolo et al., 2001). Recent new analyses of deformation and gravity data confirm the role of hydrothermal fluids in generating uplift (at least partially) and subsidence observed since the last unrest crisis (Gottsmann et al., 2003, 2006; Battaglia et al., 2006).

Physical modelling of heat and fluid flow is a useful tool to quantify the effects of hydrothermal fluid circulation. The simulations presented below describe fluid circulation within the shallow hydrothermal system that feeds surface discharges at the Solfatara crater (Todesco et al., 2003a, b, 2004; Chiodini et al., 2003; Todesco and Berrino, 2005). The role of new magmatic intrusions in the recent unrest crises is not explicitly accounted for, but it is represented in terms of variable magmatic degassing and by the emplacement of a deep source of hot fluids. Simulations were performed with the TOUGH2 geothermal simulator (Pruess, 1991; Pruess et al., 1999). The model describes the coupled heat and fluid flow through porous media for a multi-phase, multi-component system. Phase transitions (gas–liquid) and associated latent heat effects are fully accounted for. Water and carbon dioxide are the two fluid components considered in the model. Details on model formulation and solution techniques can be found in Pruess et al. (1999). Shallow hydrothermal circulation at Solfatara is simulated on a uniform, two-dimensional and axisymmetric domain (Figure 2a). A source of hot ($350°C$) water and carbon dioxide is placed at the bottom (near the symmetry axis) to represent magmatic degassing. Discharge of these hot fluids generates a wide two-phase plume, within which a shallow dry-gas region forms (Figure 2b, Todesco et al., 2003a). Existence and conditions of such single-phase gas region are in good agreement with geochemical data, postulating that fumaroles are fed by a super-heated vapour zone (Chiodini and Marini, 1998).

Using these initial system conditions the model can be applied to study the recent evolution at Solfatara. Simulations were carried out under the assumption that observed compositional changes were driven by periods of increased magmatic degassing. Unrest crises are therefore simulated as periods of higher gas flow rate and $CO_2$ content at the deep source (Chiodini et al., 2003). The model describes the fluid composition and properties throughout the simulation, allowing comparison of modelling results with available geochemical and geophysical data. The composition of the single-phase gas region is taken as representative of fumarolic gases, and is compared with observed gas composition. Appropriate number, timing and duration of each unrest period allow successful matching with the observed compositional variation (Figure 3). If magmatic degassing increases, pore pressure and fluid temperature are also expected to increase. Mechanical effects associated with such changes can be evaluated based on the calculated pressure and temperature distribution. Coupling between TOUGH2 and FLAC3D, a commercial code for rock mechanics (Itasca Consulting Group Inc., 1997), was
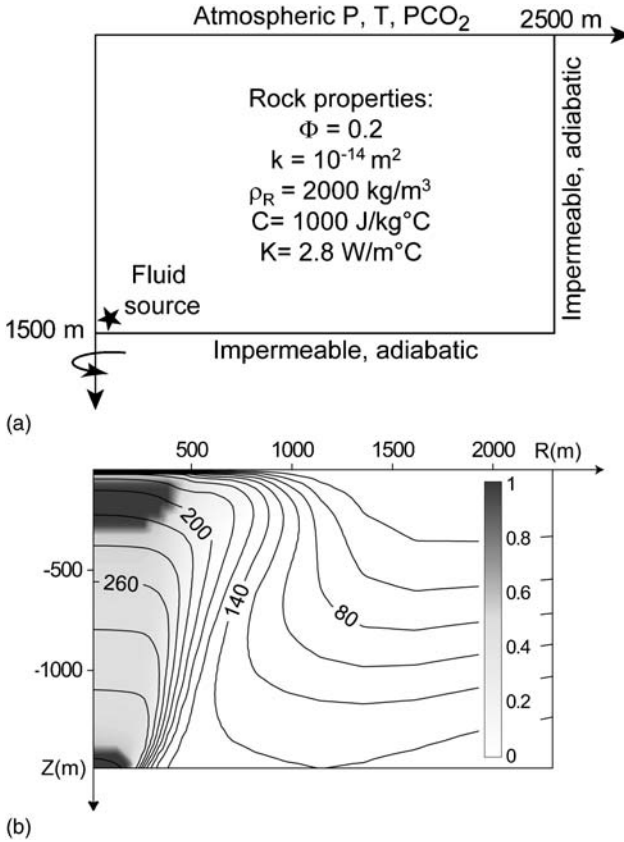
**Figure 2**    a. Computational domain, boundary conditions and rock properties utilised in
numerical simulations of hydrothermal fluid flow. The star indicates the position of a deep
source of fluids, discharging a mixture of water and carbon dioxide at 350°C (modified after
Todesco and Berrino, 2005). b. Temperature (°C, solid line) and volumetric gas fraction (shades)
obtained after a prolonged injection of hot gases at the deep source, and applied as initial
conditions in the simulations thereafter (modified after Chiodini et al., 2003). The shallow
gas-dominated region (dark grey) corresponds to the superheated vapour region that,
according to the geochemical model (Chiodini and Marini, 1998), feeds the fumaroles.

performed to study thermo–hydro–mechanical problems (Rutqvist et al., 2002).
Taking advantage of this methodology, simulations were carried out to model the
deformation arising from increased magmatic degassing, under the assumption
of pure elastic behaviour (Todesco et al., 2003b, 2004). Results from coupled
simulations showed how increased magmatic degassing can drive significant
amounts of rock deformation (Figure 4). Rapid uplift was calculated during the
2-year-long unrest period. Afterwards, a slower and longer subsidence takes place
as the magmatic contribution is strongly reduced. Even though the model only
describes a very shallow portion of the entire volcanic system, therefore neglecting
deformation arising from deeper contributions, the bell-shape form of the
uplifted region, temporal evolution of ground deformation and even the delay of
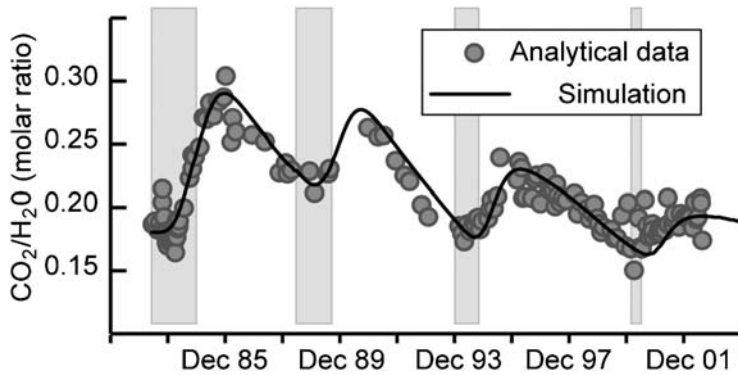
**Figure 3** Comparison between the $CO_2/H_2O$ molar ratio observed at Solfatara fumaroles (dots) and gas composition simulated by the model (solid line). Shaded bars represent the simulated periods of system unrest, characterised by higher gas flow rate and $CO_2$ content at the deep source (modified after Chiodini et al., 2003).
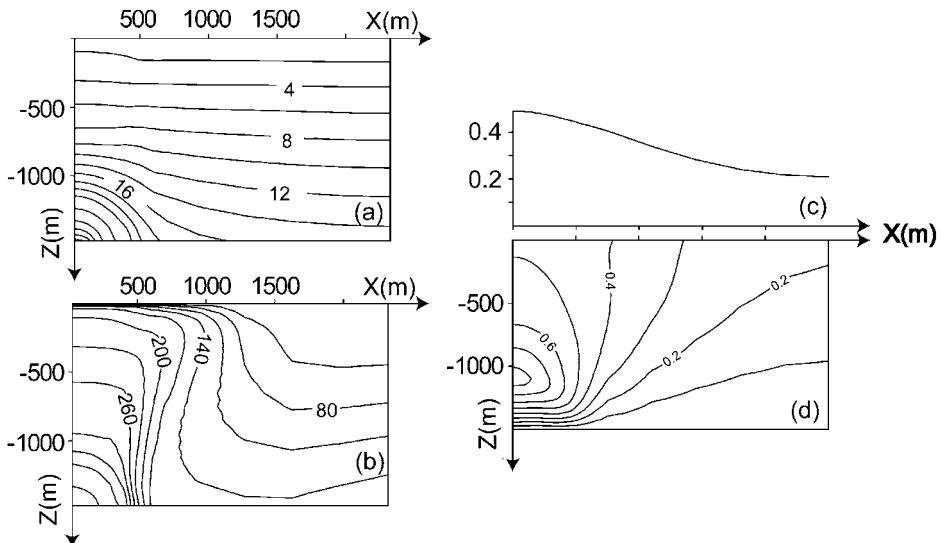


**Figure 4** Distribution of (a) pore pressure (MPa) and (b) temperature (°C) at the end of a 2-year-long unrest crisis. The corresponding ground uplift (m), resulting from heating and pressurisation, is shown in (c). The distribution of vertical ground displacement over the computational domain is shown in (d). Rock deformation is calculated assuming elastic behaviour, and low values of elastic properties due to high temperatures. Bulk modulus = 5 GPa; shear modulus = 2 GPa (modified after Todesco et al., 2003b, 2004).

compositional changes with respect to ground displacement are all consistent with the available observations (Todesco et al., 2003b, 2004). Alternating unrest and quiescent periods also drive significant changes in fluid density, arising from variable fluid composition and phase distribution. Subsurface density changes then affect the value of gravity that can be recorded at the surface. Based on modelling results,
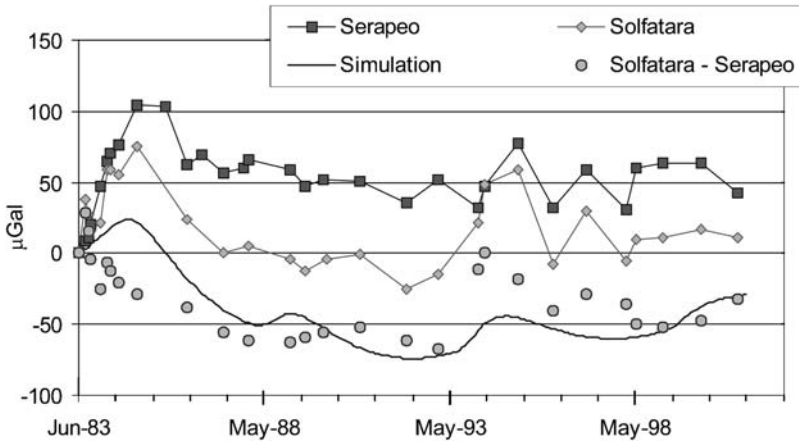
**Figure 5** Temporal variations of gravity residuals observed at Solfatara (diamonds) and Serapeo (squares). The difference between the values recorded at the two stations (dots) is compared with calculated gravity change (solid line) arising from the temporal variation of fluid density. The good correspondence confirms that anomalous gravity residuals at Solfatara are associated with the hot plume of hydrothermal fluids (modified after Todesco and Berrino, 2005).

the gravity changes arising from the simulated unrest periods were calculated (Todesco and Berrino, 2005). Each unrest period causes a sudden and short–lasting gravity increase, associated with the stronger degassing rate. As the newly injected fluids rise toward the surface, the two–phase plume widens and the average gas fraction increases. The overall effect of subsequent unrest crises is therefore to progressively reduce the value of gravity at the surface (Figure 5). Todesco and Berrino (2005) showed that this effect explains the discrepancy between gravity data measured at Solfatara and those recorded at nearby stations, where hydro–thermal fluids do not reach the surface. In this case, it was possible to compare modelling results with both geochemical and geophysical data. A good match with both data sets was obtained by progressively refining the model's initial and boundary conditions. These conditions correspond to an initially hotter system (which indeed had already experienced another important unrest crisis in 1969) and to shorter (but slightly stronger) unrest crises, characterised by a higher $CO_2/H_2O$ ratio with respect to previous simulations (Todesco and Berrino, 2005). This new characterisation of magmatic degassing is in good agreement with recent refinements of the geochemical model (Chiodini, personal communication).

The opportunity to compare modelling results with two sets of independent parameters represented a valuable chance to constrain modelling results in a field, such as volcanology, where model calibration and validation are usually impossible to carry out. Simulation of two different parameters can also be used to improve our understanding of system evolution based on monitoring data. Parametric studies can be carried out to show the different effects of selected source properties (i.e. fluid composition, gas flow rate) on fumarole composition and gravity data. The model can then be used to define different scenarios and to establish a reference framework for the interpretation of monitoring data.

# 6. Discussion and Conclusions

Hydrothermal fluid circulation is a very special feature of active volcanic systems. By controlling the transport of heat and fluids from the magma reservoir to the surface, hydrothermal fluids play a significant role in the evolution of volcanic centres. Circulating fluids affect rock properties, generate various types of geochemical and geophysical signals and can trigger shallow seismicity and ground deformation. Pore pressure build-up, followed by intense degassing, may explain uplift and subsidence cycles observed during non–eruptive unrest at many calderas in the world. Repeated crises, accompanied by ground deformation and by widespread hydrothermal alteration, can progressively weaken rocks strength and, on the long-term, this can be one of the many features favouring a renewal of the eruptive activity. Hydrothermal systems therefore represent an important key to understanding volcanic unrest. Physical modelling of hydrothermal fluid circulation is a powerful tool to study the evolution of hydrothermal systems, and to quantify their effects on selected geochemical and geophysical parameters. Volcanic surveillance collects geochemical and geophysical data, whose evolution depends on the complex interactions between the magmatic source, hot circulating fluids and the host rocks through which they circulate. It is impossible to fully assess all these interactions, but the interpretation of monitoring data should account for this complexity. Results from numerical modelling of hydrothermal circulation are promising, but the complexity of the natural systems demand further improvement to achieve satisfactory results, beyond the theoretical study. A fully multi–disciplinary approach is required to improve and further connect conceptual models, numerical models and monitoring data. We need robust conceptual models capable of describing caldera evolution in all its geochemical and geophysical aspects, consistently incorporating all available information.

Several aspects need to be further investigated to fully understand the role of fluids in unrest crises. Mechanisms controlling magma degassing and the transport of heat and fluid from the magma chamber to the hydrothermal system are still poorly constrained. Pulsating degassing, alternating phases of higher and lower gas flow rates, seems to be a common behaviour, but we lack a coherent explanation for it. A better characterisation of magmatic degassing could greatly improve our descrip-tion of hydrothermal circulation, and provide further insights on the functioning and ultimate meaning of non–eruptive unrest crises. Subsurface rock properties are usually poorly defined — few measurements may be available on thermal and acoustic properties of subsurface rocks, but information on hydraulic properties is usually missing. Data used to set up numerical models are commonly taken from the literature and are hardly representative of the natural system. Changes of rock properties through time, or with changing system conditions, are also poorly constrained and generally are not accounted for in models applied to volcanological problems. Nevertheless, these changes could play an important role during unrest crises and their effects on fluid-flow pattern, and on pressure and temperature distribution, should be assessed. More data are available on hydrothermal alteration and, in general, on chemical reactions taking place during fluid circulation. However, modelling of volcanic unrest has not yet included their description, and

does not take into account their effects on fluid circulation. Further work is needed on these coupled processes, including thermal, chemical and mechanical effects and their feedback on fluid circulation. Development of numerical models should also include a better description of fluid properties through the transition from subcritical to supercritical temperatures, and under the extreme conditions that characterise active volcanic systems. Implementation of inverse modelling, directly incorporating data from monitoring networks, would greatly improve our ability to interpret signals gathered during unrest and could contribute to volcanic hazard assessment.

Another important aspect to be considered in future research is the connection between models and observations. This should be improved to ensure at least some degree of model calibration. Therefore, it is necessary to develop models that describe parameters that can be measured in the natural system. We cannot access hydrothermal system at depths and consequently we cannot compare simulated flow variables to direct measurements of pressure or phase saturation. We need to convert modelling results into a larger number of observables, such as gravity changes, which can be actually compared with available data. Preliminary successful results are encouraging, but the comparison between observation and modelling results should be performed over a larger number of physical and chemical data. Coordinated monitoring campaigns are necessary to provide simultaneous measurements of different geochemical and geophysical parameters. Simultaneous matching of independent data sets is an effective way to validate modelling results. Monitoring data and modelling results should freely circulate inside the scientific community to ensure a continuous positive feedback, with prompt updating of the conceptual model, progressive refinement of model calibration and rational optimisation of monitoring activities.

## ACKNOWLEDGMENTS

## REFERENCES

Ague, J.J., 2003. Fluid flow in the deep crust. In: Rudnick, R. L. (Ed), The Crust. Vol. 3. Holland, H.D., Turekian, K.K. (Eds), Treatise on Geochemistry, Elsevier-Pergamon, Oxford.

Allis, R.G., 2000. Review of subsidence at Wairakei field, New Zealand. Geothermics, 29, 455–478.

Angerer, E., Crampin, S., Li, X.-Y., Davis, T.L., 2002. Processing, modelling and predicting time-lapse effects of overpressured fluid-injection in a fractured reservoir. Geophys. J. Int., 149, 267–280.

Battaglia, M., Segall, P., 2004. The interpretation of gravity changes and crustal deformation in active volcanic areas. Pure Appl. Geophys., 161, 1453–1467.

Battaglia, M., Segall, P., Roberts, C., 2003. The mechanics of unrest at Long Valley caldera, California. 2. Constraining the nature of the source using geodetic and micro-gravity data. J. Volcanol. Geotherm. Res., 127, 219–245.

Battaglia, M., Troise, C., Obrizzo, F., Pingue, F., De Natale, G., 2006. Evidence for fluid migration as the source of deformation at Campi Flegrei caldera (Italy). Geophys. Res. Lett., 33, L01307, doi: 10.1029/2005GL024904.

Bergfeld, D., Evans, W.C., Howle, J.F., Farrar, C.D., 2006. Carbon dioxide emissions from vegetation-kill zones around the resurgent dome of Long Valley caldera, eastern California, USA. J. Volcanol. Geotherm. Res., 152, 140–156.

Berrino, G., Rymer, H., Brown, G.C., Corrado, G., 1992. Gravity–height correlations for unrest at calderas. J. Volcanol. Geotherm. Res., 53, 11–26.

Bianco, F., Del Pezzo, E., Saccorotti, G., Ventura, G., 2004. The role of hydrothermal fluids in triggering the July–August 2000 seismic swarm at Campi Flegrei, Italy: evidence from seismological and mesostructural data. J. Volcanol. Geotherm. Res., 133, 229–246.

Bishoff, J.L., 1991. Densities of liquids and vapors in boiling NaCl–$H_2O$ solutions; a PVTX summary from $300°$ to $500°C$. Am. J. Sci., 291, 309–338.

Bishoff, J.L., Pitzer, K.S., 1984. Phase relations and adiabats in boiling seafloor geothermal systems. Earth Planet Sci. Lett., 75, 327–338.

Bishoff, J.L., Rosenbauer, R.J., Pitzer, K.S., 1986. The system NaCl–$H_2O$: relations of vapor–liquid near the critical temperature of water and of vapor–liquid–halite from $300°$ to $500°C$. Geochim. Cosmochim. Acta, 50, 1427–1444.

Blong, R.J., McKee, C.O., 1995. The Rabaul eruption, 1994–destruction of a town. Macquarie University, Natural Hazards Research Centre Report.

Bonafede, M., 1991. Hot fluid migration, an efficient source of ground deformation, application to the 1982–1985 crisis at Campi Flegrei — Italy. J. Volcanol. Geotherm. Res., 48, 187–198.

Bowers, T.S., Hegelson, H.C., 1983a. Calculation of the thermodynamic and geochemical consequences of nonideal mixing in the system $H_2O$–$CO_2$–NaCl on phase relations in geologic systems: equation of state for $H_2O$–$CO_2$–NaCl fluids at high pressure and temperatures. Geochim. Cosmochim. Acta, 47, 1247–1275.

Bowers, T.S., Hegelson, H.C., 1983b. Calculation of the thermodynamic and geochemical consequences of nonideal mixing in the system $H_2O$–$CO_2$–NaCl on phase relations in geologic systems: metamorphic equilibria at high pressure and temperatures. Am. Mineral., 68, 1059–1075.

Brown, G.C., Rymer, H., Stevenson, D., 1991. Volcano monitoring by microgravity and energy budget analysis. J. Geol. Soc. Lond., 148, 585–593.

Buick, I.S., Cartwright, I., 2002. Fractured-controlled fluid flow and metasomatism in the contact aureole of the Marulan Batholith (New South Wales, Australia). Contrib. Mineral. Petrol., 143(6), 733–749.

Burnham, J.K., 1985. Energy release in subvolcanic environments: implication for breccia formations. Econ. Geol., 80, 1515–1522.

Cathles, L.M., 1977. An analysis of the cooling of intrusives by ground-water convection which includes boiling. Econ. Geol., 72, 804–826.

Carroll, M.R., Webster, J.D., 1994. Solubilities of sulfur, noble gases, nitrogen, chlorine and fluorine in magmas. In: Carroll, M.R. and Halloway, J.R. (Eds), Volatiles in Magmas, Rev. Mineral. Vol. 30, pp. 231–279.

Casertano, L., Olivieri del Castillo, A., Quagliariello, M.T., 1976. Hydrodynamics and geodynamics in the Phlegrean Fields area of Italy. Nature, 264, 154–161.

Castagnolo, D., Gaeta, F.S., De Natale, G., Peluso, F., Mastrolorenzo, G., Troise, C., Pingue, F., Mita, D.G., 2001. Campi Flegrei unrest episodes and possible evolution towards critical phenomena. J. Volcanol. Geotherm. Res., 109, 13–30.

Chiodini, G., Marini, L., 1998. Hydrothermal gas equilibria: the $H_2O$–$H_2$–$CO_2$–CO–$CH_4$ system. Geochim. Cosmochim. Acta, 62, 2673–2687.

Chiodini, G., Todesco, M., Caliro, S., Del Gaudio, C., Macedonio, G., Russo, M., 2003. Magma degassing as a trigger of bradyseismic events: the case of Phlegrean Fields (Italy). Geophys. Res. Lett., 30(8), 1434–1437.

Chouet, B.A., 1996. New methods and future trends in seismological volcano monitoring. In: Scarpa, R. and Tilling, R.I. (Eds), Monitoring and Mitigation of Volcano Hazard. Springer Verlag, Berlin, pp. 23–97.

Cole, J.W., Milner, D.M., Spinks, K.D., 2005. Caldera and caldera structures: a review. Earth Sci. Rev., 69, 1–26.

Corey, A.T., Rathjens, C.H., Henderson, J.H., Wyllie, M.R., 1956. Three-phase relative permeability. Trans. AIME, 207, 349–351.

Crampin, S., Booth, D.C., 1989. Shear-wave splitting showing hydraulic dilatation of pre-existing joints in granite. Sci. Drill., 1, 21–26.

Crampin, S., Chastin, S., 2003. A review of shear wave splitting the crack-critical crust. Geophys. J. Int., 155, 221–240.

Darnet, M., Maineult, A., Marquis, G., 2004. On the origin of self-potential (SP) anomalies induced by water injections into geothermal reservoirs. Geophys. Res. Lett., 31, L19609, doi: 10.1029/2004GL020922.

De Angelis, S., McNutt, S.R., 2005. Degassing and hydrothermal activity at Mt. Spurr, Alaska, during the summer 2004 inferred from complex frequencies of long-period events. Geophys. Res. Lett., 32, L12312, doi: 10.1029/2005GL022618.

Delaney, P.T., 1982. Rapid intrusion of magma into wet rock: groundwater …and stress evolution in cooling pluton environments. Am. J. Sci., 281, 35–68.

Delmelle, P., Stix, J., 2000. Volcanic gases. In: Sigurdsson, H., Houghton, B., McNutt, S.R., Rymer, H.Stix, J. (Eds), Encyclopedia of Volcanoes. Academic Press, San Diego, pp. 803–815.

de Marsily, G., 1986. Quantitative Hydrogeology: Groundwater Hydrology for Engineers. Academic Press Inc., San Diego, 440 pp.

De Natale, G., Pingue, F., Allard, P., Zollo, A., 1991. Geophysical and geochemical modelling of the 1982–1984 unrest phenomena at Campi Flegrei caldera (southern Italy). J. Volcanol. Geotherm. Res., 48, 199–222.

De Natale, G., Troise, C., Pingue, F., 2001. A mechanical fluid-dynamical model for ground movements at Campi Flegrei caldera. J. Geodyn., 32, 487–571.

Dullien, F.A.L., 1992. Porous Media. Fluid Transport and Pore Structure. Academic Press, San Diego, 574 pp.

Elder, J.W., 1967a. Steady free convection in a porous medium heated from below. J. Fluid Mech., 27, 29–48.

Elder, J.W., 1967b. Transient convection in a porous medium. J. Fluid Mech., 27, 609–623.

Elder, J.W., 1981. Geothermal Systems. Academic Press, New York, 508 pp.

Evans, D.D., Rasmussen, T.C., Nicholson, T.J., 2001. Flow and transport through unsaturated fractured rock: an overview. In: Evans, D.D., Rasmussen, T.C., Nicholson, T.J. (Eds), Flow and Transport Through Unsaturated Fractured Rock. Geophys. Monograph 42, AGU, Washington DC, pp. 1–18.

Ferry, J.M., Wing, B.A., Penniston-Dorland, S.C., Rumble, D., III, 2002. The direction of fluid flow during contact metamorphism of siliceous carbonate rocks: new data for the Monzoni and Predazzo aureoles, northern Italy, and a global review. Contrib. Mineral. Petrol., 142, 679–699.

Foulger, G.R., Julian, B.R., Hill, D.P., Pitt, A.M., Malin, P., Shalev, E., 2004. Non-double-couple microearthquakes at Long Valley Caldera provide evidence for hydraulic fracturing. J. Volcanol. Geotherm. Res., 132, 45–71.

Fournier, R.O., 1987. Conceptual model of brine evolution in magmatic hydrothermal systems. In: Decker, R.W., Wright, T.L.Stauffer, P.H. (Eds), Volcanism in Hawaii. USGS, Professional Paper 1350, pp. 1487–1506.

Gaeta, F.S., De Natale, G., Peluso, F., Mastrolorenzo, G., Castagnolo, D., Troise, C., Pingue, F., Mita, D.G., Rossano, S., 1998. Genesis and evolution of unrest episodes at Campi Flegrei caldera: the role of thermal–fluid–dynamical processes in the geothermal system. J. Geophys. Res., 103(B9), 20921–20933.

Gaeta, F.S., Peluso, F., Arienzo, I., Castagnolo, D., De Natale, G., Milano, G., Albanese, C., Mita, D., 2003. A physical appraisal of a new aspect of bradyseism: the miniuplifts. J. Geophys. Res., 108(B8), 2363, doi: 10.1029/2002JB001913.

Giggenbach, W.F., 1996. Chemical composition of volcanic gases. In: Scarpa, R. and Tilling, R.I. (Eds), Monitoring and Mitigation of Volcanic Hazards. Springer Verlag, Berlin, pp. 202–226.

Goff, F., Janik, C.J., 2000. Geothermal systems. In: Sigurdsson, H., Houghton, B., McNutt, S.R., Rymer, H.Stix, J. (Eds), Encyclopedia of Volcanoes. Academic Press, San Diego, pp. 817–834.

Gottsmann, J., Battaglia, M., 2008. Deciphering causes of unrest at explosive collapse calderas:. Recent advances and future challenges of joint time-lapse gravimetric and ground deformation studies, 10, 417–446.

Gottsmann, J., Berrino, G., Rymer, H., Williams-Jones, G., 2003. Hazard assessment during caldera unrest at the Campi Flegrei, Italy: a contribution from gravity–height gradients. Earth Planet Sci. Lett., 211, 295–309.

Gottsmann, J., Rymer, H., 2002. Deflation during caldera unrest; constraints on subsurface processes and eruption prediction from gravity–height data. Bull. Volcanol., 64, 338–348.

Gottsmann, J., Rymer, H., Berrino, G., 2006. Caldera unrest at the Campi Flegrei: a critical evaluation of source parameters from geodetic data inversion. J. Volcanol. Geotherm. Res., 150, 132–145.

Gudmundsson, A., FJeldskaar, I., Brenner, S.L., 2002. Propagation pathways and fluid transport of hydrofractures in jointed and layered rocks in geothermal fields. J. Volcanol. Geotherm. Res., 116, 257–278.

Gudmundsson, O., Finlayson, D., Itikarai, I., Nishimura, Y., Johnson, W., 2004. Seismic attenuation at Rabaul volcano, Papua New Guinea. J. Volcanol. Geotherm. Res., 130, 77–92.

Hayba, D.O., Ingebritsen, S.E., 1997. Multiphase groundwater flow near cooling plutons. J. Geophys. Res., 102, 12235–12252.

Hellweg, M., 2000. Physical models for the source of Lascar's harmonic tremor. J. Volcanol. Geotherm. Res., 101, 183–198.

Helmig, R., 1997. Multiphase Flow and Transport Processes in the Subsurface: A Contribution to the Modelling of Hydrosystems. Springer-Verlag, Berlin, 367 pp.

Hernández, P.A., Notsu, K., Salazar, J.M., Mori, T., Natale, G., Okada, H., Virgili, G., Shimoike, Y., Sato, M., Pérez, N.M., 2001. Carbon dioxide degassing by advective flow from Usu Volcano, Japan. Science, 292, 83–86.

Hill, D.P., Prejean, S., 2005. Magmatic unrest beneath Mammoth mountain, California. J. Volcanol. Geotherm. Res., 146, 257–283.

Hon, K., Pallister, J., 1995. Wrestling with restless calderas and fighting floods of lava. Nature, 376, 554–555.

Howle, J.F., Langbein, J.O., Farrar, C.D., Wilkinson, S.K., 2003. Deformation near the Casa Diablo geothermal well field and related processes Long Valley caldera, Eastern California, 1993–2000. J. Volcanol. Geotherm. Res., 127, 365–390.

Hunt, T.M., Kissling, W.M., 1994. Determination of reservoir properties at Wairakei geothermal field using gravity changes measurements. J. Volcanol. Geotherm. Res., 63, 129–143.

Hurwitz, S., Ingebritsen, S.E., Sorey, M.L., 2002. Episodic thermal perturbations associated with groundwater flow: an example from Kilauea Volcano, Hawaii. J. Geophys. Res., 107(B11), 2297, doi: 10.1029/2001JB001654.

Hurwitz, S., Kipp, K.L., Ingebritsen, S.E., Reid, M.E., 2003. Groundwater flow, heat transport, and water-table position within volcanic edifices: implications for volcanic processes in the Cascade Range. J. Geophys. Res., 108(B12), 2557, doi: 10.1029/2003JB002565.

Ingebritsen, S.E., Rojstaczer, S.A., 1993. Controls on geyser periodicity. Science, 262, 889–892.

Ingebritsen, S.E., Rojstaczer, S.A., 1996. Geyser periodicity and the response of geysers to deformation. J. Geophys. Res., 101, 21891–21905.

Ingebritsen, S.E., Sanford, W.E., 1998. Groundwater in Geologic Processes. Cambridge University Press, New York, 365 pp.

Ingebritsen, S.E., Sorey, M.L., 1985. A quantitative analysis of the Lassen hydrothermal system, north-central California. Water Resour. Res., 21, 853–868.

Ingebritsen, S.E., Sorey, M.L., 1988. Vapor-dominated zones within hydrothermal systems: evolution and natural state. J. Geophys. Res., 93, 13635–13655.

Itasca Consulting Group Inc., 1997. FLAC3D Manual: Fast Lagrangian Analysis of Continua in 3 Dimensions — Version 2.0. Itasca Consulting Group Inc., Minnesota.

Jamtveit, B., Grorud, H.F., Ragnarsdottir, K.V., 1997. Flow and transport during contact metamorphism and hydrothermal activity: an example from the Oslo rift. In: Jamtveit, B. and Yardley, B.W.D. (Eds), Fluid Flow and Transport in Rocks: Mechanisms and Effects. Chapman and Hall, London, pp. 57–82.

Kaneshima, S., Kawakatsu, H., Matsubayashi, M., Sudo, S., Tsutsui, T., Ohminato, T., Ito, H., Uhira, K., Yamasato, H., Oikawa, J., Takeo, M., Iidaka, T., 1996. Mechanism of phreatic eruptions at Aso volcano inferred from near-field broadband seismic observations. Science, 273, 642–645.

Kawakatsu, H., Kaneshima, S., Matsubayashi, H., Ohminato, T., Sudo, Y., Tsutsui, T., Uhira, K., Yamasato, H., Ito, H., Legrand, D., 2000. Aso94: Aso seismic observation with broadband instruments. J. Volcanol. Geotherm. Res., 101, 129–154.

Kiryukhin, A., Xu, T., Pruess, K., Apps, J., Slovtsov, I., 2004. Thermal–hydrodynamic–chemical (THC) modelling based on geothermal field data. Geothermics, 33(3), 349–381.

Kissling, W., 1999. Modelling of cooling plutons in the Taupo volcanic zone, New Zealand. Proc. Twenty-Fourth Workshop on Geothermal Reservoir Engineering, Stanford University, Stanford, California, January 25–27.

Konstantinou, K.I., Schlindwein, V., 2002. Nature, wavefield properties and source mechanism of volcanic tremor: a review. J. Volcanol. Geotherm. Res,, 119, 161–187.

Maillot, B., Nielsen, S., Main, I., 1999. Numerical simulation of seismicity due to fluid injection in a brittle poro-elastic medium. Geophys. J. Int., 139, 263–272.

McKee, C.O., Johnston, R.W., Lowenstein, P.L., Riley, S.J., Blong, R.J., De Saint Ours, P., Talai, B., 1985. Rabaul Caldera, Papua New Guinea: volcanic hazards, surveillance, and eruption contingency planning. J. Volcanol. Geotherm. Res., 23, 195–237.

McKee, C.O., Lowenstein, P.L., De Saint Ours, P., Talai, B., Itikarai, I., Mori, J.J., 1984. Seismic and ground deformation crisis at Rabaul caldera: prelude to an eruption? Bull. Volcanol., 47, 397–411.

Miller, S.A., Collettini, C., Chiaraluce, L., Cocco, M., Barchi, M., Boris, J., Kraus, P., 2004. Aftershock driven by a high-pressure $CO_2$ source at depth. Nature, 427, 724–727.

Miller, V., Savage, M., 2001. Changes in seismic anisotropy after volcanic eruptions: evidence from Mount Ruapehu. Science, 293, 2231–2233.

Mori, J., McKee, C.O., Itikarai, I., Lowenstein, P.L., De Saint Ours, P., Talai, B., 1989. Earthquake of the Rabaul seismo-deformational crisis September 1983 to July 1985: seismicity on a caldera ring fault. In: Latter, J.H. (Ed), Volcanic Hazards, IAVCEI Proc., Volcanol., 1.

Murray, J.B., Rymer, H., Locke, C.A., 2000. Ground deformation, gravity, and magnetics. In: Sigurdsson, H., Houghton, B., McNutt, S.R., Rymer, H.Stix, J. (Eds), Encyclopedia of Volcanoes. Academic Press, San Diego, pp. 1121–1140.

Newhall, G.G., Albano, S.E., Matsumoto, N., Sandoval, T., 2001. Roles of groundwater in volcanic unrest. J.Geol. Soc. Phil., 56, 69–84.

Newhall, C.G., Dzurisin, D., 1988. Historical unrest at large calderas of the world. USGS Bull., 1855, 1108 pp.

Norton, D.L., 1984. Theory of hydrothermal systems. Ann. Rev. Earth Planet Sci., 12, 155–177.

Norton, D.L., Knight, J., 1977. Transport phenomena in hydrothermal system: cooling plutons. Am. J. Sci., 277, 937–981.

Nortquist, G., Protacio, J.A.P., Acuña, J.A., 2004. Precision gravity monitoring of the Bulalo geothermal field, Philippines: independent checks and constraints on numerical simulation. Geothermics, 33, 37–56.

Olivieri del Castillo, A., Quagliariello, M.T., 1969. Sulla genesi del bradisismo flegreo. Atti Ass. Geof. It., 18mo Congresso, Naples, pp. 557–594.

Oppenheimer, C., 2003. Volcanic degassing. In: Rudnick, R. L. (Ed), The Crust, Vol. 3., Holland, H.D., Turekian, K.K. (Eds), Treatise on Geochemistry, Elsevier-Pergamon, Oxford, pp. 123–166.

O'Sullivan, M.J., Pruess, K., Lippmann, M.J., 2001. The state of the art of geothermal reservoir simulation. Geothermics, 30, 395–429.

Orsi, G., Petrazzuoli, S.M., Wohletz, K., 1999. Mechanical and thermo-fluid behaviour during unrest at the Campi Flegrei caldera (Italy). J. Volcanol. Geotherm. Res., 91, 453–470.

Pitzer, K.S., Pabalan, R.T., 1986. Thermodynamics of NaCl in steam. Geochim. Cosmochim. Acta, 50, 1445–1454.

Pribnow, D.F.C., Schütze, C., Hurter, S.J., Flechsig, C., Sass, J.H., 2003. Fluid flow in the resurgent dome of Long Valley Caldera: implications from thermal data and deep electrical sounding. J. Volcanol. Geotherm. Res., 127, 329–345.

Pruess, K., 1990. Modelling of geothermal reservoirs: fundamental processes, computer simulation and field applications. Geothermics, 19, 3–15.

Pruess, K., 1991. TOUGH2 – A general purpose numerical simulator for multiphase fluid and heat flow. Report LBL 29400, Lawrence Berkeley National Laboratory, Berkeley, CA, USA.

Pruess, K., Oldenburg, C.M., Moridis, G., 1999. TOUGH2 User's Guide, Version 2.0. Lawrence Berkeley National Laboratory Report LBNL-43134, Berkeley, California.

Reid, M.E., 2004. Massive collapse of volcano edifices triggered by hydrothermal pressurization. Geology, 32, 373–376.

Rutqvist, J., Wu, Y.-S., Tsang, C.-F., Bodvarsson, G., 2002. A modelling approach for analysis of coupled multiphase fluid flow, heat transfer, and deformation in fractured porous rock. Int. J. Rock Mech., 39, 429–442.

Rymer, H., 1994. Microgravity change as a precursor to volcanic activity. J. Volcanol. Geotherm. Res., 61, 311–328.

Shapiro, S.A., Patzig, R., Rothert, E., Rindschwentner, J., 2003. Triggering of seismicity by pore-pressure perturbations: permeability related signature of the phenomenon. Pure Appl. Geophys., 160, 1051–1066.

Smithsonian Institution-GVN, 1994.– [Monthly event reports]. Bull. Global Volc. Network, 9, 1–8.

Sorey, M.L., McConnel, V.S., Roeloffs, E., 2003. Summary of recent research in Long Valley Caldera, California. J. Volcanol. Geotherm. Res., 127, 165–173.

Symonds, R.B., Gerlach, T.M., Reed, M.H., 2001. Magmatic gas scrubbing: implications for volcano monitoring. J. Volcanol. Geotherm. Res., 108, 303–341.

Tait, S., Jaupart, C., Vergniolle, S., 1989. Pressure, gas content and eruption periodicity of a shallow, crystallising magma chamber. Earth Planet Sci. Lett., 92(1), 107–123.

Todesco, M., 1995. Modelling of the geothermal activity at Vulcano (Aeolian Islands, Italy). Proceedings of the World Geothermal Congress '95., 2, 1309–1314. International Geothermal. Association, Firenze.

Todesco, M., 1997. Origin of fumarolic fluids at Vulcano (Italy). Insights from isotope data and numerical modelling of hydrothermal circulation. J. Volcanol. Geotherm. Res., 79, 63–85.

Todesco, M., Berrino, G., 2005. Modelling hydrothermal fluid circulation and gravity signals at the Phlegraean Fields caldera. Earth Planet Sci. Lett., 240, 328–338.

Todesco, M., Chiodini, G., Macedonio, G., 2003a. Monitoring and modelling hydrothermal fluid emission at La Solfatara (Phlegrean Fields, Italy). J. Volcanol. Geotherm. Res., 125, 57–79.

Todesco, M., Rutqvist, J., Chiodini, G., Pruess, K., Oldenburg, C.M., 2004. Modelling of recent volcanic episodes at Phlegrean Fields (Italy): geochemical variations and ground deformation. Geothermics, 33(4), 531–547.

Todesco, M., Rutqvist, J., Pruess, K., Oldenburg, C.M., 2003b. Multi-phase fluid circulation and ground deformation: a new perspective on bradyseismic activity at the Phlegrean Fields (Italy). Proceedings. Twenty-Eighth Workshop on Geothermal Reservoir Engineering, Stanford University, Stanford, CA, SGP-TR-173.

Troise, C., De Natale, G., Pingue, F., Tammaro, U., De Martino, P., Obrizzo, F., Boschi, E., 2008. A new uplift episode at Campi Flegrei caldera (Southern Italy):. implications for unrest interpretation and eruption hazard evaluation, 10, 375–392.

Tsang, C.-F., 1999. Linking thermal, hydrological, and mechanical processes in fractured rocks. Ann. Rev. Earth Planet Sci., 27, 359–384.

Verma, A., Pruess, K., 1988. Thermohydrological conditions and silica redistribution near high-level nuclear waste emplaced in saturated geological formations. J. Geophys. Res., 93, 1159–1173.

Villemant, B., Hammouya, G., Michel, A., Semet, M.P., Komorowski, J.C., Boudon, G., Cheminée, J.L., 2005. The memory of volcanic waters: shallow magma degassing revealed by halogen

monitoring in thermal springs of La Soufrière volcano (Guadeloupe, Lesser Antilles). Earth Planet Sci. Lett., 237, 710–728.

White, D.E., Muffler, L.J.P., Truessdell, H.A., 1971. Vapor-dominated hydrothermal systems compared with hot water systems. Econ. Geol., 66, 75–97.

Xu, T., Pruess, K., 2001. Modelling multiphase non-isothermal fluid flow and reactive geochemical transport in variably saturated fractured rocks: 1. Methodology. Am. J. Sci., 301, 16–33.

Xu, T., Sonnenthal, E., Spycher, N., Pruess, K., Brimhall, G., Apps, J., 2001. Modelling multiphase non-isothermal fluid flow and reactive geochemical transport in variably saturated fractured rocks: 2. Applications to supergene copper enrichment and hydrothermal flows. Am. J. Sci., 301, 34–59.

Yamamoto, M., Kawakatsu, H., Kaneshima, S., Mori, T., Tutui, T., Sudo, Y., Morita, Y., 1999. Detection of a crack-like conduit beneath the active crater at Aso volcano, Japan. Geophys. Res. Lett., 26, 3577–3680.

Zlotnicki, J., Nishida, Y., 2003. Review on morphological insights of self-potential anomalies on volcanoes. Surv. Geophys., 24, 291–338.

# Deciphering Causes of Unrest at Explosive Collapse Calderas: Recent Advances and Future Challenges of Joint Time-Lapse Gravimetric and Ground Deformation Studies

Joachim Gottsmann[1],[*] *and* Maurizio Battaglia[2]

## Contents

[*]Corresponding author. Tel.: 0117 9545422; Fax: 0117 9253385
*E-mail address:* j.gottsmann@bristol.ac.uk

[1] Department of Earth Sciences, University of Bristol, Wills Memorial Building, Queens Road, Bristol BS8 1RJ, UK
[2] Department of Earth Sciences, University of Rome I "La Sapienza", P.le A. Moro 5, 00185 Rome, Italy

## Abstract

Unrest at explosive collapse calderas is the manifestation of complex subsurface processes. Geophysical signals recorded during unrest can be caused by the migration and emplacement of magma, or by tectonic or hydrothermal activity. Geodetic techniques represent a crucial part of a monitoring programme as they provide means to quantify volume changes in the feeder system of restless calderas. However, deformation data alone cannot discriminate between magma and aqueous fluid intrusions. Time-lapse gravity measurements can constrain the mass of the intrusion, and consequently the combination of geodesy and gravity measurements can be used to infer the density of the intrusive fluids and can better constrain the deformation source. Here, we consider the application of gravimetric and geodetic techniques to study caldera unrest with examples from Long Valley, Campi Flegrei, Las Cañadas and Nisyros. We identify problems with current time-lapse gravimetric techniques, discuss several approaches to model the source of unrest from deformation and gravity data and provide an outlook into future challenges for integrated geodetic studies.

## 1. Introduction

Complex subsurface processes, such as the migration and emplacement of magma, and tectonic or hydrothermal activity, can trigger seismicity, ground deformation, thermal variations and changes in the potential fields at a volcano. Unrest can be the first sign of the reactivation of a volcanic system that may lead to an eruption; monitoring is an essential means to assess hazards and mitigate risks during volcanic crises (Dzurisin et al., 1999).

Time-lapse geodetic and gravimetric techniques represent a crucial part of a monitoring programme as they provide means to quantify changes in the feeder system of restless explosive calderas (e.g. Battaglia et al., 2003a, 2003b, 2006; Ukawa et al., 2006; Gottsmann et al., 2005; Furuya et al., 2003; Rymer et al., 1998; Rymer, 1994; Berrino, 1994; Rymer and Tryggvason, 1993; Berrino et al., 1984, 1992; McKee et al., 1989; Johnsen et al., 1980). For example, gravity–height gradients may enable the assessment of potential hazards sometimes months or weeks before magma flow leads to earthquakes or other eruption precursors (Dzurisin, 2003, 2006; Sparks, 2003; Gottsmann and Rymer, 2002; Rymer and Williams-Jones, 2000).

However, because of the complexity of subsurface structures beneath active volcanoes, identifying the causative source of unrest is not straightforward. Active calderas often host both hydrothermal and magmatic reservoirs at depth; physical and chemical changes in either can produce measurable geophysical signals. The challenge lies in interpreting these signals and inferring the cause of unrest prior to impending eruptions. However, not all periods of caldera unrest culminate in volcanic eruptions, and not all eruptions induce, or terminate by, caldera collapse (Newhall and Dzurisin, 1988).

Volcanic activity at calderas incorporates the entire range of volcanic eruptions, spanning from purely phreatic activity on one hand, to phreatomagmatic eruptions

or purely magmatic eruptions on the other. Erupted volumes may vary from a few tens of cubic metres in phreatic eruptions to several thousand cubic kilometres in ultra-plinian eruptions (Francis, 1993).

Well-documented examples of the dilemmas volcano scientists are confronted with during the reactivation of caldera volcanoes are the large volcanic centres of Campi Flegrei (Berrino et al., 1984), Yellowstone (Arnet et al., 1997) and Long Valley (Battaglia et al., 2003a, 2003b). In Campi Flegrei, the occurrence of about 2 m of uplift and thousands of earthquakes not only triggered the evacuation of the local population in 1984, but also a controversy on the source of unrest (Barberi et al., 1996): magma movement or hydrothermal fluid migration? The critical questions emerging from these examples are how to (a) constrain the source of unrest, (b) improve the assessment of hazards associated with the unrest and (c) refine our ability to forecast volcanic activity. It is worth noting that geodetic measurements alone cannot discriminate between magma and aqueous fluid intrusion. Gravity measurements, however, can constrain the mass of the intrusion. Combined geodesy and gravity measurements can be used to infer the density of the intrusive fluids and can better constrain the source of unrest.

In this paper, we consider some recent advances in identifying sources of unrest at explosive calderas via joint gravimetric and geodetic studies. In particular, we discuss the application of joint gravimetric and geodetic techniques, data reduction, the evaluation of gravity–height gradients and time-series inversion. Finally, we identify problems with current time-lapse gravimetric techniques and provide an outlook into future challenges and possible solutions of integrated geodetic studies.

## 2. THE SUBSURFACE BENEATH CALDERAS: HYDROTHERMAL VERSUS MAGMATIC RESERVOIRS

The subsurface beneath calderas is complex, and it may be difficult to capture the full spectrum of structural, mechanical and chemical complexities. Static investigations such as seismic tomography (Vanorio et al., 2005; Aprea et al., 2002; De Lorenzo et al., 2001; Steck and Prothero, 1994) are one way of visualising large-scale (of the order of 1 km) structures beneath calderas as are gravimetric and other potential field investigations (e.g. Campos-Enriquez et al., 2005; Campos-Enriquez and Garduno-Monroy, 1995; Araña et al., 2000).

Dynamic investigations such as geodetic (ground deformation) observations are of an intermediate resolution. These data are often directly related to volume and pressure change at depth, which may be interpreted in terms of fluid movement and temperature changes. Combining geodetic measurements (global positioning system (GPS), levelling, electronic distance meter (EDM), and interferometric synthetic aperture radar (InSAR)) with time-lapse gravity data provides an important source of information relating to the movement of fluids at depth and is a tool for understanding the factors controlling fluid migration in a volcanic system (Dzurisin, 2003, 2006; Williams-Jones et al., 2003; Dvorak and Dzurisin, 1997).

Geophysical studies identify at least three different levels of subsurface reservoirs capable of producing mass/pressure variations at depth and quantifiable geodetic signals at the ground surface:

1. hydrothermal reservoir(s) extending from surface levels to a few kilometres depth;
2. mid-crustal reservoirs, interpreted to be hosting varying fractions of melt and aqueous fluids and
3. deep reservoirs, potentially associated with underplating at the interface of the crust and upper mantle funnelling new melt to mid-crustal levels.

The comparison of results from dynamic and static geophysical studies with those from petrological and geochemical investigations can be regarded as a possible solution to the problem of discriminating between magmatic and non-magmatic reservoirs as likely sources of unrest.

# 3. Joint Ground Deformation and Gravimetric Survey

## 3.1. Introduction

The analysis of integrated geodetic (deformation and gravity) time series is a straightforward approach to quantify subsurface mass/volume/density changes. These data are obtained by time-lapse joint deformation and micro-gravity surveys, whereby individual relative gravity and crustal deformation readings are obtained at benchmarks (Figure 1). With the recent advent of portable absolute gravimeters,



**Figure 1**   A possible arrangement for the simultaneous occupation of a benchmark using a roving GPS receiver and a portable field gravimeter (photo credit: L. Wooller).

time-lapse observations are also possible using absolute readings (Berrino et al., 2006), or through a combination of absolute and relative gravity measurements (hybrid micro-gravimetry). Hybrid micro-gravimetry might be especially important in areas where there is no guarantee of temporally constant gravity at the reference site (Furuya et al., 2003).

Repeated occupation of the network leads to gravity–deformation time series that are evaluated with respect to base line data obtained at a reference that is usually located outside the area of interest. Obviously, baseline corrections are redundant if an absolute gravimeter is part of the survey network. Complexities arise particularly on small volcanic islands where it might be difficult to install a reference outside the zone of interest (Furuya et al., 2003). A reference based too close to the zone of interest results in serious ambiguities relating to subsurface processes since deep-seated mass/density changes affect gravity measurements both at the reference and the network baselines.

Gravimetric and ground deformation data can be evaluated by (a) computing the gravity–height gradients (see Section 4) or (b) forward or inverse modelling of gravity and geodetic data using single or distributed pressure sources (see Section 5).

## 3.2. Ground deformation

At the very heart of volcanology lies the search for the 'plumbing systems' and magma reservoirs that form the inner workings of Earth's active volcanoes (Dvorak and Dzurisin, 1997). Much can be learned about the physics of active calderas by recording the surface displacements that occur before and during eruptions. Away from the eruptive site, the surface rises or falls with geometric regularity as magma forces its way through the crust. Caldera deformation may be the result of a decade-long unrest. The pattern and rate of surface displacement can often be matched by models that range from simple pressure sources embedded in an elastic material (e.g. Dvorak and Dzurisin, 1997) or visco-elastic material (Newman et al, 2006; Bonafede et al, 1986), to complex 3-D numerical models (Folch and Gottsmann, 2006; Walter et al., 2005). However, the scope of this paper is not to review the application of ground deformation techniques at active volcanoes, and we refer the interested reader to recent review articles on this matter (e.g. Dzurisin, 2003, 2006; Poland et al., 2006; Dvorak and Dzurisin, 1997).

## 3.3. Time-lapse micro-gravimetry

The raw gravity measurements collected in the field are noisy. Part of the background noise can usually be eliminated using global models of Earth and ocean tides as well as of atmospheric effects (temperature and pressure). Continuous tidal recordings (using, e.g., an Earth tide gravimeter) may be needed to achieve a local, high-precision reduction. After correcting for atmospheric and tidal effects, the observed gravity change ($\Delta g_{obs}$) is the difference in gravity between a benchmark and the reference site, if relative gravimeters are employed. Field measurement errors restrict relative micro-gravity precision to about $10\,\mu Gal$, which is equivalent to an uncertainty in the vertical deformation of about $0.03\,m$. In ideal conditions,
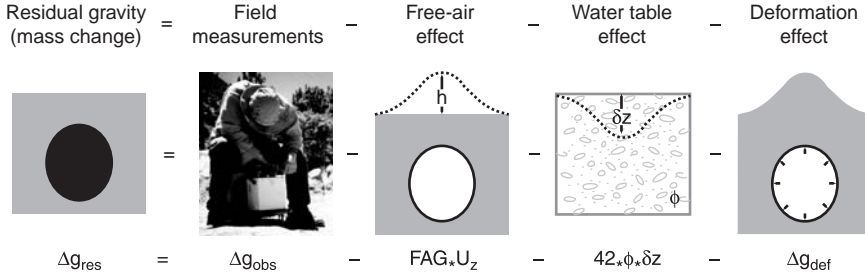
**Figure 2** The different effects that compose the gravity signal measured in the field. All constants are in $\mu\text{Gal m}^{-1}$, $U_z$ is the vertical displacement, $\phi$ the porosity and $\delta z$ the water table change.

resolvable gravity changes may be detected up to 10 km from the region of maximum ground deformation if the mass change at depth is at least $10^{12}$ kg (Williams-Jones and Rymer, 2002). In order to extract the gravity signal produced by a subsurface mass and/or density change, gravity residuals need to be quantified (Eggers, 1987). The residual gravity change at each benchmark ($\Delta g_r$) is given by (see Figure 2):

$$\Delta g_r = \Delta g_{obs} - \text{FAG} \times U_z - \Delta g_{def} - \Delta g_{wt} \tag{1}$$

where FAG is the free-air gravity gradient (the value of the theoretical gradient $\text{FAG}_T$ is $-308.6\,\mu\text{Gal m}^{-1}$; $1\,\mu\text{Gal} = 10^8\,\text{m s}^{-2}$), $U_z$ the vertical displacement, $\Delta g_{def}$ the Bouguer effect of deformation and the resulting propagation of density boundaries on gravity and $\Delta g_{wt}$ the ground water table effect. The Bouguer effect of deformation $\Delta g_{def}$ depends on the geometry of the source. It is exactly zero if the source has a spherical symmetry (Walsh and Rice, 1979), is negligible for a prolate spheroid, but can strongly bias the density estimate for a horizontal penny-shaped crack source (Battaglia et al., 2006).

Critical to the interpretation of residual gravity variations is the correction for variations in the level of the ground water table (e.g. Battaglia et al., 2003b) or gravity changes induced by an active hydrothermal system (see Sections 6 and 7). The water table correction $\Delta g_{wt}$ can be approximated by:

$$\Delta g_{wt} = 2\pi G \rho_w \phi \delta_z \tag{2}$$

where $2\pi G \rho_w = 42\,\mu\text{Gal m}^{-1}$, $G$ is the universal gravitational constant ($6.673 \times 10^{-11}\,\text{N m}^2\,\text{kg}^{-2}$), $\phi$ the effective porosity, $\rho_w$ the density of water and $\delta_z$ the vertical water table change of an unconfined aquifer.

Failure to account for such contributions may result in attributing the entire gravitational signal to deeper, usually magmatic, processes or in being unable to differentiate between the gravity signal due to the unrest and the background noise (Jachens and Roberts, 1985). Conclusions drawn may then be unrealistic and may contribute little to the precise assessment of hazards associated with caldera unrest (see also Section 7).

## 4. VERTICAL GRAVITY–HEIGHT GRADIENTS

Gravity and height changes are theoretically inversely correlated. A positive change in surface elevation (inflation) results in net gravity decrease, expressed by the free-air gravity gradient FAG. The FAG should be measured directly because implications drawn from gravity changes caused by subsurface processes might be less meaningful if the value of the *real* FAG deviates substantially from the theoretical gradient $FAG_T$. Alternatively, if the local density anomaly can be approximated by a point source, the local FAG can be estimated ($FAG_a$) from static gravity data:

$$FAG_a = FAG_T - \frac{\Delta g_b (2z + 1)}{(z + 1)^2} \tag{3}$$

where $\Delta g_b$ is the maximum amplitude of the Bouguer anomaly and $z$ the depth of the point source. At the Campi Flegrei caldera, for example, the calculated local $FAG_a$ matches the measured FAG within error (Berrino, 1994; Berrino et al., 1984).

Gravity–height data deviating from the $FAG_T$ must be interpreted in terms of subsurface mass changes. No mass change is required for data falling on this gradient, but a subsurface density change is necessary. If there is no density change, but there is a mass change, then gravity-height data will follow the Bouguer-corrected FAG (BCFAG). The value of the BCFAG depends on the density $\rho$, the geometry of the source and on the value of the FAG (Rymer, 1994). For example, the BCFAG for an infinite slab is:

$$BCFAG_s = FAG + 2 \times 10^8 \mu G \rho + FAG + 0.04191\rho \tag{4}$$

Figure 3 summarises possible subsurface processes for different gravity-height gradients.

The residual vertical gravity gradient (Gottsmann et al., 2006a):

$$\frac{\Delta g_r}{U_z} = \frac{\Delta g_{obs}}{U_z} - FAG \tag{5}$$

bears information on the dominant subsurface process, with $U_z$ as the vertical displacement. A pressure change caused by a density change (e.g. phase change) in a centre of expansion results in $\Delta g_{obs}/U_z \approx FAG$; hence $\Delta g_r/U_z$ values are around 0 (Walsh and Rice, 1979). Mass fluctuations in a point mass gives $\Delta g_{obs}/U_z \neq FAG$, and hence a $\Delta g_r/U_z \neq 0$ (Fernández et al., 2005). Applying this concept to a 13-year period of ground deflation at the Campi Flegrei caldera, Gottsmann et al. (2006a) found that the slow deflation shows a pronounced nonlinear space–gradient relationship and an absence of radial symmetry in the data. This suggests the presence of causative sources along the caldera boundary fault, in addition to a main source located beneath the centre of the caldera (Figure 4) (see also Section 6.2).

In general, vertical gravity gradients can provide a first and quick assessment of subsurface processes as they enable the discrimination between pressure change effects and mass changes. Given sufficient spatial resolution of gravity–height data, gradients can provide initial insights into source multiplicity, and poles in the spatial
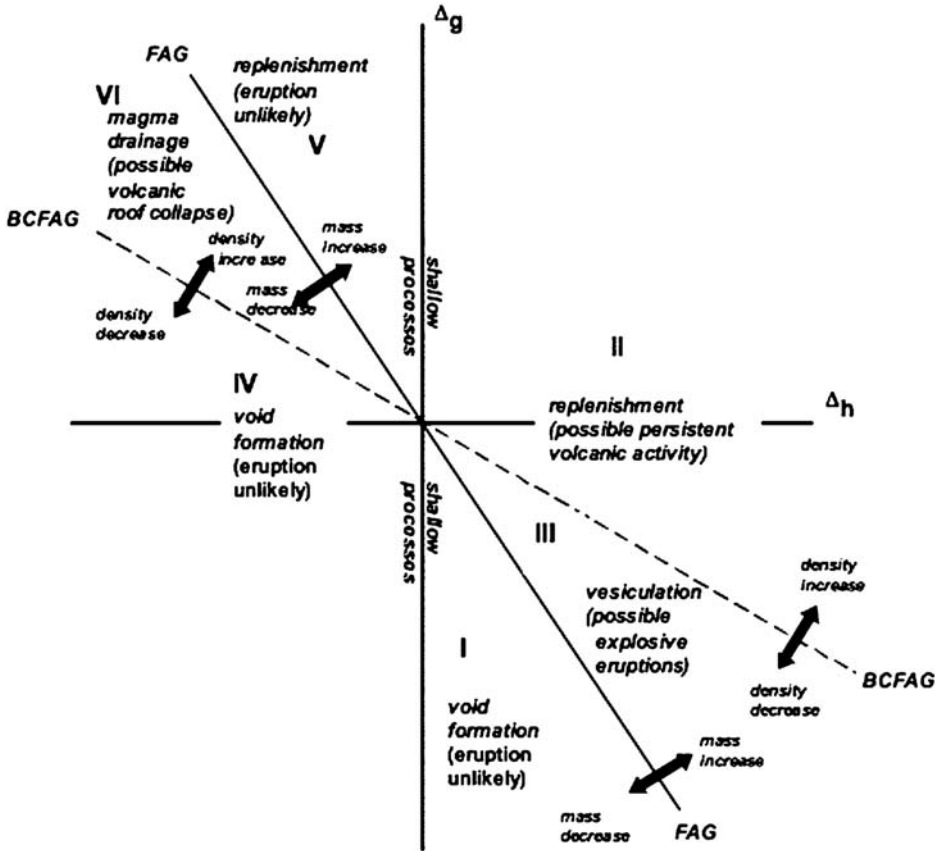
**Figure 3**   The interpretation of $\Delta g/\Delta h$ data deviating from predicted gradients (FAG and BCFAG) in terms of their identification as possible precursors to volcanic activity. Six regions (I—VI) may be discriminated (after Gottsmann et al., 2003).

gradient distribution can be used as a first proxy on source depth (Fernández et al., 2005). A first qualitative approach using gravity–height gradients can be augmented by a fully quantitative investigation of subsurface dynamics via the inversion of time-series data. As such, an integrated approach to the study of caldera unrest and related hazards could include both initial and rapid evaluation of the geodetic results using gravity gradients, followed by an in-depth study of the source parameters and their sensitivities. The latter step is explained in the following section.

# 5. Single and Distributed Sources

## 5.1. Single sources

Although the interpretation of gravity–height gradients may provide a first insight into the source of caldera unrest, a more detailed and rigorous
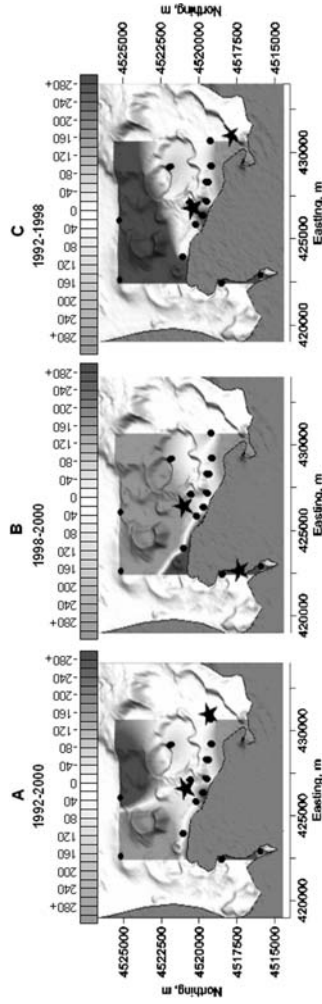
**Figure 4** Residual gravity gradients ($\mu$Gal m$^{-1}$) obtained for different episodes of caldera deflation at the Campi Flegrei. Black dots denote gravity benchmark locations and red stars indicate surface projections of source locations derived from two–source random search inversion (after Gottsmann et al., 2006a).

estimate of the source parameters requires the joint inversion of gravity and geodetic data using single (Dzurisin, 2003) or distributed sources (Vasco et al., 1990).

Single source models, like the well-known point source of dilation (Mogi source; Mogi, 1958) in an elastic, homogeneous and isotropic half-space, are widely used to interpret geodetic and gravity data at active calderas both during phases of ground inflation and deflation (e.g. de Zeeuw-van Dalfsen et al., 2005). In particular, they are used to determine the location and volume of a magma intrusion, and thus to help anticipate the onset of an eruption and mitigate its damage (Dzurisin, 2003; Dvorak and Dzurisin, 1997). Given the difference in density between silicate melts ($\sim 2,500 \, \mathrm{kg \, m^{-3}}$) and hydrothermal fluids ($\sim 1,000 \, \mathrm{kg \, m^{-3}}$), this approach can help to distinguish between possible sources of caldera unrest. Although a point source model appears at odds with the geology of volcanic regions, since magma bodies are not single point-like sources, theoretical work by McTigue (1987) demonstrated that if the radius of the body is small compared to its depth then the point-like approximation of a 3-D magma body will hold. In general, the hypothesis of a Mogi point source is valid for a source radius to depth ratio $\varepsilon < 0.25$, for values of $0.25 < \varepsilon < 0.5$, the differences of predictions from point source approximations and a finite spherical source lie in the range of centimetres (e.g. within the precision of GPS elevation measurements), whereas for $\varepsilon > 0.5$ differences can be more than 30% (Folch et al., 2000; Gottsmann et al., 2006b).

Choosing the right source model is critical for the geological interpretation of geodetic and gravity data. For example, if the actual source does not possess spherical symmetry then the standard approach of using a point source to invert uplift data will lead to biased estimates of the source parameters (e.g. a deeper location and a higher density). This results in considerable uncertainty about the nature of the intruding fluid (Battaglia et al., 2006; Battaglia and Segall, 2004). Together with the point source of dilation, there are at least two additional point-like source models widely used in volcano geodesy: the prolate spheroid (Yang et al., 1988; Clark et al., 1986) and the penny-shaped crack (Fialko et al., 2001). Since different source geometries produce similar uplift profiles, it is necessary to include both the horizontal and vertical deformation in the joint inversion to determine a unique geometry for the point-like source (Dieterich and Decker, 1975).

The joint inversion follows a two-step approach. First, the geometry and parameters (e.g. depth, radius, aspect ratio) of the source are determined. Several algorithms can be used for the inversion (Cervelli et al., 2001). The inversion covariance matrix, as well as the measurement's error, should take into account monument instability (Pollitz et al., 1998). The best-fit model can be determined using a reduced chi-square ($\chi_v^2$) test, and 95% confidence limits can be computed (Cervelli et al., 2001). Once the source parameters are determined, we can compute the effect of deformation $\Delta g_{\mathrm{def}}$ and the residual gravity $\Delta g_{\mathrm{r}}$ (see Equation (1)). Finally, we can fit the source model to the deformation and the residual gravity to estimate the mass change, volume change and density of the intrusion (e.g. Battaglia et al., 2003b).

## 5.2. Distributed sources

A distributed source allows for a more general model in which the geometry is not prescribed *a priori*. As such, a distributed model may be considered to be exploratory in nature, i.e. the geometry of the resulting model can provide information on geological structures controlling magmatic and hydrothermal processes within the caldera. One can view a distributed source as a first step in deciphering the kinematics of fluid movement beneath a collapse caldera.

We can construct a distributed source by subdividing the volume beneath the caldera into a set of nonoverlapping cells or grid-blocks, as described in Vasco et al. (1988) and Vasco et al. (2000). Each grid block may undergo a distinct fractional volume change. The displacement at any point on the surface is the combined response due to the volume change of each grid block. The background medium is assumed to behave elastically over the duration of the observation interval. As noted in Vasco et al. (1988), this does not preclude local inelastic behaviour within each grid block. Rather, one is solving for an effective elastic source, as is done in seismic source modelling (Aki and Richards, 1980). As surface deformation observations typically cannot resolve detailed volume change variations as a function of depth (Dieterich and Decker, 1975), the depth boundaries of the grid are prescribed. It is worth noting that single and distributed sources are complementary to each other. The number and depth of the distributed source model can be based upon earlier point source modelling and physical considerations due to a computational limit. The observed surface deformation is linearly related to the fractional volume change of each grid block. Thus, each observation provides a linear constraint on the subsurface volume change in the grid of cells (Vasco et al., 1988). Given an adequate spatial distribution of vertical and horizontal deformation data, one may estimate the volume change distribution within the grid. Therefore, using a regularised, linear least-squares procedure one can solve for the distribution of volume change at depth (Vasco et al., 2000).

## 6. The Search for Causative Sources of Unrest: Recent Examples of Integrated Studies from the Long Valley, Campi Flegrei and Las Cañadas Calderas

## 6.1. Long Valley caldera

The Long Valley volcanic area (Figure 5) has been active for the past 3 million years. Rhyolite lava eruptions from 2.1 to 0.8 Ma formed Glass Mountain on the northeast rim of the present caldera. The Glass Mountain eruptions, which were fed by a large, chemically evolving magma chamber in the shallow crust, culminated 0.76 Ma ago in a cataclysmic caldera-forming eruption. This massive eruption resulted in the deposition of $600 \, km^3$ of Bishop Tuff and the simultaneous subsidence of the magma chamber roof creating the present $17 \, km \times 32 \, km$ oval depression of the Long Valley caldera. Between 0.76 and 0.6 Ma ago, uplift of the caldera floor and the eruption of flows of rhyolite lava formed the resurgent dome. The most recent eruptive activity occurred 600 years ago along the Mono-Inyo craters volcanic chain (Hildreth, 2004).
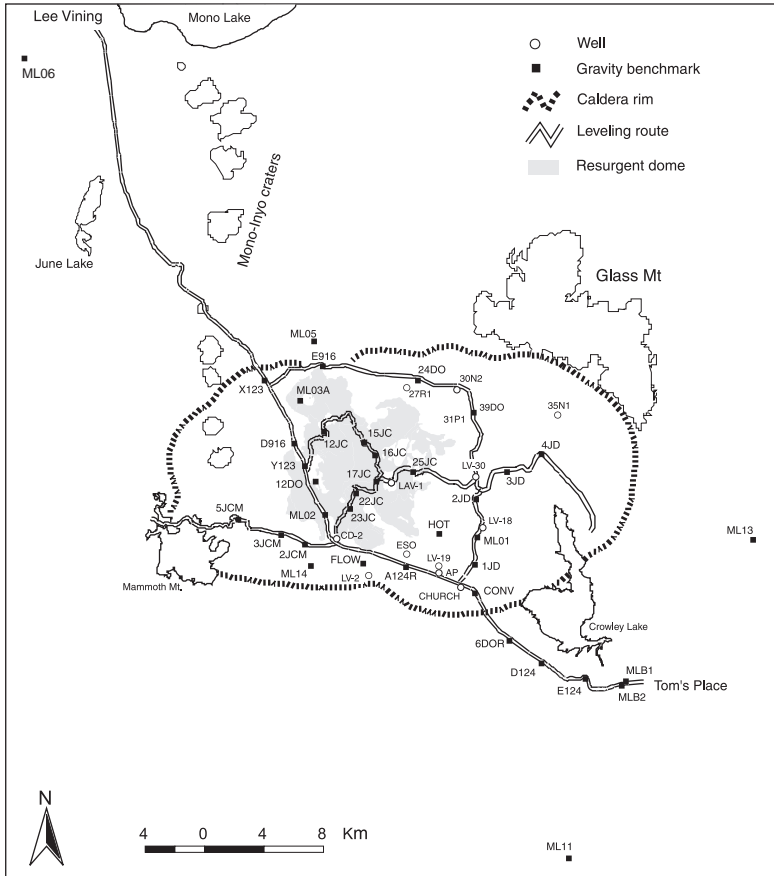
**Figure 5**    Map of Long Valley caldera, showing networks for monitoring gravity, uplift and ground water level. Gravity stations: BR, Benton Range; LV, Lee Vining; RC, Rock Creek Lake; TP, Tom's Place. All gravity readings were taken relative to Tom's Place (after Battaglia et al., 2003b).

In May 1980, a strong earthquake swarm struck the southern margin of Long Valley caldera, marking the onset of the current period of unrest (Hill, 1998). This ongoing unrest includes recurrent earthquake swarms and uplift of the resurgent dome within the central section of the caldera. After a sharp increase in the deformation rate during the summer–fall of 1997, the caldera was relatively inactive with no significant deformation since the spring of 1998 (Figure 6).

Surveys of two-colour EDM and levelling networks indicate that the principal sources of deformation are the intrusion of a magma body beneath the resurgent dome, and right lateral strike slip within the south moat of the caldera (Langbein, 2003; Tiampo et al., 2000). Radar interferometry (Fialko et al., 2001), GPS surveys and gravity measurements (Battaglia et al., 2003b) confirm the intrusion beneath the resurgent dome. In addition, there is evidence for fluid intrusion beneath the caldera south moat and Mammoth Mt. (Hill et al., 2003).
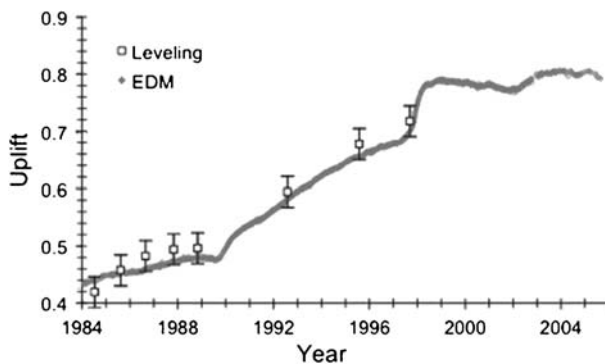
**Figure 6**   The time series of the horizontal deformation along the CASA–KRAK EDM baseline is very similar to the history of the vertical deformation at the resurgent dome (benchmark W911). The USGS has used this similarity to get a qualitative estimate of the vertical deformation at the resurgent dome when a direct measurement was missing. EDM and levelling data courtesy of the Long Valley Observatory (online at lvo.wr.usgs.gov).

Among the most fundamental questions with regard to Long Valley geodynamics is the cause of the ongoing unrest at the caldera. Combining geodetic and microgravity data can provide important constraints on the source of inflation. The United States Geological Survey (USGS) started an intensive geodetic monitoring programme in Long Valley in 1980. Data collected by the USGS include levelling surveys from 1980 to 1997 and measurements of horizontal deformation using a two-colour geodimeter from 1985 and differential GPS from 1994 (Langbein et al., 1995). The last complete levelling of Long Valley caldera occurred in July–August 1992. A network of continuously operating GPS receivers monitors crustal deformation within the caldera. The USGS occupied the Long Valley gravity network six times from 1980 to 1985. Earlier efforts at detecting and interpreting gravity changes in the Long Valley area were limited by the small amplitude of the accumulated signal, and the difficulty in correcting for the water table effect (Jachens and Roberts, 1985).

In an effort to update the vertical deformation measurements within the caldera, Battaglia et al. (2003a) resurveyed 44 of the existing levelling monuments in Long Valley in July 1999 using dual frequency GPS receivers. The gravity network (Figure 5) was occupied twice, in the summers of 1998 and 1999 (Battaglia et al., 2003b; Figure 7). Because sources with different geometry can have similar vertical deformation profiles but distinct horizontal deformation (Dieterich and Decker, 1975), both vertical and horizontal displacements were inverted. In order to improve the signal-to-noise ratio, inflation was modelled using a two-step approach (Battaglia et al., 2003a, 2003b). First, geodetic data from 1985 to 1999 (the longest time interval for which both horizontal and vertical deformation data are available) were inverted to determine the geometry and location of the source. Then, both the uplift and gravity data from 1982 to 1999 were inverted to determine the volume and density of the intrusion.

The best fitting inflation source is a vertical prolate ellipsoid located beneath the resurgent dome. A bootstrap method was employed to estimate 95% confidence
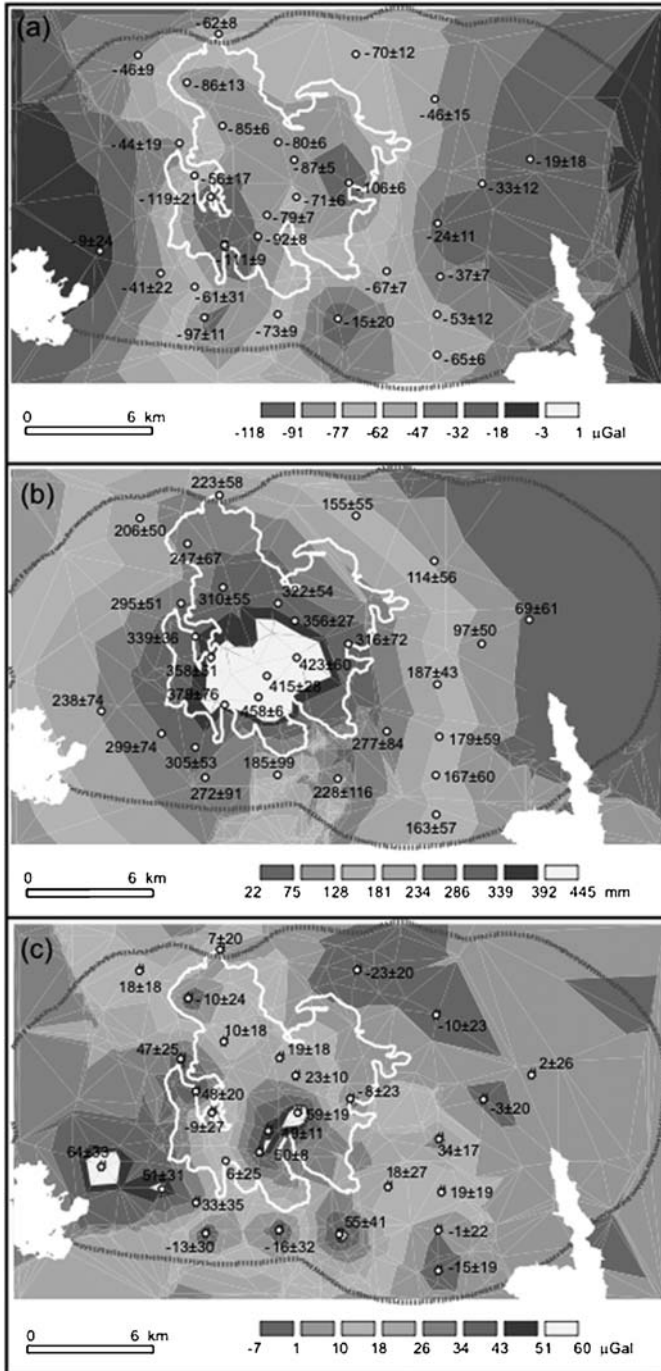
**Figure 7** (a) Gravity changes from 1982 to 1999, values in μGal, error 1 standard deviation. (b) Uplift at gravity benchmarks from 1982 to 1999, values in mm, error 1 standard deviation. (c) Residual gravity from 1982 to 1999, values in μGal, error 1 standard deviation. The white outline at the centre of the caldera is the resurgent dome (after Battaglia et al., 2003b).

bounds for the parameters of the inflation model. The authors obtained a range of 0.25–0.65 for the source geometric aspect ratio, 4.9–7.5 km for the depth, 0.105–0.187 km$^3$ for the 1982–1999 volume change and 1,180–2,330 kg/m$^3$ for the density. Their results support the intrusion of silicate melts, but there is still an uncertainty about the geometry of the magma chamber and the nature of the intruding fluid. For example, is the ellipsoidal model truly representative of the actual geological structure (e.g. a neck or volcanic plug intruding into the shallow crust), or is the inversion simply recovering average source properties? If the latter is the case, then the low-density estimate for the intrusion (1,180–2,330 kg/m$^3$) could point to a hybrid source composed of both melt and an aqueous phase (Battaglia et al., 2003b).

The so-called distributed models (Battaglia and Vasco, 2006) can provide additional insights into fluid movement beneath the Long Valley caldera. As noted in Section 5.2, a distributed source allows for a more general model in which the geometry is not prescribed *a priori*.

Using both the vertical deformation and the line-length changes provided by two-colour EDM measurements (Battaglia et al., 2003a), Battaglia and Vasco (2006) estimated the fractional volume change beneath the Long Valley caldera. The resulting distribution of fractional volume change in the three layers of the model is shown in Figure 4. Dark red and brown colours in this figure signify greater fractional volume changes. The largest fractional volume change forms a dominantly east–west body in the depth range of 5–7 km. In addition, a north–south trending component of fractional volume change roughly parallels a system of north–northwest trending faults within the caldera. This feature extends northward from the east–west anomaly to the northern edge of the caldera. The volume change in the deeper layers (7–9 km, 9–11 km) is much smaller in amplitude and similar in pattern to the overlying layer. This is most likely due to the poor depth resolution provided by the surface deformation data. The distribution of fractional volume change is suggestive in that it underlies some existing north-trending faults. In addition, the east–west component of volume change follows a hypothesised east–west fault in the south moat region. Furthermore, the east–west component of volume change connects two sets of north–south trending faults. The more easterly set extends from the central caldera to the south; the other set cuts northward through the interior of the caldera (Figure 8).

## 6.2. Campi Flegrei

Campi Flegrei, near Naples, on the west coast of southern Italy (Figure 9), has erupted only once in the past 4,000 years: an explosive eruption that lasted 10 days in A.D. 1538. Between 1905 and 1968, the centre of the Campi Flegrei caldera subsided at a rate of 14 mm yr$^{-1}$, essentially the same as the average subsidence rate determined from sea level rise at Campi Flegrei since the 1820s (Dvorak and Mastrolorenzo, 1991). Between the summer of 1968 and January 1970, the caldera centre rose by almost a metre and continued to rise at a decreasing rate until mid-1972. No earthquakes were widely felt during the uplift. The caldera subsided during the next 3 years and then showed no elevation changes until mid-1982.
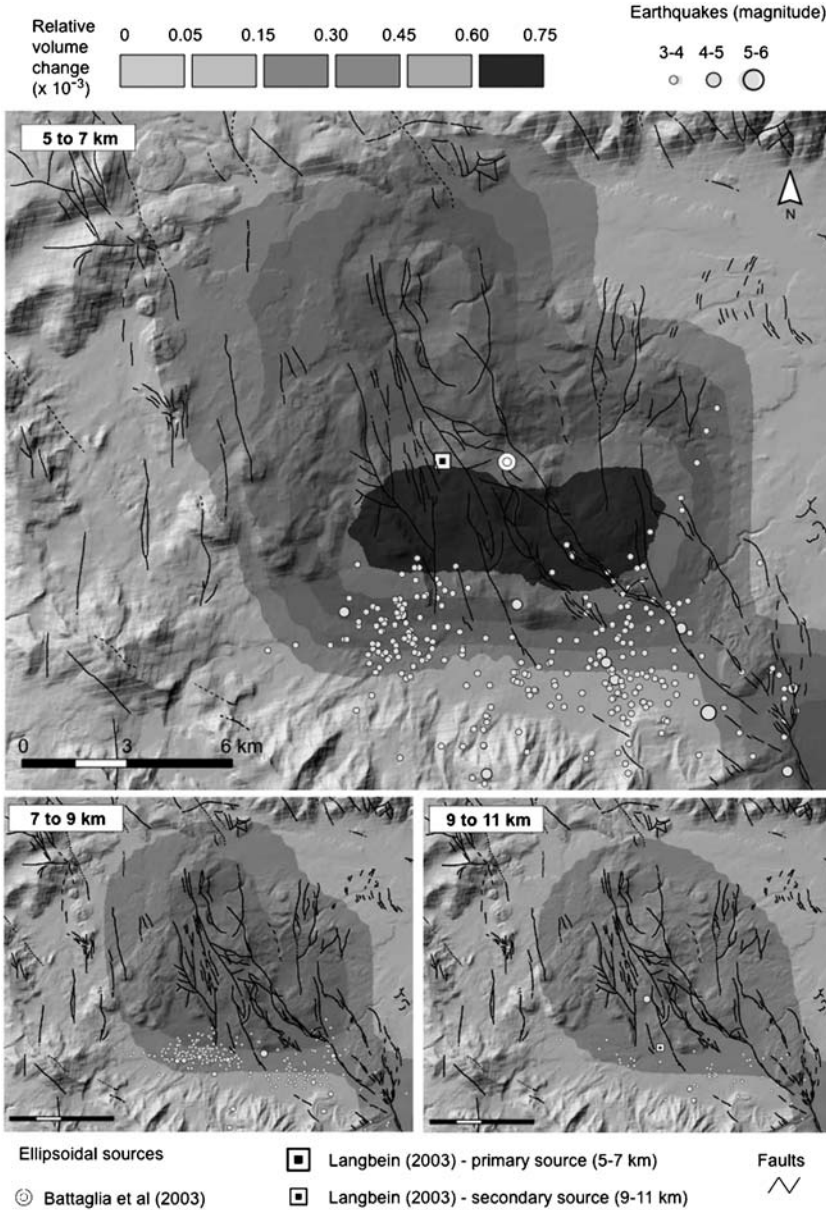
**Figure 8**    3–D distribution of relative subsurface volume changes, and earthquakes hypocentres. The inversion grid is composed of three layers; each layer is divided into a 41 × 41 grid. We show results for layers 6, 8 and 10 km deep, and the location of the ellipsoidal sources after Battaglia et al. (2003b) and Langbein (2003). Earthquake data provided by the Northern California Earthquake Data Center, online at www.ncedc.org (after Battaglia and Vasco, 2006).
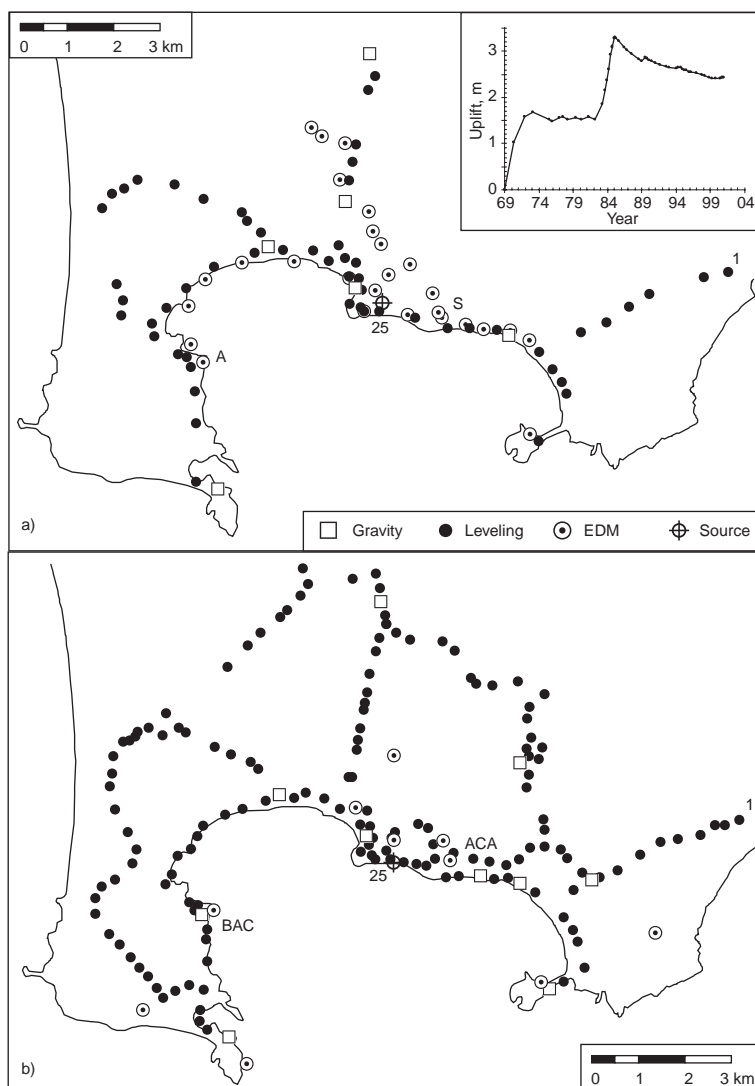
**Figure 9**   Sketch map of the levelling lines, EDM, gravity benchmarks and source location at Campi Flegrei during different periods of times, as analysed in this work: (a) between 1980 and 1983 (during inflation) and (b) between 1990 and 1995 (during deflation). The inset shows ground-level changes at the benchmark 25 (centre of Pozzuoli — where vertical displacement is maximum) from 1969 to 2001 (after Battaglia et al., 2006).

A second episode of uplift began in mid-1982 and continued at a steady rate until it ended suddenly in December 1984. The net uplift during the two episodes since 1968 was 3.0 m. The second episode was a period of intense earthquake swarms, which damaged many buildings and caused a temporary evacuation around the caldera centre. The centre of the caldera floor has subsided at a rate of 10–30 mm yr$^{-1}$ since December 1984 (Barberi et al., 1996; Dvorak and Mastrolorenzo, 1991).

The first papers on Campi Flegrei unrest (e.g. Berrino et al., 1984) ascribed the ground deformation to magmatic intrusion, and the initial interpretation of measured gravity–height change gradients confirmed this hypothesis (Berrino, 1994; Berrino et al., 1984). Later, several authors suggested the possibility of fluid intrusion to explain caldera deformation and gas emissions (e.g. Chiodini et al., 2003; Gaeta et al., 1998; De Natale et al., 1991; Bonafede, 1991). Some recent papers on gravity changes invoke a single hybrid source including both magmatic and hydrothermal components (Gottsmann et al., 2006b, 2006c; Bonafede and Mazzanti, 1998).

Compared to previous analyses of gravity changes at Campi Flegrei caldera, Battaglia et al. (2006) (1) evaluated the background gravity noise due to water table fluctuations and to the coupling between elastic deformation and gravity (the so-called deformation effect; Walsh and Rice, 1979) to avoid bias in the density estimate; while the noise from the water table changes is negligible, the deformation effect significantly bias the estimate of the density of the intrusion and (2) included all available vertical, horizontal and gravity measurements in the joint inversion of geodetic and gravity data to better determine the source parameters; in particular, it is the first time that horizontal measurements are used to model the caldera deflation.

The data set included levelling, EDM and gravity measurements collected by the Osservatorio Vesuviano (Figure 9). First-order optical levelling data, referenced to benchmark 1 in Naples, are available for the whole period 1980–1995, at a number of points increasing with time. Distance changes in an EDM network covering the caldera were determined for 13 baselines between 1980 and 1983 (during inflation, Dvorak and Berrino, 1991), and 21 baselines between 1991 and 1995 (during deflation, Berrino, 1995). The number of gravity stations available for the analysis is 6 sites between 1981 and 1983, and 10 sites between 1991 and 1995 (Gottsmann et al., 2003; Berrino, 1994).

The inversion was performed using a weighted least-squares algorithm with search grid. The covariance matrix, as well as the measurements' errors included an error of $\pm 2\,\mathrm{mm/yr}^{-0.5}$, taking into account monument instability. The best fit model was determined using a reduced chi-square ($\chi_v^2$) test, and 95% confidence limits are computed by a bootstrap percentile method (Efron and Tibshirani, 1986). Battaglia et al. (2006) tested three source geometries: a spherical source (McTigue, 1987), a vertical prolate spheroid (Yang et al., 1988; Clark et al., 1986) and a horizontal penny-shaped source (Fialko et al., 2001), all in an elastic, homogeneous, isotropic half-space.

Inversion results show that the source best fitting the deformation and gravity data during the inflation period is a horizontal penny-shaped crack located beneath the town of Pozzuoli at a depth between 2.5 and 3.5 km, with a radius from 1.6 to 2.7 km, a volume increase between 0.021 and 0.027 km$^3$ and a density between 142 and 1,115 kg m$^{-3}$ (Figure 10). On the other hand, the best fit source for the deflation period is a vertical prolate spheroid 1.9–2.2 km deep, aspect ratio (defined as the ratio between the semi-minor and the semi-major axes) 0.39–0.54, volume decrease 0.005–0.006 km$^3$ and density between 902 and 1,015 kg m$^{-3}$ (Figure 10). The inversion is insensitive to the magnitude of the spheroid semi-major axis.
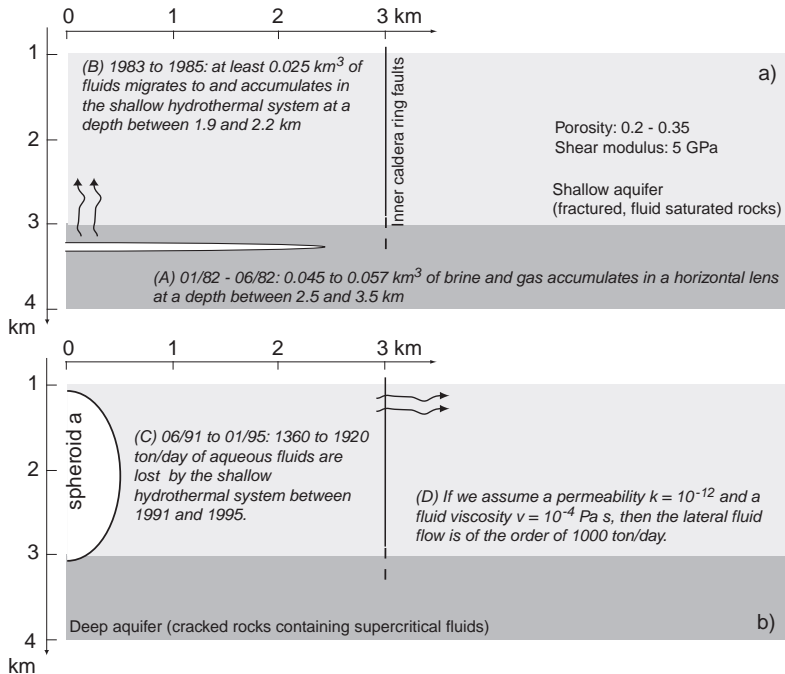
**Figure 10** A possible scenario for unrest at Campi Flegrei (see discussion for explanation): (a) between 1980 and 1983 (during inflation) and (b) between 1990 and 1995 (during deflation) (after Battaglia et al., 2006).

## 6.3. Las Cañadas caldera

Although ground deformation is a frequent phenomenon accompanying the reactivation of calderas, the recent unrest at Tenerife (Canary Islands, Spain) indicates that significant subsurface mass migration may occur without significant ground deformation.

The central volcanic complex (CVC) on Tenerife is the third-highest volcanic complex on Earth, rising almost 7,000 m from the seafloor. The complex includes the 16 km × 9 km-wide Las Cañadas caldera (LCC), which formed during three large-scale volcanic eruptions over the past 1 Ma (Martí et al., 1994). After almost a century of quiescence (the last eruption was in 1909), the complex reactivated in spring 2004 when a number of earthquake swarms (volcano-tectonic events) were felt on the island. An increase in fumarolic activity at the summit of Teide volcano was noted in October 2004, and a new fissure with fumarolic activity formed along the volcano's NE flank in December 2004 (García et al., 2006).

Joint micro-gravity and deformation data collected between May 2004 and July 2005 (Gottsmann et al., 2006d) reflects a mass addition of up to $10^{11}$ kg at depth with maximum positive amplitudes in the northern and western parts of the LCC (Figure 11a). Surprisingly, the gravity changes were not accompanied with widespread ground deformation. In the absence of significant surface deformation, subsurface mass changes cannot be directly related to volume changes and so the
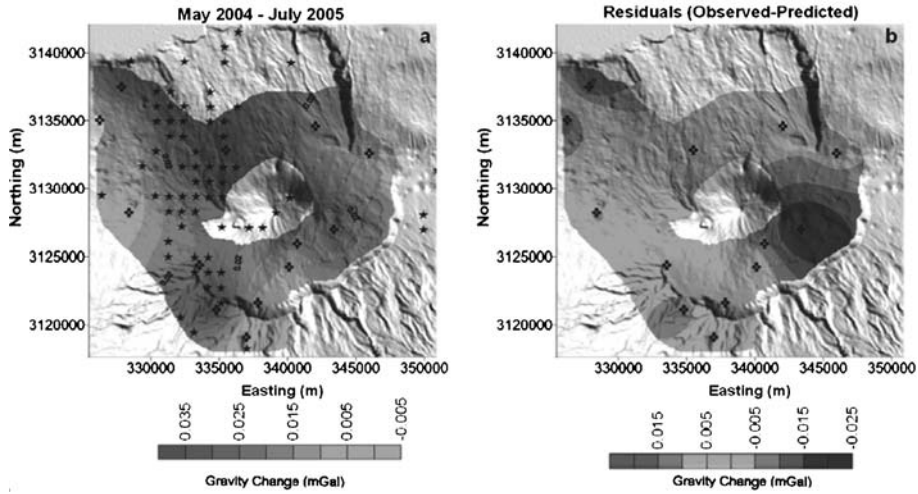
**Figure 11** (a) Residual gravity changes between May 2004 and July 2005 draped over a DEM of the CVC of Tenerife (28.3°N, 16.7°W). Uncertainty in gravity changes is on average $\pm 0.015$ mGal. Benchmark location (crosses) and epicentre locations (stars) of seismicity recorded between May 2004 and July 2005 are also shown. Both gravity increase and seismicity appear to be spatially and temporally correlated. (b) Residuals between observed and predicted gravity changes (mGal) at the benchmarks for the period May 2004 and July 2005 from inversion for an infinite horizontal cylinder at 2,000 m depth below the surface. This body is an approximation of the zone undergoing mass/density increase during fluid migration at the northern and western slopes of the CVC complex. Red colour indicates that the model is predicting higher gravity changes than observed while blue colour indicates the opposite. Green colour indicates match between predictions and observations.

density of the intrusion remains ambiguous. Gottsmann et al. (2006d) found little evidence supporting the hypothesis that the mass increase is solely due to magma movement (i.e. dyke emplacement). An alternative explanation is that the observed gravity increase is due to aqueous fluid migration through the CVC. For example, the volcano–tectonic seismic events may have triggered the release and upward migration of hydrothermal fluids from a deep reservoir. Alternatively, fluid migration may have resulted from the perturbation of an existing deep hydrothermal reservoir due to magma injection, or from the pressurisation of seawater saturated rocks and resultant fluid movement. Based on the evaluation of seismic data, aqueous fluid migration as the causative source for this period of unrest is also proposed by Almendros et al. (2007). Migration of (hydrothermal) fluids through a permeable medium creates little surface deformation, but the filling of pore space increases the bulk density of the material resulting in a gravity increase at the ground surface. The source of the observed gravity increase was approximated by Gottsmann et al. (2006d) by an infinite horizontal cylindrical source, and the inversion of the available data gave a source depth of ca. 2,000 m below the surface. The residuals between observed and predicted gravity changes are shown in Figure 11b.

## 7. The Problem of Aliasing of Time-Lapse Micro-Gravity Data

Gravity-change time series obtained from time-lapse micro-gravity surveys may suffer from distortion when comparing data between individual surveys. This problem was addressed by Gottsmann et al. (2005) who reported significant gravity changes over periods of tens of minutes (Figure 12) at the Nisyros caldera, Greece. The caldera (Figure 12) hosts a complex hydrothermal system extending to depths of at least 1.2 km that overlies a magma reservoir of unknown depth (Caliro et al., 2005). There are reports of at least 13 historic phreatic eruptions, the last in 1888, but there are no reports on historical magmatic or phreato–magmatic activity. A seismic crises, together with a ground uplift of more than 14 cm, occurred between 1996 and 2000 (Lagios et al., 2005; Sachpazi et al., 2002).

The amplitude of the short-term gravimetric oscillations was on the same order of magnitude as the gravity changes observed within the caldera between two annual surveys. The short-term gravity changes were observed within the caldera depression but not around the flanks of the caldera, ruling out atmospheric or tidal perturbations as causative sources. The recorded gravity waveforms indicate the presence of subsurface dynamic processes. The wavelength of the area affected by short-term changes is rather small, suggesting a shallow source (a few hundred metres deep) causing the short-term mass/density changes. Short–period oscillations were also detected in a subsequent field survey at the caldera using a combination of geodetic, gravimetric, seismic and electromagnetic observations (Gottsmann et al., 2007). There is strong evidence that the hydrothermal system is the source for the short-term gravity oscillations. The recorded variations are likely to be triggered by transient changes in the subsurface density during anomalous or non-steady state degassing. In another study, using a multi–day gravimetric record, Tikku et al. (2006) interpret variations in micro-seismicity recorded in an active geyser basin at the Yellowstone caldera (USA) as tremor induced by fluid flow causing also significant gravity variations.

Care must be taken from survey to survey when inferring subsurface processes during traditional time-lapse observations, especially in volcanic areas with active hydrothermal systems that operate on different timescales than magma reservoirs (see also Todesco, 2008). In order to better quantify fundamental subsurface processes and their associated timescales, it is essential to obtain long–term gravity/ height change time series at restless calderas, for instance, via the joint installation of continuously recording gravimeters and GPS receivers (see Section 9).

## 8. The Effect of Lateral Discontinuities on Ground Deformation and Residual Gravity Changes

De Natale et al. (1997) recognised the influence of collapse structures on the deformation pattern at a number of restless calderas, and concluded that subsurface volume and pressure increases (deduced by inverting ground deformation time
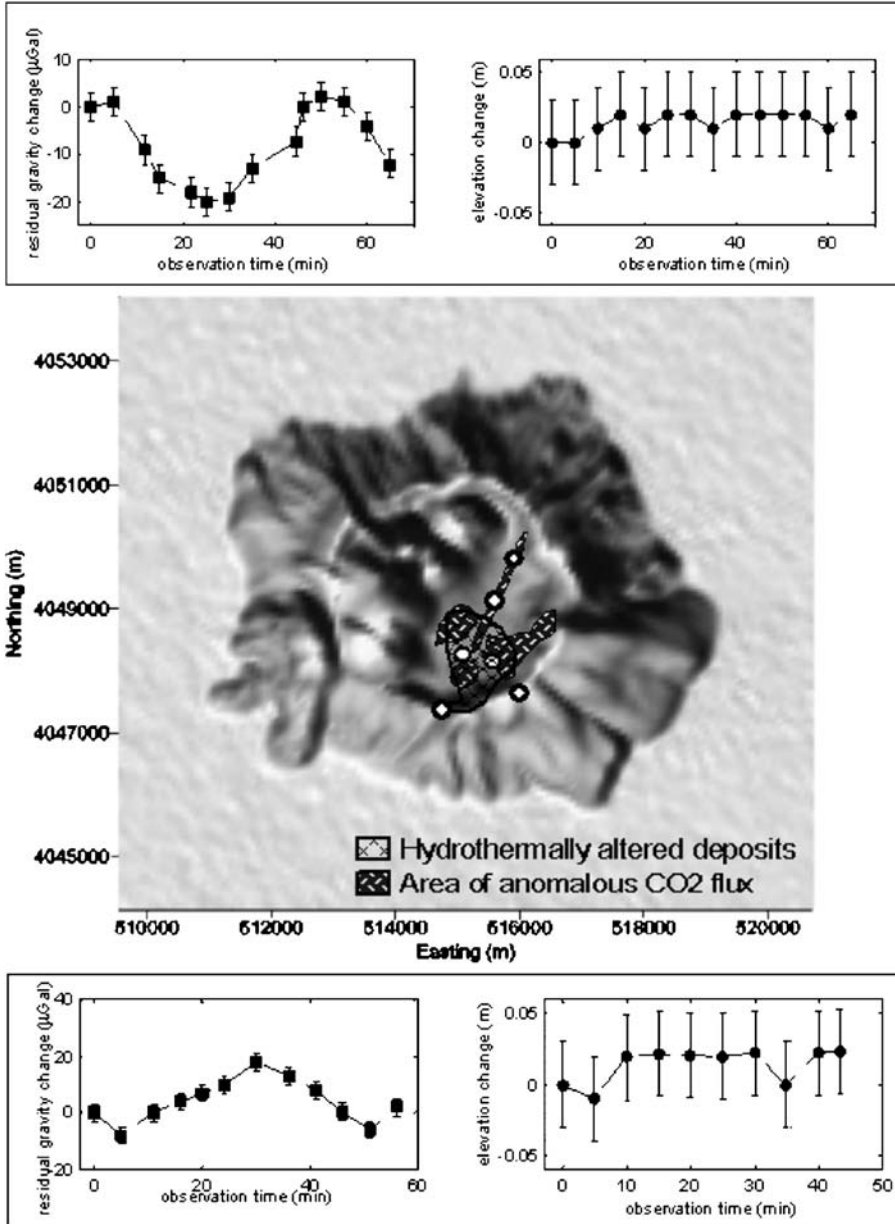
**Figure 12**    Shaded DEM image of Nisyros (36.4°N, 27.2°E) showing areas of hydrothermally altered deposits and areas of anomalously high $CO_2$ flux along the caldera floor (Caliro et al., 2005). Short-term residual gravity changes were recorded at locations indicated by circles. Time-series plots show examples of recorded residual gravity changes and 5 min averages of 1 Hz GPS measurements (after Gottsmann et al., 2005).

series) depend strongly on whether or not lateral discontinuities are accounted for. A recent 3-D numerical analysis (Folch and Gottsmann, 2006) shows that intra-caldera or caldera ring faults can significantly amplify and distort the ground deformation pattern during unrest. Data inversion using models that do not contemplate lateral discontinuities such as isotropic and homogenous half-space models can provide erroneous results on source parameter such as pressure change and source depth. The degree of amplification and distortion in the form of abrupt changes in displacement/distance gradients in proximity to faults is dependent on source geometry. Prolate bodies represent a particularly critical geometry for which pressure increases may be overestimated by a factor of up to three (Figure 13). Bodies such as sills or oblate spheroids are very effective in concentrating deformation directly above their upper surface because the induced displacement vectors tend to be vertical. In contrast, spherical or prolate bodies distribute their displacement vectors predominantly nonvertically (i.e. in the direction normal to subvertical ring faults), and thus require a significantly higher pressure increase than oblate geometries in order to trigger the same amount of surface displacement. As a consequence, the effect of faults on the displacement field becomes more pronounced for the latter geometries compared to the former. The presence of faults may alter notably the shape of both vertical and radial deformation patterns as well as their absolute value. The 3-D analysis suggests that amplification effects can be much larger than predicted by 2-D models (De Natale et al., 1997). Relevant parameters are, by order of importance, source geometry, fault to source distance, fault length and position, and dip angle.

A further important point of accounting for lateral discontinuities concerns time-lapse micro-gravimetric data obtained simultaneously with deformation data. In contrast to their application in isotropic and homogenous half-space models, gravity measurements need to be corrected for the deformation effect (see Section 3) whatever the source geometry, due to the coupling between gravity and elastic deformation in a heterogeneous medium (Bonafede and Mazzanti, 1998).

## 9. Summary, Conclusions and Outlook

Combined geodetic and gravimetric measurements allow us to infer the density of intrusive bodies and better constrain deformation sources in volcanic areas. The joint gravimetric and ground deformation studies reviewed in this paper show that great care must be taken in accounting for possible contributions of water table fluctuation, the effect of the propagation of density boundaries and the effect of boundary faults. For example, the work by Battaglia et al. (2006) shows that the effect of the propagation of density boundaries can reduce the observed gravity changes by up to 80%. Folch and Gottsmann (2006) prove that pressure increases inferred from ground deformation data may be overestimated by up to 300%, if stress concentration in areas bounded by ring faults is not considered.

First approximations of the source of unrest via gravity–height gradients need to be augmented by a rigorous estimate of the source parameters and their sensitivities, via the joint inversion of gravity and geodetic data. We have reported on recent case
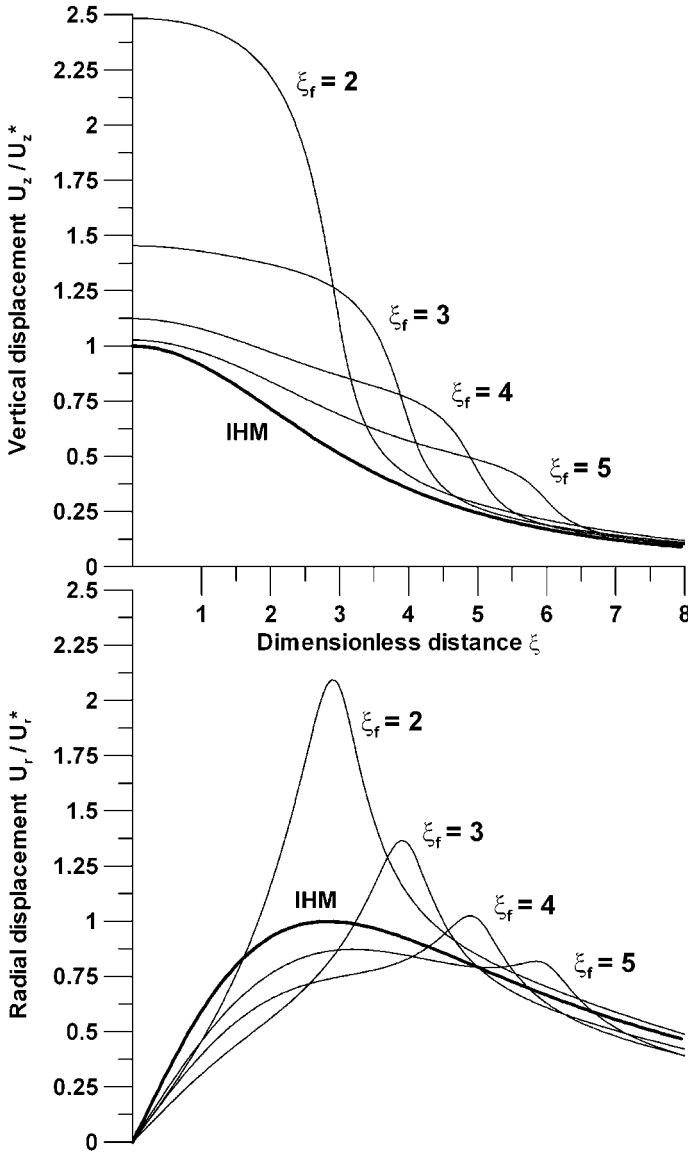
**Figure 13**    The effect of a fault on vertical (top) and radial (bottom) surface displacements pattern caused by a pressurised spherical source. Fault distance is expressed as the ratio between radial distance and source radius, $\xi_f$. Radial distance is normalised to the source radius, i.e. for $x = 3$, distance is three times the source radius. Results for faults located at distances $\xi_f$ of 2, 3, 4 and 5 are shown. Bold lines indicate the predictions for a pressurised spherical source using an isotropic, homogeneous half-space model (IHM). Displacements are normalised to $U_z^*$ and $U_r^*$, the maximum vertical and radial displacements, respectively, as obtained from the IHM. Model parameters for these solutions are source radius of 1 km, source depth of 4 km, vertical fault length of 3.725 km and a dip angle of $15°$ towards the source. The distance between the top of the fault and the free surface is 10% of the fault length (after Folch and Gottsmann, 2006).

studies at the Long Valley, Campi Flegrei, Las Cañadas and the Nisyros caldera and have highlighted some of the complexities involved in the hunt for sources of caldera unrest. Hydrothermal fluid migration appears to be an important source, and more detailed studies, particularly on short-term (high-frequency) mass/density changes, may be necessary. We have shown that joint ground deformation and time-lapse micro-gravity monitoring of active calderas can provide vital insights into their subsurface dynamics, particularly when structural complexities and heterogeneous mechanical properties of the subsurface do not obey a simple linearly elastic relationship of stress generation and resultant ground deformation.

A standard approach in geodetic data analysis is the use of relatively simple mathematical models assuming pure elasticity of the Earth's crust. While such models may account for phenomena resulting in a linear gravity–height signature, nonlinear gravity–height change relationships, in addition to gravity changes associated with negligible ground deformation (or vice versa), are difficult to interpret. A number of applications (Fernández et al., 2005; Tiampo et al., 2004; Fernández and Rundle, 1994) suggest that gravitational coupling effects may be fundamental for explaining gravity changes at active volcanoes, which are not accompanied by significant displacement.

Despite the geologically plausible results obtainable from integrated geodetic data inversions, we have to discuss several limitations of model results.

First, within the concept of elastic rheology, there is a high degree of uncertainty in the value of rigidity. Inferred source pressure changes are directly dependent on rock rigidity, i.e. the higher the rigidity value, the higher the pressure change required to match the amplitude of ground deformation. Few studies have been performed to directly quantify mechanical properties of caldera fill and host rocks, yet directly deduced rigidities differ significantly from generic values (Vanorio et al., 2003, 2005). Accurate knowledge of mechanical properties is required so that inversion results can be considered realistic.

Second, viscoelastic relaxation can play an important role in deep-seated magmatic sources. A viscoelastic halo around the deep source might reduce the deduced pressure changes by up to one order of magnitude (Newman et al., 2001, 2006; Fernández et al., 2001). However, deducing 'realistic' visco-elastic property values such as structural relaxation times or the dimension of a visco–elastic halo around a magma reservoir is difficult and may be prone to large errors.

Third, medium heterogeneity in the form of structural discontinuities (e.g. faults) can have significant effects on both deformation and gravity fields (see Chapter 8).

To tackle the problem of data aliasing, it is essential to obtain long time series of gravity and deformation data via continuous observations. The latter is developing into a standard tool in volcano monitoring, whereas continuous gravimetry still plays a minor role, if any at all, due to high operating costs and problems with the reduction of the background noise (Andò and Carbone, 2004). Continuous time series would give critical baseline data via the statistical analysis of data including spectral analysis. This approach could provide an important tool for the discrimination of short-term changes due to intrinsic physico-chemical processes in hydrothermal reservoirs from fundamental long-term magma movement and

replenishment processes. A more economical solution could be employing two gravimeters operating simultaneously, one in continuous mode, while a second is employed following the routine of time-lapse micro-gravity surveys. This setup can help circumvent the pitfall of data aliasing of traditional periodic surveys. Continuous gravimetry is certainly not yet standard for volcano monitoring, although a few long-term continuous gravity observations have provided important constraints on subsurface dynamics (Berrino et al., 2006; Carbone et al., 2003).

The quantification of subsurface volume/pressure/mass changes should be regarded as essential for the detection of potential pre-eruptive signals from restless calderas. Integrated geodetic studies can provide important insight into the dynamic processes causing unrest and should be considered a vital component in any monitoring programme.

## *ACKNOWLEDGEMENTS*

## *REFERENCES*

Aki, K., Richards, P.G., 1980. Quantitative Seismology, Vol. 1, Freeman and Company, New York, NY.

Almendros, J., Ibanez, J.M., Carmona, E., Zandomeneghi, D., 2007. Array analyses of volcanic earthquakes and tremor recorded at Las Canadas caldera (Tenerife Island, Spain) during the 2004 seismic activation of Teide volcano. J. Volcanol. Geotherm. Res., 160(3-4), 285–299.

Andò, B., Carbone, D., 2004. A test on a Neuro-Fuzzy algorithm used to reduce continuous gravity records for the effect of meteorological parameters. Phys. Earth Planet. Inter., 142, 37–47.

Aprea, C.M., Hildebrand, S., Fehler, M., Steck, L., Baldridge, W.S., Roberts, P., Thurber, C.H., Lutter, W.J., 2002. Three-dimensional Kirchhoff migration: imaging of the Jemez volcanic field using teleseismic data. J. Geophys. Res., 107(B10), 2247, doi: 10.1029/2000JB000097.

Araña, V., Camacho, A.G., Garcia, A., Montesinos, F.G., Blanco, I., Vieira, R., Felpeto, A., 2000. Internal structure of Tenerife (Canary Islands) based on gravity, aeromagnetic and volcanological data. J. Volcanol. Geotherm. Res., 103(1-4), 43–64.

Arnet, F., Kahle, H.-G., Klingele, E., Smith, R.B., Meertens, C.M., Dzurisin, D., 1997. Temporal gravity and height changes of Yellowstone caldera, 1977–1994. Geophys. Res. Lett., 24(22), 2741–2744.

Barberi, F., Cassano, E., La Torre, P., Sbrana, A., 1996. The problem of volcanic unrest: the Campi Flegrei case history. In: Scandone, R. (Ed.), Monitoring and Mitigation of Volcano Hazards. Springer, Berlin, pp. 771–786.

Battaglia, M., Segall, P., 2004. The interpretation of gravity changes and crustal deformation in active volcanic areas. Pure Appl. Geophys., 161(7), 1453–1467.

Battaglia, M., Segall, P., Murray, J., Cervelli, P., Langbein, J., 2003a. The mechanics of unrest at Long Valley caldera, California: 1. Modeling the geometry of the source using GPS, leveling and two-color EDM data. J. Volcanol. Geotherm. Res., 127(3-4), 195–217.

Battaglia, M., Segall, P., Roberts, C., 2003b. The mechanics of unrest at Long Valley caldera, California. 2. Constraining the nature of the source using geodetic and micro-gravity data. J. Volcanol. Geotherm. Res., 127(3-4), 219–245.

Battaglia, M., Troise, C., Obrizzo, F., Pingue, F., De Natale, G., 2006. Evidence for fluid migration as the source of deformation at Campi Flegrei caldera (Italy). Geophys. Res. Lett., 33, L01307, doi: 10.1029/2005GL024904.

Battaglia, M., Vasco, D., 2006. The search for magma reservoirs in Long Valley caldera: single vs. distributed sources. In: Troise, C., De Natale, G., Kilburn, C.R.J. (Eds), Mechanisms of Activity and Unrests at Large Calderas. Geological Society of London, Vol. 269, pp. 173–180.

Berrino, G., 1994. Gravity changes induced by height–mass variations at the Campi Flegrei caldera. J. Volcanol. Geotherm. Res., 61(3–4), 293–309.

Berrino, G., 1995. Misure distanziometriche ai Campi Flegrei–Giugno 1995, Internal report, Osserv. Vesuviano, Naples, Italy.

Berrino, G., Corrado, G., Luongo, G., Toro, B., 1984. Ground deformation and gravity changes accompanying the 1982 Pozzuoli uplift. Bull. Volcanol., 47(2), 188–200.

Berrino, G., Corrado, G., Riccardi, U., 2006. On the capability of recording gravity stations to detect signals coming from volcanic activity: the case of Vesuvius. J. Volcanol. Geotherm. Res., 150(1-3), 270–282.

Berrino, G., Rymer, H., Brown, G.C., Corrado, G., 1992. Gravity–height correlations for unrest at calderas. J. Volcanol. Geotherm. Res., 53, 11–26.

Bonafede, M., 1991. Hot fluid migration, an efficient source of ground deformation: application to the 1982–1985 crisis at Campi Flegrei, Italy. J. Volcanol. Geotherm. Res., 48, 187–198.

Bonafede, M., Dragoni, M., Quareni, F., 1986. Displacement and stress fields produced by a centre of dilation and by a pressure source in a viscoelastic half-space: application to the study of ground deformation and seismic activity at Campi Flegrei, Italy. Geophys. J. R. Astron. Soc., 87, 455–485.

Bonafede, M., Mazzanti, M., 1998. Modelling gravity variations consistent with ground deformation in the Campi Flegrei caldera, Italy. J. Volcanol. Geotherm. Res., 81, 137–157.

Caliro, S., Chiodini, G., Galluzzo, D., Granieri, D., La Rocca, M., Saccorotti, G., Ventura, G., 2005. Recent activity of Nisyros volcano (Greece) inferred from structural, geochemical and seismological data. Bull. Volcanol., 67(4), 358–369.

Campos-Enriquez, J.O., Dominguez-Mendez, F., Lozada-Zumaeta, M., Morales-Rodriguez, H.F., Andaverde-Arredondo, J.A., 2005. Application of the Gauss theorem to the study of silicic calderas: the calderas of La Primavera, Los Azufres, and Los Humeros (Mexico). J. Volcanol. Geotherm. Res., 147(1-2), 39–67.

Campos-Enriquez, J.O., Garduno-Monroy, V.H., 1995. Los Azufres silicic center (Mexico): inference of caldera structural elements from gravity, aeromagnetic, and geoelectric data. J. Volcanol. Geotherm. Res., 67(1-3), 123–152.

Carbone, D., Budetta, G., Greco, F., Rymer, H., 2003. Combined discrete and continuous gravity observations at Mount Etna. J. Volcanol. Geotherm. Res., 123(1–2), 123–135.

Cervelli, P., Murray, M., Segall, P., Aoki, Y., Kato, T., 2001. Estimating source parameters from deformation data, with an application to the March 1997 earthquake swarm off the Izu Peninsula, Japan. J. Geophys. Res., 106(B6), 11,217–11,238.

Chiodini, G., Todesco, M., Caliro, S., Del Gaudio, C., Macedonio, G., Russo, M., 2003. Magma degassing as a trigger of bradyseismic events: the case of Phlegrean Fields (Italy). Geophys. Res. Lett., 30(8), 1434, doi: 10.1029/2002GL016790.

Clark, D.A., Saul, S.J., Emerson, D.W., 1986. Magnetic and gravity anomalies of a triaxial ellipsoid. Explor. Geophys., 17, 189–200.

De Lorenzo, S., Zollo, A., Mongelli, F., 2001. Source parameters and three-dimensional attenuation structure from the inversion of microearthquake pulse width data: Qp imaging and inferences of the thermal state of the Campi Flegrei caldera (southern Italy). J. Geophys. Res., B, Solid Earth Planets, 106(8), 16,265–16,286.

De Natale, G., Pingue, F., Allard, P., Zollo, A., 1991. Geophysical and geochemical modelling of the 1982–1984 unrest phenomena at Campi Flegrei caldera, southern Italy. J. Volcanol. Geotherm. Res., 48, 199–222.

De Natale, G., Petrazzuoli, S.M., Pingue, F., 1997. The effect of collapse structures on ground deformation in calderas. Geophys. Res. Lett., 24, 1555–1558.

de Zeeuw-van Dalfsen, E., Rymer, H., Sigmundsson, F., Sturkell, E., 2005. Net gravity decrease at Askja volcano, Iceland: constraints on processes responsible for continuous caldera deflation, 1988–2003. J. Volcanol. Geotherm. Res., 139(3–4), 227–239.

Dieterich, J.H., Decker, R., 1975. Finite element modeling of surface deformation associated with volcanism. J. Geophys. Res., 80, 4094–4102.

Dvorak, J., Berrino, G., 1991. Recent ground movement and seismic activity in Campi Flegrei, southern Italy, episodic growth of a resurgent dome. J. Geophys. Res., 96, 2309–2323.

Dvorak, J., Mastrolorenzo, G., 1991. The mechanisms of recent vertical crustal movements in Campi Flegrei caldera, southern Italy. Spec. Pap. Geol. Soc. Am., 263, 54.

Dvorak, J.J., Dzurisin, D., 1997. Volcano geodesy: the search for magma reservoirs and the formation of eruptive vents. Rev. Geophys., 35(3), 343–384.

Dzurisin, D., 2003. A comprehensive approach to monitoring volcano deformation as a window on the eruption cycle. Rev. Geophys., 41, doi: 10.1029/2001RG000107.

Dzurisin, D., 2006. Volcano Deformation: New Geodetic Monitoring Techniques. Springer, Berlin, p. 441.

Dzurisin, D., Wicks, J.C., Thatcher, W., 1999. Renewed uplift at the Yellowstone caldera measured by levelling surveys and satellite radar interferometry. Bull. Volcanol., 61(6), 349–355.

Efron, B., Tibshirani, R., 1986. Bootstrap methods for standard errors, confidence intervals, and other measures of statistical accuracy. Stat. Sci., 1, 54–77.

Eggers, A.A., 1987. Residual gravity changes and eruption magnitudes. J. Volcanol. Geotherm. Res., 33, 201–216.

Fernández, J., Rundle, J.B., 1994. Gravity changes and deformation due to a magmatic intrusion in a two-layered crustal model. J. Geophys. Res., 99, 2737–2746.

Fernández, J., Tiampo, K.F., Rundle, J.B., 2001. Viscoelastic displacement and gravity changes due to point magmatic intrusions in a gravitational layered solid earth. Geophys. J. Int., 146, 155–170.

Fernández, J., Tiampo, K.F., Rundle, J.B., Jentzsch, G., 2005. On the interpretation of vertical gravity gradients produced by magmatic intrusions. J. Geodyn., 39(5), 475–492.

Fialko, Y., Kazhan, Y., Simons, M., 2001. Deformation due to a pressurized horizontal circular crack in an elastic half-space, with applications to volcano geodesy. Geophys. J. Int., 146, 181–190.

Folch, A., Fernandez, J., Rundle, J., Marti, J., 2000. Ground deformation in a viscoelastic medium composed of a layer overlying a half space: a comparison between point and extended sources. Geophys. J. Int., 140, 37–50.

Folch, A., Gottsmann, J., 2006. Faults and ground uplift at active calderas. In: Troise, C., De Natale, G., Kilburn, C.R.J. (Eds), Mechanisms of Activity and Unrests at Large Calderas. Geological Society of London, Special Publications, pp. 109–120.

Francis, P.W., 1993. Volcanoes: a planetary perspective. Oxford University Press, 443 pp.

Furuya, M., Okubo, S., Sun, W., Tanaka, Y., Oikawa, J., Watanabe, H., Maekawa, T., 2003. Spatiotemporal gravity changes at Miyakejima volcano, Japan: caldera collapse, explosive eruptions and magma movement. J. Geophys. Res., 108(B4), 2219, doi: 10.1029/2002JB001989.

Gaeta, F.S., De Natale, G., Peluso, F., Mastrolorenzo, G., Castagnolo, D., Troise, C., Pingue, F., Mita, D.G., Rossano, S., 1998. Genesis and evolution of unrest episodes at Campi Flegrei caldera: the role of thermal fluid–dynamical processes in the geothermal system. J. Geophys. Res., 103, 20,921–20,933.

García, A., Vila, J., Ortiz, R., Macia, R., Sleeman, R., Marrero, J.M., Sánchez, N., Tárraga, M., Correig, A.M., 2006. Monitoring the reawakening of Canary Islands' Teide volcano. EOS Trans. Am. Geophys. Union, 87(6), 61.

Gottsmann, J., Berrino, G., Rymer, H., Williams-Jones, G., 2003. Hazard assessment during caldera unrest at the Campi Flegrei, Italy: a contribution from gravity–height gradients. Earth Planet. Sci. Lett., 211, 295–309.

Gottsmann, J., Camacho, A., Fernandez, J., Tiampo, K.F., 2006a. Spatio-temporal variations in vertical gravity gradients at the Campi Flegrei caldera (Italy): a case for source multiplicity during unrest? Geophys. J. Int., 167, 1089–1096.

Gottsmann, J., Carniel, R., Coppo, N., Wooller, L., Hautmann, S.D., Rymer, H., 2007. Oscillations in hydrothermal systems as a source of periodic unrest at caldera volcanoes: multiparameter insights from Nisyros, Greece. Geophys. Res. Lett., 34, L07307, doi: 10.1029/2007GL029594.

Gottsmann, J., Folch, A., Rymer, H., 2006b. Unrest at Campi Flegrei: a contribution to the magmatic versus hydrothermal debate from inverse and finite element modeling. J. Geophys. Res., 111(B07203), doi: 10.1029/2005JB003745.

Gottsmann, J., Rymer, H., 2002. Deflation during caldera unrest: constraints on subsurface processes and eruption prediction from gravity–height data. Bull. Volcanol., 64, 338–348.

Gottsmann, J., Rymer, H., Berrino, G., 2006c. Unrest at the Campi Flegrei caldera (Italy): a critical evaluation of source parameters from geodetic data inversion. J. Volcanol. Geotherm. Res., 150, 132–145.

Gottsmann, J., Rymer, H., Wooller, L.K., 2005. On the interpretation of gravity variations in the presence of active hydrothermal systems: insights from the Nisyros caldera, Greece. Geophys. Res. Lett., 32(L23310), doi: 10.1029/2005GL024061.

Gottsmann, J., Wooller, L.K., Marti, J., Fernandez, J., Camacho, A.G., Gonzalez, P., Garcia, A., Rymer, H., 2006d. New evidence for the reactivation of Teide volcano. Geophys. Res. Lett., 33(L20311), doi: 10.1029/2006GL027523.

Hildreth, W., 2004. Volcanological perspectives on Long Valley, Mammoth Mountain, and Mono Craters: several contiguous but discrete systems. J. Volcanol. Geotherm. Res., 136, 169–198.

Hill, D.P., 1998. 1998 SSA meeting presidential address: science, geologic hazards, and public in a large, restless caldera. Seismol. Res. Lett., 69(5), 400–404.

Hill, D.P., Langbein, J.O., Prejean, S., 2003. Relations between seismicity and deformation during unrest in Long Valley caldera, California, from 1995 through 1999. J. Volcanol. Geotherm. Res., 127, 175–193.

Jachens, R., Roberts, C., 1985. Temporal and areal gravity investigations at Long Valley caldera, California. J. Geophys. Res., 90, 11,210–11,218.

Johnsen, G.V., Bjornsson, A., Sigurdsson, S., 1980. Gravity and elevation changes caused by magma movement beneath the Krafla caldera, northeast Iceland. J. Geophys., 47, 132–140.

Lagios, E., Sakkas, V., Parcharidis, I., Dietrich, V., 2005. Ground deformation of Nisyros volcano (Greece) for the period 1995–2002: results from DInSAR and DGPS observations. Bull. Volcanol., 68(2), 201–214.

Langbein, J., 2003. Deformation of the Long Valley caldera, California: inferences from measurements from 1988 to 2001. J. Volcanol. Geotherm. Res., 127, 247–267.

Langbein, J., Dzurisin, D., Marshall, G., Stein, R., Rundle, J., 1995. Shallow and peripheral volcanic sources of inflation revealed by modeling two-color geodimeter and leveling data from Long Valley caldera, California, 1988–1992. J. Geophys. Res., 100, 12,487–12,495.

Martí, J., Mitjavila, J., Villa, I.M., 1994. Stratigraphy, structure and geochronology of the Las Cañadas Caldera (Tenerife, Canary Islands). Geol Mag, 131, 715–727.

McKee, C., Mori, J., Talai, B., 1989. Microgravity changes and ground deformation at Rabaul caldera, 1973–1985. In: Latter, J. (Ed.), IAVCEI Proceedings in Volcanology. Springer, Berlin, pp. 399–431.

McTigue, D.F., 1987. Elastic stress and deformation near a finite spherical magma body: resolution of the point source paradox. J. Geophys. Res., 92, 12931–12940.

Mogi, K., 1958. Relations between eruptions of various volcanoes and the deformations of the ground surfaces around them. Bull. Earth. Res. Inst., 36, 99–134.

Newhall, C.G., Dzurisin, D., 1988. Historical unrest at large calderas of the world. US Geological Survey Bulletin. US Geological Survey, Reston, VA, 1108 pp.

Newman, A.V., Dixon, T.H., Gourmelen, N., 2006. A four-dimensional viscoelastic deformation model for Long Valley caldera, California, between 1995 and 2000. J. Volcanol. Geotherm. Res., 150, 244–269.

Newman, A.V., Dixon, T.H., Ofoegbu, G.I., Dixon, J.E., 2001. Geodetic and seismic constraints on recent activity at Long Valley caldera, California: evidence for viscoelastic rheology. J. Volcanol. Geotherm. Res., 105, 183–206.

Poland, M., Hamburger, M., Newman, A., 2006. The changing shapes of active volcanoes: history, evolution, and future challenges for volcano geodesy. J. Volcanol. Geotherm. Res., 150, 1–13.

Pollitz, F.F., Buergmann, R., Segall, P., 1998. Joint estimation of afterslip rate and postseismic relaxation following the 1989 Loma Prieta earthquake. J. Geophys. Res., 103(B11), 26,975–26,992.

Rymer, H., 1994. Microgravity change as a precursor to volcanic activity. J. Volcanol. Geotherm. Res., 61, 311–328.

Rymer, H., Cassidy, J., Locke, C., Sigmundsson, F., 1998. Post-eruptive gravity changes from 1990 to 1996 at Krafla volcano, Iceland. J. Volcanol. Geotherm. Res., 87, 141–149.

Rymer, H., Tryggvason, E., 1993. Gravity and elevation changes at Askja, Iceland. Bull. Volcanol., 55, 362–371.

Rymer, H., Williams-Jones, G., 2000. Volcanic eruption prediction: magma chamber physics from gravity and deformation measurements. Geophys. Res. Lett., 27(16), 2389–2392.

Sachpazi, M., Knotoes, C., Voulgaris, N, Laigle, M., Vougioukalakis, G., Sikioti, O., Stavrakakis, G., Baskoutas, J., Kalogeras, J., Lepine, J.C., 2002. Seismological and SAR signature of unrest at Nisyros caldera, Greece. J. Volcanol. Geotherm. Res., 116(1–2), 19–33.

Sparks, R.S.J., 2003. Forecasting volcanic eruptions. Earth Planet. Sci. Lett., 210, 1–15.

Steck, L.K., Prothero, W.A., Jr., 1994. Crustal structure beneath Long Valley caldera from modeling of teleseismic P wave polarizations and Ps converted waves. J. Geophys. Res., 99, 6881–6898.

Tiampo, K.F., Fernández, J., Jentzsch, G., Charco, M., Rundle, J.B., 2004. New results at Mayon, Philippines, from a joint inversion of gravity and deformation measurements. Pure Appl. Geophys., 161, 1433–1452.

Tiampo, K.F., Rundle, J.B., Fernandez, J., Langbein, J.O., 2000. Spherical and ellipsoidal volcanic sources at Long Valley caldera, California, using a genetic algorithm inversion technique. J. Volcanol. Geotherm. Res., 102(3-4), 189–206.

Tikku, A.A., McAdoo, D.C., Schenewerk, M.S., Willoughby, E.C., 2006. Temporal fluctuations of microseismic noise in Yellowstone's Upper Geyser Basin from a continuous gravity observation. Geophys. Res. Lett., 33, L11306, doi: 10.1029/2006GL026113.

Todesco, M., 2008. Hydrothermal fluid circulation and its effect on caldera unrest (this issue).

Ukawa, M., Fujita, E., Ueda, H., Kumagai, T., Nakajima, H., Morita, H., 2006. Long-term geodetic measurements of large scale deformation at Iwo-Jima caldera, Japan. J. Volcanol. Geotherm. Res., 150(1–3), 98–118.

Vanorio, T., Prasad, M., Nur, A., 2003. Elastic properties of dry clay mineral aggregates, suspensions and sandstones. Geophys. J. Int., 155(1), 319–326.

Vanorio, T., Virieux, J., Capuano, P., Russo, G., 2005. Three-dimensional seismic tomography from P wave and S wave microearthquake travel times and rock physics characterization of the Campi Flegrei caldera. J. Geophys. Res., 110, B03201, doi: 10.1029/2004JB003102.

Vasco, D.W., Johnson, L.R., Goldstein, N.E., 1988. Using surface displacement and strain observations to determine deformation at depth, with an application to Long Valley caldera, California. J. Geophys. Res., 93, 3232–3242.

Vasco, D.W., Karasaki, K., Doughty, C., 2000. Using surface deformation to image reservoir dynamics. Geophysics, 65, 132–147.

Vasco, D.W., Smith, R.B., Taylor, C.L., 1990. Inversion of sources of crustal deformation and gravity change at the Yellowstone caldera. J. Geophys. Res., 95, 19,839–19,856.

Walsh, J.B., Rice, J.R., 1979. Local changes in gravity resulting from deformation. J. Geophys. Res., 84, 156–170.

Walter, T.R., Acocella, V., Neri, M., Amelung, F., 2005. Feedback processes between magmatic events and flank movement at Mount Etna (Italy) during the 2002–2003 eruption. J. Geophys. Res., 110, doi: 10.1029/2005JB003688.

Williams-Jones, G., Rymer, H., 2002. Detecting volcanic eruption precursors: a new method using gravity and deformation measurements. J. Volcanol. Geotherm. Res., 113, 379–389.

Williams-Jones, G., Rymer, H., Rothery, D.A., 2003. Gravity changes and passive $SO_2$ degassing at the Masaya caldera complex, Nicaragua. J. Volcanol. Geotherm. Res., 123(1–2), 137–160.

Yang, X., Davis, P.M., Dieterich, J.H., 1988. Deformation from inflation of a dipping finite prolate spheroid in an elastic half-space as a model for volcanic stressing. J. Geophys. Res., 93, 4249–4257.

# The Failure Forecast Method: Review and Application for the Real-Time Detection of Precursory Patterns at Reawakening Volcanoes

Marta Tárraga[1],[*], Roberto Carniel[2], Ramon Ortiz[1] *and* Alicia García[1]

## Contents

## Abstract

This paper sets out to assess the failure forecast method (FFM) and its application to volcanology. After first reviewing the history of its development and the published literature, a special focus will be given to the possible use of FFM in the analysis of reawakening volcanoes and caldera unrest. We present results from its application to the recent episode of unrest at the Las Cañadas caldera, Tenerife (Spain). Here the FFM procedure was automated, solving the problem of subjectivity in the application of FFM.

[*]Corresponding author. Tel.: +34 914 111 328, Ext. 1186; Fax: +34 915 644 740
*E-mail address:* marta.tarraga@gmail.com

[1] Departamento de Volcanología. Museo Nacional de Ciencias Naturales, CSIC, Madrid, Spain
[2] Dipartimento di Georisorse e Territorio, Università di Udine, Via Cotonificio 114, 33100 Udine, Italy

# 1. Introduction

One of the main objectives in volcanology is to forecast volcanic eruptions. Over the last few decades notable advances have been made — thanks to the observation and recognition of a number of precursory phenomena. The steps involved include the detection and characterisation of potential precursors, in particular those relating to persistence (Carniel et al., 2008a, 2008b), followed by close monitoring, in order to study their subsequent evolution. In some cases, this temporal evolution has shown the presence of recognizable patterns or "laws" (often empirical) before an eruptive event.

Unrest episodes in calderas and composite volcanoes are common, but are unfortunately not always well understood. There are a number of cases in which unrest did not culminate in eruption, even after significant unrest of the volcanic system (Hill et al., 2003; Todesco et al., 2004). However, there are examples where eruptions have occurred seemingly without significant precursory signals. In some cases, the precursors are simply too difficult to identify from the data (Alekseev et al., 1995; Carniel et al., 2006). Volcanic eruptions are driven by the ascent of magma from a reservoir to the surface, but not all episodes of dyke injection necessarily lead to an eruption. In fact, it is likely that most dyke injections become arrested at depth (Gudmundsson et al., 1999) and never reach the surface. As a consequence, only a small percentage of unrest episodes, triggered by magma injection, end in a new eruption.

Collapse calderas are structurally heterogeneous systems, due to intensive faulting both syn– and post collapse, and many host well–developed hydrothermal systems. Changes of the physico-chemical properties of hydrothermal systems are also inferred to cause unrest (Todesco et al., 2004, Todesco, 2008). Signals from hydrothermal systems may be superimposed on magmatic signals, thus masking the magmatic unrest indicators. For this reason it is crucial to discriminate between magmatic and non–magmatic unrest in order to accurately forecast volcanic activity.

Several authors have observed an increase in the rate of change of observables, such as ground deformation, seismicity and gas emission, at different time scales before an eruption. For instance, at Bezymyanny volcano in Kamchatka, Russia, Tokarev (1963) observed an increase in the rate of seismic energy release ahead of 13 eruptions in October 1959, April 1957 and March 1961. The increase was defined by a hyperbolic fit of the cumulative square root of energy release versus time. These seismic precursors were detected between 30 and 50 days before the eruptions. Tokarev (1983) also used these hyperbolic laws to make extrapolations and to forecast eruptions at other Kamchatkan volcanoes, including Sheveluch in 1964 and Tolbachik in 1975.

Later, Swanson et al. (1983) used the observation of precursory changes in seismic activity, deformation and (harder to define) gas emissions, to forecast 13 eruptions at Mount St. Helens, USA, between June 1980 (soon after the catastrophic eruption of May 18th the same year) and December 1982. The majority of these forecasts were issued anywhere between tens of minutes up to several hours before the eruptions. The last seven eruptions, from mid–April 1981 onwards, were forecasted well ahead of their occurrence, from 3 days to 3 months

in advance. Similarly, Malone et al. (1983) noted an abrupt increase in the seismic energy release (associated with medium–low frequency seismic events located at a depth of less than 3 km) before the majority of eruptions at Mount St. Helens between October 1980 and the end of 1982. This seismic precursor usually appeared in the week before the eruption, when the inter-eruptive repose period was of the order of two months. Two "extreme" cases were also documented, including the longest and shortest repose periods. The former (4.5 months) ended with an eruption whose precursors had been observed one month earlier. The latter (2 weeks) ended with precursors 24 hours before the eruption. Using ground deformation rather than seismic data for the same period, Chadwick et al. (1983) and Dzurisin et al. (1983) were able to forecast the occurrence of eruptions at Mount St. Helens between 3 and 19 days ahead.

Voight (1988) proposed a general law of material failure governed by accelerating creep in order to characterise precursory phenomena. This gave birth to the material failure forecast method (FFM). The underlying hypothesis of this methodology is that deterministic models can be applied to volcanic systems. Pressurisation of a magma reservoir results in material failure, due to fracturing of the host rock. Voight's (1988) original approach has subsequently been applied and further developed in a number of studies in order to forecast eruptions or volcano-related seismic events at a number of different volcanoes (Voight and Cornelius, 1991; Cornelius and Voight, 1994, 1996; Kilburn and Voight, 1998; De la Cruz-Reyna and Reyes-Dávila, 2001; Kilburn, 2003; Ortiz et al., 2003; Carniel et al., 2006; Tárraga et al., 2006) which we review in Section 7. The practical application of FFM as a real-time forecasting tool has been made possible in the 1990s — thanks to a marked increase in CPU speed.

Major theoretical advances were made by Cornelius and Scott (1993), who related the equations of FFM to the theory of damage accumulation by studying the nature of creep acceleration. In 2001, De la Cruz-Reyna and Reyes-Dávila published a study of FFM, based on the use of linear models of viscoelasticity, allowing the identification of different behaviour linked to different stress conditions enabling fast estimations of the failure time of the material.

The present contribution reviews the application of the FFM in volcanology and describes it as a potential tool to discriminate between volcanic and purely tectonic unrests. We evaluate its main advantages and drawbacks in interpreting precursory signals produced during unrest episodes.

## 2. Theory of Precursors

Volcanoes are complex dynamical systems controlled by the interaction of many processes that usually show either non-linear (Carniel and Di Cecca, 1999) or stochastic behaviour (Jaquet and Carniel, 2001). The high-level of uncertainty in the parameters governing these processes makes predicting the behaviour of volcanic systems highly problematic. However, these complex and possibly chaotic systems can occasionally show regular or even periodic behaviour (Sparks, 2003). The identification of repetitive patterns prior to an eruption would, of course, be

an important tool, but these patterns could or could not be directly related to the beginning of the eruptive activity. Only in the positive case could these patterns help in highlighting possible future eruptive behaviour (Sandri et al., 2004) and therefore be considered "precursors". Moreover, precursors of a volcanic eruption do not generally appear in a clear and isolated form, but rather as changes (sometimes very slight) in the full spectrum of local activity.

The search for precursors of volcanic eruptions and earthquakes is usually done in hindsight via an empirical approach by looking at all anomalous signals that may be interpreted as a warning. In practice, one looks for the best correlation between the time series of the phenomenon and its possible precursor. Once an acceptable correlation is found the precursor could be deemed as meaningful, although it could also result from a pure coincidence (Keilis-Borok et al., 1988; Mulargia, 1992; Shebalin et al., 2006). To define a signal as "precursory", one has to relate the number of successful forecasts to the number of pure coincidences (Ortiz and García, 2000). A detailed example of a Bayesian evaluation is given in Section 7.3 for the case of Las Cañadas Caldera, Tenerife (Tárraga et al., 2006).

Phenomenon 'A' is said to be a precursor of another phenomenon 'B', if 'A' happens before 'B', and the following conditions are verified (Mulargia and Gasperini, 1996; Ortiz and García, 2000):

- a known phenomenological relationship must exist between 'A' and 'B' (cause and effect).
- 'A' must be known and the characteristics of 'B' must be perfectly defined.
- the time window between 'A' and 'B' must be known.

The most difficult part in the quantification of precursors is defining the window. If the window is too long then any phenomenon becomes a precursor, and within a long enough window any event might happen (Mulargia, 1997). Therefore, one has to reduce the length of the window and also consider the possibility of a time delay in this window. Finally, one has to study the various possible combinations; i.e. (1) several precursors can precede a single event; (2) several events can follow a single precursor or (3) several precursors precede several events (most frequently). From a practical point of view, a requirement for a precursor to be deemed meaningful is that the related time window must be defined with sufficient precision and the forecast issued with sufficient premonition to allow authorities to take appropriate measures. For this to be possible, the minimum forecast parameters that must be provided to authorities are the length of the time window, the probability of occurrence and the type of expected (eruptive) event(s).

## 3. The Theory of the Material Failure Forecast Method (FFM)

The material FFM (here applied to forecast eruptions) was originally developed to study in particular the mechanics of landslides, with several

experimental data acquisitions and subsequent modelling by different authors. In the work of Fukuzono (1985), Fukuzono and Terashima (1985) and Fukuzono (1990) analogue models were created where soil layers deposited at different angles on inclined planes were subjected to an increasing load due to artificial rain. After a given time the surface displacement, $x$, of the layers with different slopes increased, and material failure was observed after several hours. Empirically, the increase of the logarithm of acceleration was observed to be proportional to the logarithm of displacement velocity immediately before failure. This behaviour was modelled with the following differential equation:

$$\frac{d^2x}{dt} = A\left(\frac{dx}{dt}\right)^{\alpha} \tag{1}$$

where $x$ is the displacement, $t$ the time and $A$ and $\alpha$ the two empirical constants derived from the experimental data. The value of $\alpha$ was experimentally determined to lie in the range from 1.5 to 2.2.

Assuming $A > 0$ (see Equation (1)), and using different values of $\alpha$, we obtain the following expressions for velocity $dx/dt$:

Case $\alpha < 1$:

$$\frac{dx}{dt} = [A(1-\alpha)]^{1/(1-\alpha)}(t_1 + t)^{1/(1-\alpha)} \tag{2}$$

Case $\alpha = 1$:

$$\frac{dx}{dt} = \exp[A(t_2 + t)] \tag{3}$$

Case $\alpha > 1$:

$$\frac{dx}{dt} = [A(\alpha-1)]^{-1/(\alpha-1)}(t_r - t)^{-1/(\alpha-1)} \tag{4}$$

where $t_1$, $t_2$ and $t_r$ are integration constants.

An estimate of the timing of material failure can then be derived on a graph of inverse velocity $(1/v)$ versus time, and extrapolating the curve to get $t = 1/v = 0$.

Transforming Equation (4) into:

$$\frac{1}{v} = [A(\alpha-1)]^{1/(\alpha-1)}(t_r - t)^{1/(\alpha-1)} \tag{5}$$

where $1/v$ is $1/(dx/dt)$, we can see that the resulting curve is decreasing with time and is linear if $\alpha = 2$, convex if $\alpha > 2$ and concave if $1 < \alpha < 2$.

When $\alpha = 2$, Equation (4) has an hyperbolic increase in deformation rate, and as a consequence the inverse velocity curve (Equation (5)) becomes linear. This is used to forecast the time of failure, via linear extrapolation to the intersection of the time axis. In the experiment of Fukuzono (1985), the forecast generated using this linear extrapolation method was issued several tens of minutes before the actual material failure. For values of $\alpha$ not equal to 2 the extrapolations can be carried out using a different (and slightly more complicated) graphical method, as explained in detail in Fukuzono (1985).

Voight (1988) proved that Equation (1) reflects a general physical law that governs different forms of material failure, for constant conditions of stress and temperature. Substituting displacement $x$ with $\Omega$ in Equation (1), where $\Omega$ is an experimental observable linked to a physical change of the system (such as ground displacement, tilt, seismic energy release, etc.), according to Fukuzono (1985) we see a linear relationship between the logarithm of the acceleration of the observable $\ddot{\Omega}$ and the rate of the observable $\dot{\Omega}$. Defining $\dot{\Omega} = \dot{\Omega}_0$, and the initial condition at the time $t = t_0$, we rewrite Equation (1) as:

$$\ddot{\Omega} = A\dot{\Omega}^{\alpha} \tag{6}$$

$$\dot{\Omega} = [A(1-\alpha)(t-t_0) + \dot{\Omega}_0^{(1-\alpha)}]^{1/(1-\alpha)} \quad \text{for } \alpha < 1 \tag{7}$$

$$\dot{\Omega} = \dot{\Omega}_0 e^{A(t-t_0)} \quad \text{for } \alpha = 1 \tag{8}$$

$$\dot{\Omega} = [A(\alpha-1)(t_f-t) + \dot{\Omega}_f^{(1-\alpha)}]^{1/(1-\alpha)} \quad \text{for } \alpha > 1 \tag{9}$$

where $t_f$ is the time of failure, and $\dot{\Omega}_f$ the rate of increase of the observable at the time of failure. Equation (9) shows there is a certain time for which the rate of increase of the observable becomes infinite, i.e. there is a singularity. For this reason there exists an upper-bound solution for the time of failure $t_f$. The time of failure is thus computed at $t = t_a$ and $\dot{\Omega} = \dot{\Omega}_a$ by:

$$t_f - t_a = \frac{\dot{\Omega}_a^{(1-\alpha)} - \dot{\Omega}_f^{(1-\alpha)}}{A(\alpha-1)} \tag{10}$$

Assuming an infinite $\dot{\Omega}_f$, we obtain an upper-bound solution given by:

$$t_f - t_a = \frac{\dot{\Omega}_a^{(1-\alpha)}}{A(\alpha-1)} \tag{11}$$

By solving analytically Equations (10) and (11) we obtain values of $A$ and $\alpha$. Voight (1989) estimated these values experimentally for the time preceding failure in volcanic domes. Similar to the results from landslides, $\alpha$ was estimated to be generally close to 2.

The constant of proportionality $A$ depends on $\alpha$, which is a dimensionless constant. For Equations (1) and (6), we observe that $A = [T^{(\alpha-2)}L^{(1-\alpha)}]$, where $T$ has dimensions of time and $L$ has the same dimensions as $\Omega$ (length, energy, etc.). In the special case of $\alpha = 2$, $A = [1/L]$, or in other words, the dimensions of $A$ are the inverse of length. '$A$' is always positive because deformation is always increasing (Cornelius and Voight, 1995).

## 4. Techniques of Analysis

Cornelius and Voight (1995) discuss five different techniques, one graphical and four numerical, to determine the time of failure from a set of experimental data. The graphical technique (shown above) is based on the inverse of the rate of increase in the observable versus time. This technique is not limited to linear extrapolations — one can also select either a more general curve or piece-meal linear trend to be fitted manually. The graphical approach is the fastest and simplest to use, and it is therefore the most suitable for use in the field during a crisis when time plays a major role. Moving on to the numerical techniques, three of them are based on least-square fitting of linear trends while the last one uses a non-linear fitting procedure. The general idea is to determine the value of '$A$' and $\alpha$ from Equation (6). The first numerical technique is called "*linearised least-squares technique*" and is simply a numerical version of the graphical approach described above. It is based on the linear form of Equations (7) and (9), where $\alpha \neq 1$ and can be determined by iteration, maximising the correlation coefficient of the linear fit for different choices of $\alpha$. The second numerical technique is called "*log rate versus log rate acceleration technique*" and uses the logarithmic form of Equation (6). It does not require an iterative process in order to compute $\alpha$ and $A$, and its linearity clearly shows how an experimental data set follows the material failure law. The third numerical technique, called "*hindsight technique*", is mainly applied to the characterisation of small time segments immediately after or before material failure, using the logarithmic form of Equation (11) (only for $\alpha > 1$). Finally, the fourth technique is called "*non-linear least-square technique*" and can be applied for any value of $\alpha$. Special algorithms are required to minimise the variance between the given function and the experimental data through the search of an n-dimensional space of variables (Bevington, 1969; Cornelius and Voight, 1995).

## 5. Viscoelastic Model

De la Cruz-Reyna and Reyes-Dávila (2001) propose a linear Kelvin—Voigt viscoelastic model (Bland, 1960) to describe the observed accelerating behaviour of seismicity and deformation recorded at various volcanoes before an eruption. Each behaviour can be described by a simple mathematical function, derived from a viscoelastic process, which estimates of time of failure of a system that has been subjected to a load or stress.

When subjected to stress, the materials show different responses in terms of deformation below the elastic limit. This behaviour is known as creep. Many materials follow three different creep states with time: the primary creep, with a high initial strain rate as the load is applied followed by a reduced strain rate (i.e. deceleration); the secondary creep (or pseudoviscous flow state) where the strain rate is low and almost uniform and the tertiary creep, where the deformation accelerates up to the point of failure. In a general form, the response of the deformation rate to an applied constant stress (moving from primary to secondary

and then tertiary creep states) can be expressed through the following relaxation law (De la Cruz-Reyna and Reyes-Dávila, 2001):

$$\dot{\varepsilon}(t) = \frac{B}{1 + st} \tag{12}$$

where $\dot{\varepsilon}$ is the deformation rate, $t$ the time and $B$ and $s$ the parameters that are dependent on the creep state of the material. The former scales proportionally to the applied stress. Whether creep is primary or tertiary depends on the sign of $s$. If $s = 0$, Equation (12) describes secondary creep, i.e. pseudoviscous flow.

De la Cruz-Reyna and Reyes-Dávila (2001) analysed the creep behaviour of viscoelastic bodies subjected to different load histories: constant stress, stress linearly increasing to a time $t_c$ or stress monotonically growing in a linear fashion up to a time $t_c$ and constant afterwards. The results show that the body has an exponential distribution of retardation frequency that converges or diverges as a function of the creep state (or, equivalently, as a function of the sign of $s$). According to the model, the tertiary creep state implies a degradation of the material, i.e. the medium becomes less resistant, and as a consequence shows an increase in the rate of deformation and released seismic energy. For this reason, experimental field data enables detection of tertiary creep and thus the time of failure of the material to be forecast according to the two parameters, $s$ and $B/st_c$, which depend on the stress applied to the material.

## 6. Seismicity as the Observable for FFM

Examining the time evolution of seismic activity is probably the simplest and most effective way to approach the problem of forecasting using the material FFM. The data can be acquired continuously and sent in real-time via radio or internet (Tárraga et al., 2006). As we have seen, the FFM model is based on monitoring material deformation. It is therefore essential to establish the missing link between material deformation and seismic activity.

We start by examining the real-time seismic amplitude measurement (RSAM) (Endo and Murray, 1991) as the seismic observable for the FFM. The RSAM is an average of the modulus of the amplitude of the seismic signal over a given time window (typically 1, 5 or 10 min). It can be expressed in the form:

$$\text{RSAM} = \frac{1}{N} \sum_{i=1}^{N} |A_i| \tag{13}$$

where $N$ is the length of the time window used for averaging and $A_i$ the single seismic amplitude samples.

The main advantage of the RSAM is, as its name suggests, that it can provide information in real-time. The units employed may simply be counts or volts, or can be measured in units of average ground velocity (i.e. meters per second) by using the appropriate sensor conversion factor. The RSAM does not distinguish between different potential seismic sources, and is therefore unable to discount the

contribution to seismic energy from factors unrelated to the main process resulting in possible material failure. Therefore, events such as teleseisms, surface noise (e.g. rockfalls), anthropogenic noise, sea noise, wind noise, etc. have to be used with caution. A partial solution is to condition the acceptance of a given energy contribution to its spectral content. This leads to the definition of formulas similar to Equation (13), but is limited by given frequency bands. The derived quantity is called seismic spectral amplitude measurement (SSAM) (Stephens et al., 1994; Rogers and Stephens, 1995).

The RSAM can be related to the reduced displacement (RD), which is defined as the ground displacement $U$ (considered to be the root-mean-square (rms) of Rayleigh waves) corrected for geometric spreading and instrument amplification. It can be written as follows (Aki and Koyanagi, 1981; Fehler, 1983; Cornelius and Voight, 1995):

$$\text{RD} = \text{rms}(U)\sqrt{\lambda\Delta} \tag{14}$$

The dimensions of RD are length squared $[L^2]$ as $\lambda$ is the wavelength considered, $\Delta$ the distance from the source and the rms of the seismic ground displacement is:

$$\text{rms}(U) = \left[\frac{\sum U^2}{N}\right]^{1/2} \tag{15}$$

The quantity $\text{rms}(U)$ is half the measured peak-to-peak amplitude of $U$, and if we assume that the signal is composed of sine waves (Fehler, 1983; Cornelius and Voight, 1995) it can be written as follows:

$$\text{rms}(U) = \left(\frac{U^2}{2\pi}\int_0^{2\pi}\sin^2x\,dx\right)^{1/2} = \frac{U}{\sqrt{2}} \tag{16}$$

The ground displacement, again in the case of sine waves, is related to the ground velocity through a phase shift of $-\pi/2$, and the RSAM can be shown to follow the following proportionality relationship:

$$\text{RSAM} \propto \left(\frac{U}{2\pi}\int_{-\pi/2}^{3\pi/2}|\sin x|dx\right) = \frac{U}{\pi} \tag{17}$$

We therefore deduce that the RSAM is proportional to the RD and this is proportional to the seismic moment rate or energy rate (both expressed in Joules per second (Fehler, 1983; Cornelius and Voight, 1995)). This provides proof that the RSAM record can be directly employed as the observable $\dot{\Omega}$ in Equation (6), even when the constants of proportionality are not precisely known (Cornelius and Voight, 1995).

Another seismic parameter used in the literature to estimate the deformation rate (strictly linked to the RSAM) is the real-time seismic energy measurement (RSEM) (De la Cruz-Reyna and Reyes-Dávila, 2001; Reyes-Dávila and De la Cruz-Reyna, 2002; Tárraga et al., 2006), which is the square root of the average

squared seismic amplitude:

$$\text{RSEM} = k\sqrt{\frac{1}{N}\sum_{i=1}^{N}(A_i - A_{avg})^2} \tag{18}$$

where $A_i$ is the seismic signal amplitude sample, $A_{avg}$ the average of $N$ samples and $k$ a constant that depends on the analogue–digital converter.

The energy density of the motion over a period $T$ is:

$$E_d = \frac{1}{2}\rho f \int_0^T \dot{x}^2 dt \tag{19}$$

where $\rho$ is the ground mass density, $f$ the frequency and $\dot{x} = V_0\sin(2\pi f t)$ with $V_0 = (-2\pi f a)$ where $a$ is the amplitude.

Therefore, if every period of the seismic wave carries $1/2(\rho V_0^2)$, $n$ periods with a total duration of $t_0$ seconds of a wave travelling with velocity $\beta$ carry an energy density flux equal to:

$$\dot{E}_d = \frac{1}{2}\rho V_0^2 \beta t_0 \tag{20}$$

which is directly proportional to the RSEM as defined above.

## 7. FFM Applied to the Studies of Volcanoes

### 7.1. Persistently active volcanoes and volcanoes with multiple recent eruption episodes

Most of the work published so far focuses on volcanoes that can be described as either persistently active (and mostly basaltic in magma composition; e.g. Stromboli, Kilauea) or volcanoes with a recent history of multiple volcanic eruptions (e.g. Mount. St. Helens). These examples are discussed in more detail in the next section. Table 1 details a number of these studies where FFM was applied to forecast failure during volcanic processes, both in hindsight and foresight. Experience gained from applying FFM to reawakening volcanoes after long repose periods (decades or centuries) is far more limited. For the particular case of applying FFM at basaltic volcanoes, the work by Bell and Kilburn (2006) is noteworthy. Generally, at basaltic volcanoes seismicity only increases a short time before the onset of an eruption. However, in some cases (in particular at Kilauea and Mauna Loa in Hawaii and at Etna in Italy) an exponential increase in the number of volcano-tectonic events has been observed a few months beforehand. The authors demonstrate that the time scales at which these accelerations appear present an inverse correlation with the rate of seismicity that can be considered "normal", which is in turn related to the stress state of the volcanic edifice. This new observation can be used to better constrain the forecasted time of failure at basaltic volcanoes that are the most difficult to predict with sufficient anticipation (as we show in Table 1).

**Table 1** List of application of FFM at persistently active volcanoes and those with recent episodes of activity.

| Author(s) | Volcano | Eruption date | Eruption type | Ω | Forecast period | Forecast type | Findings/results |
|---|---|---|---|---|---|---|---|
| Voight (1988) | Bezymyanny (Kamchatcka) | 12th Apr., 1960 | Explosive activity | Cumulative seismic strain release | ~10 days | Hindsight | Value of $\alpha$ close to 2 |
| Voight (1988) | Mt. St. Helens | 6th Sep., 1981 | Dome-building activity | Fault movement | ~10 days | Hindsight | Value of $\alpha$ close to 2 |
| Voight (1988) | Mt. St. Helens | 19th Mar., 1982 | Dome-building and explosive activity (minor) | Line length change | ~10 days | Hindsight | Value of $\alpha$ close to 2 |
| Voight (1988) | Mt. St. Helens | 19th Mar., 1982 | Dome-building and explosive activity (minor) | Tilt | ~3 weeks | Hindsight | Value of $\alpha$ close to 2 |
| Voight and Cornelius (1991) | Mt. St. Helens | 28th May, 1985 | Dome-building activity and lava extrusion | RSAM | ~12 days | Hindsight | FFM can be influenced by the structural mechanisms and conditions of load or stress |
| Voight and Cornelius (1991) | Mt. St. Helens | 22nd Oct., 1986 | Dome-building activity and lava extrusion | RSAM | ~5 days | Hindsight | FFM can be influenced by the structural mechanisms and conditions of load or stress |
| Voight and Cornelius (1991) | Redoubt (Alaska) | 14th Dec., 1989 | Major explosive eruption | RSAM | ~1 day | Hindsight | FFM can be influenced by the structural mechanisms and conditions of load or stress |
| Voight and Cornelius (1991) | Redoubt (Alaska) | 2nd Jan., 1990 | Major explosive and dome-destroying eruption | RSAM | ~8 days | Hindsight | FFM can be influenced by the structural mechanisms and conditions of load or stress |

**Table 1** (*Continued*)

| Author(s) | Volcano | Eruption date | Eruption type | Ω | Forecast period | Forecast type | Findings/results |
|---|---|---|---|---|---|---|---|
| Cornelius and Voight (1994) | Redoubt (Alaska) | Period after 2nd Jan., 1990 (Jan. through Apr.) | Succession of dome collapse eruptions | SSAM (freq. band near 2 Hz) | Several hours to few days | Hindsight | SSAM good tool for FFM |
| De la Cruz-Reyna and Reyes–Dávila (2001) | Colima (Mexico) | 21st Jul., 1994 | Moderate phreatic eruption | RSEM | ~6 days | Hindsight | Viscoelastic model |
| De la Cruz-Reyna and Reyes–Dávila (2001) | Colima (Mexico) | 20th Nov., 1998 | Dome-building activity and lava extrusion | RSEM | ~3 days | Foresight | Viscoelastic model |
| Reyes–Dávila and De la Cruz–Reyna (2002) | Colima (Mexico) | 10th Feb., 1999 17th Jul., 1999 29th Jul., 1999 | Moderate explosive eruptions | RSEM | Unrecognizable precursors | No forecast | No seismic precursors due to a open system (or complex open –close system) |
| Reyes–Dávila and De la Cruz–Reyna (2002) | Colima (Mexico) | 10th May 1999 22nd Feb., 2001 | Moderate explosive eruptions | RSEM | Precursors difficult to recognize few hours prior the event | Hindsight | Acceleration of seismicity at Colima could be associated to a closed system |
| Ortiz et al. (2003) | Villarrica (Chile) | 27th Oct., 2000 | Violent explosion | RSAM | ~7 days (Fig. 1) | Hindsight | The two forecasted explosions are related to the re-opening magmatic conduct |
| Ortiz et al. (2003) | Villarrica (Chile) | 29th Oct., 2000 | Violent explosion | RSAM | ~4 days (Fig. 1) | Hindsight | The two forecasted explosions are related to the re-opening magmatic conduct |

| Chastin and Main (2003) | Kilauea (Hawaii, USA) | 35 eruptions: period 1959–2000 | Effusive | Rate of seismic events | No precursors or short time scale (hours to few days) | Hindsight Statistical study | No threshold on the rate of events and no changes in the scaling exponent: no reliable indicators of pre-eruptive episodes |
|---|---|---|---|---|---|---|---|
| Grasso and Zaliapin (2004) | Piton de la Fournaise (La Reunion, France) | 15 eruptions: period 1988–2001 | Effusive | Number of seismic events | ~5 days | Hindsight Statistical study | Applicability limited by large number of false alarms. Main advantage: only count of daily events |
| Carniel et al. (2006) | Stromboli (Italy) | 5th Apr, 2003 | Powerful explosion | RSAM SSAM | ~2 days (Fig. 3) | Hindsight | Combination of different approaches: dynamical analysis and FFM |

## 7.2. Reawakening volcanoes

Cornelius and Voight (1996) used RSAM records of Pinatubo volcano, Philippines, to forecast an eruption with FFM. This was the first time that the method was successfully used in foresight rather than in hindsight. The observable was the inverse of the RSAM; its graphical representation between 1st and 10th June 1991 was extrapolated linearly to forecast an intersection (i.e. a failure) on 12th June. The forecast of an explosive eruption on 12th was issued, but the results of the analysis did not reach the authorities responsible for hazard evaluation. In any case, on 12th June a series of explosive eruptions began and produced pyroclastic flows. The series culminated on 15th June with a catastrophic eruption. In hindsight the analysis was then extended with the application of FFM to the observable SSAM. Different frequency bands were used and the results compared to those obtained by the RSAM. In this instance RSAM and SSAM showed similar patterns and the use of SSAM did not produce any significant advance over RSAM. This is in contrast to the case of Redoubt after 2nd January 1990, where the precursory seismic behaviour was related to LP events (Stephens et al., 1994).

Kilburn and Voight (1998) compared Equation (6) with new relationships for $\Omega$ derived from the growth of *microscopic* cracks, under the assumption that large scale fracturing produces the measured seismic events. The method was tested on the Soufrière Hills volcano, Montserrat, West Indies, where about 3 days before the breakout of andesitic lava on 15th November 1995 (and after more than 3 years of increased seismicity and phreatic explosions) the number of earthquakes increased by a factor of 10. This increase in the rate of seismic events was consistent with a growth, possibly episodic, of the fracture system through which the magma reached the surface. The recognition of this increased fracturing allowed the simplification of the linear interpretation of the inverse of the seismic events rate as a function of time. Using data from the 12 days prior to the lava breakout, Kilburn and Voight (1998) showed in hindsight that with a great dispersion of the data (the correlation coefficient was 0.79) the forecasted time of failure was 16th November (1 day after the real breakout). The authors also proved that using all the dataset with a non–linear fit produced a forecast date that was even further off the mark (19th–20th November). On the other hand, using only the last 4 days' worth of data (the correlation coefficient here is 0.94) the linear forecast was correctly issued for 15th November. The interpretation of this result is that in the datasets two significantly different trends are observed, i.e. two different data populations could be fitted with two different lines: one intersecting the time axis on the 15th (with a correlation coefficient $r^2 = 0.99$) and the other on the 21st (with $r^2 = 0.87$). The intermittent advance of a simple fracture system has been used to explain the presence of the two data populations, where the intermittency is induced by the different resistance of the various layers of rock being fractured or by the temporal increase in the effective resistance of the damaged zone.

The model proposed by Kilburn (2003) addresses the relation between two significant factors present before the eruption of volcanoes that have been quiescent for long periods. The first factor is the acceleration of seismicity, and the second is a slow extension of conduit faults that keep growing until they connect to

a pre-existing array of subvertical fractures and thus open a new path for the magma to reach the surface. In other words, the final state of the ascending magma is the result of the control imposed by the rock fracturing (between the magma front and the surface) at a given time. In particular, the fractures grow as they coalesce with other smaller pre-existing cracks. The failure is therefore the result of a multiscale process, where microscopic fracturing slowly leads to macroscopic failure. The equations governing the growth of the cracks are invariant under scale transformation, i.e. they do not depend on the size of the cracks or the duration of the process. The aim is to anticipate similar seismic patterns among eruption precursors, irrespective of the timescale used to measure the event rate. This model was tested in hindsight on the material failures at Pinatubo and at Soufrière Hills; two andesitic volcanoes that reawakened after centuries of quiescence. Therefore, this is a model that is potentially applicable in similar cases where forecast is difficult due to the lack of specific instrumental seismic data from previous eruptions (Figure 1).

Tárraga et al. (2004) applied FFM to forecast an explosive eruption that produced a 5 km high-eruptive column at the Tungurahua volcano in Ecuador. The start of the eruption was linked with the occurrence of an earthquake near the volcano, which a few hours later triggered the first explosion and an eruptive
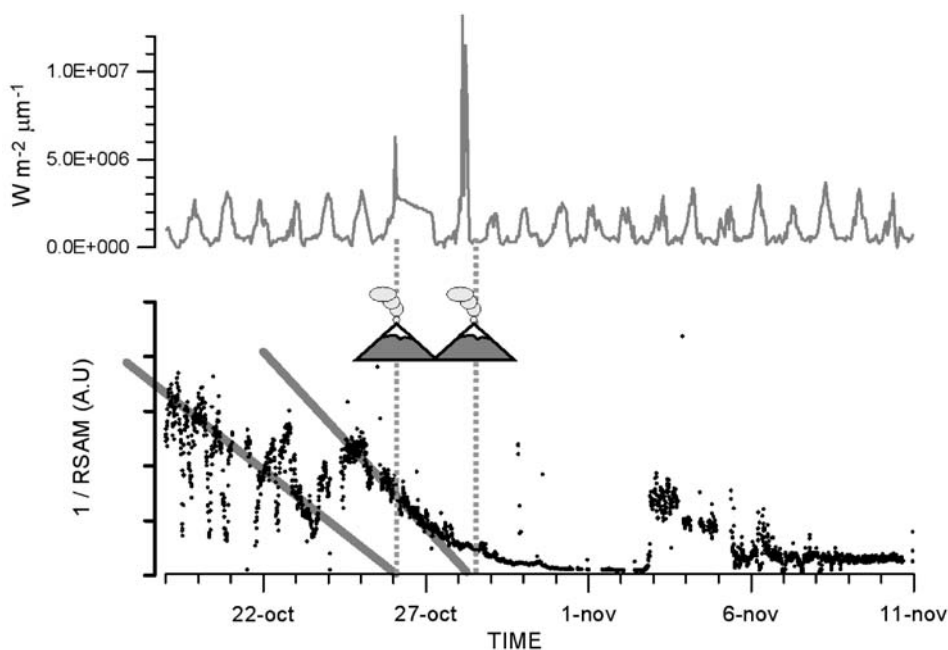


**Figure 1** Application of FFM to forecast the explosions at Villarrica volcano, Chile, on 26th and 29th October, 2000. Above: the two explosions are detected by the radiance around Villarrica crater by the Hot Spot monitoring program using GOES satellite images of the Hawaii Institute of Geophysics and Planetology (Harris et al., 2001). Below: the corresponding FFM forecasts using the RSAM observable (from Ortiz et al., 2003).

phase that continued for several days. The application of FFM to real-time seismic data (subjected to a low pass filter below the frequency of the characteristic tremor, i.e. 2.5 Hz) allowed the forecast of the onset of the explosive phase with more than 6 hours advance warning (Figures 2 and 3).
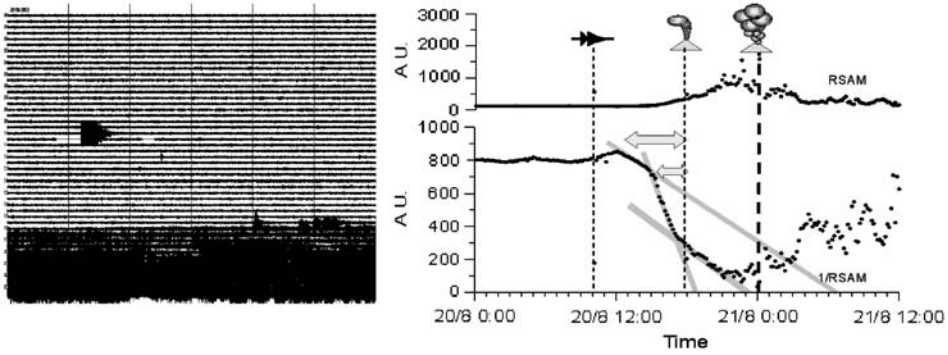


**Figure 2**    Left: Seismic record of Tungurahua volcano, Ecuador, on 20th August, 2003. A tectonic seismic event (M = 4.5) can be clearly seen in the graph, triggering the eruption of the volcano about 8 hours later. Right: Application of the FFM forecast to the SSAM, computed with a low pass filter at 2 Hz.
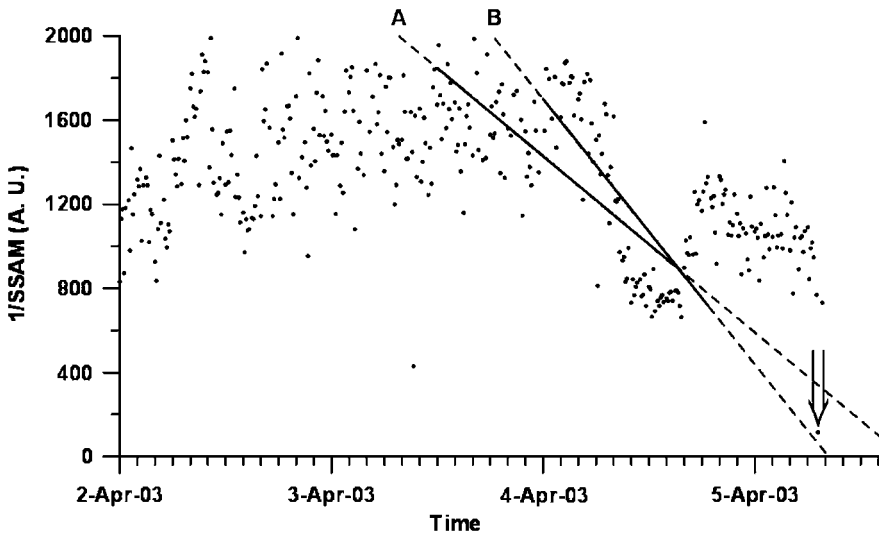


**Figure 3**    Application of the FFM forecast to the 5th April, 2003, explosion of Stromboli volcano, Italy. Time evolution of the inverse of the SSAM with a band-pass filter (FIR, centre frequency 1.2 Hz, attenuation 80 dB at 0.5 and 2.0 Hz) using 20 min time windows. The least-squares fit is carried out on the data recorded from 3rd April, 2003, 12:00 GMT to 4th April, 2003, 16:00 GMT (continuous line A), and from 4th April, 2003, 00:00 GMT to 4th April, 2003, 19:00 GMT (continuous line B). The extrapolated intersection of these lines (dashed lines) with the horizontal axis gives the forecasted time of the paroxysm, while the arrow indicates the actual occurrence of the paroxysm (5th April, 2003, 07:12 GMT) (data from Carniel et al., 2006).

## 7.3. Automated use of FFM in the evaluation of caldera unrest

One of the main drawbacks of FFM is its subjectivity. Any decrease in the evolution of the inverse of an observable versus time, e.g. 1/RSAM, can be potentially fitted with a linear function and generate a forecast for the time of failure. In order to avoid this subjectivity Tárraga et al. (2006) developed a fully automated program to generate, evaluate and validate the forecasts. The specific aim was to assess the situation on the island of Tenerife (Canary Islands, Spain), where after about a century of quiescence the possibility of reactivation within the Las Cañadas caldera is now debated. Firstly, the raw time series of the observable (RSEM or, more efficiently, its band-passed version SSEM) was broken down into a *seasonal* component, a *trend* component and a *remainder* component. This allowed a reduction in the effect of anthropogenic noise (a major problem on Tenerife). Maxima in the trend of the 1/SSEM time series were then sought and the subsequent decreasing part was used to fit a linear trend and forecast the time of failure. Although a high number of potential forecasts were generated, only those that fulfilled specific requirements were accepted. The criteria were as follows: a minimum number of data points in the decreasing section, a minimum quality of the fit in the least-square sense and finally a limited time difference between the maximum that initiates the decrease and the zero crossing that ends it (or, equivalently, a slope of minimal increase). The evaluation of the forecasts was completely automated with no human intervention. Of course, parameter values in the criteria above could be used to fine-tune the performances. The first decision to make was where to start a decreasing fit. The most natural choice was to start fitting a decrease at a maximum. The best results were obtained by choosing the local maximum in a 6-hour time window. Above all, this option produces a significant decrease in the number of false alarms. Figure 4 shows an example of how an automatic fit is generated. Testing of the program was conducted using several months' worth of seismic data recorded on Tenerife. This test process differs in one important aspect from the other studies discussed — namely that the forecasts related not to explosions, but tectonic events whose relationship to volcanic unrest is only speculated. The automation allowed the authors to carry out an in-depth statistical analysis of the forecasts and to evaluate the results in a Bayesian sense. Of particular note was the introduction of an objective evaluation factor. Let hypothesis 'H' be "day with a seismic event" and evidence 'E' equal "day with issued forecast". In the Bayesian evaluation:

$$P(H|E) = P(H)\frac{P(E|H)}{P(E)} \tag{21}$$

the quantity $P(E|H)/P(E)$ (which we call *forecast gain*) should be as great as possible. In particular, a forecast gain greater than 1 means that we *do* gain something by applying the forecast procedure, i.e. for those days for which a forecast is issued we *do* have a greater probability of having a seismic event than on a day chosen at random using only the prior statistics of days with and without events. It is noteworthy that in all the periods of seismic activity recorded in Tenerife and considered in the study the forecast gain is always found to be greater than 1.
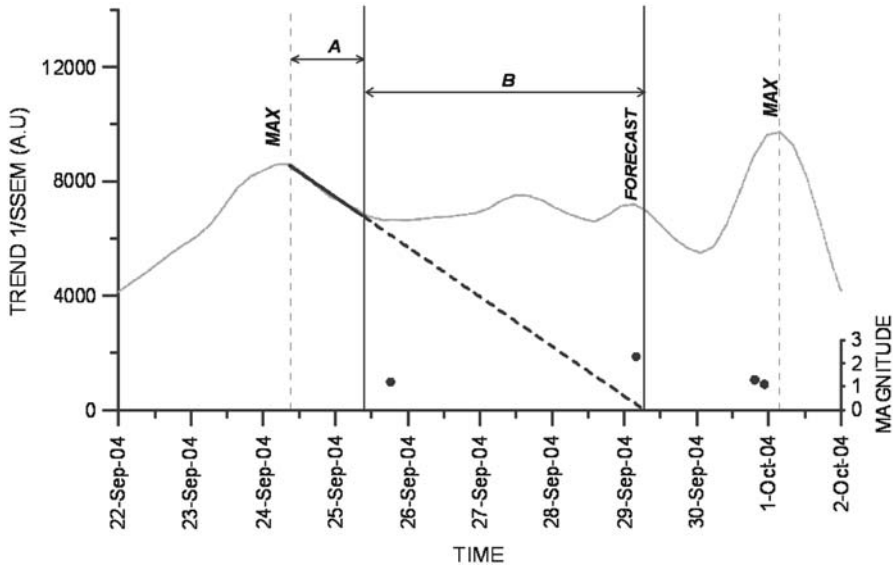
**Figure 4** Example of application of the automatic FFM forecast at Las Cañadas caldera, Tenerife, Spain. The black dots represent the seismic events (with their magnitudes as computed by Instituto Geográfico Nacional). The vertical dashed lines represent automatically detected maxima, *A* is the minimum number of data points required to generate the first fit (144) and corresponds to a time window of one day. *B* is the time difference between the generation of the forecast and the time of the forecast itself. In this case, the forecast was issued 3.8 days in advance — close to the maximum number of data points allowed, which is set to 4 days (data from Tárraga et al., 2006).

Moreover, changing the parameters involved in the rules of definition for the generation and subsequent validation of the automatic forecasts could still optimise the forecast gain. The main conclusion of the analysis of Tárraga et al. (2006) is that the seismic noise recorded in Tenerife, despite its strong anthropogenic contamination, contains significant information about the forthcoming tectonic events, i.e. a significant percentage must be of "volcanic" origin (where the term "volcanic" should be taken in its widest sense) and could include both directly magmatic effects and indirect effects. In fact, no examples are known in a purely tectonic setting where the occurrence of purely tectonic events can be forecasted by using continuous seismic noise recorded nearby. Moreover, the lack of statistically significant differences in the results obtained from the data of 2004 and 2005 clearly indicate that the Las Cañadas caldera currently remains in a state of disequilibrium (October 2006). The automated FFM analysis made it possible to prove the existence of a single process that both contributes to the generation of the seismic noise and to the generation of tectonic events, a process not previously observed in Tenerife and which may be related to a reawakening of the Las Cañadas caldera. We can only speculate on the nature of this process. Our preferred model is one that produces an accumulation of stress that finally leads to the generation of earthquakes. The stress changes also affect the magmatic system, which in turn excites the shallow hydrothermal system and finally produces the continuous

seismic noise. The earthquakes are often clustered in time, and clusters often include events both outside and below the island (Tárraga et al., 2006). This phenomenon suggests a stress propagation and would explain why tectonic events located outside the island can also be forecasted using the noise.

## 8. CONCLUSIONS

FFM is one of the few forecast methods with the capacity to define a time window during which a given eruptive event can be expected, as successfully demonstrated on several occasions over the last few years. These include actual forecasts in advance of moderate explosions, and hindcasts (or retrospective analyses) that show that the availability of continuously recorded seismic data could have forecast volcanic events if a different means of processing that information had been employed.

The observable that is linked to FFM (most commonly seismicity or ground deformation) accelerates as the fracturing of the system grows and the time of material failure becomes closer. It should be stated that on many occasions this observable, which is always a very indirect measure of the state of the system, could only be indirectly linked to the magmatic system through its interaction with the superficial system of fractures of the volcanic system or, especially in the case of calderas, of the superficial hydrothermal system. In these cases the forecasted "event" may not be an eruption, but instead another superficial phenomena such as tectonic faulting, landslide, or a change in the gas flux or gas composition of a fumarole due to modification of the feeder system.

Despite the positive examples observed, especially at well-instrumented stratovolcanoes, the FFM should still be considered a young methodology with room for improvement. However, once optimised it could be applied to other cases such as the "birth" of new monogenetic volcanic cones for which no published analysis is known. With respect to the specific case of calderas, the results are promising. The a posteriori analysis of past events qualitatively shows repetitive patterns suggesting that FFM methodology may well be useful. This was shown, for example, at the beginning of the Rabaul crisis in 1983 (Archbold et al., 1988) that ended with the eruption of 1994. Here, the increment in seismicity was observed during less than 24 h (GVN, 1994). Similar behaviour was observed at the Miyakejima caldera in 2000 (Geshi et al., 2002) where a forecast could have been made for the onset of the eruption that ended with a collapse phase. On the other hand, during the Campi Flegrei caldera crisis of 1983–85 (see Figure 5 in SEAN, 1984) the process did not result in an eruption. In this case the FFM might have highlighted the changes in parameters like deformation and fumarolic activity; thus demonstrating a change in the volcanic and/or hydrothermal system, but of course a forecasted time of failure in this instance would not have been useful.

Given the ratio between cost and performance, it is highly recommended that FFM methodology be established as a routine processing of seismic and/or deformation data. In fact, it would not require any major investment in terms of

new instrumentation. All that is required is the installation of new software, which can possibly run on the same platform already used for data acquisition.

Of course, FFM is not the perfect solution to the uncertainties of forecasting and the methodology should be always applied with caution. In particular, one has to take into account the fact that the model presented here, if applied to real monitoring data, can give forecasts at very different time scales and these are often too short. The consequences of its application for civil defence purposes could be serious, and forecasts could create genuine false alarms as the failure process can be aborted at any time or even be misinterpreted from the data in the first place (see De la Cruz-Reyna and Reyes-Dávila, 2001; Reyes-Dávila and De la Cruz-Reyna, 2002).

One of the major drawbacks of the FFM is its subjectivity. However, this can be overcome with complete automation of the processing tools (including the generation and validation of the forecasts), as has been demonstrated by the study at Las Cañadas caldera (Tárraga et al., 2006). Of course the generated forecasts should be assessed and utilised by trained personnel, but not indiscriminately. This should be done when the specific type of precursors used show a clear accelerating behaviour or when other dynamical parameters also show anomalies — for example the successful multiparametric approach applied at Stromboli volcano (Carniel et al., 2006). It is also important to note how the long term use of the FFM at a quiet or dormant volcano is an essential prerequisite in order to define the baseline or "normal behaviour" of the FFM, thus effectively reducing the number of potential false alarms.

## ACKNOWLEDGEMENTS

## REFERENCES

Aki, K., Koyanagi, R.Y., 1981. Deep volcanic tremor and magma ascent mechanism under Kilauea, Hawaii. J. Geophys. Res., 86, 7095–7109.

Alekseev, V.A., Alekseeva, N.G., Muravyev, Ya.D., Biryukova, T.P., Kuznetsov, I.P., 1995. Aerosols Precursor to the Avachinsky Volcano Eruption (Kamchatka) in January 1991. Dokl. AN, 345(5), 667–670.

Archbold, M.J., McKee, C.O., Talai, B., Mori, J., De Saint Ours, P., 1988. Electronic distance measuring network monitoring during the Rabaul seismicity deformational crisis of 1983–1985. J. Geophys. Res., 93(B10), 12123–12136.

Bell, A., Kilburn, C., 2006. Changing seismicity as a medium–term precursor to basaltic eruptions. Poster in Symposium IV-B: volcano monitoring; International Conference "Cities on Volcanoes 4", Quito, Ecuador. January 23–27, 2006.

Bevington, P.R., 1969. Data Reduction and Error Analysis for Physical Sciences. McGraw Hill, New York, NY, 336 pp.

Bland, D.R., 1960. The Theory of Linear Viscoelasticity. Pergamon Press, New York, pp. 1–125.

Carniel, R., Di Cecca, M., 1999. Dynamical tools for the analysis of long term evolution of volcanic tremor at Stromboli. Annali di Geofisica, 42(3), 483–495.

Carniel, R., Jaquet, O., Tárraga, M., 2008a. Perspectives of application of the geostatistical approach to volcano forecasting at different timescales. In: Gottsmann, J. and Martí, J. (Eds), Caldera volcanism. Analysis, modelling and response, Developments in Volcanology book series, Elsevier, pp. 471–489.

Carniel, R., Ortiz, R., Di Cecca, M., 2006b. Spectral and dynamical hints on the timescale of preparation of the 5 April 2003 explosion at Stromboli volcano. Can. J. Earth Sci., 43, 41–55.

Carniel, R., Tárraga, M., Jaquet, O., Ortiz, R., García, A., 2008b. The seismic noise at Las Cañadas volcanic caldera, Tenerife, Spain: persistence characterization, and possible relationship with regional tectonic events. J. Volcanol. Geotherm. Res., (in press).

Chadwick, W.W., Swanson, D.A., Iwatsubo, E.Y., Heliker, C.C., Leighley, T.A., 1983. Deformation monitoring at Mount St. Helens in 1981 and 1982. Science, 221, 1378–1380.

Chastin, S.F.M., Main, I.G., 2003. Statistical analysis of daily seismic event rate as a precursor to volcanic eruptions. Geophys. Res. Lett., 30(13), 1671.

Cornelius, R.R., Scott, P.A., 1993. A materials failure relation of accelerating creep as empirical description of damage accumulation. Rock Mech. Rock Eng., 26, 233–252.

Cornelius, R.R., Voight, B., 1994. Seimological aspects of the 1989–1990 eruption at Redoubt Volcano, Alaska: The Materials Failure Forecast Method (FFM) with RSAM and SSAM seismic data. In: Miller, T.P. and Chouet, B.A. (Eds), The 1989–1990 eruptions of Redoubt Volcano. Alaska: J. Volcanol. Geotherm. Res., Vol. 62, pp. 469–498.

Cornelius, R.R., Voight, B., 1995. Graphical and PC-software analysis of volcano eruption precursors according to the Materials Failure Forecast Method (FFM). J. Volcanol. Geotherm. Res., 64, 295–320.

Cornelius, R.R., Voight, B., 1996. Real-time seismic amplitude measurement (RSAM) and seismic spectral amplitude measurement (SSAM) analyses with the materials failure forecast method (FFM), June 1991 explosive eruption at Mount Pinatubo. In: Newhall, C.G. and Punongbayan, R.S. (Eds), Fire and Mud: Eruptions and Lahars of Mount Pinatubo, Philippines. University of Washington Press, Seattle, pp. 249–268.

De la Cruz-Reyna, S., Reyes-Dávila, G., 2001. A model to describe precursory material-failure phenomena: application to short-term forecasting at Colima volcano. Mexico Bull. Volcanol., 63, 297–308.

Dzurisin, D., Westphal, J.A., Johnson, D.J., 1983. Eruption prediction aided by electronic tiltmeter data at Mount St. Helens. Science, 221, 1381–1383.

Endo, T.E., Murray, T., 1991. Real-time seismic amplitude measurement (RSAM). A volcano monitoring and prediction tool. Bull. Volcanol., 53, 533–545.

Fehler, M., 1983. Observations of volcanic tremor at Mount St. Helens volcano. J. Geophys. Res., 88, 3476–3484.

Fukuzono, T., 1985. A new method for predicting the failure time of a slope. In: Proc. IV International Conference and Field Workshop on Landslides, Tokyo.

Fukuzono, T., 1990. Recent studies on time prediction of slope failure. Landslide News, 4, 9–12.

Fukuzono, T., Terashima, H., 1985. Experimental study of slope failure in cohesive soils caused by rainfall. In: Int Symp on Erosion, Debris Flow and Disaster Prevention. Tsukaba, Japan.

Geshi, N., Shimano, T., Chiba, T., Nakada, S., 2002. Caldera collapse during the 2000 eruption of Miyakejima Volcano, Japan. Bull. Volcanol., 64, 55–68.

Grasso, J.-R., Zaliapin, I., 2004. Predictability of volcano eruption: lessons from a basaltic effusive volcano. Geophys. Res. Lett., 31(5), L05602, doi: 10.1029/2003GL019022.

Gudmundsson, A., Marinoni, L.B., Marti, J., 1999. Injection and arrest of dykes: implications for volcanic hazards. J. Volcanol. Geotherm. Res., 88(1-2), 1–13.

GVN, 1994. Rabaul. Smithsonian Institution Global Volcanism Network Bull. 19, 09.

Harris, A.J.L., E. Pilger, E., Flynn, L.P., 2001. Web-based hot spot monitoring using GOES: what it is and how it works. Adv. Environ. Monit. Model., 1, 3–31.

Hill, D.P., Langbein, J.O., Prejean, S., 2003. Relations between seismicity and deformation during unrest in Long Valley Caldera, California, from 1995 through 1999. J. Volcanol. Geotherm. Res., 127(3-4), 175–193.

Jaquet, O., Carniel, R., 2001. Stochastic modelling at Stromboli: a volcano with remarkable memory. J. Volcanol. Geotherm. Res., 105, 249–262.

Keilis-Borok, V.I., Knopoff, L., Rotwain, I.M., Allen, C.R., 1988. Intermediate-term prediction of occurrence times of strong earthquakes. Nature, 335(6192), 690–694.

Kilburn, C.R.J., 2003. Multiscale fracturing as a key to forecasting volcanic eruptions. J. Volcanol. Geotherm. Res., 125, 271–289.

Kilburn, C.R.J., Voight, B., 1998. Slow rock fracture as eruption precursor at Soufriere Hills volcano, Montserrat. Geophys. Res. Lett., 25(19), 3665–3668.

Malone, S.D., Boyko, C., Weaver, C.S., 1983. Seismic precursors to the Mount St. Helens eruptions in 1981 and 1982. Science, 221, 1376–1378.

Mulargia, F., 1992. Time association between series of geophysical events. Phys. Earth Planet Inter., 71, 147–153.

Mulargia, F., 1997. Retrospective validation of the time association of precursors. Geophys. J. Int., 131, 500–504.

Mulargia, F., Gasperini, P., 1996. Precursor candidacy and validation. Geophys. Res. Lett., 23(11), 1323–1326.

Ortiz, R., García, A., 2000. Seguimiento y pronóstico de erupciones. In: Astiz, M. and García, A. (Eds), Curso Internacional de Volcanología y Geofísica Volcánica. Servicio de Publicaciones Excmo. Cabildo Insular de Lanzarote, Serie Casa de los Volcanes no. 7, pp. 215–226.

Ortiz, R., Moreno, H., García, A., Fuentealba, G., Astiz, M., Peña, P., Sánchez, N., Tárraga, M., 2003. Villarrica volcano (Chile): characteristics of the volcanic tremor and forecasting of small explosions by means of a material failure method. J. Volcanol. Geotherm. Res., 128, 247–259.

Reyes-Dávila, G.A., De la Cruz-Reyna, S., 2002. Experience in the short-term eruption forecasting at Volcán de Colima, México, and public response to forecasts. J. Volcanol. Geotherm. Res., 117, 121–127.

Rogers, J.A., Stephens, J.A., 1995. SSAM: Real Time Seismic Spectral Amplitude Measurement on PC and its application to volcano monitoring. Bull. Seism. Soc. Am., 85, 632–639.

Sandri, L., Marzocchi, W., Zaccarelli, L., 2004. A new perspective in identifying the precursory patterns of eruptions. Bull. Volcanol., 66, 263–275.

SEAN, 1984. Campi Flegrei. Smithsonian Institution Global Volcanism Network Bull. 09,04.

Shebalin, P., Keilis-Borok, V., Gabrielov, A., Zaliapin, I., Turcotte, D., 2006. Short-term earthquake prediction by reverse analysis of lithosphere dynamics. Tectonophysics, 413, 63–75.

Sparks, R.S.J., 2003. Forecasting volcanic eruptions. Earth Planet. Sci. Lett., 210, 1–15.

Stephens, C.D., Chouet, B.A., Page, R.A., Lahr, J.C., Power, J.A., 1994. Seismological aspects of the 1989–1990 eruptions at Redoubt Volcano, Alaska: The SSAM perspective. J. Volcanol. Geotherm. Res., 62, 153–182.

Swanson, D.A., Casadevall, T.J., Dzurisin, D., Malone, S.D., Newhall, C.G., Weaver, C.S., 1983. Predicting eruptions at Mount St. Helens, June 1980 through December 1982. Science, 221, 1369–1376.

Tárraga, M., Carniel, R., Ortiz, R., Marrero, J.M., García, A., 2006. On the predictability of volcano-tectonic events by low frequency seismic noise analysis at Teide-Pico Viejo volcanic complex, Canary Islands. Nat. Hazards Earth Syst. Sci., 6, 365–376.

Tárraga, M., Ortiz, R., García, A., Hall, M., Molina, I., Llinares, A., 2004. Aplicación del Material Failure Forecast Method (FFM) para el pronóstico de la reactivación del Volcán Tungurahua (Ecuador) en Agosto de 2003. Resúmenes 4ª Asamblea Hispano–Portuguesa de Geodesia y Geofísica, 591–592.

Todesco, M., 2008. Hydrothermal fluid circulation and its effect on caldera unrest. In: Gottsmann, J. and Martí, J. (Eds), Caldera volcanism. Analysis, modelling and response, Developments in Volcanology book series, Elsevier, pp. 393–410.

Todesco, M., Rutqvist, J., Chiodini, G., Pruess, K., Oldenburg, C.M., 2004. Modeling of recent volcanic episodes at Phlegrean Fields (Italy): geochemical variations and ground deformation. Geothermics, 33(4), 531–547.

Tokarev, P.I., 1963. On a possibility of forecasting of Bezymianny volcano eruptions according to seismic data. Bull. Volcanol., 26, 379–386.

Tokarev, P.I., 1983. Experience in predicting volcanic eruptions in the USSR. In: Tazieff, H. and Sabroux, J.C. (Eds), Forecasting Volcanic Events. Elsevier, Amsterdam, pp. 257–268.

Voight, B., 1988. A method for prediction of volcanic eruptions. Nature, 332(10), 125–130.

Voight, B., 1989. A relation to describe rate-dependent material failure. Science, 243, 200–203.

Voight, B., Cornelius, R.R., 1991. Prospects for eruption prediction in near real-time. Nature, 350, 695–698.

This page intentionally left blank

# Perspectives on the Application of the Geostatistical Approach to Volcano Forecasting at Different Time Scales

Roberto Carniel[1,*], Olivier Jaquet[2] *and* Marta Tárraga[3]

## Contents

## Abstract

In the problem of forecasting a volcanic eruptive scenario, empirical or observational time series must be examined in order to look for precursory behaviour. A key concept in

*Corresponding author. Tel.: +39 0432 558749; Fax: +39 0432 558700
*E-mail address:* roberto.carniel@uniud.it

[1] Dipartimento di Georisorse e Territorio, Università di Udine, Via Cotonificio 114, 33100 Udine, Italy
[2] In2Earth Modelling Ltd, Switzerland
[3] Departamento de Volcanología, Museo Nacional de Ciencias Naturales, CSIC, Madrid, Spain

this respect is that of memory or persistence of a given time series. A time series that does not keep some memory of its past cannot, in fact, provide information about the future of the evolving volcanic process, i.e. it cannot help to forecast an eruption. The geostatistical approach aims to identify this memory, if it exists, quantify its duration and exploit its potential in forecasting, and can be applied not only in the time but also in the space domain. In this paper, a review is presented of the state of the art, and an application to the case of a possible reawakening of a caldera is presented.

## 1. INTRODUCTION

A key problem in volcanology is the issue of forecasting, with purposes that can range from pure research (e.g. demonstrating the validity of a theoretical model to explain a given phenomenon) to civil protection (e.g. moderating the potentially catastrophic consequences for society of a volcanic eruption).

Volcanic risk can be separated into three factors, i.e. hazard, vulnerability and exposure. Given a specific time window and a specific geographical area of interest, hazard generally is taken to represent the probability of occurrence of a potentially damaging event (although other definitions are sometimes used). We then need to consider the extent to which a given object suffers damage by this event. This, by analogy to seismic risk (Riuscetti et al., 1997), defines the vulnerability. Finally, we have to weigh the value of this object, potentially exposed to the event, and this leads to the concept of exposure. Of course, the concept of 'object' can be extended to any element at risk, to arrive to a final definition of volcanic risk (UNDRO, 1979) that is a measure of the expected number of lives lost, persons injured, damage to property or disruption of economic activity due to a given volcanic event.

Vulnerability can, in general, be reduced; in contrast, volcanic hazard cannot, in general, be mitigated, and forecasts of volcanic hazards are, therefore, an essential input for risk assessment. The time scale we are concerned about is also of paramount importance. We can assess volcanic hazards at short term (days to weeks), e.g. while following the course of an eruption, or with the purpose of scheduling tourist visits to a crater area, at mid term (months to years), e.g. while monitoring an active volcano or an active caldera and trying to record the first signs of an upcoming eruption, or at long term (few years to hundreds of thousands of years), e.g. when choosing the site for an industrial plant or a nuclear waste repository.

An increase in monitoring capabilities has offered the availability of multi–parametric datasets on several volcanoes, a source of information which can and should be exploited (e.g. Ripepe et al., 2002; Harris et al., 2005; Green and Neuberg, 2005; Jones et al., 2006). At the same time, forecasting based on these datasets has become more quantitative, and research in this field is still under strong development. At short term, many authors have tackled the problem of forecasting in a deterministic sense, e.g. by introducing the material failure forecast method (FFM), proposed after the Mt. St. Helens eruption, by Voight (1988), Voight and Cornelius (1991) and Cornelius and Voight (1995), based on the hypothesis that the growth of magma paths is driven by rock failure in the edifice induced by

overpressure in the magma chamber. Several case histories with this kind of approach are described in another paper in this volume (Tárraga et al., 2008). However, due to their deterministic nature, aleatory and epistemic uncertainties (Woo, 1999) have not been associated with such forecasting, which suffers also from a high degree of subjectivity that only recently has been the subject of research (Tárraga et al., 2006). The uncertainty can be mainly ascribed to the inevitably imperfect knowledge of nonlinear volcanic processes and to the insufficient amount of monitoring information, always affected by logistical and economical limitations. For these reasons, the most common approach, and probably the most sensible, to the forecasting of volcanic eruptions, especially at medium–long term, is based on a probabilistic formalism (Sparks, 2003) rather than on a deterministic approach.

## 2. The Probabilistic Approach

We can date early probabilistic approaches back to forecasting at mid–long term to the 1960s, when Wickman (1966) and Reyment (1969) proposed stochastic models for the study of volcanic eruption patterns on specific volcanoes. Since then, several stochastic models have been developed, e.g. for establishing a radioactive waste facility at Yucca Mountain in Nevada. In the latter case, the models proposed were first based on a complete space–time independence of the eruptive events, which led to the choice of a homogeneous Poisson model (Crowe et al., 1982). The Poisson process is the most common model to generate events in space–time where the occurrence of one event does not affect the generation of subsequent events, i.e. it is a process without memory neither in time nor in space. A first time-dependence is introduced by the Markovian models (Aspinall et al., 2006) where the current event depends only on the immediate preceding state and not on the previous history of the system. The introduction of a time-dependence led Ho (1991) to propose a Weibull–Poisson model for the estimation of eruption recurrence rate, and Ho and Smith (1998) to propose a nonhomogeneous spatio–temporal Poisson model. The Weibull distribution, in particular, is related to material, rock-mechanical failure models. More recently, Connor and Hill (1995) proposed nearest-neighbour nonhomogeneous Poisson models that allowed them to estimate the probability of volcanic eruptions taking into account the spatial distribution of volcanic centres, models which were then extended by Martin et al. (2004) in a Bayesian framework to be applied to the Tohoku volcanic arc in Japan. However, there is still a lack of an adequate characterisation of potentially complex space-time structure that is observed on volcanoes, which cannot be represented by a simple Poisson (no memory) or Markov (one-step memory) process.

For short-term forecasting, a probabilistic approach was proposed by Connor et al. (2003). They showed that a probability distribution characterised by competing processes could explain the repose intervals between 75 vulcanian explosions of Soufrière Hills volcano, Montserrat, in 1997. The physical basis proposed to justify the use of a probabilistic log-logistic model for this sequence involves the presence of

two competing processes operating in the upper volcano conduit on different time scales: pressurization on one hand, due to rheological stiffening and gas exsolution, and depressurization on the other, due to development of permeability and gas escape.

Another probabilistic method proposed in the literature is the Event Tree approach (Newhall and Hoblitt, 2001; Marzocchi et al., 2004). The procedure is based on a Bayesian approach that produces a probability estimation of any possible event making use of all available information including not only monitoring (current) data but also models, historical and geological data. The theoretical knowledge is used to estimate an *a priori* probability distribution that can then be modified on the basis of new monitoring data or other information that becomes available. The scheme allows epistemic and aleatoric uncertainties (Woo, 1999) to be dealt with in a formal way, through estimation of probability distributions at each node of the event tree. The scheme was applied to Vesuvius (Marzocchi et al., 2004) to quantitatively estimate both long- and short-term volcanic hazard, showing that there is a probability of up to 20% that next eruption could be larger than the so-called 'maximum expected event' currently used by the Italian Civil Protection Department in the emergency response plan. Another scheme that allows us to mix datasets of heterogeneous origin, the results of their analysis and even expert opinions is the framework of Bayesian Belief Networks (BBN) (Aspinall et al., 2003). Recently, the introduction of formal logic in this scheme has become the subject of research (Pshenichny et al., 2005), in order to formally separate the knowledge present in the models and expert judgments from what all that can on the contrary be considered 'data', and to introduce proper tools for processing such different forms of knowledge.

One common problem that limits many classical statistical techniques is the availability of geophysical datasets that are not only small but also show gaps (missing data). As a result, for forecasting purposes, multivariate stochastic methods in the space–time domain are needed that must be able to handle these data gaps. The importance of the use of multivariate data has been recognised recently (e.g. Jaquet and Carniel, 2003), along with complementary approaches such as pattern recognition (e.g. Sandri et al., 2004).

Geostatistics (Chilès and Delfiner, 1999) provides a general framework as well as methods and models adaptable to forecasting issues in space and time. In what follows, we summarise some theoretical aspects of geostatistical methods and models for the analysis and estimation of volcanic hazards at short and long term, and present a number of case studies.

## 3. The Geostatistical Approach

In a context rather distant from volcanology, i.e. the field of ore-reserve estimation, Matheron (1962) introduced the concept of geostatistics, which was then applied to a wide range of fields spanning from hydrology to geology and meteorology, where it was further developed methodologically (Chilès and Delfiner, 1999), until finally reaching the field of volcanology where it was

introduced first, in a space–time context, for the estimation of volcanic hazards in the Osteifel region (Jaquet et al., 2000), then to study the temporal patterns of Stromboli volcano eruptive activity in a monoparametric sense (Jaquet and Carniel, 2001), and later still in a multiparametric sense (Jaquet and Carniel, 2003). The geostatistical methodology can be schematically subdivided into four phases: (a) detection of (cross) correlation, (b) modelling of (cross) correlation, (c) identification of precursors and (d) stochastic forecasting.

## 3.1. Detection of (cross) correlation

One key point that differentiates this approach from the others mentioned above is the recognition that volcanic events do not seem to occur at random in time; on the contrary, the evidence is that events are clustered in time, i.e. correlated in time, and the process thus exhibits a kind of memory of its (more or less recent) past. The length of time this memory lasts is an important characterisation of the system, which can be quantified using a tool called variogram, introduced by Matheron (1962) in the field of geostatistics, again first in a spatial domain rather than in the time domain. In other words, the variogram quantifies the scales at which correlations occur in the time domain. This memory of past activity expresses the persistence of its behaviour, and that persistence is obviously the first clue to look at when considering a time series as a potential source of information on precursors. The classical autocovariance can also provide similar information, but the variogram $\gamma_{ii}(\tau)$ has wider applicability, as it only requires the stationarity of the increments of the studied stochastic process in order to obtain the following definition in the monovariate case:

$$\gamma_{ii}(\tau) = \frac{1}{2} E[(V_i(t + \tau) - V_i(t))^2] \tag{1}$$

where $V_i(t)$ is a stochastic process of index $i$, $\tau$ the time lag and $E[\,]$ the mathematical expectation. Further details are given in Jaquet et al. (2006b).

In the multivariate case, if $K$ intrinsic stochastic processes are considered, we need a multivariate definition that aims to quantify the cross correlation in time via a new entity called cross variogram $\gamma_{ij}(\tau)$ (Wackernagel, 2003):

$$\gamma_{ij}(\tau) = \frac{1}{2} E[(V_i(t + \tau) - V_i(t))(V_j(t + \tau) - V_j(t))] \tag{2}$$

where each $V_i(t)$, $V_j(t)$ is a stochastic process ($i, j = 1, \ldots, K$). Of these theoretical variograms and cross variograms, their empirical 'estimates' can be directly computed from observed time series:

$$\gamma_{ij}^*(\tau) = \frac{1}{2n_\tau} \sum_{\alpha=1}^{n_\tau} (V_i(t_\alpha + \tau) - V_i(t_\alpha))(V_j(t_\alpha + \tau) - V_j(t_\alpha)) \tag{3}$$

using all the $n_\tau$ pairs of data which are separated in time by the same time lag $\tau$, which for irregular sampled time series can be considered with a certain tolerance by subdividing values into 'classes'.

## 3.2. Modelling of (cross) correlation

The empirical variogram can be then modelled in order to parameterise observed behaviour. The properties required by a variogram model are discussed by Chilès and Delfiner (1999). As an example, a model $\gamma_M(\tau)$ of a spherical variogram with a discontinuity at the origin was used by Jaquet and Carniel (2001) and Jaquet and Carniel (2003) to describe the behaviour of seismic time series at Stromboli volcano:

$$\gamma_M(\tau) = b_0 + b_1 \left[ \frac{3}{2}\frac{\tau}{a} - \frac{1}{2}\frac{\tau^3}{a^3} \right], \qquad \tau \leq a$$
$$\gamma_M(\tau) = b_0 + b_1, \qquad \tau > a$$

(4)

The 'memory time scale' needed to characterise persistence is given by the parameter $a$, while the two parameters $b_0$ and $b_1$ represent the intensity of the random and stochastic components of the time series, respectively.

## 3.3. Identification of precursors and stochastic forecasting at short term

As already mentioned, potential precursors can be found only within a time series that shows some level of persistence. Once this is established, we can, for example, monitor the variogram parameters $b_0$ and $b_1$ mentioned above as a function of time, and study their relative behaviour when approaching the onset of eruptive events (Jaquet et al., 2006a). Another way of looking for potential precursors is the stochastic decomposition of experimental time series, e.g. by kriging analysis (Chilès and Delfiner, 1999).

Once a persistent time series is identified, its behaviour can be used to examine the precursors of selected eruptive scenarios for forecasting, i.e. estimate their probability of occurrence in a given future time window, given the associated uncertainty. For instance, stochastic simulation (Chilès and Delfiner, 1999) can be used within the framework of Monte Carlo methods. A number of simulations which respect the data points of the empirical time series are generated, possibly taking into account all the latest time history that could come from the monitoring (Jaquet et al., 2006a). It is obvious that this must always be related to a given time scale, i.e. a given time window in the future.

## 3.4. Stochastic forecasting at medium–long term

Passing from a short time window to a medium- or long-time scale, spatial considerations inevitably come into play. Just as in a related field such as landslide hazard (Ayalew and Yamagishi, 2005), this is true even in the limited spatial context of a volcanic caldera (Gomes et al., 2005). Not only that, one should take into account the propensity (or susceptibility) of a given area to become the locus of a new vent (Cornella et al., 2004; Martí et al., 2006) or even of a completely new volcanic centre (Jaquet et al., 2000, 2006c), i.e. the problem moves from a

time-only domain and, of necessity, becomes spatio–temporal. Of course, susceptibility is only the first step, as further complications can arise before reaching an hazard estimate for a given location, such as the modelling of ash dispersion (Costa et al., 2006), lava flow coverage (Damiani et al., 2006) etc. In summary, the final product we are looking at is the probability that a specific area (space-dependence) will be reached by volcanic products during a given time window (time-dependence). For this reason, in a related geostatistical model, both dependencies should be taken into account.

For the time component, a Cox point process (Cox, 1955) is usually selected (Jaquet et al., 2000; Jaquet and Carniel, 2001) which corresponds to a Poisson point arrival process whose intensity is, in turn, a stochastic process (Lantuéjoul, 2002). The probability system becomes therefore doubly stochastic. For the spatial component, a hazard function $H(x)$ should, as mentioned above, provide an estimate of the probability of a given point of coordinate $x$ to be affected by a given volcanic product in a given time window. Also, in space the volcanic sources are not located at random but show spatial clustering, suggesting one might apply the Cox process also in space (Jaquet et al., 2000, 2006c). If sophisticated modelling (Costa et al., 2006; Damiani et al., 2006) is not available, the surface covered by a given eruption product can be roughly modelled by using simple geometrical shapes with random variables generating their parameters. As in the purely time-dependent case, so also in the spatio–temporal case, can the Monte Carlo approach be used to evaluate the probability of occurrence of a series of possible volcanic scenarios. Further details can be found in Jaquet and Carniel (2006).

## 4. Case Studies

In the following, the geostatistical approach is applied to the study of volcanic activity in the short term at Stromboli, Italy and Soufrière Hills, Montserrat, which represent two published case studies exhibiting features that could represent a possible full range of different volcanoes. Then, the long-term case is illustrated by two other published examples: Osteifel, Germany and Tohoku, Japan. Finally, the application of the concept to the evaluation of the crisis related to the possible reawakening of the Las Cañadas caldera in Tenerife is presented.

## 4.1. Stromboli volcano

Stromboli volcano (Italy) is the archetype for strombolian activity (Carniel and Iacop, 1996), and another important feature of this volcano is the presence of continuous volcanic tremor (Ripepe and Gordeev, 1999) which is an invaluable source of information on the dynamics of the volcanic system (Carniel and Di Cecca, 1999). About twice a year, on average, the volcano shows paroxysmal activity that can easily affect tourists visiting the volcano. Jaquet and Carniel (2001) examined Stromboli seismic data recorded between 1992 and 2001 (Alean et al., 2006) with a geostatistical approach, using both the daily number of strombolian

events and the tremor intensity. The empirical variograms and cross variograms allowed Jaquet and Carniel (2001) to highlight the remarkable memory of the system that can last more than 400 days, and two memory regimes with different time scales (Jaquet and Carniel, 2001) which were a medium memory of 60 days, and a longer memory of 190 days. These were identified from the variogram behaviour; two structures with different growing slopes are, in fact, observed on the experimental curve.

Jaquet and Carniel (2003) investigated further how these memory effects can be used for forecasting. Taking a stochastic decomposition by multivariate kriging analysis, the time behaviour of the two memory components (60 and 190 days) can be jointly analysed in relation to the occurrences of the paroxysmal phases, revealing the following traits. Two small lava flows seem to form a distinct statistical population, being associated with high values of both components. On the other hand, the vast majority of the explosive paroxysmal phases is associated with a negative value of at least one of the two components. This finding led Jaquet and Carniel (2003) to propose the definition of a 'grade of concern'. Of course, entering the highest grade of concern does not mean we will inevitably have a paroxysm, and there is nothing like a 'no concern' state, due to the continuous activity of Stromboli.

## 4.2. Soufrière Hills volcano

Soufrière Hills volcano (Montserrat, West Indies) entered a dome-growing eruption in July 1995, which is still continuing (MVO, 2007). The andesite dome growth (Sparks and Young, 2002) was interrupted twice by dormancy stages (MVO, 2007). Jaquet et al. (2006a) investigated a long part of this eruption (1996–2003) with a stochastic approach, in particular, investigating the onset of the new dome growth after the first dormancy. The daily number and the cumulative energy of seismic events recorded at Montserrat were used in the study, as currently classified by MVO: volcano-tectonic (VT), rockfall (RF), long-period (LP) and hybrid (H), although the significance of the distinction between LP and H events is currently being questioned (Green and Neuberg, 2006). The time evolution of variogram parameters was monitored, highlighting different behaviour for periods of dome growth and dormancy. Most important, however, was the recognition of trends that developed in the variograms before the new dome growth of November 1999, indicating the precursory emergence of structured and persistent behaviour. The realisation of forecasts with uncertainty requires Monte Carlo simulation for potential volcanic scenarios (Jaquet et al., 2006a). The estimated probabilities then correspond to an uncertainty measure of hazard occurrence for a given period, which can be used for risk analysis.

Jaquet et al. (2006b) studied a series of 75 vulcanian explosions (Connor et al., 2003) that occurred following the collapse of the lava dome on 21st September 1997. The data include the time of each explosion and the real-time seismic amplitude measurement (RSAM). The variogram results show that the system had a memory of 60–87 h at that time, which means that some influence from an individual explosion was retained for about eight subsequent explosions. Thus, the

history of pressure variations is 'stored' in the ascending magma by kinetic effects related to degassing, crystallization and rheological stiffening. Jaquet et al. (2006b) then showed how this memory could help constrain the physical parameters of the system (ascent rates, conduit cross sections etc.) and contribute to forecasting also by establishing how sequential volcanic events are correlated.

## 4.3. Osteifel volcanic region

The Osteifel region in Germany is a volcanic field where the last eruption occurred about 13 ky BP — one of the youngest in central Europe — but with no current signs of magmatic activity. However, any reactivation now could be catastrophic due to modern day population and industrial density; hence, estimates of the probability of eruptions constitute an important contribution to the hazard and risk analysis of the area (Jaquet et al., 2000). Most of the eruptions, in fact, produced just mafic cinder cones, maars and tuff rings, but some showed a phonolitic composition and include few plinian, large-scale eruptions. To estimate the relative probabilities of occurrence of such eruptions, a 650 ky long geologic dataset was used. A 'sampling period' of 12 ky is the maximum time resolution achievable, and a clear clustering in time is observed, indicating that the number of eruptions is correlated up to ca. 80 ky. This 'memory of the volcanic field' can be interpreted as the average duration of volcanic activity and repose periods. The age of last eruption — only 13 ky ago — is then a clear indication that the Osteifel volcanic field should not be considered extinct.

On the basis of the past observed volcanic activity, different eruptive scenarios were considered, ranging from relatively quiet cinder cones to potentially plinian phonolitic centres, and Monte Carlo simulations were carried out to estimate the mean number of future events in time and space. The resulting hazard maps display the probability of a specific volcanic event that can potentially occur in the future over a period of 12 ky. An important consideration is that one can assume that the occurrence of volcanic events in the Osteifel region is random at the scale of a century. Therefore, probability estimates for the next 100 years can be easily derived, leading to a 'qualitatively low' volcanic risk estimate (Jaquet et al., 2000).

## 4.4. Tohoku volcanic region

For safety reasons, the performance of potential sites for the geologic storage of high-level radioactive waste (HLW) must be evaluated over periods of $10^5$–$10^6$ years. At this time scale, volcanic events are likely to occur, and their consequences through a geological HLW repository are substantial. Therefore, hazards associated with such events are required to be assessed. In relation to HLW repository issues in Japan (Apted et al., 2004), probabilistic models are currently being developed for the forecasting at long term of volcanic events (Jaquet et al., 2006c). In this case, the problem is the estimation of the probability of a new volcano forming within a small area of the region of interest (e.g. a monogenetic volcanic field). This issue was addressed in a probabilistic framework by introducing the concept of potential of volcanism, which was used as a basis for the development of a set of probabilistic

models. The proposed outcome is a probabilistic methodology for the long-term assessment of volcanic hazard that uses a suite of probabilistic models (Poisson, nonhomogeneous Poisson and Cox processes) for the assessment of event uncertainty from conceptual to parametric. Such method will become operational and will provide the necessary input for decision-making in the stages of investigation of the concerned regions. The same authors are now expanding the concept of potential of volcanism by accounting for multivariate correlation. In particular, data from seismic tomography (Hasegawa and Nakajima, 2004) is being integrated into the probabilistic calculations of volcanic hazards.

## 4.5. Las Cañadas caldera

Tenerife is the largest island of the Canaries archipelago in the Atlantic ocean, with a large, composite, subaerial basaltic shield structure built between 12 and 3.3 My BP, and additional, more differentiated, magmas erupted in the last 3.5 My at the central, composite Las Cañadas volcanic complex (Martí et al., 1994). The construction of the Las Cañadas edifice was truncated by the formation of the Las Cañadas caldera, currently attributed to a series of vertical collapses (Martí and Gudmundsson, 2000). A double stratovolcano has formed on the northern border of the Caldera over the last 0.18 Ma: the Teide–Pico Viejo complex, which shows a complete series of eruptive styles from basaltic (effusive) to phonolitic (explosive). The subplinian eruption of Montaña Blanca, about 2,000 years BP, is one of the most recent phonolitic events on the southern Teide flank. Several minor basaltic eruptions have occurred in historical times, the last in 1909 in Chinyero, near Pico Viejo on the lower Santiago rift to the NW, which, together with the Dorsal rift to the NE, mainly controls contemporary basaltic volcanism on the island (Ablay and Martí, 2000).

Several seismic stations were installed on the island of Tenerife in the last few years as the result of an increase in seismicity. The material FFM (Voight, 1988) was applied by Tárraga et al. (2006), after so-called seasonal decomposition of time series by the Loess technique (Cleveland et al., 1990) was applied to remove the effect of a strong anthropogenic 24 h cyclic component. An automatic algorithm then provided a linear fit to the decreasing trend component of the 1/SSEM time series (SSEM, spectral seismic energy measurement) and determined, at the zero crossing, the forecast times of local tectonic events. FFM is a very subjective method, and one of the major innovations of the work of Tárraga et al. (2006) is the full automatization of the process that allows one to evaluate forecasts in a statistical, Bayesian sense. Further details can be found in Tárraga et al. (2008) in this volume. The thoughtful choice of the specific values of the parameters that constrain the automatic fits allows further improvement in the results. In particular, studying the persistence (i.e. the memory) of the system could provide useful information with which to optimise the choice of the length of the time windows involved in the forecast. As already noted, volcanic events are correlated in time. The length of time this memory lasts is an important characterisation of the system, which can be quantified using the variogram. The memory of past activity expresses the persistence of its behaviour, a persistence which is a key step when considering time

series as a potential source of precursors. Rather than using raw seismic data, a series of methodologies — real time seismic energy measurement (RSEM), the already cited SSEM, main- and average frequency, dynamical embedding parameters such as delay time and embedding dimension (Carniel and Di Cecca, 1999) etc. — are applied by Carniel et al. (2006) to the data in order to carry out a so-called 'data reduction'. New time series are obtained, with an effective sampling rate of one every 60 min, which are then analysed to estimate their persistence. It is worth noting that the persistence results do not change significantly if the reduced data are computed on shorter time windows (even 1 min). The choice of 60 min is therefore a good compromise between computing time and variogram detail. The use of the 1/RSEM instead of the RSEM allows some reduction in the effect of bad data possibly contaminating the dataset.

Results of the variogram analysis of the RSEM (Carniel et al., 2006) highlight the strong contamination of the seismic data by anthropogenic noise, which shows up with clear 24 h oscillations. This effect can be strongly reduced by applying a Loess seasonal decomposition to the reduced time series (Cleveland et al., 1990). However, the general shape of the variogram for unfiltered data, once 24 h oscillations are not taken into account, resembles the persistence at time scales longer than one day. As an example, the memory of the seismic noise in March 2005 was evaluated using different approaches. Using the RSEM on the raw time series, strong daily anthropogenic oscillations appear in the variogram. A good indication that a time series is not contaminated by anthropogenic noise is the partial or total disappearance of these daily cycles. This can be clearly observed in the variogram of the RSEM trend remaining after the seasonal decomposition has been applied, but also on the variogram of the SSEM computed using only the frequency band 0.5–2.0 Hz, as shown in Figure 1.

The majority of the parameters analysed show a memory (20–100 h), which suggests a potential for precursors on a timeframe of up to 4 days. There is also a time variation of the duration of this persistence, which varies according to the month in which it is computed, a topic that will be further investigated, as it could be significant. Also, in relation to the occurrence of tectonic events inside and outside the island, the (time varying) persistence could provide hints on the time scale at which FFM forecasts could be performed.

In addition, the variograms computed for the different frequency bands of the spectrogram can help to distinguish anthropogenic from natural seismic noise. In the example of October 2004, we see, for instance, that the 2–2.4 Hz frequency band (Figure 2) is dominated by the volcanic signal, while in the 2.8–3.2 Hz band the 24 h cycle dominates but the memory effect is still visible, while in the 4.4–4.8 Hz band the anthropogenic noise completely hides the volcanic signal.

Furthermore, the parameters needed to determine the embedding (i.e. dimension and delay time) for a dynamical analysis (Carniel and Di Cecca, 1999) show changes with time, with a degree of persistence of the same order of the other parameters. Again, the daily cycles are usually superimposed on a longer memory trend if data are not filtered by the seasonal decomposition. Carniel et al. (2006) showed in particular the potential of the singular value decomposition (SVD), which decomposes a signal into principal components and which can be more or
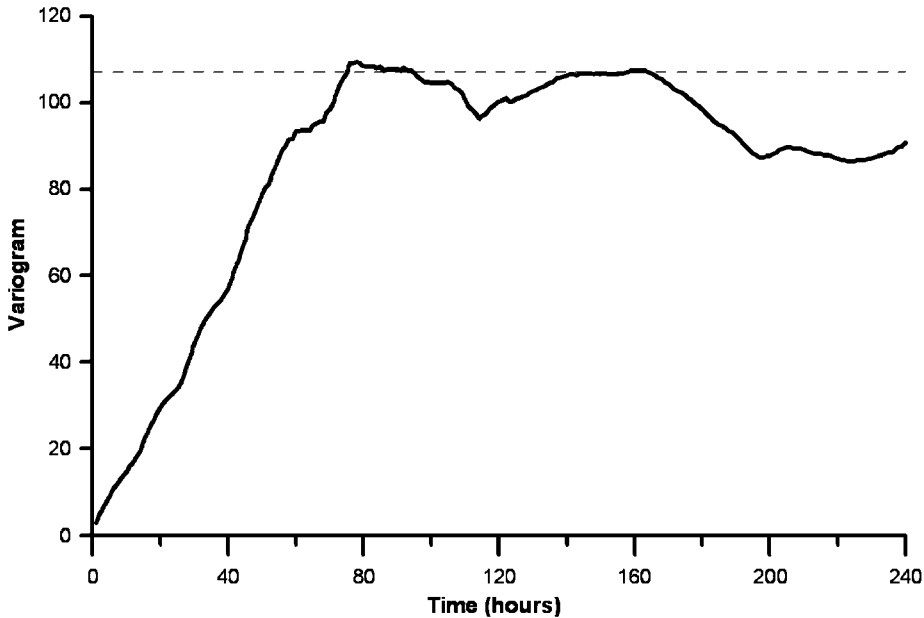
**Figure 1**  The memory of the seismic noise recorded in March 2005 close to Las Cañadas caldera, Tenerife (Spain), is analysed using the variogram tool. While the RSEM variogram computed on raw data shows strong daily oscillations due to anthropogenic contamination, in the variogram of the SSEM shown here, computed using only the 0.5—2.0 Hz frequency band, oscillations are strongly reduced, better highlighting the memory of the volcanic process (about 80 h).

less dominated by natural noise or by the anthropogenic contamination. For instance, the variogram of December 2004 computed on the first (most important) SVD (Figure 3) shows that this principal component is the result of the superposition of both natural and human noise. Carniel et al. (2006) also show a rare case where the third singular value is almost completely free from the 24 h cycle, meaning that the third principal component should be completely related to the volcanic process.

The stochastic approach in the time domain has allowed further evidence (i.e. the presence of a memory effect in the process generating the seismic noise, or — better — generating the volcanic tremor signal) to be provided of a state of unrest in the caldera of Las Cañadas in the island of Tenerife, which supplements the evidence obtained from the successful application of the FFM to forecast tectonic events (Tárraga et al., 2006). As far as the space domain is concerned, this approach could further improve the results of the susceptibility analysis currently carried out for both basaltic (Cornella et al., 2004) and phonolitic (Martí et al., 2006) eruptions on Tenerife. Susceptibility is the spatial probability density function for the opening of a future vent, derived from all relevant geological information (locations of previous vents, structural lineations, stress field information etc). The two approaches (spatial and time) can and should, of course, be integrated when a
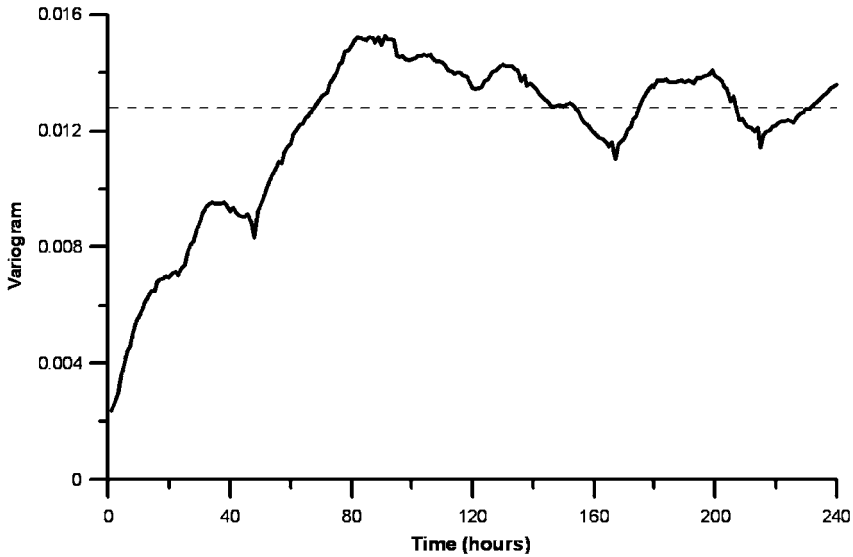
**Figure 2** Computing the variogram of different spectrogram frequency bands of the seismic noise is another way to distinguish anthropogenic from natural seismic noise close to Las Cañadas caldera. In October 2004, the 2—2.4 Hz frequency band shown here is dominated by the volcanic signal, highlighting again a memory of about 80 h.
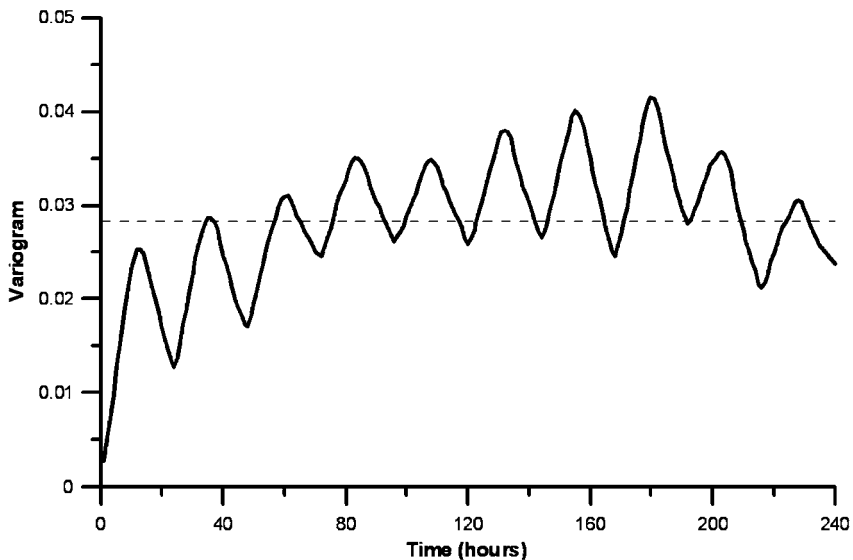


**Figure 3** The SVD of the seismic noise recorded close to Las Cañadas caldera also allows to distinguish between natural and anthropogenic noise. Here, the variogram of the most important SVD singular value of the seismic noise recorded in December 2004 shows daily cycles (due to anthropogenic noise) superimposed on a longer memory trend, indicating the presence of a natural source with longer memory (again, about 80 h).

crisis develops. At this stage, when short-term assessment is needed, the key role is played by the most recent monitoring data.

## 5. Conclusions and Perspectives

Geostatistics is a general framework of tools and methods that aids analysis of spatio–temporal volcanic data, and allows the construction of models with which to estimate the probability of occurrence of a given volcanic scenario and the variation of such probability with time and with space. The key concept is the memory, i.e. the persistence that a volcanic process possesses both in time and in space. In this paper, we have presented results from several studies that have demonstrated the wide applicability of this approach to a spectrum of time and space scales.

The (cross) correlation in space or in time is detected through (cross) variogram calculations applied to space–time data, where the alternative 'cross' prefix indicates the use of multiparametric data, in a natural extension of 1-D stochastic models. These correlations are then modelled to parameterise them in terms of behaviour type, scale and intensity. Precursors can be identified either by seeking out changes in variogram parameters (Jaquet et al., 2006a) or by stochastic decomposition (Jaquet and Carniel, 2001; Jaquet and Carniel, 2003). These methods were applied to the monitoring of active volcanoes using multiparametric geophysical datasets. Stochastic models were developed for hazard estimation: (a) in the short term by inspecting time series sampled at active volcanoes (Stromboli and Soufrière Hills) and (b) in the long term using space–time data from a volcanic region (Osteifel and Tohoku). Finally, we have shown how the stochastic approach can provide evidence of unrest at a caldera like Las Cañadas at Tenerife, e.g. in terms of the appearance of a memory effect in the seismic noise. The (possibly changing) time span of this memory can provide useful hints to other methods of forecasting such as the material FFM. In the other (i.e. space) domain, the approach can help by characterising the so-called susceptibility, i.e. if an eruption is impeding, by relative probabilities of *where* the vent could appear.

An important observation is that the geostatistical approach provides hazard estimates that can be accompanied by evaluations of associated uncertainty, as is required for probabilistic risk assessments. Moreover, the geostatistical analysis results can be utilised as one of the number of possible inputs, providing possibly contrasting pieces of evidence that can be integrated with tools such as the BBN, as applied by Aspinall et al. (2003) or Event Trees (Newhall and Hoblitt, 2001) as applied by Marzocchi et al. (2004).

The models proposed here are contributions to the challenging issue of deducing future volcanic activity, sufficiently general to be able to handle almost any type of data, be it geological, historical or geophysical. It is important to understand that adopting the stochastic approach does not mean we are assuming the process behind the generation of volcanic eruption has a stochastic character, i.e. it is a methodological choice. Even if the process could be completely described deterministically, because it is nonlinear and because initial conditions can only

be known with a certain (usually large) degree of uncertainty, one can demon-strate that predictions based on numerical models would not be able to reach reliable outcomes due to the likely chaotic nature of the system. This is a strong reason in favour of choosing stochastic models as one pathway to our objectives in volcanic hazard estimation.

## ACKNOWLEDGEMENTS

## REFERENCES

Ablay, G.J., Martí, J., 2000. Stratigraphy, structure, and volcanic evolution of the Pico Teide–Pico Viejo formation, Tenerife, Canary Islands. J. Volcanol. Geotherm. Res., 103, 175–208.

Alean, J., Carniel, R., Fulle, M., 2006. Stromboli online: information about Stromboli, Etna and other volcanoes. http://www.stromboli.net

Apted, M., Berryman, K., Chapman, N., Cloos, M., Connor, C.B., Kitayama, K., Sparks, S., Tsuchi, H., 2004. Locating a radioactive waste repository in the ring of fire. Eos Trans. Am. Geophys. Union, 85(45), 465–480.

Aspinall, W., Carniel, R., Jaquet, O., Woo, G., Hincks, T., 2006. Using hidden multi-state Markov models with multi-parameter volcanic data to provide empirical evidence for alert level decision-support. J. Volcanol. Geotherm. Res., 153(1–2), 112–124.

Aspinall, W.P., Woo, G., Voight, B., Baxter, P.J., 2003. Evidence-based volcanology: application to eruption crises. J. Volcanol. Geotherm. Res., 128(1–3), 273–285.

Ayalew, L., Yamagishi, H., 2005. The application of GIS-based logistic regression for landslide susceptibility mapping in the Kakuda-Yahiko mountains, central Japan. Geomorphology, 65, 15–31.

Carniel, R., Di Cecca, M., 1999. Dynamical tools for the analysis of long term evolution of volcanic tremor at Stromboli. Annali di Geofisica, 42(3), 483–495.

Carniel, R., Iacop, F., 1996. On the persistency of crater assignment criteria for Stromboli explosion-quakes. Annali di Geofisica, 39(2), 347–359.

Carniel, R., Tárraga, M., Jaquet, O., Garcia, A., 2006. On the memory of seismic noise recorded at Teide–Pico Viejo volcanic complex, Tenerife, Spain. Geophys. Res. Abstr., 8, 01929.

Chilès, J.P., Delfiner, P., 1999. Geostatistics: Modelling Spatial Uncertainty. Wiley Series in Probability and Mathematical Statistics, John Wiley & Sons Inc., Hoboken, New Jersey, 695 pp.

Cleveland, R.B., Cleveland, W.S., McRae, J.E., Terpenning, I., 1990. STL: a seasonal-trend decomposition procedure based on Loess. J. Official Stat., 6, 3–73.

Connor, C.B., Hill, B.E., 1995. Three nonhomogeneous Poisson models for the probability of basaltic volcanism: application to the Yucca mountain region, Nevada. J. Geophys. Res., 100(B6), 10,107–10,125.

Connor, C.B., Sparks, R.S.J., Mason, R.M., Bonadonna, C., Young, S.R., 2003. Exploring links between physical and probabilistic models of volcanic eruptions: the Soufrière Hills volcano, Montserrat. Geophys. Res. Lett., 30, 1701, doi:10.1029/2003GL017384.

Cornelius, R.R., Voight, B., 1995. Graphical and PC-software analysis of volcano eruption precursors according to the materials failure forecast method (FFM). J. Volcanol. Geotherm. Res., 64, 295–320.

Cornella, O., Martí, J., Hurlimann, M., Satacana, N., Felpeto, A., Galindo, I., Pérez, N., 2004. Susceptibility analysis of basaltic eruptions at Tenerife (Canary Islands). Geophys. Res. Abstr., 6, 04750.

Costa, A., Macedonio, G., Folch, A., 2006. A three-dimensional Eulerian model for transport and deposition of volcanic ashes. Earth Planet. Sci. Lett., 241(3–4), 634–647.

Cox, D.R., 1955. Some statistical methods connected with series of events. J. R. Stat. Soc. B (Methodological), XVII(2), 129–164.

Crowe, B.M., Johnson, M.E., Beckman, R.J., 1982. Calculation of the probability of volcanic disruption of a high-level nuclear waste repository within southern Nevada, USA. Radioactive Waste Manag. Nucl. Fuel Cycle, 3, 167–190.

Damiani, M.L., Groppelli, G., Norini, G., Bertino, E., Gigliuto, A., Nucita, A., 2006. A lava flow simulation model for the development of volcanic hazard maps for Mount Etna (Italy). Comput. Geosci., 32(4), 512–526.

Gomes, A., Gaspar, J.L., Goulart, C., Queiroz, G., 2005. Evaluation of landslide susceptibility of Sete Cidades volcano (S. Miguel Island, Azores). Nat. Hazards Earth Syst. Sci., 5, 251–257.

Green, D., Neuberg, J., 2006. Waveform classification of volcanic low-frequency earthquake swarms and its implication at Soufrière Hills volcano, Montserrat. J. Volcanol. Geotherm. Res., 153(1–2), 51–63.

Green, D.N., Neuberg, J., 2005. Seismic and infrasonic signals associated with an unusual collapse event at the Soufriere Hills volcano, Montserrat. Geophys. Res. Lett., 32(7), L07308, doi:10.1029/2004GL022265.

Harris, A.J., Carniel, R., Jones, J., 2005. Identification and modelling of variable convective regimes at Erta Ale lava lake. J. Volcanol. Geotherm. Res., 142(3–4), 207–223.

Hasegawa, A., Nakajima, J., 2004. Geophysical constraints on slab subduction and arc magmatism. Geophys. Monogr. 150, IUGG, 19, 81–93.

Ho, C.-H., 1991. Time trend analysis of basaltic volcanism at the Yucca mountain site. J. Volcanol. Geotherm. Res., 46, 61–72.

Ho, C.-H., Smith, E.I., 1998. A spatial-temporal/3-D model for volcanic hazard assessment: application to the Yucca mountain region. Math. Geol., 30(5), 497–510.

Jaquet, O., Carniel, R., 2001. Stochastic modelling at Stromboli: a volcano with remarkable memory. J. Volcanol. Geotherm. Res., 105, 249–262.

Jaquet, O., Carniel, R., 2003. Multivariate stochastic modelling: towards forecasts of paroxysmal phases at Stromboli. J. Volcanol. Geotherm. Res., 128, 261–271.

Jaquet, O., Carniel, R., 2006. Estimation of volcanic hazards using geostatistical models. In: Mader, H.M., Coles, S.G., Connor, C.B. and Connor, L.J. (Eds), Statistics in Volcanology. IAVCEI Publications IAV001, Geological Society of London, ISBN 978-1-86239-208-3, 296 pp.

Jaquet, O., Carniel, R., Sparks, R.S.J., Thompson, G., Namar, R., Di Cecca, M., 2006a. DEVIN: a forecasting approach using stochastic methods applied to the Soufrière Hills volcano. J. Volcanol. Geotherm. Res., 153(1–2), 97–111.

Jaquet O., Connor C.B., Connor L., 2006c. Probabilistic methodology for long term assessment of volcanic hazards. Proceedings of the International High-Level Radioactive Waste Management Conference, Las Vegas, NV, April 30–May 4, 2006.

Jaquet, O., Löw, S., Martinelli, B., Dietrich, V., Gilby, D., 2000. Estimation of volcanic hazards based on Cox stochastic processes. J. Phys. Chem. Earth A, 25(6–7), 571–579.

Jaquet, O., Sparks, R.S.J., Carniel, R., 2006b. Magma memory recorded by statistics of volcanic explosions at the Soufrière Hills volcano, Montserrat. In Mader, H.M., Coles, S.G., Connor, C.B. and Connor, L.J. (Eds), Statistics in Volcanology. IAVCEI Publications IAV001, Geological Society of London, ISBN 978-1-86239-208-3, 296 pp.

Jones, J., Carniel, R., Harris, A.J.L., Malone, S., 2006. Seismic characteristics of variable convection at Erta Ale lava lake, Ethiopia. J. Volcanol. Geotherm. Res., 153(1–2), 64–79.

Lantuéjoul, C., 2002. Geostatistical Simulation: Models and Algorithms. Springer, Berlin, 256 pp.

Martí, J., Gudmundsson, A., 2000. The Las Cañadas caldera (Tenerife, Canary Island): an overlapping collapse caldera generated by magma-chamber migration. J. Volcanol. Geotherm. Res., 103, 161–173.

Martí, J., Geyer, J., Felpeto, A., 2006. Susceptibility analysis of phonolitic eruptions at Teide volcano (Canary Islands). Geophys. Res. Abstr., 8, 04047.

Martí, J., Mitjavila, J., Araña, V., 1994. Stratigraphy, structure and geochronology of the Las Cañadas caldera (Tenerife, Canary Islands). Geol. Mag., 131, 715–727.

Martin, A.J., Umeda, K., Connor, C.B., Weller, J.N., Zhao, D., Takahashi, M., 2004. Modeling long-term volcanic hazard through Bayesian inference: an example from the Tohoku volcanic arc, Japan. J. Geophys. Res., 109, B10208, doi:10.1029/2004JB003201.

Marzocchi, W., Sandri, L., Gasparini, P., Newhall, C., Boschi, E., 2004. Quantifying probabilities of volcanic events: the example of volcanic hazard at Mount Vesuvius. J. Geophys. Res., 109, B11201, doi: 10.1029/2004JB003155.

Matheron, G., 1962. Traité de Géostatistique Appliquée. Tome 1. Editions Technip, Paris, 334 pp.

MVO (2007). The Montserrat volcano observatory. http://www.mvo.ms.

Newhall, C., Hoblitt, R., 2001. Constructing event trees for volcanic crises. Bull. Volcanol., 64(1), 3–20.

Pshenichny, C., Carniel, R., Akimova, V., 2005. Decreasing the uncertainty of BBN technique by means of complex formal approach to volcanological information treatment. Geophys. Res. Abstr., 7, 01016.

Reyment, R.A., 1969. Statistical analysis of some volcanologic data regarded as series of point events. Pure Appl. Geophys., 74, 57–77.

Ripepe, M., Gordeev, E., 1999. Gas bubble dynamics model for shallow volcanic tremor at Stromboli. J. Geophys. Res., 104(B5), 10,639–10,654.

Ripepe, M., Harris, A.J.L., Carniel, R., 2002. Thermal, seismic and infrasonic evidences of variable degassing rates at Stromboli volcano. J. Volcanol. Geotherm. Res., 118, 285–297.

Riuscetti, M., Carniel, R., Cecotti, C., 1997. Seismic vulnerability assessment of masonry buildings in a region of moderate seismicity. Annali di Geofisica, XL(5), 1405–1413.

Sandri, L., Marzocchi, W., Zaccarelli, L., 2004. A new perspective in identifying the precursory patterns of eruptions. Bull. Volcanol., 66, 263–275.

Sparks, R.S.J., 2003. Forecasting volcanic eruptions. Earth Planet. Sci. Lett., 210, 1–15.

Sparks, R.S.J., Young, S.R., 2002. The eruption of Soufrière Hills volcano, Montserrat: overview of scientific results. In: Druitt T.H. and Kokelaar, B.P. (Eds), The Eruption of Soufrière Hills Volcano, Montserrat, from 1995 to 1999. Geological Society, London, Memoirs, Vol. 21, pp. 45–69.

Tárraga, M., Carniel, R., Ortiz, R., García, A., 2008. The failure forecast method: review and application for the real-time detection of precursory patterns at reawakening volcanoes (this volume, Chapter 13).

Tárraga, M., Carniel, R., Ortiz, R., Marrero, J.M., García, A., 2006a. On the predictability of volcano-tectonic events by low frequency seismic noise analysis at Teide–Pico Viejo volcanic complex, Canary Islands. Nat. Hazards Earth Syst. Sci., 6, 365–376.

UNDRO 1979. Natural disasters and vulnerability analysis. Office of the United Nations Disaster Relief Co-ordinator (UNDRO), Report of Expert Group Meeting (9–12 July 1979), UNDRO, Geneva.

Voight, B., 1988. A method for prediction of volcanic eruptions. Nature, 332(10), 125–130.

Voight, B., Cornelius, R.R., 1991. Prospects for eruption prediction in near real-time. Nature, 350, 695–698.

Wackernagel, H., 2003. Multivariate Geostatistics, 3rd edn. Springer-Verlag, Berlin, 387 pp.

Wickman, F.E., 1966. Repose period patterns of volcanoes. V. General discussion and a tentative stochastic model. Arkiv Miner. Geol., 4, 351–367.

Woo, G., 1999. The Mathematics of Natural Catastrophes. Imperial College Press, London, 292 pp.

This page intentionally left blank

# Subject Index